

Dissertation  
zur Erlangung des akademischen Grades  
Doctor rerum naturalium  
(Dr. rer. nat.)

---

# Charge Carrier Trap Spectroscopy on Organic Hole Transport Materials

---

vorgelegt von

Paul Pahner

geboren am 16. Mai 1986 in Hoyerswerda

Institut für Angewandte Photophysik  
Fachrichtung Physik  
Fakultät Mathematik und Naturwissenschaften  
Technische Universität Dresden

April 2016

Eingereicht am 25.04.2016

Verteidigt am 16.09.2016

1. Gutachter: Prof. Dr. Karl Leo
2. Gutachter: Prof. Dr.-Ing. Björn Lüssem

## Abstract

Electronic circuits comprising organic semiconductor thin-films are part of promising technologies for a renewable power generation and an energy-efficient information technology. Whereas TV and mobile phone applications of organic light emitting diodes (OLEDs) got ready for the market awhile ago, organic photovoltaics still lack in power conversion efficiencies, especially in relation to their current fabrication costs. A major reason for the low efficiencies are losses due to the large number of charge carrier traps in organic semiconductors as compared to silicon. It is the aim of this thesis to identify and quantify charge carrier traps in vacuum-deposited organic semiconductor thin-films and comprehend the reasons for the trap formation. For that, the techniques impedance spectroscopy (IS), thermally stimulated currents (TSC), and photoelectron spectroscopy are utilized.

In order to assess the absolute energy of charge carrier traps, the charge carrier transport levels are computed for various hole transport materials such as MeO-TPD, pentacene, and ZnPc. Unlike inorganics, organic semiconductors possess in first-order approximation Gaussian distributed densities of states and temperature-dependent transport levels. The latter shift by up to 300 meV towards the energy gap-mid when changing from room temperature to 10 K as it is done for TSC examinations.

The frequency-dependent capacitance response of charge carrier traps in organic Schottky diodes of pentacene and ZnPc are studied via impedance spectroscopy. In undoped systems, deep traps with depths of approx. 0.6 eV and densities in the order of  $10^{16} \dots 10^{17} \text{ cm}^{-3}$  are prevailing. For pentacene, the deep trap density is reduced when the material undergoes an additional purification step. Utilizing p-doping, the Fermi level is tuned in a way that deep traps are saturated. Vice versa, the freeze-out of p-doped ZnPc provides further insight into the influence of trap-filling, impurity saturation and reserve on the Fermi level position in organic semiconductors. Furthermore, charge carrier traps are investigated via thermally stimulated currents. It is shown that the trap depths are obtained correctly only if the dispersive transport of the released charge carriers until their extraction is considered. For the first time, the polarity of charge carrier traps in MeO-TPD, ZnPc, and m-MTDATA is identified from TSC's differences in release time when spacer layers are introduced in the TSC samples. Simultaneously, tiny hole mobilities in the order of  $10^{-13} \text{ cm}^2 \text{ Vs}^{-1}$  are detected for low-temperature thin-films of the hole transporter material Spiro-TTB. It is shown for Spiro-TTB co-evaporated with the acceptor molecule F<sub>6</sub>-TCNNQ and a p-doped ZnPc:C<sub>60</sub> absorber blend that the doping process creates shallow trap levels. Finally, various organic hole transport materials are examined upon their stability in water and oxygen atmosphere during sample fabrication and storage of the organic electronics. In case of pentacene, ZnPc, MeO-TPD, and m-MTDATA, hole traps are already present in unexposed thin-films, which increase in trap density upon oxygen exposure. A global trap level caused by oxygen impurities is found at energies of 4.7...4.8 eV that is detrimental to hole transport in organic semiconductors.

## Kurzfassung

Elektronische Bauelemente aus Dünnschichten organischer Halbleiter sind Teil möglicher Schlüsseltechnologien zur regenerativen Energiegewinnung und energieeffizienten Informationstechnik. Während Fernseh- und Mobilfunkanwendungen organischer Leuchtdioden (OLEDs) bereits vor einiger Zeit Marktreife erlangt haben, ist die organische Photovoltaik (OPV) noch durch zu hohe Fertigungskosten in Relation zu unzureichenden Effizienzen unrentabel. Ein wesentlicher Grund für die niedrigen Wirkungsgrade sind Verluste durch die im Vergleich zu Silizium hohe Zahl an Ladungsträgerfallen in organischen Halbleitern. Ziel dieser Arbeit ist es, mittels Impedanz-Spektroskopie (IS), thermisch stimulierten Strömen (TSC) und Photoelektronenspektroskopie methodenübergreifend Ladungsträgerfallen in vakuumverdampften organischen Dünnschichten zu identifizieren, zu quantifizieren und ihre Ursachen zu ergründen.

Um die Energie von Ladungsträgerfallen absolut beziffern zu können, wird zunächst für verschiedene Lochtransportmaterialien wie z.B. MeO-TPD, Pentazen und ZnPc die Transportenergie aus den in erster Ordnung gaußförmigen Zustandsdichten berechnet. Im Gegensatz zu anorganischen Halbleitern ist die Transportenergie in organischen Halbleitern temperaturabhängig. Sie verschiebt sich beim Übergang von Raumtemperatur zu 10 K, wie für TSC Untersuchungen bedeutsam, um bis zu 300 meV in Richtung der Bandlückenmitte.

Mittels Impedanz-Spektroskopie wird die frequenzabhängige Kapazitätsantwort von Ladungsträgerfallen in organischen Schottky-Dioden aus Pentazen und ZnPc untersucht. In undotierten Systemen dominieren Defekte mit Tiefen um 0.6 eV, deren Dichte in der Größenordnung von  $10^{16} \dots 10^{17} \text{ cm}^{-3}$  liegt, sich aber im Fall von Pentazen durch einen zusätzlichen Materialaufreinigungsschritt halbieren lässt. Über p-Dotierung wird das Fermi-Level so eingestellt, dass tiefe Fallen abgesättigt werden können. Umgekehrt liefert das Ausfrieren von p-dotiertem ZnPc weitere Belege für den Einfluss von Fallenzuständen, Störstellen-Erschöpfung und Reserve auf das Fermi-Level in dotierten organischen Halbleitern.

Im Weiteren werden Ladungsträgerfallen über thermisch stimulierte Ströme untersucht. Es wird gezeigt, dass die Fallentiefen nur dann konsistent bestimmt werden, wenn der dispersive Transport von freigesetzten Ladungsträgern zur Extraktionsstelle berücksichtigt wird. Durch Einführung von 'Abstandshalterschichten' werden erstmalig über TSC die Polaritäten von Ladungsträgerfallen in MeO-TPD, ZnPc und m-MTDATA per Laufzeitunterschied bestimmt. Gleichzeitig werden geringste Löcherbeweglichkeiten in der Größenordnung von  $10^{-13} \text{ cm}^2 \text{ Vs}^{-1}$  für stark gekühlte Dünnschichten des Lochtransporters Spiro-TTB gemessen. Wie für Spiro-TTB koverdampft mit dem Akzeptormolekül F<sub>6</sub>-TCNNQ und p-dotierte Mischschichten der Absorbermaterialien ZnPc und C<sub>60</sub> gezeigt, erzeugt Dotierung relativ flache Störstellen. Abschließend werden verschiedene organische Lochtransporter-Materialien auf ihre Stabilität in Wasser- und Sauerstoffatmosphären während der Prozessierung und der Lagerung fertiger elektronischer Bauelemente untersucht. Für Pentazen, ZnPc, MeO-TPD und m-MTDATA werden Löcherfallen in intrinsischen Dünnschichten nachgewiesen. Bei Kontakt mit Sauerstoff nimmt deren Defektdichte zu. Es findet sich ein universales Fallenniveau bei rund 4.7...4.8 eV, verursacht durch Sauerstoffverunreinigungen, welches den Lochtransport in organischen Halbleitern limitiert.



## Articles

- A. Fischer, P. Pahner, B. Lüssem, K. Leo, R. Scholz, T. Koprucki, J. Fuhrmann, K. Gärtner, and A. Glitzky: *Self-heating effects in organic semiconductor crossbar structures with small active area*, Organic Electronics **13**, 2461 (2012). doi: 10.1016/j.orgel.2012.06.046
- P. Pahner, H. Kleemann, L. Burtone, M. L. Tietze, J. Fischer, K. Leo, and B. Lüssem: *Pentacene Schottky diodes studied by impedance spectroscopy: Doping properties and trap response*, Physical Review B **88**, 195205 (2013). doi: 10.1103/PhysRevB.88.195205
- A. Fischer, P. Pahner, B. Lüssem, K. Leo, R. Scholz, T. Koprucki, K. Gärtner, and A. Glitzky: *Self-Heating, Bistability, and Thermal Switching in Organic Semiconductors*, Physical Review Letters **110**, 126601 (2013). doi: 10.1103/PhysRevLett.110.126601
- B. Lüssem, M. L. Tietze, A. Fischer, P. Pahner, H. Kleemann, A. Günther, D. Kasemann, and K. Leo: *Beyond Conventional Organic Transistors - Novel Approaches with Improved Performance and Stability*, Proc. SPIE 9185 (2014). doi:10.1117/12.2061878
- L. E. Polander, P. Pahner, M. Schwarze, M. Saalfrank, C. Körner, and K. Leo: *Hole-transport material variation in fully vacuum deposited perovskite solar cells*, APL Materials **2**, 081503 (2014). doi: 10.1063/1.4889843
- M. L. Tietze, P. Pahner, K. Schmidt, K. Leo, and B. Lüssem: *Doped Organic Semiconductors: Trap-Filling, Impurity Saturation and Reserve Regimes*, Advanced Functional Materials **25**(18):2701 (2015). doi: 10.1002/adfm.201404549
- J. Fischer, D. Ray, H. Kleemann, P. Pahner, M. Schwarze, C. Körner, K. Vandewal, and K. Leo: *Density of states determination in organic donor-acceptor blend layers enabled by molecular doping*, J. Appl. Phys. **117**, 245501 (2015). doi: 10.1063/1.4922587
- P. Pahner, M. L. Tietze, M. Schwarze, K. Vandewal, B. Lüssem, F. Bussolotti, S. Kera, and K. Leo: *Density of States in Disordered Organic Semiconductors: Quantitative Analyses and Implications on Temperature-Dependent Transport Levels*, submitted (2016).
- P. Pahner, M. Schwarze, M. L. Tietze, S. Kunze, and K. Leo: *Global oxygen-induced trap levels in organic hole transport materials*, in preparation (2016).
- P. Pahner, M. L. Tietze, M. Schwarze, and K. Leo: *Trap states in p-doped hole transport layers identified by thermally stimulated currents*, in preparation (2016).
- M. L. Tietze, P. Pahner, J. Benduhn, M. Schwarze, K. Vandewal, and K. Leo: *Freeze-Out of Molecular Doping: Temperature control of the Fermi level and Doping Efficiency in a p-doped Organic Semiconductor*, in preparation (2016).
- M. Schwarze, B. D. Naab, M. L. Tietze, P. Pahner, F. Bussolotti, S. Kera, B. Lüssem, D. Kasemann, Z. Bao, and K. Leo: *Doping mechanism of the efficient air-stable n-doping small molecule o-MeO-DMBI-Cl*, in preparation (2016).

- N. Sergeeva, P. Pahner, C. Körner, K. Vandewal, and K. Leo: *The identification and characterization of trap states in DCV5T-Me:C60 based organic solar cells*, in preparation (2016).

## External Project

- P. Pahner and J. Blochwitz-Nimoth: *Literature study: New uses for doping*, Internal review paper for Novaled GmbH, (2015).

---

# Conferences

## Presenting author

- P. Pahner, H. Kleemann, L. Burtone, M. L. Tietze, K. Leo, and B. Lüssem: *Pentacene Schottky diodes studied by impedance spectroscopy - Doping properties and trap response*, International Conference on Organic Electronics, 20th June 2013, Grenoble, France (Talk).
- P. Pahner, J. Fischer, D. Kasemann, K. Leo, and B. Lüssem: *Trap Distributions in Pristine and Oxygen/Air Exposed Hole Transport Layers*, MRS Spring Meeting, 25th April 2014, San Francisco, USA (Talk).

## Contributions

- H. Kleemann, P. Pahner, A. A. Zakhidov, B. Lüssem, and K. Leo: *Organic pin-diodes for electronic applications*, Plastic Electronics, 20th October 2010, Dresden, Germany (Poster).
- H. Kleemann, C. Schünemann, P. Pahner, A. A. Zakhidov, B. Lüssem, and K. Leo: *Organic pin-Diodes with Adjustable Current-Voltage Applicable at Ultra-High Frequencies*, DPG Frühjahrstagung, 17th March 2011, Dresden, Germany (Talk).
- M. L. Tietze, P. Pahner, B. Lüssem, and K. Leo: *Molecular doping: Achieving high doping efficiencies in p- and n-type doped Pentacene and ZnPc*, MRS Spring Meeting, 2nd April 2013, San Francisco, USA (Poster).
- M. Schwarze, M. L. Tietze, P. Pahner, B. Naab, Z. Bao, B. Lüssem, D. Kasemann, and K. Leo: *Photoelectron spectroscopy studies on two air-stable molecular n-dopants*, DPG Frühjahrstagung, 3rd April 2014, Dresden, Germany (Talk).
- B. Lüssem, M. L. Tietze, A. Fischer, P. Pahner, H. Kleemann, A. Günther, D. Kasemann, and K. Leo: *Beyond conventional organic transistors: novel approaches with improved performance and stability*, SPIE Optics + Photonics, 18th August 2014, San Diego, USA (Talk).
- M. L. Tietze, P. Pahner, B. Lüssem, and K. Leo: *Doped Organic Semiconductors: Trap-Filling, Impurity Saturation, and Reserve Regimes*, MRS Fall Meeting, 3rd December 2014, Boston, USA (Talk).
- M. Schwarze, M. L. Tietze, P. Pahner, B. Naab, Z. Bao, B. Lüssem, D. Kasemann, and K. Leo: *Photoelectron spectroscopy studies on efficient air-stable molecular n-dopants*, DPG Frühjahrstagung, 2015, Berlin, Germany (Talk).
- N. Sergeeva, J. Fischer, P. Pahner, L. Burtone, C. Körner, K. Vandewal, and K. Leo: *DCV5T-Me:C60 Solar Cells on Presence of Traps*, DPG Frühjahrstagung, 2015, Berlin, Germany (Talk).
- N. Sergeeva, P. Pahner, C. Körner, K. Vandewal, and K. Leo: *The identification and characterization of trap states in DCV5T-Me:C60 based organic solar cells*, SPIE Organic Photonics + Electronics, 2016, San Diego, USA (Talk).



---

# Contents

<b>1. Introduction</b>	<b>1</b>
<b>2. The Fundamentals of Molecular Semiconductors</b>	<b>5</b>
2.1. From Organic Molecules to Organic Thin Films . . . . .	5
2.1.1. Molecular Orbitals - an Introduction to LCAO Theory . . . . .	5
2.1.2. Hybridization and Delocalized $\pi$ -Systems . . . . .	7
2.1.3. Formation of Organic Solids . . . . .	9
2.1.4. Excited Molecules - Absorption, Emission, and Excitons . . . . .	11
2.1.5. Orientation and Morphology . . . . .	13
2.1.6. Interface Formation in Organic Semiconductors . . . . .	14
2.2. Charge Carrier Transport . . . . .	16
2.2.1. Towards Band-Like Transport in Highly Ordered Crystals . . . . .	16
2.2.2. Hopping Transport Concepts in Disordered Systems . . . . .	17
2.2.3. Theories on the Transport Level . . . . .	23
<b>3. Molecular Doping</b>	<b>29</b>
3.1. Terms and Definitions of Molecular Doping . . . . .	29
3.2. Prevailing Theories on Charge Transfer in Host:Dopant Systems . . . . .	32
3.2.1. Integer Charge Transfer Model . . . . .	32
3.2.2. Intermolecular Hybridization . . . . .	33
3.2.3. Classical Semiconductor Approach with Effective $E_A$ . . . . .	34
3.3. Literature Overview on Results in the Field of Doped Molecular Semiconductors . . . . .	36
3.4. Application of Molecular Doping to Optoelectronics . . . . .	40
3.4.1. The p-i-n Concept in Organic Solar Cells . . . . .	40
<b>4. Spectroscopy of Charge Carrier Traps in Molecular Semiconductors</b>	<b>41</b>
4.1. Trap States . . . . .	41
4.2. Impedance Spectroscopy . . . . .	43
4.2.1. Basic Math of Impedance Spectroscopy . . . . .	44
4.2.2. Data Inspection . . . . .	45
4.2.3. The Depletion Capacitance of Schottky Contacts . . . . .	48
4.2.4. Trap Distribution from Frequency Dependent Capacitance . . . . .	52
4.2.5. Experimental Details . . . . .	55
4.3. Thermally Stimulated Currents . . . . .	56
4.3.1. Introduction . . . . .	56
4.3.2. Evaluation of TSC Spectra . . . . .	58
4.3.3. Experimental Details . . . . .	63
4.4. Additional Measurement Techniques . . . . .	65
4.4.1. Photoelectron Spectroscopy . . . . .	65
4.4.2. Conductivity . . . . .	69
4.5. Investigated Materials . . . . .	69
4.5.1. Hole Transport Materials . . . . .	70

4.5.2. Molecular Dopants . . . . .	71
4.5.3. Solar Cell Materials . . . . .	73
4.6. Sample Preparation . . . . .	74
<b>5. Estimation of the Transport Level in Organic Hole Transporting Layers</b>	<b>77</b>
5.1. UPS Spectra . . . . .	77
5.1.1. Analytical Description of the HOMO DOS . . . . .	78
5.1.2. Amorphous-Type HTL Materials . . . . .	80
5.1.3. (Poly-)Crystalline HTL Materials . . . . .	82
5.1.4. Estimation of Charge Carrier Densities from HIBs . . . . .	84
5.1.5. Influence of Charge Screening on the IP . . . . .	85
5.1.6. Conclusions on DOS Widths determined by UPS . . . . .	86
5.2. Temperature Dependent Transport Levels . . . . .	90
5.2.1. Models and Influence of DOS Parameters . . . . .	90
5.2.2. DOS Parametrizations of the HTL Materials . . . . .	95
5.2.3. Temperature Dependent Transport Level for HTL Materials . . . . .	97
5.3. Summary . . . . .	98
<b>6. Trap Response and Dopant Regimes in Organic Schottky Diodes</b>	<b>99</b>
6.1. Depletion Zones and Mott-Schottky Analysis: Doping Efficiency . . . . .	99
6.2. Frequency Dependent Trap Capacitance . . . . .	104
6.2.1. Deep Traps in P5 and ZnPc . . . . .	107
6.2.2. Shallow Traps in p-doped P5 and ZnPc . . . . .	109
6.3. Freeze-Out of p-Doping in ZnPc . . . . .	110
6.4. Summary . . . . .	115
<b>7. Thermally Stimulated Currents in Organic Semiconductors</b>	<b>117</b>
7.1. Assessments of TSC: Spectra Fitting, Hoogenstraaten-, $T^4$ -, and Chen's-Method . . . . .	117
7.2. Dispersive Transport of Thermally Stimulated Currents . . . . .	120
7.3. Summary . . . . .	126
<b>8. Doping Induced Gap States in Organic Neat and Blend Layers</b>	<b>127</b>
8.1. Motivation . . . . .	127
8.2. Doping Induced Gap States in Spiro-TTB . . . . .	128
8.3. Dependence on Layer Thickness and Doping Concentration . . . . .	132
8.4. Doping Induced Gap States in ZnPc:C <sub>60</sub> Blends . . . . .	137
8.5. Summary: Indications for an Acceptor Level? . . . . .	140
<b>9. Oxygen and Water Related Defects in Organic Hole Transporting Layers</b>	<b>145</b>
9.1. Motivation . . . . .	145
9.2. Aged Pentacene Schottky Diode . . . . .	146
9.3. Trap Signatures in Fresh and Aged HTLs . . . . .	150
9.4. Influence of Oxygen and Humid Air During the Sample Preparation . . . . .	153
9.5. Trap Polarity, O <sub>2</sub> Storage, and Low-T Mobility . . . . .	155
9.6. Summary: Global Oxygen Trap . . . . .	159
<b>10. Conclusion and Outlook</b>	<b>163</b>

<b>A. Appendix</b>	<b>169</b>
A.1. Trap Capacitance Fitting - Burtone Model . . . . .	169
A.2. Python Calculation of the Transport Level . . . . .	175
A.3. Python TSC Experiment Procedure . . . . .	180
A.4. Conductivities . . . . .	186
A.5. List of Important Abbreviations . . . . .	187
A.6. List of Important Symbols . . . . .	188
A.7. List of used Materials . . . . .	189





---

# Introduction

It is 2016 and the world is facing immense challenges for the next decades. Newspapers, TV shows, and social media could be easily depressing any follower. World news' most featured topics are war, violence, forced migration, pollution, corruption, poverty, and diseases. The world is tremendously imbalanced as half of its wealth is in hands of one percent of the population.<sup>[1]</sup> While the first-world giants Facebook, Google, Microsoft, and Apple promote next-gen technologies such as virtual reality, true reality suffers from still 16,000 deaths of 'third world' children-under-five-years each day.<sup>[2]</sup> For those escaping the bottom part of the GDP<sup>1</sup> ranking, i.e. emerging nations, strongly growing population and technization cause multiple problems. More and more people demand food, clean water, energy, and income, most of the time clumped at concentrated places to live in. Super-large urban sprawls such as Mexico City, Karachi, Cairo, or the Chinese mega-cities Beijing and Shanghai suffer already heavily from environmental pollution.<sup>[3]</sup> Speaking of China, the red dragon has overcome the state of an emerging nation.<sup>[4]</sup> Despite world-wide stagnation, the Chinese economy has been growing for the last years by rates as high as seven to ten percent, eventually surpassing the economical power of the biggest industry nations.<sup>[5]</sup> Improving standards of living are observed, e.g. a wider motorization of its residents. Beijing, for instance, approached a total number of six million registered vehicles during the last years,<sup>[6]</sup> causing immense rates of particulate matter and a swiftly growing demand for mobile energy sources.<sup>[6,7]</sup>

Rapid economic development, industrial expansion, and technization during the last few decades have more than doubled the global energy consumption from 71,000 TWh in 1973 to approx. 158,000 TWh in 2013.<sup>[8]</sup> World-wide, the vast majority of the energy (approx. 80%) is gained from fossil fuels such as oil, coal, and natural gas.<sup>[8]</sup> Recent discoveries of new oil and gas fields in Canada, Brazil, Norway, or Russia, the controversial launch of hydraulic fracturing (fracking) led by the US, and the future prospect of accessing Arctic's resources<sup>[9,10]</sup> have postponed the oil depletion and rendered the peak oil assumption premature.<sup>[11]</sup> For the year 2014, the proven world oil reserves were 1,493 billion barrels, at an annual crude oil production of 26.8 million barrels.<sup>[12]</sup> Hereby, over fifty percent of the resources are located in the middle east, which has become a scenery for permanent political crisis since the mid of the 20<sup>th</sup> century.<sup>[13]</sup> In order to satisfy their economies' and populations' thirst for cheap energy, sadly the future will bear further conflicts of nations and interest groups battling for financial and geopolitical advantages.

Already today, the usage of fossil fuels is judged highly detrimental, since the burning for energy generation produces large amounts of the greenhouse gas carbon dioxide. For 2015, global CO<sub>2</sub> emissions of 35.7 gigatons per year were predicted,<sup>[14]</sup> which have induced an average monthly atmospheric CO<sub>2</sub> concentration over 400 ppm for the first time in at least 800,000 years.<sup>[14]</sup> Simultaneously, fourteen of the fifteen hottest years on human weather record have occurred since 2000. A global warming of 1 °C as compared to the pre-industrial age (1850-1900) has been reached most recently in 2015.<sup>[15]</sup> Although the world's climate has been alternating between cold and warm periods throughout past geological eras, typical cycle lengths were ten thousands of years, which is why today's time frame is alarming. Probably the most striking example that

---

<sup>1</sup>Gross Domestic Product

consequences of global warming are already present, is the reduction of glacier ice around the world.<sup>[16–22]</sup> Polar regions such as Greenland,<sup>[16]</sup> Iceland,<sup>[17]</sup> or Antarctica,<sup>[18]</sup> the Himalaya,<sup>[19]</sup> Patagonia<sup>[20]</sup> but likewise alpine glaciers<sup>[21,22]</sup> suffer from heavy loss of their ice volume, i.e. glacier length and thickness. In the long run, not only the sea level rises, threatening the livings of several hundred million people, but significant fresh water reservoirs are lost.<sup>[23]</sup> Further predicted consequences for an ongoing exaggerated warming are manifold. Extreme weather situations including higher intensities and frequencies of heat waves, droughts and tempests<sup>[24]</sup> are accompanied by a deoxygenation of the oceans<sup>[25]</sup>, and the extinction of many species due to increased temperatures and atmosphere CO<sub>2</sub> concentrations.

In order to limit the impact global warming, the United Nations agreed in late 2015 on limiting the temperature increase to less than 2 °C as compared to the pre-industrial age,<sup>[26]</sup> which requires a drastic decrease of greenhouse gas emissions. This consensus is, however, in strong contraction to the energy demands of a steadily growing earth population. Nuclear energy bears the potential to fill this gap, whereas the nuclear meltdowns of Three Miles Island in 1979,<sup>[27]</sup> Chernobyl in 1986,<sup>[28]</sup> and Fukushima in 2011<sup>[29]</sup> exposed its tremendous risks. Consequently, several countries decided to phase-out from nuclear energy. In 2012, the German government agreed on the so-called 'Energiewende',<sup>[30]</sup> i.e. a drastic increase of renewable energies and energy efficiency to eventually abolish the use of fossil fuels and nuclear energy in the long run. Massive invests in research, development, and setup of renewable energies from wind, biomass, water, geothermal, and solar power is required as the remaining German nuclear power plants will close already in 2022.<sup>[31]</sup> Ever since the decisions of Paris' climate congress in late 2015, it is highly worth to focus upon (re)new(able) energy concepts: first, to establish know-how and future technological leadership in prospective markets. Second, to grow autarky towards resources from crisis zones. And most importantly third, to relinquish a world worth to live in for upcoming generations.

One of the promising technologies in the renewable energy cocktail are organic photovoltaics (OPV). Future large-scale applications such as printable<sup>[32]</sup> and flexible organic solar cells<sup>[33]</sup> (OSCs) bear the potential to exploit nearly every existing surface directed towards the sun to generate electric energy in a cheap and low-carbon<sup>2</sup> fashion. Such surfaces are for instance rooftops, house fronts, vehicle bodies, or just your casual bag containing your mobile phone or laptop.

Since the first reasonably efficient OSC published by Tang in 1986,<sup>[34]</sup> the solar power conversion efficiency (PCE) has been drastically improved from about 1 % up to 13.2 %, most recently published by Heliatek in February 2016.<sup>[35]</sup> Whereas the sibling technology of organic light emitting diodes (OLEDs) has successfully entered the market and is commercially available in smart phones or next-generation TVs, OPV still struggles. Although OSCs have reached the efficiency of amorphous silicon cells,<sup>[36]</sup> much scientific effort is necessary to improve the ratio of generated power to production costs. The latter could be lowered by printing,<sup>[32]</sup> stamping,<sup>[37]</sup> or spin-casting techniques<sup>[38]</sup> of polymeric organic semiconductors, which render costly vacuum conditions redundant. At the same time, the control of the thin-film purity and morphology is inevitable to obtain performant and long-term stable devices.

A major reason for the limited PCE are charge carrier traps in the organic semiconductor thin-films,<sup>[39–44]</sup> where they reduce the mobility and the lifetime of electrons and holes generated upon light absorption. Such traps can be caused by impurities, which intermingle the organic semiconductor material at all stages, i.e. during synthesis, storage, fabrication, and operation in the finished OSC. Moreover, traps originate from the intrinsic energetic disorder of an organic semiconductor,<sup>[45]</sup> which is further increased by molecular intermixing in donator:acceptor blends of an OSC<sup>[46]</sup> or by Coulomb interaction with charged molecules in an electrically doped thin-film.<sup>[47,48]</sup>

---

<sup>2</sup>For the sake of integrity, the carbon emission from fabricating OPV devices must be considered though.

---

The scope of the present thesis is to identify charge carrier traps in organic semiconductors, spectroscopically quantify their density and energetic depth as well as provide insight into their origin. After a brief introduction to the basics of organic semiconductors, charge carrier transport in disordered materials is intensively discussed in Chapter 2. In particular, several ways to determine the temperature-dependent transport level are reviewed in Sec. 2.2.3. Chapter 3 aims to give a summary on molecular doping, which is utilized to inspect and suspected to cause traps at the same time. Prevailing theories on its working principle and literature results for doped molecular semiconductors are presented. Chapter 4 contains the experimental details on the charge carrier trap spectroscopy conducted in this thesis. After a definition of the term 'charge carrier trap' and a literature review on their possible origins in Sec. 4.1, the techniques Impedance Spectroscopy (IS) and Thermally Stimulated Currents (TSC) are discussed in Sec. 4.2 and Sec. 4.3, respectively. Further, the fundamentals of ultraviolet photoelectron spectroscopy (UPS), utilized to obtain information on the energetic disorder in the thin-films, are given in Sec. 4.4. Key properties of the investigated organic semiconductor materials are described in Sec. 4.5. Hereby, the samples are fabricated under ultra-high vacuum (UHV) conditions to maintain best possible purity and reproducibility as summarized in Sec. 4.6. The scientific results of the thesis are discussed in Chapter 5 to 9. In Chapter 5, various organic hole transport materials are examined by UPS, accessing their Fermi level positions, the ionization potentials, and the energetic disorder parameters. The data are used to compute the temperature-dependent position of the hole transport level in each material. Chapter 6 mainly discusses the trap information extraction from the capacitance function of organic semiconductor Schottky diodes. Here, the hole transport materials pentacene (P5) and zinc-phthalocyanine (ZnPc) are intentionally p-doped to 'make trap states visible' via IS. The other way around, dopant freeze-out and its consequences are examined via UPS and IS measurements for cooled p-ZnPc thin-films in Sec. 6.3.

The Chapters 7 to 9 deal with results from thermally stimulated current experiments. Chapter 7 starts with a review on reported methods to evaluate TSC spectra from trap site distributions, typically seen in organic semiconductors. Consistency with field-dependent TSC measurements is achieved when the thermal release of charge carriers is combined with their dispersive transport towards the extraction points, as done in Sec. 7.2. In Chapter 8, this model is applied to TSC spectra from intentionally p-doped 2,2',7,7'-tetrakis-(N,N-di-methylphenylamino)-9,9'-spirobifluorene (Spiro-TTB) and p-doped ZnPc:C<sub>60</sub> solar cells. TSC spectra for different layer thicknesses and doping concentrations are examined, clearly indicating a gap-state formation caused by molecular doping. Chapter 9 contains degradation experiments for various hole transport materials. The influences of water and oxygen impurities during sample fabrication and storage on the inherent trap distributions are investigated. In particular, a global oxygen-caused trap distribution is found in various organic semiconductors such as N,N,N',N'-tetrakis(4-methoxyphenyl)benzidine (MeO-TPD), 4,4',4''-tris(3-methylphenylphenylamino)-triphenylamine (m-MTDATA), P5, and ZnPc. Introducing a spacer layer concept to TSC samples, the polarity of the global oxygen trap is identified experimentally. Furthermore, tiny low-temperature charge carrier mobilities are measured by this technique, which have been commonly inaccessible prior to this.

Finally, the findings of the thesis are summarized in Chapter 10 and suggestions for further investigations are delineated.



# The Fundamentals of Molecular Semiconductors

*This first chapter covers the state of knowledge in the field of organic semiconductors, particularly important for this thesis. Starting with a brief introduction of the LCAO theory and its application to explain hybridization and electron delocalization, the formation of organic solids is described. Subsequently, relaxation processes, interaction with light, and morphological growth for organic thin-films as well as energy level alignments at metal/organic and organic/organic interfaces are presented in a nutshell. Main charge carrier transport theories are discussed step-by-step, with special emphasis on the definition of the transport level.*

## 2.1. From Organic Molecules to Organic Thin Films

Organic substances comprise all types of hydrocarbon-based compounds and exhibit the widest diversity in the field of chemistry. Carbon possesses the possibility to form covalent bonds with different atom species and other carbon atoms at the same time, sharing electron pairs. Employing just the very basic elements carbon and hydrogen already leads to very different realizations of covalently bond compounds, e.g. the 1d gaseous ethylene, the highly conductive 2d graphene, or the 'hard as rock' 3d diamond. Adding few further atom species like nitrogen, oxygen, fluorine, sulfur, or several metals allows for complex compounds such as amino acids, proteins, alcohols, esters, or organometallic complexes, which are essentials for life.

Organic compounds show only a limited symmetry in contrast to mostly highly symmetric inorganic compounds. Often times, they consist of dozens up to hundreds of atoms. Determining for the semi-conducting properties is the existence of a delocalized  $\pi$ - electron system whose formation is explained in the following.

### 2.1.1. Molecular Orbitals - an Introduction to LCAO Theory

Already a single molecule has to be treated as a many body problem, consisting of  $K$  nuclei and  $N$  electrons. The static *Schrödinger equation*  $\hat{H}\Psi = E\Psi$  yields the Eigenenergies  $\{E_n\}$  of the system with the eigenfunctions  $\{\Psi_n\}$ .<sup>[49]</sup> The Hamiltonian  $\hat{H} = \sum_i^{K,N} T_i + V_i$  includes all kinetic  $T_i$  and potential  $V_i$  energies of the interacting particles (positively charged nuclei and negatively charged electrons), but renders the Schrödinger equation not entirely analytically solvable. Hence, the ionized  $H_2^+$  hydrogen molecule ( $K=2$ ,  $N=1$ ) shall be regarded in the following. Still, the introduced thoughts remain applicable to more complex molecule systems.

With respect to the much larger nucleus mass as compared to the electron mass, one can separate the eigenfunctions  $\{\Psi_n(\vec{r}, \vec{R}_1, \vec{R}_2)\}$  into their vibronic  $\{\Psi_{n,v}(\vec{R}_1, \vec{R}_2)\}$  and electronic  $\{\Psi_{n,e}(\vec{r})\}$  part (*Born-Oppenheimer approximation*).<sup>[50]</sup> Assuming fixed nuclei with an inter-atomic distance  $R = |\vec{R}_1 - \vec{R}_2|$ ,

$r_A = |\vec{r} - \vec{R}_1|$  and  $r_B = |\vec{r} - \vec{R}_2|$  simplifies the Hamiltonian of the electronic system to

$$\hat{H}_e = -\frac{\hbar^2}{2m_e} \Delta(\vec{r}) - \frac{e^2}{4\pi\epsilon_0} \left( \frac{1}{r_A} + \frac{1}{r_B} - \frac{1}{R} \right). \quad (2.1)$$

While the Coulomb attraction between the protons and the electron lowers the system energy, the electrostatic repulsion of the nuclei defines stability and equilibrium distance of the molecule. The related Schrödinger equation  $\hat{H}_e \Psi_e(\vec{r}) = E_e \Psi_e(\vec{r})$  is exactly solvable. However, a more general approach should be discussed here as it can be easily transferred to more complex systems: the linear combination of atomic orbitals (LCAO). The LCAO method approximates molecular wave functions by superposition of individual atomic wave functions, e.g. staying with the  $H_2^+$  example, a molecular orbital  $\Psi(\vec{r})$  is composed of

$$\Psi(\vec{r}) = c_1 \chi_A + c_2 \chi_B, \quad (2.2)$$

where  $c_{1,2}$  are expansion coefficients and  $\chi_{A,B}$  are atomic wave functions, e.g. 1s orbitals of the single hydrogen atoms. Symmetry and normalization of the solutions for the Schrödinger equation demand  $c_1 = \pm c_2$  and  $(|c_1|^2 = |c_2|^2)$  which results in a symmetric  $\Psi_+$  and an anti-symmetric  $\Psi_-$  wave function

$$\Psi_{\pm} = \frac{1}{\sqrt{2 \pm 2S}} (\chi_A \pm \chi_B) \quad (2.3)$$

with the corresponding eigenvalues

$$E_{\pm}(R) = \frac{H_{AA} \pm H_{AB}}{1 \pm S}. \quad (2.4)$$

Herein,  $H_{ij}$  name the Hamiltonian integrals and  $0 \leq S \leq 1$  is the overlap integral with

$$H_{i,j} = \int \chi_i^* \hat{H} \chi_j d\vec{r} \quad \text{and} \quad S_{i,j} = \int \chi_i^* \chi_j d\vec{r}. \quad (2.5)$$

The energy eigenvalue of the electron in the atomic orbital of one nucleus equals  $H_{ii}$  while  $H_{ij}$  represents the resonance term of the system. Furthermore, it can be shown that  $S \equiv S_{AB} = S_{BA}$  and, due to identical nuclei in the  $H_2^+$  molecule,  $H_{AA} = H_{BB}$ .

Regarding the obtained wave functions  $\Psi_{\pm}$  and their energies  $E_{\pm}$ , there are differences as depicted in Fig. 2.1. The symmetric eigenfunction  $\Psi_+$  exhibits a probability density  $|\Psi_+|^2 > 0$  between the nuclei, forming a bond between the hydrogen atoms with an energetic minimum at  $R = R_0$ . For the anti-symmetric solution  $\Psi_-$ , the probability of the electron  $|\Psi_-|^2$  to be present in between the nuclei vanishes at  $R/2$  while the electron is kept close to either one of the hydrogen cores. Hence,  $E_-(R)$  decreases monotonously with no distinct energetic minimum (anti-bonding) but all the way on an elevated energy level, in contrast to  $E_+(R)$ . This split up and the occupation of the bonding orbital enables a lowering of the systems energy as compared to the single hydrogen atom  $\tilde{E}$ . The orbitals  $\Psi_i$  of more complex molecules can be formed analogously with the LCAO method as

$$\Psi_i = \sum_j c_{ij} \chi_j. \quad (2.6)$$

Depending on the orientation of the combined molecular orbital one distinguishes  $\sigma/\sigma^*$ -orbitals parallel arranged to the bonding axis from perpendicular oriented  $\pi/\pi^*$ - orbitals. The energetic split up between the bonding and the anti-bonding (\*) orbital is stronger for  $\sigma$ -type orbitals due to the increased overlap of the atomic wave functions  $S$  (cf. Fig. 2.1) as compared to  $\pi$ -type orbitals. In contrast,  $\pi$ - and  $\pi^*$ -bonds split close to the initial state. Hence, they determine the energy gap between the highest occupied molecular orbital

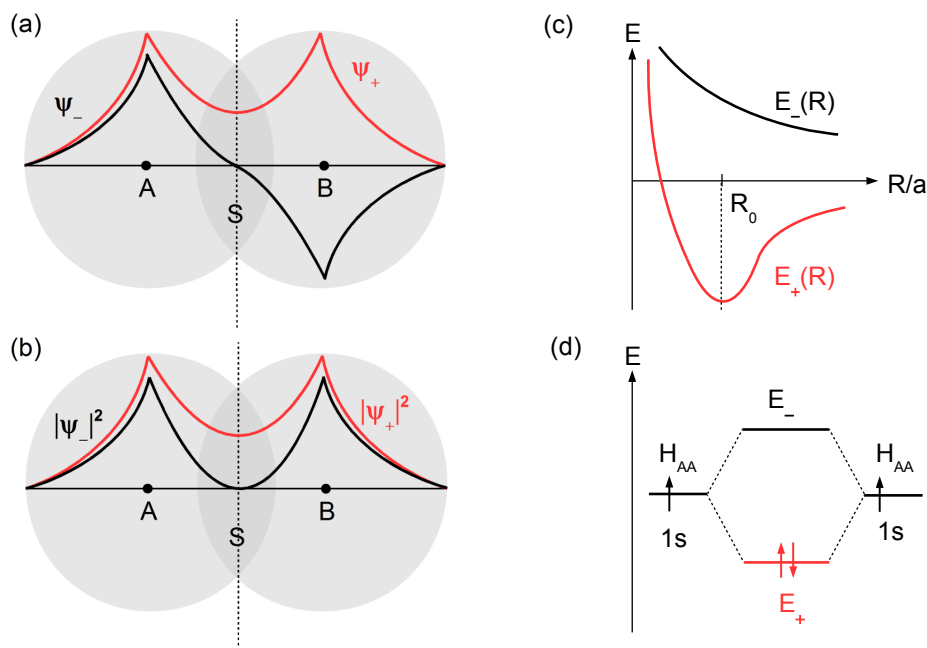


**Figure 2.1.:** (a) Cross-section along the bonding axis of the nuclei (A and B) in the  $H_2^+$  molecule. Symmetric wave function  $\Psi_+$  and anti-symmetric wave function  $\Psi_-$  represent the LCAO solutions of the spherical 1s orbitals (illustrated in gray shades, with overlap  $S$ ). (b) The mean values  $|\Psi_{\pm}|^2$  depict the electron probability densities around A and B. (c) Formation of bonding  $E_+$  and anti-bonding  $E_-$  eigenstates as function of nuclei distance  $R$  and corresponding energy splitting as compared to the atomic level  $H_{AA}$  of the 1s orbital (d).

(HOMO) and the lowest unoccupied molecular orbital (LUMO) of the molecule. Not only linear combinations of solely atomic  $s$ -,  $p$ -, or in more rare cases  $d$ - orbitals are possible but also an LCAO of mixed orbitals resulting from so-called *hybridization*. This hybrid formation is responsible for the existence of delocalized electrons and semi-conducting properties in organic solids which are briefly discussed in the following section.

### 2.1.2. Hybridization and Delocalized $\pi$ -Systems

Carbon in its ground state features the electron configuration  $1s^2 2s^2 2p_x 2p_y$  with two unpaired electrons distributed among the degenerated  $p_x, p_y, p_z$ -orbitals. In the presence of an external potential, e.g. a hydrogen atom, it is often energetically favorable to promote a  $2s$  electron into a  $2p$  state. The combination of  $s$ - and  $p$ -orbital is a *hybrid* orbital, which offers an increased bonding strength and lowers the system energy. The resulting possibilities are illustrated in Fig. 2.2. In case of  $sp$ -hybridization, one  $s$ - is mixed with one  $p$ -orbital (without loss of generality) by:

$$\chi_{sp(1,2)} = \frac{1}{\sqrt{2}} (\chi_{2s} \pm \chi_{2pz}). \quad (2.7)$$

The two hybrid orbitals  $\chi_{sp(1,2)}$  face diametrically. Together with the still singly occupied  $p_x$ - and  $p_y$ - orbitals, they allow for the built-up of four bonds for carbon. For instance, pairing up with hydrogen and another  $sp$ -hybridized carbon atom results in acetylene ( $C_2H_2$ ,  $H-C \equiv C-H$ ). At that, two  $sp$ -orbitals, one of each carbon atom, provide a  $\sigma/\sigma^*$ - solution while additional  $\pi$ -bonds are formed by the overlapping perpendicular  $p_x$  and  $p_y$  orbitals. The remaining  $sp$  orbitals are combined with the 1s orbitals of the hydrogen. The concept of hybridization can be extended to linear combinations of  $\chi_{2s}$  with  $\chi_{2px}$  and  $\chi_{2py}$  ( $sp^2$ -hybridization) or  $\chi_{2s}$  with  $\chi_{2px}$ ,  $\chi_{2py}$ , and  $\chi_{2pz}$  ( $sp^3$ -hybridization). In case of  $sp^2$  hybridized carbon, three  $sp^2$  orbitals are formed within a plane and  $120^\circ$  of angular distance, e.g. for ethylene ( $C_2H_4$ ) two of them build  $\sigma$ -bonds with

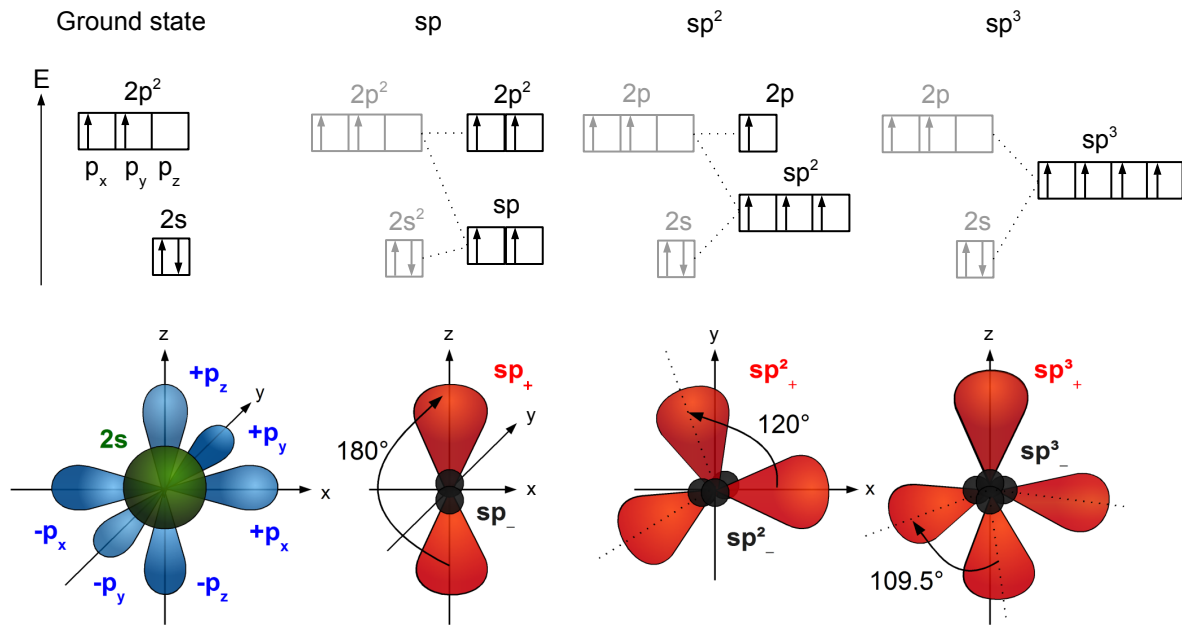


**Figure 2.2.:** Electron configuration of carbon in its ground state and transition to  $sp$ -,  $sp^2$ -, and  $sp^3$ - hybridization (top), corresponding orbital shapes (bottom).

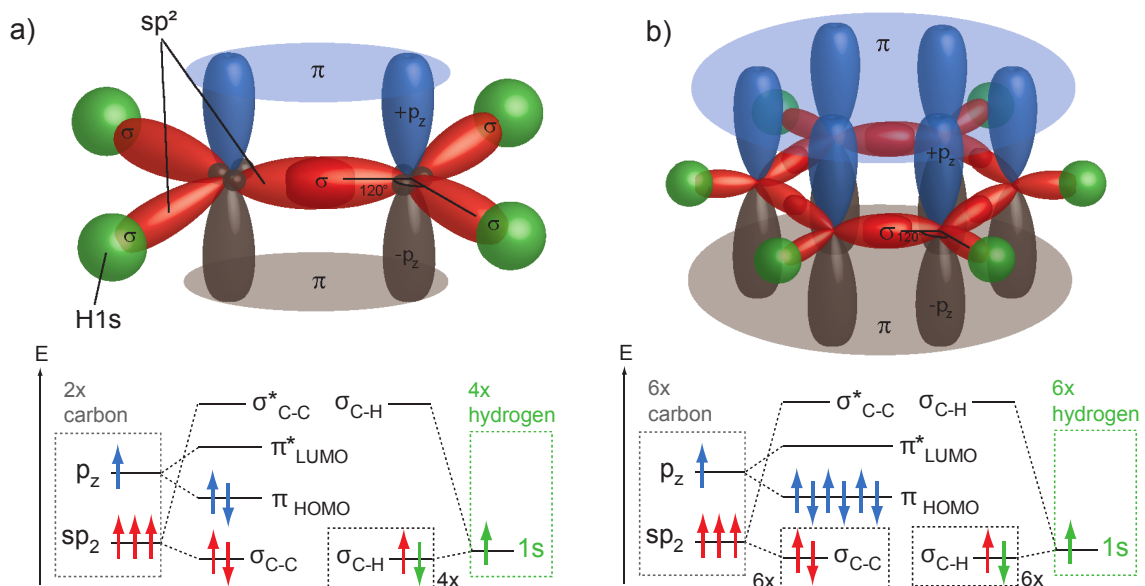


**Figure 2.3.:** (a) Two  $sp^2$ -hybridized carbon atoms form an ethylene molecule via a  $\pi$ - and a  $\sigma$ - bond. The four remaining  $sp^2$ -orbitals are saturated by hydrogen valences. (b) In case of benzene, six  $sp^2$ -hybridized carbons are arranged in a ring structure, creating a delocalized electronic  $\pi$ -system which is important for semi-conducting properties of e.g. acenes.



hydrogen while one  $sp^2$  forms a  $\sigma$ -bond to set the C=C structure together with the remaining  $\pi$ -bond of the  $p_z$  orbitals. For  $sp^3$ -hybridized carbon, the  $\pi$ -bonds are absent since the valence electrons occupy four  $sp^3$ -orbitals. These shape a tetrahedron with the most possible spherical distance of  $109.5^\circ$  as seen in methane ( $\text{CH}_4$ ) or ethane ( $\text{C}_2\text{H}_6$ ).<sup>[51]</sup>

The existence of weakly bound  $\pi$ -systems is mandatory for having delocalized electrons, which is why conjugated molecules are the backbone of organic semiconductors. As shown in Fig. 2.3, all of the six carbon atoms in benzene are  $sp^2$ -hybridized and build  $\sigma$ -bonds with two neighboring C-atoms, forming the aromatic ring structure, while the remaining  $sp^2$ -hybrids are saturated with hydrogen. The perpendicularly oriented  $p_z$ -orbitals arrange to a spread  $\pi$ -system, where the six  $p_z$ -electrons share a delocalized probability density. By that means, charge carriers are able to 'propagate' through the whole benzene molecule. Adding further conjugated rings enhances the  $\pi$ -system and simultaneously increases the spatial uncertainty of the electrons. It has been observed that likewise the energy gap between HOMO and LUMO decreases continuously with higher chain length<sup>[52]</sup>, e.g. from benzene to pentacene (cf. Fig 2.4 (d)).

### 2.1.3. Formation of Organic Solids

Both attractive and repulsive forces are needed to form stable bonds and set any system to its lowest energetic state. In organic solids, electrically neutral, organic molecules are closely packed arrangements, which interact via their charge carrier density distributions. The latter is approximately described in terms of the *Lennard-Jones-Potential*:

$$V_{L-J} = \epsilon \left[ \left( \frac{r_0}{r} \right)^{12} - 2 \left( \frac{r_0}{r} \right)^6 \right]. \quad (2.8)$$

The  $(1/r)^{12}$  term is very short-ranged and describes the repulsion of electron densities in overlapping molecular orbitals due to Coulomb interaction and *Pauli's principle*. The attractive part  $-(1/r)^6$  characterizes the *van-der-Waals* forces. Non-static electron density distributions in the frontier orbitals of the molecules create fluctuating multipole moments, which can polarize adjacent molecules, creating further multipoles. The resulting electrostatic interactions are attractive but weak ( $\approx 0.1 \text{ eV}$ )<sup>1</sup> as compared to ionic (3...7 eV) or covalent (2...8 eV) bonds. Hence, melting and boiling temperatures of organic solids are comparably low and often in the range of RT.

**Polarization in Organic Solids.** Fundamental properties such as absorption or charge carrier transport capabilities of isolated molecules are still present in solids, but their energetics are often shifted due to polarization effects such as electronic, vibronic, or phononic couplings. Particularly, the required minimum energy to remove an electron from the molecule, i.e. the ionization potential IP, and the net energy gain when adding an electron to a molecule, i.e. the electron affinity EA, are affected (cf. Fig. 2.4 (a)-(c)). This fact explains e.g. the measured difference in IP of pentacene in gaseous phase ( $\text{IP}_g = 6.6 \text{ eV}$ ) and solid state ( $\text{IP}_s = 4.9 \text{ eV}$ ) by  $P_+ = 1.7 \text{ eV}$ . Van-der-Waals interactions between adjacent molecules diminish (increase) the IP (EA) in the bulk by Coulomb interaction energies  $P_+$  ( $P_-$ ) which can cover up to several 100 meV (cf. Fig. 2.4 (d)).

<sup>1</sup>As an example: the interaction between stacked pyridine dimers is found to be 4 kcal/mol which equals 0.17 eV per molecule<sup>[53]</sup>

Random mutual orientations of neighboring molecules within organic thin-film layers introduce static disorder. Hence, polarization strengths and as a consequence thereof IPs and EAs are statistically distributed. Molecular films with a larger degree of disorder, i.e. ones less crystalline, usually feature a stronger broadening of their energy levels.<sup>[54]</sup>

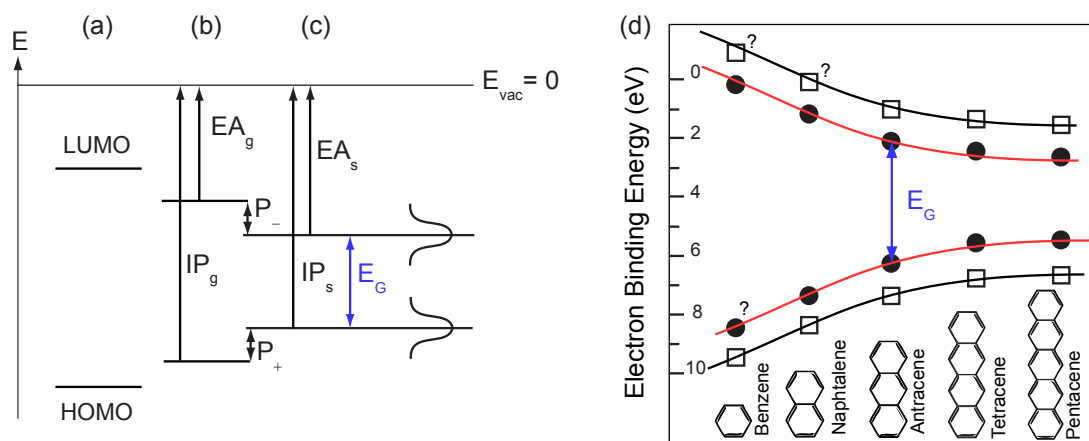


**Figure 2.4.:** Energy scheme in the (a) isolated single molecule, (b) ionized single molecule and (c) solid bulk where the energy levels are approximatively Gaussian distributed. The energy gap  $E_G$  is reduced by polarization energies  $P_{\pm}$ . With increasing chain length,  $E_G$  is further lowered in aromatic molecules (d).<sup>[55]</sup> Here, red (black) lines mark the solid state (gaseous phase) while question marks indicate experimentally not accessible data.

**Relaxation Processes in an Organic Crystal Lattice.** Moreover, the introduction of a localized charge carrier on a centered molecule, at the time  $t = 0$ , forces further changes in probability density, orbital shape, and energy levels of the molecules in the vicinity. The relaxation occurs on different time scales as illustrated in Fig. 2.5. Within  $10^{-16}$ ... $10^{-15}$  s dipoles are induced in the surrounding molecules reducing (increasing) the IP (EA) of the solid by polarization energies  $P_{\pm} = 1$ ...2 eV.<sup>[56]</sup> The localized charge carrier is now stabilized by its polarization cloud and hence called *polaron*. Subsequently, the molecular orbitals re-arrange on a timescale  $10^{-14}$ ... $10^{-13}$  s by intra-molecular vibrations (*vibronic polaron*) with interaction energies of 0.1...0.3 eV. Based on the already discussed differences in mass of the electronic charge and the heavy nuclei, the relaxation

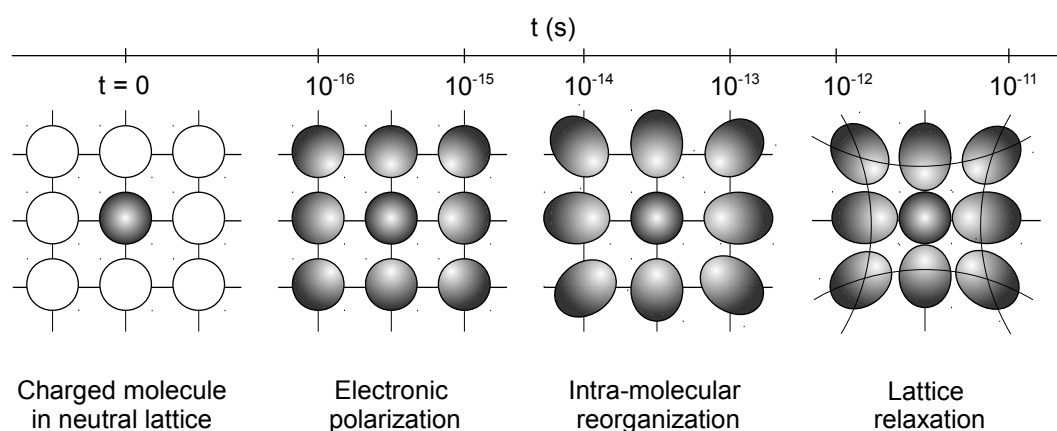


**Figure 2.5.:** Electronic and phononic reorganization of the surroundings in molecular crystal upon insertion of a localized charge at  $t = 0$  at its center.

of the molecular lattice is the slowest process ( $\sim 10^{-11}$  s).<sup>[57]</sup> Interaction energies for the *lattice phonon* are rather low (10...30 meV) and phononic coupling is of minor impact for the energy landscape of localized charge carriers. Nevertheless, the concept of the polaron quasi-particles has proven to be important to describe the charge carrier transport in organic solids. Ideal molecular crystals feature band-like transport in so-called polaron bands, which considers coupling of electronic states and lattice phonons. By contrast, disordered materials show hopping transport in terms of phonon-assisted tunneling of polarons between neighboring molecules. Extending these considerations, in-depth descriptions for the transport of charge carriers in amorphous organic semiconductors shall be presented in Sec. 2.2.

### 2.1.4. Excited Molecules - Absorption, Emission, and Excitons

Organic molecules can interact with light both radiatively, in terms of absorption or emission of a photon, and non-radiatively by internal conversion or inter-system crossing. As discussed in Sec. 2.1.3, the optical properties of the single molecules are only slightly disturbed by the weak van-der-Waals forces thus prevail nearly unchanged upon thin-film aggregation. The possible processes are sketched in Fig. 2.6 a).

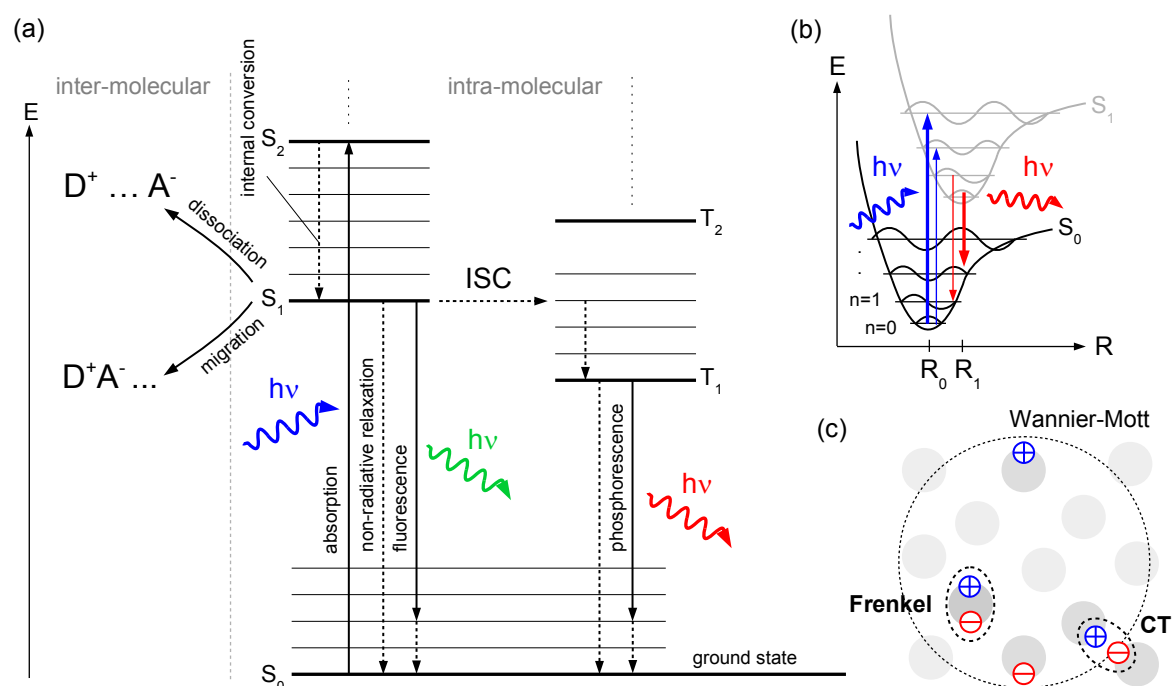


**Figure 2.6.:** **a)** Jablonski diagram to summarize intra-molecular transitions between singlet  $S_i$  and triplet states  $T_j$ . Non-radiative transitions, e.g. internal conversion or spin-flipping ISC are drawn in dashed lines while radiative processes involving absorption/emission of a photon are represented by solid lines. Upon exciton formation, migration to an adjacent molecule or dissociation of the exciton creating a charged donor/acceptor-pair are the most important inter-molecular transitions (redrawn after Ref.<sup>[58]</sup>). **b)** Illustration of Franck-Condon principle and Stokes shift between photon emission and photon absorption, shown for singlet states  $S_0$  and  $S_1$  with vibrational substructure as indicated. By photo excitation, the orbital shape of the molecule is distorted, resulting in a larger mean electron bonding radius  $R_1 > R_0$ . The arrow strength displays the transition probability. **c)** Semiconductor lattice depicting the spatial differences between Wannier-Mott, Frenkel, and charge-transfer type exciton formations.

The *absorption* of a photon promotes an electron from the ground state  $S_0$  to an excited singlet state  $S_n$ . As all electronic states split in vibrational and rotational substructures, the molecule most possibly relaxes through *internal conversion* (IC) within ps via phonon interaction with its surroundings. Radiative relaxation

to the ground state  $S_0$  by emission of a photon usually occurs from the lowest vibronal state of  $S_1$  and is known as *fluorescence*. All those transitions preserve the system spin  $S = 0$  which results from all electrons anti-parallel paired up in the molecule HOMO at  $S_0$ .

Especially in presence of heavy atoms, however, spin-orbit-coupling enables to access triplet states  $S = 1$  upon *inter-system crossing* (ISC). Quantum mechanically forbidden, spin-flip processes are most unlikely to happen thus rendering lifetimes in triplet states ( $\mu\text{s}$  to  $\text{ms}$ ) considerably larger than those of singlet states ( $\text{ps}$  to  $\text{ns}$ ). An excited triplet state can decay via IC and ISC towards  $S_0$ , the radiative relaxation  $T_1 \rightarrow S_0$  is called *phosphorescence*. Phosphorescent emission is red shifted since triplets (i.e. electrons with parallel paired spins) are lower in energy than singlets due to Pauli principle and Coulomb repulsion.

Comparing absorption and emission spectra of an organic semiconductor, one typically observes an additional red shift. The transition probability between initial and final states quantum mechanically obeys *Fermi's Golden Rule*. Further, the Franck-Cordon principle explains that transitions more likely happen if the vibronic wave functions overlap more significantly. Photo excitation leads to relocation of the charge probability density and the molecular lattice (cf. Sec. 2.1.3). By Born-Oppenheimer approximation, the electronic relaxation is much faster than the nuclear motion. Hence, transitions for a minimal  $\Delta R$  are favored, always leading to a red (Stokes) shift of the emission spectra as illustrated in Fig. 2.6 b).

**Excitons.** The picture of excitons is frequently used when describing the interaction of organic matter with light. An exciton is a quasi-particle with either spin  $S = 0$  (singlet) or  $S = 1$  (triplet) and represents an excitation of an organic molecule. Herein, an electron is located at the LUMO while and hole sits at the HOMO of the molecule. In theory, one distinguishes excitons by their interaction radius  $R'$  (cf. Fig. 2.6 c)): inorganic semiconductors exhibit large dielectric constants  $\epsilon_r$  and hence low exciton binding energies of only few meV. Their so-called *Wannier-Mott* excitons are rather delocalized over the entire solid. In contrast, *Frenkel* excitons in organic semiconductors are strongly localized thus the electron-hole pair is situated closely within few Å. In context of the low  $\epsilon_r = 3...5$  in organic semiconductors, this results in binding strength of a few 100 meV. Cases of special interest herein are the *Charge Transfer type* excitons, where electron and hole pair are located on adjacent molecules. Deploying dissociation energy e.g. by an electric field and/or temperature creates free charge carriers - a principle exploited by (organic) photovoltaics or the doping technique.

In the molecular solid, excitons are able to migrate within short distance via simultaneous hopping of electron and hole requiring overlapping wave functions with the neighboring molecule (*Dexter* transfer).<sup>[59]</sup> Longer distances can be bypassed in terms of resonant tunneling, i.e. dipole-dipole interaction via virtual photons (*Förster* transfer).<sup>[60]</sup> It is found that the former is the prominent transport mechanism for triplet excitons while the latter is only possible for singlet excitons, however, enabling traveling distances  $> 10$  nm. The exciton movement in the thin-film is described by its diffusion length  $l_D = \sqrt{D\tau}$ , characterized by the diffusion constant  $D = 10^{-4}...10^{-3} \text{ cm}^2\text{s}^{-1}$  <sup>[61-63]</sup> and the lifetime which is for singlet excitons approx.  $\tau_s \sim \text{ns}$ <sup>[64]</sup> and for triplet excitons in the range of  $\tau_t \sim \mu\text{s}$ <sup>[65]</sup>...ms.<sup>[66]</sup> Consequently, organic semiconductors exhibit exciton diffusion lengths in the range of  $l_D \sim 10$  nm.<sup>[62,67,68]</sup> Recently published results on  $l_D$  exceeding  $1 \mu\text{m}$  in inorganic perovskite materials,<sup>[69,70]</sup> however, could strongly favor organic-inorganic hybrid solutions as both can be deposited from vacuum vapor phase.<sup>[71]</sup>

### 2.1.5. Orientation and Morphology

As presented in Sec. 2.1.3, inter-molecular bonds motivated by van-der-Waals forces are rather weak.<sup>[72,73]</sup> While  $\pi$ -orbital delocalization<sup>[74]</sup> and hybridization effects<sup>[75]</sup> control the size of the energy gap and the positions of HOMO and LUMO, the molecular shape governs the thin-film aggregation. Molecule size, planarity, rigidity, aspect ratio, and the presence of solubilize/ reactive side chains dictate molecular packing, surface alignment, and solubility in solvents for liquid processing<sup>[76]</sup> or other molecular species for molecular intermixing, i.e. domain sizes and phase separation.<sup>[77]</sup> Materials that arrange in a periodic lattice or in aggregates often exhibit superior charge transport properties.<sup>[77]</sup> Pentacene for example (cf. Fig. 2.7 (c)) is known to form an edge-to-edge herringbone structure (1).<sup>[56]</sup> Adding solubilize triisopropyl groups in TIPS<sup>2</sup>-pentacene induce a face-to-face brickwork-like packing (2),<sup>[78]</sup> while shifting the side group to position 5,14 (o-TIPS-P5) creates a sandwich herringbone motif (3),<sup>[79]</sup> mostly due to steric hindrance.<sup>[77]</sup> Associated with the packing scheme, molecular ordering, orbital overlap, and resonance govern charge transport mechanisms<sup>[80]</sup> in organic thin-films which will be discussed in Sec. 2.2 in detail and explain anisotropies, e.g. of charge carrier mobility.<sup>[81]</sup> Representing the starting point of thin-film aggregation, initial nucleation on a surface is important and has been manipulated, e.g. via substrate temperature<sup>[82,83]</sup> or surface chemistry (SAMs<sup>3</sup>).

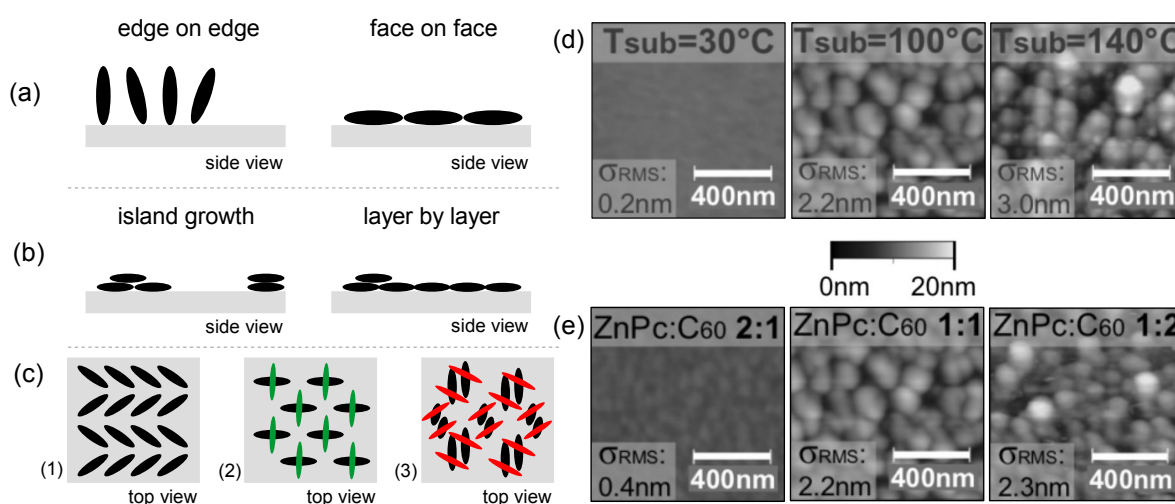


**Figure 2.7.:** (a)-(b) Observed growth modes for organic semiconductors. (c) Additional solubilizing side chains (green) change the molecular packing of pentacene (black) from a herringbone structure (1) to a brickwork-like one of TIPS-pentacene (2).<sup>[78]</sup> If the side groups (red) are not centered on the P5 molecule (3), steric hindering causes a sandwich herringbone motif.<sup>[79]</sup> (d)-(e) AFM measurements on phase aggregation in ZnPc:C<sub>60</sub> blends on glass/C<sub>60</sub> for various substrate temperatures (1 : 1 ratio) and different mixing ratios (140° C) (taken from Ref. [83]).

The formation of the first monolayer, e.g. decisive for the charge transport in a transistor structure, is strongly influenced by surface roughness and surface potential of the underlying substrate. Different types of substrate templates typically force different orientations of the subsequent organic film (cf. Fig. 2.7 (a)).<sup>[84,85]</sup> For instance, metal phthalocyanines (PCs) tend to exhibit an edge-on-orientation on substrates like SiO<sub>2</sub>, indium-tin-oxide (ITO), or PEDOT:PSS<sup>4</sup> due to their weak interfacial interaction.<sup>[86,87]</sup> The orientation is changed when an additional layer enabling strong interfacial coupling with the organic bulk film is applied.<sup>[88]</sup>

<sup>2</sup>6,13-bis(triisopropyl-silylethynyl)

<sup>3</sup>self assembled monolayers

<sup>4</sup>poly(3,4-ethylenedioxythiophene) polystyrene sulfonate

Template layers such as copper iodine nanocrystals<sup>[88]</sup>, PTCDA,<sup>[89]</sup> tetracene,<sup>[90]</sup> or pentacene<sup>[87]</sup> have been shown to induce a preferred face-on orientation of the PCs. This morphological configuration has been shown to improve absorption and exciton dissociation, i.e. solar cell performance<sup>[87,88,90]</sup>, and shifts the HOMO level position.<sup>[91]</sup> After the first monolayer, consecutive layers might arrange differently, to form either a closed layer<sup>[92]</sup> or separated islands<sup>[73]</sup> (cf. Fig. 2.7 (b)) depending on the preferred packing and the deposition conditions, e.g. temperature or deposition rate.<sup>[93]</sup>

The situation even complicates for blends of different molecular species, e.g. the levels of crystallization and phase separation in ZnPc:C<sub>60</sub> has been found to strongly depend on substrate temperature and mixing ratio (cf. Fig. 2.7 (d)-(e)).<sup>[82,83]</sup> All these thoughts are summarized in the term 'morphology'. Linking the results of elaborated techniques like various types of X-ray scattering or AFM<sup>5</sup> e.g. to charge transport concepts and their experimental observations is still challenging.

### 2.1.6. Interface Formation in Organic Semiconductors

**Intrinsic Metal/Organic Interfaces.** Figure 2.8 (a) exemplary shows the alignment of MeO-TPD on a gold substrate. Naturally, one expects a vanishing hole injection barrier  $\phi$  after vacuum level alignment of comparable metal work function and organic ionization potential. Instead, ultraviolet electron spectroscopy reveals  $\phi = 1.1$  eV due to an interface dipole  $\Delta$  that exists between the metal surface and the organic layer.<sup>[94]</sup> Several origins for such dipoles are discussed in literature, e.g. *pinning* of the Fermi level either at tailing states of the DOS<sup>[95,96]</sup> or at *integer charge transfer states*<sup>[97–99]</sup> formed between the metal surface and interface polaron states.

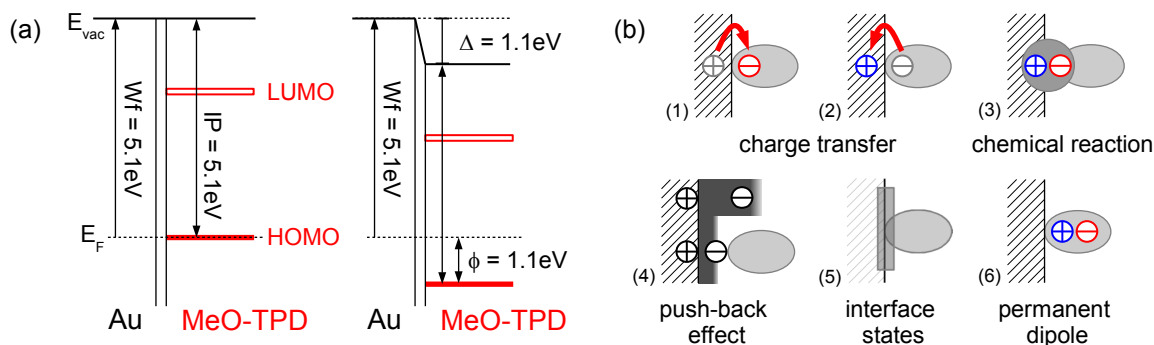


**Figure 2.8.:** (a) Energy level alignment of MeO-TPD on gold as expected (left) and obtained by UPS (right) (data taken from Ref. <sup>[94]</sup>). (b) Possible explanations for dipoles  $\Delta$  occurring at metal/organic interfaces (redrawn after Ref. <sup>[100]</sup>).

Moreover, reactive molecules can chemically bind to the metal surface. As reported for Alq<sub>3</sub><sup>6</sup>, the organometallic complexes establish new intra-gap states and alter the energy alignment.<sup>[101–103]</sup> A similar result has been found in terms of *metal induced gap states* (MIGS)<sup>[104,105]</sup> at which the metal electron wave functions decay into the semiconductor and broaden its DOS. Charge transfer between the Fermi level of the metal and the induced interface gap states (typical densities are  $\sim 10^{14}$  cm<sup>2</sup>eV<sup>−1</sup>)<sup>[104]</sup> occurs and results in dipole formation. In reserve, the *pillow* or *push-back effect* is observed. At the metal surface, the positive charge

<sup>5</sup>atomic force microscopy

<sup>6</sup>tris(8-hydroxy-quinolino)-aluminum

carrier distribution of the nuclei drops abrupt while the electron density extends into the vacuum and decays exponentially. If a molecule adsorbs onto the metal surface, the Coulomb repulsion suppresses these tailing states and lowers the work function of the substrate. This effect is particularly important for noble metals and explains the dipole in Fig. 2.8(a).

Detailed descriptions of these mechanisms are found in literature,<sup>[100]</sup> however it has been calculated using Poisson equation that for a typical configuration ( $n = 10^{15} \text{ cm}^{-3}$ ,  $\varepsilon = 3$ ,  $\Delta W_f = 0.5 \text{ eV}$ ) complete Fermi level alignment in an intrinsic organic layer is only reached after  $\sim 400 \text{ nm}$  of film thickness.<sup>[94]</sup> An experimental validation is reported by Hayashi *et al.* who measured a Fermi level alignment in  $\text{C}_{60}$  with  $n = 4.5 \times 10^{14} \text{ cm}^{-3}$  after  $\sim 500 \text{ nm}$  film thickness on substrates of Au, Ag, and Cu.<sup>[106]</sup> by Kelvin probe microscopy. This is alerting since organic electronic devices are rarely designed to exceed 100...800 nm in overall film thicknesses.<sup>[107–109]</sup>

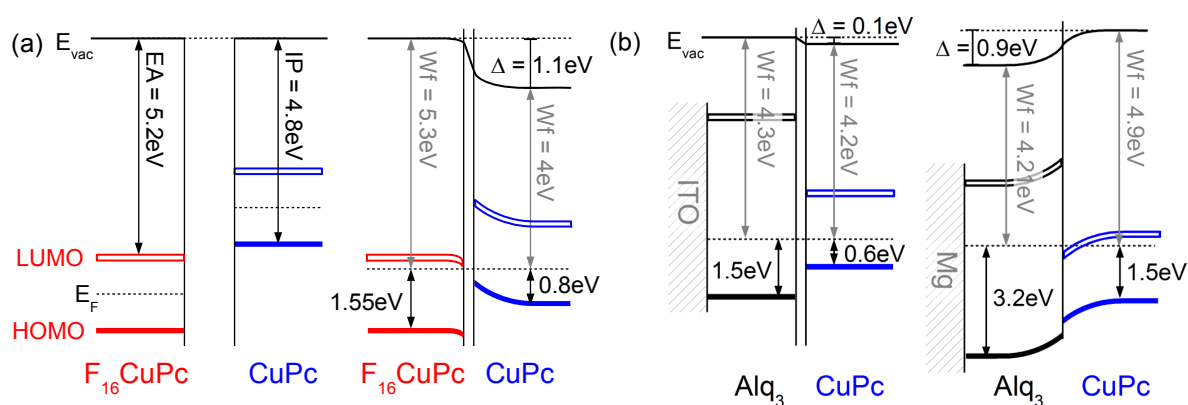


**Figure 2.9.:** Energy level alignment in flat heterojunctions of intrinsic organic semiconductors. **(a)** Due to non-overlapping energy gaps of  $\text{F}_{16}\text{CuPc}$  and  $\text{CuPc}$ , charge transfer and level bending occurs at the interface upon merging (left) to (right) (redrawn after Ref. <sup>[110]</sup>). **(b)** Substrate dependent alignment of  $\text{Alq}_3/\text{CuPc}$  junctions. While no dipole is present in case of deposition on ozone treated ITO (left),  $\text{Alq}_3$  undergoes charge transfer with the Mg surface thus pinning  $E_F$  and altering the work function (right)(adapted from Ref. <sup>[111]</sup>).

**Intrinsic Organic/Organic Interfaces.** In case of organic/organic interfaces, mostly vacuum level alignment is observed.<sup>[112–114]</sup> However, in case of strongly differing  $IP$ s or  $EA$ s, e.g. for the combination of the electron donating  $\text{TTF}^7$  and the electron accepting  $\text{TCNQ}$  ( $\Delta = 0.6 \text{ eV}$ ),<sup>[115]</sup> interface dipoles are reported. The dipole strength is even increased for combinations of molecular species with non-overlapping energy gaps, e.g. interface charge transfer resulting in  $\Delta = 1.1 \text{ eV}$  in  $\text{F}_{16}\text{CuPc}$  ( $EA = 5.2 \text{ eV}$ ) /  $\text{CuPc}$  ( $IP = 4.8 \text{ eV}$ )(cf. Fig. 2.9(a)). Moreover, substrate dependencies are reported for organic heterojunctions.<sup>[110,111,116,117]</sup> Existing interface dipoles, e.g. originating from Fermi level pinning in the organic semiconductor close to the substrate, cause bending of the molecular orbitals at the organic/organic interface and suppresses vacuum level alignment (cf. Fig. 2.9(b)).<sup>[111]</sup>

**Doped Metal/Organic Interfaces.** The typically low intrinsic charge carrier densities in organic semiconductors can be raised via introduction of doping molecules (cf. Ch. 3). The generated free charge carriers alter the energy level alignment at the interface upon charge transfer with the metal surface. For such a so-called *Schottky contact*, one observes the formation of a depletion zone in the organic layer near the interface and a level bending. Fermi level alignment of the organic bulk layer is typically reached after a few

<sup>7</sup>tetrathiafulvalene

nm. Ohmic losses are minimized as charge carriers are able to tunnel through the thin injection barrier  $\phi$  into the organic semiconductor. Hence, a possible device operation becomes independent on the actually used contact material next to doped organic layers. However, in our case the formation of a defined depletion zone will be used to study doping properties and examine charge carrier traps in the organic material, which is why Schottky contacts are discussed in Sec. 4.2.3 in detail.

## 2.2. Charge Carrier Transport

The manifold ways to align and orient organic molecules determine the electronic transport in organic semiconductors. Extensive reviews on this topic are found in literature<sup>[118–120]</sup>. Depending on the level of crystallization and the examined temperature regime, one observes a transition between two borderline cases: polaronic band-like transport and hopping transport, both delimited by their temperature dependence of the mobility  $\mu(T)$ . While delocalized phonon-assisted transport in polaron bands is only observed in highly purified crystalline phases at low temperatures, hopping transport over localized sites is commonly observed in amorphous or microcrystalline organic films. Taking a step back to a more general introduction of band transport in highly ordered films, both types of charge carrier transport shall be reviewed here.

### 2.2.1. Towards Band-Like Transport in Highly Ordered Crystals

One of the most basic charge carriers transport theories, the *Drude model*, was introduced in 1900 to explain the conductivity in metals and solids containing free electrons. In this picture, electrons are classically accelerated by an applied electric field within the material until they collide with heavy, positively charged lattice ions. Upon collision, the electrons scatter by random angle, before they are accelerated again and the next collision occurs. Despite the erroneous interpretation of the actual nature of the scattering centers, an explanation of Ohm's law and Joules heat was given. With emerging quantum mechanics, a detailed microscopical description became accessible, identifying the scattering centers as structural defects, chemical contaminations, or lattice phonons. However, in the case of undisturbed propagation, the translation symmetry of the crystal potential  $V(\vec{r} + \vec{R}_n) = V(\vec{r})$  with lattice vector  $\vec{R} = \vec{R}_n/n$  demands periodic solutions of the Schrödinger equation that suit the Bloch condition

$$\Psi_{\vec{k}}(\vec{r} + \vec{R}_n) = \exp(i\vec{k} \circ \vec{R}_n) \Psi_{\vec{k}}(\vec{r}). \quad (2.9)$$

The wave functions  $\Psi_{\vec{k}}$  can be computed from solutions of the atomic orbitals (tight-binding-approximation) and result in electronic (conduction and valence) bands. Their shape depends on the crystal lattice symmetry, while the band width  $W$  is proportional to the overlap  $J_{m,m'}$  of neighboring atomic orbitals  $\chi_i$  of the lattice points  $m$  and  $m'$  with

$$W \propto J_{m,m'} = \langle \chi_{\vec{r}-\vec{R}_m} | \hat{H} | \chi_{\vec{r}-\vec{R}_{m'}} \rangle, \quad (2.10)$$

similar to the findings in LCAO theory in Sec. 2.1.1. Electrons and holes are restricted to be at areas of constant energies, i.e. ellipsoids

$$E(\vec{k}) = E_{C,V} \pm \hbar^2 \left( \frac{k_1^2}{2m_1} + \frac{k_2^2}{2m_2} + \frac{k_3^2}{2m_3} \right), \quad (2.11)$$

which are determined by the effective masses  $m_{1,2,3}$  and the position of the area itself in the  $\vec{k}$ -space.<sup>[121]</sup> The effective mass of an electron or a hole  $m_i$  towards the respective axis  $i$  is given by the corresponding



dispersion relation

$$m_i = \hbar^2 \left( \frac{d^2 E(k)}{dk_i^2} \right)^{-1}. \quad (2.12)$$

Since the electronic states are extended over the whole crystal, free charge carriers can propagate within the bands. The transport is a drift and the mobility  $\mu_i$  of charge carriers in the band is given by

$$\mu_i = \frac{e\tau_i}{m_i} \quad (2.13)$$

with the mean time between two scattering processes at lattice defects, impurities or phonons denoted as  $\tau_i$ . Transport in extended bands is only meaningful, if  $\tau \gg \hbar/W$  and the resulting mean free path is larger than the lattice constant, i.e. charge carrier motion is extended to several unit cells. For highly crystalline inorganic materials, mobilities reach  $\mu_e \approx 1.4 \times 10^4 \text{ cm}^2/\text{Vs}$  in Si or  $\mu_e \approx 9.2 \times 10^4 \text{ cm}^2/\text{Vs}$  in GaAs. These values are only exceeded in low dimensional systems, e.g. single layers of graphene ( $2 \times 10^5 \text{ cm}^2/\text{Vs}$  at RT)<sup>[122]</sup>. The highest reported mobilities are observed in 2D heterostructures of AlGaAs/GaAs ( $3.5 \times 10^7 \text{ cm}^2/\text{Vs}$ )<sup>[123]</sup> close to 0 K. Due to suppressing of phonon modes at low temperatures, the scattering probabilities are lowered. In general, the theory of ideal band transport predicts a temperature dependence of the mobility in the form of  $\mu \propto T^{-3/2}$ . However, measured scaling laws differ from this result, e.g.  $\mu_h \propto T^{-2.3}$  and  $\mu_e \propto T^{-1.5}$  for Ge<sup>[124]</sup> or  $\mu_h \propto T^{-2.2}$  for Si, due to non-parabolic bands and defect scattering.

For organic semiconductors, measured mobilities are lower by orders of magnitude. The prevailing reason for that is their limited inter-molecular coupling. Consequently, the bandwidth of organic semiconductors is small as compared to inorganics and band transport is observed only in case of highly-ordered and pure crystals at low temperatures.<sup>[125]</sup> While organic benchmark materials such as singlecrystalline rubrene can compete at least with inorganic  $\alpha$ -Si,<sup>[126]</sup> thin-films of small molecules<sup>[127–130]</sup> and polymers<sup>[131,132]</sup> exhibit only low mobility values. Herein, it has been shown that thin-film morphology and orientation are important, e.g. to explain intra-grain and inter-grain transport in polymer backbones, emphasizing the importance of molecular  $\pi$ -stacking. In addition to the observation of band transport in several high purity organic solids at low temperatures by Karl *et al.*,<sup>[125]</sup> negative temperature coefficients of the mobility (i.e.  $d\mu/dT < 0$ ) have been reported for few ten K in solution processed FETs<sup>[133,134]</sup>. Referred to as band-like transport, the results are explained by field-assisted promotion from shallow states into more extended states<sup>[133]</sup> and polaronic transport<sup>[134]</sup>. In transport theory, polaron bands formed due to electron-phonon interaction, exhibit a  $\mu \propto T^{-3/2}$  dependency and are narrower as compared to entirely electronic bands. In experiments, mobility drops with  $\mu \propto T^{-n}$  and  $n > 1.5$  (i.e. band-like). However, the bandwidth  $W$  decreases with increasing temperature (dynamic disorder) until complete localization of the charge carriers and the charge carrier motion transitions into hopping transport. Hence, charge carrier hopping is considered the predominant transport mechanism at room temperature especially in organic films with greater disorder, e.g. amorphous or poorly crystalline layers of small molecules. They are discussed in the following section.

### 2.2.2. Hopping Transport Concepts in Disordered Systems

Governed by weak inter-molecular van-der-Waals interactions in molecular solids, the overlap of frontier orbitals of neighboring molecules is very limited. Considering a mostly amorphous organic film, charge carriers remain localized at their molecular sites and polaron bands are suppressed. In disordered media, the charge carrier motion is attributed to occasional hopping steps, the fundamental problem is set by the master equation:<sup>[135]</sup>

$$\frac{\partial}{\partial t} n_i(t) = - \sum_{j \neq i} W_{ji} n_i(t) [1 - n_j(t)] + \sum_{j \neq i} W_{ij} n_j(t) [1 - n_i(t)] - \lambda_i n_i(t). \quad (2.14)$$

A change in occupation probability  $n_i(t)$  of site  $i$  can occur via interaction with all surrounding sites  $j$ , e.g. a hop of a charge carrier from  $i$  to an empty site  $j$  (first term) or from  $j$  in case of an empty site  $i$  (second term). The transition rates  $W_{ji}$  and  $W_{ij}$  are commonly equal. The third term denotes decay rates  $\lambda_i$  in case of excited states or recombination. The most prominent description for the transition rates  $W$  was given by Anderson with the so-called *Miller-Abrahams* expressions<sup>[136]</sup> denoted as

$$W_{ij} = \nu_0 \exp(-2\gamma |R_{ij}|) \begin{cases} \exp\left(\frac{-(\varepsilon_j - \varepsilon_i)}{k_B T}\right) & \forall \varepsilon_j > \varepsilon_i \\ 1 & \text{else} \end{cases} \quad (2.15)$$

where  $\nu_0$  is the phonon vibration frequency i.e. 'jump-attempt' rate,  $\gamma$  is the inverse localization radius (caused by the overlap integrals of the molecular orbitals), and  $\varepsilon_i$  and  $\varepsilon_j$  are the energies of the respective sites  $i$  and  $j$  with the inter-site distance  $|R_{ij}|$ . An illustration is given in Fig. 2.10. The transport process is regarded as phonon-assisted tunneling between sites further apart and jumps between neighboring sites. Herein, jumps towards sites of lower energy happen immediately whereas jumps to energies higher than the initial energy are temperature activated (Arrhenius-type). The major simplification is that no polaron relaxation after a successful jump is considered, i.e. the energy landscape remains unchanged.

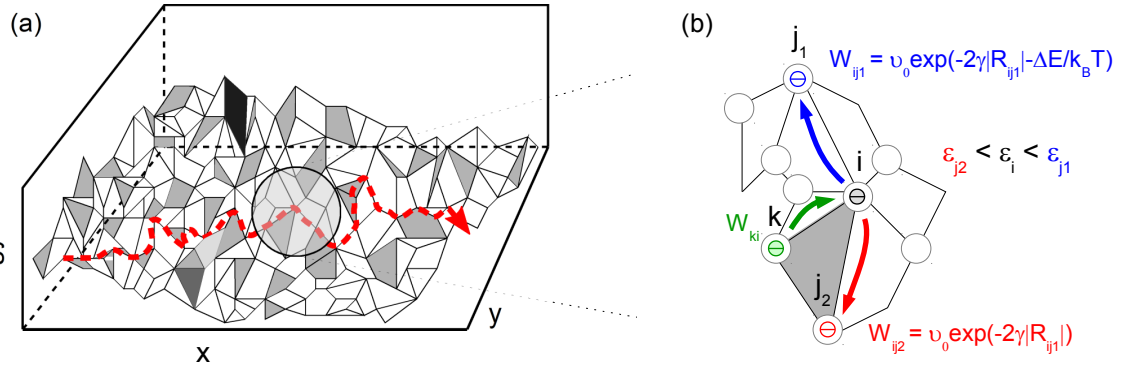


**Figure 2.10:** (a) Charge carrier transport in an energetically and spatially disordered system. (b) Microscopically, the occupation of site  $i$  changes when the residing charge carrier hops to a neighboring, empty site  $j_1$  or  $j_2$  (rates given as  $W_{ij}$ ). Jumps upwards in energy obey an energy penalty while jumps downwards are only limited by spatial tunneling probabilities. The emptied site  $i$  can be re-occupied by backward hops or a charge carrier jumping from nearby site  $k$ .

Mott included this effect in his polaron hopping model, assuming that hops may occur between sites in resonance (dependent on temperature)<sup>[137]</sup>. The total energy does not depend on the site the charge carrier is situated at. The hopping rate between two sites separated by energy  $\Delta E = |\varepsilon_j - \varepsilon_i|$  is proportional to  $\exp(-\Delta E / 2k_B T)$ . Both models yield similar transport currents for steady state conditions and room temperature, but differ for low temperatures. Here, the occupation of phonon modes changes which promotes polaron relaxation. In case of correlated site energies (i.e. for the CDM<sup>8</sup>), the solutions are insensitive to the chosen expression of the transition rates<sup>[138]</sup>. Regardless of the transfer rate of choice, Eq. (2.14) needs to be solved in terms of most probable jump distance, i.e. in energy  $\Delta E_{max}$  and spatial distance  $R_{max}$ . Subsequently, major approaches and their outcome are briefly explained.

<sup>8</sup>Correlated Disorder Model

### Mott's Variable Range Hopping (VRH)

Efficient hopping transfer requires the initial jump site to be filled and the final site to be empty (cf. Eq. (2.14)). In a disordered film, such sites are distributed spatially and energy-wise, and transport is a trade-off problem. Although energetically favorable sites to jump do exist, they might be fairly distant rendering the tunneling probability negligible. On the other hand, targeted sites nearby could cause diminished hopping probabilities because of potential energy penalties  $\propto \exp(-\Delta E/k_B T)$ . However, it is natural to expect the charge carriers to hop in vicinity of the Fermi level where filled and unfilled states are closest (cf. Fig. 2.11 (a)). Assuming a uniform site distribution  $g(E) = g$ , a charge carrier has  $\frac{4}{3}\pi R^3 g \Delta E$  options to hop within its spherical surroundings by an energy  $\Delta E$  over the distance  $R$ , but needs an empty site to perform a successful hop, i.e.

$$\frac{4}{3}\pi R^3 g \Delta E \simeq 1. \quad (2.16)$$

Using e.g. the Miller-Abrahams expressions (cf. Eq. (2.15)), the maximum jump rate with respect to  $R$  is derived as

$$W_{ij}|_{max} = \nu_0 \exp \left( -\gamma \left( \frac{1}{8\gamma k_B \pi g} \frac{1}{T} \right)^{1/4} - \frac{1}{k_B T \frac{4}{3}\pi \left( \frac{1}{8\gamma k_B \pi g} \frac{1}{T} \right)^{3/4} g} \right) \quad (2.17)$$

or

$$\sigma(T) \sim W_{ij}|_{max} \propto \exp \left[ - \left( \frac{T_0}{T} \right)^{1/4} \right].$$

It is known as Mott's temperature activated hopping formula<sup>[139]</sup> with the optimized distance  $R_{opt}$  and energy step  $\Delta E_{opt}$  given by

$$R_{opt}^4 = \frac{1}{8\gamma k_B \pi g} \frac{1}{T} \quad \text{and} \quad \Delta E_{opt} = \frac{(8\gamma k_B T)^{3/4}}{\frac{4}{3}(\pi g)^{1/4}}. \quad (2.18)$$

At room temperature, typical values of  $g = 10^{21} \text{ cm}^{-3} \text{ eV}^{-1}$  and  $\gamma = 1 \text{ nm}^{-1}$  yield  $R_{opt} \approx 1 \text{ nm}$  and  $\Delta E_{opt} \approx 0.2 \text{ eV}$ , which is in good agreement with a very localized hopping motion. Similar calculations for exponential site (i.e. DOS) distributions show that the carrier motion happens at states situated slightly above the location of the charge carrier equilibrium distribution (cf. Fig. 2.11 (b)).<sup>[118]</sup> With a steeper DOS, the current flows at elevated energies where more states are available (cf. Fig. 2.11 (c)).

### Ambegaokar's Percolation Approach

Mott's variable range hopping calculations suggested that charge carriers take the fastest way through a landscape of disordered sites. This shows itself similar to the problem of water running i.e. percolating in dry sand. As percolation theories were powerful and already advanced, in one of the most important contributions Ambegaokar *et al.* proposed to describe charge carrier transport in disordered media.<sup>[141]</sup> Following the illustration in Fig. 2.12, the spatial lattice of the hopping sites is transformed into a resistor network. It is the aim to obtain the critical (i.e. fastest) path way through the system by minimizing the systems overall resistance. Miller-Abrahams jumps between sites of the energy  $\varepsilon_i$  and  $\varepsilon_j$  at the distance  $R_{ij}$  are expressed by current flow through conductors as

$$G_{ij} \approx \frac{q\nu_0}{k_B T} \exp(-2\gamma |R_{ij}|) \exp \left( -\frac{|\varepsilon_j - E_F| + |\varepsilon_i - E_F| + |\varepsilon_j - \varepsilon_i|}{2k_B T} \right). \quad (2.19)$$

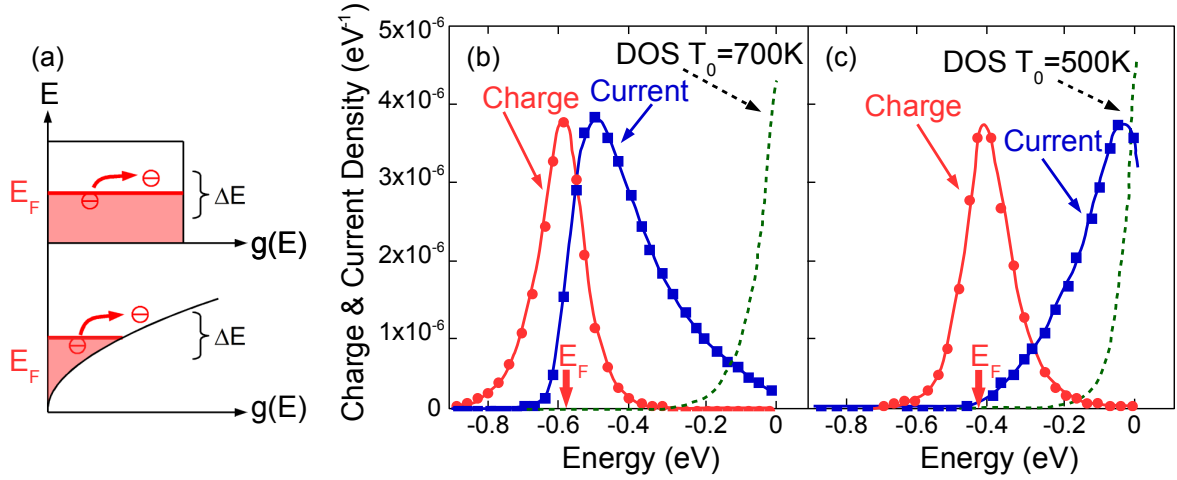


**Figure 2.11:** (a) As shown for uniform (top) and exponential (bottom) distribution of density of states  $\rho$ , charge carrier hopping occurs within  $\Delta\epsilon$  around the Fermi level where occupied and empty sites are in close vicinity. (b) Normalized charge carrier density, current density and density of states for exponential DOS of  $T_0 = 700$  K and 500 K (c). In both cases, the filling factor of the DOS is  $10^{-4}$  and the Fermi level position is indicated by a thick arrow. Computed by VRH, charge carrier transport takes place at elevated energies as compared to  $E_F$ .<sup>[118,140]</sup>

Here, the site energies distant from the Fermi level provoke only low jump probabilities. After transcription, the conductors are subsequently added into an empty site landscape starting with the lowest values until a (critical) percolation path is formed and the critical (necessary) conductivity  $\sigma(T) = G_C$  is obtained. Applying this percolation approach to a 3D uniform site distribution leads again to Mott's formula (cf. Eq. (2.17)), and shows the consistency of these two approaches.

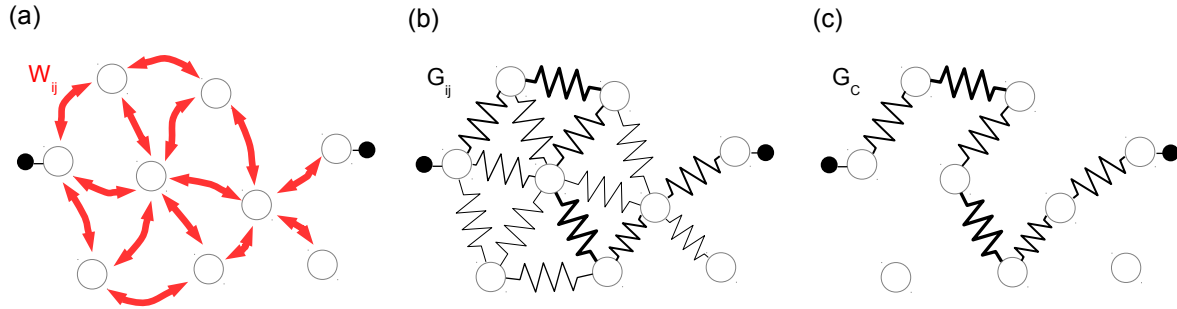


**Figure 2.12:** For a percolation description of the charge carrier transport, the hopping system (a) turns into a resistor network (b). Step-by-step, resistors are removed in a way that only the highest conductors are kept to ensure a percolation path through the disordered film (c).

Most relevantly in context of organic semiconductors, Vissenberg and Matters applied the percolation approach to an exponentially distributed DOS<sup>[142]</sup>, addressing the issue that the site density at the Fermi level is dependent on the actual Fermi level position (i.e. charge carrier densities  $p(E) = \frac{1}{N_t} \int dE g(E) f(E)$ ). For the conductivity in such a system, they derived

$$\sigma(p, T) = \sigma_0 \left( \frac{\pi N_t p (T_0/T)^3}{(2\gamma)^3 B_e \Gamma(1 - T/T_0) \Gamma(1 + T/T_0)} \right)^{T_0/T} \quad (2.20)$$

with  $\Gamma(z) = \int_0^\infty dx \exp(-x) x^{z-1}$  and  $B_c \approx 2.8$  nearest neighbors in a 3D lattice.<sup>[143]</sup> In case of low charge carrier densities ( $p \ll N_t$ ) and low temperatures ( $T < T_0$ ), an Arrhenius-like temperature dependence of the conductivity<sup>[142,144,145]</sup> employing the activation energy  $E_{A,\sigma}$  to

$$\sigma(T) = \sigma_0 \exp\left(-\frac{E_{A,\sigma}}{k_B T}\right) \quad (2.21)$$

is found. With that, Eq. (2.20) and Eq. (2.21) comprise two main results for an exponential DOS: The characteristic hop is a temperature activated jump from the Fermi energy towards a specific transport energy where much more available sites exist.<sup>[146,147]</sup> Secondly, the conductivity increases superlinearly with the charge carrier density ( $\sigma \propto p^{T_0/T}$ ). Filling the DOS increases the average energy of charge carriers in the system thus facilitating an easier access towards more target sites. The effective activation energy is reduced. For Gaussian DOS functions, similar percolation approaches can be found in literature.<sup>[148,149]</sup>

### Computational Approaches: Bässler Model, EGDM, and ECDM

Besides the considerations on variable range hopping and percolation path theory already presented above, extensive studies were published on computational approaches of charge carrier transport in organic films. In early work of Bässler *et al.*, the master equation Eq. (2.14) is solved on a finite cubic lattice with periodic boundary conditions using Miller-Abrahams rates and Monte Carlo simulations.<sup>[150]</sup> Following Fig. 2.13, they assume a DOS which is Gaussian distributed (hence the model is known as GDM<sup>9</sup>) in both energy space as

$$g(E) = \frac{N_0}{\sqrt{2\pi}\tilde{\sigma}} \exp\left(-\frac{(E - E_0)^2}{2\tilde{\sigma}^2}\right) \quad (2.22)$$

with the energetic (static) disorder  $\tilde{\sigma}$  and spatial space as

$$g(\Gamma) = \frac{1}{\sqrt{2\pi}\Sigma} \exp\left(-\frac{(\Gamma - \gamma R_0)^2}{2\Sigma^2}\right) \quad (2.23)$$

with the off-diagonal disorder  $\Sigma$ . The latter is caused by varying orbital overlaps of neighboring molecules with  $\Sigma = 2\gamma |R_{ij}|$ .

In progress of the Monte Carlo experiment, the motion of randomly inserted charge carriers motivated by an external electric field  $F$  is tracked. Upon multiple simulation passes, their movement speed converges and the actual position of the charge carriers becomes insignificant. The mean time and the accomplished way of the charge carriers towards the extracting contacts yield the mobility, depending on the disorder. For a single charge carrier in the DOS, Bässler *et al.* found it to be located around  $E_\infty = E_0 - \sigma^2/k_B T$  for  $t \rightarrow \infty$ , while the mobility function is derived to<sup>[150]</sup>

$$\mu(\tilde{\sigma}, \Sigma, F, T) = \mu_0 \exp\left[-\left(\frac{T_0}{T}\right)^2\right] \begin{cases} \exp\left[C\left((3/2\frac{T_0}{T})^2 - \Sigma^2\right)\sqrt{F}\right] & , \Sigma \geq 1.5 \\ \exp\left[C\left((3/2\frac{T_0}{T})^2 - 2.25\right)\sqrt{F}\right] & , \Sigma < 1.5 \end{cases} \quad (2.24)$$

with the empirical constant  $C = 2.9 \times 10^{-4} (\text{cm/Vs})^{1/2}$  and  $T_0 = 2\sigma/3k_B$ . For low charge carrier densities and high field strengths ( $F \geq 10^6 \text{ V/cm}$ )<sup>[151,152]</sup>, the result agrees well with the experimentally observed

<sup>9</sup>Gaussian Disorder Model

Poole-Frenkel behavior  $\mu \propto \exp(\sqrt{F})$ , as observed e.g. in time-of-flight experiments.<sup>[150,153–155]</sup> Deviations at low to intermediate fields are resolved in the CDM assuming correlated site energies.<sup>[138]</sup>

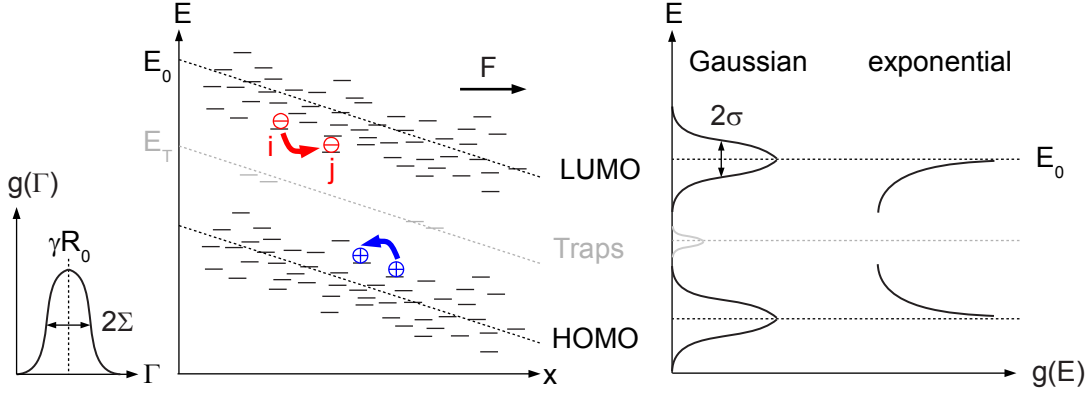


**Figure 2.13.:** Illustration of electron and hole transport in disordered systems in presence of an electric field  $F$ . In the (E)GDM, spacial overlap of adjacent sites ( $\Gamma$ ) and site energies ( $E$ ) are commonly assumed to be Gaussian distributed.<sup>[150,156,157]</sup> Computations considering the extension of the DOS towards the energy gap often use exponential distributions.<sup>[142,144,145]</sup>

However, findings of Tanase *et al.* in OFETs of the disordered polymer<sup>10</sup> demonstrated a strong dependence of the mobility on charge carrier concentration<sup>[158]</sup>. In the EGDM<sup>11</sup> Pasveer, Coehoorn, and coworkers solved the master-equation Eq. (2.14) numerically to obtain a drift mobility dependent on temperature  $T$ , electric field  $F$ , charge carrier density  $p$ , and disorder  $\sigma$  as (cf. plot in Fig. 2.14)<sup>[156,157,159]</sup>

$$\mu(\hat{\sigma}, F, p, T) = \mu_0(\hat{\sigma}, T) \cdot f(E, \hat{\sigma}, T) \cdot g(p, \hat{\sigma}, T), \quad (2.25)$$

with

$$\mu_0(\hat{\sigma}, T) = \mu_0 \exp[-C\hat{\sigma}^2], \quad (2.26)$$

$$f(E, \hat{\sigma}, T) = \exp \left[ 0.44 \left( \hat{\sigma}^{3/2} - 2.2 \right) \cdot \left( \sqrt{1 + 0.8 \left( \frac{F e a}{\sigma} \right)^2} - 1 \right) \right], \quad (2.27)$$

$$g(p, \hat{\sigma}, T) = \exp \left[ \frac{1}{2} (\hat{\sigma}^2 - \hat{\sigma}) \cdot (2 p a^3)^\delta \right], \quad (2.28)$$

and

$$\hat{\sigma} = \frac{\sigma}{k_B T}, \quad \delta = \frac{2}{\hat{\sigma}^2} [\ln(\hat{\sigma}^2 - \hat{\sigma}) - \ln(\ln 4)], \quad C = \text{const.} \quad (2.29)$$

Independent of the exact formalism, all discussed descriptions of charge carrier transport in a Gaussian distributed density of states propose the same scenario. At equilibrium, the charge carriers reside in the low energy tail of the DOS. However in case of transport, they take their route towards states of higher energy but also higher density near the center of the Gaussian DOS and in the vicinity of a distinct transport level. Thereby, upward hops are promoted by (thermal) activation energy. However, the exact location of the transport level  $E_T$  has attracted in-depth research and is fundamental for further understanding of the work in this thesis, thus, the main theories shall be presented in the following section.

<sup>10</sup>Poly(3-hexylthiophene-2,5-diyl)

<sup>11</sup>Extended Gaussian Disorder Model

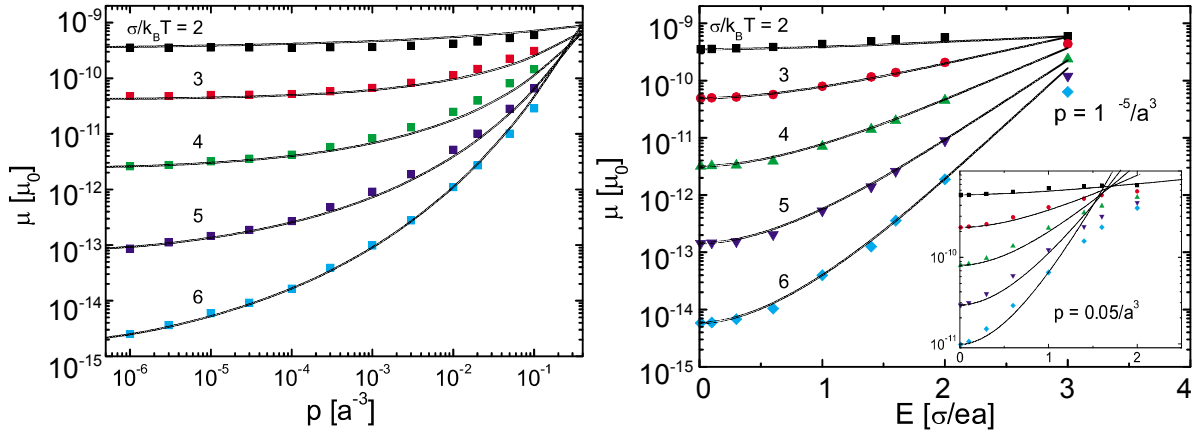


**Figure 2.14.:** Results from Pasveer et al.<sup>[156]</sup> at various temperatures - Left: Charge carrier density dependence of the mobility at vanishing field. Right: Field dependence of the mobility for typical densities in OLEDs (low, main) and OFETs (high, inset). Numerical results of the master equation (symbols) are fitted (lines) according to the parametrization given in Eq. (2.25).

### 2.2.3. Theories on the Transport Level

**Introduction.** The treatment of charge carrier motion in organic semiconductors in the frame of a defined transport level is beneficial since it allows for a straight-forward transcription of well established inorganic semiconductor physics. Adapting the multiple trapping model with its sharp mobility edge, it has been suggested that charge carrier transport happens via states of high  $\mu$ . Localized states below a threshold energy, i.e. the transport level  $E_{Tr}$ , trap charge carriers. Consequently, they require an activation energy to take part in transport again.<sup>[146,148]</sup> Herein, the position of  $E_{Tr}$  will show itself to be dependent on the assumed DOS distribution (exponential or Gaussian), determining the residence of the charge carriers.

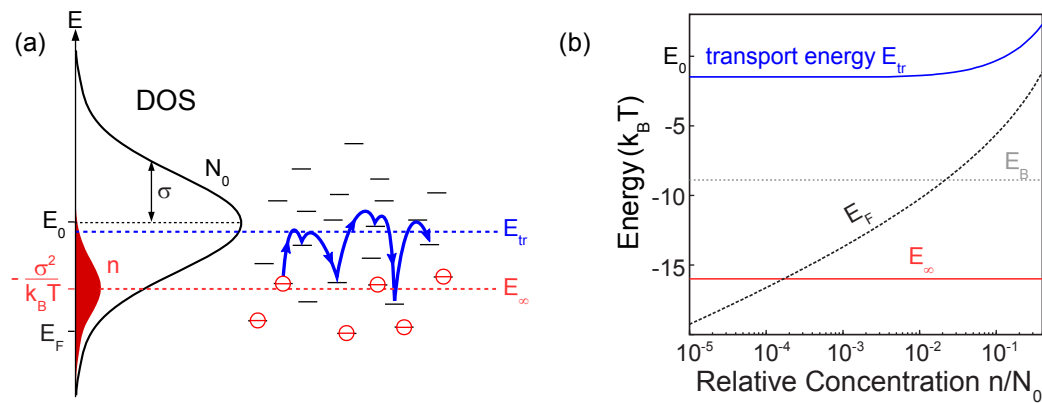


**Figure 2.15.:** (a) Charge carrier transport in a Gaussian DOS, where the charge carriers reside around the equilibrium energy  $E_{\infty} = E_0 - \sigma^2/k_B T$  and move at the transport energy  $E_{Tr}$ . (b) Upon partial filling of the DOS,  $E_{Tr}$  remains constant for concentrations up to  $n/N_0 \approx 0.05$ .<sup>[161]</sup> The positions of  $E_F$ ,  $E_{\infty}$  and  $E_B \approx E_0 - (5/9)\sigma^2/k_B T$  are plotted for  $\sigma/k_B T = 4$  and  $N_0\gamma^3 = 0.01$ .

**Early Approaches.** Since Bässler *et al.* found that a charge carrier resides at an equilibrium energy of  $E_\infty = E_0 - \sigma^2/k_B T$  within the tail of a Gaussian DOS (cf. Fig. 2.15), it is natural to estimate the transport level from the temperature dependence of the low-field mobility as<sup>[156]</sup>

$$\mu \propto \left[ -C \left( \frac{\sigma}{k_B T} \right)^2 \right] \quad (2.30)$$

where  $C$  is a numerical constant close to  $4/9$ . In this context, it was claimed that the transport to happen at  $E_B \approx E_0 - (5/9) \sigma^2/k_B T$ .<sup>[160]</sup> However, it has been argued that charge carriers are distributed in the range of  $\sigma$  around  $E_\infty$  which should be reflected in the hopping rates and  $E_{Tr}$ .<sup>[119]</sup>

Although much effort was put into this topic, the exact position and the interpretation of such a transport level is still controversially debated. A first analytical approach was suggested by Schönherr *et al.*<sup>[162]</sup>, who solved the percolation problem assuming only nearest-neighbor-hopping (NNH) for a Gaussian DOS. They define the transport level as energy  $E_{crit}$  of sites conducting the most current once a critical (percolation) path is formed through the medium, i.e.

$$\int_{-\infty}^{E_{crit}} g(E) dE = c_p. \quad (2.31)$$

For the three-dimensional simple cubic lattice, the critical concentration for percolation is  $c_p = 0.31$ , hence  $E_{crit} - E_0 \approx -0.6\sigma$ . Similar results were recently published by Cottaar *et al.* who in addition addressed the strong dependency of the critical energy on the lattice formation (i.e.  $E_{crit,sc} - E_0 = -0.49\sigma$  and  $E_{crit,fcc} - E_0 = -0.84\sigma$ ).<sup>[163]</sup> Despite detailed derivations for different DOS types are found in literature<sup>[142,145,164]</sup>, it has been argued that percolation description is not suitable for finding the real transport energy in disordered systems.<sup>[119]</sup> Charge transport involves spatial propagation of the charge carriers, hence it should always be equally described by activation to an elevated energy and tunneling to sites further apart (cf. Sec. 2.2.2).

**Arkhipov's Theory.** Considering a spatially random distribution of sites in a steep density of states ( $\partial g(E)/\partial E \sim 10^{-4}$ ), Arkhipov *et al.* derived from the number of possible shallower hopping sites the most probable jump-to-energy  $E_j$  as<sup>[165–169]</sup>

$$\int_{-\infty}^{E_j} g(E) (E - E_j)^3 dE = \frac{6}{\pi} (\gamma k_B T)^3. \quad (2.32)$$

This result is obtained disregarding backward carrier jumps into starting sites, which do not contribute to spacial hopping transport, but end up in charge carrier oscillation. In case of allowing backward carrier jumps, an increased number of short range hopping events is observed in charge carrier transport simulations.<sup>[119,170]</sup> Hence it has been argued that the most frequently visited energy  $E_j$  is not completely identical to the transport level.<sup>[119,171]</sup> However, after an upward jump over the inter-site distance  $r$ , a charge carrier will not return to the initial site if there is another hopping neighbor of the targeted site with a smaller hopping parameter  $2\gamma r$  outside the sphere of radius  $r$  centered at the starting site.<sup>[165]</sup> The average number of such



neighboring sites  $n_b(E_i, r)$  has been calculated by Arkhipov *et al.* as

$$\begin{aligned}
 n_b(E_i, r) &= 2\pi \int_0^r dr' r'^2 \int_{\arccos(r'/2r)}^\pi d\theta \sin \theta \int_{-\infty}^{E_i + 2\gamma k_B T(r-r')} g(E) dE \\
 &= \frac{\pi r^3}{12} \left\{ 11 \int_{-\infty}^{E_i} g(E) dE \right. \\
 &\quad \left. + \int_{E_i}^{E_i + 2\gamma k_B T \gamma r} g(E) dE \left[ 8 \left( 1 - \frac{E - E_i}{2\gamma k_B T \gamma r} \right) \right. \right. \\
 &\quad \left. \left. + 3 \left( 1 - \frac{E - E_i}{2\gamma k_B T \gamma r} \right)^4 \right] \right\}.
 \end{aligned} \tag{2.33}$$

It increases in a DOS  $g(E)$  with increasing both initial energy  $E_i$  and spacial distance  $r$ . Basically, Eq. (2.33) summarizes all target sites which are reachable from a site energy  $E_i$ . Down- or backward jumps happen without any energy restriction to sites of an energy lower than  $E_i$  (c.f. first integral in second equation). The inverse charge carrier localization length  $\gamma$  and the thermal energy  $k_B T$  in the system define the 'action radius'  $2\gamma k_B T r$  around the site energy  $E_i$ . Within this sphere, a number of neighboring sites are reachable via upward jumps (c.f. second integral in second equation). The probability  $\lambda(E_i, r)$  that the site of energy  $E_i$  has at least one hopping neighbor of a hopping parameter smaller than  $2\gamma r$  is determined by the Poisson distribution:<sup>[165]</sup>

$$\lambda(E_i, r) = 1 - \exp[-n_b(E_i, r)]. \tag{2.34}$$

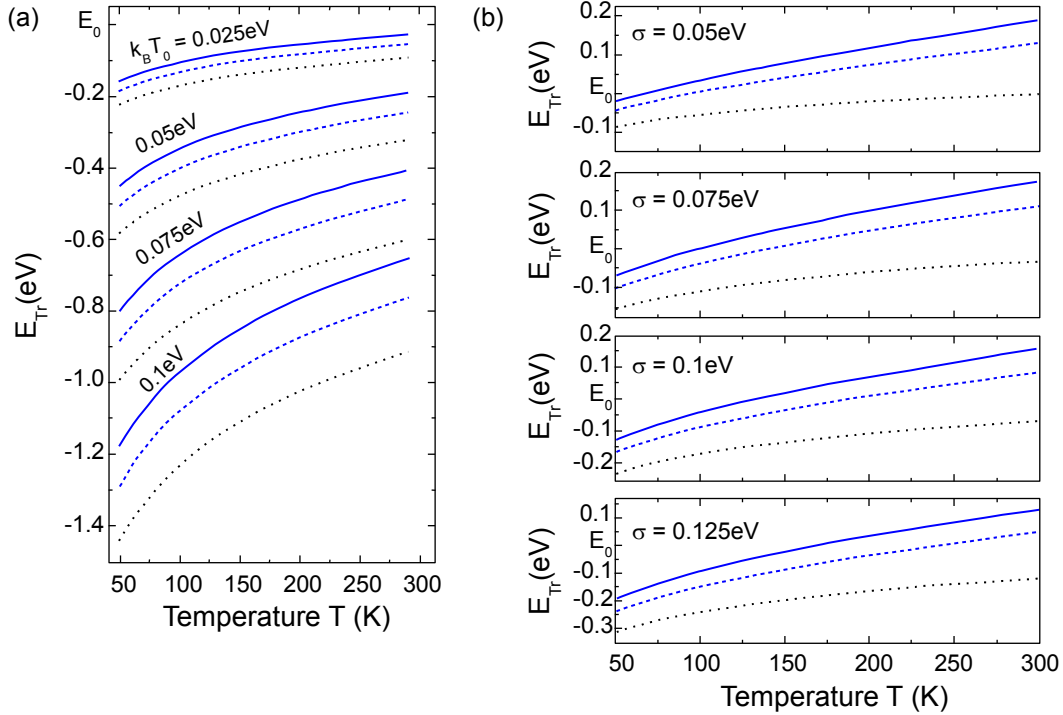


**Figure 2.16.:** Temperature dependence of the effective transport level (solid lines) and the energy of most probable jumps (dashed lines) in a disordered system as reported by Arkhipov<sup>[165]</sup> with (a) exponential DOS ( $\gamma=1\text{nm}^{-1}$ ,  $g_0=10^{23}\text{cm}^{-3}\text{eV}^{-1}$ ) and (b) Gaussian DOS ( $\gamma=10\text{nm}^{-1}$ ,  $N_0=10^{22}\text{cm}^{-3}\text{eV}^{-1}$ ). For comparison, the most targeted energy by VRH is shown (dotted lines).

Considering only upward jumps to target sites from which a jump back to the starting site is improbable, Arkhipov *et al.* derived an alternative description of the transport energy  $E_{Tr}$  using Eq. (2.33) and Eq. (2.34) to<sup>[165]</sup>

$$\int_{-\infty}^{E_{Tr}} g(E) dE \int_0^{(E_{Tr}-E)/2\gamma k_B T} r^2 \{1 - \exp[-n_b(E, r)]\} dr = \frac{1}{4\pi}. \quad (2.35)$$

The application of Eq. (2.32) and Eq. (2.35) to an exponential and a Gaussian DOS

$$g_\beta(E) = N_0 \exp\left(\frac{E - E_0}{k_B T_0}\right) \quad \text{and} \quad g_\sigma(E) = \frac{N_0}{\sqrt{2\pi}\sigma} \exp\left[-\frac{(E - E_\sigma)^2}{2\sigma^2}\right] \quad (2.36)$$

and the derived temperature dependencies are depicted in Fig. 2.16. They are compared to findings on most probable jumps from Mott's VRH theory<sup>[146,147]</sup>, i.e.

$$g(E_j) \left[ \int_{-\infty}^{E_j} g(E) dE \right]^{-4/3} = \frac{1}{k_B T} \left( \frac{9\pi}{2\gamma^3} \right)^{1/3}. \quad (2.37)$$

Although Eq. (2.37) predicts a deeper level of most probable carrier jumps, its temperature dependence mimics that of both,  $E_{Tr}$  and  $E_j$  calculated by Arkhipov.<sup>[165]</sup> The offsets increase with larger disorder  $T_0$ , but remain typically less than 0.2 eV around room temperature. For low temperatures (low thermal energy), the charge carrier hopping happens deep in the exponential tail with reduced mobility.<sup>[172]</sup> This explanation holds true for a Gaussian DOS (cf. Fig. 2.16 (b)), although the temperature dependencies deviate more strongly. The crossing of  $E_0$  at certain temperatures, however, seems unreasonable and is considered to be an artifact of the tunneling contribution.<sup>[165,172]</sup> Since the DOS further away from the center  $E_0$  is low and decreases steeply, most charge carriers are expected to hop around  $E_{tr,RT} \approx E_0$  for RT.

Considering partial filling of the DOS, the transport level has been reported to be stable up to concentrations of  $n/N_0 \approx 0.05$ .<sup>[161]</sup> Charge carriers are able to hop to a sufficient number of states close-by in energy to propagate through the system.<sup>[147,148]</sup> Only for elevated densities  $n$  (i.e.  $E_F$  exceeding the equilibrium position  $E_\infty$  of a charge carrier in a DOS by significant extent), the transport level increases towards  $E_0$  where more empty sites exist (cf. Fig. 2.15 (b)).<sup>[161,167]</sup>

**Recent Advances.** An interesting approach towards finding the transport energy has lately been suggested by Oelerich *et al.*<sup>[119]</sup> Assuming a Gaussian DOS, they solve the hopping problem for the NNH regime after removing small slices of the DOS ( $\varepsilon_{crit} \pm \Delta E$ ) leaving those parts inaccessible during charge transport (cf. Fig. 2.17). Depending on how important the withdrawn sites are, i.e. close to  $E_{Tr}$ , the cutting more or less severely effects the mobility of the system. At room temperature, a strong drop of  $\mu$  is observed close to the DOS center  $E_0$  indicating the position of the transport level. For decreased temperatures,  $E_{Tr}$  shifts towards lower energies. Note that cuts close to the equilibrium energy  $E_\infty$  force some charge carriers to populate sites of higher energy and slightly increase the mobility due to less required activation energy.

As shown, the transport level depends significantly on temperature and disorder parameters of the organic thin-films, a fact that has to be considered in further parts of this work. Only linking structural properties and predictive transport theories allows for a correct description of the energetic landscape, i.e. intra-gap states which are mainly addressed in the thesis.

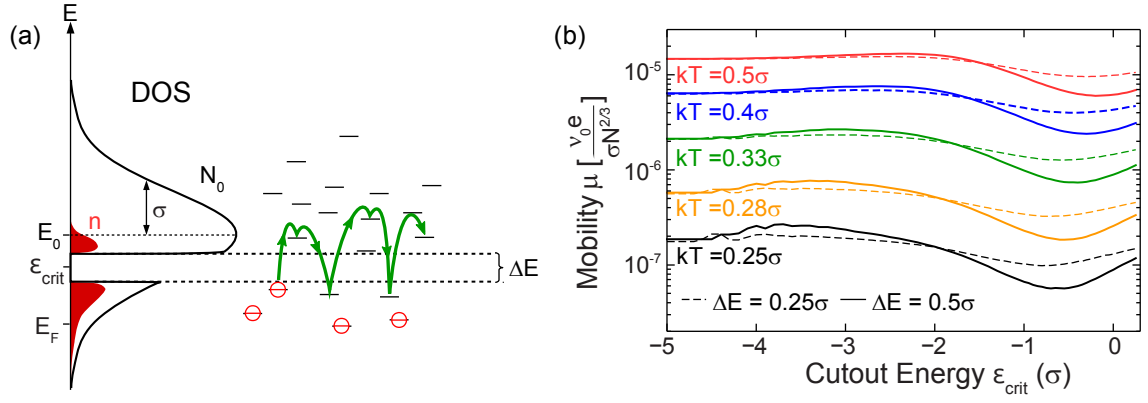


**Figure 2.17.:** (a) Modified Gaussian DOS after Oelerich et al. with sites cut within  $\Delta E$  around  $\varepsilon_{crit}$  that are inaccessible for charge carrier transport. (b) Calculated hopping mobility for cut systems and different temperatures  $k_B T$ . Larger cuts close to the transport energy  $E_{Tr}$  show a stronger drop in  $\mu$  as transport relevant sites are eliminated (redrawn after Ref. <sup>[119]</sup>).



# Molecular Doping

*Key to the experimental parts of this thesis, the fundamentals of molecular doping are discussed. Following an introduction of the technical concept and a short overview on common molecular doping compounds, prevailing theories on the microscopic charge transfer are summarized. Within a classical semiconductor approach, the difference between deep and shallow dopant states and its implication on the Fermi level position are described. The chapter ends with a summary of major theoretical and experimental studies in the field of molecular doping, and examples of the application of the doping technique in organic optoelectronic devices.*

## 3.1. Terms and Defintions of Molecular Doping

Due to strong localization (hence low mobilities  $\mu$ ) and low intrinsic free charge carrier concentrations  $n, p$  organic semiconductors exhibit only low conductivities

$$\sigma = e \cdot n, p \cdot \mu. \quad (3.1)$$

The number of intrinsic charge carriers in a classical semiconductor, i.e. those created via thermal generation across the energy gap  $E_g$ , is

$$n_i \cdot p_i = n_i^2 = N_C \cdot N_V \exp\left(-\frac{E_g}{k_B T}\right), \quad (3.2)$$

where  $N_C$  and  $N_V$  are the density of states at the conduction band and the valence band. Assuming  $N_C = N_V \approx 10^{20} \text{ cm}^{-3}$ , organic semiconductors exhibit intrinsic charge carrier densities  $p_i = 10^3 \dots 10^7 \text{ cm}^{-3}$  due to the larger  $E_g$  as compared to inorganic semiconductors, e.g. GaAs with  $E_g = 1.42 \text{ eV}$ .<sup>[47]</sup> Measured free charge carrier concentrations differ between  $p = 10^9 \dots 10^{14} \text{ cm}^{-3}$  for small molecule semiconductors and  $p = 10^{15} \dots 10^{17} \text{ cm}^{-3}$  for  $\pi$ -conjugated polymers, mostly risen from electro-active impurities and structural defects that form intra-gap states. However, these free charge carrier densities are not controllable in type and amount.

Excess charge carrier densities can only be created via: *i)* illumination *ii)* injection *iii)* field effect or *iv)* charge transfer from introduced dopant molecules to the host material. The latter requires a very well matched energy level alignment between both molecular species. As depicted in Fig. 3.1(a) in case of *p*-(*n*)-doping, the LUMO (HOMO) of the dopant has to lie energetically below (above) the HOMO (LUMO) of the host material. For efficient charge transfer, energy differences are typically found to be less than 0.5 eV.<sup>[174]</sup> Despite extensive research on this topic, a unified theory on the doping process is absent up to now.<sup>[91,175]</sup> While the idea of integer charge transfer has been more established in early work,<sup>[176,177]</sup> recently more hints are found supporting doping undergoing charge transfer hybrid formation.<sup>[178,179]</sup> After an introduction of important quantities of the doping technique and a brief review on widely used doping compounds, both theories of the doping process thus shall be presented in the following sections.

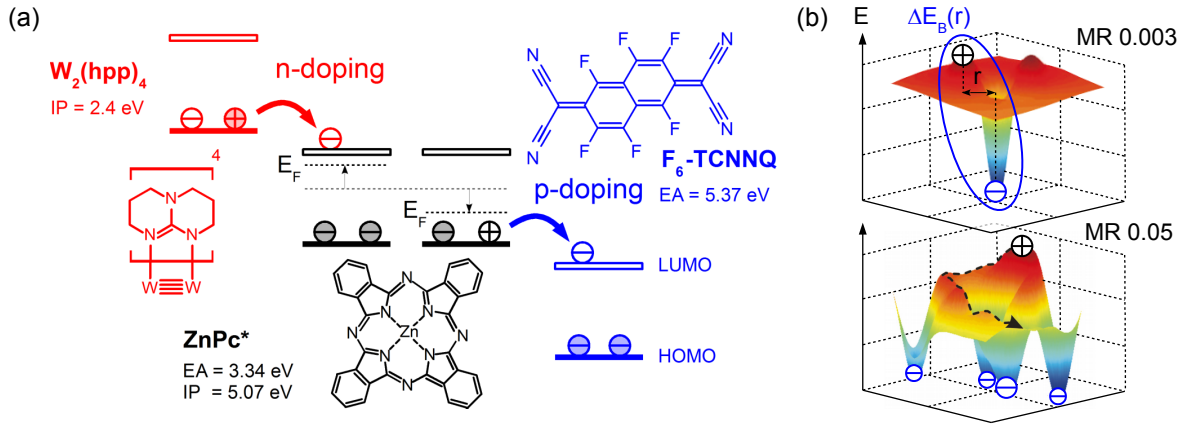


**Figure 3.1.:** (a) Principle of n/p-doping, here shown for zinc-phthalocyanine (\* respective energy values for thin-film aggregation on organic sublayer) with W<sub>2</sub>(hpp)<sub>4</sub> or F<sub>6</sub>-TCNNQ. Following the traditional integer charge transfer model, n(p)-type doping is provided by electron transfer from the HOMO of the dopant(host) to the LUMO of the host(dopant). (b) According energy landscape in a host:dopant system at different doping concentrations as calculated by Mityashin et al. for P5:F<sub>4</sub>-TCNQ.<sup>[173]</sup> At higher MR and thus higher energetic disorder, the CT complex dissociation probability is increased.

### Quantities and Units of Doping Concentration

Mainly related to higher defect densities, doping concentrations in organic semiconductors commonly exceed the ppm<sup>1</sup> range known from inorganic semiconductors, especially in case of highly purified single-crystalline semiconductors. Most essential is the molar doping ratio MR as it defines the ratio of dopant  $n_D$  and host molecules  $n_H$  in a mixed film. The doping concentration  $c_n$  on the other hand states on the number of dopants relative to the overall number of molecules within the film, i.e.

$$\text{MR} = \frac{n_D}{n_H}, \quad c_n [\text{mol}\%] = 100\% \cdot \frac{n_D}{n_D + n_H}, \quad c_n = 100\% \cdot \frac{\text{MR}}{\text{MR} + 1}. \quad (3.3)$$

Originating from the detection of evaporated masses during thin-film preparation with quartz crystal microbalances in vacuum, another representation is commonly used. The weight ratio WR defines the deposited dopant mass  $m_D$  per deposited host mass  $m_H$ . Likewise, the mass doping concentration is the dopant mass divided by the overall film mass, i.e.

$$\text{WR} = \frac{m_D}{m_H}, \quad c_m [\text{wt}\%] = 100\% \cdot \frac{m_D}{m_D + m_H}, \quad c_m = 100\% \cdot \frac{\text{WR}}{\text{WR} + 1}. \quad (3.4)$$

Using the molar masses  $M_i$  with  $m_i = n_i \cdot M_i \cdot V_i$  both representation types can be translated into each other following

$$\text{WR} = \text{MR} \cdot \frac{M_D}{M_H}. \quad (3.5)$$

Charge transport layers in modern applications like OLEDs or OSCs exhibit doping concentrations of a few weight percent to ensure very thin depletion zones and ohmic contacts. In this thesis, however, reasonably large depletion zones at MR  $10^{-2}$  and below<sup>[180–183]</sup> are exploited to study charge carrier traps and the doping process itself.

<sup>1</sup>parts per million

### Dopant Compounds for Small Molecule Semiconductors

Early attempts to dope organic semiconductors often utilized strongly oxidizing gases, e.g. iodine or bromine, where one achieves high conductivities for materials such as phthalocyanines or polymers like polypyrrole.<sup>[184–188]</sup> A main drawback is the small size of such dopants as they show a high tendency to diffuse leaving it impossible to form long-term stable doped layers. More frequently used, electron donating alkali metal atoms like (fluorinated)<sup>[189]</sup> lithium<sup>[190]</sup> (complexes)<sup>[191]</sup> or cesium<sup>[192,193]</sup> suffer from the same issue. Despite being deposited as thin interfacial layer, e.g. Parthasarathy reports on strong diffusion of Li into bulk layers of CuPc, BCP, or Alq<sub>3</sub> of up to 100 nm<sup>[194]</sup> which causes exciton quenching and reduced lifetimes in devices like OLEDs or OSCs.<sup>[195,196]</sup> Moreover, such n-doping, e.g. of Bphen with Cs,<sup>[108,193]</sup> requires high concentrations, at the same time adding a large number of ionized metal cores, i.e. deep Coulomb traps. Hence, alkali metals are increasingly replaced by molecular dopants recently.

Molecular p-doping has been reported in the last decades, employing organic acceptor materials such as ortho-chloranil,<sup>[197]</sup> tetracyano-quinodimethane (TCNQ),<sup>[198]</sup> and dicyano-dichloro-quinone (DDQ)<sup>[199]</sup> for phthalocyanines or oligothiophenes. However, their dopant strength has been limited, e.g. for TCNQ with an electron affinity of only  $EA = 4.5$  eV.<sup>[175]</sup> Fluorinated derivatives drastically improved the potency. Consequently, F<sub>4</sub>-TCNQ shows  $EA = 5.24$  eV<sup>[200]</sup> and became a standard dopant for many HTL<sup>2</sup> materials, e.g. (MeO)-TPD,<sup>[201,202]</sup>  $\alpha$ -NPD,<sup>[203]</sup> m-MTDATA,<sup>[204]</sup> and various phthalocyanines.<sup>[107,200,205,206]</sup> Advancements in chemical synthesis of dopants within the last years spawned today's state-of-the-art acceptor materials F<sub>6</sub>-TCNNQ<sup>[128,182,183,207]</sup> and the fluorinated buckminster fullerene C<sub>60</sub>F<sub>36</sub>.<sup>[182,183,208]</sup> Both exhibit a high molar mass, allowing for controlled lower doping, and do not show the low vapor pressure of F<sub>4</sub>-TCNQ causing contamination of evaporation chambers. Recently, large band gap transition metal oxides such as molybdenum trioxide MoO<sub>3</sub>,<sup>[209–212]</sup> tungsten oxide WO<sub>3</sub>,<sup>[213]</sup> and rhenium oxide ReO<sub>3</sub><sup>[214]</sup> have been reported as possible dopant candidates in organic devices. Due to their large electron affinity, they are able to p-dope even host with high IP, e.g. CPB<sup>3</sup> (IP= 6.23 eV) doped by MoO<sub>3</sub> (EA= 6.7 eV).<sup>[209]</sup> A main drawback herein are the commonly required doping concentrations of 20...50 mol%<sup>[212,213]</sup> to reach sufficient conductivity values, creating a large amount of Coulomb traps by the dopant species<sup>[209,215]</sup> and limiting the doping efficiencies to few percent.<sup>[209–211,215]</sup>

N-doping of organic semiconductors using molecular dopants is much more challenging. The dopants must feature high lying HOMO levels to ensure efficient charge carrier transport to the LUMO levels of the host. Typical hosts materials feature electron affinities in the range of 3 eV.<sup>[107,175]</sup> This fact renders most of the pure dopants prone to oxidation in air and demands for special storage and treatment, e.g. in case of the potent W<sub>2</sub>(hpp)<sub>4</sub> and Cr<sub>2</sub>(hpp)<sub>4</sub><sup>[216–218]</sup> which lead to conductivities of up to 4 S/cm in C<sub>60</sub> films.<sup>[130,219]</sup> Due to a self-passivation effect lately reported by Tietze *et al.*, the mixed films retain a conductivity in air up to a factor of 1/3 (after heating in vacuum).<sup>[220]</sup> However, another possibility to circumvent the air instability of the pure dopants is the use of air-stable precursor molecules. For this concept introduced by Werner, in their case n-doping NTCDA with pyrodine B,<sup>[221,222]</sup> donors are provided *in situ* by activation of stable precursors via thermal energy or illumination (e.g. AOB doped C<sub>60</sub>)<sup>[223,224]</sup> during or after evaporation of the mixed film. Further, the mechanism of splitting a less reactive dimer molecule in two radical monomers donating electrons to the host is commonly exploited.<sup>[224–226]</sup>

Despite manifold realizations of doping compounds, their working principle in the host matrix is still under debate and is discussed in the following.

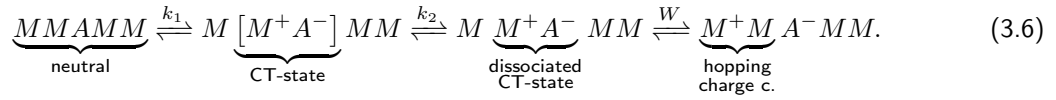
<sup>2</sup>hole transport layer

<sup>3</sup>4,4'-bis(N-carbazolyl)-1,1'-biphenyl

## 3.2. Prevailing Theories on Charge Transfer in Host:Dopant Systems

### 3.2.1. Integer Charge Transfer Model

Commonly, doping is considered as two-step process:<sup>[227,228]</sup> first, for *p*-doping electrons are transferred from the matrix molecule *M* to an acceptor molecule *A* incorporated in the system and a charge transfer (CT) complex  $[M^+A^-]$  is formed.<sup>[229]</sup> Secondly,  $[M^+A^-]$  dissociates. Both processes are balanced by the reaction constants  $k_1$  and  $k_2$  which indicate, whether the equilibrium state is on the respective left or right of the equation. The eventually created positive charge + moves away from the ionized acceptor  $A^-$  along the matrix *M* as



While the eventually yielded free charge carriers hop in the DOS with the jump probability *W* as discussed in Sec. 2.2.2, their generation can be estimated by the law of mass action as<sup>[91]</sup>

$$\eta = \frac{N_{M^+} N_{A^-}}{N_M N_A} = \exp\left(\frac{-\Delta E}{k_B T}\right). \quad (3.7)$$

The number densities of the molecular species *i* are given as  $N_i$  and  $\eta$  accounts for the balance of the two-step reaction in Eq. (3.6), hence the efficiency of the doping process. Typically, the equilibrium constant  $\eta = k_1 \cdot k_2$  shows low values of a few percent<sup>[132,207,230]</sup>, thus the reaction balance is shifted to the left site, although the probability of charge transfer (i.e.  $k_1$ ) is close to unity<sup>[107]</sup> (assuming perfect intermixing of matrix and dopant, i.e. no clustered dopants).

The limiting factor for  $\eta$  is the dissociation barrier. The CT complex has to overcome it, as it is caused by the Coulomb attraction of generated charge carrier and ionized dopant molecule. The binding energy  $\Delta E_B$  of the CT complex can be estimated as

$$\Delta E_B(r) = \frac{1}{4\pi\epsilon_0} \frac{e}{r^2} + P_{e-h}(r) - (P_e + P_h) \simeq \frac{1}{4\pi\epsilon_0\epsilon_r} \frac{e}{r^2} \quad (3.8)$$

with the energy  $P_{e-h}$  gained by the CT complex upon polarization of its surroundings and the polarization values  $P_{e,h}$  for a free pair of electron and hole. Similarly, the binding energy can be approximated by Coulomb interaction of two point charges separated by the distance *r* in the system with the dielectric constant  $\epsilon_r$ . Common values of  $\epsilon_r \approx 3$  and an inter-molecular distance of  $r \simeq 1$  nm result in  $\Delta E_B = 0.5$  eV that exceeds by far  $k_B T = 0.025$  eV at room temperature. The assumption of a thermal Boltzmann activation  $\exp(-\Delta E_B/k_B T)$  hence could explain why only a small fraction of CT states dissociates. Nevertheless, this simple picture neither considers polaronic effects due to the many-body interaction of free charge carriers and ionized dopants<sup>[173]</sup> nor the net energy gain of the electron/hole upon charge transfer in the host:dopant system, which could possibly support the CT state dissociation. In this context, Mityashin *et al.* report on an strong increase of the dissociation probability hence doping efficiency with higher MR in F<sub>4</sub>-TCNQ doped pentacene.<sup>[173,231]</sup> Infringing a threshold concentration of dopants, stronger energetic disorder creates more percolation paths supporting hole jumps further apart from the ionized acceptor molecule (cf. Fig. 3.1(b)).



### 3.2.2. Intermolecular Hybridization

In contrast to the 'traditional' CT state picture, the group of Norbert Koch proposed a hybridization model for the doping process.<sup>[178,232–234]</sup> Motivated by observations of polaronic sub gap states via UPS in doped thiophene systems,<sup>[235,236]</sup> they propose hybridization of overlapping host and dopant orbitals. The generation of a free charge carrier is hence considered a process involving three molecules. Sketched in Fig. 3.2, the HOMO of a host molecule and the LUMO of a dopant molecule form two hybrid orbitals at first. Both electrons from the former host HOMO occupy the bonding orbital of the hybrid. In a second step, *p*-doping is gained by an upward hop of an electron from the HOMO of another host nearby, thus leaving free hole in the host matrix.<sup>[178]</sup>

The poor occupation of the sub gap hybrid orbitals obeys Fermi-Dirac statistics thus gives an explanation for low doping efficiencies.<sup>[178]</sup> The activation energy  $E_A$  for the charge transfer is governed by the energy splitting of the hybrid states. For maximized doping efficiencies  $\eta$ , the host HOMO and the dopant LUMO need to match as closely as possible. A large inter-molecular orbital overlap  $S$ <sup>[237]</sup> is however disadvantageous<sup>[233]</sup> since it increases the energy splitting. In experiment, alkylated benzothieno-benzothiophene (HOMO  $\approx 5.7$ ) *p*-doped with tetracyanoquinodimethane at different fluorination stages, i.e. F<sub>*n*</sub>-TCNQ (*n* = {0, 1, 2, 4}) and F<sub>6</sub>-TCNNQ shows such trends. GIXRD<sup>4</sup> measurements hint on similar aggregation of dopants in the mixed thin-films (i.e.  $S$  is expected to remain unchanged) with increasing fluorination of the dopant. In contrast to neat films, additional sub gap absorption features arise in UV/Vis, attributed to formed hybrid states. With deeper lying LUMO = -4.23 ... -5.36 eV of the dopants, the found transitions from bonding (HOMO) to anti-bonding orbital (LUMO) and HOMO-1 to LUMO of the hybrid shift equally to lower energies, indicating a smaller energy split with larger EA of the dopant.<sup>[234]</sup>

Measurements of the doping efficiency  $\eta$  directly proving the theory are, however, missing up to now. Nevertheless, the reported increase in IP in blends up to 1:1 of F<sub>4</sub>-TCNQ and pentacene respectively  $\alpha$ -sexithiophene supports the hybrid model (an intermixing of host and hybrid signal is assumed).<sup>[178]</sup> The calculated activation energy  $E_A$  of several 100 meV for the charge transition to the hybrid LUMO in P5:F<sub>4</sub>-TCNQ qualitatively agrees with the reported low doping efficiencies.<sup>[173]</sup>

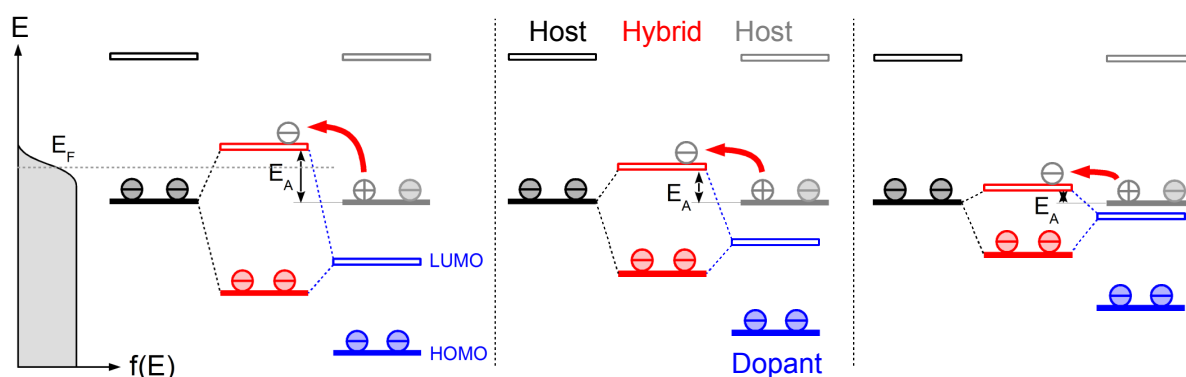


**Figure 3.2.:** Formation of hybrid orbitals (red) due to overlap of molecular frontier orbitals, namely HOMO of a host molecule (black) and LUMO of a dopant (blue). In case of *p*-doping, an electron is transferred from the HOMO of another host (gray) to the unoccupied hybrid orbital. The activation energy  $E_A$  of this process is governed by the energy splitting (from left to right), while the occupation of the molecular levels obeys the Fermi-Dirac distribution.

<sup>4</sup>grazing incidence X-ray diffraction

### 3.2.3. Classical Semiconductor Approach with Effective $E_A$

Despite the prevailing inconsistencies concerning the charge transfer mechanism in doped systems, recently Tietze *et al.* introduced an adequate model to explain Fermi level shifts upon doping of various host systems over a wide range of doping concentrations.<sup>[181,183,207]</sup> They utilize a classical semiconductor approach, where doping occurs via thermal activation from dopant levels in the energy gap to the edges of conduction or valence band ( $E_C$  and  $E_V$ ). The equilibrium condition for all states obeys Fermi-Dirac statistics

$$f(E, E_F) = \frac{1}{1 + \exp\left(\frac{E - E_F}{k_B T}\right)}, \quad (3.9)$$

with the occupation probability  $f(E, E_F)$  for electrons at site energies  $E$  in a system with the electro-chemical potential at the position of the Fermi Level  $E_F$ . Consequently, the occupation of a (single) acceptor level  $E_A$  in case of p-doping shows as

$$N_A^- = \frac{N_A}{1 + \exp\left(\frac{E_A - E_F}{k_B T}\right)}. \quad (3.10)$$

Here,  $N_A^-$  represents the number of ionized acceptors, i.e. those undergoing charge transfer, and  $N_A$  is the overall number of sites at  $E_A$ . The assumption of a discrete acceptor level is however strongly idealized, since (especially in case of organic semiconductors) DOS distributions are broadened and of rather complex shape. The number of occupied states for any distribution of states is defined by the respective Fermi-Dirac integral, e.g. for the number of free holes in the valence band with typically  $g_V(E) \propto \sqrt{E - E_V}$  as

$$p = \int_{-\infty}^{+\infty} dE g_V(E) [1 - f(E, E_F)]. \quad (3.11)$$

The notation  $[1 - f(E, E_F)]$  is mandatory since the occupation of states with holes means the absence of electrons. Using Boltzmann approximation  $E - E_V \gg k_B T$ , the Fermi-Dirac integral yields

$$p = N_V \exp\left(\frac{E_V - E_F}{k_B T}\right) \quad (3.12)$$

with  $N_V$  as effective density of states at the valence band edge  $E_V$ . The number of free holes  $p$ , satisfying the charge neutrality equation  $p = N_A^-$  determines the position of the Fermi level with respect to the transport edge. Increasing the amount of  $N_A$  thus  $p$  shifts  $E_F$  closer towards  $E_V$ . In general, classical semiconductor theory distinguishes between two extreme cases: shallow and deep dopant states. Both are illustrated in Fig. 3.3(a).

**Shallow Dopant States.** For shallow dopants, the Fermi level lies energetically above the impurity level  $E_A$ , independent on doping concentration or temperature. Hence all the dopant molecules are ionized at all times, i.e.  $p = N_A^- = N_A$  and adding more dopants  $N_A$  linearly increases the number of free charge carriers  $p$ . In direct consequence, the Fermi level shift towards the band edge as

$$E_F(T) = E_V - k_B T \ln \frac{N_A}{N_V}. \quad (3.13)$$

**Deep Dopant States.** In case of deep dopant states, the Fermi level is situated between  $E_A$  and  $E_V$  thus according to Eq. (3.10) only a fraction of  $N_A$  is ionized. The activation energy  $\Delta E_p$  towards the valence band edge is given by

$$\Delta E_p = \frac{E_A - E_V}{2}, \quad (3.14)$$

and the number of free charge carriers is calculated similarly to Eq. (3.11) as

$$p \simeq \sqrt{N_A N_V} \exp\left(-\frac{\Delta E_p}{k_B T}\right). \quad (3.15)$$

The shift of the Fermi level with the logarithm of the number of acceptor molecules from Eq. (3.13) is reduced by a factor of two as

$$E_F(T) = \frac{E_A + E_V}{2} - k_B T \ln \frac{N_A}{N_V}. \quad (3.16)$$

Obviously, the presence of such deep states  $N_A$  pins the Fermi level as positions closer than  $(E_A + E_V)/2$  to  $E_V$  are not reachable. Nevertheless, the number of free charge carriers  $p$  at the valence band edge is equal for all distinct positions of  $E_F$ .

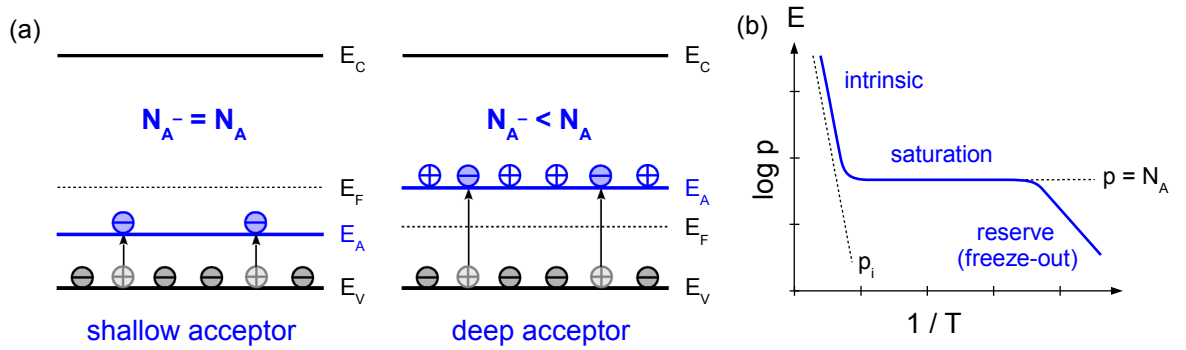


**Figure 3.3.:** (a) Energy levels in context of classical semiconductor theory for a p-doped semiconductor with either shallow or deep acceptor level  $E_A$ . (b) Corresponding plot of free hole density  $p$  versus  $1/T$  at fixed acceptor concentration  $N_A$  featuring dopant reserve, saturation, and intrinsic temperature regime (redrawn after<sup>[91]</sup>).

The impurity depth, i.e. shallow or deep, only affects the number of required acceptor molecule to shift the Fermi level to same positions. For a fixed dopant density  $N_A$ , impurity levels can appear as either shallow or deep distributions, dependent on the actual temperature  $T$ . With decreasing  $T$ , the Fermi-Dirac statistics sharpens and less thermal activation energy is provided. At a certain temperature,  $E_F$  intersects with  $E_A$  which marks the transition to deep state behavior ( $N_A^- < N_A$ ). Following Fig. 3.3(b), this regime is called *impurity reserve* or, attributed to the decrease of active dopants, *freeze-out*. In contrast, increasing  $T$  yield more active dopants, eventually reaching  $p = N_A^- = N_A$ , entering the *dopant saturation* regime. For sake of completeness since generally not observed in organic semiconductors, the intrinsic charge carrier concentration in Eq. (3.2) exceeds  $p$  introduced by doping at very elevated temperatures. However, a transition between dopant saturation and dopant reserve can be forced at fixed temperature by manipulating the Fermi-Dirac statistics upon introduction of a large number of  $N_A$ .<sup>[91]</sup> This established statistical model has been shown to be applicable for a series of organic host:dopant systems, e.g. describing p-doping in MeO-TPD:C<sub>60</sub>F<sub>36</sub><sup>[181,207]</sup> as well as n-doping in ZnPc:W<sub>2</sub>(hpp)<sub>4</sub>,<sup>[183]</sup> and allows for the quantification of inherent trap distributions at the same time.

In general, results show that the assumption of deep impurity levels is more suited for organic semiconductors at room temperature. Following Eq. (3.13), typical doping concentrations of  $N_A/N_V = 0.01$  would imply at most  $E_A = 120$  meV for dopant saturation, i.e.  $E_F = E_A$  and  $\eta = 100\%$ . Strong doping, e.g.  $N_A/N_V = 0.1$  would require an even shallower impurity level of  $E_A = 60$  meV to guarantee dopant saturation. As previously discussed, doping efficiencies are often limited to few (ten) percent and calculated CT state binding energies<sup>[238]</sup> / activation energies for hybrid charge transfer<sup>[234]</sup> in the range of a few 100 meV. Hence the formation of reasonably deep dopant states is most likely. The hopping nature of charge transport in organic semiconductors however might alter their exact depth level, especially since the transport level is found to be temperature dependent,<sup>[165,172]</sup> in contrast to classic inorganic semiconductors.

### 3.3. Literature Overview on Results in the Field of Doped Molecular Semiconductors

The mechanism of doping in organic semiconductors has been studied further quite extensively, utilizing conductivity,<sup>[130,177,202]</sup> photoelectron spectroscopy, Seebeck,<sup>[130,177]</sup> and IR spectroscopy measurements.<sup>[107]</sup> The main results will be successively presented to provide an overview on the state of knowledge. Conductivity studies can be done experimentally quite easily *in situ*, although they comprise ambiguous physics as

$$\sigma(N_A, T) = e \cdot p(N_A, T) \cdot \mu(p, T). \quad (3.17)$$

Often times, a superlinear increase of the conductivity with the doping concentration is observed, e.g. in case of MeO-TPD:F<sub>4</sub>-TCNQ (slope 1.85) or ZnPc:F<sub>4</sub>-TCNQ (1.6) (cf. Fig. 3.4(a)).<sup>[177,202]</sup> Even assuming shallow dopant states and impurity saturation  $p = N_A$  underestimates these results. Besides, linear<sup>[130,180,221]</sup> and sublinear<sup>[219]</sup> slopes are to be found as well as transitions to other regimes, e.g. in case of very low doping of C<sub>60</sub> with the reactive dimer [RuCp\*(mes)]<sub>2</sub>.<sup>[180]</sup> However, following Eq. (3.17), precise measurements of charge carrier density  $p$  and charge carrier mobility  $\mu$  are indispensable to conclude on reasons for the conductivity behavior.

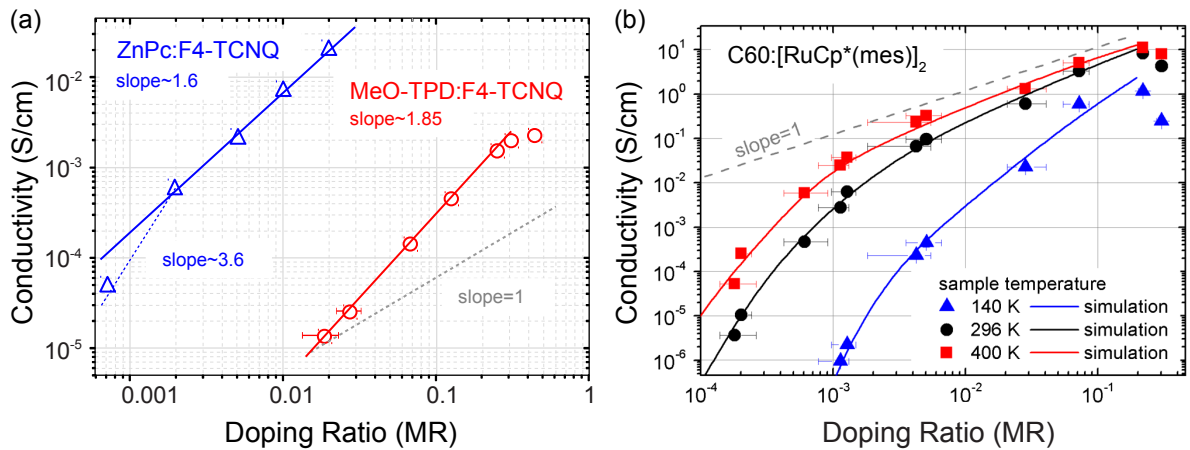


**Figure 3.4.:** (a) Thin-film conductivity versus concentration of dopant F<sub>4</sub>-TCNQ in MeO-TPD and ZnPc. In such experiments, for  $MR \simeq 0.01$  and above, typically a superlinear increase is seen (data taken from Ref. <sup>[177]</sup> and Ref. <sup>[202]</sup>). (b) Conductivity in C<sub>60</sub>:[RuCp\*(mes)]<sub>2</sub>. Merely expected to happen for p-doping but reported for n-doping: strong divergence from slope=1 attributed to incomplete trap filling at low MR and temperatures (redrawn from Ref. <sup>[180]</sup>).

One possibility to estimate  $p$  is via thermoelectric, i.e. Seebeck measurements. The Seebeck coefficient  $S$  corresponds to a thermo voltage  $U$  upon a temperature difference  $\Delta T$  within a semiconductor, defined as

$$S(T) = \lim_{\Delta T \rightarrow 0} \frac{U(T, \Delta T)}{\Delta T} \quad (3.18)$$

and equals the energetic distance of Fermi level and respective transport energy  $E_{Tr}$

$$S(T) = \frac{E_F(T) - E_{Tr}}{eT}. \quad (3.19)$$

This relation holds for band-transport with bandwidths  $\leq k_B T$  and hopping transport likewise. In combination with Eq. (3.12) it approximates the number of free holes as

$$p = N_{tr} \exp\left(-\frac{E_F(T) - E_{Tr}}{k_B T}\right) \simeq N_{tr} \exp\left(-\frac{e}{k_B} S(T)\right). \quad (3.20)$$

Seebeck coefficients  $S$  and derived hole densities  $p$  for  $F_4$ -TCNQ doped ZnPc are shown in Fig. 3.5(a), both indicating a shift of  $E_F$  closer to  $E_{Tr}$  for higher MR. The increase in  $p$  is however again strongly superlinear, rendering the assumption of deep dopant states, hence  $p \propto \sqrt{N_A}$ , wrong. This fact is supported by the temperature independence of the Seebeck energy (cf. Fig. 3.5 inset). Similar studies can be found in literature.<sup>[176,219]</sup> However, in case of VoPc<sup>5</sup> doped by  $F_4$ -TCNQ,  $S$  and with that  $p$  show themselves slightly temperature dependent ( $E_{act} \sim 0.1$  eV).<sup>[176]</sup> Nevertheless, the acceptor depth  $E_A$  is found to be smaller than  $E_F - E_{Tr}$  for all MR, supporting shallow state formation of the dopants.<sup>[176]</sup> From both rather contrary results it might be likely, that this host:dopant system finds itself close to the transition point of impurity saturation and reserve regime, i.e. shallow and deep dopants.

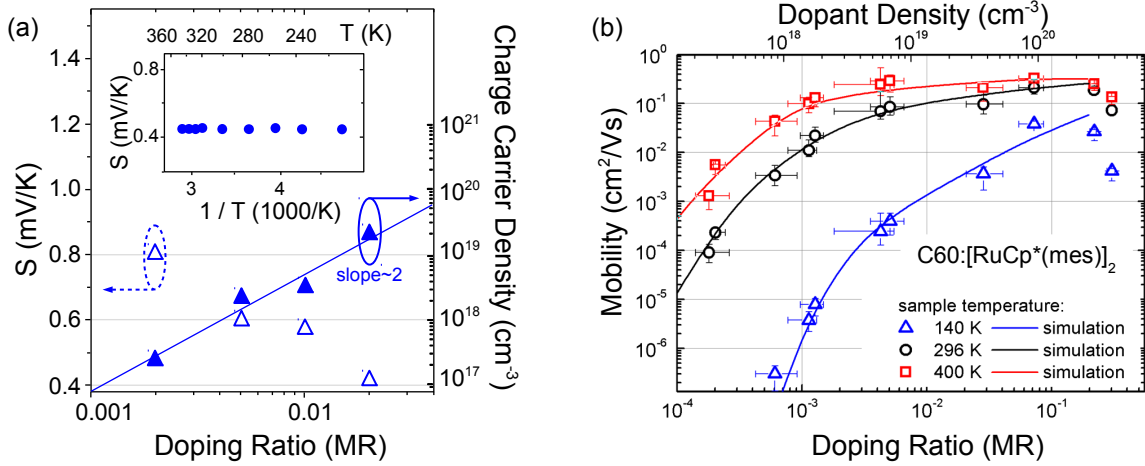


**Figure 3.5.:** (a) Seebeck coefficient  $S$  and deduced charge carrier density  $p$  versus molar doping ratio in ZnPc doped by  $F_4$ -TCNQ. Inset:  $S$  shows to be temperature independent, here for MR 0.02 (data taken from Ref.<sup>[177]</sup>). (b) Mobility in  $C_{60}$  upon trap filling deduced from the conductivity data shown in Fig. 3.4(b) using  $\mu_e = \sigma/en$  and  $n = N_D$ . The curves represent results of corresponding Monte Carlo simulations. (redrawn after Ref.<sup>[180]</sup>).

The superlinear increase of  $\sigma$  is still striking and in contradiction to the assumption of shallow states  $p \propto N_A$ . One possible explanation that has already been discussed in this thesis is the increasing CT state dissociation probability due to stronger energetic disorder thus more percolation pathways at higher amounts of doping molecules in the matrix.<sup>[173]</sup> Despite a qualitative agreement on the experimentally seen decrease of activation

<sup>5</sup>vanadyl-phthalocyanine

energy at higher MR<sup>[180,206,239,240]</sup>, still high conductivities of  $10^{-3}$  S/cm<sup>[128]</sup> and above as well as large doping efficiencies up to 0.98<sup>[182]</sup> are reported for the same or similar material systems whereat Mityashin *et al.* calculated a charge generation efficiency of zero (cf. Tab. 3.1).<sup>[173]</sup> A similar approach finds itself in accordance with experimental results in n-doped PPEEB<sup>6</sup> though, as the superlinear increase of  $\sigma$  with higher MR

$$\sigma = e\mu_e N_D \exp\left(-\frac{E_D}{k_B T}\right) \quad (3.21)$$

is governed by an activation energy  $E_D$

$$E_D = E_{D,max} - \beta N_D^{1/3} \quad (3.22)$$

with the electron donor density  $N_D$  at the donor level  $E_D$  ( $\simeq 0.3$  eV). The fit parameter  $\beta = 6.5 \times 10^{-8}$  eV cm is of the order  $e^2/4\pi\epsilon_0\epsilon_r$  and yields  $\epsilon_r = 7.2$  which is remarkably higher than for the undoped film ( $\epsilon_r = 4$ ). Gregg *et al.* explain their findings by an increase in polarizability of the organic films by the number of electrons in bound but delocalized states near dopant cations,<sup>[241]</sup> supporting CT state dissociation.

An advanced approach for the conductivity dependence has been suggested by Männig *et al.*, examining F<sub>4</sub>-TCNQ doped ZnPc, VoPc, and TDATA<sup>7</sup>.<sup>[206]</sup> They adapt the percolation description of transport in disordered organics by Vissenberg and Matters<sup>[142]</sup> who found an Arrhenius-type temperature activation  $\sigma \propto \exp(-E_A/k_B T)$  as well as a superlinear increase in conductivity  $\sigma \propto p^{T_0/T}$  (cf. Eq. (2.20) and Eq. (2.21)). An exponential DOS with  $T_0$  in the range of 450...520 K and only the assumption of shallow dopant states ( $E_A = 0.18...0.34$  eV) allows to reproduce conductivity and field effect mobility measurements over a range of doping ratios (MR 0.002...0.02) and temperatures (160...360 K). The activation energy  $E_A$  is again found to decrease monotonously with higher doping and deep dopant formation can be excluded by producing sublinear, i.e. incorrect,  $\sigma(N_A)$  relations. The percolation nature of this ansatz however, i.e. considering only critical jumps, impedes the evaluation of Seebeck coefficients which are determined by average hops<sup>[206]</sup> (cf. Sec. 2.2.3).

Deviations, i.e. transition kinks and strong superlinear shifts in the low doping regime have been addressed to trap limited mobilities.<sup>[180,242]</sup> Olthof *et al.* assume a doping efficiency of 1 ( $n = N_D$ ) and calculate the mobility from their conductivity data as depicted in Fig. 3.4(b) and Fig. 3.5(b). Below a threshold in doping concentration of MR  $2 - 6 \times 10^{-3}$ , Fermi level position and charge transport are limited by an exponential trap distribution with the density  $\sim 10^{18}$  cm<sup>-3</sup>. After occupying all those trapping sites via doping induced charge carriers, the  $\mu$  saturates around typical values of  $0.1 - 0.2$  cm<sup>2</sup>/Vs and  $E_F$  is no longer pinned.<sup>[180]</sup> A direct proof of this explanation via measuring  $\mu$  experimentally even for MR down to  $10^{-3}...10^{-4}$  is absent though. However, predictive Monte Carlo simulation by Mehraeen *et al.* (solid lines added in Fig. 3.4/3.5(b)) support the findings. They use a composite DOS with a centered Gauss and an exponential distribution toward the energy gap. Both hopping and mobility edge model conclude that two regimes for  $\sigma(N_D)$  are dominant: a (trap-limited) superlinear and a linear part. The transition point, i.e. charge carrier density, is situated where the DOS of both distributions are balanced.<sup>[242]</sup> A major simplification is still the negligence of a thermal activation energy for charge generation and just the assumption of existing charge carriers, independent on the temperature.

<sup>6</sup>perylene diimide

<sup>7</sup>4,4',4''-tris(N,N-diphenylamino)-triphenylamine

The position of the Fermi level Eq. (3.13) and Eq. (3.16) has been previously discussed to depend on the amount of incorporated dopants hence the number of generated free charge carriers. In ultraviolet spectroscopy measurements, Olthof *et al.* report on a stabilization of  $E_F$  around 0.4 eV for  $MR \simeq 0.1$  in MeO-TPD:F<sub>4</sub>-TCNQ (cf. Fig. 3.6, green symbols).<sup>[202]</sup> Since measurements of Tietze *et al.* confirm this pinning at doping with F<sub>6</sub>-TCNQ and C<sub>60</sub>F<sub>36</sub> (cf. Fig. 3.6, red and blue), they conclude on deep dopant formation in the MeO-TPD films which agrees with the calculated acceptor level of  $E_A = 0.46$  eV.<sup>[181,207]</sup> Seebeck experiments by Menke for the identical material combination however, seem to be contradictory as the Seebeck Energy, i.e.  $E_S = E_F - E_{Tr}$  decreases further for  $MR > 0.1$ .<sup>[240]</sup> This fact is puzzling, as the transport level  $E_{Tr}$  has been calculated to shift only closer towards the DOS center, i.e. further away from the energy gap and  $E_F$ .<sup>[130,161]</sup> Possibly, the assumption of an equal lattice formation for low and high mixing ratios is wrong and substantial amounts of another molecular species, e.g. dopants, add percolation pathways strongly influencing  $E_{Tr}$ .

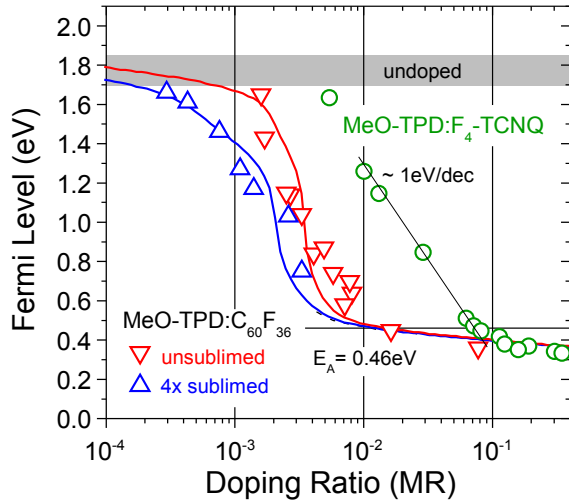


**Figure 3.6.:** Fermi level positions versus doping concentration in MeO-TPD doped with F<sub>4</sub>-TCNQ or C<sub>60</sub>F<sub>36</sub>. The strong shifts at  $MR \approx 2 \times 10^{-3} \dots 5 \times 10^{-2}$  are due to pinning of  $E_F$  at deep trap levels  $E_T \simeq 1.4 \dots 1.7$  eV to the HOMO onset ( $E = 0$ ). The trap density  $N_T$  is in the range of  $10^{18} \text{ cm}^{-3}$  but reduced upon host purification (data taken from Ref.<sup>[181,202,207]</sup>).

Host:Dopant	$c_n$ [mol%]	$\eta$ [%]	Ref.
MeO-TPD: F <sub>4</sub> -TCNQ	3.1	3	Ref. [202]
	17	3	
	27	14	
MeO-TPD: F <sub>6</sub> -TCNNQ	0.8	20	Ref. [207]
	2.4	12	
	14.4	7	
MeO-TPD: C <sub>60</sub> F <sub>36</sub>	0.09	36	Ref. [207]
	0.7	23	
	6.9	10	
P5: F <sub>4</sub> -TCNQ	0.3	0	Ref. [173]
	1.0	6	
	3.0	14	
	5.0	23	
C <sub>60</sub> :W <sub>2</sub> (hpp) <sub>4</sub>	3.0	4	Ref. [130]
Ir(piq) <sub>3</sub> : NDP2	1.1	63	Ref. [243]
	2.2	95	
	4.3	85	
	8.5	64	

**Table 3.1.:** Published results of doping efficiency  $\eta = p/N_A$  in small molecule systems, examined via UPS<sup>[202,207]</sup>, combined Seebeck and conductivity<sup>[130]</sup>, impedance,<sup>[243]</sup> or simulation<sup>[173]</sup>.

The strong shifts of about 1 eV/decade in Fermi level versus molar doping ratio (cf. Fig. 3.6) are characterized by Tietze in terms of an extended classical semiconductor model including trap distributions.<sup>[91,207]</sup> Similar to the conductivity data presented above (cf. Fig. 3.4), inherent deep traps are found to limit the number of free charge carriers, hence pinning the Fermi level for low doping concentrations. As soon as the traps (in case of MeO-TPD:  $E_T \simeq 1.35$  eV,  $N_T \simeq 10^{18} \text{ cm}^{-3}$ )<sup>[207]</sup> are filled by adding consecutively more dopants,  $E_F$  shifts away from the mid energy gap towards the hole transport level eventually saturating at  $E_A$ . In this range, i.e.  $MR \approx 2 \times 10^{-3} \dots 10^{-1}$ , the doping efficiency  $\eta = p/N_A$  is expected to reach its maximum.<sup>[91]</sup> Reported values of doping efficiency however strongly depend on the material system, the doping ratio, and the experimental technique used. An overview is given in Tab. 3.1. While estimated values from ultraviolet spectroscopy are low, it is supposed that electric fields such as the built-in field in impedance spectroscopy support the CT state dissociation which could explain the higher values of  $\eta$ .

## 3.4. Application of Molecular Doping to Optoelectronics

### 3.4.1. The p-i-n Concept in Organic Solar Cells

In organic solar cells, following concepts given in Sec. 2.1.4, light is absorbed in the photo active layer and converted into electric current. Due to the high exciton binding energy  $\Delta E_B$ , a spontaneous splitting of the electron-hole pair is unlikely. The conversion efficiency is tremendously increased by the introduction of an exciton splitting interface as illustrated in Fig. 3.7. Herein, a preferably electron transporting material (acceptor) is combined with an (donor) material favoring hole transport. Both are either merged closely, i.e. in a flat heterojunction, or co-deposited as a bulk heterojunction.

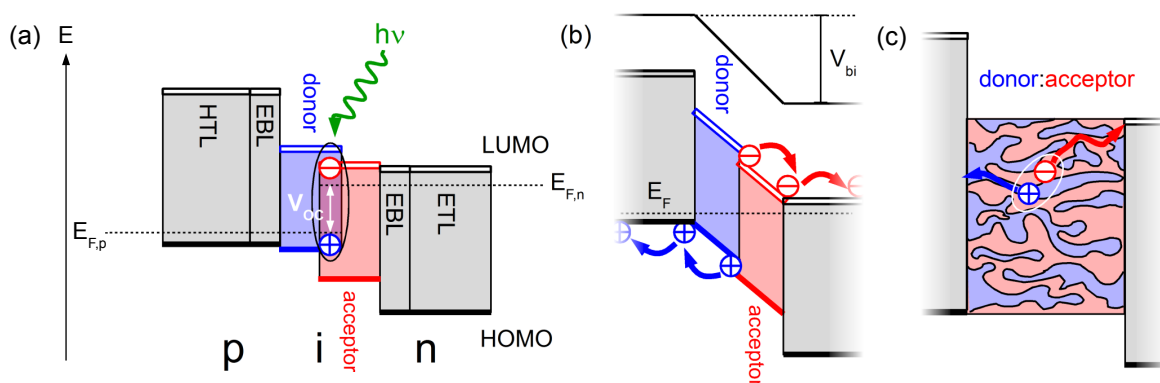


**Figure 3.7.:** (a) Organic solar cell layer sequence with p-i-n structure in open-circuit configuration. Upon illumination, excitons are generated in photo active areas and are separated at the donor-acceptor interface. Consequently, the Fermi level splits into  $E_{F,p}$  and  $E_{F,n}$ , which determines the open-circuit voltage  $V_{oc}$ . (b) In case of short-circuit, separated electrons and holes migrate, motivated by the built-in voltage  $V_{bi}$ , to the corresponding electrodes. (c) Blending of donor and acceptor material in bulk heterojunctions can partly compensate the poor exciton diffusion length in organic semiconductors limiting flat heterojunctions (e.g. shown in (b)).

After absorption of an incoming photon, an exciton is created on either of these molecular species and can diffuse to a donor-acceptor interface. Benefited by the energy offset between the HOMO of the donor and the LUMO of the acceptor, typically in the range of 0.5...0.6 eV, a separation of the exciton is possible. In direct consequence, the Fermi level splits into two quasi-Fermi levels which can be measured as *open-circuit voltage*  $V_{oc}$ , depending on the HOMO-LUMO difference as well as  $\Delta E_B$ .<sup>[244]</sup> Electron and hole are afterwards transported to the corresponding extracting electrodes via electron transport layer (ETL) and hole transport layer (HTL). Such transport layers are typically electrically doped to ensure high charge carrier conductivities<sup>[71]</sup> and have large bandgaps to minimize parasitic absorption. Additionally, hole/electron blocking layers (HTL/EBL) are present to prevent a diffusion of charge carriers (majorly excitons) to the 'wrong' electrode, i.e. quenching.

As briefly discussed in Sec. 2.1.4, a major limitation to organic solar cells is the exciton diffusion length of only  $\sim 10$  nm. Photo active layers are hence restricted to small film thicknesses which limits their absorption capabilities. Bulk heterojunctions however allow for thicker films, as the molecular intermixing of donor and acceptor phase guarantees still reachable exciton separating interfaces within few nm. Still, this demands for a precise control of the thin-film morphology (cf. Sec. 2.1.5). Furthermore, novel organic/inorganic device concepts featuring perovskite absorbers with large exciton diffusion length<sup>[71]</sup> or tandem solar cells employing multiple stacked absorber cells<sup>[109]</sup> are found in literature.



# Spectroscopy of Charge Carrier Traps in Molecular Semiconductors

*Conceptually introduced in the previous sections as additional intra-gap states, this chapter starts with a short overview on causing effects of trap states. Afterwards, the used characterization techniques for examining trap distributions in density, energy, and shape are presented. Impedance spectroscopy including the depletion capacitance and the frequency dependent trap capacitance are discussed in detail. The method of thermally stimulated currents and all important approaches for data analysis to obtain detailed trap DOS profiles are explained in-depth. Utilized to gain information about the energy/distribution of HOMO levels and Fermi level positions, the principles of ultraviolet photoelectron spectroscopy are briefly summarized. Further, this chapter includes experimental details on the measurement setups, the sample preparation, and the examined materials to spectroscopically identify trap states.*

## 4.1. Trap States

Trap states are unwanted sites in the energy gap of an (organic) semiconductor. Utilizing the introduction of a transport level  $E_{Tr}$  as given in the previous section puts up a simple definition: states below (above)  $E_{tr,e}$  ( $E_{tr,h}$ ) are considered as electron (hole) traps.<sup>[245]</sup> Those intra-gap states lower the mobility via multiple charge carrier trapping and release events<sup>[180]</sup>, eventually leading to charge carrier recombination losses if the retention time for the trapping site exceeds the charge carrier lifetime in the system. Depending on temperature and minority/majority carrier concentration, such recombination centers limit the power conversion efficiencies in state-of-the-art OLEDs or OSCs. Delayed reversal of traps causes parasitic capacitances and hysteresis in switching terminals. For instance, the threshold voltage of OFETs is strongly influenced by the presence of traps.<sup>[41,246]</sup>

According to semiconductor statistics, the electron (hole) trap occupation  $N_T^\mp(E)$  is given by the Fermi-Dirac integral

$$N_T^- = \int_{-\infty}^{\infty} dE g_T^-(E) f(E, E_T) \quad , \quad N_T^+ = \int_{-\infty}^{\infty} dE g_T^+(E) (1 - f(E, E_T)) \quad (4.1)$$

with the electron (hole) trap densities  $g_T^\mp(E)$  and the Fermi-Dirac statistics  $f(E, E_T)$ . Hence, the position of the Fermi level is determining the interaction of traps and free charge carriers, namely described in terms of conductivity, mobility, trap-and-release, or capacitance of the system which is explained in further parts of this thesis. Subsequently, causes for existing trap distributions are discussed briefly.

### Disordered DOS

As discussed above, the density of states in organic semiconductors is broadened due to thin-film aggregation and fluctuations of polarization energies. The DOS towards the energy gap is commonly approximated by a Gaussian and/or an exponential distribution<sup>[158,247,248]</sup> where charge carriers reside at the lower energy tail, i.e. sites close to the energy gap. Intrinsically, temperature and the disorder parameters  $\sigma$  and  $k_B T_0$  govern the position of the transport level, i.e. whether parts of the DOS are considered as hopping sites or traps. Increasing disorder and decreasing temperature shift  $E_{T_r}$  further into the energy gap and away from the DOS center (cf. Sec. 2.2.3).

### Chemical Impurities

Additional trap states deep within the energy gap are often impurity related.<sup>[246,249]</sup> Species with different chemical compositions, e.g. contaminations or degraded source molecules, show altered energy levels thus act as traps in the matrix.<sup>[250]</sup> Residuals of imperfect material sublimation are suspected to form deep trap states.<sup>[41,181]</sup> Hence, advanced purification techniques are mandatory for organic semiconductors, though the material quality lags far behind what has been achieved in inorganics such as silicon.<sup>[246]</sup>

Moreover, organic semiconductors are reported to be sensitive to vapor, e.g. of water, oxygen,<sup>[251–253]</sup> or ambient air. As discussed in Section 2.1.3, inter-molecular interactions in an organic semiconductor film are dominated by the relatively weak van-der-Waals forces, making organic semiconductor materials particularly susceptible to the incorporation of chemical impurities, such as solvent and ambient gas molecules.<sup>[246,254,255]</sup> Vapor molecules are able to penetrate deeply into organic semiconductor films<sup>[256,257]</sup>, either increasing the morphological disorder<sup>[256]</sup> or creating dipole moments, locally altering the energy landscape.<sup>[257,258]</sup> In this context, Nicolai *et al.* report on a generic trap level for electron transport caused by water-oxygen exposure in a series of conjugated polymers displaying varying LUMO levels.<sup>[43]</sup> They suspect the formation of  $(H_2O)_n-O_2$  complexes<sup>[259,260]</sup> as well as photo-oxidation of the polymers surrounded by hydrated oxygen complexes to cause a trap distribution around  $E_T = -3.6$  eV with respect to the vacuum level. In general, chemical reactions (up to a complete fraction of the molecules as seen for the air-sensitive n-dopant  $W_2(hpp)_4$ <sup>1</sup>)<sup>[220]</sup> are expected to happen at reactive parts of the organic molecules, e.g. thiol groups or in the center of extended carbon chains. The latter has been reported for e.g. pentacene, where either two oxygen or hydrogen atoms form double bonds with the carbon atoms at the 6,13-positions.<sup>[249]</sup> The resulting 6,13-pentacenequinone and 6,13-dihydropentacene are considered to be important impurities within pentacene films.<sup>[261–264]</sup>

### Structural Defects

Besides chemical impurities and the prevailing disorder, structural defects a major cause for traps in organic semiconductors. Despite elaborated fabrications (e.g. zone-melting<sup>[265]</sup> or solution shearing<sup>[266]</sup>), extended defects such as edge and screw dislocations or vacancies can be present in significant densities even in organic crystals.<sup>[74]</sup> Grain boundaries can hinder the charge carrier transport<sup>[267]</sup>, especially since thin-films of the small molecules investigated in this thesis are at best polycrystalline. Measurements on pentacene transistors show decreased charge carrier mobilities for smaller grain sizes (manipulated by either deposition rate or substrate preparation), i.e. more grain boundaries with respect to the total film thickness.<sup>[268–271]</sup> Though, interpretations on the interaction of grain boundaries with passing charge carriers are manifold and

---

<sup>1</sup>tetrakis(1,3,4,6,7,8-hexahydro- 2H-pyrimido[1,2-a]pyrimidinato)ditungsten(II)

controversial.<sup>[246,249]</sup> Experiments using Kelvin probe microscopy on operating pentacene OTFTs<sup>2</sup> reveal that charge trapping is inhomogeneously distributed for thick bulk films and does not appear to be confined solely to grain boundaries.<sup>[272]</sup> For few monolayers of film thickness however, grain boundaries are decisive for charge trapping.<sup>[273,274]</sup> Theoretical studies on the thin-film growth predict a relaxation of most defects of the monolayer into ideal crystal configuration, leaving the densities of remaining defects lower than  $10^{16}\text{cm}^{-3}$ .<sup>[275]</sup> Hence, crystalline grains represent favorable configurations of low energy. Grain boundaries feature low molecular overlap, thus creating a barrier which hinders the charge carriers from hopping between adjacent grains. In other words, charges are trapped *by* high-energy grain boundaries not *on* them.<sup>[246]</sup> Still, they leave the crystallites 'vulnerable', e.g. to penetrating impurity molecules or occurring point defects.

### Molecular Intermixing

In case of mixing different molecular species the situation complicates. For phase separation as used in bulk heterojunction OSCs<sup>[109]</sup>, the trap distributions of the neat films add up for mixed materials, e.g. as reported for polymeric blends of P3HT:PC<sub>61</sub>BM.<sup>[46]</sup> Besides, additional trap tailing is observed, probably due to increased disorder at the material interfaces.<sup>[46]</sup> Moreover, strong phase separation always includes the possibility of dead end areas<sup>[276]</sup> with high extraction barriers, thus trapping charge carriers on a finite phase surrounded by parts of a different material. In systems with another molecular species dissolved in the matrix, e.g. molecular doping, the DOS disorder remains unaffected only for low concentrations ( $< \text{MR } 0.001$ ). Arkhipov *et al.* predict a significant DOS broadening and an increased number of deep traps caused by Coulomb interaction of ionized dopant molecules and charge carriers for matrix:dopant mixing ratios higher than 100:1.<sup>[277]</sup> Experimentally, depending on the size and the energetics of the incorporated molecules, a broadening of the DOS<sup>[182,278,279]</sup> and an affected charge carrier mobility<sup>[167,280]</sup> are commonly seen at elevated densities ( $> \text{MR } 0.001$ ), e.g. as shown by Kleemann *et al.* for P5:F<sub>4</sub>-TCNQ and P5:F<sub>6</sub>-TCNNQ. SEM<sup>3</sup> pictures reveal an aggregation of charged molecules at the grain boundaries<sup>[128]</sup> up to a complete loss of crystallinity of pentacene in (GI)XRD<sup>4</sup> measurements at a molar ratio of 10:1.<sup>[128,178]</sup>

## 4.2. Impedance Spectroscopy

Impedance spectroscopy (IS) is a characterization technique which analyses the linear response of a system upon small-signal excitation. The general electrical approach is to apply an electric stimulus e.g. a voltage or a current to the system and to monitor the resulting current or voltage. During the ongoing measurement, the general material properties of the system are considered to be time-invariant. The physical properties of interest are examined typically in the frequency domain, in more rare cases they are Fourier transformed from the time domain. Although the IS method was originally meant to measure the influence of atmospheric conditions on electrochemical sensors,<sup>[281]</sup> a multitude of processes are accessible depending on their characteristic time frame, e.g. from slow chemical reactions<sup>[282]</sup> or diffusion/recombination phenomena<sup>[283–285]</sup> to charge carrier relaxation/transport processes.<sup>[286–290]</sup> In this thesis, IS is utilized to gain information on the occupation of inherent charge carrier trap distributions.

Despite the possibility to excite the system with a voltage step function or a composed white noise signal which benefits fast and easy data acquisition, a single-frequency small signal voltage (current, alternatively) stimulus is most commonly used. The applied sinusoidal signal  $v(t) = v_0 \cdot \sin(\omega t)$  perturbs the system and

<sup>2</sup>organic thin-film transistors

<sup>3</sup>Scanning Electron Microscopy

<sup>4</sup>Grating Incidence X-Ray Diffraction

the resulting current  $i(t) = i_0 \cdot \sin(\omega t + \varphi)$  is measured in phase  $\varphi$  and amplitude, or real and imaginary part by fast Fourier transformation (FFT) of the current response. By that, the acquired data is already translated to the frequency domain which simplifies further analysis. The complete impedance spectrum  $Z(\omega)$  is composed of a set of measurements for different frequencies  $\omega$ . What occurs time consuming since single measurements take seconds (MHz) to hours (mHz) depending on the measurement frequency, significantly improves signal-to-noise ratio. Thus, the stimulus amplitude  $v_0$  can be reduced to values below the thermal voltage (approximately 25 mV at 295 K) to ensure linear response of the system and suppress distortion of the FFT signal.

#### 4.2.1. Basic Math of Impedance Spectroscopy

The impedance function  $Z(\omega)$  is a more general approach to resistance of an electrical system which considers differences in phase angle. Thus, the notation is typically done in the complex plane, either in rectangular or polar coordinates

$$Z(\omega) = R(\omega) + jX(\omega) = |Z(\omega)| \cdot \exp[j\varphi(\omega)] \quad (4.2)$$

with real part (*resistance*)  $R(\omega)$  and imaginary part (*reactance*)  $X(\omega)$ , or the modulus (*amplitude*)

$$|Z(\omega)| = \sqrt{R(\omega)^2 + X(\omega)^2}, \quad (4.3)$$

and the *phase angle*

$$\varphi = \tan^{-1} \left( \frac{X(\omega)}{R(\omega)} \right), \quad (4.4)$$

respectively. It has to be noted that the impedance is time-invariant, although usually depending on the excitation frequency  $\omega$  in all its components. From those, not only the impedance function but a number of important further quantities is derived. First is the *admittance*  $Y(\omega)$

$$Y(\omega) = Z(\omega)^{-1} = \frac{R(\omega)}{|Z(\omega)|^2} - j \frac{X(\omega)}{|Z(\omega)|^2} = G(\omega) + jB(\omega) \quad (4.5)$$

which is the inverse of the impedance and consists of the *conductance*  $G(\omega)$  and the *susceptance*  $B(\omega)$ . Second, the admittance allows to calculate the complex *dielectric function*  $\varepsilon(\omega)$  of the system:

$$\varepsilon(\omega) = \frac{Y(\omega)}{j\omega C_0} = \varepsilon'(\omega) + j\varepsilon''(\omega). \quad (4.6)$$

The dielectric function is normalized by the vacuum capacitance  $C_0$  of the empty system. Here in, the simplest assumption in geometry of the system would be a plate-capacitor-like device with

$$C_0 = \frac{\varepsilon_0 A}{d} \quad (4.7)$$

with the dimensions  $A$  and  $d$ , and the vacuum permittivity  $\varepsilon_0$ . Depending on the device physics, it is useful to define further, more specific quantities with the use of impedance and admittance function. Those quantities are often paired with appropriate equivalent circuit models and summarized as *immittances*. Mostly important and discussed throughout this thesis is the capacitance function  $C(\omega)$ , defined by the susceptance  $B(\omega)$  and the angular frequency  $\omega$  to

$$C(\omega) = \frac{B(\omega)}{\omega} = -\frac{X(\omega)}{\omega |Z(\omega)|^2}. \quad (4.8)$$

### 4.2.2. Data Inspection

Analyzing and modeling of an obtained IS spectrum is often ambiguous and requires first a basic idea of the given device, and second, knowledge of some fundamental equivalent circuits and their impedance response. In case of simple structured and 'ideally' behaving samples, e.g. for characterization of conducting electrodes, insulating capacitors or trap-free single neat organic films, already graphical inspections yield a basic understanding of the device properties. Herein, impedance related data is depicted in two ways. In the complex plane of the *Nyquist* plot the imaginary part  $X(\omega)$  is plotted versus the real part  $R(\omega)$  of the impedance, and the excitation frequency  $\omega$  is used implicitly. Moreover, the frequency can be considered explicitly, showcasing either negative phase angle  $-\varphi(\omega)$ , modulus  $|Z(\omega)|$ , or the calculated *capacitance function*  $C(\omega)$  of the underlying circuit (*Bode* plots).

In order to properly obtain the characteristic properties of the investigated circuitry, it is however beneficial to perform a fitting procedure of the acquired data. Most commonly, this is done utilizing the *Complex Nonlinear Least Squares* technique, introduced by Macdonald and Gaber<sup>[291]</sup> and later implemented in all standard impedance analysis software.<sup>5</sup> To obtain a fit, the weighted sums of the squared imaginary and real part residuals are minimized

$$S = \sum_{i=1}^k \left\{ \lambda_i^R [R_m(\omega_i) - R_s(\omega_i, \mathbf{P})]^2 + \lambda_i^X [X_m(\omega_i) - X_s(\omega_i, \mathbf{P})]^2 \right\}. \quad (4.9)$$

The measured values  $(R, X_m)$  are subtracted for each frequency  $\omega_1 \dots \omega_k$  by the simulated ones  $(R, X_s)$  which are calculated for an assumed theoretical model of the device circuit employing the parameters  $\mathbf{P}$ . By minimization of  $S$ , the best set of  $\mathbf{P}$  is obtained. The choice of the theoretical model is either governed by a mathematical description of the physical system as used in this thesis for the examination of inherent trap states in organic thin-film layers and further explained in Sec. 4.2.4. Another approach is the modeling via equivalent circuits that however demands for an interpretation of the derived quantities in terms of the physical device properties.<sup>[292]</sup> In this case, the fitting procedure is less complicated while physical insights are provided already for 'simple' device structures. Hence, basic concepts of equivalent circuits are discussed in the following.

### Equivalent Circuit Modeling

The purpose of the use of equivalent circuits is to model key electrical properties of the system under investigation which is kept as simple as possible. Equivalent circuits often contain only linear and passive elements, are able to mimic the impedance response of a stimulated system from IS, and allow an interpretation of accessible device physics. Resistors represent a conductive path, e.g. an electrode with a certain sheet resistance, a bulk layer with a defined conductivity, or an injection barrier for charge carriers at a material interface. Capacitive elements characterize regions of space charge in a device, resulting either from depletion or accumulation of charge carriers. Inductive elements are neglected here in this work, since measurement and device layout are optimized to minimize inductive behavior, e.g. by short leads.

Physical imperfections of the system can be accounted for by constant phase elements (CPE), for example to cover leakage paths in capacitors e.g. by non-ideal dielectrics. Inhomogeneities of the examined system are modeled with distributed elements, mostly a number of inter-connected circuits to allow for a distribution of characteristic time constants.<sup>[281]</sup> For instance, one could imagine a morphologically rough material interface

<sup>5</sup>In this thesis, we use the commercial software Zview®(Scribner Associates Inc, United States).

of a system<sup>[293,294]</sup> which has to be described by a number of individual microscopic 'plain' interfaces, each represented by its own designated circuit. Another application of distributed elements are diffusive phenomena in non-infinite systems,<sup>[283,284]</sup> since diffusion is a spatially set problem and the resulting IS response is not describable with entirely ideal components.

**RC Series Circuit.** One of the most fundamental combinations of a resistor and a capacitor is the R-C-series circuit as depicted in Fig. 4.1 (a). The impedance of the resistor  $R_S$  and the capacitor  $C_S$  add up to the impedance of the circuit:

$$Z(\omega) = R_S + \frac{1}{j\omega C_S}. \quad (4.10)$$

In the complex plane (Nyquist plot, cf. Fig. 4.1 (b) left), the impedance function is a vertical line which intercepts the real axis at the value of the series resistance  $R_S$ . At low frequencies  $\omega$ , the capacitor impedance  $1/j\omega C_S$  dominates the IS response (cf. Fig. 4.1 (b) middle, negative phase angle at  $90^\circ$ ) and the circuit capacitance is frequency independent at the value  $C_S$ . With increasing frequency  $\omega$ , the impedance modulus scales proportional to  $1/\omega$  and eventually the negative phase angle drops below  $45^\circ$  ( $|X(\omega)| \leq R_S$ ). From there, the series resistance dominates while the capacitor impedance tends to zero, resulting in a plateau  $|Z(\omega)| = R_S$ . The capacitance function  $C(\omega)$  (cf. Fig. 4.1 (b) right, Eq. (4.8)) drops to zero as well. Its point of inflection shifts to higher  $\omega$  with smaller  $R_S$ .

**RC Parallel Circuit.** The second circuit to be considered is a parallel connection of resistor  $R_P$  and capacitor  $C_P$ , hence the impedance functions calculates as

$$Z(\omega) = \frac{R_P}{1 + j\omega R_P C_P} \quad (4.11)$$

and describes a semicircle with the diameter  $R_P$  in the Nyquist plot (cf. Fig. 4.1 (d)). For low frequencies, the capacitor impedance exceeds  $R_P$  by far. The circuit behaves entirely resistive ( $-\varphi \rightarrow 0$ ,  $|Z| \rightarrow R_P$ ). With increasing frequency, the capacitor impedance vanishes and shunts the resistor. The overall impedance  $|Z|$  tends to zero and the negative phase angle  $-\varphi$  reaches  $90^\circ$ , indicating a perfectly capacitive response of the circuit. The capacitance function Eq. (4.8) is constant to the value of the capacitor  $C_P$  and equals the susceptance  $B(\omega)$  divided by the frequency  $\omega$ .

**R-RC Circuit.** This last example is most relevant since it already allows for the description of simple organic electronic devices, e.g. Schottky diodes, as it combines an RC parallel circuit with a series resistance  $R_S$  (cf. Fig. 4.1 (e)). Therefore the impedance function is a sum of the previously discussed parts and shows

$$Z(\omega) = R_S + \frac{R_P}{1 + j\omega R_P C_P}. \quad (4.12)$$

Again (cf. Fig. 4.1 (f)),  $Z(\omega)$  plotted in the complex plane is a semicircle with the diameter  $R_P$  but here shifted by the series resistance on the real axis. Determined by the RC parallel branch, the IS response transitions between two states. At low frequencies, once again the capacitor impedance tends to infinity and the impedance modulus exhibits a plateau at  $R_P + R_S$  ( $-\varphi = 0^\circ$ ). With higher  $\omega$ , the capacitive pathway becomes conducting and starts to dominate the impedance response (increasing  $-\varphi$  and pronounced maximum). At very high frequencies, the capacitor shunts the RC parallel circuit and  $Z(\omega)$  of the entire element has a lower limit at the series resistance ( $-\varphi \rightarrow 0$ ). The capacitance function behaves similar to the previous discussed RC parallel circuit. However, the low frequency plateau does not exactly match the parallel

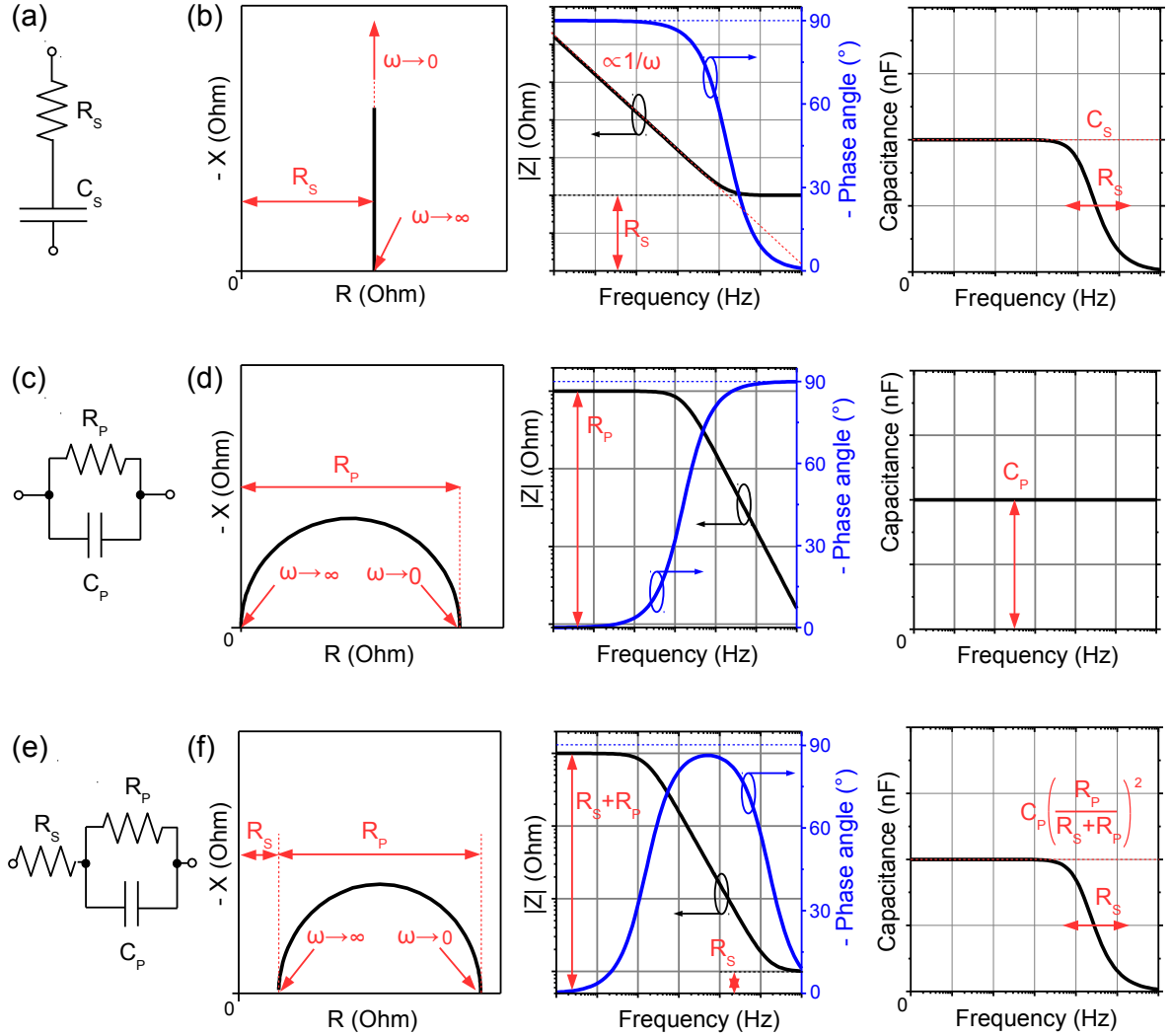


**Figure 4.1.:** (a)-(b) RC series circuit consisting of resistor  $R_S$  and capacitor  $C_S$ . In the high frequency regime, the circuit impedance is determined by  $R_S$  while the impedance of the capacitor  $1/j\omega C_S$  dominates in the low frequency regime. (c)-(d) RC parallel circuit of resistor  $R_P$  and capacitor  $C_P$ . The capacitance of the circuit is frequency independent. At high frequencies the capacitor impedance drops to zero hence shunts the resistor which is dominant at low  $\omega$ . (e)-(f) R-RC circuit consisting of RC parallel unit and a series resistance  $R_S$ . The features of impedance spectra are sums of the two previous circuitries.

capacitance  $C_P$  since a part of the applied voltage drops over the series resistance. The capacitance can be derived as

$$C(\omega) = \frac{C_P R_P^2}{(R_P + R_S)^2 + (\omega R_P C_P)^2}, \quad (4.13)$$

and results for the limit  $\omega \rightarrow 0$  in

$$C(\omega \rightarrow 0) = C_P \left( \frac{R_P}{R_P + R_S} \right)^2. \quad (4.14)$$

Only in case of  $R_P \gg R_S$  the capacitance plateau equals  $C_P$  (transition to RC parallel), else the ratio of parallel resistance to series resistance is determining  $C(\omega \rightarrow 0)$ .

**Equivalent Circuits in Organic Electronic Devices.** Impedance spectra of thin-film devices such as OLEDs or OSCs can be often identified with R-RC circuits. Series resistances  $R_S \sim 100 \Omega$  represent electrode and injection performance, while typically large parallel resistances  $R_P \sim \text{k}\Omega \dots \text{M}\Omega$  dominate the impedance over a wide frequency range. Hence, Nyquist plots show semicircles with large diameters and the plateau of  $Z(\omega \rightarrow 0)$  is fairly not reached within the measurement frequency range. For a single organic layer,  $R_P$  is attributed to its resistivity (i.e. conductivity) while the capacitance  $C_P$  describes possible charge depletion/accumulation. As intrinsic organic layers typically exhibit very low concentrations of free charge carriers (cf. Sec. 3), they are commonly identified with the depletion or so-called *geometrical* capacitance. Especially since OLEDs and OSCs consist of pin junctions, their interpretation in terms of a R-RC circuit seems natural. If there exists more than one depletion layer, the equivalent circuit has to be extended by an equal number of RC parts. The Nyquist plot then shows multiple semicircles which overlap depending on the similarity of their characteristic response times  $\tau_i = RC$ . The capacitance function exhibit multiple plateaus.

In this thesis, depletion zones near doped Schottky contacts are of particular interest, since capacitance and resistance are tuned by the doping concentration. The modulation of the depletion zone allows for a determination of trap densities whose response is typically seen as low frequency contribution exceeding the capacitance spectra of a standard R-RC circuit and is further explained in the consecutive parts of this section.

### 4.2.3. The Depletion Capacitance of Schottky Contacts

It has been discussed in Sec. 2.1.6 that not only energy levels but also interface dipoles resulting from chemical reactions, charge transfer, and/or interface states are crucial to the energy level alignment at intrinsic metal/organic contacts. Additional charges introduced by doping the organic semiconductor compensate such interfacial effects and allow for Fermi level alignment within few nm from the contacts. Hence, the level alignment is not anymore a property of the metal/organic material combination, but largely determined by the Fermi level position, i.e. the doping concentration.

#### Formation of Trap-Free Space Charge Regions

The formation of such a Schottky contact is treated similarly to inorganic semiconductor physics. Here considered for  $p$ -doping, metal and organics with work functions  $W_{\text{metal}}^f < W_{\text{organics}}^f$  are assembled. After contacting, priorly generated holes move from the organics into the metal until Fermi level equilibrium between both materials is established. Consequently, negatively charged dopant ions remain in the depleted organic layer and form a space charge region (SCR) of width  $w$  which causes an energy level bending (cf. Fig. 4.2 (a)). The voltage drop over this layer equals the built-in voltage  $V_{bi}$ . Assuming an abrupt  $n^+p$ -junction, the



space charge  $\rho(x)$  is described as

$$\rho(x) = \begin{cases} -eN_A^- & , 0 \leq x \leq w \\ 0 & , x > w \end{cases}. \quad (4.15)$$

The profiles of field  $F(x)$  and potential  $V(x)$  within the SCR are obtained by solving the Poisson equation

$$-\frac{d^2V(x)}{dx^2} = \frac{dF(x)}{dx} = \frac{\rho(x)}{\varepsilon_0\varepsilon_r}. \quad (4.16)$$

Considering the boundary condition of a vanishing field outside the depletion zone

$$\left. \frac{dV(x)}{dx} \right|_{x \geq w} = 0, \quad (4.17)$$

the integration of Eq. (4.16) yields

$$F(x) = \frac{eN_A^-}{\varepsilon_0\varepsilon_r}(w-x) \quad \text{and} \quad V(x) = \frac{eN_A^-}{2\varepsilon_0\varepsilon_r}(w-x)^2. \quad (4.18)$$

For a built-in potential  $qV_{bi} \gg k_B T$ <sup>6</sup> and, without loss of generality, a voltage drop between  $V(x=0) = V_{bi}$  and  $V(x=w) = 0$  results in space charge region width

$$w = \sqrt{\frac{2\varepsilon_0\varepsilon_r V_{bi}}{eN_A^-}}. \quad (4.19)$$

From measured values of  $V_{bi}$ ,  $w$ , and the relative permittivity  $\varepsilon_r$ , it should be possible to calculate the number of ionized dopants  $N_A^-$ , i.e. to gain information about the doping efficiency  $\eta$ . In experiment however, the picture of the built-in potential

$$V_{bi} = Wf_{organics} - Wf_{metal} \quad (4.20)$$

being the difference between the work functions is oversimplified since especially for lower doping concentrations, interface dipoles  $\Delta$  change  $V(x=0)$  significantly. The influence of intermixing of host and matrix molecules on the dielectric screening, i.e. the permittivity remains unknown. Furthermore, inherent trap distributions alter the charge carriers occupation and hence the electric field which is why they must be considered in the following.

### Formation of Trap-Limited Space Charge Regions

As discussed in Sec. 3.3, charge carrier traps distributions pin the Fermi level in the semiconductor by reducing the number of free charge carriers. In case of hole transport, the respective work function  $Wf_{organics}$  and with that the built-in potential are decreased. The level bending has to be discussed now for a semiconductor with two (for simplification discrete) acceptor levels, a shallow level at  $E_1$  below  $E_F$  and a deep level at  $E_2$  which lies above  $E_F$  if the level bending is small. Thus if  $eV_{bi} < (E_F - E_2)$ , the occupation probability for electrons of states at  $E_2$  is low and the space charge region forms similar to the trap-free regime.<sup>[295]</sup>

For strong level bending  $eV_{bi} > (E_F - E_2)$ , the Fermi level intersects with the deep level at the distance  $X$  from the contact and splits the depletion zone (cf. Fig. 4.2 (b)). In  $w_1$ , the Fermi level is above  $E_2$  and the

<sup>6</sup>the  $k_B T \sim 25$  meV at RT are typically guaranteed for our material combinations to be exceeded

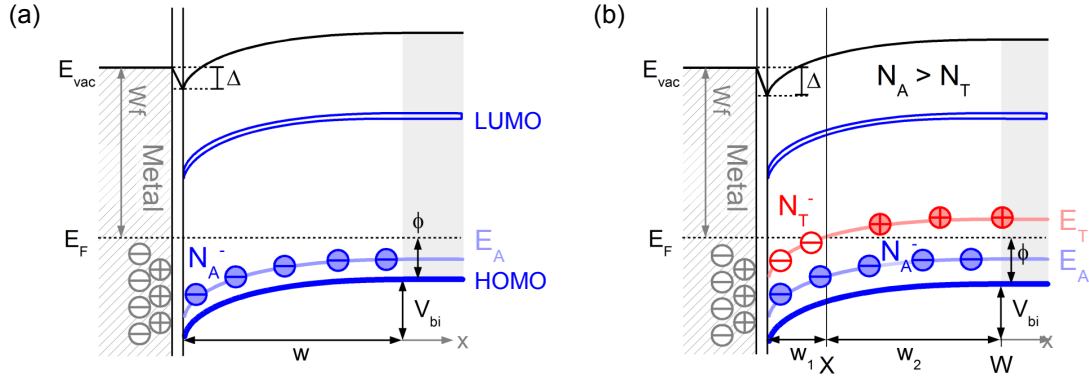


**Figure 4.2.:** Depletion layer formation and level bending at a Schottky contact featuring **(a)** a shallow impurity level  $E_A$  or **(b)** a shallow and a deep impurity level  $E_T$ .

states are able to capture electrons, i.e. are charged. In  $w_2$  ( $E_F < E_2$ ) holes populate the deep states at  $E_2$  which are hence neutral and do not contribute to the space charge.<sup>[296]</sup> The space charge density  $\rho(x)$  is re-written to

$$\rho(x) = \begin{cases} -e(N_1 + N_2) & , w_1 : 0 \leq x < X \\ -eN_1 & , w_2 : X \leq x < W \\ 0 & , x \geq W \end{cases} . \quad (4.21)$$

With respect to the boundary conditions  $\forall x \geq W : F(x) = V(x) = 0$ , the Poisson Eq. (4.16) is solved for both parts of the depletion zone in Eq. (4.21) individually,<sup>[295]</sup> In  $w_2$  the electric field is calculated as

$$-\frac{dV(x)}{dx} = F(x) = \frac{eN_1}{\varepsilon_0\varepsilon_r} (x - W) , \quad (4.22)$$

and further integration yields the potential

$$V(x) = -\frac{eN_1}{2\varepsilon_0\varepsilon_r} (W - x)^2 . \quad (4.23)$$

Similarly, one obtains at  $w_1$

$$F(x) = \frac{e(N_1 + N_2)}{\varepsilon_0\varepsilon_r} (x - X) + \frac{eN_1}{\varepsilon_0\varepsilon_r} (x - W) \quad (4.24)$$

and

$$V(x) = -\frac{e}{\varepsilon_0\varepsilon_r} \left( \frac{(N_1 + N_2)}{2} (x - X)^2 + N_1 (X - W) (x - X) + \frac{N_1}{2} (X - W)^2 \right) . \quad (4.25)$$

Again, the potential drop over the entire space charge region is described by the built-in voltage, i.e. according to Eq. (4.25) for  $V(x=0) = V_{bi}$  this yields

$$V_{bi} = -\frac{e}{2\varepsilon_0\varepsilon_r} (N_2 X^2 + N_1 W^2) . \quad (4.26)$$

Comparing the result to the trap-free relation of Eq. (4.19), the occurrence of the deep level shifts the built-in voltage by  $N_2 X^2$ , i.e. without knowledge of the trap level  $E_2$  and the intersection point  $X$  with  $E_F$  an access to  $V_{bi}$  and further the number of ionized dopants  $N_A^-$  is not possible.

### Depletion Capacitance and Mott-Schottky Analysis

**Shallow impurity level, uniform doping.** The depletion zone separates electrons in the metal near the contact and those deeper in the bulk of the semiconductor, hence it possesses a capacitance similar to a plate capacitor arrangement

$$C = \varepsilon_0 \varepsilon_r \frac{A}{w}. \quad (4.27)$$

Upon application of a reverse bias voltage  $V$ , electrons in the bulk are even further repulsed from the contact which results in an increase in depletion layer width  $\delta w$ . Consequently, the change of the space charge  $Q$  defines as

$$Q = eN_A^- w A \quad (4.28)$$

determines the differential capacitance  $C = |\delta Q / \delta V|$ . Together with Eq. (4.27) and (4.19) this leads to the capacitance of a space charge region employing one shallow acceptor level  $N_A$ ,

$$\frac{1}{C^2} = \frac{2(V_{bi} - V)}{A^2 e \varepsilon_0 \varepsilon_r N_A^-} \quad (4.29)$$

which is the famous Mott-Schottky equation, and allows for the determination of the ionized shallow acceptor concentration  $N_A^-$  from

$$\frac{d}{dV} \frac{1}{C^2} = -\frac{2}{A^2 e \varepsilon_0 \varepsilon_r N_A^-}. \quad (4.30)$$

In case of a uniform doping profile, the slope Eq. (4.30) is a straight line yielding  $N_A^-$  (cf. Fig. 4.3 (a)).

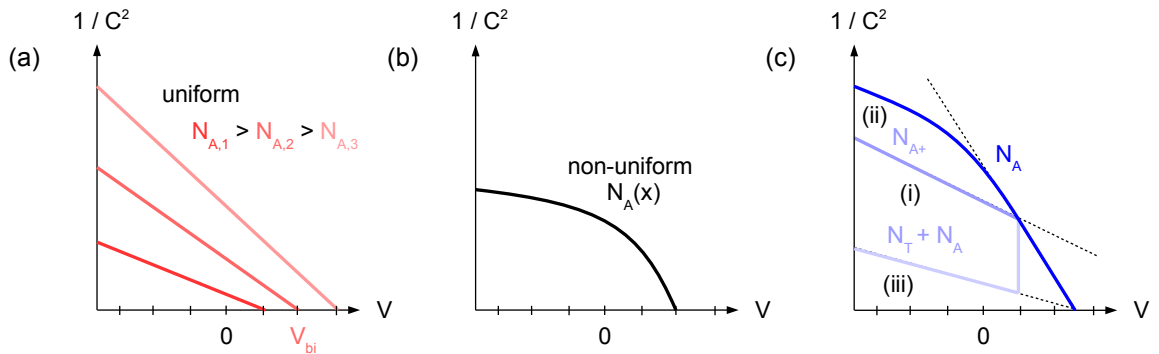


**Figure 4.3.:** Characteristic behavior of Mott-Schottky plots in case of **(a)** uniform doping with varying shallow acceptor concentrations  $N_{A,i}$  **(b)** non-uniform doping  $N_A(x)$  or **(c)** two acceptor levels. In detail, it is illustrated (i) an abrupt increase of acceptor level density from  $N_{A+}$  to  $N_A$ , (ii) the high frequency limit, and (iii) the low frequency limit of a sample with a density  $N_A$  of shallow impurities and a density  $N_T$  of deep level impurities.

**Non-uniform doping.** For an arbitrary doping profile  $N_A^-(x)$  (cf. Fig. 4.3 (b)), e.g. important for rough films, gradient doping, or separated host and dopant domains, Eq. (4.28) no longer holds and must be replaced by  $Q = \int eN_A^-(x) dx$ .<sup>[297]</sup> The Mott-Schottky relation reveals now the ionized acceptor density  $N_A^-(w)$  at the edge of the depletion zone in terms of the *profiler* equation<sup>[201]</sup>

$$N_A^-(w) = \frac{C^3}{e \varepsilon_0 \varepsilon_r A^2} \left[ \frac{dC}{dV} \right]^{-1}. \quad (4.31)$$

Here, changing the bias voltage thus  $w$  allows for a determination of the entire  $N_A^-(x)$ .

**Shallow and Deep Impurity Level.** Introducing a deep acceptor level  $N_T$  (i.e. a hole trap) in an addition to the existing shallow acceptor level  $N_A$  complicates the situation. The small-signal capacitance depends on the occupation (ionization) probabilities for both levels, i.e. is given by<sup>[295]</sup>

$$C = \frac{dQ}{dV} = -e \left( N_T \frac{dX}{dV} + N_A \frac{dW}{dV} \right). \quad (4.32)$$

It has been shown that the change of the capacitance with applied voltage is frequency dependent.<sup>[298]</sup> In the high frequency regime  $\omega \rightarrow \infty$ , the deep acceptor states are not able to follow the impedance stimulus. Hence, only majority carriers charging and discharging the shallow level at the edge of the depletion zone can respond to the applied signal and  $(dX/dV) = 0$ . For this case, the capacitance-voltage relation is derived to<sup>[295]</sup>

$$\frac{1}{C^2} = -\frac{2}{A^2 e \varepsilon_0 \varepsilon_r N_A^-} \left\{ V_{bi} - \frac{N_A^- N_T^-}{(N_A^- + N_T^-)^2} \right. \\ \left. \times V_X \left\{ \left[ 1 + \left( \frac{N_A^- + N_T^-}{N_A^-} \right) \left( \frac{V_{bi}}{V_X} - 1 \right) \right]^{1/2} - 1 \right\}^2 \right\} \quad (4.33)$$

with  $V_X = V(x) = V_{bi} - V$ .

As depicted in Fig. 4.3 (c), the Mott-Schottky plot shows a kink or a smeared out curvature, the latter is attributed to the broadened DOS of the acceptor levels.<sup>[299]</sup> For low frequencies  $\omega \rightarrow 0$  however, the deep level is able to respond to the excitation signal. The capacitance-voltage relation reads in this case

$$\frac{1}{C^2} = -\frac{2}{A^2 e \varepsilon_0 \varepsilon_r (N_A^- + N_T^-)} \left( V_{bi} - V - \frac{N_T^-}{N_A^- + N_T^-} V_X \right). \quad (4.34)$$

The apparent concentration is now the sum of the two acceptors, obtained from the slope  $1/(N_A^- + N_T^-)$  in  $1/C^2(V)$  for stronger reverse biases after a sudden drop at  $V = V_{bi} - (E_F - E_T)/q$ .<sup>[297]</sup> Intermediate frequencies, however, reveal responses from both deep and shallow impurity levels. The observed capacitance is regarded as a rather complicated function of the impurity level energy and distribution, bias voltage, and excitation frequency. This demands for an elaborated model analysis as utilized throughout this thesis and presented in the following.

#### 4.2.4. Trap Distribution from Frequency Dependent Capacitance

**Via an Equivalent Circuit Model.** As already briefly introduced, the capacitance function of organic diodes is typically dependent on the excitation frequency and exhibits an increasing signal contribution for low frequencies. This behavior has been attributed to charge carrier traps.<sup>[182,289]</sup> However, an explanation in terms of an equivalent circuit model is complicated. An attempt is reported by Losee,<sup>[300]</sup> who incorporates a number of RC series elements, each of them representing a single discrete trap level (cf. Fig. 4.4). The capacitance is a measure for the amount of stored charges while the resistance models the release energy, i.e. the trap depth. Both combined yield the characteristic time constant  $\tau = R \cdot C$  of the impurity level which responds upon IS excitation of  $\omega \sim 1/\tau$  and provides a rise in  $C(\omega)$ . For a description of organic semiconductors however, this method has proven itself to be impractical.<sup>[39]</sup> Trap distributions in organics are typically broad  $\sim$  several  $k_B T$  which could be only accounted for by a quasi-infinite number of RC elements, i.e. a huge number of fitting parameters.<sup>[292]</sup>

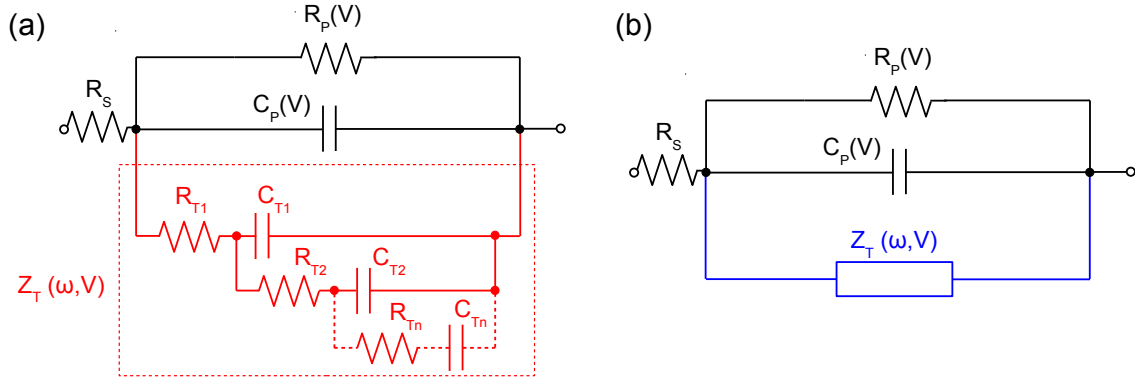


**Figure 4.4.:** (a) Equivalent circuit model of organic diodes with a transmission line model for inherent trap states. Each RC element represents a distinct trap level  $E_T$  following Losee model.<sup>[300]</sup> Only an infinite number of elements could cover the impedance of a trap distribution  $Z_T(\omega, V)$ . (b) In contrast, the IS response of a generic trap distribution  $g_T(E)$  is describable in terms of the physical model presented in Ref.<sup>[39,289,301–303]</sup> and adapted in this thesis.

**Via a Physical Model.** In this thesis, a physical model which has been introduced in previous work<sup>[39,289,301–303]</sup> is used to examine the trap response part in the capacitance function. Here in, a generic trap distribution  $g_T(E)$  can be considered to account for a realistic scenario in organic semiconductors. In the following, the validity of Boltzmann approximation and the presence of only one trap species (i.e. hole traps) are assumed.

The density of free holes  $p$  is given by evaluation of the Fermi integral using Boltzmann approximation to

$$p = \int_{-\infty}^{+\infty} g(E) [1 - f(E)] dE = N_0 \exp\left(-\frac{E_{tr,h} - E_F}{k_B T}\right) \quad (4.35)$$

with the effective density of states  $N_0$  at the transport level energy  $E_{tr,h}$  of holes in the HOMO. The number of holes  $p_t(E)$  occupying the distribution of hole traps  $g_T(E)$  is

$$p_T(E) = \int g_T(E) [1 - f(E)] dE. \quad (4.36)$$

Interaction between traps and elevated states at the transport level occurs via charge carrier release and capture, the balance equation reads

$$\frac{\partial p}{\partial t} = -\frac{\partial p_T}{\partial t} = \int g_T(E) \frac{\partial f(E)}{\partial t} dE, \quad (4.37)$$

$$\frac{\partial f(E)}{\partial t} = \beta p [1 - f(E)] - \epsilon f(E). \quad (4.38)$$

Here, the quantities  $\beta$  and  $\epsilon$  represent the time constants for hole capture and release respectively (cf. Fig. 4.5). The frequency dependent capacitance is derived for a small perturbation of the system (i.e. an IS stimulus), hence steady-state quantities  $\bar{y}$  are distinguished from small perturbation quantities  $\hat{y}$ . Regarding steady-state conditions, the time derivatives are equal to 0. Hence, the occupation probability  $\bar{f}(E_T)$  of a trapping site at the trap energy  $E_T$  and given  $E_F$  is balanced by competing emission and capture of holes according to Eq. (4.38) to

$$\bar{f}(E_T) = \left[1 + \frac{\epsilon}{\beta p}\right]^{-1} = 1 - \left[1 + \exp\left(\frac{E_T - E_F}{k_B T}\right)\right]^{-1}. \quad (4.39)$$

Together with Eq. (4.35), the emission rate  $\epsilon(E_T)$  is determined by

$$\epsilon(E_T) = \beta N_0 \exp\left(\frac{E_{tr,h} - E_T}{k_B T}\right). \quad (4.40)$$

In case of a perturbed system, the complex capacitance function  $C^*(\omega)$ , defined by dividing the admittance  $Y(\omega)$  by  $j\omega$ , represents the ratio between charge carrier density variation  $\hat{Q}$  and perturbing voltage signal  $\hat{V}$ , i.e. [304]

$$C^*(\omega) = \frac{\hat{Q}}{\hat{V}} = \frac{e}{\hat{V}} (\hat{p} + \hat{p}_T) = \frac{e}{\hat{V}} \left( \hat{p} + \int g_T(E) \hat{f}(E) dE \right). \quad (4.41)$$

In the low frequency regime, the response of the free majority charge carriers can be considered as instantaneous. Consequently, the Fermi level is varied to  $dE_F = -e dV$  resulting in

$$\hat{p} = \frac{d\bar{p}}{dV} \hat{V} = \frac{C_0}{e} \hat{V}. \quad (4.42)$$

The variation of the hole density is described in terms of a chemical capacitance  $C_0$

$$C_0 = e \frac{d\bar{p}}{dV} = \frac{e^2}{k_B T} \bar{p}. \quad (4.43)$$

Solving Eq. (4.35) for a small perturbation yields the occupation probability function for a trap level  $E_T$  to [301,304]

$$\hat{f}(E_T) = \frac{1}{\bar{p}} \frac{\bar{f}(E_T) [1 - \bar{f}(E_T)]}{1 + j\omega/\omega_T} \hat{p} = \frac{e}{k_B T} \frac{\bar{f}(E_T) [1 - \bar{f}(E_T)]}{1 + j\omega/\omega_T} \hat{V} \quad (4.44)$$

where  $\omega_T$  is the characteristic trap frequency

$$\omega_T(E_T) = \frac{\epsilon(E_T)}{1 - \bar{f}(E_T)}. \quad (4.45)$$

Substituting Eq. (4.44) into Eq. (4.41) finally results in the complex capacitance function  $C^*(\omega)$  depending only on steady-state quantities and the integration of the trap state distribution

$$C_T^*(\omega) = \frac{Y_T^*(\omega)}{j\omega} = \frac{e^2}{k_B T} \int \frac{\bar{f}(E) [1 - \bar{f}(E)]}{1 + j\omega/\omega_T} g_T(E) dE. \quad (4.46)$$

This Eq. (4.46) is solved for the whole device which requires knowledge of the Fermi level position with respect to the hole transport level at every position of the sample.

**Fermi Level Positions and Energy Levels.** As previously mentioned, the calculation of the trap distribution demands information on the Fermi level position and the transport level. Here, UPS measurements yield the HOMO shape with its center position  $E_0$ . From there,  $E_{tr,h}$  is estimated depending on the temperature and charge carrier density. The Fermi level position with respect to  $E_{tr,h}$ , i.e. the level bending, is obtained from drift-diffusion simulations. Details on the calculation model are found the work of Schober [305–307], successfully applied to hole and electron transport in OLEDs. In short, a system of differential equations considering drift and diffusive motion of charge carriers obeying continuity and Poisson equation is solved using Boltzmann approximation. In particular, either ohmic or thermionic contacts are assumed. Recombination is neglected since free electrons are considered absent for hole only devices. The simulation code stops once a steady-state result is obtained. Consequently, the impedance analysis is performed and the trap data is re-inserted in the drift-diffusion simulation to verify the results.

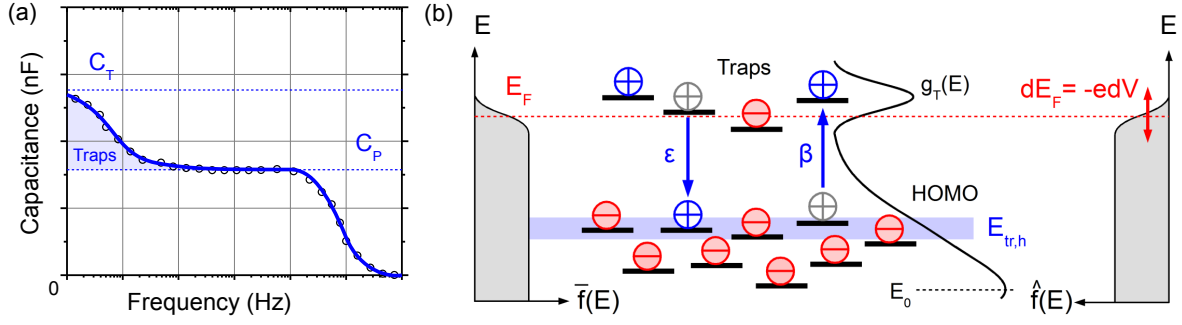


**Figure 4.5.:** (a) Schematic illustration of low frequency capacitance contribution of inherent traps in an organic diode. The depletion capacitance  $C_P$  is exceeded by an additional, frequency dependent trap capacitance  $C_T$ , which is examined with the physical model explained above to gain information on the trap parameters. (b) Balanced emission and capture of holes between a deep hole trap and the hole transport level  $E_{tr,h}$ . Upon IS stimulus, the Fermi level is altered, resulting in varying charge carrier densities thus the additional capacitance  $C_T^*(\omega)$ .

#### 4.2.5. Experimental Details

Impedance spectroscopy measurements are carried out with an *Autolab PGSTAT302N LCR Precision Meter* (Metrohm Autolab B.V., Utrecht, Netherlands). Excitation frequencies range typically from  $10^{-1}$  to  $10^6$  Hz while bias voltages can be swept  $-5 \dots +5$  V. The amplitude of the oscillating signal is set to 15 mV to avoid nonlinear signal response. Upon excitation, the out-of-phase current response is measured, directly displaying real ( $R$ ) and imaginary part ( $X$ ) of the impedance. All measurements are conducted in the dark.

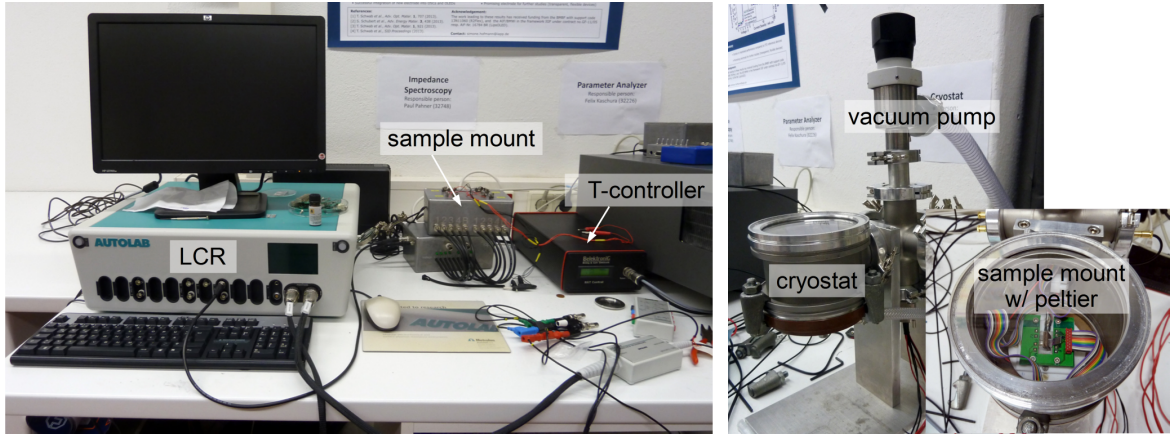


**Figure 4.6.:** Impedance measurement setup with Autolab LCR meter, multi sample mount, and the possibilities to measure under illumination or temperature variation. Only the latter was used in this thesis, employing a vacuum pumped peltier cryostat.

Temperature-dependent experiments down to  $\sim 220$  K are taken in a Peltier cryostat. Being  $\Delta T \simeq \pm 1$  K at room temperature, the temperature uncertainty  $\Delta T$  increases, limited by the sensor placements of the setup, to  $\pm 5$  K for 220 K. Temperatures below are reached in a liquid helium driven continuous flow cryostat *STVP-100* (JANIS, Massachusetts, United States) (details are found in Sec. 4.3),  $\Delta T$  is within  $\pm 0.1$  K. The encapsulation must be removed prior to cooling to minimize the possibility of sample damage (cf. Sec. 4.6). Inside the cryostats, the samples are kept under vacuum conditions  $p \sim 100$  mbar and the measurements are taken as fast as possible (same day) to suppress degradation effects.

## 4.3. Thermally Stimulated Currents

### 4.3.1. Introduction

Thermally stimulated techniques, e.g. *thermally stimulated luminescence* (TSL) and - in our case - *thermally stimulated current* (TSC) are useful methods to examine trap distributions. Both involve cooling of the sample to temperatures comparably low to the trap activation energies and flooding it with excess charge carriers. Once steady state is reached and gap states are occupied, i.e. the sample is charged, the system temperature  $T(t) = T_0 + \beta t$  is increased linearly at a heating rate  $\beta \sim \text{K/min}$ . In this process, trapped charges are released from progressively deeper localized states with increasing  $T$  and thus higher thermal energy.

**Thermally Stimulated Luminescence.** In case of TSL, released charge carriers recombine radiatively with charge carriers of opposite sign whom are typically de-trapped likewise. The luminescence signal is directly recorded, thus rendering the trap peak unaffected by charge carrier transport properties, i.e. inevitable for very low mobility materials. Detrimently, it is not possible to distinguish hole and electron traps.

**Thermally Stimulated Currents Experiments.** The TSC method, which this thesis and its work will focus on, however, allows for the examination of unipolar samples. Motivated by an electric field  $F$ , the released charge carriers are moving towards corresponding electrodes and are extracted yielding a current signal. States within a narrow range of the gradually rising energy  $E_{\text{TSC}}(T) \propto k_B T$  provide the largest contribution to the trap signal, eventually generating a peak in the TSC spectrum. This involves information about the trap energy, density, and distribution, and moreover about the properties governing the transport of the de-trapped charge carriers. A sketch of the TSC experiment is shown in Fig. 4.7.

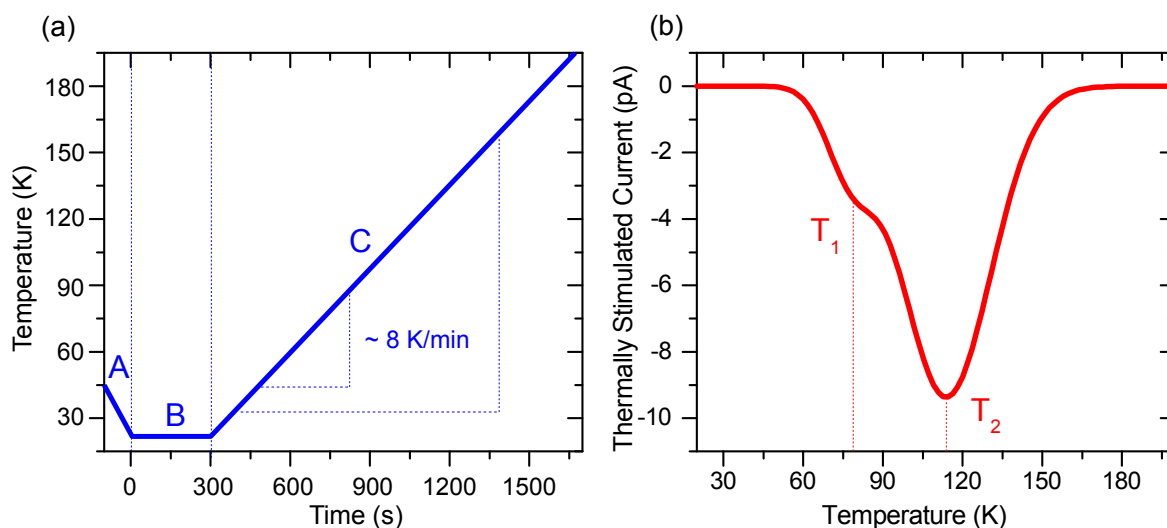


**Figure 4.7.:** (a) Thermally stimulated current experiment in its three phases: cool down (A), trap filling and sample resting (B), and linear heat-up (C), here shown for a rate  $\beta \sim 8 \text{ K/min}$ . (b) Corresponding TSC spectrum employing a trap shoulder at  $T_1$  and a peak at  $T_2$ .

**Trap Filling.** Filling of traps at low temperatures is achieved by applying a forward bias to the sample hence driving a filling current injected from the corresponding electrodes (electrical filling). The choice of the electrode material is made according to the energy levels of the organic semiconductors, since the species of



the injected charge carrier is determined by the injection barriers at the metal/organic interface. Alternatively, the traps can be filled optically. Assuming a highly absorbing material, excitons are generated within the photo-active layer and split either under the influence of an external or a built-in field, e.g. at a donor-acceptor interface. Within the thermalization time, the separated electrons and holes occupy the (deep) gap states (first). Subsequently, the sample is set to rest at low  $T$  for few min to achieve an equilibrium occupation of deep traps. Remaining 'free' charge carriers close to the transport level, i.e. moving in the device, are extracted via built-in potential.

**Fractional TSC (FTSC).** Fractional TSC is a frequently reported method<sup>[245,308,309]</sup> to distinguish between several closely packed monoenergetic trap levels or to examine trap distributions, specifically important for organic semiconductors. Following the illustration in Fig. (4.8), traps are filled at  $T_0$  and a TSC run (*pre-release*) is conducted up to a temperature  $T_{\text{stop}}$ . Reaching this turning point, the sample is immediately cooled down again to  $T_0$ . From here, another TSC run is conducted but without previously filling the trapping sites. Similar to the pre-release run, an initial rise of the TSC from the shallowest occupied trap states is observed. These traps are however deeper in energy since all lower lying trap levels have been already previously emptied. Consequently, the initial rise of the TSC occurs at higher  $T$ . By varying  $T_{\text{stop}}$  it is possible to slice the entire TSC spectrum. Integration and subtraction of the FTSC curves yields a lower limit in trap density of each slice. Estimation of the trap energies, e.g. by the initial rise method, allows to calculate the entire trap DOS  $g_T(E)$ .

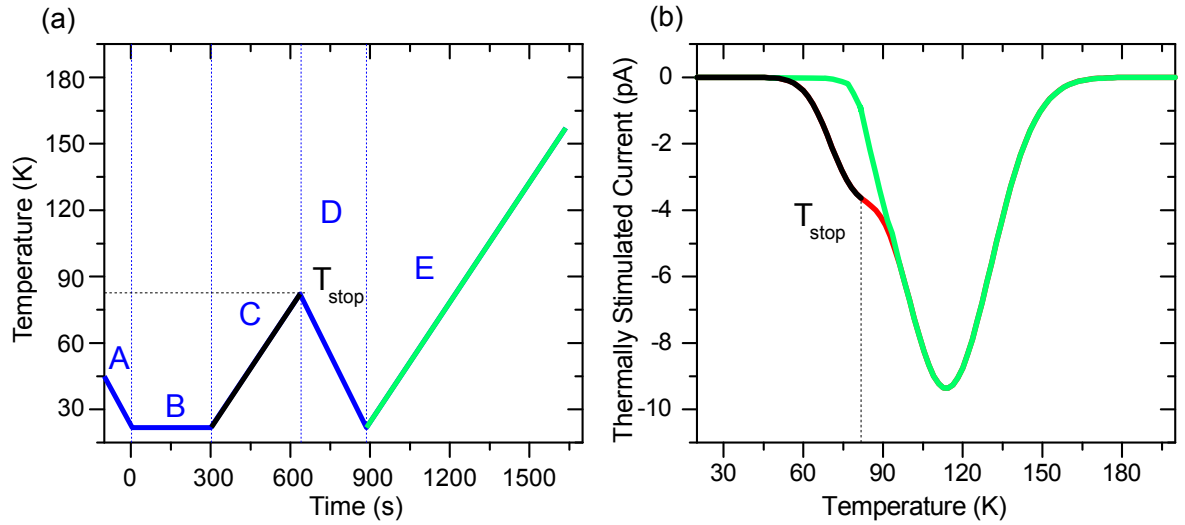


**Figure 4.8.:** (a) Sketch of a fractional thermally stimulated current experiment to map trap distributions  $g_T(E)$ : cool down (A), trap filling and sample resting (B), pre-release run up to stopping temperature  $T_{\text{stop}}$  (C), immediate cool down (D), and (E) full heat-up TSC run. (b) Corresponding FTSC curves with pre-release spectrum (black), coinciding with the complete TSC spectrum (red) up to  $T_{\text{stop}}$ , and full heat-up TSC spectrum (green line).

### 4.3.2. Evaluation of TSC Spectra

Despite a straightforward experimental sequence, several assumptions must be taken to completely explain a TSC spectrum. Similarly to the balance equation Eq. (4.37) for the trap occupation in IS, rate equations can be defined for the two level system of transport level and trap level to<sup>[310]</sup>

$$\frac{dp_T}{dt} = -p_T N_0 S v \exp\left(-\frac{E_{tr,h} - E_T}{k_B T}\right) + p (N_T - p_T) S v, \quad (4.47a)$$

$$\frac{dp}{dt} = -\frac{p}{\tau} - \frac{dp_T}{dt}. \quad (4.47b)$$

The occupation density  $p_T$  of a trap level  $E_T$  is changed by emission of previously trapped holes to states of density  $N_0$  at the hole transport level  $E_{tr,h}$ . Simultaneously, free charge carriers of density  $p$  are possibly recaptured by empty trap sites ( $N_T - p_T$ ). Both mechanics in Eq. (4.47a) depend on the capture cross section  $S$  for holes and a thermal velocity  $v$  of the holes around the transport level.<sup>7</sup> There, the occupation density  $p$  is determined by the interaction with the trap level and possible recombination with respect to the charge carrier lifetime  $\tau$  (cf. Eq. (4.47b)).

However, solving this set of differential equations requires knowledge not only of trap specific quantities (depth, distribution, and density) to yield the TSC signal, but also of temperature dependent material parameters (in particular:  $E_{tr,h}$ ). In the following, several evaluation concepts are discussed whether they are applicable to provide information on trap distributions from TSC in organic semiconductors.

**Estimation of Trap Density.** A lower limit of the trap density  $p_T$  can be obtained when integrating the measured signal  $I(T) \propto I(t)$  to<sup>[311]</sup>

$$\int I(t) dt = Q \leq e A d N_T \quad (4.48)$$

where  $A \cdot d$  is the sample volume to be extracted from. The inequality is given for two reasons: either the traps are filled incompletely or the charge carriers recombine after release before they can be extracted. The latter is important in bipolar devices where hole and electron (traps) are present. In the absence of a radiative recombination center, i.e. an emitter molecule like used in TSL, the obtained trap density is diminished. The first reason can be attributed to recombination losses as well. In a bipolar sample structure, e.g. an illuminated solar cell, incident light not only generates new electron-hole pairs, but also release already trapped charges.<sup>[312]</sup> For electrical filling, it has been discussed that the trap induced electric field can annihilate an external field effectively preventing charge injection and trap filling.<sup>[311]</sup> Anyways, the established occupation is lower than the actual trap density. Moreover, an elevated TSC starting temperature means that very shallow trap states are not occupied at all and can not be measured, thus reducing the observed  $N_T$  even further.

**Initial Rise Method.** The most frequently used method<sup>[44,131,245,308,309,313–316]</sup> to determine the energy of a trap level is the *initial rise* method introduced by Garlick and Gibson.<sup>[317]</sup> They found the TSC signal at the beginning of the peak to be proportional to an activation energy  $\Delta E$ , i.e.

$$I(T) \propto \exp\left(-\frac{\Delta E}{k_B T}\right) \quad (4.49)$$

---

<sup>7</sup>In fact, the definition was originally given for inorganic semiconductor where the thermal velocity  $v_{th}$  of charge carriers in the respective transport band can be estimated from e.g. Hall measurements.

Plotting  $\ln I(T)$  versus  $1/T$  yields what is commonly identified with the trap energy  $E_T = \Delta E$ . An advantage of this method is that already a small temperature range, i.e. the onset of the peak signal, is sufficient to determine the trap energy. Consequently, the temperature dependence of material parameters is neglected. However, the obtained trap energy represents only a lower limit and can not resolve typically broad densities of trap states in organic semiconductors. Because of that, the initial rise method is mostly paired with fractional TSC experiments to profile the trap DOS (cf. Sec. 4.3).

### TSC Spectra Fitting for Monoenergetic Trap Levels

Haering/Adams and Garlick/Gibson solved Eq. (4.47a) and (4.47b) to yield the thermally stimulated current  $I(T) = AF e \mu(T) p(T)$  <sup>[318]</sup> considering two borderline cases: slow re-trapping (*first-order kinetics*) with  $\tau^{-1} \gg (N_T - p_T) S \nu$  and fast re-trapping (*second-order kinetics*) following  $\tau^{-1} \ll (N_T - p_T) S \nu$ . <sup>[310,317]</sup>

**First-Order Kinetics (Slow Re-trapping).** Assuming that the recombination rate  $\tau^{-1}$  (which can be treated as considerably small e.g. in hole-only devices) is larger than the capturing rate of free charge carriers to the trap, the TSC spectrum is derived to <sup>[310]</sup>

$$I(T) = AF e \mu \tau N_T \nu \exp \left[ -\frac{E_T - E_{Tr}}{k_B T} - \frac{\nu}{\beta} \int_{T_0}^T \exp \left( -\frac{E_T - E_{Tr}}{k_B T'} \right) dT' \right] \quad (4.50)$$

Note that the temperature dependences of mobility  $\mu(T)$ , lifetime  $\tau(T)$ , and  $\nu(T)$  must be neglected to enable an analytic solution. Here, the prefactors  $N_0 S \nu$  are combined and yield a term  $\nu$  which can be considered similar to an attempt-to-escape frequency for a transition from a lower to a higher energy level. As seen from Eq. (4.50), the TSC spectrum not only strongly depends on  $E_T$  but also on  $\nu$ , and the heating rate  $\beta$ . In Figure 4.9, various TSC spectra computed from Eq. (4.50) are plotted to illustrate the influence of  $E_T$ ,  $\nu$ , and  $\beta$ . Note that already a discrete trap level  $E_T$  produces a broadened TSC peak. This can be understood thinking in terms of probabilities. For considerable low temperatures, the release rate of trapped charges carries is zero, which increases exponentially approaching higher  $T$  due to Boltzmann statistics. However, the integral term in Eq. (4.50) gradually diminishes the TSC signal once the peak temperature  $T_{max}$  is passed and the majority of trapped charges is released.

For a monoenergetic trap level, the width of the TSC spectrum depends on the trap energy, the heating rate, and the attempt-to-escape frequency (cf. Fig. 4.9). The deeper the trap, the faster the heat up and the lower  $\nu$ , the more broadened is the TSC spectrum. Moreover, a larger  $E_T$  shifts the TSC peak to higher temperatures since more thermal energy is required to release the charge carriers. A similar shift of  $T_{max}$  to higher temperatures is observed when assuming a lower attempt-to-escape frequency. Figuratively speaking, the trapped charges try to escape from the trapping site less often which reduces their release rate for statistical reasons. Consequently, the trap peak is observed for a constant  $\beta$  at higher temperatures. An analog explanation can be given for a variation of the heating rate  $\beta$ . For a fixed  $E_T$  and  $\nu$ , the TSC peak appears at higher  $T$ . Herein, the peak height  $I(T_{max})$  is increased for larger  $\beta$  which becomes obvious when plotting the TSC versus time (cf. Fig. 4.9 (d)). Although more charges are released within a shorter time frame, the peak sum, i.e. the overall number of extracted charge carriers, stays constant for all  $\beta$ .

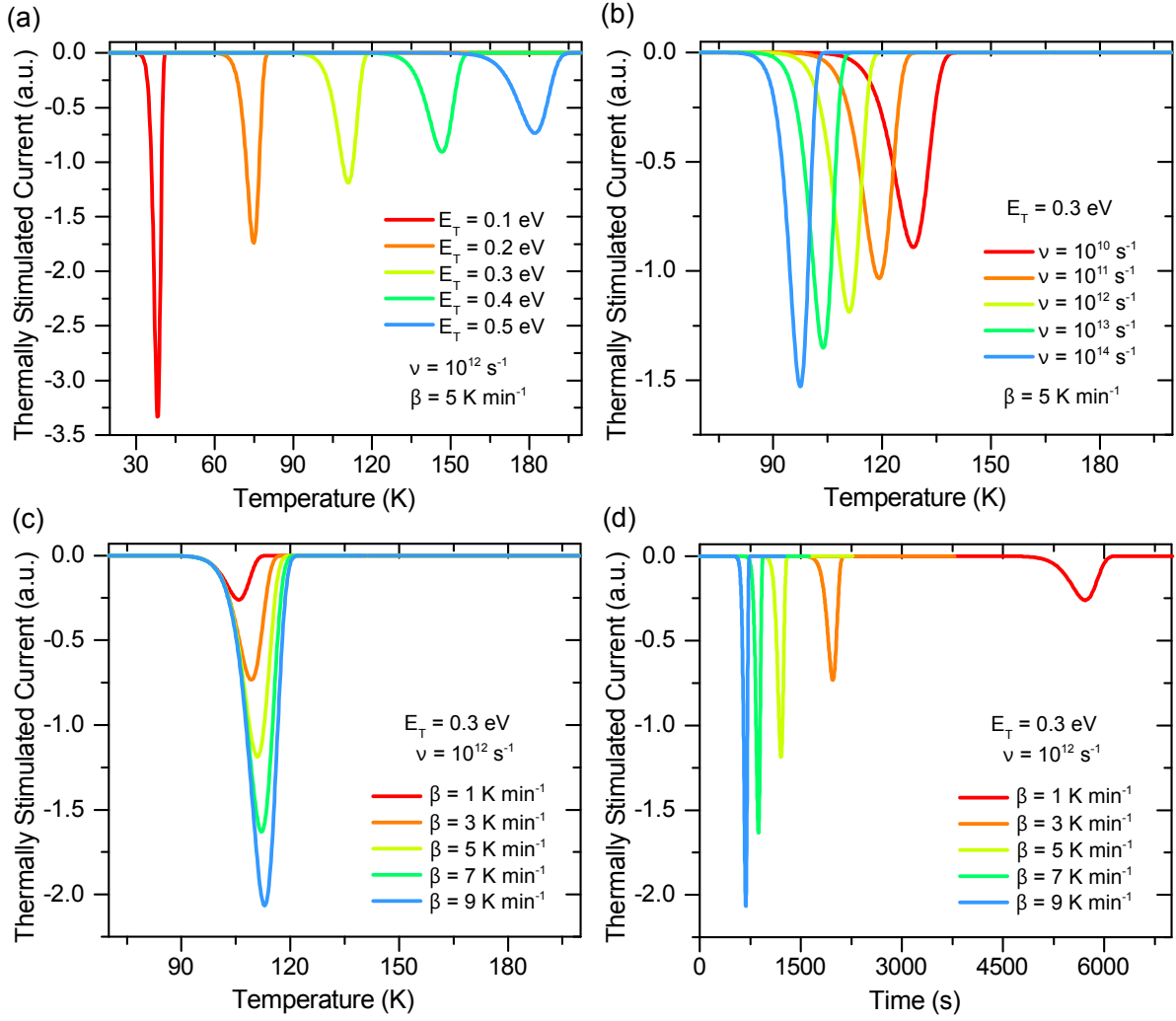


**Figure 4.9.:** Simulated TSC spectra for a monoenergetic trap level without charge carrier re-trapping (first-order kinetics) according to Eq. (4.50). The parameter variations show the dependence of the TSC spectra on **(a)** the trap energy  $E_T$ , **(b)** the attempt-to-escape frequency  $\nu$ , and **(c)-(d)** the heating rate  $\beta$  (adapted from Ref. [312]).

**Second-Order Kinetics (Fast Re-trapping).** If re-trapping of previously released charge carriers by empty trap sites can not be neglected, Garlick and Gibson derived the second-order equation [317]

$$I(T) = AF e \mu \tau \nu \frac{p_{T0}^2 \exp\left(-\frac{E_T - E_{Tr}}{k_B T}\right)}{N_T + \left[1 \frac{p_{T0} \nu}{N_T \beta} \int_{T_0}^T N_0 \exp\left(-\frac{E_T - E_{Tr}}{k_B T'}\right) dT'\right]^2}. \quad (4.51)$$

In particular, the shape of the TSC spectrum depends on the number of initially occupied trap sites  $p_{T0}$  and the overall number of trap sites  $N_T$ . Once more,  $\nu$ ,  $\mu$ , and  $\tau$  are considered to be temperature independent. The TSC parameter dependencies shown in Fig. 4.9 hold for second-order kinetics whereas the TSC peak height is reduced approximatively by the ratio  $p_{T0}/N_T$ . The signal at the high temperature flank is significantly increased as compared to first-order kinetics (cf. Fig. 4.10). Both features are attributed to re-trapping and re-emission of initially released charge carriers thus a delayed extraction at the contacts of the sample. Moreover, recombination losses diminish the overall number of extracted charges when the traveling time of the charge carriers exceeds their lifetime. This effect is more pronounced for smaller initial trap occupations  $p_{T0}$  (cf. Fig. 4.10 (b)).

**Distinction Between 1st and 2nd-Order Kinetics: Chen's Method.** Commonly, the shape of the TSC peak is examined to obtain information on the trap kinetics and the trap energy. Starting from the peak maximum temperature  $T_{\max}$  and the low and high temperatures at half signal intensity  $T_1$  and  $T_2$ , one defines form factors<sup>[319]</sup>

$$\mu_g = \delta/\omega \quad \text{with} \quad \omega = T_2 - T_1, \delta = T_2 - T_{\max}. \quad (4.52)$$

Chen examined a multitude of TSL and TSC spectra,<sup>[319–322]</sup> where the symmetry factor  $\mu_g$  indicates if re-trapping is a dominant process. For first order kinetics, usually a quickly vanishing high temperature signal is observed. Values of  $0.42 < \mu_g < 0.44$  are reported.<sup>[319,322]</sup> TSC curves corresponding to second order kinetics are found to decrease more slowly at the high temperature range. Comparing Fig. 4.10 (a), TSC spectra assuming re-trapping are nearly symmetric, derived values of  $\mu_g$  are as high as 0.78...0.85.<sup>[319]</sup> Furthermore, Chen summarizes in Ref.<sup>[320]</sup> a number of semi-empirical and analytical calculations to estimate the trap energy from the peak shape. A generalized formula is presented to

$$E_T - E_{tr,h} = 2.8k_B T_{\max}^2/\alpha \quad (4.53)$$

with  $\alpha = \tau/\mu_g = \tau\omega/\delta$  and  $\tau = T_{\max} - T_1$ .<sup>[319]</sup> Neglecting the temperature dependence, the attempt-to-escape frequency  $\nu$  can be estimated to (first-order kinetics)<sup>[320]</sup>

$$\nu = \left[ 2\beta \frac{1.26T_{\max}/\omega - 1}{2.718^2 T_{\max}} \right] \exp(2.52T_{\max}/\omega). \quad (4.54)$$

However, analyzing the TSC fit functions Eq. (4.50) and (4.51), the integral term is vanishing for temperatures  $T$  close to  $T_0$  thus leaving  $I(T) \propto \exp(-\Delta E/k_B T)$  which is the already given result Eq. (4.49). Consequently, the initial rise method can be considered as valid independent on the trap kinetics.

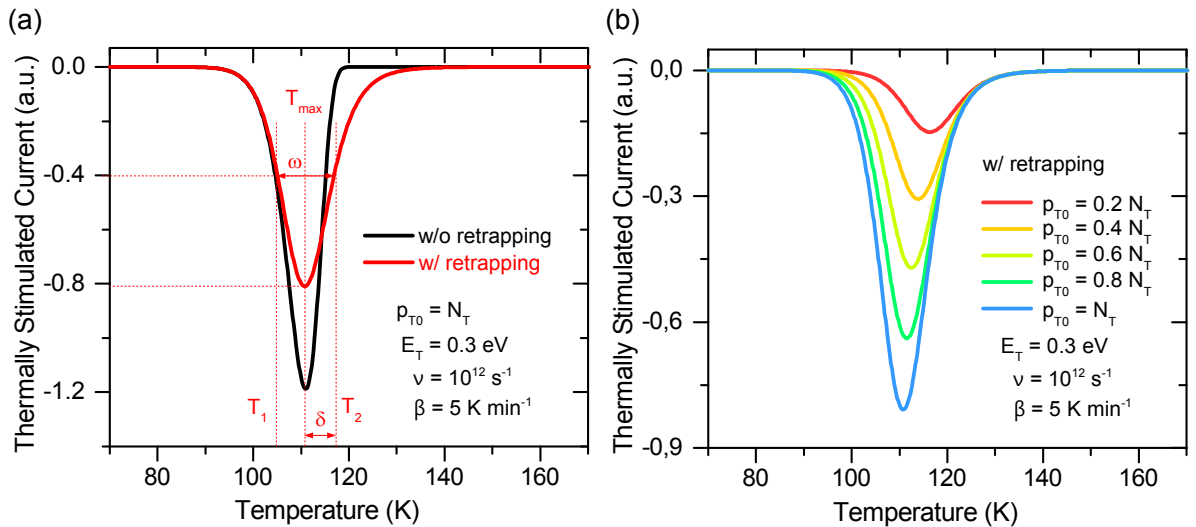


**Figure 4.10.:** (a) Comparison of TSC spectra for first (black) and second (red line) order kinetics according to Eq. (4.50) and (4.51). In case of re-trapping, the high temperature flank  $\delta = T_2 - T_{\max}$  is significantly increased. The peak is more symmetric with the ratio  $\delta/\omega \rightarrow 1$ . (b) Varying the ratio of initially filled traps  $p_{T0}$  and overall number of trapping sites  $N_T$  influences the TSC peak maximum and the collected charge carrier density.

**Simplified Peak Fitting after Cowell and Woods.** In case of 1st-order kinetics, Cowell and Woods have shown that repeated integration of Eq. (4.50) yields a converging infinite series.<sup>[323]</sup> For trap depths  $E_T/k_B T > 1$ , the result can be simplified to

$$I(T) \simeq \tilde{A} \exp[-\Theta - B \exp(-\Theta) \Theta^{-2}] \quad (4.55)$$

with  $\tilde{A} = AF e \mu \tau N_T \nu$ ,  $B = \nu \Delta E / \beta k_B$ , and  $\Theta = \Delta E / k_B T$ . The parameter  $B$  is obtained by differentiation of Eq. (4.55) to

$$B = \exp(\Theta_{\max}) \Theta_{\max}^2 \quad (4.56)$$

with  $\Theta_{\max} = \Delta E / k_B T_{\max}$ . Numerical fitting of Eq. (4.55) and Eq. (4.56) yield the parameters  $\tilde{A}$ ,  $T_{\max}$ , and  $\Delta E$ .<sup>[324]</sup> Afterwards, the attempt-to-escape frequency  $\nu$  can be calculated from  $B$ .<sup>[325]</sup> Similarly, for 2nd-order kinetics, Eq. (4.51) can be evolved to

$$I(T) \simeq C \exp[-\Theta - D \exp(-\Theta) \Theta^{-7/2}] \quad (4.57)$$

using  $C = AF e \mu \nu p_{T0} / N_T$  and  $D \simeq \exp(\Theta_{\max}) \Theta_{\max}^{9/2} / (\Theta_{\max} + 15)$ <sup>[323]</sup>, and fitted to the TSC spectra in the same manner.

**Hoogenstraaten- and T<sup>4</sup>- Method.** As discussed according to Fig. (4.9), the peak maximum temperatures  $T_{\max}$  shift to higher  $T$  for faster heating. Hoogenstraaten and later Bube made use of this observation. Assuming a constant attempt-to-escape frequency  $\nu$  and setting  $dI(T_{\max})/dT = 0$ , they formulate the relation<sup>[326,327]</sup>

$$\ln\left(\frac{T_{\max}^2}{\beta}\right) = \frac{E_T - E_{Tr}}{k_B T_{\max}} - \ln\left(\frac{E_T - E_{Tr}}{k_B \nu}\right). \quad (4.58)$$

The slope of the plot  $\ln(T_{\max}^2/\beta)$  versus  $1/T_{\max}$  directly yields the trap energy<sup>[315]</sup> while the intersection with the abscissa allows for an estimation of  $\nu$ .

At times, the T<sup>4</sup>-method is utilized for a fast approximate estimation of the trap energy, e.g. in C<sub>60</sub> field effect transistors<sup>[328]</sup> or polymeric P3HT:PC<sub>61</sub>BM solar cells.<sup>[329]</sup> Assuming an attempt-to-escape frequency  $\nu \propto T^2$ , commonly observed in inorganic semiconductors, the method by Hoogenstraaten in Eq. (4.58) simplifies to<sup>[330]</sup>

$$E_T = k_B T_{\max} \ln\left(\frac{T_{\max}^4}{\beta}\right). \quad (4.59)$$

Now, the trap energy can be estimated without variation of the heating rate which reduces the number of required TSC runs. However, Schafferhans has shown that the T<sup>4</sup>-method overestimates the depth of shallow impurity states ( $< 150$  meV) as compared to data from the initial rise method in PC<sub>61</sub>BM,<sup>[312]</sup> mainly due to the strong assumptions made on  $\nu$ .<sup>[330]</sup>

### TSC Spectra Fitting for Distributed Trap Levels

Previously discussed concepts for the examination of monoenergetic trap levels hold only partially for organic semiconductors as they feature typically broad energy distributions  $g_T(E)$ . The peak maximum positions  $T_{\max}$  remain unaffected, thus an evaluation with the Hoogenstraaten- or T<sup>4</sup>-method characterizes the energetic position of the dominant trap level. However, an explanation of the entire TSC spectra can only be given when adapting Eq. (4.50) and (4.51) by an additional integration over the energy distribution of the trapping

sites. Without re-trapping, the TSC signal reads

$$I(T) \propto \nu \int_{-\infty}^{+\infty} dE g_T(E) \exp \left[ -\frac{E_T - E_{Tr}}{k_B T} - \frac{\nu}{\beta} \int_{T_0}^T \exp \left( -\frac{E_T - E_{Tr}}{k_B T'} \right) dT' \right]. \quad (4.60)$$

The trapping sites distribution  $g_T(E)$  can represent any shape but is typically given in a Gaussian form, i.e.

$$g_T(E) = \frac{N_T}{\sqrt{2\pi}\sigma_T} \exp \left( -\frac{(E - E_T)^2}{2\sigma_T^2} \right). \quad (4.61)$$

In Fig. 4.11, the TSC of a Gaussian trap distribution with varying width  $\sigma_T$  at a trap depth of  $E_T = 0.3$  eV is compared with a monoenergetic trap level at the same position calculated from Eq. (4.60) and (4.51). While the peak temperature  $T_{\max}$  stays approximatively the same, the TSC spectra becomes reasonably broadened with higher  $\sigma_T$ . A similar trend can be observed when re-trapping is considered.<sup>[312]</sup>

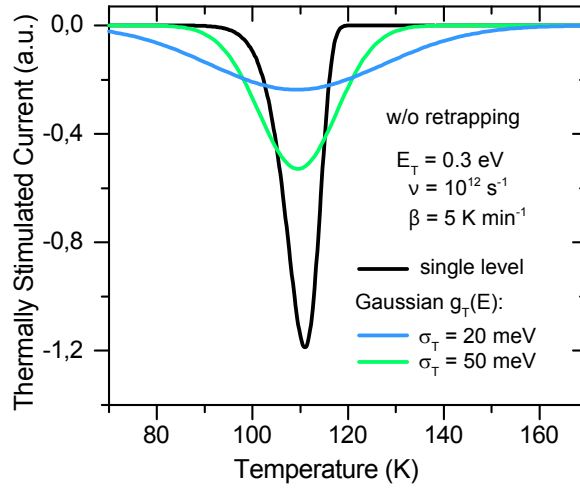


**Figure 4.11.:** Simulated TSC spectra (blue, green) for a Gaussian distributed trap level of varying DOS width  $\sigma_T$  following Eq. (4.60) and (4.61). For comparison, an monoenergetic trap level (black line, equal to  $\sigma_T = 0$  meV) at the same energy position  $E_T = 0.3$  eV is drawn. Integration of the curves yield equal trap densities  $N_T$ .

In summary, the evaluation of TSC spectra, especially finding a suitable fitting set, for organic semiconductors is not trivial and involves a number of assumptions on material parameters and trap kinetics. Occurring, broad trap distributions and a reported temperature dependence of the transport level  $E_{tr,h} = E_{tr,h}(T)$  hamper the data interpretation which is why a cross check with other evaluation methods are necessary. Main assumptions for the examination steps and conclusions will follow in the consecutive result chapters. Particularly important will be fractional TSC measurements which are able to map the trap DOS  $g_T(E)$  experimentally.

### 4.3.3. Experimental Details

Thermally stimulated current measurements are performed in a STVP-100 continuous flow cryostat (JANIS, Massachusetts, United States) driven with liquid helium which allows to reach a minimum temperature of  $T = 4.2$  K. The entire setup is illustrated in Fig. (4.12). A closed vacuum shell ( $p < 10^{-6}$  mbar, established using a molecular turbo pump Turbovac 50 (Oerlikon Leybold Vacuum, Cologne, Germany) connected to a pre-vacuum pump Trivac D 16 B (Oerlikon Leybold Vacuum)) minimizes heat input to the system by suppressing heat conduction. The cryostat is equipped with two calibrated silicon diode temperature sensors,

one (A) close to the vaporizer where cold gas from the liquid helium dewar enters the cryostat via the evacuated transfer line ( $p \simeq 10^{-6}$  mbar). A second sensor (B) is positioned close to the TSC sample. Both are monitored via a two-terminal PID temperature controller Lakeshore 336 which can additionally heat the cooling gas at the sample and the vaporizer position via two separated heating circuits (max. thermal power: 50/100 W). In the process of a TSC run, the setpoints of the PID units are ramped according to the heating rate  $\beta$  simultaneously. This guarantees an equal temperature distribution of the cooling gas around the sample and prevents thermo voltages.

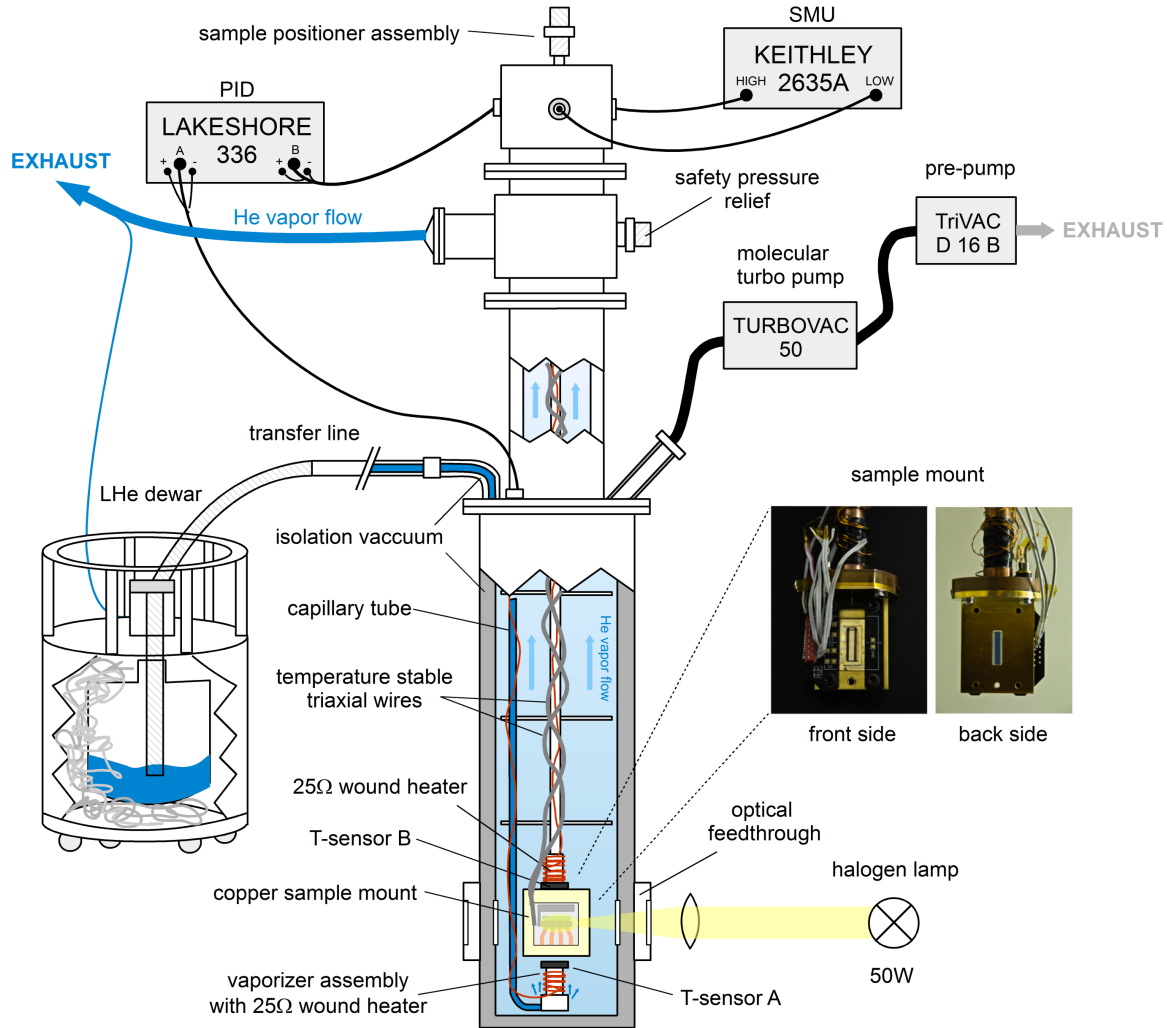


**Figure 4.12.:** Detailed sketch of the thermally stimulated current experimental setup. The sample temperature is balanced via a liquid helium flow and a two-terminal PID temperature controller. Trap-filling is done either electrically via a filling current or optically via illumination. In case of low temperature impedance spectroscopy (see Sec. 4.6), the source-measure unit is replaced by the Autolab PGSTAT302N LCR Precision Meter.

Electrically, the investigated TSC sample is connected via triaxial wires, employing an inner and an outer electrical shield to minimize signal noise, to an external source-measure-unit (SMU). The SMU is a KEITHLEY 2635A (Keithley, Ohio, United States) which is able to resolve currents down to 10 fA when probing a sample. Alternatively, the SMU is used to electrically fill the trap applying forward bias and allows for temperature dependent current-voltage measurements.



Before starting a TSC, the samples are de-encapsulated and immediately transferred to the cryostat where they are kept under inert atmosphere to slow possible degradation. Trap filling is typically done at  $T_0 = 10$  K, either realized electrically or by illumination with a bright white light 50 W halogen lamp through optical feedthroughs ( $T = 0.95$ )<sup>[58]</sup> of the cryostat. The filling conditions (e.g. applied bias, duration) are checked prior to the TSC run. In case of optical filling, the illumination angle is optimized to yield a maximal short-circuit current. The extraction of released charge carriers during the TSC experiment is, if not stated differently, led by the built-in potential. Only a small voltage  $\sim 1$  meV is applied to suppress minor leakage currents.

Except for the halogen lamp and the helium flow control, the entire experiment is computer-controlled via a self-written *python* program (for source code see Sec. A.3). Recently, the system has been extended to allow batch processing consecutive TSC runs of one sample and relieve the experiment operator. Limited by a slow cool down ( $\sim 1...2$  h) and maximum stable linear  $\beta \sim 9$  K/min due to the size of the recipient, the measurement duration especially for a complete FTSC is between 24...48 h.

## 4.4. Additional Measurement Techniques

### 4.4.1. Photoelectron Spectroscopy

#### Basics of Photoelectron Spectroscopy

Photoelectron spectroscopy (PES) is the most important methods to study the chemical and electrical properties of thin-film organic semiconductors in a single experiment, allowing for a characterization directly after fabrication without breaking ultra high vacuum (UHV) conditions. The technique is very surface sensitive and for most material systems non-destructive.

Photoelectron spectroscopy measurements exploit the external photo-effect, described by Einstein in early 1905 following

$$E_{\text{kin,max}} = h\nu - \Phi, \quad (4.62)$$

which relates the frequency  $\nu$  of an incident photon from an ideally monochromatic light source directed onto a metal or semiconductor to the maximum kinetic energy  $E_{\text{kin,max}}$  of an electron escaping from the sample with work function  $\Phi$ . Examinations with varying  $\nu$  identify both  $\Phi$  and the Planck's constant  $h$ . In PES, elaborated electrostatic analyzer systems are used to map the whole spectrum on kinetic energies  $E_{\text{kin}}$  of the emitted photoelectrons. Depending on the energy of the utilized photons, either the DOS of the valence structure of the system or characteristic binding energies of respective core levels for the individual atoms are resolved. Hence, it is distinguished between UV photoelectron spectroscopy (UPS) for  $h\nu < 50$  eV and x-ray photoelectron spectroscopy (XPS) with energies above. Such excitations are typically realized via gas discharge lamps, soft x-ray,<sup>[220]</sup> or synchrotron<sup>[331]</sup> sources.

The photoemission process can be described in terms of three successive steps, i.e. *i*) local photoionization upon photon absorption and electron excitation, *ii*) migration of the excited electron in the bulk layer towards the surface, and *iii*) escape of the electron to the vacuum. Details on these parts can be found in Ref.<sup>[332]</sup>. For the two latter steps, the mean free path of electrons  $\lambda$  within dense matter is crucial. As depicted in Fig. 4.13,  $\lambda$  depends strongly on the electron kinetic energy.<sup>[333]</sup> Typical excitation energies for UPS, e.g. the He-I irradiation at  $h\nu = 21.22$  eV result in  $\lambda = 1...2$  nm. In case of XPS, it shows  $\lambda \sim 10$  nm

( $\text{AlK}_{\alpha}$ :  $h\nu = 1486.6 \text{ eV}$ ). Despite photon penetration depths of a few  $\mu\text{m}$  in organic thin-films, hence the released electrons originate from the very first monolayers. This fact explains why surface contaminations, e.g. by physisorption must be prevented at all cost and UHV conditions are mandatory during PES experiments.

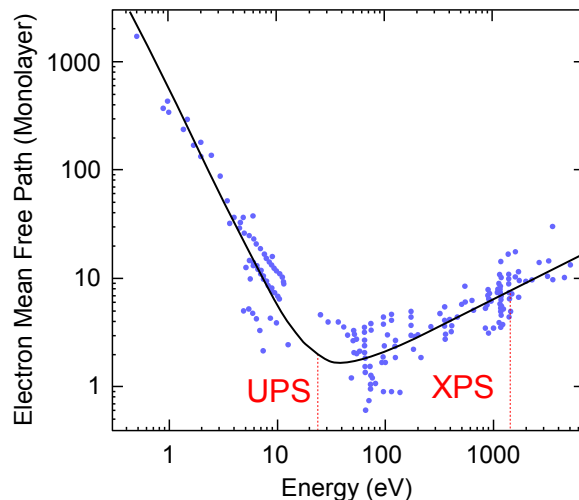


**Figure 4.13.:** Mean free path of electrons in solids as function of their kinetic energy. The (blue) data points represent electrons in different elements (redrawn after Ref.<sup>[333]</sup>). The red dotted lines indicate typical electron energies in UPS and XPS experiments throughout this thesis.

Moreover, bulk properties inspected by PES have to be viewed with care. Alignments at organic/organic or metal/organic interfaces, e.g. level bending at a Schottky contact, have to be inspected incrementally by evaporating the second layer in Åsteps onto the first one and checking the DOS for every layer thickness.<sup>[94]</sup> Compared to the underlying layers it was however found that the topmost layer experiences different polarization and electron screening effects due to its contact with the vacuum. Consequently, the ionization potential of the thin-film is usually increased by a few 100 meV.<sup>[334–336]</sup>

### Details on the Experimental Setup

The photoelectron spectroscopy system used in this thesis has been described extensively in Ref.<sup>[91]</sup> and Ref.<sup>[94]</sup> where most of the information presented here are taken from and further details can be found. The PES setup is a *Phoibos 100* (Specs GmbH, Berlin, Germany), which is illustrated in Fig. 4.14. It is attached to the UHV evaporation cluster tool UFO and consists of an UHV analysis chamber with a heat filament and a (liquid  $\text{N}_2$ ) coolable sample mount, UV- and x-ray sources, an electrical lens system, a hemispherical analyzer (HSA), and a multi channeltron detector (MCD). Photo excitation sources are usually the He-I line ( $h\nu = 21.22 \text{ eV}$ ) of a gas discharge lamp (*Specs UVS10/35*) for UPS and the  $\text{AlK}_{\alpha}$  ( $1486.6 \text{ eV}$ ) irradiation (*Specs XR-50*) for XPS.

**Vacuum Conditions.** Prior to thermal evaporation of the organics, the sample surface is cleaned *in-situ* via  $\text{Ar}^+$  sputtering. During the PES experiment, the base pressure is kept  $< 10^{-10} \text{ mbar}$  to prevent surface contamination. Assuming a sticking coefficient of unity, one monolayer is formed from a residual gas at a pressure of 1 Torr ( $= 1.332 \text{ mbar}$ ) within  $10^{-6} \text{ s}$  according to Langmuir's law of surface adsorption. A pressure  $\sim 10^{-8} \text{ mbar}$ , common for evaporation chambers, results in few minutes while only a pressure of  $10^{-10} \text{ mbar}$  ( $\sim 4 \text{ h}$ ) grants an adequate level of purity within the time frame of a PES experiment.

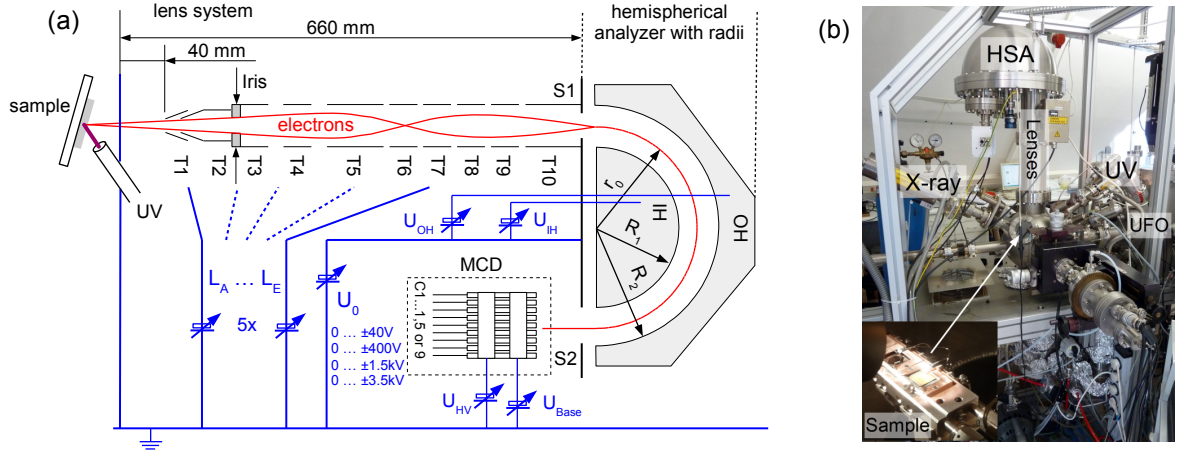


**Figure 4.14.:** (a) Schematic sketch (adapted from Ref. <sup>[91]</sup> and Ref. <sup>[94]</sup>) and (b) photograph of the PES setup Phoibos 100 (Specs, Germany). The inset of (b) shows an UPS sample mounted and contacted inside the PES chamber.

**Lens System and Hemispherical Analyzer (HSA).** Photo excited electrons escaping from the sample are collected through an aperture iris by an array of electrical lenses T1...T10 which speed them up or down while guiding to the entrance slit S1 of the hemispherical analyzer. The HSA is operated in *Fixed Analyzer Transmission (FAT)* mode, i.e. its pass energy  $E_{\text{pass}}$  is kept constant. Consequently, the retardation potential  $U_0$  of the lens systems is swept to force all electrons to the fixed  $E_{\text{pass}}$ , i.e.

$$eU_0 = E_{\text{kin}} - E_{\text{pass}}. \quad (4.63)$$

The hemispherical analyzer itself consists of two half-spheres IH and OH with the radii  $R_1 = 75 \text{ mm}$  and  $R_2 = 125 \text{ mm}$ . An radial electrical field between those spheres deflect the incoming electrons to elliptical trajectories with the mean radius  $r_0$  where they pass with the energy

$$E_{\text{pass}} = -e \frac{R_1 R_2}{2r_0 (R_2 - R_1)} (U_{\text{OH}} - U_{\text{IH}}) = -0.9375e (U_{\text{OH}} - U_{\text{IH}}). \quad (4.64)$$

Herein, the transmission is broadened dependent on the slit/beam geometry and the pass energy.<sup>[337]</sup> Though, in *FAT* lens mode the analyzer resolution is equal for all energies since  $E_{\text{pass}}$  is kept constant.<sup>[91]</sup>

**Multi Channeltron Detector (MCD).** An array of five channel electron multipliers C1...C5 finally detect the incoming photo electrons. Each of the channeltrons consists of a glass tube coated with a high resistance material. Under a voltage  $U = U_{\text{HV}} - U_{\text{Base}}$  between the ends of the tubes typically as high as  $\sim 3 \text{ keV}$  to ensure saturation, the walls of the glass tubes acts as continuous dynode. Secondary electrons lead to an avalanche effect and a signal gain in the range of  $10^8$ . Importantly, sample and detector are electrically connected to align the respective Fermi levels. Since their work functions are typically different, the detector measures a shifted  $E'_{\text{kin}}$  instead of  $E_{\text{kin}}$ . In case of a common Fermi level, one yields

$$E_{\text{kin}} + Wf_{\text{sample}} = E'_{\text{kin}} + Wf_{\text{detector}}. \quad (4.65)$$

The work function of the detector has been determined to  $Wf_{\text{detector}} = 4.56 \text{ eV}$ .<sup>[91]</sup>

### Principles of UPS Experiments and Data Evaluation

In order to explain how thin-film properties are accessible via ultraviolet photoelectron spectroscopy, Fig. 4.15 shows exemplary an UPS measurement for a 10 nm thick  $C_{60}$  layer on a silver substrate. The detected distribution of the kinetic energy directly maps the DOS shape of the bound electrons. The binding energy is however calculated from

$$E_B = h\nu - E_{kin} - Wf_{sample} = h\nu - E'_{kin} - Wf_{detector}. \quad (4.66)$$

Additionally, the sample bias voltage of  $-8\text{ V}$  applied to increase the photoelectron yield is subtracted. The polynomial background in  $E_{kin}$  originates from electrons undergoing inelastic scattering on their way to the sample surface, hence are lowered in kinetic energy. The point of the lowest kinetic energy  $E_{kin} \simeq 0$ , where also the secondary electrons background signal drops abruptly, is called *high binding energy cut-off* (HBEC). Here, the photo excitation  $h\nu$  is only just sufficient to overcome the sample work function and promote electrons to the vacuum level  $E_{vac}$ . By that means, a calculation of the sample work function is possible, i.e.

$$Wf_{sample} = h\nu - E_{HBEC}. \quad (4.67)$$

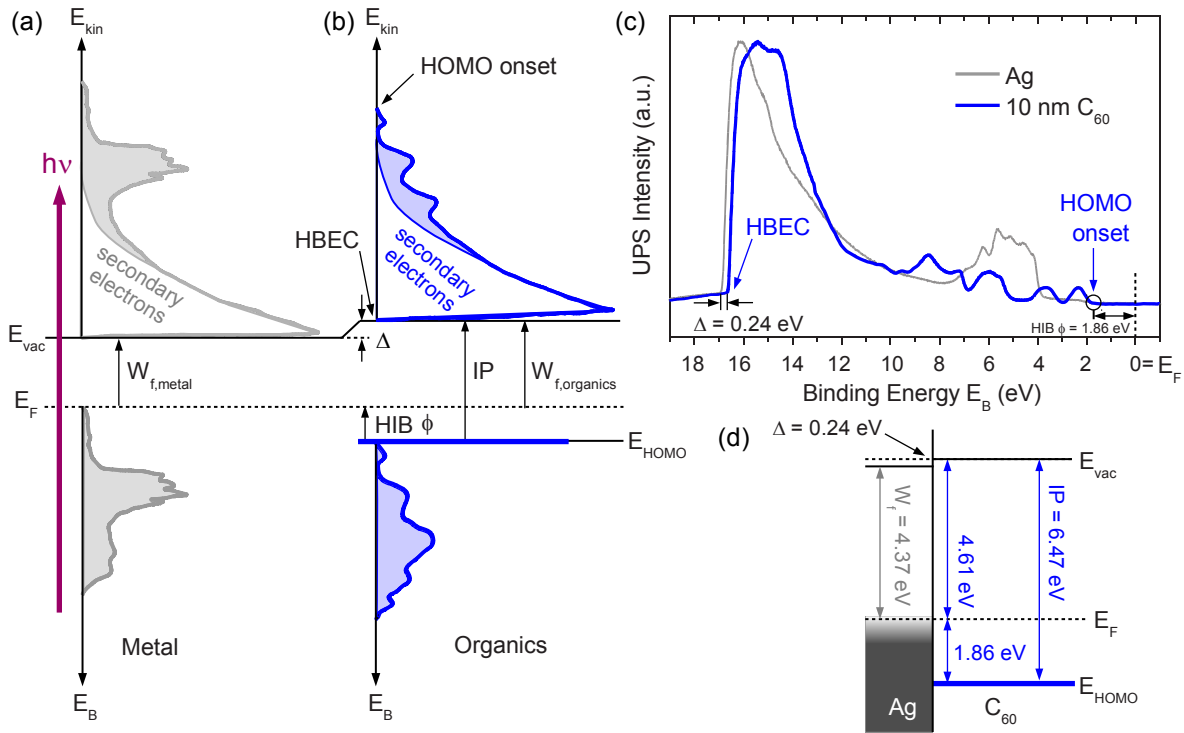


**Figure 4.15.:** Illustration of the UV excitation of a sample of (a) silver and (b)  $C_{60}$  (10 nm) with photons of an energy  $h\nu$ . Obtained are the work function ( $W_f$ ), the ionization potential (IP), the hole injection barrier ( $\phi$ ) and the interface dipole ( $\Delta$ ). (c) UPS signal intensity of the two materials versus electron binding energy  $E_B$  and kinetic energy  $E_{kin}$ . (d) Derived energy level alignment between the Ag substrate and  $C_{60}$  (adapted from Ref. [91,94,174]).

In case of the Ag substrate  $W_f = 4.37\text{ eV}$  is obtained. The fastest electrons, however, originate for a metal surface from the position of the Fermi edge  $E_F$  at  $E_B = 0\text{ eV}$ . For an organic semiconductor,  $E_F$  lies in the energy gap and the fastest photo electrons come from the HOMO onset  $E_{HOMO}$  at which the HOMO DOS

increases significantly. Consequently, the hole injection barrier *HIB*  $\phi$  to the metal is  $\phi = E_F - E_{HOMO}$ . The thin-film ionization potential IP is calculated from

$$IP = Wf_{organics} + \phi = h\nu - (E_{HBEC} - E_{HOMO}). \quad (4.68)$$

As depicted in Fig. 4.15 (d), 10 nm C<sub>60</sub> on Ag show  $\phi = 1.86$  eV and an IP = 6.47 eV. Often times, the vacuum level  $E_{vac}$  is not aligned throughout the sample, but shows an interface dipole  $\Delta$  in between two adjacent materials. Several effects causing this phenomena are discussed in Sec. 2.1.6. In UPS, interface dipoles are observed by a shift of the HBEC, i.e.

$$\Delta = E_{HBEC}^{metal} - E_{HBEC}^{organics} = Wf_{organics} - Wf_{metal}, \quad (4.69)$$

in case of Ag/C<sub>60</sub> to  $\Delta = 0.24$  eV. In conclusion, the important parts of the UPS spectrum for this thesis are the HBEC and the HOMO onset region. The corresponding values  $E_{HBEC}$  and  $E_{HOMO}$  are determined by fitting straight lines to the flanks of the signal and examining the intersection with the energy axis. Moreover, the DOS shape towards the HOMO tail is approximated by Gaussian and exponential fit functions as explained later in Sec. 6.

The signal broadening has been previously estimated by measurements of the gold Fermi edge to just 10 meV<sup>[94]</sup> whereas the experimental error due to reproducibility (e.g. sample preparation) is around 50 meV.<sup>[91]</sup> Excitation features due to satellite emissions (23.09 eV, 23.75 eV and 24.05 eV) of the He-I discharge lamp are subtracted prior to data evaluation. Further experimental details including measurement parameters can be found in Ref.<sup>[91]</sup>

#### 4.4.2. Conductivity

Conductivity measurements are performed *in-situ* during thin-film deposition at the evaporation tool UFO1. Prior, a meander type electrode configuration with two interlaced finger contacts is prepared through a overlay shadow mask on a glass substrate, in a combination of Cr/Au for the investigation of hole transport materials. An applied bias of  $V = 10$  V results in a current  $I$  between the contacts which rises with increasing film thickness  $d$  (monitored via QCM) and yields the conductivity  $\sigma$ :

$$\sigma = \frac{I}{V} \frac{l}{b \cdot d}. \quad (4.70)$$

The aspect ratio  $l/b$  is determined by the distance  $l$  and the width  $b$  of the contacts and is minimized, i.e. here to  $0.5 \text{ mm}/111 \text{ mm} = 4.5 \times 10^{-3}$  to examine even very low conductivities. The current is recorded with a Keithley 236 source measure unit, featuring a resolution limit of 100 fA which is increased to  $\sim 10$  pA due to long cable connections and imperfect shielding. Thus, conductivities such low as  $5 \times 10^{-10} \text{ S/cm}$  are resolvable from the slopes of  $I$  versus  $d$  plots with this configuration. Further details are found in Ref.<sup>[338]</sup>

### 4.5. Investigated Materials

In the following section, the organic semiconductor materials investigated in this thesis are presented. The overview covers eight hole transport materials, four molecular dopants, and two electron transporting/absorber materials used in solar cells. Figure 4.16 summarized the respective molecular structures. 3-zone-gradient vacuum sublimation

### 4.5.1. Hole Transport Materials

#### Pentacene (Sensient, Wolfen, Germany)

*Pentacene* (P5) is a polycyclic aromatic hydrocarbon ( $C_{22}H_{14}$ ), consisting of five benzene rings. One molecule possesses a length of 14 Å.<sup>[339]</sup> Vapor deposited, pentacene forms polycrystalline thin-films<sup>[128]</sup> ( $\rho = 1.32 \text{ g/cm}^3$ ),<sup>[73]</sup> mostly ordered predominantly in a herringbone structure,<sup>[56]</sup> and exhibits a surface roughness in the range of the film thickness. Ionization potential and electron affinity depend on the thin-film growth mode and are in the range of 4.9 eV<sup>[94]</sup> and 2.7 eV,<sup>[340]</sup> respectively. Hence, n-doping by strong donors such as  $W_2(hpp)_4$  has been realized.<sup>[183,341]</sup> P-doping is achieved utilizing the acceptors  $C_{60}F_{36}$  and  $F_6$ -TCNQ.<sup>[128,182,183]</sup> Despite having an optical gap of 1.82 eV,<sup>[94]</sup> pentacene is rarely reported as absorber material in organic solar cells.<sup>8</sup> Exposed to UV radiation, pentacene oxidizes strongly in air.<sup>[344]</sup> However, due to its strong conjugation and large grain sizes,<sup>[345]</sup> high charge carrier mobilities  $\sim 10^0 \text{ cm}^2/\text{Vs}$  and on/off ratios  $10^6 \dots 10^8$  are reported from OFET experiments,<sup>[127,346]</sup> which can be further improved controlling the morphology,<sup>[347]</sup> e.g. in case of solution processed TIPS-pentacene. Vapor deposited pentacene films at IAPP typically show mobilities  $10^{-3} \dots 10^{-1} \text{ cm}^2/\text{Vs}$ .<sup>[129,348]</sup> Three-times sublimed material is utilized. For impedance studies on the purification grade, two-times sublimed P5 is used, too.

#### ZnPc (CreaPhys, Dresden, Germany)

*Zinc-phthalocyanine* (ZnPc) is a standard absorber and commonly used as donor material in (bulk) heterojunctions of organic solar cells.<sup>[349–352]</sup> Neat thin-films of the material ( $\rho = 1.55 \text{ g/cm}^3$ )<sup>[353]</sup> are typically polycrystalline, and feature triclinic ( $\alpha$ ) and/or monoclinic ( $\gamma$ ) phases.<sup>[353]</sup> Surface orientation, film roughness and crystallite size are defined and controllable by the substrate (type and temperature) and the evaporation conditions.<sup>[83]</sup> Consequently, the ionization potential ranges within 5.0...5.4 eV.<sup>[91]</sup> The optical gap has been measured to 1.55 eV, which results in an electron affinity  $\sim 3.5 \text{ eV}$  (IPES: 3.34 eV).<sup>[354]</sup> The mobility is in the range of  $10^{-3} \text{ cm}^2/\text{Vs}$ .<sup>9</sup> In this work, three-times sublimed ZnPc is utilized.

#### Spiro-TTB (LumTec, Taiwan)

*2,2',7,7'-tetrakis-(N,N-di-methylphenylamino)-9,9'-spirobifluoren* (Spiro-TTB) has recently advanced to an alternative HTL material in OLEDs,<sup>[306,355]</sup> e.g. as it shows no remarkable hole injection barrier towards the electron blocking layer and red emitter host material NPB.<sup>[356]</sup> A conductivity increase is achieved by p-doping with  $F_6$ -TCNNQ.<sup>[306,355]</sup> Spiro-TTB consists of two *N,N,N',N'*-tetrakis(4-methylphenyl)benzidine (TTB) groups that spiro-carbon linked.<sup>10</sup> The wide-gap material ( $> 3 \text{ eV}$ )<sup>[357]</sup> has an ionization potential  $\sim 5.3 \text{ eV}$ <sup>[71]</sup> and forms smooth amorphous layers.<sup>[358]</sup> A hole mobility  $\sim 10^{-5} \text{ cm}^2/\text{Vs}$  is reported for intrinsic Spiro-TTB.<sup>[359]</sup> Prior to evaporation, the material is sublimated two times.

#### MeO-TPD (Sensient)

*N,N,N',N'*-tetrakis(4-methoxyphenyl)benzidine (MeO-TPD) has been frequently used as HTL material in OLED<sup>[108,360,361]</sup> and OPV<sup>[350,362]</sup> applications as it energetically aligns well with injection contacts and is easy p-dopable, e.g. by  $F_6$ -TCNNQ<sup>[207]</sup> or  $C_{60}F_{36}$ .<sup>[208]</sup> The thin-film IP is reported to 5.07 eV<sup>[91]</sup>, whereas

<sup>8</sup>Actually, only in case of singlet fission to receive two low-energy excitons upon absorption of one high energy photon P5 is extensively used in solar cells.<sup>[342,343]</sup> Pentacene solar cells typically suffer from low  $V_{OC}$ , e.g. in combination with  $C_{60}$ , and shortcuts due to rough layers.

<sup>9</sup>taken from: internal OSOL database

<sup>10</sup>Spiro compounds are bicyclic organic compounds with rings connected through just one atom. The connecting atom is the spiro (carbon) atom.

the literature values of for the optical gap differ from 2.96 eV<sup>[94]</sup> to 3.2 eV<sup>[363]</sup> thus leaving the material transparent. Hence, EA can be estimated to maximal 1.9 eV which hampers n-doping.<sup>[91]</sup> MeO-TPD forms amorphous layers ( $\rho = 1.463 \text{ g/cm}^3$ ), but suffers from a low glass transition temperature  $T_g = 67^\circ\text{C}$  which is known to lead to undesired crystallization.<sup>[364]</sup> Prior to evaporation, the material is sublimated twice.

#### BF-DPB (Sensient)

*N,N'-((diphenyl-N,N'-bis)9,9-dimethyl-fluoren-2-yl)-benzidine* (BF-DPB) is a common p-dopable hole transport material ( $\rho = 1.21 \text{ g/cm}^3$ ) in OPV.<sup>[109]</sup> Its structure is similar to MeO-TPD with differences only in the side chains.<sup>[363]</sup> Likewise, it forms amorphous films and shows an OFET mobility  $\sim 10^{-5} \text{ cm}^2/\text{Vs}$ .<sup>[130]</sup> However, the ionization potential is increased to  $\sim 5.2 \text{ eV}$ .<sup>[355]</sup> In this work, two-times sublimed BF-DPB is utilized.

#### NPB (Sensient)

*N,N'-Di(naphthalen-1-yl)-N,N'-diphenyl-benzidine* (NPB, also known as  $\alpha$ -NPD) matches with the previously introduced hole transport materials performance-wise, i.e. shows smooth layer formation ( $\rho = 1.14 \text{ g/cm}^3$ ), sufficient hole mobility<sup>[365]</sup>, and transparency (optical gap  $\sim 4 \text{ eV}$ ).<sup>[366]</sup> The IP is further increased to 5.4 eV,<sup>[305]</sup> which requires strong acceptors such as NDP9 for p-doping or a larger amount of dopant molecules as the doping efficiency is reduced (e.g. for F<sub>6</sub>-TCNNQ). NPB is mainly used in OLEDs as blocker material to contain electrons in the emission zone and host material for red emitters.<sup>[193,355,367]</sup> In this work, two-times sublimed NPB is utilized.

#### m-MTDATA or 'Starburst' (LumTec)

*4,4',4''-tris(3-methylphenylphenylamino)-triphenylamine* (m-MTDATA) is a rather 'oldfashioned' amorphous wide-gap (3.2 eV)<sup>[368]</sup> hole transport material for OLED applications.<sup>[368,369]</sup> It has an IP around 5.1 eV and a hole mobility  $\sim 10^{-5} \text{ cm}^2/\text{Vs}$ .<sup>[370]</sup> The material is utilized as obtained without any further purification.

### 4.5.2. Molecular Dopants

#### p-Dopants: F<sub>6</sub>-TCNNQ, NDP9 (Novaled GmbH, Dresden), and C<sub>60</sub>F<sub>36</sub> (Ionic Liquids Technologie GmbH, Heilbronn, Germany)

The p-dopant *1,3,4,5,7,8-hexafluorotetracyanonaphthoquinodimethane* (F<sub>6</sub>-TCNNQ) is the most frequently used one in this thesis. In literature it is further known as F<sub>6</sub>-TNAP<sup>[371]</sup> and similar to the prominent F<sub>4</sub>-TCNQ.<sup>[234]</sup> However, F<sub>6</sub>-TCNNQ is superior since it exhibits less volatility in vacuum, i.e. does not contaminate evaporation chambers. Its electron affinity is reported to be 5.37 eV,<sup>[371]</sup> however in-house cyclic voltammetry measurements yield 5.00 eV.<sup>11</sup>

The proprietary Novaled p-dopant NDP9 (short for *Novaled Dopant Positive 9*) can not be shown structure-wise, but is potent to dope materials of an IP up to 5.6 eV.<sup>[109]</sup> In this thesis, it is used for p-doping the deep lying hole transporter BPAPF in organic solar cells.

For the *fluorinated buckminster fullerene* C<sub>60</sub>F<sub>36</sub> an electron affinity of 5.38 eV is reported.<sup>[208]</sup> Hence, it is suited to p-doped the majority of HTL materials and due to its large molar mass of 1404.59 g/mol low doping concentrations (up to a factor 4 lower than for F<sub>6</sub>-TCNNQ) are achievable without technical modifications, e.g. a rotating shutter system.<sup>[91]</sup> Further, the molecules are expected to be stable in vacuum and thin-films, i.e. do not diffuse. All dopant molecules are utilized as obtained.

<sup>11</sup>Measured by Marion Wrackmeyer at IAPP, unpublished results

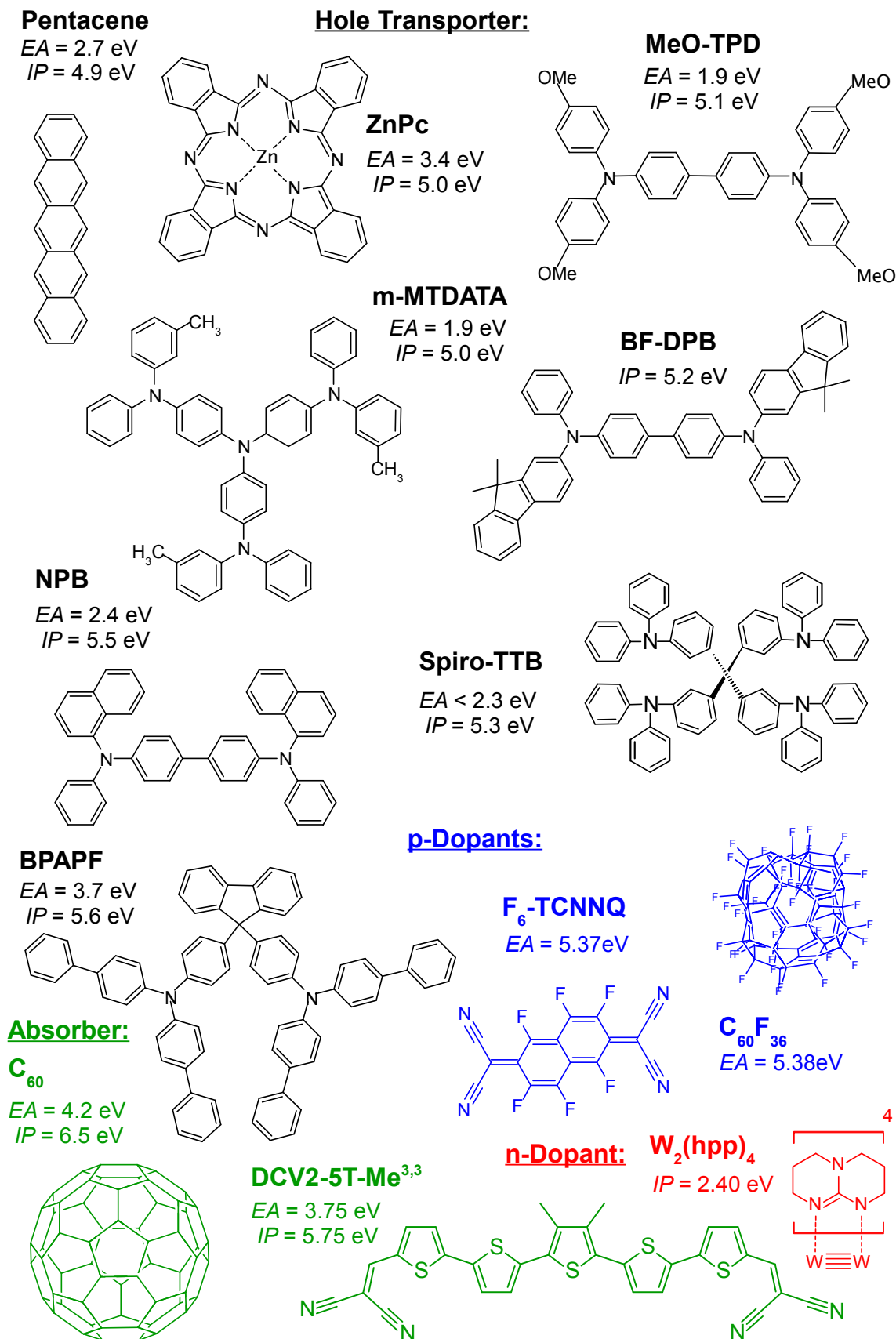


**Figure 4.16.:** Structures of molecules investigated in this thesis. Ionization potentials and electron affinities as reported in literature and measured by cyclic voltammetry or UPS. Further details are found in the text.



**n-Dopant:  $W_2(hpp)_4$  (NovaLED GmbH)**

*Tetrakis(1,3,4,6,7,8-hexahydro-2H-pyrimido[1,2-a]pyrimidinato)ditungsten (II)* is a di-metal anion complex and was first reported by Cotton *et al.* in 2002.<sup>[216]</sup> Its ionization potential was measured by UPS to 2.40 eV,<sup>[91]</sup> hence it acts a strong electron donor, but the pure material is prone to degradation in air and must be stored and handled with care.<sup>[220]</sup> In this thesis,  $W_2(hpp)_4$  is utilized to n-dope  $C_{60}$  in organic solar cell stacks and used as obtained.

**4.5.3. Solar Cell Materials****Absorber Materials:  $C_{60}$  (CreaPhys) and DCV2-5T-Me(3,3) (Synthon, Ulm, Germany)**

The buckminster fullerene  $C_{60}$  is commonly applied in small molecule organic solar cells as acceptor in combination with either  $(F_n^-)ZnPc$  or oligothiophenes, e.g. DCV derivatives.<sup>[82,109,351,372]</sup> Beneficial for high speed switching applications<sup>[373,374]</sup> are the naturally high mobility  $\sim 10^{-3} \text{ cm}^2/\text{Vs}^{12}$  and conductivities which can be increased to more than 1 S/cm upon n-doping, e.g. with  $W_2(hpp)_4$ .<sup>[219]</sup> For optimized surface wetting and the gate dielectrics, OFET mobilities of up to  $4.9 \text{ cm}^2/\text{Vs}$  are found in literature.<sup>[375]</sup> Driven at elevated current densities, even Joule's heating of single carrier n-i-n devices has been observed.<sup>[376,377]</sup>  $C_{60}$  forms micro-crystalline thin-films ( $\rho = 1.63 \text{ g/cm}^3$ ) with a mixture of mostly fcc (lattice constant  $a = 14.1 \text{ \AA}$ ) and hcp phases.<sup>[378]</sup> An ionization potential of 6.5 eV is observed in UPS and absorption measurements yield an optical gap of 2.3 eV which results in an EA in the order of 4.2 eV.<sup>[91]</sup> Recently,  $C_{60}$  is more and more replaced as ETL material by wide-gap transport materials, e.g. Bis-HFI-NTCDI, to reduce parasitic absorption in OSCs.<sup>[379]</sup> In this work,  $C_{60}$  is used as received.

Oligothiophenes have emerged in the last years,<sup>[380]</sup> improving over the established ZnPc donor material and allowing for new record efficiency solar cells with PCEs of 7.7 %<sup>[58]</sup> to 8.3 %<sup>[109]</sup> for single junctions and 9.7 % for triple junction cells.<sup>[109]</sup> The variety of DCV2-*n*T materials is provided by different length of the thiophene chain (*n*T) and possible attached side groups, altering the absorption properties and the HOMO position of the molecules. Similar to the acenes (cf. Sec. 2.1.3) the HOMO is shifted upwards for longer chains.<sup>[58]</sup> In this thesis, the benchmark material 2,2'-((3'',4''-dimethyl-[2,2':5',2'':5'',2''':5''',2''''-quinquethiophene]-5,5'''-diyl)bis(methanylylidene))dimalononitrile (DCV2-5T-Me<sup>3,3</sup>) is used in donor:acceptor blends with  $C_{60}$ . The IP is measured to 5.75 eV by UPS,<sup>[58]</sup> maximizing the  $V_{OC}$ . The optical gap is  $\sim 1.7 \text{ eV}^{13}$  and the material features strong absorption with a high extinction coefficient around  $\lambda = 600 \text{ nm}$ . In this work, DCV2-5T-Me<sup>3,3</sup> is used as obtained.

**Hole Transport Materials: BPAPF, Spiro-MeO-TAD, Spiro-MeO-TPD, Spiro-TAD**

9,9-bis[4-(*N,N*-bis-biphenyl-4-yl-amino)phenyl]-9H-fluorene (BPAPF) is used in solar cells to match the deep HOMO of DCV2-5T-Me<sup>3,3</sup> and minimize energy barriers. It has an IP = 5.6 eV, an optical gap of 2.9 eV, and is p-dopable by NDP9. The spiro derivatives differ in side chains thus range in IP = 5.0...5.4 eV and are used in HTM studies in perovskite solar cells.<sup>[71]</sup> The conductivities are summarized in the appendix A.4.

<sup>12</sup>Measured by Moritz P. Hein in OFET geometry at IAPP, unpublished results.

<sup>13</sup>taken from: internal OSOL database

## 4.6. Sample Preparation

### Conductivity, Impedance, and UPS Samples

Most of the investigated samples with exception of the ones for TSC measurements have been built at the evaporation multi chamber tool UFO1 (cf. Fig. 4.17 (d)). Its inter-connected vacuum chambers keep the samples at a base pressure of  $10^{-6}$ ... $10^{-9}$  mbar at all time, maintained by a set of oil diffusion and turbo molecular pumps. Each of the five individual evaporation chambers allows for the deposition of designated material (combinations), i.e. intrinsic organic films, p-doped and n-doped layers, or metal films as contacting electrodes. Finished samples are directly characterized in the attached UPS chamber (base pressure here  $\sim 10^{-11}$  mbar), kept in the storage for later measurements or transferred to the nitrogen atmosphere of the adjacent glovebox where they can be boxed, e.g. for transportation to an encapsulation robot. The

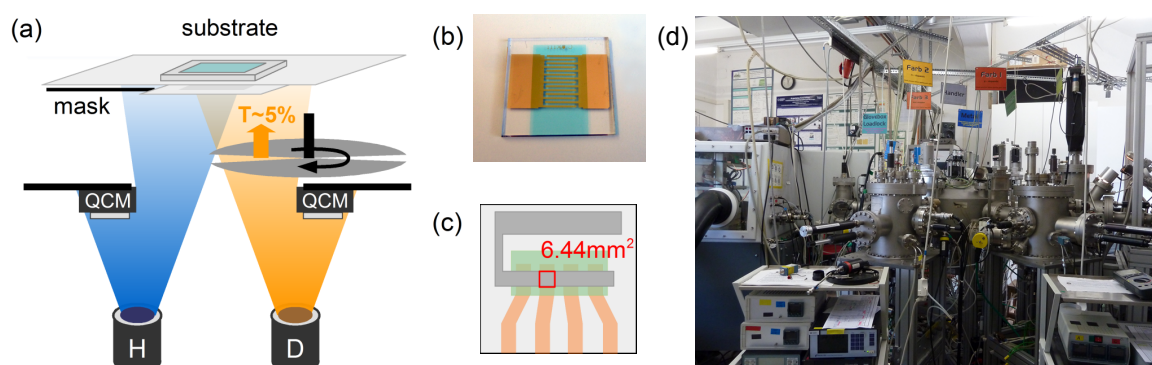


**Figure 4.17.:** (a) Schematic sketch of QCM controlled co-evaporation of a host:dopant system through a shadow mask on a substrate. The rotating shutter placed over the dopant source reduces the deposited amount to 5% of the incoming molecules. (b) Conductivity sample after in-situ characterization, here with a p-doped ZnPc film (blue) between a Cr/Au meander type electrode. (c) Standard diode layout for impedance samples and solar cells. The overlap of the bottom electrode (orange) with the top electrode (gray) both sandwiching the organic layer (green) defines the active area of 6.44 mm<sup>2</sup>. (d) Multi chamber evaporation tool UFO1.

organic molecules are typically materialized in forms of crystalline flakes or powders and purchased from material suppliers such as Sigma-Aldrich or Sensient. After multiple runs of tri-zone gradient sublimation to enhance the purification grade, the organic materials are mounted in ceramic crucibles at the bottom of the evaporation chambers. Wrapped by copper coils, the crucibles are heated via PID-controlled power circuits to elevated temperatures resulting in sublimation of the organics. Comparing Fig. 4.17 (a), the vapor flow is directed upwards through a shadow mask determining the film geometry onto the substrate. The thin-film deposition is controlled via quartz crystal micro-balances (QCMs) operating independently in the chamber to e.g. monitor both the material vapor flows in host:dopant systems. Upon evaporation, material perpetually stick at the QCMs hence changing their mass and their resonance frequency, respectively. Deposition rates used in this thesis are in the range 0.1...2 Å/s. Particularly important is the *tooling*, since the QCMs are mostly close to the crucible thus further away from the substrate. Utilizing a second QCM at the substrate position, this geometrical mismatch is determined as a calibration factor. Knowing the material density and the tooling, one is able to precisely control the thin-film growth.

Doping ratios as low as  $MR 10^{-5}$ <sup>[183]</sup> are realized with the aid of an additional rotating shutter ( $f = 1...3$  Hz), placed in the vapor flow between the monitoring QCM and the substrate. In that way, the controllable amount

of deposited dopant molecules is no longer limited to the resolution limit of the QCM and the host deposition rate can be kept as low as  $\sim 1 \text{ \AA/s}$ . The circular shutter has slit openings which enable a transmission of  $\sim 5\%$  which is verified by XPS and tooling QCM measurements.

Starting point for the investigated samples in this thesis are  $1 \times 1''$  glass substrates, either fully blank (conductivity) or ITO-coated (impedance, Thin Film Devices Ltd, United States). The glasses, pre-treated with acetone, ethanol, and isopropyl, are ozone cleaned (4 min, 250 W) before deposition. In case of conductivity, the contact finger structure (1 nm Cr, then Au/Ag) is prepared at first using an overlay shadow mask (cf. Fig. 4.17 (b)). UPS experiments are performed on  $\text{Ar}^+$ -sputtered, typically random orientated micro crystalline silver or gold foils (MaTeCK, Jülich, Germany) with a purity of 99.995% and a size of  $\sim 1 \times 1 \text{ cm}^2$ , which is conductively taped to an Omicron molybdenum sample holder.<sup>[91]</sup> Impedance samples are commonly finished with a 100 nm aluminum top contact, evaporated at deposition rates  $\sim 2 \text{ \AA/s}$  from a thermally more stable tungsten bucket. The overlap between the bottom electrode and the top electrode defines the active area of a single device to  $A = 6.44 \text{ mm}^2$  (cf. Fig. 4.17 (c)).

### TSC Samples

Since thermally stimulated currents are able to resolve in-depth trap distributions, best material and sample quality are required. For ensuring the highest possible level of sample stability (TSC measurements on one device can take up to several days), comparability, and reproducibility, TSC samples are processed at a commercial evaporation cluster tools (Kurt J. Lesker, Jefferson Hills, PA, United States) by designated technical staff. The evaporation technique is similar, however it is possible to handle large  $6 \times 6$  substrate wafers at once. The standard base pressure is  $\sim 5 \times 10^{-8}$  mbar, and various shutters and shadow masks as well as 12 organic and 3 metal material sources allow for a realization of different stack designs and film parameters (e.g. 'wedges' of film thickness, doping ratio) in one 'run'. Herein, the wafer is constantly rotating in a plane to maximize the homogeneity of the deposited film. Moreover, the substrates can be heated prior and while evaporation and residual gases such as  $\text{O}_2$  can be initialized during the sample fabrication process. Afterwards, the finished devices are encapsulated with glass and UV curable glue.

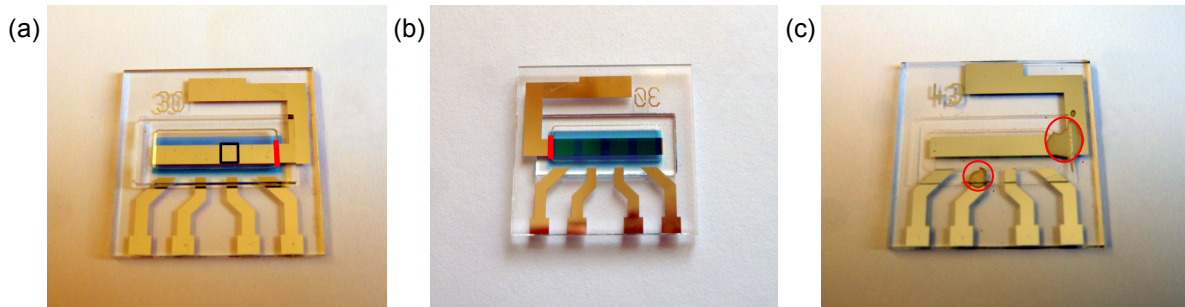


**Figure 4.18.:** (a) Front-side view (active area indicated by black square) and (b) back-side view of encapsulated samples for thermally stimulated currents as produced by Lesker. (c) In order to prevent device malfunction while sample cooling (contact rip-off is usually seen at the spot marked with a red bar), the encapsulation is removed prior the experiment and the electrodes are painted with colloidal silver (in red circles).

However, it has been found in this thesis that the initial encapsulation is not sufficient for temperature dependent measurements below 240 K. Probably due to diverse thermal expansion coefficients, glass and glue relax differently thus creating mechanical strains and eventually ripping apart the metal contacts underneath. As depicted in Fig. 4.18, the encapsulation is removed carefully before undertaking the first TSC measurement

on the sample. The contacts are strengthened with colloidal silver paint and the TSC runs are carried out as soon as possible, keeping the sample in the 'inert' atmosphere of the cryostat at all time until the characterization is finished.

# Estimation of the Transport Level in Organic Hole Transporting Layers

*Fermi level positions, hole injection barriers, and the HOMO DOS are determined for various hole transporting materials. UPS experiments are conducted on pristine organic semiconductor films grown on both, metal substrates as well as on a p-doped HTL Spiro-TTB interlayer. The DOS is modeled with a Gaussian distribution, which must be rescaled to correct signal broadening from UPS. Utilizing this data and the analytic approach of Arkhipov et al.<sup>[165]</sup> presented earlier in this thesis, solutions for the temperature dependent position of the transport level are calculated. In particular, hole transport is identified to occur at energies slightly above the HOMO onset at room temperature. At reduced temperatures, the transport level shifts deeper into the energy gap.*

While the charge carrier transport level  $E_{Tr}$  is clearly defined by the band edges in inorganic semiconductors, it is expected to be highly influenced by the broadened DOS for organic semiconductors. Especially for experimental techniques utilizing temperature variations such as TSC or DLTS<sup>1</sup>, the knowledge of  $E_{Tr}(T)$  is essential to obtain correct trap depths. Unfortunately, direct measurements of  $E_{Tr}(T)$  are not possible. Still, as discussed earlier in Sec. 2.2.3, Arkhipov et al. presented a sophisticated method to numerically obtain the position of the transport level as a function of temperature.<sup>[165]</sup> Their computational method is adapted and discussed in Sec. 5.2 for the investigated HTL materials. It demands a functional parametrization of the HOMO DOS  $g(E)$ , which is accessed via ultraviolet photoelectron spectroscopy measurements described in Sec. 5.1.

## 5.1. UPS Spectra

Employing BF-DPB, MeO-TPD, Spiro-TTB, m-MTDATA, pentacene (P5), and ZnPc, a selection of the most common hole transport materials in small molecule OLEDs, OSCs, and OTFTs is investigated. However, the substrate type can strongly affect the thin-film growth mode of the investigated materials.<sup>[93,353,381,382]</sup> Hence, UPS experiments are performed on different substrate types to provide a complete data set. The intrinsic HTLs are typically evaporated on sputter-cleaned silver substrates ( $W_f = 4.3$  eV) covered by a 7 nm p-doped decoupling layer. For the latter, Spiro-TTB:F<sub>6</sub>-TCNNQ (4 wt%) is used, which has evolved into a standard material combination in injection/extraction layers of OLEDs<sup>[355]</sup> and OSCs.<sup>[71]</sup> The intrinsic HTL films are deposited at a rate of 1 Å/s until they appear closed, i.e. no UPS signal from the materials underneath is visible anymore. For most (amorphous) thin-films, a thickness of 10 nm is sufficient. Rough layers, e.g. of P5, require 30...50 nm to appear closed. Since the origin of hole trap states is easier to identify in neat sample stacks<sup>2</sup>, the assembly of intrinsic HTLs on bare metal(-like) surfaces must be examined likewise.

<sup>1</sup>deep level transient spectroscopy

<sup>2</sup>especially important for the interpretation of TSC spectra in Ch. 8 and Ch. 9

Here, already existing and in-house measured UPS data (in particular by Dr. Selina Olthof<sup>[94]</sup>, Dr. Max L. Tietze,<sup>[183]</sup> and MSc Martin Schwarze<sup>[71]</sup>) is used and completed by additional measurements.

In Fig. 5.1 (a), respective UPS spectra of ZnPc, P5, m-MTDATA, Spiro-TTB, MeO-TPD, and BF-DPB on Ag/p-Spiro-TTB substrates are shown. For comparison, the UPS spectrum of sole Ag/p-Spiro-TTB is given. The HOMO onsets and HBECs are indicated by circles. Both yield the IPs following Eq. (4.68), which are summarized in Tab. 5.1 on pg. 80 and Tab. 5.3 on pg. 89. The difference between the Fermi level ( $E_B = 0$  eV) and the HOMO onset defines the hole injection barrier (HIB)  $\phi$  from the underlying Ag substrate into the organic layer. P-doping shifts the UPS spectrum towards lower binding energies (compare p-Spiro-TTB with Spiro-TTB), which results in a lower HIB (0.39 eV to 0.72 eV).<sup>[91,183]</sup> Simultaneously, the HBEC is observed at lower  $E_B$ , i.e., the work function of the thin-film increases. Interface dipoles between the underlying substrate and the thin-film, however, can not be quantified. The HBEC shifts originating from the interface dipole and the energy level alignment/bending in bulk layers can not be separated. For that purpose, UPS spectra of incremental monolayers rather than single bulk layers on the substrate must be considered.<sup>[202]</sup>

### 5.1.1. Analytical Description of the HOMO DOS

The calculation of the hole transport level requires an appropriate analytical expression  $g(E)$  for the HOMO DOS. The procedure to obtain  $g(E)$  is illustrated for Ag/p-Spiro-TTB as example in Fig. 5.1 (b) and (c). The quantities deduced from the UPS spectrum are listed in Tab. 5.1. The parameters of all other investigated HTL materials, classified by the substrate they are grown on, are summarized in Tab. 5.4 on pg. 89.

**Gaussian DOS Assumption.** Typically, the low binding energy flank is fitted manually with a tangent function to obtain the HOMO onset  $E_{\text{HOMO}}$ ,<sup>[91,94,205]</sup> i.e. the distance to the Fermi level (0.394 eV for p-Spiro-TTB). Remarkably broadened, the HOMO DOS can be identified with at least one Gaussian distribution in the form of

$$g(E) = \frac{N_\sigma}{\sqrt{2\pi}\sigma_{\text{UPS}}} \exp \left[ -\frac{(E - E_0)^2}{2\sigma_{\text{UPS}}^2} \right]. \quad (5.1)$$

Reviewing the materials in Fig. 5.1 (a), apparently at least two Gaussian distributions are necessary to entirely describe the UPS HOMO DOS double peaks in the related (tetrakis-benzidine type) materials BF-DPB, MeO-TPD, and (p-)Spiro-TTB. However, it is sufficient to include only the low energy Gaussian for further calculation of the transport level. Hole transport favorably happens at lower energies, which agrees with transport level predictions presented earlier in this thesis (cf. Sec. 2.2.3). Therefore, only the Gaussian distribution drawn black in Fig. 5.1 (b) is discussed in further steps for the examined Ag/p-Spiro-TTB sample. The fitted Gaussian distribution coincides with the manual tangent fit function (blue) for a wide range of the low energy flank. The Gaussian's turning points are situated at  $E_0 \pm \sigma_{\text{UPS}}$ . The tangent through  $E = E_0 - \sigma_{\text{UPS}}$  has the form

$$t_\sigma(E) = \frac{N_\sigma}{\sqrt{2\pi}\sigma_{\text{UPS}}} \exp \left[ -\frac{1}{2} \right] \left( 2 + \frac{E - E_0}{\sigma_{\text{UPS}}} \right) \quad (5.2)$$

and intersects zero at

$$E_{\text{HOMO}}^* = E_0 - 2\sigma_{\text{UPS}}. \quad (5.3)$$

The difference between the obtained  $E_{\text{HOMO}}^*$  of the Gaussian function and the manually fitted  $E_{\text{HOMO}}$  is below the UPS resolution limit ( $\sim 50$  meV).<sup>[91]</sup> This observation holds for all examined HTLs in this thesis, e.g. for p-Spiro-TTB ( $\sigma_{\text{UPS}} = 0.204$  eV),  $E_{\text{HOMO}}^* - E_{\text{HOMO}} = 0.408$  eV  $- 0.394$  eV = 0.014 eV.

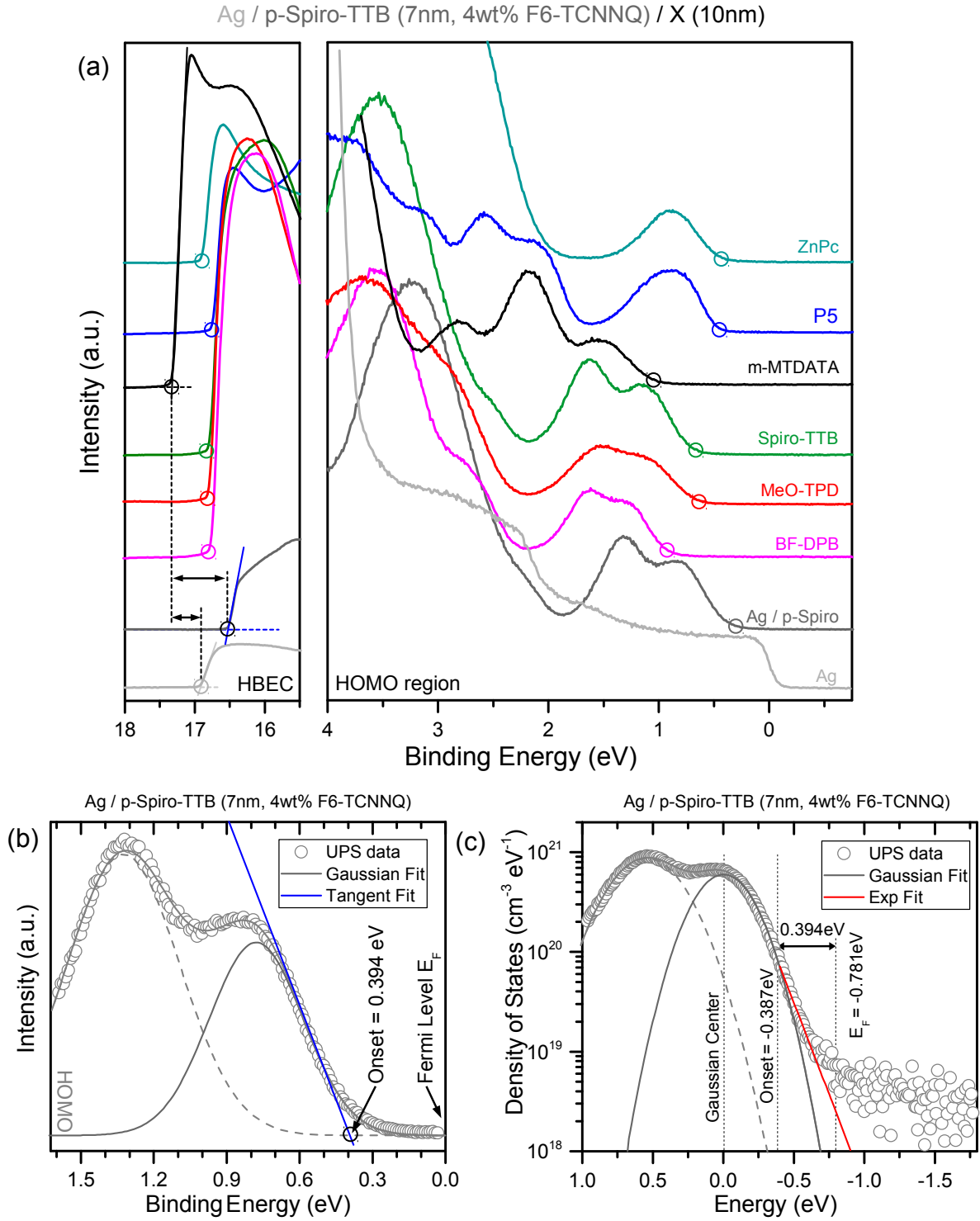


**Figure 5.1.:** (a) UPS spectra of various HTL materials (10 nm) on Ag/p-Spiro-TTB (7 nm, doped with 4 wt% F<sub>6</sub>-TCNNQ) substrates. (b) HOMO region of the p-doped Spiro-TTB layer on Ag. The black circle indicates the HOMO onset at 0.394 eV with respect to  $E_F$ . A set of Gaussians describes the UPS signal distribution and coincides with the tangent, yielding the HOMO onset, at the low energy flank. In (c), the signal is normalized to the effective density  $N_0 = 7.13 \times 10^{20} \text{ cm}^{-3}$ , assuming a thin-film density of  $\rho = 1.3 \text{ g/cm}^3$ . The energy axis is rescaled to match the center of the low energy Gauss  $E_0 = 0.0 \text{ eV}$ . For the latter, the turning point  $E = -2\sigma_{\text{UPS}}$  coincides with the HOMO onset. Starting here, an additional exponential function is added to describe the tail signal of the UPS spectrum (red line).

**Table 5.1.:** UPS data and HOMO DOS parametrization calculated from Fig. 5.1 (a)-(c) for Spiro-TTB doped by 4 wt% of F<sub>6</sub>-TCNNQ on Ag.

IP (eV)	$E_F^*$ (eV)	Onset* (eV)	$\phi$ (eV)	$N_\sigma$ (cm <sup>-3</sup> )	$\sigma_{\text{UPS}}$ (eV)	$N_\beta$ (cm <sup>-3</sup> )	$\beta$ (eV)
5.11	-0.781	-0.387	0.394	$2.88 \times 10^{20}$	0.192	$8.48 \times 10^{18}$	0.118

**Energy Axis and Normalization.** Since the hole transport level will be calculated with respect to the Gaussian DOS maximum, the energy axis of the UPS spectrum is rescaled by setting  $E_0 \stackrel{!}{=} 0$  (cf. Fig. 5.1 (c)). Consequently, the HOMO onset is at  $E_{\text{HOMO}} \simeq E_{\text{HOMO}}^* = -2\sigma_{\text{UPS}}$ . Furthermore, the UPS signal intensity is normalized. The area under the complete HOMO peak is identified with the molecule density  $N_0$ , estimated from the mass density  $\rho$  and the molar mass  $M$ . The density of states  $N_\sigma$  is a fraction of  $N_0$ , given by the peak area ratio of the (low energy) Gaussian distribution and the entire HOMO double peak.

**Exponential Tailing.** The semi-log plot of the UPS spectra reveals increasing deviations of the Gaussian DOS fit for energies  $E < E_{\text{HOMO}}^*$  (cf. Fig. 5.1 (c)). An exponential distribution

$$g_\beta(E) = \frac{N_\beta}{\beta} \exp\left[\frac{E - E_\beta}{\beta}\right] \quad (5.4)$$

is used to account for the tailing UPS signal. The energy  $E_\beta$  marks here the transition point between the Gaussian and the exponential distribution. Throughout all UPS measurements, it is found that

$$E_\beta \simeq E_{\text{HOMO}} \simeq E_{\text{HOMO}}^*. \quad (5.5)$$

The exponential description of possibly existing tail states is, however, restricted to the measurement noise level. As soon as the UPS signal is in the range of the noise level (e.g. for Ag/p-Spiro-TTB around  $E_{\text{cut}} = -0.75$  eV), the analytical fit is not unambiguous anymore. Possible appearances of tail states are discussed further in Sec. 5.2.2. In order to increase the signal-to-noise ratio, a higher number of repetitive UPS scans can be recorded. However, this leads to charging effects and distorted UPS spectra, especially for weakly conductive thin-films. Moreover, the signal underground originating e.g. from secondary excitation lines remains.

### 5.1.2. Amorphous-Type HTL Materials

Fig. 5.2 illustrates the HOMO regions of UPS spectra for BF-DPB, MeO-TPD, Spiro-TTB, and m-MTDATA - all grown on Ag/p-Spiro-TTB (top). They are compared with corresponding UPS spectra for the thin-films on metal(-like) substrates (bottom). Gaussian and exponential fits are included. The fitting parameters are found in Tab. 5.3 on pg. 89 and the results are discussed in the following.

**BF-DPB, MeO-TPD, Spiro-TTB.** In this series of structural similar molecules, the UPS spectrum of BF-DPB (0.185 eV) exhibits the smallest Gaussian width on Ag/p-Spiro in comparison to Spiro-TTB (0.204 eV) and MeO-TPD (0.211 eV) (cf. Fig. 5.2). The exponential tails are in the same order of magnitude ( $N_\beta = 1...2 \times 10^{19}$  cm<sup>-3</sup>,  $\beta = 0.16...0.19$  eV). Deviations arise where it is difficult to distinguish UPS signals from noisy background. The smaller  $\sigma_{\text{UPS}}$  suggests that BF-DPB is energetically less disordered than MeO-TPD and Spiro-TTB on Ag/p-Spiro due to reasons of either morphology or polarizability. However, this fact could explain that the intrinsic mobility of BF-DPB ( $5.7 \times 10^{-5}$  cm<sup>2</sup>/Vs) is higher than for intrinsic MeO-



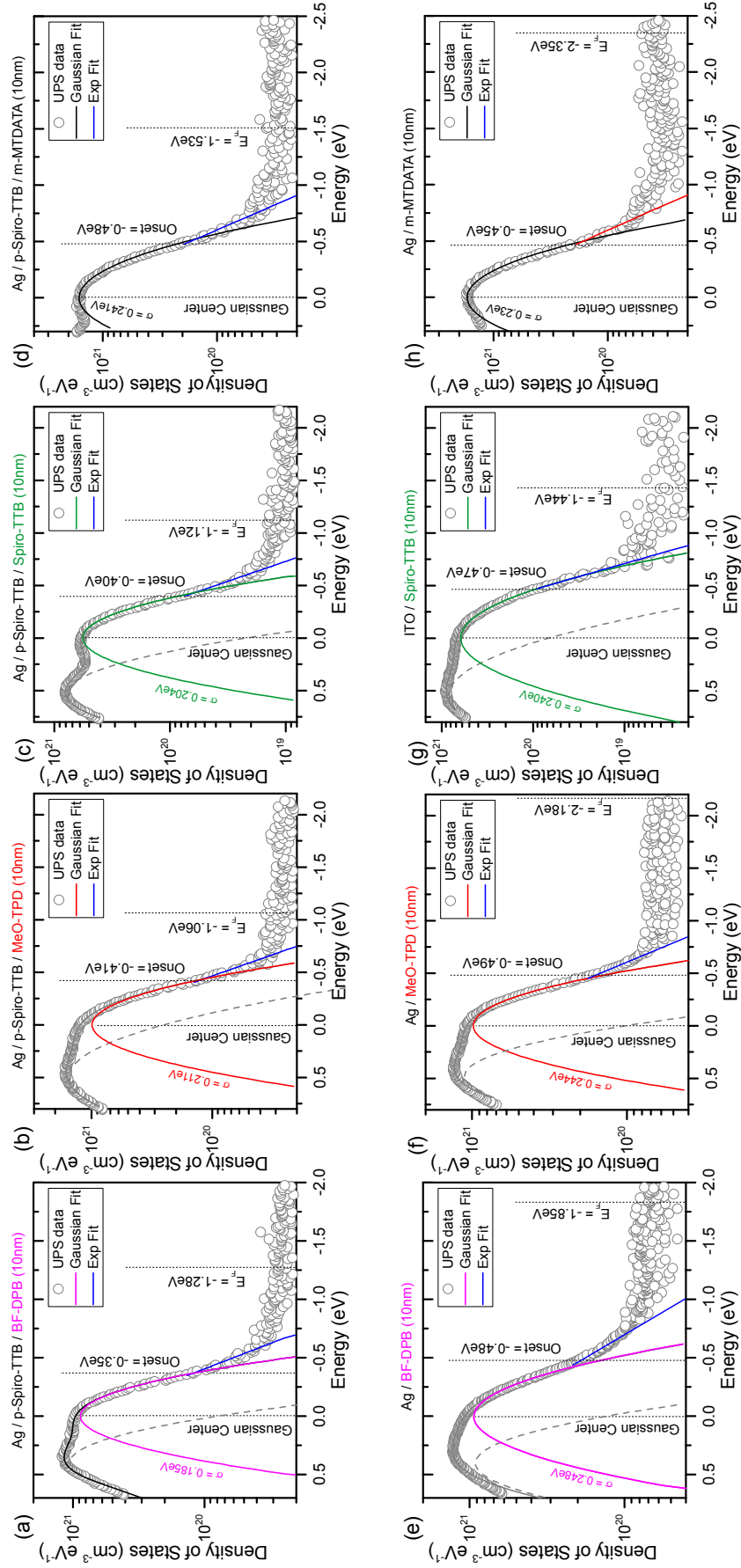


**Figure 5.2.:** Normalized and fitted UPS spectra of intrinsic BF-DPB, MeO-TPD, Spiro-TTB, and m-MTDATA on Ag/p-Spiro-TTB (7 nm, doped with F<sub>6</sub>-TCNNQ) substrates (a)-(d). UPS measurements for HTL films grown on pure silver or ITO substrates are shown in (e)-(h). The low energy flanks are described by Gaussian distributions. Tailing signals are quantified via exponential functions. The fit parameters are summarized in Tab. 5.4.

TPD ( $2.3 \times 10^{-5} \text{ cm}^2/\text{Vs}$ ) as reported by Menke *et al.*<sup>[240]</sup> When grown on a bare Ag or ITO substrate, all three molecules form strongly disordered films. The Gaussian width  $\sigma_{\text{UPS}}$  of their HOMO spectra increases to 0.248 eV (BF-DPB), 0.244 eV (MeO-TPD), and 0.240 eV (Spiro-TTB). At the same time, the Fermi level is located further away from the HOMO, e.g. for BF-DPB from  $-1.28 \text{ eV}$  on Ag/p-Spiro to  $-1.85 \text{ eV}$  on bare Ag. This trend will be explained when discussing pentacene on differently doped substrates in Sec. 5.1.3.

**m-MTDATA.** The hole transport material m-MTDATA exhibits, independently of the substrate, a broad HOMO. The Gaussian HOMO widths  $\sigma_{\text{UPS}}$  are 0.241 eV on p-Spiro/Ag and 0.230 eV on Ag (cf. Fig. 5.2 (d) and (h)). These results agree with observations made by Shirota *et al.*, who introduced m-MTDATA as highly amorphous HTL in OLEDs back in 1994.<sup>[368]</sup> A strong drawback of m-MTDATA is its low glass transition temperature of approximately  $75^\circ\text{C}$ , which is why m-MTDATA has been abandoned in OLED applications recently.

### 5.1.3. (Poly-)Crystalline HTL Materials

**Pentacene.** Fig. 5.3 (a) provides a comparison of UPS spectra for pentacene evaporated on various substrates. For 30 nm P5 grown on bare Ag, the silver Fermi edge is still visible at  $E_B = 0 \text{ eV}$  (compare purple and gray curves). This is attributed to pentacene's typically rough layer formation,<sup>[128]</sup> with a surface roughness in the range of the layer thickness. Incident UV light is able to penetrate the silver substrate and releases photo electrons at low binding energies. In areas of incomplete thin-film covering, e.g. at grain boundaries, the mean free path of free electrons is much higher than in the thin-film. Consequently, released photo electrons from the substrate are able to reach the detector. Hence, the P5 HOMO spectrum is superimposed by features of the Ag spectrum and thus appears broadened. Fitting of the HOMO spectrum with a comparably narrow Gaussian distribution fails and instead yields a width of  $\sigma_{\text{UPS}} = 0.380 \text{ eV}$ . In the following, P5 grown on Ag is not considered any further.

Tietze showed that introducing a thin 4 nm MeO-TPD spacer layer solves the roughness problem.<sup>[91]</sup> At a thickness of 30 nm P5, neither the Fermi edge of the Ag substrate nor features of the MeO-TPD layer are visible in the UPS spectrum (cf. Fig. 5.3 (b)) anymore. The Gaussian width of the HOMO spectrum is fitted to  $\sigma_{\text{UPS}} = 0.162 \text{ eV}$ , which indicates a less disordered thin-film. The  $E_F$  position at  $-1.72 \text{ eV}$  is identical to the situation without the spacer layer and matches very well with reported values of undoped pentacene.<sup>[183]</sup>

With an n-doped P5 layer underneath,  $\sigma_{\text{UPS}}$  is determined as 0.176 eV. The Fermi level of the intrinsic P5 on top shifts by 0.6...0.7 eV away from the HOMO and is at  $-2.4 \text{ eV}$  w.r.t. the HOMO maximum ( $-2.28 \text{ eV}$  to the Gaussian center, cf. Fig. 5.3 (a) and (c)). The HIB increases to 1.89 eV. Evaporated on p-doped Spiro-TTB, the situation inverts. The Fermi level is in this case close to the HOMO ( $-0.79 \text{ eV}$  to the Gaussian center). The hole injection barrier is strongly reduced to only 0.47 eV. Both observations are caused by Fermi level alignment across the doped sublayers and the intrinsic pentacene. Within the resolution limit of the UPS system (50 meV), the P5 HOMO exhibits a similar disorder parameter ( $\sigma_{\text{UPS}} = 0.154 \text{ eV}$ ) on Ag/p-Spiro and on Ag/MeO-TPD.

The shift of  $E_F$  and the change in HIB can be explained by earlier layer-by-layer UPS experiments for pentacene pin and nip homojunctions performed by Olthof.<sup>[94]</sup> Upon deposition of a p(n)-doped layer on the Ag substrate, a gradual level bending indicates the formation of a charge carrier depletion zone close to the substrate interface. HBEC and HOMO-onset are shifted to lower(higher) binding energies. Upon deposition

of an intrinsic layer on top, the Fermi level re-aligns through the layer stack. The HBEC position and the HOMO onset increase (decrease) gradually. An alternative notion is given in terms of charge carrier density profiles. The free hole (electron) density in p(n)-doped layers exceeds the respective number in intrinsic layers. Hence in the p(n)-doped layer, the Fermi level is close (far away) from the HOMO. For an adjacent intrinsic layer, the charge carrier density does not change abruptly, but diffusively decays into the undoped region. Hence, the Fermi level shifts gradually. The diffusion length of the free charge carriers is at least in the order of the pristine P5 on top. Only for sufficiently thick intrinsic layers (several 100 nm), the Fermi level positions (and consequently the HIBs) become independent of the layer underneath.<sup>[106]</sup> This explains the different  $E_F$  and HIB values for 30...50 nm P5 on intrinsic, p- and n-doped substrates. In the same way,  $E_F$  and the HIBs of all other HTLs differ on Ag/p-Spiro-TTB from their equivalents on bare Ag (cf. Fig. 5.2 and Tab. 5.3).

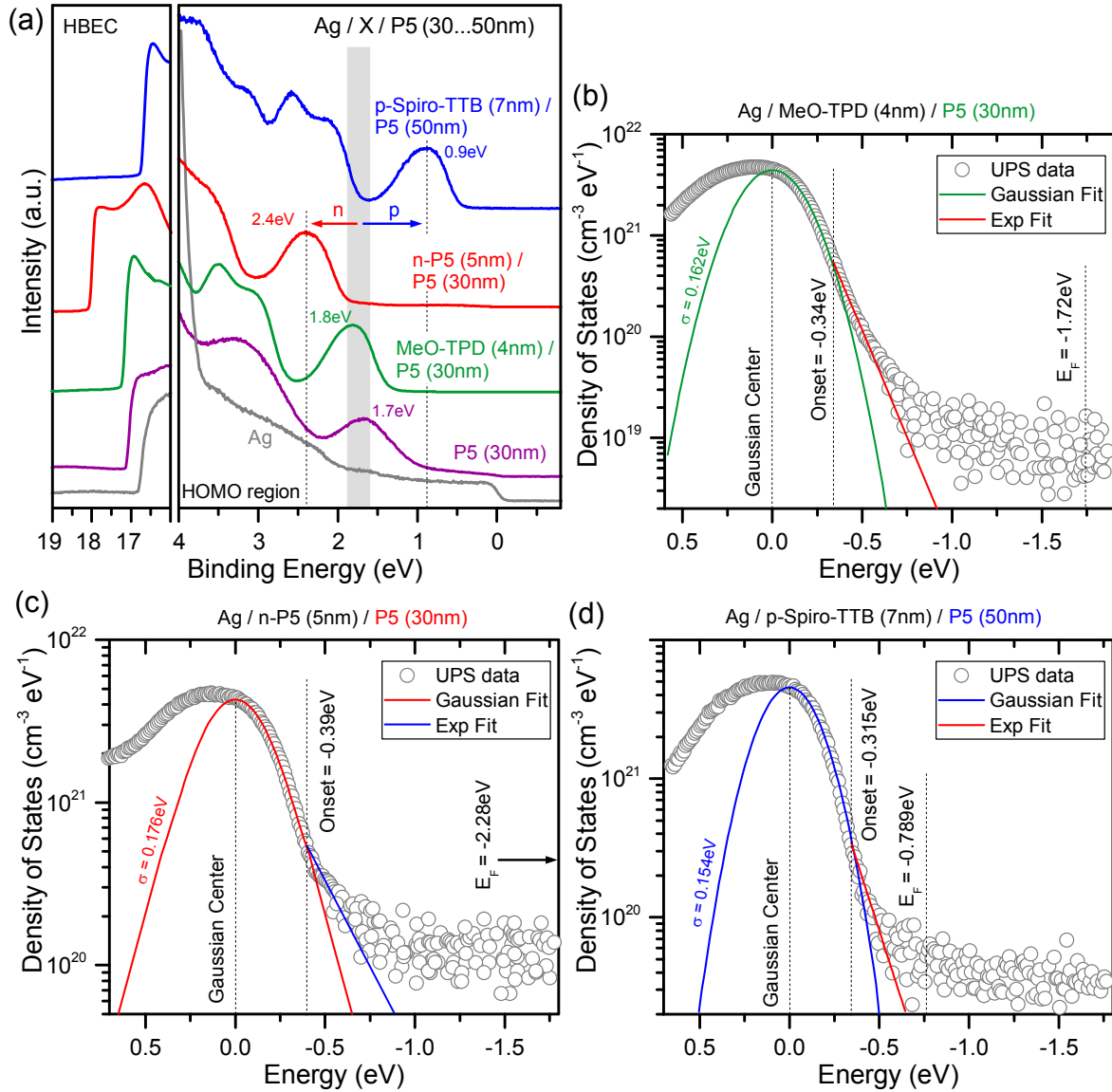


**Figure 5.3.:** (a) Pentacene UPS spectra on different substrate types. Introducing an intrinsic MeO-TPD interlayer does not significantly change the Fermi level position w.r.t. the HOMO peak maximum. An n-doped P5 spacer layer increases the HIB for P5, a p-doped Spiro-TTB layer decreases the HIB. In all three cases, the P5 HOMO is fitted by a Gaussian and an exponential distribution (b)-(d).

**ZnPc.** Fig. 5.4 depicts the UPS spectra for ZnPc grown on Ag/p-Spiro-TTB (a) or a sputter-cleaned Au substrate (b). The Fermi level position is deeper in the ZnPc gap ( $E_F = -1.55$  eV) on Au as compared to ZnPc on Ag/p-Spiro-TTB ( $E_F = -0.888$  eV) due to charge carrier diffusion from the sublayer. The differences in Gaussian width of the HOMO spectra for ZnPc on Ag/p-Spiro-TTB ( $\sigma_{\text{UPS}} = 0.219$  eV) and ZnPc on Au ( $\sigma_{\text{UPS}} = 0.180$  eV) suggest a strong influence of the substrate on the thin-film morphology. Tietze showed a strong difference in the IP (4.9...5.4 eV) between weakly (organic) and strongly (Ag) interacting substrates.<sup>[183]</sup> Re-examining this data reveals a ZnPc HOMO width of 0.180 eV on 0.7 nm MeO-TPD covered Ag and 0.160 eV on bare Ag. Despite similar IPs for Ag/p-Spiro-TTB/ZnPc (5.02 eV) and Au/ZnPc (5.07 eV), it is most likely that different substrate interactions lead to the diverging  $\sigma_{\text{UPS}}$ . Variable angle spectroscopic ellipsometry and GIXRD measurements of Schünemann *et al.* reveal a tilted orientation for ZnPc films on metal substrates that interact strongly with the  $\pi$ -system of the organic molecules.<sup>[382]</sup> In contrast, on weakly interacting substrates such as amorphous organic layers, the ZnPc molecules are found to stand upright on the substrate surface. Hence, the UPS spectra are likely to differ depending on molecular orientation and the thin-film growth mode induced by the orientation of the first organic monolayer. Similar observations are reported by Duhm for flat lying and upright standing sexithiophene derivatives.<sup>[381]</sup>

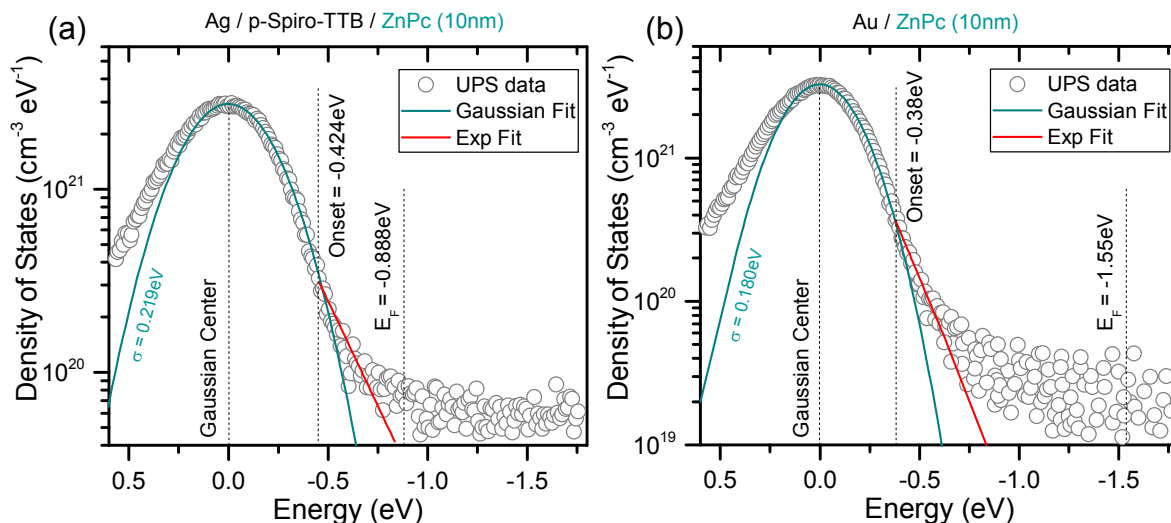


**Figure 5.4.:** UPS spectra and respective Gaussian and exponential fit functions for ZnPc grown on (a) Ag/p-Spiro-TTB or (b) bare Ag. The thin-film formation is substrate dependent and with a smaller disorder parameter  $\sigma_{\text{UPS}}$  for the strongly interacting metal surface.

#### 5.1.4. Estimation of Charge Carrier Densities from HIBs

The HIBs obtained in Sec. 5.1.2 and Sec. 5.1.3 are compared to reported values for intentionally doped layers. This allows to conclude on the number of majority charge carriers at the surface of the intrinsic HTLs, originating from the doped sublayer. Tietze *et al.* published HIB values for a large number of molar doping ratios in various HTL materials.<sup>[181,183,207]</sup> Fig. 5.5 is adapted from Ref.<sup>[183]</sup> to illustrate the p- and n-doping of P5 and ZnPc. Data for MeO-TPD is shown in Fig. 3.6 or can be found in Ref.<sup>[181,207]</sup>. Assuming a doping efficiency of  $\eta = 1$ , the free hole(electron) density  $p, n$  is approximated from  $p, n = \eta \times N_0 \times \text{MR} = N_0 \times \text{MR}$ .

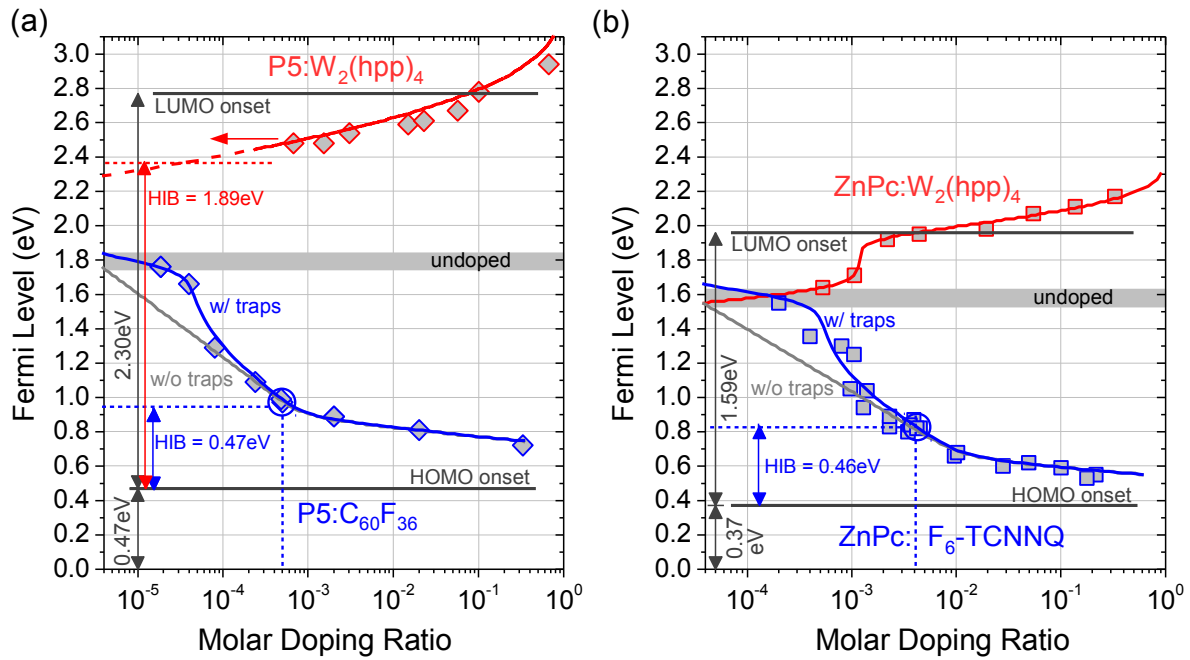


**Figure 5.5.:** UPS data for p-(blue) and n-(red) doping of (a) P5 and (b) ZnPc. The Fermi level is depicted with respect to the HOMO maximum. The HIBs refer to the HOMO onset. Solid lines illustrate the statistical model by Tietze<sup>[207]</sup> to describe the dependence of the Fermi level position on the molar doping ratio. Blue circles indicate the HIB of P5/ZnPc films on p-Spiro-TTB. Adapted from Ref. <sup>[183]</sup>

An HIB of 0.47 eV of P5 (on Ag/p-Spiro) corresponds to a hole concentration of  $p \simeq 1.4 \times 10^{18} \text{ cm}^{-3}$  (MR  $5 \times 10^{-4}$ ). For ZnPc, an HIB of 0.46 eV is identified with a hole concentration of  $p \simeq 6.5 \times 10^{18} \text{ cm}^{-3}$  (MR  $4 \times 10^{-3}$ ). MeO-TPD exhibits an HIB of 0.66 eV at  $p \simeq 5.8 \times 10^{18} \text{ cm}^{-3}$  (MR  $4 \times 10^{-3}$ ) holes.<sup>[207]</sup> The free hole concentration for the two latter is higher than for P5 because of their smaller layer thicknesses (10 nm versus 50 nm). In case of n-doping and an HIB of 1.89 eV for P5, an electron concentration slightly below  $n = 10^{18} \text{ cm}^{-3}$  (MR  $3.5 \times 10^{-4}$ ) can be deduced. In summary, diffusive tailing of majority charge carriers from doped sublayers is significant, even for intrinsic film thicknesses  $\simeq 30\text{...}50 \text{ nm}$ . This is crucial for modern OLED stack architectures, where significant charge carrier densities tailing from doped transport layers into the emission zone can cause triplet polaron quenching. Considering holes, the estimated charge carrier densities exceed the trap densities calculated by Tietze (P5:  $9.6 \times 10^{16} \text{ cm}^{-3}$ , ZnPc:  $7.2 \times 10^{17} \text{ cm}^{-3}$ , MeO-TPD:  $3.5 \times 10^{18} \text{ cm}^{-3}$ ). Consequently, trap filling from doped sublayers can be assumed for thinner intrinsic organic semiconducting layers. This mechanism is important, e.g. for contact doping in organic thin-film transistors.

### 5.1.5. Influence of Charge Screening on the IP

Interestingly, the ionization potential of pentacene depends slightly on the doping type of the sublayer. Whereas P5 on intrinsic MeO-TPD shows an IP of 5.02 eV, the IP for P5 on a p-doped layer increases to 5.06 eV. Evaporated on an n-doped layer, the IP of P5 decreases to 4.95 eV. Similar tendencies are reported for intentionally doped layers of P5, where the IP ranges from 4.9 eV (n-doped by MR 0.02 of Novaled property dopant NDN1) and 5.1 eV (intrinsic) to 5.3 eV (p-doped by MR 0.02 of Novaled NDP2).<sup>[94]</sup> A similar increase in ionization potential is observed upon p-doping of MeO-TPD with F<sub>4</sub>-TCNQ.<sup>[94]</sup> For an 1:1 blend of P5 and F<sub>4</sub>-TCNQ, Salzmann *et al.* measured even an IP = 5.75 eV.<sup>[178]</sup> They explained this increase with the

formation of molecular hybrid orbitals between P5 and the p-dopant. The bonding hybrid orbitals exhibit a larger IP. They are filled by CT electrons, which are accessible via UPS excitation. At increasing dopant MR, they consequently dominate the UPS signal. However, this theory does not apply here. The examined HTLs are undoped and a diffusion of entire dopant molecules from the substrate to the top of the sample stack is unlikely. Alternatively, the change in IP was explained by Olthof as being caused by weakened Coulomb screening. Upon p-doping, the additional positive charges weaken the electrostatic screening of a hole that is produced in the photoemission process. Consequently, the polarization energy decreases and therefore the IP increases. Upon n-doping the situation is vice versa. This mechanism is suggested to govern here the exact value of the IP. However, following Sec. 5.1.4, the density of free charge carriers is expected to be approximately one order of magnitude lower than for intentionally doped layers. The change in electrostatic screening is consequently lower and the IP split smaller. The deviations observed in IP are smaller than for intentionally p- or n-doped organic layers. However this effect must be considered when comparing IPs of thin-films on different sublayers.

### 5.1.6. Conclusions on DOS Widths determined by UPS

The Gaussian widths  $\sigma_{\text{UPS}}$  determined by fitting the DOS spectra in this chapter range from 0.15 eV (P5, on Ag/p-Spiro-TTB) and 0.18 eV (ZnPc, on Au) to 0.24...0.25 eV (BF-DPB, MeO-TPD, Spiro-TTB, and m-MTDATA). These results are similar to those obtained earlier by Tietze (P5: 0.16 eV and ZnPc: 0.17 eV, both on Ag/MeO-TPD, and MeO-TPD on Ag: 0.23 eV)<sup>[91,207]</sup> with the identical UPS setup. In general, materials with a more crystalline aggregation (P5 and ZnPc) tend to have a smaller disorder parameter  $\sigma$  than amorphous-type HTL materials. Substrate interactions with the adjacent molecules alter the energetic disorder  $\tilde{\sigma}$  or the spacial disorder  $\Sigma$  of the thin-films eventually yielding a different  $\sigma$ . Structural examinations such as (GI)-XRD in future work should clarify how strongly such thin-film are spatially distorted.

For the present UPS measurement system, Olthof estimated the signal broadening for the gold Fermi edge.<sup>[94]</sup> At RT, its width was measured to be 120 meV while Fermi-Dirac statistics predict 110 meV. Assuming the same broadening, a HOMO of  $\sigma_{\text{UPS}} = 150...240$  meV would exhibit an experimental error in its width of 12.5...20 meV. Furthermore, Schober discussed that UPS might be methodically erroneous to determine the disorder parameter  $\sigma$  for transport simulations.<sup>[306,307]</sup> It was argued that UPS is a surface-sensitive technique, and at the surface to the vacuum, the reduced dielectric stabilization causes electrostatic screening effects.<sup>[383]</sup> This affects the correlation in site energies and consequently the width of the DOS. Secondly, immanent features of the organics, such as vibronic modes of the ionized molecules, contribute to broaden the UPS signal.<sup>[306,383]</sup> In spite of that and due to a lack in alternatives,  $\sigma_{\text{UPS}}$  obtained from UPS measurements has been taken when concluding on the DOS disorder in organic semiconductors.<sup>[96,305,306]</sup>

However, most recent advances in computing DOS disorder parameters by quantum mechanical approaches<sup>[383–388]</sup> have strengthened the concerns about the applicability of UPS data. By employing molecular polarizability calculations from dipole interactions (Thole model)<sup>[384,389]</sup>, Schrader *et al.* reported  $\sigma \simeq 0.1$  eV for DCV-*n*T donor materials in 2012.<sup>[385]</sup> For the potent DCV2-5T-Me(3,3)<sup>[109]</sup>, Poelking *et al.* calculated  $\sigma = 0.10$  eV.<sup>[383]</sup> Here, the UPS spectrum of 12 nm DCV2-5T-Me(3,3) on Ag,<sup>3</sup> shown in Fig. 5.6 (a), exhibits a Gaussian width of  $\sigma_{\text{UPS}} = 0.22$  eV. A similar mismatch between UPS results and theoretical calculations is found for ZnPc and P5, where the findings in this chapter are  $\sigma_{\text{UPS}} = 0.18...0.22$  eV and  $\sigma_{\text{UPS}} \simeq 0.16$  eV, but Poelking *et al.* yield  $\sigma = 0.08$  eV and  $\sigma = 0.03$  eV, respectively. Resembling values were computed by Yavuz *et al.*, namely  $\sigma = 0.068$  eV for P5,  $\sigma = 0.075$  eV for the P5 modification DNTT<sup>4</sup>, and  $\sigma = 0.091$  eV for DCV-4T.<sup>[386]</sup>

<sup>3</sup>measured by Dr. Max Tietze, IAPP

<sup>4</sup>dinaphtho[2,3-b:2',3'-f]thieno[3,2-b]thiophene

**Table 5.2.:** Comparison of (HOMO) disorder parameters  $\sigma$  obtained via different experimental and theoretical methods for several small molecule organic semiconductors.

Material	$\sigma$ (eV)	Method	Ref.
P5	0.15...0.18	UPS	this work
	0.163	UPS	Ref. [91]
	0.068	Thole model sim.	Ref. [386]
	0.03	Thole model sim.	Ref. [383]
	0.07	KPFM <sup>5</sup> + TFT	Ref. [390]
	0.20...0.25	photocurrents	Ref. [391]
ZnPc	0.18...0.22	UPS	this work
	0.170	UPS	Ref. [91]
	0.08	Thole model sim.	Ref. [383]
(MeO-)TPD	0.21...0.24	UPS	this work
	0.225	UPS	Ref. [181,207]
	0.13	DFT	Ref. [388]
$\alpha$ -NPD	0.14	DFT	Ref. [388]
Spiro(MeO-TAD,TTB)	0.20...0.24	UPS	this work
	0.122	time-of-flight	Ref. [392]
DCV2-5T-Me(3,3)	0.22	UPS	this work
	0.10	Thole modelsim.	Ref. [383,385]
C <sub>60</sub>	0.2...0.3 (HOMO)	UPS	Ref. [91,362]
	0.3...0.4 (LUMO)	IPES	Ref. [91,362]
	0.06...0.08	mol. dynamics sim. + DFT	Ref. [387]

Pursuing a DFT approach, Friederich *et al.* published  $\sigma = 0.13...0.14$  eV for the strongly disordered benzidine derivatives  $\alpha$ -NPD (NPB) and TPD. [388] The structural similar MeO-TPD shows  $\sigma_{\text{UPS}} = 0.21...0.24$  eV.

Table 5.2 summarizes the deviations between the UPS results and alternative/computational approaches towards  $\sigma$ . Across the board, photo excitation techniques lead to values  $\sigma$  increased by approx. 100 meV as compared to the computational findings. Here, electron-phonon interactions, i.e. vibronic signal broadening are suspected. [383] Besides UPS, photocurrent measurements (e.g. Lang *et al.* measured  $\sigma = 0.20...0.25$  eV for P5, [391]) and inverse photoelectron spectroscopy results are significantly broadened and do not apply one-to-one to the disorder of an organic semiconductor DOS. Signal broadening of IPES is illustrated in Fig. 5.6 (b), which illustrates the combined UPS/IPES spectra<sup>6</sup> for C<sub>60</sub> on Au (taken from Ref. [362]). Both HOMO ( $\sigma_{\text{UPS}} \simeq 0.2$  eV) and LUMO width ( $\sigma_{\text{IPES}} = 0.3...0.4$  eV) exceed the theoretical predictions ( $\sigma = 0.06...0.08$  eV) published by Tummala *et al.* most recently, examining the static and dynamic disorder in fullerenes. [387] In contrast to photo excitation techniques, charge carrier transport measurements obviously do not suffer from signal broadening. Time-of-flight measurements on Spiro-MeO-TAD, structurally similar to the benzidines investigated in this thesis, reveal an energetic disorder  $\tilde{\sigma} \simeq 0.1$  eV and a spatial disorder  $\Sigma \simeq 0.07$  eV. [392] Both combine to  $\sigma = \sqrt{\tilde{\sigma}^2 + \Sigma^2}$  [387]  $\simeq 0.12$  eV, which is approx. 100 meV smaller than typical UPS results (cf. Tab.5.2). For P5, Yogev *et al.* manipulated its growth mode on SiO<sub>2</sub> via an HMDS seed layer and obtained  $\sigma = 0.07$  eV by Kelvin probe force microscopy and thin-film transistor measurements. [390]

<sup>6</sup>measured by Selina Olthof at Princeton University

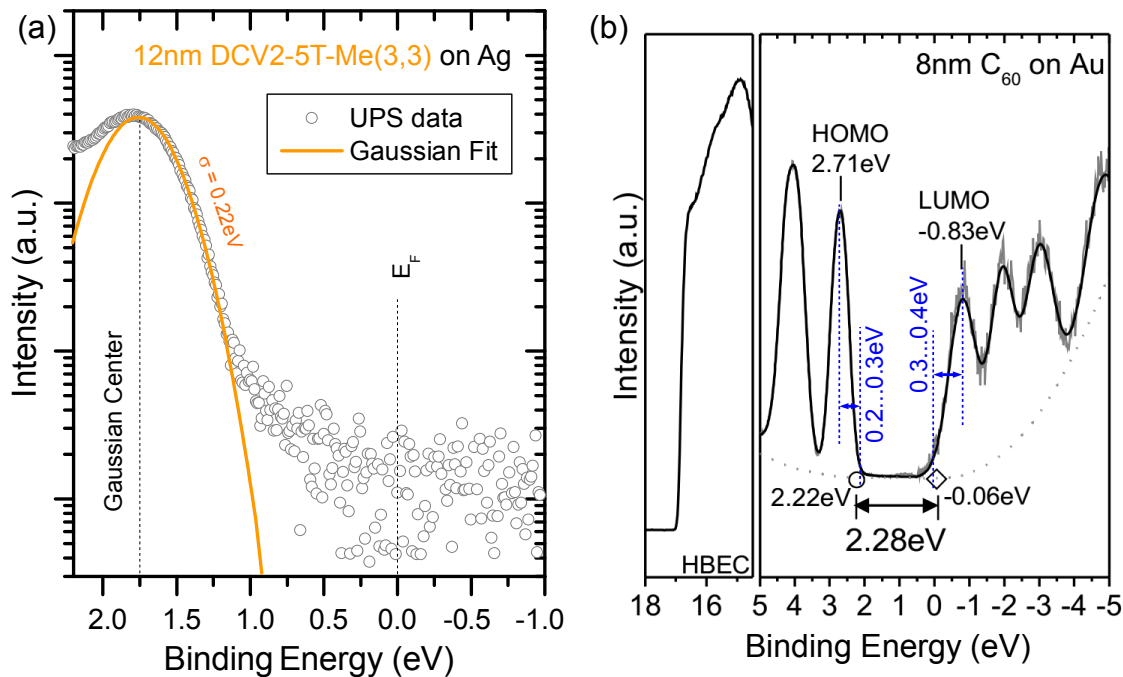


**Figure 5.6.:** (a) UPS spectrum of the donor material DCV2-5T-Me(3,3) grown on Au, measured by Dr. Max Tietze, IAPP. The HOMO signal is fitted with a Gaussian distribution of  $\sigma = 0.22$  eV. (b) IPES/UPS of  $C_{60}$  on Au, measured by Dr. Selina Olthof at Princeton University (taken from Ref. <sup>[91,362]</sup>). The DOS widths are indicated by blue lines.

In summary, the site energy disorder parameters  $\sigma_{\text{UPS}}$  obtained from fitting UPS spectra are considerably enlarged by approx. 100 meV. For most of the various HTL materials examined in Sec. 5.1, this equals a broadening by a factor two. Subsequently, the Gaussian DOS widths  $\sigma$  and the exponential tailing parameters  $\beta$  must be adapted, i.e. divided by a factor two, when approaching the transport levels for the HTL materials in the following section.



**Table 5.3.:** Summary of thin-film properties and UPS data for various HTL materials, separated by the substrates they are grown on.

Material	$\rho$ (g/cm <sup>3</sup> )	M (g/mol)	$N_0$ (cm <sup>-3</sup> )	Substrate	IP (eV)	$E_F^*$ (eV)	Onset* (eV)	HIB $\phi$ (eV)
BF-DPB	1.21	720.941	$1.01 \times 10^{21}$	Ag*	5.23*	-1.85*	-0.48*	1.37*
				Ag/p-Spiro	5.377	-1.275	-0.354	0.921
MeO-TPD	1.463	608.725	$1.45 \times 10^{21}$	Ag*	5.037*	-2.18*	-0.486*	1.694*
				Ag/p-Spiro	5.194	-1.064	-0.405	0.659
Spiro-TTB	1.3	1097.47	$7.13 \times 10^{20}$	ITO <sup>†</sup>	5.237 <sup>†</sup>	-1.44	-0.47	0.970 <sup>†</sup>
				Ag/p-Spiro	5.279	-1.117	-0.400	0.717
m-MTDATA	1.3	789.018	$9.92 \times 10^{20}$	Ag	5.007	-2.35	-0.45	1.898
				Ag/p-Spiro	4.991	-1.531	-0.478	1.053
ZnPc	1.55	577.932	$1.62 \times 10^{21}$	Au <sup>◇</sup>	5.070 <sup>◇</sup>	-1.55 <sup>◇</sup>	-0.38 <sup>◇</sup>	1.170 <sup>◇</sup>
				Ag/p-Spiro	5.015	-0.888	-0.424	0.464
P5	1.32	278.35	$2.86 \times 10^{21}$	Ag <sup>◇</sup>	5.06 <sup>◇</sup>	-1.71	(-0.77)	0.940 <sup>◇</sup>
				Ag/MeO-TPD	5.02	-1.72	-0.34	1.38
				Ag/p-Spiro	4.95	-0.789	-0.315	0.474
				Ag/n-P5*	5.06*	-2.28	-0.39	1.89*

**Table 5.4.:** Determined Gaussian and exponential DOS parameters,  $(\sigma, \beta) = 0.5 \times (\sigma, \beta)_{\text{UPS}}$ .

	Substrate	$N_G$ (cm <sup>-3</sup> )	$\sigma_{\text{UPS}}$ (eV)	$\sigma$ (eV)	$N_\beta$ (cm <sup>-3</sup> )	$\beta_{\text{UPS}}$ (eV)	$\beta$ (eV)	$E_{\text{cut}}$ (eV)
BF-DPB	Ag	$5.91 \times 10^{20}$	0.248	0.12	$6.62 \times 10^{19}$	0.345	0.17	-0.75
	Ag/p-Spiro	$4.64 \times 10^{20}$	0.185	0.09	$2.42 \times 10^{19}$	0.189	0.09	-0.62
MeO-TPD	Ag	$6.82 \times 10^{20}$	0.244	0.12	$4.52 \times 10^{19}$	0.270	0.14	-0.70
	Ag/p-Spiro	$5.83 \times 10^{20}$	0.211	0.11	$2.49 \times 10^{19}$	0.175	0.09	-0.70
Spiro-TTB	ITO	$3.71 \times 10^{20}$	0.24	0.12	$9.61 \times 10^{18}$	0.108	0.05	-0.70
	Ag/p-Spiro	$3.01 \times 10^{20}$	0.204	0.10	$1.21 \times 10^{19}$	0.164	0.08	-0.65
m-MTDATA	Ag	$9.88 \times 10^{20}$	0.23	0.12	$4.16 \times 10^{19}$	0.196	0.10	-0.75
	Ag/p-Spiro	$9.92 \times 10^{20}$	0.241	0.12	$3.52 \times 10^{19}$	0.190	0.10	-0.75
ZnPc	Au	$1.45 \times 10^{21}$	0.18	0.09	$5.98 \times 10^{19}$	0.131	0.07	-0.65
	Ag/p-Spiro	$1.45 \times 10^{21}$	0.219	0.11	$6.22 \times 10^{19}$	0.189	0.05	-0.68
P5	Ag	-	(0.388)	-	-	-	-	-
	Ag/MeO-TPD	$1.93 \times 10^{21}$	0.162	0.08	$5.97 \times 10^{19}$	0.104	0.05	-0.60
	Ag/p-Spiro	$1.91 \times 10^{21}$	0.154	0.08	$4.80 \times 10^{19}$	0.108	0.05	-0.60
	Ag/n-P5	$1.97 \times 10^{21}$	0.176	0.09	$4.67 \times 10^{19}$	0.110	0.06	-0.55

<sup>†</sup> measured by PhD student Martin Schwarze, IAPP, published in Ref. [71]

\* measured by Dr. Selina Olthof, IAPP.

<sup>◇</sup> measured by Dr. Max Tietze, IAPP, published in Ref. [183]

## 5.2. Temperature Dependent Transport Levels

### 5.2.1. Models and Influence of DOS Parameters

Previously introduced in Sec. 2.2.3, the hopping model calculations by Arkhipov *et al.* allow to compute the temperature dependent transport level in an energetically and spatially disordered system of localized states. By employing a Gaussian or an exponential DOS, they showed fundamental correlations between the DOS shape and  $E_{Tr}(T)$ . The application to a real system was reported by Kadashchuk *et al.* to explain TSL measurements for a methyl-substituted ladder-type poly(paraphenylene).<sup>[166]</sup> The authors fitted their TSL spectra assuming  $E_{Tr}(T)$  and an attempt-to-escape frequency  $\nu_0$  and found two narrow Gaussian distributions ( $\sigma_1 = 0.069$  eV and  $\sigma_2 = 0.042$  eV). They were identified with the HOMO DOS and tailing of states towards the energy gap. However up to now, no implementation of disordered DOS data from UPS or theoretical calculations in transport level simulations has been published. Besides, it is still under debate whether backward hops from the target site to the initial site must be excluded in the  $E_{Tr}$  calculation or not. In their early work, Arkhipov *et al.* emphasized that suppressing charge carrier jumps back to their initial states means actual conductivity.<sup>[165]</sup> Otherwise, charge carrier can take round-trips in isolated areas of the disordered DOS without any spatial propagation in the mean of time. Hence, introduced in Sec. 2.2.3, the transport level position  $E_{Tr'}(T)$  must obey the relation

$$\int_{-\infty}^{E_{Tr'}} g(E) dE \int_0^{(E_{Tr'} - E)/2\gamma k_B T} r^2 \{1 - \exp[-n_b(E, r)]\} dr = \frac{1}{4\pi} \quad (2.35)$$

with the number of accessible neighboring hopping sites  $n_b$  as

$$\begin{aligned} n_b(E_j, r) &= 2\pi \int_0^r dr' r'^2 \int_{\arccos(r'/2r)}^{\pi} d\theta \sin \theta \int_{-\infty}^{E_j + 2\gamma k_B T(r-r')} g(E) dE \\ &= \frac{\pi r^3}{12} \left\{ 11 \int_{-\infty}^{E_j} g(E) dE \right. \\ &\quad \left. + \int_{E_j}^{E_j + 2k_B T \gamma r} g(E) dE \left[ 8 \left( 1 - \frac{E - E_j}{2k_B T \gamma r} \right) \right. \right. \\ &\quad \left. \left. + 3 \left( 1 - \frac{E - E_j}{2k_B T \gamma r} \right)^4 \right] \right\}. \end{aligned} \quad (2.33)$$

The energy of the targeted sites is denoted as  $E_j$ , the inverse localization length is represented by  $\gamma$ . However, this expression has been replaced shortly afterwards by the authors.<sup>[167,393]</sup> In literature, their simplified description of the transport level, introduced in the initial publication Ref.<sup>[165]</sup>, is found almost exclusively.<sup>[166,167,169]</sup> Here, the transport level is identified with the most frequently visited energy  $E_{Tr'}(T)$  and follows the equation

$$\int_{-\infty}^{E_{Tr''}} g(E) (E - E_{Tr''})^3 dE = \frac{6}{\pi} (\gamma k_B T)^3. \quad (2.32)$$

It has been addressed that the Mott  $T^{-1/4}$  law<sup>[139]</sup> for the derived conductivities and the temperature dependency of the transport energy are not significantly affected by round-trips of charge carriers.<sup>[394]</sup> In the context of this thesis, *python* calculation routines have been written to solve both transcendent integral equations Eq. (2.32) and Eq. (2.35), yielding  $E_{Tr''}(T)$  and  $E_{Tr'}(T)$ . The source code is documented in Sec. A.2.

In the following, the dependence of  $E_{Tr'}(T)$  and  $E_{Tr''}(T)$  on the DOS shape  $g(E)$  and inverse localization parameters  $\gamma$  are examined. First, the results published by Arkhipov *et al.* for a Gaussian ( $\sigma = 0.05...0.125$  eV) and an exponential DOS ( $\beta = 0.0025...0.1$  eV) are reproduced in a series of simulations. Second, Fig. 5.7 illustrates solutions of  $E_{Tr'}(T)$  and  $E_{Tr''}(T)$  for variations of  $\sigma$  and  $N_\sigma$  within the ranges presented above in Sec. 5.1. Basically, both energy levels are shifted by a few 100 meV towards the energy gap-mid for decreasing temperatures and increasing DOS width or density. Below, the results for a Gaussian DOS are discussed more in detail. Similar dependencies hold for an exponential DOS.

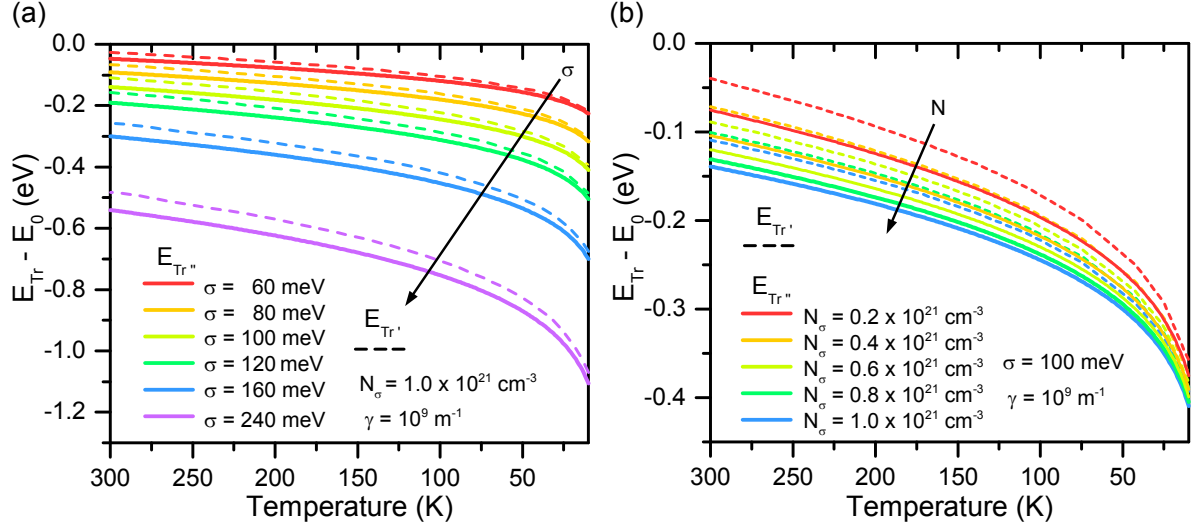


**Figure 5.7.:** Transport level positions  $E_{Tr'}$  (dashed lines) and  $E_{Tr''}$  (solid lines, most probable jump-to-energy) versus temperature, calculated from Eq. (2.35) and Eq. (2.32). For both illustrations, a Gaussian DOS is assumed. In particular, (a) shows a variation of the Gaussian width  $\sigma$  for a fixed  $N_\sigma = 10^{21} \text{ cm}^{-3}$ . (b) Variation of the number of states  $N_\sigma$  for  $\sigma = 100 \text{ meV}$ .

**Transport Level versus Most Probable Jump-to-Energy.** The solutions for  $E_{Tr'}(T)$  and  $E_{Tr''}(T)$  both move monotonously with lower temperature towards the energy gap-mid. At a specific DOS (indicated by equal colors in Fig. 5.7 (a) and (b)), the difference between the solution suppressing backward jumps  $E_{Tr'}$  and the most probable jump-to-energy  $E_{Tr''}$  is well below 50 meV. Being 20...25 meV for DOS widths of  $\sigma = 60...120 \text{ meV}$  at RT,  $|E_{Tr'} - E_{Tr''}|$  decreases towards 10 meV at lower temperatures. Similar to the findings of Arkhipov *et al.*,  $|E_{Tr'}(T)| < |E_{Tr''}(T)|$  w.r.t the HOMO center for  $\forall T$ . Consequently, a charge carrier originating from a deep gap state needs slightly more energy to escape to a mobile state and take part in conductivity than to just jump to the most frequently visited energy and subsequently back. However, it is beyond the scope of this thesis to conclude the superior transport level model. The observed temperature dependencies  $E_{Tr'}(T)$  and  $E_{Tr''}(T)$  are almost coinciding and the differences for both solutions at a distinct  $T$  are typically below the uncertainty on  $\sigma$  from the UPS measurements. Here, already a variation in  $\sigma$  of 10 meV causes a difference of approx. 25 meV for the transport level position. Hence, for sake of computational simplicity, the transport level position is identified with the most probable jump-to-energy  $E_{Tr}(T) \stackrel{!}{=} E_{Tr''}(T)$  and no distinction is made.

**Influence of the DOS Width.** For a broader DOS, the transport level is located deeper in the energy gap (cf. Fig. 5.7 (a)). Herein, a variation in  $\sigma$  of 20 meV causes a relocation of  $E_{Tr}$  by approx. 50 meV. Spanning  $T$  from 10 K to RT,  $E_{Tr}$  shifts by 180 meV ( $\sigma = 60 \text{ meV}$ ) up to 315 meV ( $\sigma = 120 \text{ meV}$ ) towards the HOMO

center. The differences are due to the contribution of the Gaussian DOS to Eq. (2.33), which led to Eq. (2.32) in the initial publication of Arkhipov *et al.*<sup>[165]</sup> Following the simplified picture in Fig. 5.8 (a), a broader DOS (sketched in blue) means a higher density of states  $N(E)$  at low energies. For instance at an energetic distance of 0.5 eV from the HOMO center, a Gaussian DOS of  $\sigma = 0.120$  meV possesses  $6 \times 10^{17}$  states per  $(\text{cm}^3 \text{ eV})$ . For  $\sigma = 0.060$  meV, there are only  $9 \times 10^6 \text{ cm}^{-3} \text{ eV}^{-1}$ . Consequently, in a broader DOS, the charge carriers reside at lower energies. They are accompanied by a number of accessible neighboring hopping sites  $n_b$ , which is yet smaller than for a less disordered DOS, i.e. when charge carriers are hopping at energies closer to the HOMO center. For decreasing  $T$ , charge carriers are more susceptible to trapping whereby conductivity and mobility are lowered by several orders of magnitude.<sup>[41,242]</sup> Still, charge carrier migration is observed even at temperatures well below 100 K.<sup>[44,131,245]</sup> With increasing  $T$ , the charge carriers gain more thermal energy which enables energetically wider jumps.<sup>[150]</sup> As known from percolation theory, the average hop distance of a charge carrier in a DOS scales with the disorder, but is inverse to the temperature.<sup>[169]</sup> In case of a steeply rising DOS (i.e. small  $\sigma$ ), significantly more target sites are reachable within a small energy interval  $E_i + \varepsilon$  than for a shallow DOS (cf. compare red and blue triangles). The average hop distance is short. For a broader DOS, the charge carriers must to perform higher energy jumps  $T$ , i.e. the  $E_{\text{Tr}}(T)$  scales stronger with  $T$ .

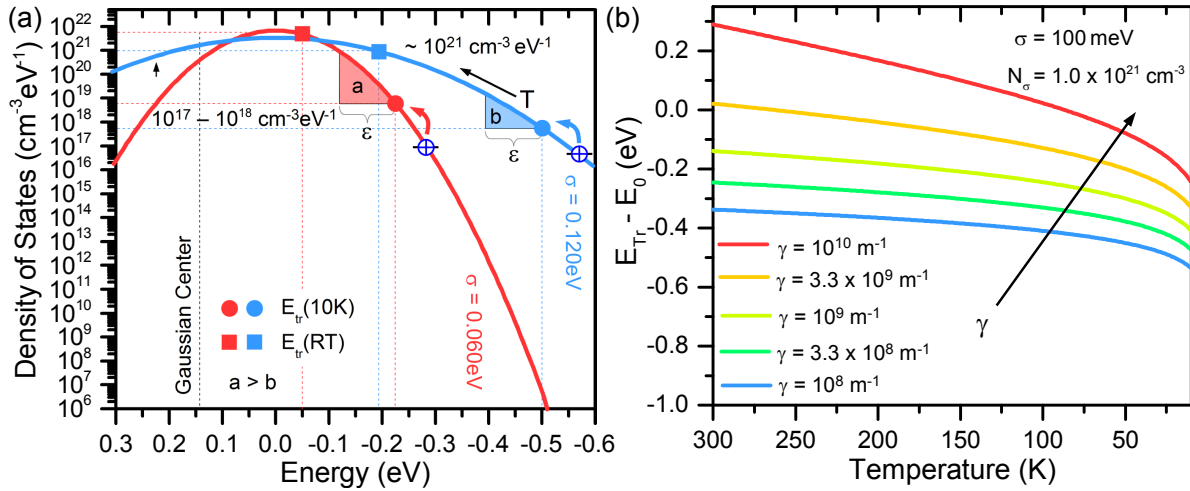


**Figure 5.8.:** (a) Gaussian DOS at widths of  $\sigma = 0.060$  eV (red) and  $\sigma = 0.120$  eV (blue). The positions of the transport level are taken from Fig. 5.7. Circles indicate  $E_{\text{Tr}}$  at 10 K, squares show  $E_{\text{Tr}}$  at room temperature. (b) Results on the  $E_{\text{Tr}}(T)$  calculations from Eq. (2.35) for varied inverse localization radius  $\gamma$  and a Gaussian DOS ( $\sigma = 100$  meV,  $N_\sigma = 10^{21} \text{ cm}^{-3}$ ).

**Transport Level at RT and Influence of Site Numbers.** A remarkable observation from Fig. 5.7 (a) is that the transport level is between  $\sigma$  and  $2\sigma$  away from the Gaussian HOMO center at RT. Together with the results of the previous section, this finding indicates that  $E_{\text{Tr}}$  is located slightly above the HOMO onset energy  $E_\beta \simeq E_{\text{HOMO}} \simeq E_{\text{HOMO}}^*$  at room temperature. The exact position is further influenced by the absolute density of states  $N_\sigma$ . Shown in Fig. 5.7 (b), the spread of  $E_{\text{Tr}}(\text{RT})$  is up to 65 meV when varying  $N_\sigma$  from  $0.2 \times 10^{21} \text{ cm}^{-3}$  to  $1.0 \times 10^{21} \text{ cm}^{-3}$  for  $\sigma = 100$  meV. A larger  $N_\sigma$  means a higher number of accessible sites  $n_b$  and a deeper lying transport level. Interestingly,  $E_{\text{Tr}}(\text{RT})$  is found throughout all  $N_\sigma$  and  $\sigma$  at site densities of  $\sim 10^{21} \text{ cm}^{-3} \text{ eV}^{-1}$  in the DOS. This is in agreement with previous assumptions made for simulations of charge carrier transport in organic semiconductors.<sup>[157,306]</sup> However, at 10 K, charge carrier transport occurs at energies with site densities around  $10^{17} \dots 10^{18} \text{ cm}^{-3} \text{ eV}^{-1}$ .

**Influence of the Fermi Level Position.** The equilibrium charge carrier distribution  $p(E)$  in a disordered system is the product of the DOS  $g(E)$  and the Fermi-Dirac statistics, i.e.

$$p(E) = g(E) \cdot f(E) = \frac{g(E)}{1 + \exp\left(\frac{E - E_F}{k_B T}\right)}. \quad (5.6)$$

Determined by the Fermi level position,  $p(E)$  limits the number of accessible hopping sites  $n_b$ . Sites further away from the DOS center than  $E_F$  are occupied by charge carriers and due to Pauli principle and electrostatic interactions inaccessible. The integrand in Eq. (2.32) is replaced by the density of vacant sites  $g(E) - p(E)$  and reads<sup>[167]</sup>

$$\int_{-\infty}^{E_{Tr}} \frac{g(E) (E - E_{Tr})^3}{1 + \exp\left(-\frac{E - E_F}{k_B T}\right)} dE = \frac{6}{\pi} (\gamma k_B T)^3. \quad (5.7)$$

The solutions of Eq. (5.7) are illustrated in Fig. 5.9 (a) and (b) for a Gaussian DOS ( $N_\sigma = 10^{21} \text{ cm}^{-3}$ ,  $\sigma = 120 \text{ meV}$ ). As long as  $E_F$  is far away from the DOS center,  $E_{Tr}(T)$  remains unaffected and equals the result from Eq. (2.32) in Fig. 5.7. Upon successive filling of the DOS with charge carriers,  $E_F$  shifts further towards the intrinsic transport level position for a charge carrier in an empty DOS. Once  $E_F$  is closer than

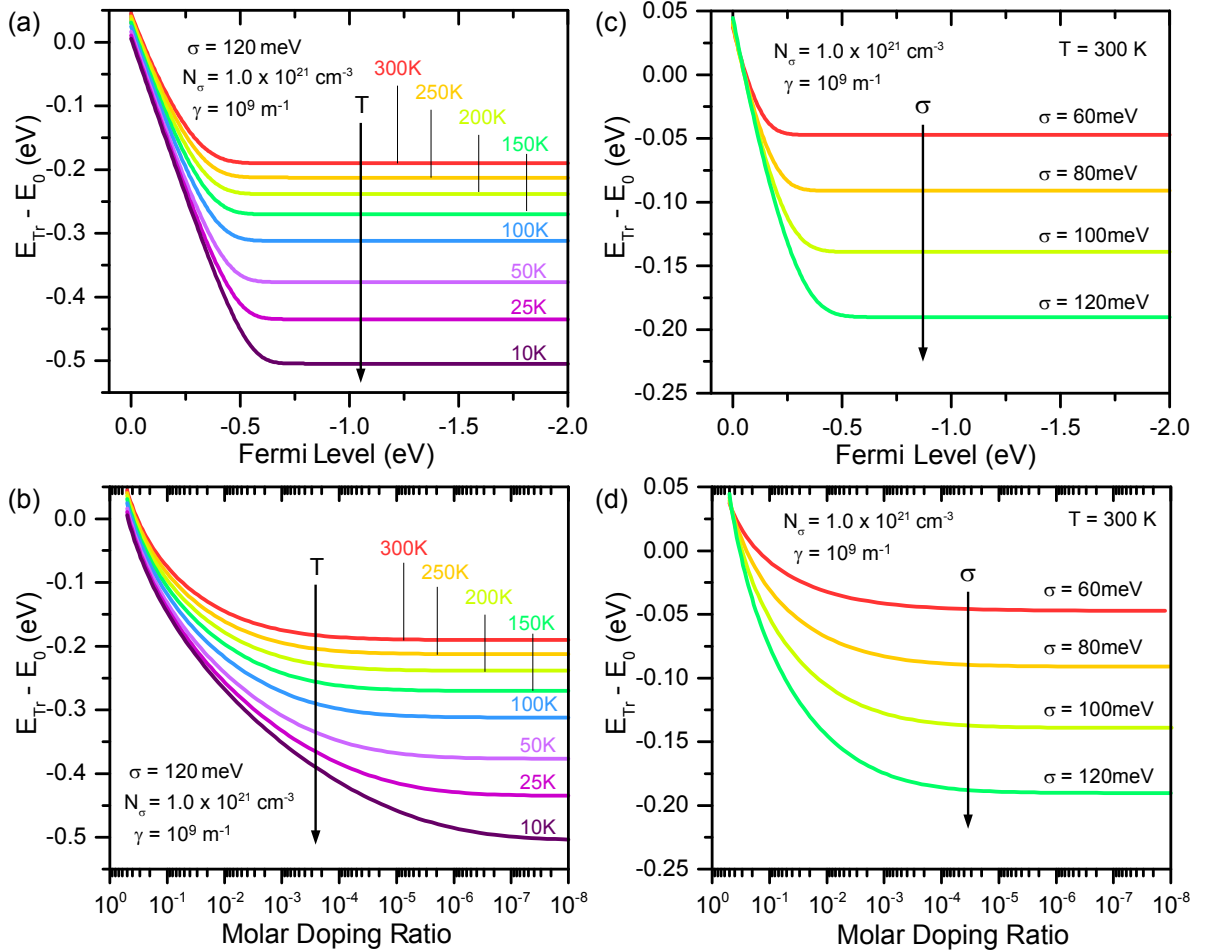


**Figure 5.9.:** Transport level positions calculated from Eq. (5.7) in a Gaussian DOS ( $N_\sigma = 10^{21} \text{ cm}^{-3}$ ) partially filled by charge carriers.  $E_{Tr}$  is plotted versus (a) the Fermi level  $E_F$  and (b) the dopant MR assuming  $p = N_A^- = N_A$  for different temperatures  $T$  and  $\sigma = 120 \text{ meV}$ . Likewise, (c) and (d) depict  $E_{Tr}$  versus  $E_F$  and MR for different DOS widths  $\sigma$  and  $T = 300 \text{ K}$ .

few  $k_B T$  to this position (approx.  $-0.5$  eV at 10 K and  $-0.2$  eV at 300 K for the distinct DOS here),  $E_{Tr}$  shifts strongly towards the DOS center (cf. Fig. 5.9 (a)), since a substantial number of target hopping sites in the DOS is now occupied. Assuming without loss of generality a doping efficiency  $\eta = 1$ , it is in  $p = N_A^- = N_A$ , where the charge carrier density is obtained from

$$p = \int_{-\infty}^{\infty} g(E) f(E) dE. \quad (5.8)$$

Utilizing Eq. (5.8), the shift of the transport level energy with respect to the molar doping ratio  $MR = p/N_\sigma$  is shown in Fig. 5.9 (b). At low charge carrier densities (MRs) in the order of  $p/N_\sigma = 10^{-6} \dots 10^{-5}$ ,  $E_{Tr}$  is only affected for temperatures  $T < 100$  K, i.e. when charge carrier transport happens at low energies. For elevated temperatures up to RT, the occupation of the low energy part of the DOS, i.e. doping by MRs up to  $10^{-3}$  does not alter  $E_{Tr}$ . Here, the charge carriers possess a sufficiently large thermal energy to jump to sites closer to the DOS center. For excessively high charge carrier concentrations ( $\sim MR 0.1$ ),  $E_{Tr}(T)$  shifts remarkably (approx. 100 meV) towards higher energies. By filling the half of the DOS (MR 0.5), the transport energy is forced beyond the DOS center. Fig. 5.9 (c) and (d) illustrate the transport level shift at  $T = 300$  K for different DOS widths  $\sigma$ . In case of a broader DOS, where the charge carriers reside at lower energies and  $E_{Tr}$  is at lower energies towards the energy gap, the transport level position is more susceptible for an increasing  $E_F$ . Hence,  $E_{Tr}$  starts to rise when  $E_F$  is crossing  $-0.5$  eV (MR  $10^{-5}$ ) for  $\sigma = 120$  meV, while it increases not until  $E_F = -0.3$  eV (MR 0.006) for  $\sigma = 60$  meV.

The Fermi level positions for the various HTL materials examined in Sec. 5.1 are typically 1...2 eV away from the HOMO center (cf. Tab. 5.3), pinned by inherent trap distributions near the energy gap-mid.<sup>[181,183,207]</sup> Although the Gaussian DOS discussed in Fig. 5.9 is a simplification of the real HTL materials DOS and tailing DOS states alter  $E_{Tr}(T)$ , it is most likely that the transport level position is independent on the exact position of  $E_F$ . Hence, the UPS resolution limit of 50 meV<sup>[94]</sup> for the distance between the HOMO center and the Fermi level can be neglected. However, in case of intentionally doped HTLs, the Fermi level position changes remarkably as compared to intrinsic materials thus  $E_F$  must be considered for the calculations of  $E_{Tr}(T)$ . Especially for measurements on doped HTL at varying temperatures, knowledge of  $E_F(T)$ , e.g. from temperature dependent UPS measurements, is required.

**Influence of Inverse Localization Radius.** The inverse localization radius  $\gamma$  has been introduced in Sec. 2.2 in the context of the Miller-Abrahams equations. Strongly delocalized charge carriers experience a long decay length  $\gamma^{-1}$  of the electronic wave functions around the molecular sites. Following Eq. (2.15), the hopping rates to a neighboring molecule increase for a decreasing  $\gamma$ . Fig. 5.8 (b) illustrates how the transport level position is affected. For a delocalized system, i.e. a small  $\gamma$  of approx.  $10^8 \text{ m}^{-1}$ ,  $E_{Tr}(T)$  shifts deeper in the gap. The charge carriers are more enabled by a stronger overlap of the molecular frontier orbitals to tunnel between sites further apart. In contrast, a stronger localization of the charge carriers at the molecules implies an  $E_{Tr}(T)$  closer to the DOS center. At  $\gamma = 10^{10} \text{ m}^{-1}$ , the transport level position even crosses  $E = 0$  for  $T > 100$  K. This artifact was previously observed by Arkhipov *et al.* (cf. Fig. 2.16 (b)), however, its origin could not be entirely clarified. A localization smaller than the molecule size likely introduces an erroneous assumption on the hopping model.

The implicit use of an intermediate value of  $\gamma = 10^9 \text{ m}^{-1}$  in the previous simulations (cf. Fig. 5.7) is easily justified when comparing with literature on transport in organic semiconductors. Bässler<sup>[150]</sup> chose  $\gamma = 2.5 \dots 8.3 \times 10^9 \text{ m}^{-1}$  for Monte-Carlo simulations in amorphous TAPC.<sup>7</sup> Abate *et al.* included

<sup>7</sup>1,1-bis(di-4-tolylaminophenyl)cyclohexane

$\gamma = 2 \times 10^9 \text{ m}^{-1}$  for Spiro-OMeTAD.<sup>[395]</sup> Publications on polyphenylene vinylene (PPV) derivatives by Coehoorn<sup>[157]</sup> and Pasveer<sup>[156]</sup> use  $\gamma = 3...5 \times 10^9 \text{ m}^{-1}$ , which are estimated from  $N_0/\gamma^3 = 10^{-2}$  and an average inter-site distance of  $N_0^{-1/3} = 1.5...1.8 \text{ nm}$ . Similar considerations are taken by Nenashev *et al.*<sup>[164]</sup> and Kadashchuk *et al.*,<sup>[166]</sup> who assumed  $N_0/\gamma^3 = 0.3^3$  and  $N_0/\gamma^3 = 1/64$ . The reported values, however, are determined only for simplified geometries, i.e. perfect cubic lattices. For real thin-films, the (inverse) localization length must be statistically distributed<sup>[150,396]</sup> and structural examinations of the geometry (XRD, etc.) are necessary. This is beyond the scope of this thesis but shall be considered in future work. Nevertheless, the lattice constants for small molecules are in the range of  $1...2 \text{ nm}$ .<sup>[397,398]</sup> Since electron delocalization can be easily extended over a few molecules,<sup>[47]</sup> it is not completely irrational to assume an inverse localization length of  $\gamma = 10^9 \text{ m}^{-1}$ .

### 5.2.2. DOS Parametrizations of the HTL Materials

The obtained DOS parameters of Tab. 5.4 are applied to Eq. (5.7) to compute the temperature dependent hole transport level positions  $E_{\text{Tr}}(T)$  for BF-DPB, MeO-TPD, Spiro-TTB, m-MTDATA, pentacene, and ZnPc. Since the thin-film growth mode thus the disorder parameter  $\sigma$  typically differ depending on the substrate type,  $E_{\text{Tr}}(T)$  is calculated for both cases: a strongly interacting (Ag, Au, ITO) and a weakly interacting (Ag/p-Spiro-TTB) substrate. Fig. 5.10 exemplarily depicts several parametrizations for the HOMO DOS of pentacene and their solutions for  $E_{\text{Tr}}(T)$  (cf. Fig. 5.10 (d)). The initially measured UPS spectrum of P5 on Ag/p-Spiro-TTB in Fig. 5.10 (a) ( $\sigma_{\text{UPS}} = 0.16 \text{ eV}$ ) is rescaled as discussed in Sec. 5.1.6 to reduce the impact of UPS signal broadening and is shown in Fig. 5.10 (b) ( $\sigma = 0.08 \text{ eV}$ , blue line). Furthermore, the description of the low energy sites is important for the position of the transport level. Due to the DOS uncertainty below the noise level (red dashed line), several assumptions for exponential distributions ( $\beta = \{25, 50, 100, 200\} \text{ meV}$ ) describing possible tailing sites are examined. These parametrizations and the appearing  $E_{\text{Tr}}(T)$  are compared in the following, in particular with high-res UPS data on  $\text{SiO}_2/\text{P5}$ , extracted from Bussolotti *et al.*<sup>[256]</sup> (Chiba, Japan) and shown in Fig. 5.10 (c).

The most natural parametrization of the rescaled P5 DOS in Fig. 5.10 (b) is given by a single Gaussian distribution ( $N_\sigma = N_0 = 2.86 \times 10^{21} \text{ cm}^{-3}$ ,  $\sigma = 0.08 \text{ eV}$ ) (blue curve).  $E_F = -0.78 \text{ eV}$  is taken directly from the UPS measurements Fig. 5.10 (a), since the distance from the DOS center to the Fermi level exceeds the  $50 \text{ meV}$  UPS resolution limit by far. Following Eq. (5.7),  $E_{\text{Tr}}$  shifts between  $-0.12 \text{ eV}$  at RT and  $-0.33 \text{ eV}$  at  $10 \text{ K}$  with respect to the HOMO center. However, the continuation of the DOS beyond the cutoff energy  $E_{\text{cut}} = -0.25 \text{ eV}$  is hardly predictable. There, the UPS signal of the thin-film intersects with the noise level (red dotted line) of the UPS measurement system. Possibly existing DOS tail states for energies smaller than the HOMO onset are assumed to be exponentially distributed ( $E_\beta = -0.187 \text{ eV}$  with the parameters  $\beta = \{200, 100, 50, 25\} \text{ meV}$  and  $N_\beta = \{8.73, 4.37, 2.18, 2.69\} \times 10^{19} \text{ cm}^{-3}$ ). Due to a substantially higher DOS at low  $E$ , the transport levels is deeper in the energy gap for a larger tailing (cf. Sec. 5.2.1). Compared to the solution for a single Gaussian DOS,  $E_{\text{Tr}}(T)$  shifts up to  $500 \text{ meV}$  towards the energy gap-mid as shown in Fig. 5.10 (d). At energies, where the transport level position is close to  $E_F$ ,  $E_{\text{Tr}}(T)$  flattens since states at energies deeper than  $E_F$  are not accessible. In case of a steeply exponential DOS ( $\beta = 25 \text{ meV}$ ), the DOS and consequently the transport level positions agree with the results for a single Gaussian DOS (compare turquoise and blue lines in Fig. 5.10).

In contrast to the IAPP UPS system, which is only able to resolve DOS approx.  $10^{19} \text{ cm}^{-3} \text{ eV}^{-1}$ , the group of Nobuo Ueno (Chiba, Japan) showed UPS spectra of pentacene<sup>[248,256]</sup> down to a density of states approx.  $10^{16} \text{ cm}^{-3} \text{ eV}^{-1}$  around the Fermi level position, thus proving the existence of low energy states

towards the energy gap. The high resolution UPS data of P5 reported by Bussolotti *et al.*,<sup>[256]</sup> and shown in Fig. 5.10 (c) is fitted by a single Gaussian distribution ( $\sigma = 0.11$  eV), covering a DOS down to  $10^{16}$  cm<sup>-3</sup> eV<sup>-1</sup>. Concurrently, the signal broadening of the hi-res UPS is expected to be smaller, since the occurring HOMO  $\sigma$  is smaller by approx. 50 meV as compared to the IAPP system ( $\sigma = 0.16$  eV). Both facts together rise the strong indication that the P5 DOS is very well approximated by a Gaussian distribution down to at least three orders of magnitude in site densities less than what has been resolved with the IAPP system in Sec. 5.1. The tailing UPS signal is considered as artificial, most likely originating from signal broadening, noise, and non-monochrome excitation. Hence, for the final computation of the transport level position for the HTL materials, only the (rescaled) Gaussian DOS is utilized. The site densities  $N_\sigma$  are normalized to the molecule densities  $N_0$  in Tab. 5.3. The results are presented in the following section.

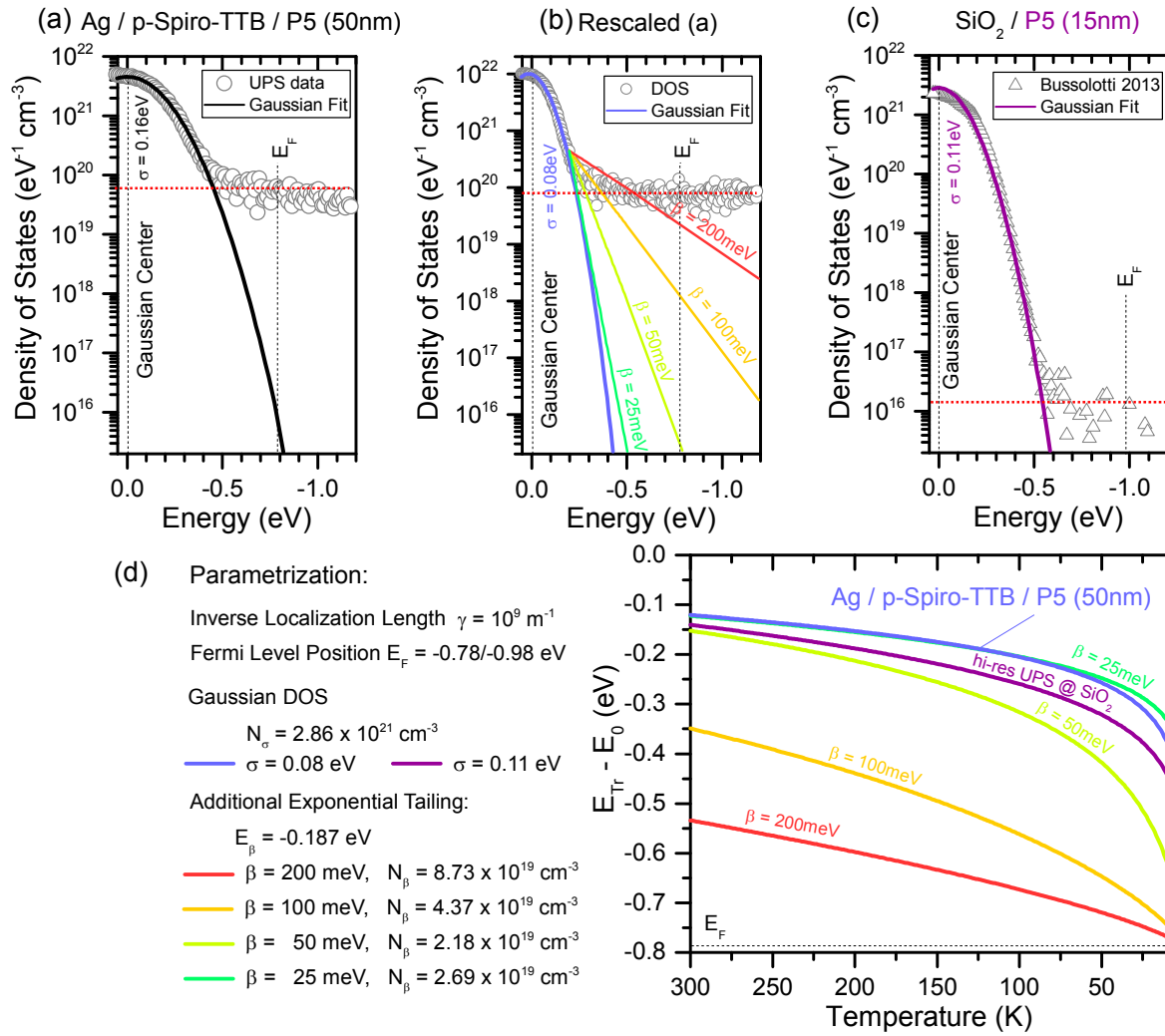


**Figure 5.10.:** Top: Comparison of DOS distributions and Gaussian fit functions for pentacene obtained via (a) UPS at IAPP ( $\sigma = 0.16$  eV, cf. Fig. 5.3), (b) rescaling of the UPS spectrum (a) ( $\sigma = 0.08$  eV) to compensate for signal broadening occurring in UPS (Sec. 5.1.6), and (c) high-resolution UPS ( $\sigma = 0.11$  eV) by Bussolotti *et al.* (Chiba, Japan, data adapted from Ref. [256]). For the second, exponential functions ( $\beta = 25 \dots 200$  meV) to model not ascertainable DOS tailing below the noise limit (red dashed line) are included. Bottom: (d) Charge carrier transport levels from Eq. (5.7) for the different parametrizations of the pentacene DOS.



### 5.2.3. Temperature Dependent Transport Level for HTL Materials

Figure 5.11 summarizes the transport level positions for the various hole transport materials grown on strongly (top) and weakly interacting substrates (bottom). While Fig. 5.11 (a) and (c) illustrate  $E_{Tr}(T)$  relative to the HOMO DOS center  $E_0$ , the energy axis is rescaled to the vacuum level in Fig. 5.11 (b) and (d). In the latter case,  $E_0$  is set to IP +  $2\sigma$  for each individual HTL material. The HOMO onsets of the materials are represented by squares, indicating the ionization potentials from Tab. 5.3.

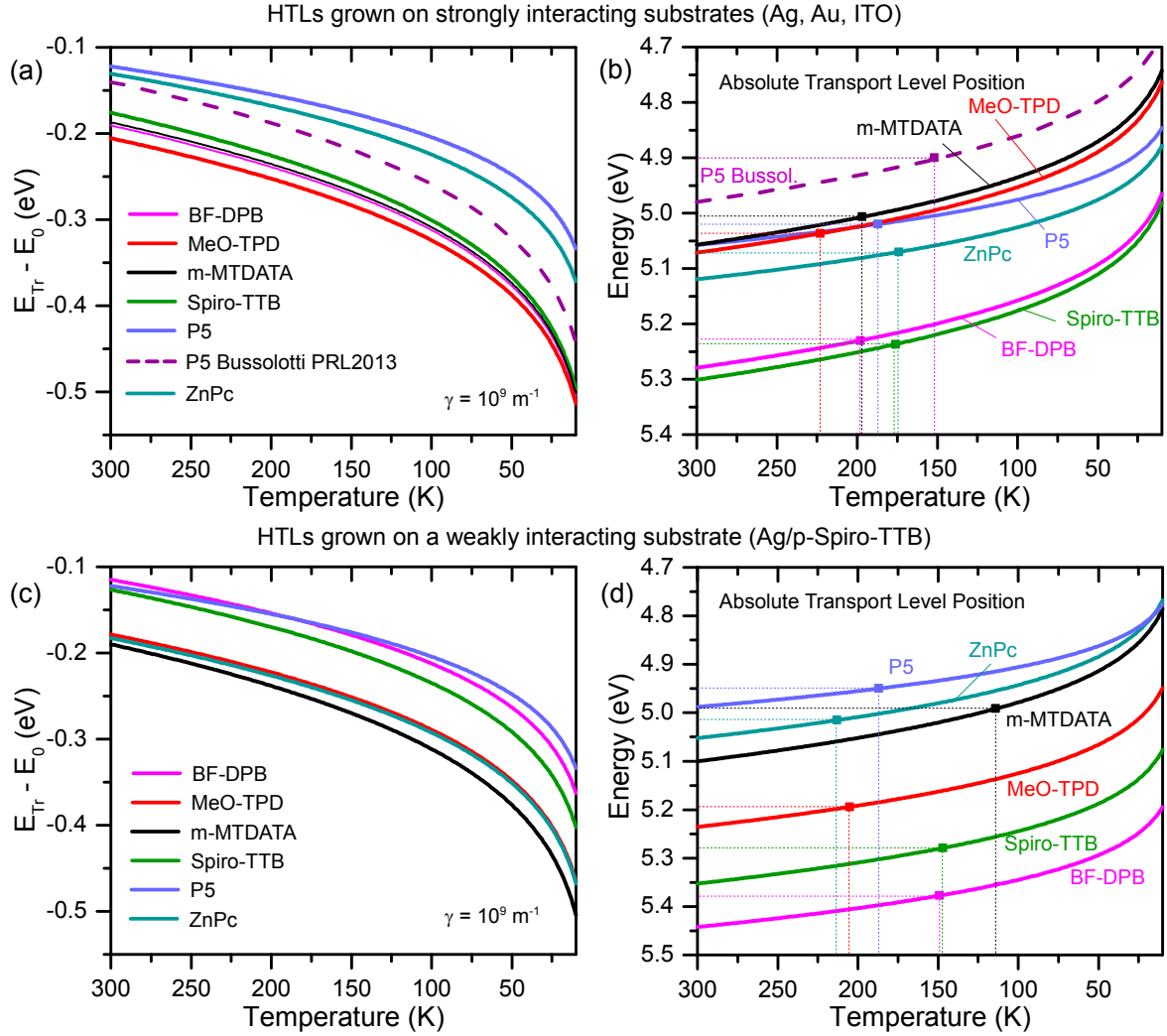


**Figure 5.11.:** (a),(c) Transport level positions calculated from Eq. (5.7) versus temperature for the examined set of hole transporting materials. The thin-films are grown on strongly/weakly interacting substrates (top/bottom). Each DOS is identified with a Gaussian distribution. The DOS parameters are found in Tab. 5.4, where the DOS widths are rescaled from the UPS spectra according to Sec. 5.1.6 and the site densities equal  $N_0$ . An inverse localization length  $\gamma = 10^9 \text{ m}^{-1}$  is assumed. (b),(d) The energy axis is rescaled to the vacuum level with squares indicating the HOMO onset and the IP of each material.

At room temperature, the transport level positions are above the HOMO onsets (50 to 100 meV). This is remarkable, since the energetic position of the charge carrier movement at RT often identified without a general concern with the IP.<sup>[39,182,207,399]</sup> Furthermore, the correct route to determine trap energies should be taken by referring not to the ionization potential but to the temperature dependent transport level. In general, the results in Fig. 5.10 resemble the findings earlier in Sec. 5.2.1. Materials with a larger disorder

parameter  $\sigma$  (e.g. m-MTDATA:  $\sigma = 0.12$  eV, as compared to P5:  $\sigma = 0.08$  eV on Ag/p-Spiro-TTB) exhibit a transport level deeper in the gap ( $E_0 - 190$  meV,  $E_0 - 122$  meV at RT). With decreasing temperature, a stronger shift in  $E_{Tr}(T)$  is observed for more disordered materials (m-MTDATA: 315 meV, P5: 211 meV for RT to 10 K). Interestingly, the different growth modes of ZnPc on strongly and weakly interacting substrates causing diverging disorder parameters  $\sigma = 0.09$  eV (on Au) and  $\sigma = 0.11$  eV (on Ag/p-Spiro-TTB) affect the position of respective the transport level remarkably.

### 5.3. Summary

UPS measurements on the HTL materials BF-DPB, Spiro-TTB, MeO-TPD, m-MTDATA, pentacene, and ZnPc have been performed and analyzed to gain information on the temperature dependent position of their hole transport levels  $E_{Tr}(T)$ . Hopping model calculations published by Arkhipov *et al.* were adapted and an analytical description  $g(E)$  of the HOMO DOS was used to compute  $E_{Tr}(T)$ .

The UPS spectra of the HTL systems were fitted with a main Gaussian distribution. Its low energy flank coincided with the common tangent fit to obtain the HOMO onset. The latter has been found at the energy  $E_\sigma - 2\sigma_{UPS}$  of the Gaussian DOS. The disorder parameters  $\sigma_{UPS}$  obtained from the UPS spectra ranged between 0.15 eV (P5) and 0.24 eV (m-MTDATA). However, these results were broadened by approx. factor two (80...120 meV), which was corrected by rescaling the energy axis. In comparison to literature values from quantum mechanical calculations and charge carrier transport experiments, the UPS method most likely suffer from electron-phonon interaction, i.e. vibronic broadening, and secondary line excitations as well as a low signal-to-noise ratio. Examining high-resolution UPS data<sup>[256,400]</sup> (Chiba, Japan) indicated that the HOMO DOS were in first order Gaussian distributed down to site densities of approx.  $10^{16} \text{ cm}^{-3} \text{ eV}^{-1}$ . Deviations in the UPS spectra at energies lower than the HOMO onset, initially fitted by exponential functions in Sec. 5.1, were probably induced by the signal broadening and were not considered for  $E_{Tr}(T)$ . Grown on weakly interacting organic substrates (Spiro-TTB p-doped by F<sub>6</sub>-TCNNQ), especially P5 and, to lesser extent, BF-DPB formed less disordered films with a Gaussian DOS width well below 100 meV. Spiro-TTB, MeO-TPD, and m-MTDATA thin-films were heavily disordered ( $\sigma = 0.10...0.12$  eV) with even increasing disorder when grown on strongly interacting metal surfaces. ZnPc however, behaved the opposite way as films on metal showed a smaller  $\sigma$ .

In case of doped sublayers, charge carrier diffusion up to 30 to 50 nm into the adjacent intrinsic layer was concluded. From a comparison with the HIB of intentionally doped films of ZnPc and P5, the densities of diffused free charge carriers have been estimated to  $\sim 10^{18} \text{ cm}^{-3}$ , which would exceed the intrinsic trap densities. Besides, a charge screening effect altering the IP, Fermi level position, and hole injection barrier of the intrinsic film was suspected.

In order to correctly refer trap energies to the vacuum energy level, transport level computations have been conducted. The influence of the HOMO DOS width as well as the number of states and the inverse localization radius on the transport level were discussed. In conclusion, more low energy states caused a charge carrier transport deeper in the gap. A strong delocalization (smaller  $\gamma$ ) had an identical effect. Introducing a charge carrier density raised the Fermi level in the DOS thus occupying low energy sites and shifting the transport level to towards the DOS center. The rescaled disorder parameters  $\sigma = [0.08...0.12]$  eV were used to finally determine the transport level positions of the HTL materials. In particular,  $E_{Tr}(\text{RT})$  is above the HOMO onset. At lowered temperatures, the transport levels relocate for several 100 meV towards the energy gap-mid.

# Trap Response and Dopant Regimes in Organic Schottky Diodes

*The charge carrier trap densities and trap energies in organic Schottky diodes consisting of the hole transporting pentacene and ZnPc are examined by impedance spectroscopy. In particular, the position of the Fermi level is found to be decisive for the trap level response. For both materials, a substantial concentration of deep hole traps is found, which saturates upon p-doping, while additional shallow traps arise. In case of P5, the observed number of deep trap states depends on the material purification. For p-ZnPc, dopant deactivation is demonstrated by temperature-dependent impedance spectroscopy and ultraviolet photoelectron spectroscopy. The results are another strong evidence for the most recently reported existence of the dopant reserve, dopant saturation, and trap-filling regime in organic semiconductors.<sup>[182,183]</sup>*

p-Doping by F<sub>4</sub>-TCNQ, F<sub>6</sub>-TCNNQ, or C<sub>60</sub>F<sub>36</sub> molecules enhances the hole conductivity of HTLs up to values of 10<sup>-3</sup>...10<sup>-1</sup> S cm<sup>-1</sup>.<sup>[71,128,208,240]</sup> Although such high values are desirable for commercial applications of organic electronics, only doping concentrations below a MR of 0.01 ensure the formation of a sufficiently large charge carrier depletion zone. The energy level bending in the depletion zone allows the Fermi level to cross large parts of the energy gap, including inherent hole trap distributions. The oscillatory excitation via impedance spectroscopy causes charge reversal of trapping sites near  $E_F$ , which is observed as additional (trap) capacitance  $C_T$ . Employing the physical model from Sec. 4.2.4, trap densities and energies with respect to the hole transport level are quantified.

The present chapter starts with an examination of the depletion zones in p-doped Schottky diodes of P5 and ZnPc. Mott-Schottky analyses are discussed to obtain the number of free holes, leading to doping efficiencies  $\eta$  and the energy level diagrams. Consequently, in Sec. 6.2, the frequency-dependent capacitance spectra of p-doped P5 and ZnPc samples are examined at RT. The influence of the Fermi level position on the observed trap capacitance is studied in Sec. 6.2.2 by varied intentional doping. An alternative approach to manipulate  $E_F$  is presented in Sec. 6.3, where impedance spectroscopy is performed during the freeze-out of doping in ZnPc:F<sub>6</sub>-TCNNQ to 10 K. Accompanied by temperature-dependent UPS measurements, the results provide further evidence for dopant saturation and reserve regimes in organic semiconductors.<sup>[183]</sup>

## 6.1. Depletion Zones and Mott-Schottky Analysis: Doping Efficiency

**Impedance of p-doped Schottky Diodes.** All Schottky diodes investigated in this chapter are built asymmetrically. The work function of sputter-cleaned ITO is close to the HOMO onset and  $E_{Tr}$  (RT) of P5 and ZnPc (cf. Sec. 5.2.3) at 4.7...4.9 eV.<sup>[205]</sup> Hence, this contact is assumed to be ohmic and its impact on the

capacitance of the device is neglected. The Schottky contact and the decisive space charge region (SCR) are formed between organic semiconductor and the Al top contact ( $W_f = 4.2$  eV).

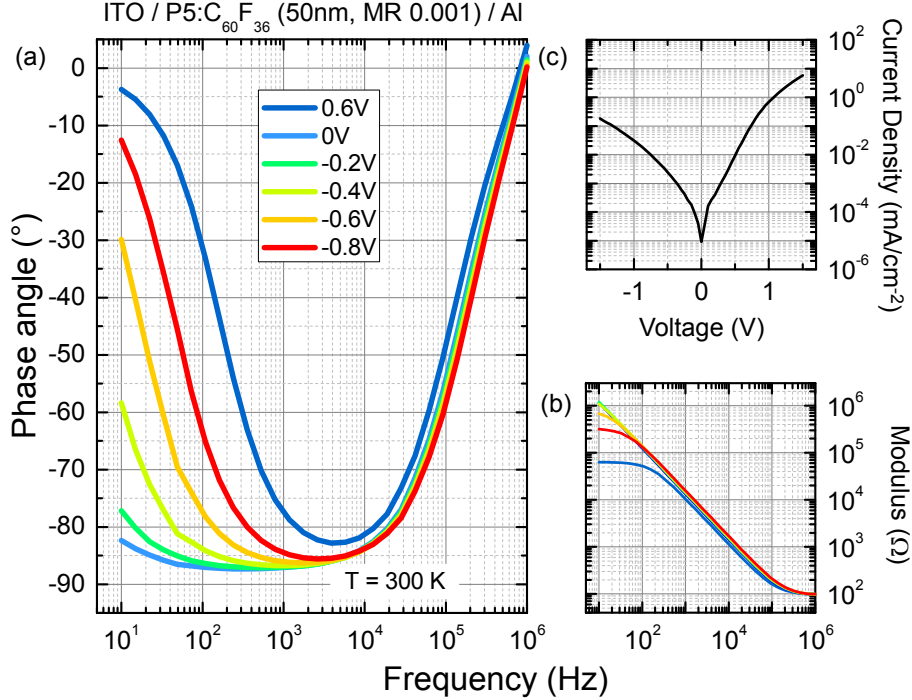


**Figure 6.1.:** Impedance response of 50 nm P5 p-doped with 0.5 wt%  $\text{C}_{60}\text{F}_{36}$  (MR 0.001), separated in (a) phase angle  $\varphi$  and (b) modulus  $Z$ .  $\varphi \sim -90^\circ$  indicates an impedance governed by the space charge depletion capacitance of the device. For high frequencies, the modulus equals  $R_S$  of the device. At very low frequencies,  $R_P$  dominates. (c) The corresponding current-voltage characteristic is attributed to the diode behavior of the device.

As shown exemplarily in Fig. 6.1 for P5: $\text{C}_{60}\text{F}_{36}$  (50 nm, MR 0.001), the Schottky diodes exhibit asymmetric current-voltage-characteristics. A pronounced plateau of phase angle  $\varphi \simeq -90^\circ$  forms for 0V and moderate reverse voltages (cf. Fig. 6.1 (a)), which corresponds to a capacitive character of the devices. Subsequently, this frequency regime is used for capacitance voltage measurements, enabling conclusions on the depletion capacitance  $C_P$  of the Schottky diodes. However, for frequencies above  $10^4$  Hz, the series resistance of the ITO starts to dominate the impedance response of the diodes. The phase angle increases while the modulus  $|Z| = \sqrt{R^2 + X^2}$  approaches the voltage independent value of the series resistance  $R_S$  (90...100  $\Omega$ ) (cf. Fig. 6.1 (b)). The increase in  $\varphi$  for frequencies  $< 10^2$  Hz is caused by the injection of charge carriers in forward direction (0.6V) as well as an increasing contribution of leakage current for larger reverse bias. In physical terms, this is expressed by a parallel, voltage-dependent leakage resistance  $R_P$  (k $\Omega$ ...M $\Omega$ ). Hence, neglecting charge carrier traps here, the diodes are identified with a simple  $R_S$ - $R_P$  $C_P$  equivalent circuit.

**Space Charge Regions and Mott-Schottky Plots.** The extent of the charge carrier depletion zone can be modulated. By applying reverse bias, free holes are pushed even further away from the positive Al Schottky contact towards the negative ITO contact. The width of the depleted layer increases and the depletion capacitance decreases (cf. Eq. (4.27) in Sec. 4.2). Vice versa, the charge carrier depletion zone shrinks and finally collapses upon starting hole injection for increasing forward bias. Here, Figure 6.2 (a) compares Mott-Schottky plots, i.e.  $1/C^2$  versus applied bias voltage  $V$ , for P5 and ZnPc Schottky diodes,

p-doped by either  $C_{60}F_{36}$  or  $F_6$ -TCNNQ, and dopant concentrations MR 0.001...0.01. The plots yield straight lines around 0 V and their slopes reveal the number of ionized acceptor molecules  $N_A^-$  following Eq. (4.30). For doping ratios  $MR \geq 0.01$  (cf. blue triangles in Fig. 6.2 (a)), however, that straight line fit is only viable for small bias voltage intervals (here  $V = +0.1... -0.3$  V in case of ZnPc: $F_6$ -TCNNQ MR 0.01). With increasing doping concentrations, both contacts of the Schottky diodes tend to be ohmic. A substantial amount of charge carriers is able to tunnel into the organic semiconductor through the thin injection barrier at the aluminum and thus floods the device even at reverse bias. Hence, the Schottky diode is not capacitive anymore.

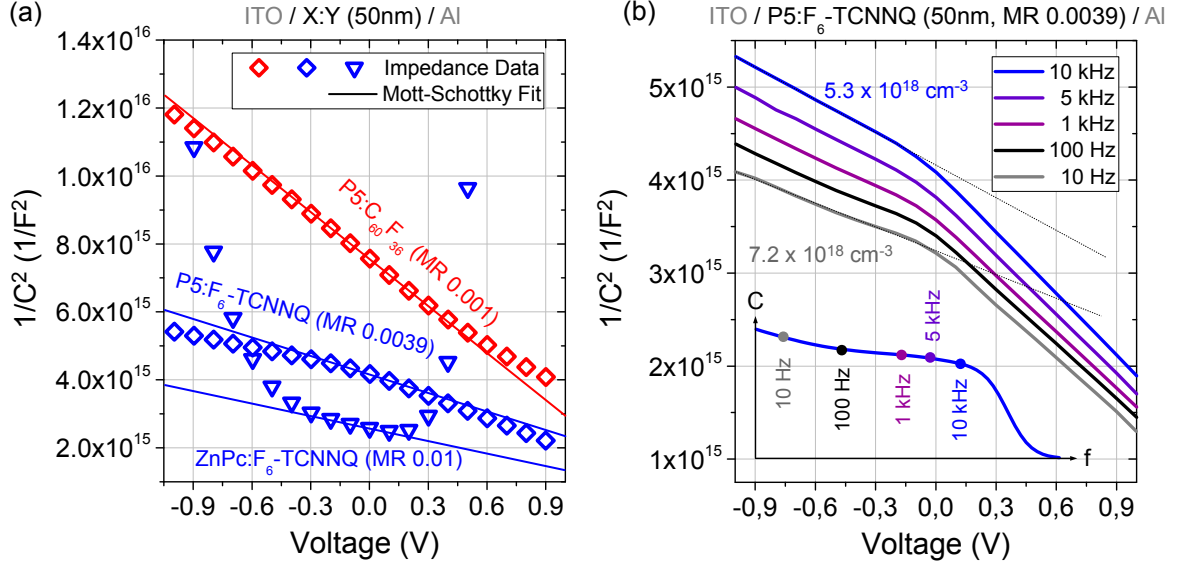


**Figure 6.2.:** (a) Mott-Schottky plots of capacitance-voltage measurements at a frequency of 10 kHz, shown here for p-doped pentacene and ZnPc at RT. The slope of the plots reveals the number of ionized acceptor molecules  $N_A^-$ . It is steeper for lower MR. (b) Capacitance (inset) and Mott-Schottky plots are governed at lower frequencies by the trap response.

Another limitation of the Mott-Schottky analysis is its frequency dependence when charge carrier traps are present. Figure 6.2 (b) shows Mott-Schottky plots for P5: $F_6$ -TCNNQ (50 nm, MR 0.0039), taken at various excitation frequencies  $10^1...10^4$  Hz, while the inset of the figure depicts a complete  $C(f)$  scan for 0 V. The latter exhibits a permanent increase in capacitance for decreasing frequencies, which is explained by charge carrier trap response to the oscillatory excitation<sup>[182,289,301]</sup> and discussed further in Sec. 6.2. Consequently, the Mott-Schottky plots are shifted by offsets in Fig. 6.2 (b) and reveal different slopes thus different  $N_A^-$  values. For 10 kHz, a number of ionized acceptors of  $N_A^- = 5.3 \times 10^{18} \text{ cm}^{-3}$  is obtained, while it is  $N_A^- = 7.2 \times 10^{18} \text{ cm}^{-3}$  at 10 Hz and heavily influenced by the trap response. In the following,  $C(V)$  measurements are taken at the highest possible frequencies, i.e. where the trap response is minimal but the series resistance is not governing the  $C(f)$  spectrum anymore (phase angle  $\varphi \simeq -90^\circ$ ).

**p-Doping Efficiencies in P5 and ZnPc.** Figure 6.3 summarizes a series of  $C(V)$  measurements for p-doped pentacene (a) and p-doped ZnPc (b). The dielectric constants  $\epsilon_r$  are 5.8<sup>[182]</sup> and 4.7<sup>[39]</sup>, respectively. The derived numbers of ionized dopants  $N_A^-$  are divided by the numbers of introduced dopants, yielding estimates of the doping efficiency  $\eta$ . For P5 p-doped by  $C_{60}F_{36}$  (red diamonds), the doping efficiency decreases steadily with increasing dopant MR from 98 % (MR  $2 \times 10^{-4}$ ) down to 45 % (MR  $10^{-3}$ ). Doped by  $F_6$ -TCNNQ, it is  $\eta = 48$  % at MR 0.0039 (blue diamond). The decrease in  $\eta$  for higher dopant MRs

might be surprising at first glance, however, Tietze *et al.* recently published an explanation for this trend. In UPS studies, they found the Fermi level position to be controlled by a distinct acceptor level  $E_A = 0.88$  eV (with respect to the HOMO center) and deep traps with a density of  $N_T = 9.6 \times 10^{16} \text{ cm}^{-3}$ .<sup>[183]</sup> Tietze *et al.* calculated the doping efficiency, i.e.  $\eta = p/N_A$ , as well as the trap filling  $N_T^+/N_T$ , and the dopant ionization  $N_A^-/N_A$  versus the dopant MR from a statistical model. Details are found in Ref.<sup>[183]</sup>, the three quantities as computed for p-doped P5 are plotted in Fig. 6.3 (a) in solid lines. For  $\text{MR} < 5 \times 10^{-5}$ , the deep traps pin the Fermi level as trap filling is not complete, i.e.  $N_T^+/N_T < 1$  (green line). Consequently, the doping efficiency is low and almost no free charge carriers are created. This fact changes as soon as all trap are filled and  $\eta$  drastically increases eventually reaching almost 100 % at  $\text{MR} 3 \dots 5 \times 10^{-4}$  (cf. black line). The doping efficiency obtained via IS is at 98 % for  $\text{MR} 2 \times 10^{-4}$  and thus in agreement to the predicted dopant saturation. When the doping concentration increases further,  $E_F$  shifts towards the HOMO level position, approaching and passing the acceptor level position  $E_A$ .<sup>[181,183,207]</sup> In other words, the acceptor level transitions from a shallow impurity  $E_A < E_F$  to a deep impurity  $E_A > E_F$  (cf. Sec. 3.2.3). For the latter, the promotion probability of electrons from the HOMO to the acceptor level and thus the generation of free holes in the host HOMO is substantially decreased. The acceptor ionization  $N_A^-/N_A$  (cf. purple line) and the doping efficiency (black line) decrease monotonously, eventually reaching values of only few percents for  $\text{MR} > 0.01$ . However, these low  $\eta$  are not observable via IS as the Schottky contacts for such high doping concentrations are ohmic and the diodes show no stable capacitance.

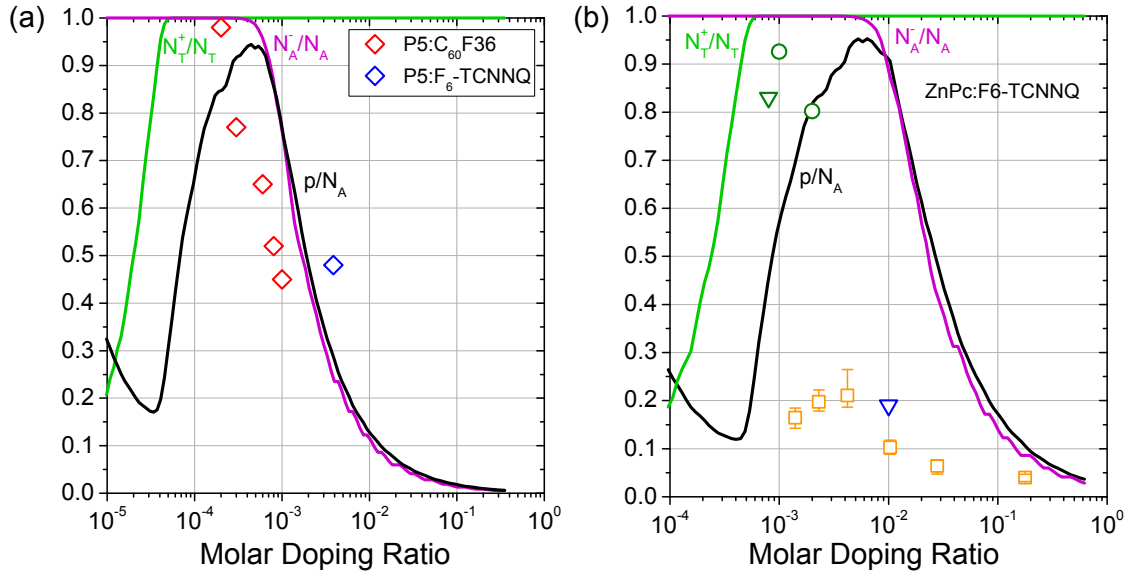


**Figure 6.3.:** Calculated doping efficiency  $p/N_A$  (black line), trap filling  $N_T^+/N_T$  (green line), and acceptor ionization  $N_A^-/N_A$  (purple line) after Tietze<sup>[183]</sup> for (a) pentacene and (b) ZnPc. For P5, doping efficiencies obtained from Mott-Schottky analysis are added (diamonds). In case of ZnPc, UPS measurements (orange squares) from Ref.<sup>[183]</sup> are compared with impedance results of  $n^+p$  HOMO junctions<sup>[292]</sup> (green circles), p-ZnPc on a C<sub>60</sub>F<sub>36</sub> sublayer<sup>[401]</sup> (green triangle) and ITO/p-ZnPc (blue triangle). All ZnPc films are doped by F<sub>6</sub>-TCNNQ.

For ZnPc p-doped by F<sub>6</sub>-TCNNQ (cf. Fig. 6.3 (b)), a doping efficiency of 18 % is obtained from the Mott-Schottky plot in Fig. 6.2 (a) at  $\text{MR} 0.01$ . Although further doping concentrations are not investigated in the context of this thesis, literature reports on  $\eta = 80 \dots 92$  % for ZnPc:F<sub>6</sub>-TCNNQ at  $\text{MR} 9 \times 10^{-4} \dots 2 \times 10^{-3}$ ,<sup>[292,401]</sup> obtained via impedance spectroscopy (green symbols). The deviations between the doping efficiencies predicted by Tietze *et al.* (cf. black lines and symbols in Fig. 6.3) are probably due to doping concentration variance during device preparation or different deep trap densities  $N_T$  as various host material batches are used.

Tietze performed doping efficiency measurements assessing the energy level bending via UPS in ZnPc:F<sub>6</sub>-TCNNQ.<sup>[91]</sup> Although he obtained declining values of  $\eta$  for  $MR > 4 \times 10^{-3}$ , the observed maximum value was only at  $\eta = 21\%$  for  $MR 0.00042$  (cf. orange symbols in Fig. 6.3 (b)). Here, it is suspected that the absent built-in field due to the missing top contact in UPS samples lowers the probability of charge (CT) separation and thus the doping efficiency as compared to impedance spectroscopy experiments. Further comparative investigations are highly suggested.

**Charge Carrier Diffusion Profiles.** When  $C(V)$  measurements are performed for thin-films grown on doped/dopant substrates, non-uniform doping profiles are obtained as illustrated in Fig. 6.4. Here, 100 nm ZnPc is grown on either 5 nm MeO-TPD:F<sub>6</sub>-TCNNQ ( $MR 0.088$ ) (red line), 5 nm ZnPc:F<sub>6</sub>-TCNNQ ( $MR 0.084$ ) (cyan), or 1 nm of the pure p-dopant C<sub>60</sub>F<sub>36</sub>. All Mott-Schottky plots in Fig. 6.4 (a) feature non-constant slopes. As shown in Fig. 6.4 (b), the application of the *profiler equation* from Sec. 4.2,

$$N_A^-(w) = \frac{C^3}{e\epsilon_0\epsilon_r A^2} \left[ \frac{dC}{dV} \right]^{-1}, \quad (4.31)$$

yields an estimate for the ionized acceptor density  $N_A^-$ , i.e. approx the free hole density  $p$  at the end of the space charge region of width  $w$ .

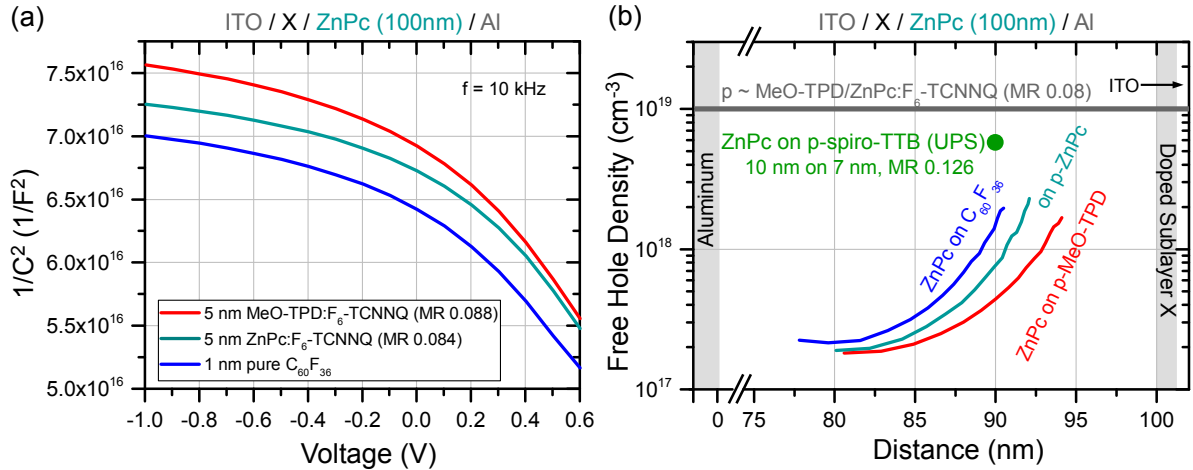


**Figure 6.4.:** (a) Mott-Schottky plots at 10 kHz for intrinsic ZnPc on various p-doped substrates show non-uniform charge carrier distributions within the ZnPc layer. (b) Computed via the profiler equation Eq. (4.31), the number of free holes  $p(x)$  is  $\leq 10^{17} \text{ cm}^{-3}$  deeper in the ZnPc layer. Close to the doped sublayer, the charge carrier concentration is strongly increased. The green circle represents the estimation of  $p$  from UPS measurements in ZnPc (10 nm) on Spiro-TTB:F<sub>6</sub>-TCNNQ (7 nm,  $MR 0.126$ ) as done earlier in Sec. 5.1. Intentional p-doping in MeO-TPD or ZnPc induces  $p \sim 10^{19} \text{ cm}^{-3}$  for  $\sim MR 0.08$ <sup>[183,207]</sup> (dark gray line).

For all three substrates,  $p$  increases from approx.  $2 \times 10^{17} \text{ cm}^{-3}$  deep within the 100 nm ZnPc layer up to  $2...3 \times 10^{18} \text{ cm}^{-3}$  for a distance  $< 10 \text{ nm}$  from the doped sublayer. This result is remarkable, since the 100 nm ZnPc layer is intentionally undoped. Hence, the obtained charge carrier density profile has to be a diffusion profile, revealing the diffusion of free holes originating from the doped sublayer X (cf. Fig. 6.4 (b)) with respect to the electric field in the devices. A similar finding has been made previously in Sec. 5.1, where hole diffusion from a p-doped Spiro-TTB sublayer (7 nm, F<sub>6</sub>-TCNNQ,  $MR 0.126$ ) shifted the Fermi level in the adjacent intrinsic layers towards their HOMO. As indicated by a green dot in Fig. 6.4 (b), the free hole



density <sup>1</sup> is still  $p \simeq 6 \times 10^{18} \text{ cm}^{-3}$  after 10 nm intrinsic ZnPc on top of p-Spiro-TTB (7 nm, F<sub>6</sub>-TCNNQ, MR0.126). Satisfyingly, the results for IS and UPS are in good agreement. For comparison, an intentionally p-doped ZnPc or MeO-TPD layer (MR 0.08 of F<sub>6</sub>-TCNNQ) features approx.  $p = 10^{19} \text{ cm}^{-3}$ .<sup>[183,207]</sup> Hence, even for several ten nm away from doped layers, intrinsic thin-films still exhibit significant charge carrier densities that otherwise would require at least moderate doping.

## 6.2. Frequency Dependent Trap Capacitance

For a generic trap distribution  $g(E)$  interacting with the respective transport level  $E_{\text{Tr}}$  (RT) upon small-signal excitation, the trap capacitance function is calculated as discussed in Sec. 4.2.4. The computation is done by a calculation routine, which was first coded by Burton<sup>[292]</sup>, later extended, and translated to *python* in the framework of the thesis. Its source code is listed in the appendix A.1. The trap distribution function  $g(E)$  is represented either by a Gaussian density of trap states  $g'(E)$ , an exponential distribution  $g''(E)$ , or a sum of both. In the following, hole traps are discussed exclusively. However, the same principles apply for electron traps. The Gaussian distribution is denoted as

$$g'(E) = \frac{N_{T,g}}{\sqrt{2\pi}\sigma^2} \exp\left(-\frac{(E - E_{T,g})^2}{2\sigma^2}\right), \quad (6.1)$$

with an energetic depth  $E_{T,g}$  referring to the hole transport level, a broadening factor  $\sigma$ , and a trap density  $N_{T,g}$ . Exponentially decaying trap distributions  $g''(E)$  are described by

$$g''(E) = \frac{N_{T,\text{exp}}}{k_B T_0} \exp\left(-\frac{E_{\text{Tr}} - E}{k_B T_0}\right), \quad (6.2)$$

i.e. their density decays above the hole transport level  $E_{\text{Tr,h}}$  towards mid-gap. The trap site concentration is given by  $N_{T,\text{exp}}$ , while the scaling factor is  $k_B T_0$ . The hole capture factor  $\beta$  is in the range  $10^{-9} \dots 10^{-10} \text{ cm}^3/\text{s}$ <sup>[182,301]</sup> (cf. Sec. 4.2.4), where a deviation of  $\beta$  of one order of magnitude leads to an error in trap depth of approx. 50 meV.

**Energy Level Diagrams.** A fundamental requirement to calculate capacitive trap responses is knowledge of the respective energy level diagrams. The latter are computed utilizing the IAPP-internal charge carrier simulation tool MOST, written by Matthias Schober. Details on that are found in Ref.<sup>[306,307]</sup> The influential input parameters are the free hole density  $p$ , the transport level energies for holes  $E_{\text{Tr,h}}$  and electrons  $E_{\text{Tr,e}}$  as well as the organic layer thickness (50 nm), and the work functions  $\phi$  of the contacts.  $p$  is obtained from Mott-Schottky analyses as discussed previously in Sec. 6.1. The transport level positions are taken from the respective RT values in Sec. 5.2.3, while the work functions are here  $\phi_{\text{Al}} = 4.2 \text{ eV}$  and  $\phi_{\text{ITO}} = 4.7 \text{ eV}$ .

Figure 6.5 shows the energy level diagrams for undoped and p-doped P5 / ZnPc. In case of undoped P5 / ZnPc, no level bending occurs.  $E_F$  (positioned approx. at the mean value of the two metal work functions) is close to the gap-mid<sup>[183]</sup> and the semiconductors are completely depleted (cf. Fig. 6.5 (a) and (c)). For p-P5 and p-ZnPc significant level bending is caused by doping. P5 doped by C<sub>60</sub>F<sub>36</sub> (MR 0.001,  $p = 1.2 \times 10^{18} \text{ cm}^{-3}$ ) exhibits a space charge region width of  $w_{\text{SCR}} = 32 \text{ nm}$  (cf. Fig. 6.5 (b)). For ZnPc doped by F<sub>6</sub>-TCNNQ (MR 0.01,  $p = 2.9 \times 10^{18} \text{ cm}^{-3}$ ), the SCR of  $w_{\text{SCR}} = 12 \text{ nm}$  is smaller due to the higher density of free holes (cf. Fig. 6.5 (d)). Within the SCR,  $E_F$  can cross large parts of the inherent charge carrier

<sup>1</sup>as calculated from the  $E_F$  position<sup>[183]</sup>



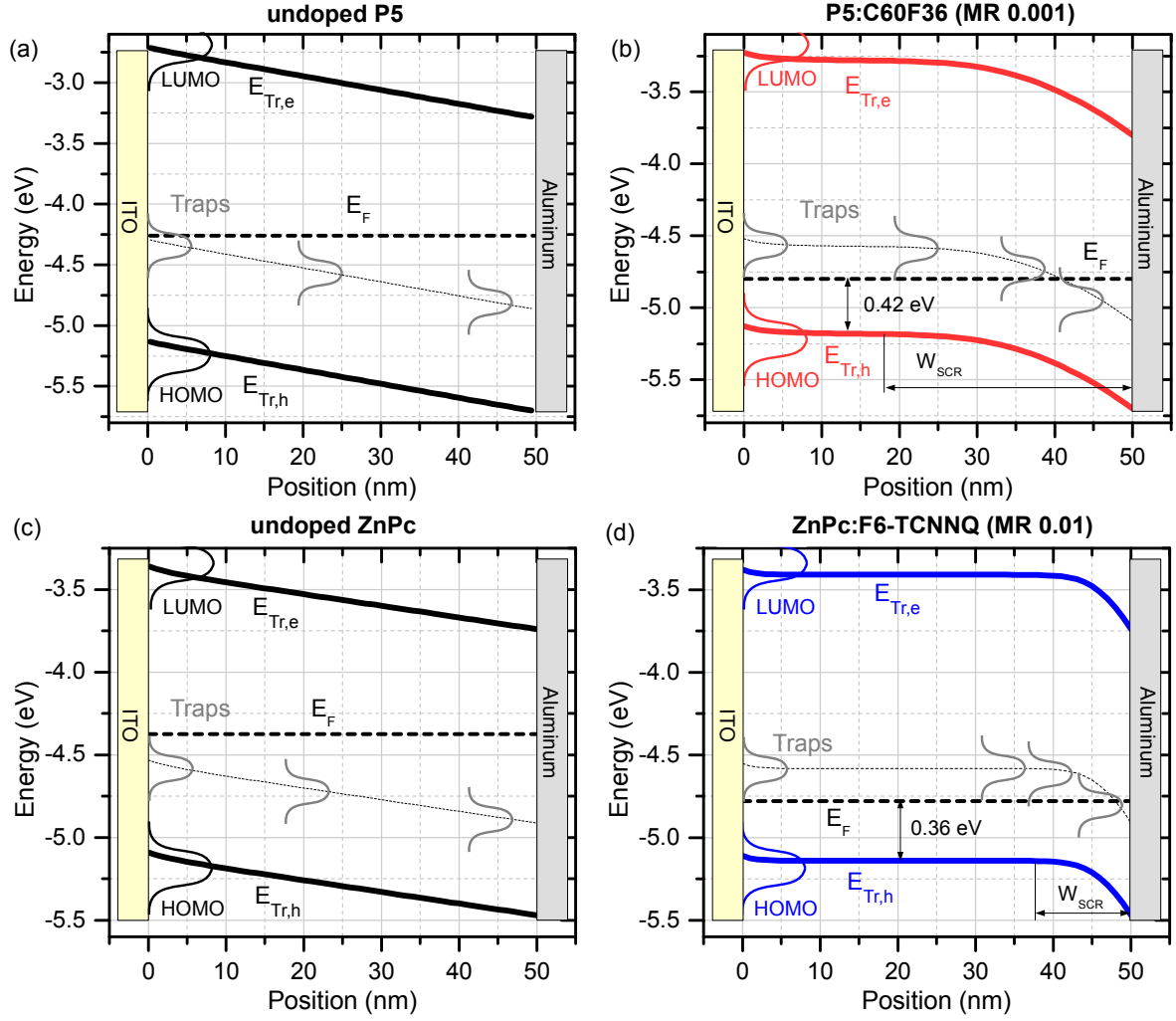


**Figure 6.5.:** Energy level diagrams for organic Schottky diodes consisting of 50 nm (a) intrinsic P5, (b) P5:C<sub>60</sub>F<sub>36</sub> (MR 0.001), (c) intrinsic ZnPc, or (d) ZnPc:F<sub>6</sub>-TCNNQ (MR 0.01), calculated via the MOST simulation tool written by Matthias Schober.<sup>[306,307]</sup> The hole transport level  $E_{Tr,h}$  and the electron transport level  $E_{Tr,e}$  are depicted in solid lines. In case of doped Schottky diodes, the level bending marks the space charge region with the depletion width  $w_{SCR}$ . Capacitive trap response originates from parts of the device, where the Fermi level  $E_F$  (dashed black line) crosses inherent trap distributions (gray).

trap distribution. Further away from the SCR, i.e. where the level bending is close to zero,  $E_F$  is 0.43 eV (P5) and 0.36 eV (ZnPc) away from the respective hole transport level. It is worth to note that these results agree well with UPS studies by Tietze *et al.*, who obtained for the same material combinations and doping concentrations a distance of 0.43 eV (p-P5) and 0.33 eV (p-ZnPc) from  $E_F$  to the HOMO onset.<sup>[183]</sup> Although  $E_{Tr,h}$  (RT) is not identical with the HOMO onset, the difference is typical  $\leq 50$  meV as obtained in Sec. 5.2.3.

**Capacitance Functions.** The measured frequency-dependent capacitance functions of pentacene and ZnPc, intrinsic (cf. black symbols) as well as p-doped with either C<sub>60</sub>F<sub>36</sub> (red symbols) or F<sub>6</sub>-TCNNQ (blue symbols) are shown in Fig. 6.6. Hereby, all  $C(f)$  spectra are taken at 0 V. In first-order approximation,  $R_S$ - $R_P$ - $C_P$  equivalent circuits, discussed in Sec. 4.2.2, are sufficient to describe the swing of the obtained capacitance functions between  $10^6$  Hz and  $5 \times 10^3$  Hz (dotted lines). An equivalent circuit fitting routine

(done with the commercial program Zview)<sup>2</sup> helps to acquire data on the series resistance  $R_S$  ( $\sim 100\ \Omega$ ) and the parallel resistance  $R_P$  ( $\sim \text{k}\Omega \dots \text{M}\Omega$ ) as well as the capacitance  $C_P$  of the SCR ( $\sim 5 \dots 20\ \text{nF}$ ). Doped layers exhibit a smaller  $R_P$  and larger  $C_P$  due to more free charge carriers inside, i.e. a thinner SCR. The series resistance  $R_S$  is independent on the doping.

An additional capacitance contribution is observed for lower frequencies. This increasing offset is attributed to charge carrier traps.<sup>[39,182,289,301]</sup> In the following, the deep and shallow traps identified in P5 and ZnPc are discussed. All obtained trap distributions are summarized in Fig. 6.7 and their parameters are listed in Tab. 6.1.

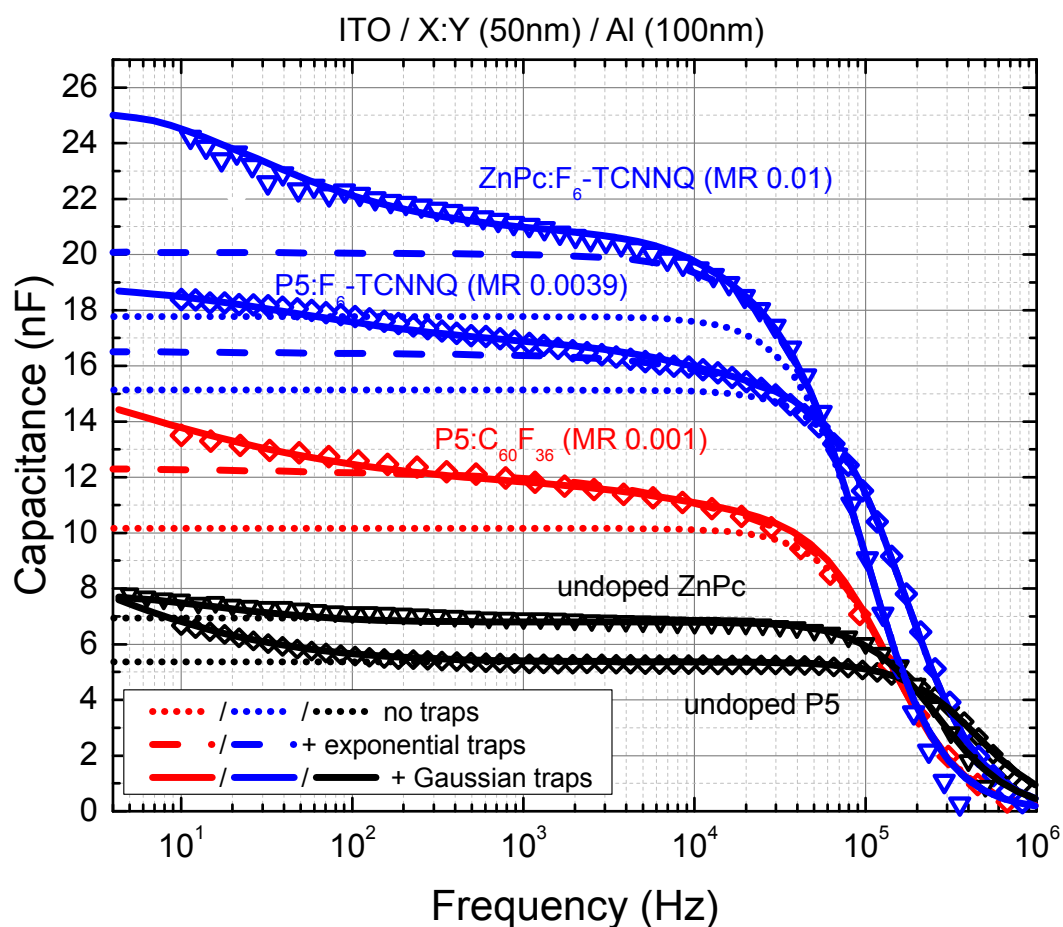


**Figure 6.6.:** Capacitance spectra for pentacene (depicted as diamonds) and ZnPc (triangles) Schottky diodes, comprising dopant molecules  $\text{C}_{60}\text{F}_{36}$  (red) or  $\text{F}_6\text{-TCNNQ}$  (blue) at zero bias. The measured data (symbols) is compared with the simulated capacitance spectra: only calculating the impact of the depletion layer (dotted line), incorporating exponentially distributed trap states (dashed line) and featuring additional Gaussian distributed deep trap states (solid line). For comparison, entirely undoped pentacene and ZnPc samples are plotted (black), exhibiting deep traps but no exponential trap distribution (black solid line).

<sup>2</sup>trial version available at <http://www.scribner.com>

### 6.2.1. Deep Traps in P5 and ZnPc

Examining the  $C(f)$  spectrum of undoped P5, a Gaussian-type trap DOS ( $N_{T,g} = 5.0 \times 10^{16} \text{ cm}^{-3}$ ,  $E_{T,g} = 0.65 \text{ eV}$ ,  $\sigma = 0.055 \text{ eV}$ ) is identified (cf. black solid line in Fig. 6.6 and Fig. 6.7 (a)). When p-doped by  $\text{C}_{60}\text{F}_{36}$  (MR 0.001), the device capacitance  $C_P$  increases to approx. 10 nF (due to the thinner SCR, cf. Fig. 6.5). At the same time, a stronger trap response is recorded. It originates from the same deep, relatively narrow ( $\sigma = 0.055 \text{ eV}$ ) Gaussian trap distribution ( $E_{t,g} = 0.60 \text{ eV}$ ), but here a density of  $N_{T,g} = 1.2 \times 10^{17} \text{ cm}^{-3}$  is obtained. P-doping by  $\text{F}_6\text{-TCNNQ}$  (MR 0.0039) reveals once more these deep Gaussian distributed traps at  $E_{T,g} = 0.58 \text{ eV}$  and a density of  $N_{T,g} = 1.1 \times 10^{17} \text{ cm}^{-3}$ , which is equal to the result of  $\text{P}_5\text{:C}_{60}\text{F}_{36}$ .

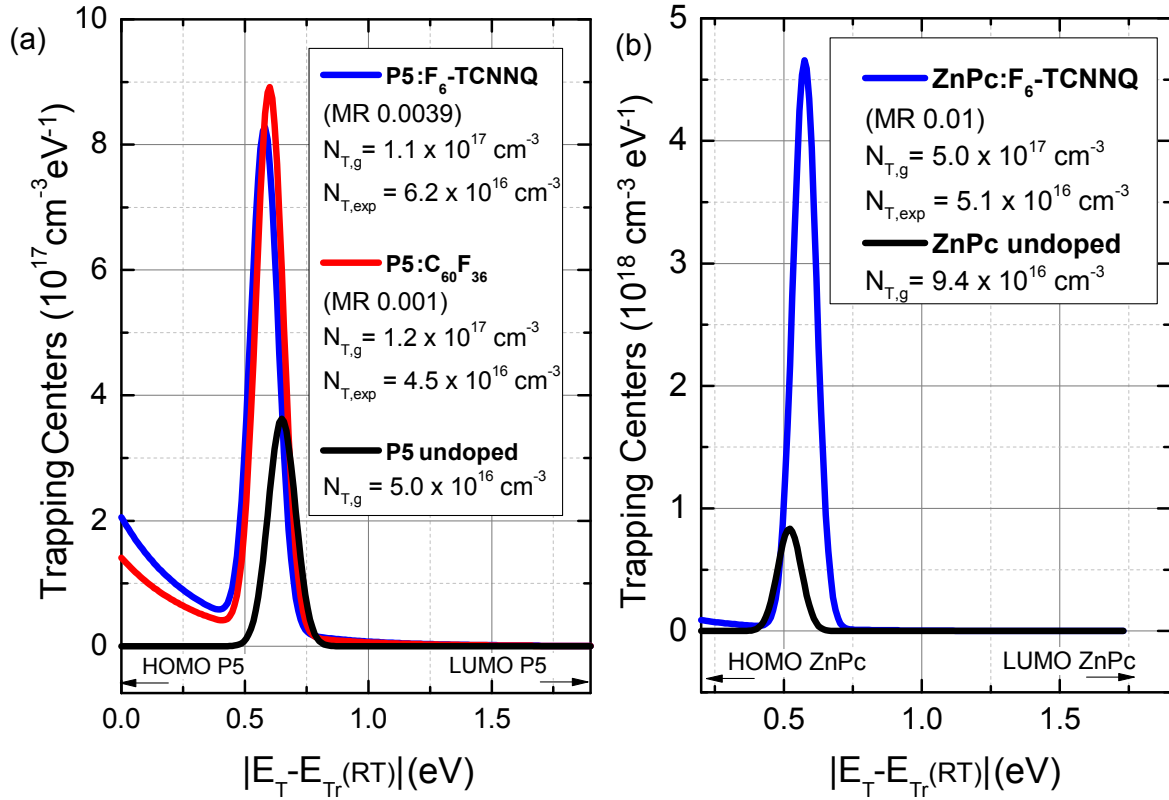


**Figure 6.7.:** Hole trap distributions in (a) pentacene and (b) ZnPc obtained by fitting the capacitance functions of the corresponding Schottky diodes. In the undoped materials, only one deeper lying Gaussian distributed trap is visible (black). Employing p-doping by  $\text{F}_6\text{-TCNNQ}$  (blue) or  $\text{C}_{60}\text{F}_{36}$  (red), a combination of exponentially tailing and deeper lying Gaussian distributed trap centers is observed. All fit parameters are summarized in Tab. 6.1.

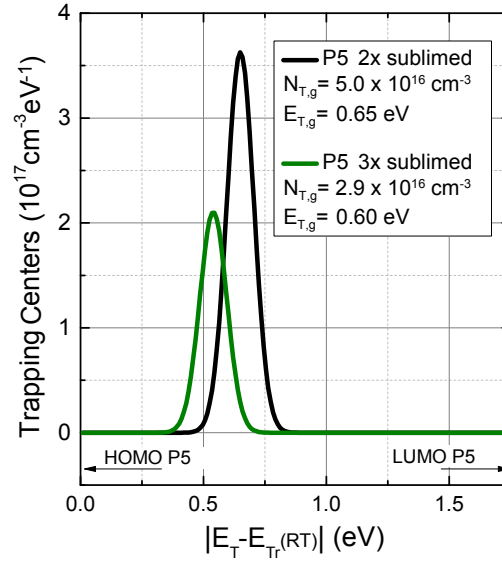
Undoped ZnPc (cf. Fig. 6.6, black triangles) exhibits a low-frequency trap response, which originates from a Gaussian-type trap distribution at  $E_{T,g} = 0.52 \text{ eV}$  with  $\sigma = 0.043 \text{ eV}$ . The trap density is found to be  $9.0 \times 10^{16} \text{ cm}^{-3}$ . When p-doped by  $\text{F}_6\text{-TCNNQ}$  (MR 0.01), an increased amount of these deep traps is identified ( $N_{T,\text{exp}} = 5.0 \times 10^{17}$ ).

Comparing the found trap distributions, it is most likely that the deep Gaussian distributed traps (0.52...0.65 eV) are characteristic for pentacene and ZnPc, since they occur in doped as well as undoped samples independently. Furthermore, the introduction of dopant molecules increases the *observable* amount of deep traps.

**Table 6.1.:** Parametrization of hole trap states in 2x and 3x sublimed P5, and ZnPc as obtained from the low frequency part of the respective capacitance functions in Fig. 6.6.

		$E_{T,\sigma}$ (eV)	$N_{T,\sigma}$ (cm <sup>-3</sup> )	$\sigma$ (eV)	$N_{T,\beta}$ (cm <sup>-3</sup> )	$k_B T_0$ (eV)
P5 (2x subl.)	undoped	0.65	$5.0 \times 10^{16}$	0.055	-	-
	C <sub>60</sub> F <sub>36</sub> (MR 0.001)	0.60	$1.2 \times 10^{17}$		$4.5 \times 10^{16}$	0.319
	F <sub>6</sub> -TCNNQ (MR 0.0039)	0.58	$1.1 \times 10^{17}$		$6.2 \times 10^{16}$	0.302
P5 (3x subl.)	undoped	0.60	$2.9 \times 10^{16}$	0.055	-	-
ZnPc	undoped	0.52	$9.0 \times 10^{16}$	0.043	-	-
	F <sub>6</sub> -TCNNQ (MR 0.01)	0.57	$5.0 \times 10^{17}$		$5.3 \times 10^{16}$	0.259

Here, the results are in excellent agreement with UPS studies by Tietze *et al.*, who identified deep traps of  $N_T = 9.6 \times 10^{16} \text{ cm}^{-3}$  in P5 and  $N_T = 7.2 \times 10^{17} \text{ cm}^{-3}$  in ZnPc.<sup>[183]</sup> Such deep charge carrier traps are commonly caused by material impurities<sup>[252,402]</sup> or structural defects<sup>[312]</sup> as discussed in Chapter 9, where water and oxygen-related defects in HTL materials are investigated.

**Figure 6.8.:** Comparison of the obtained hole trap distributions in pentacene for different material purification grades. For an additional sublimation step, the deep trap density is reduced by approx. a factor two (green) as compared to two-times sublimed P5 (black).

Material sublimation is the standard technique to remove impurities and purify organic semiconductor materials.<sup>[181]</sup> In this context, Fig. 6.8 compares the deep trap distributions obtained for two- (black line) and three-times (green line) sublimed, intrinsic pentacene. The former is the same as the trap DOS from Fig. 6.7 (a), the latter is obtained from the C(f) spectrum in Fig. 6.9 (a). While the trap depths are comparable at approx. 0.60...0.65 eV, the observed trap density is almost halved to  $2.9 \times 10^{16} \text{ cm}^{-3}$  after the additional purification step. This puts a hint on the material purity to cause deep traps within organic semiconductors. Further studies, especially comparing (un)purified material batches and different storing conditions are highly suggested.

### 6.2.2. Shallow Traps in p-doped P5 and ZnPc

Shallow trap levels, here modeled with an exponential distribution, are necessary to describe the capacitance functions of p-doped P5 and p-doped ZnPc in Fig. 6.6 between approx.  $10^4$  Hz and  $10^2$  Hz. For P5:C<sub>60</sub>F<sub>36</sub> (MR0.001), the trap DOS parameters are  $N_{T,\text{exp}} = 4.5 \times 10^{16} \text{ cm}^{-3}$  and  $k_B T_0 = 319 \text{ meV}$ . In case of P5:F<sub>6</sub>-TCNNQ (MR0.0039, they are  $N_{T,\text{exp}} = 6.2 \times 10^{16} \text{ cm}^{-3}$  and  $k_B T_0 = 302 \text{ meV}$ . Similarly, an exponential trap distribution ( $N_{T,\text{exp}} = 5.3 \times 10^{16} \text{ cm}^{-3}$ ,  $k_B T_0 = 259 \text{ meV}$ ) describes the C(f) spectrum in the range of  $10^4 \dots 10^3$  Hz for ZnPc:F<sub>6</sub>-TCNNQ (MR0.01).

All these shallow trap states appear only upon doping and their origin is not clear. They might be present in the intrinsic materials and become visible when the  $E_F$  crosses the trap energies within the depletion region. On the other hand, these additional trap states can be *caused by doping*. Arkhipov *et al.* calculated an increased energetic disorder in the host upon Coulomb interaction with ionized dopants, i.e. broad deep tails of the DOS and additional deep states.<sup>[277]</sup>

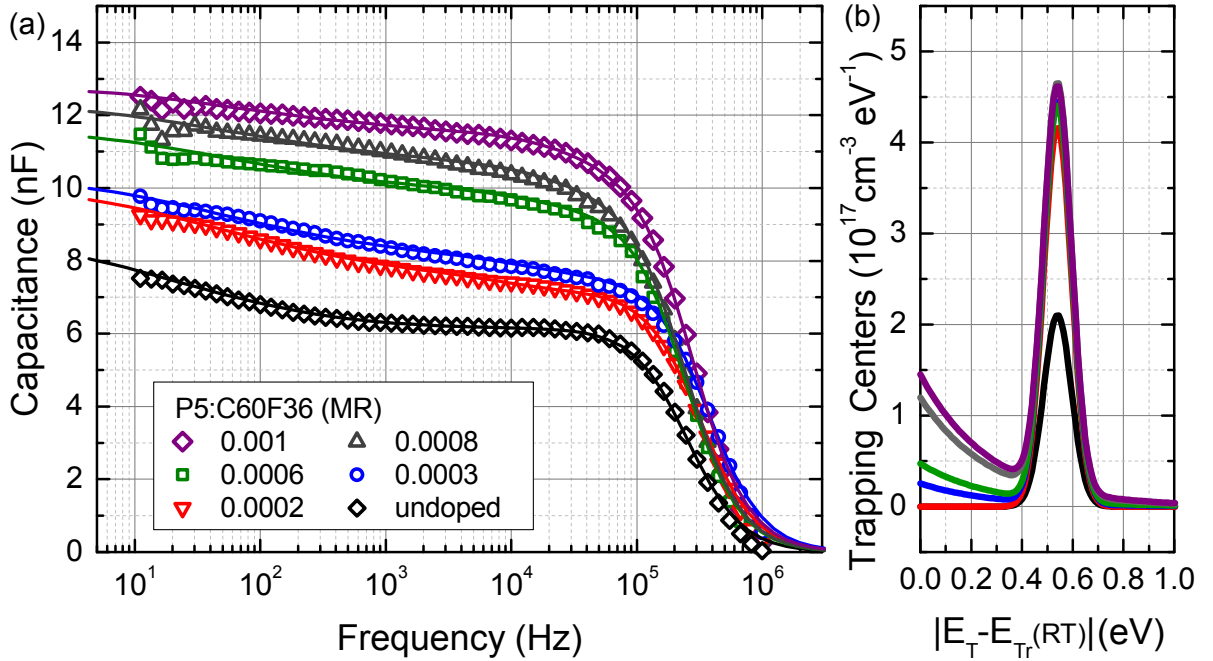


**Figure 6.9.:** Comparison of the obtained hole trap distributions in pentacene for different material purification grades. For an additional sublimation step, the deep trap density is reduced by approx. a factor two (green) as compared to two-times sublimed P5 (black).

In the following, the correlation between dopant MR and the obtained trap DOS is further investigated. Figure 6.9 shows the C(f) spectra of pentacene Schottky diodes at various doping concentrations and the obtained trap DOS. In particular, three-times sublimed P5 is used and the dopant MR is varied from 0 (undoped, black) to 0.001 (purple) of C<sub>60</sub>F<sub>36</sub>. For undoped P5, only deep traps at  $E_T = 0.54 \text{ eV}$  and  $N_T = 2.9 \times 10^{16} \text{ cm}^{-3}$  are visible. With increasing doping concentration, the determined deep trap concentration saturates at approx.  $6 \times 10^{16} \text{ cm}^{-3}$  (cf. Fig. 6.9 (b)). This trend is observed first for MR 0.0002 (red line), where only deep traps but no shallow traps with  $E_T < 0.4 \text{ eV}$  are obtained. If the dopant concentration is above MR 0.0002, the deep trap concentration  $N_{T,g}$  remains constant but additional shallow traps appear. The latter increase in density with the doping concentration and are described here by exponential distributions. Table 6.2 presents the relevant trap DOS parameters. It must be noted that the shallow trap response in Fig. 6.6 and Fig. 6.9 (a) between approx.  $10^2$  Hz and  $10^4$  Hz is not unambiguously assigned

**Table 6.2.:** Parametrization of hole trap states in 3x sublimed P5 at various C<sub>60</sub>F<sub>36</sub> dopant concentrations, as obtained from the capacitance functions in Fig. 6.9 (a).

	MR	$E_{T,\sigma}$ (eV)	$N_{T,\sigma}$ (cm <sup>-3</sup> )	$\sigma$ (eV)	$N_{T,\beta}$ (cm <sup>-3</sup> )	$k_B T_0$ (eV)
P5	undoped	0.54	$2.9 \times 10^{16}$	0.055	-	-
	0.0002		$5.8 \times 10^{16}$		-	-
	0.0003		$6.1 \times 10^{16}$		$7.2 \times 10^{15}$	0.276
	0.0006		$6.0 \times 10^{16}$		$1.3 \times 10^{16}$	
	0.0008		$6.2 \times 10^{16}$		$3.3 \times 10^{16}$	
	0.001		$6.1 \times 10^{16}$		$4.0 \times 10^{16}$	

to exponentially distributed charge carrier traps. In Chapter 8, thermally stimulated current experiments on the p-doped HTL Spiro-TTB disclose shallow, Gaussian distributed traps, which increase with doping concentration. Here, it is probable that for increased doping,  $E_F$  crosses larger parts of the inherent trap distributions for the discussed reasons while the Coulomb interaction of more and more ionized dopants with the host system generates additional (shallow) charge carrier traps.

### 6.3. Freeze-Out of p-Doping in ZnPc

**Motivation.** UPS studies by Tietze showed that the Fermi level position in a doped organic semiconductor shifts towards the gap-mid, i.e. less free charge carriers are present, when the temperature decreases.<sup>[91]</sup> In this thesis, the principle is adapted to progressively tune  $E_F$ , starting from the RT position of intentionally p-doped ZnPc, to the gap-mid at temperatures as low as 20 K. The charge carrier depletion and the trap response are studied for a varying amount of free holes down to  $10^{17}$  cm<sup>-3</sup>, which would require otherwise experimentally elaborated ultra-low doping.<sup>[183]</sup> However, direct measurements of the free hole densities versus temperature via Mott-Schottky examinations are problematic. Inherent trap capacitances and their temperature dependence superimpose the SCR signal and led to divisive results, e.g. increasing  $N_A^-$  for decreasing temperatures.<sup>[401]</sup> In the present study, the Fermi level position and thus the number of free holes relative to the deep traps are accessed via studies on  $E_F$  versus the molar doping ratio<sup>[183]</sup> and  $E_F(T)$ -measurements.

**Capacitance Freeze-Out and Trap-Filling Regime.** Figure 6.10 (a) illustrates C(f)-spectra for 50 nm ZnPc, p-doped by MR 0.01 F<sub>6</sub>-TCNNQ, and taken at temperatures from RT down to 20 K in steps of  $\Delta T = 10$  K. Related to that, Fig. 6.10 (b) shows the Fermi level position in ZnPc:F<sub>6</sub>-TCNNQ versus the dopant MR as obtained by Tietze *et al.*<sup>[183]</sup> At room temperature (cf. red arrow),  $E_F$  is approx. 0.3 eV above the HOMO onset. The respective capacitance function (cf. red line in Fig. 6.10 (a)) is determined by the depletion capacitance of the SCR as well as deep and shallow traps in the particular frequency ranges (cf. Sec. 6.2). Note that the C(f) spectrum is taken only for frequencies  $\geq 10^1$  Hz. Below, the excitation is slow as compared to the charge carrier injection, the phase angle approaches 0° and the device is not capacitive.

With decreasing temperature to approx. 150 K, the shapes of the C(f)-spectra do not change. Only lowering offsets caused by the extending SCR are observed (cf. orange line for 200 K). The trap responses remain at similar levels, which indicates that the traps are still saturated. Tietze *et al.* observed this result for a Fermi level position at approx. 0.5 eV above the HOMO onset (cf. orange arrow). For temperatures below 150 K, the SCR width increases strongly and the depletion capacitance drops. At the same time, the shallow trap response decreases. At 100 K (cf. turquoise line), almost no additional trap capacitance is observed between  $10^4$  Hz and  $10^5$  Hz and thus no shallow traps are identified. Only deep trap contributions at frequencies

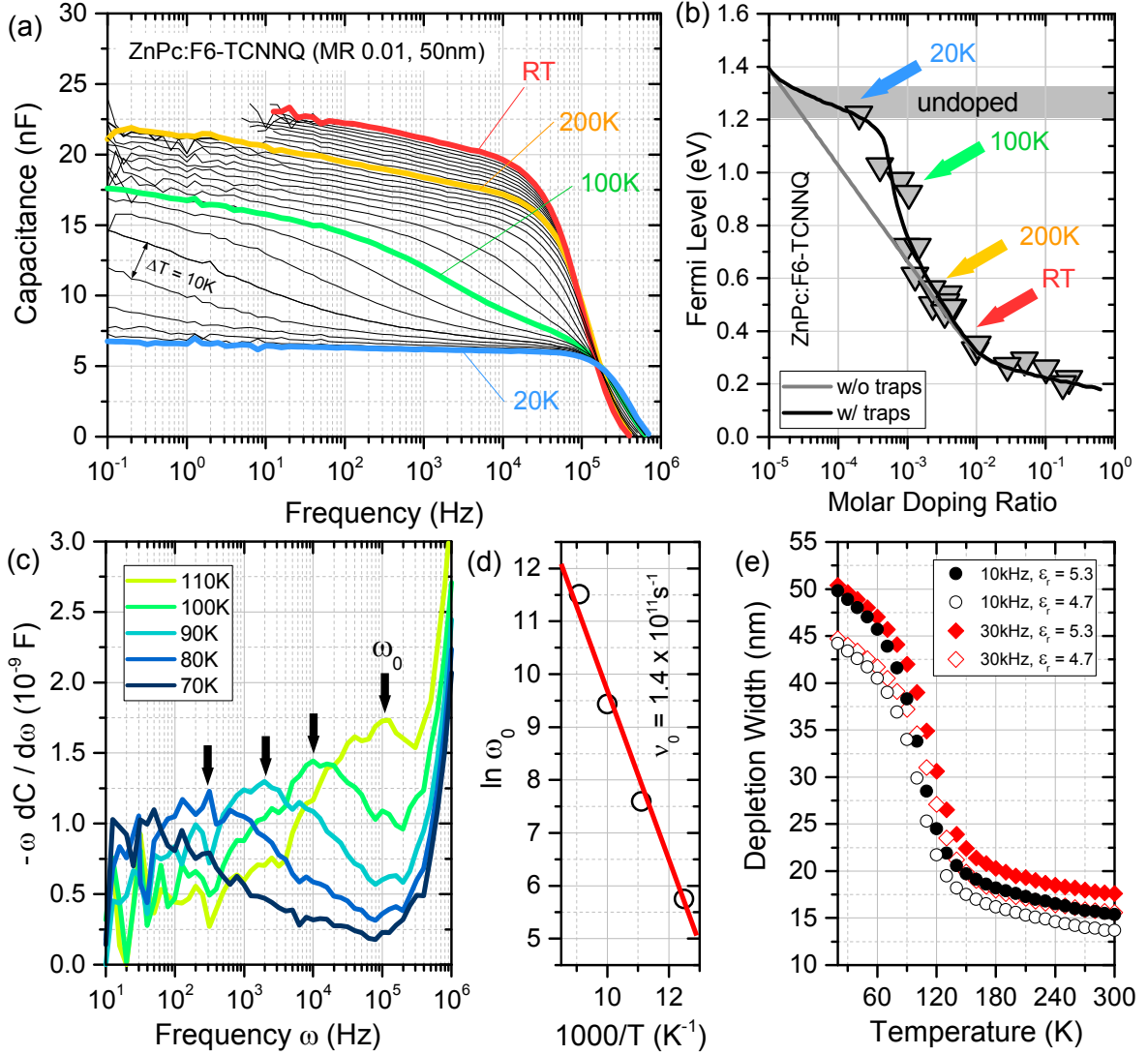


**Figure 6.10.:** (a) Capacitance spectra for p-doped ZnPc (F<sub>6</sub>-TCNNQ, MR 0.01) between ITO and Al at zero bias and sample temperatures from RT to 20 K in steps of  $\Delta T = 10$  K. The doping freeze-out causes a increasing depletion of the device and a vanishing trap response. (b) Fermi level positions with respect to the HOMO onset versus molar doping ratio in ZnPc:F<sub>6</sub>-TCNNQ at room temperature, adapted from Ref. [183]. Colored arrows indicate the  $E_F$  position for MR 0.01 at various temperatures as qualitatively presumed from the results of  $C(f,T)$  in (a). (c) Frequency dependence of the deep trap contribution to the capacitance change  $-\omega dC/d\omega$ . The maximums  $\omega_0$  are marked by black arrows. Their temperature dependence yields (d) the attempt-to-escape frequency  $\nu_0$  of the deep traps. (e) Space charge region width versus sample temperature, calculated from (a) for 10 kHz and 30 kHz and  $\epsilon = [4.7, 5.3]$ .

$\leq 10^4$  Hz are found, which, however, decrease once the sample temperature is further lowered. This observation agrees with the finding of a trap-filling regime in p-doped ZnPc at doping concentrations  $< \text{MR } 3\ldots 6 \times 10^{-4}$  most recently. [183]

At 20 K, the p-ZnPc Schottky diode is entirely depleted. The capacitance is not frequency dependent anymore but stable at approx. 6 nF, which equals a depletion width of 50 nm (assuming  $\epsilon = 5.3$ ). All dopants are frozen, i.e. no free holes are generated, and the Fermi level is deep in the gap ( $E_F > 1.2$  eV, cf. blue arrow in Fig. 6.10).

**Attempt-to-Escape Frequency.** Fitting of all capacitive trap responses in Fig. 6.10 (a) is complex and not unambiguously done due to the large number of free parameters. The number of free holes, i.e. the Fermi level and the energy level diagram, as well as the hole transport level (cf. Sec. 5.2) change with temperature. Moreover, the hole capture rate is temperature-dependent.<sup>[403]</sup> Hence, the shallow and deep trap distributions are determined only for room temperature as done in Sec. 6.2. In particular, a deep trap concentration  $N_T = 5 \times 10^{17} \text{ cm}^{-3}$  has been identified at energies 0.52...0.57 eV above  $E_{T,h}$  (RT). However, the capacitance swing of the deep trap response between  $10^3 \text{ Hz}$  and  $10^4 \text{ Hz}$  and  $T = 70...110 \text{ K}$  bears the attempt-to-escape frequency  $\nu$  of these deep traps. The latter is an important simulation parameter, which is required to model the charge carrier release from trap levels when assessing thermally stimulated currents in Chapter 7-9. Hence obtaining an estimate value for  $\nu$  is of special interest. The so-called Walter method examines the temperature dependence of the inflection point  $\omega_0$  from the capacitance change  $-\omega dC/d\omega$ ,<sup>[404]</sup> as plotted in Fig. 6.10 (c). For each sample temperature, a peak maximum  $\omega_0(T)$  is obtained (cf. black arrows). The activation energy  $E_{A,T}$  of a discrete, i.e. prominent, trap level with respect to the transport level is given by<sup>[404]</sup>

$$E_{A,T} = k_B T \ln \frac{2\nu}{\omega_0}. \quad (6.3)$$

Consequently, the Arrhenius plot in Fig. 6.10 (d) yields an attempt-to-escape frequency  $\nu = 1.4 \times 10^{11} \text{ s}^{-1}$  for the particular deep trap distribution in ZnPc. Similar results have been reported recently for traps in several donor:acceptor blends. Fischer *et al.* obtained  $\nu = 0.5...2 \times 10^{11} \text{ s}^{-1}$  for ZnPc:C<sub>60</sub>,<sup>[40]</sup> while Kraner *et al.* found  $\nu = 1...7 \times 10^{11} \text{ s}^{-1}$  for aza-BODIPY<sup>3</sup>:C<sub>60</sub> blends.<sup>[406]</sup> In both cases, the traps originated from the donor (HTL) phase. The determined order of magnitude for  $\nu$  is not surprising, since the charge carrier release is suspected to happen via phonon interaction.<sup>[119]</sup> The phonon frequency is  $\nu_0 \simeq 10^{12} \text{ s}^{-1}$ ,<sup>[119]</sup> while the hopping frequency of a charge carrier is assumed to decrease exponentially with the hopping distance by<sup>[407]</sup>

$$\nu = \nu_0 \cdot \exp(-2\gamma |R_{ij}|). \quad (6.4)$$

The latter equation is equal to the pre-factor in the *Miller-Abrahams* transition rate expression (cf. Sec. 2.2.2),<sup>[136]</sup> where  $\gamma$  is the inverse localization radius and  $|R_{ij}|$  the inter-site distance. In that sense, a charge carrier hop from a localized trap site at one molecule to a more mobile state at an adjacent molecule (i.e.  $1/\gamma \simeq |R_{ij}|$ ) conceivably relates to an attempt-to-escape frequency of  $\nu = 0.1 \cdot \nu_0 \simeq 10^{11} \text{ s}^{-1}$ .

**SCR(T): Dopant Regimes.** Although the capacitance spectra in Fig. 6.10 (a) are heavily influenced by trap responses, information on the space charge region are provided at frequencies  $\geq 10^4 \text{ Hz}$ . Here, the excitation is too fast for the majority of the traps to respond during an oscillatory cycle (cf. Sec. 6.2). The plate capacitor approximation

$$d = \varepsilon_0 \varepsilon_r \frac{A}{C} \quad (6.5)$$

is used to calculate the depletion width of the SCR for each temperature from the measured capacitance value. Figure 6.10 (e) depicts the results for excitation frequencies of 10 kHz (black symbols) and 30 kHz (red symbols). For the relative permittivity literature value of  $\varepsilon_r = 4.7$ ,<sup>[39,40]</sup> the SCR is not extended over the entire 50 nm ZnPc thin-film at 20 K, but has a width of approx 45 nm. This result is unphysical, since the flat  $C(f)$ -spectra at ultra-low temperatures indicate that no free charge carriers are present and the thin-film is completely depleted (cf. Fig. 6.10 (a)). Re-adjusting the relative permittivity to  $\varepsilon_r = 5.3$  eliminates this inconsistency. Possible reasons for a different  $\varepsilon_r$  could be the considerable dopant MR mixed into the ZnPc film or a temperature-dependence of the permittivity.

<sup>3</sup>benzannulated 4,4-difluoro-4-bora-3a,4a-diaza-s-indacen, a near-infrared absorber material class<sup>[405]</sup>



Throughout all temperatures, the obtained SCR widths are a little lower for 10 kHz as compared to 30 kHz (cf. black and red symbols in Fig. 6.10 (e)), since the capacitance tends to be overestimated for lower frequencies due to residuals of the trap response. However, all depletion-width-versus-temperature plots feature the same shape, which strongly reminds of the Fermi level versus dopant MR relation (cf. compare Fig. 6.10 (b) and (e)). Hence, the same explanation seems natural. Following the sketch in Fig. 6.11, the p-doped ZnPc thin-film (MR 0.01) is in dopant saturation at RT.<sup>[183]</sup> With decreasing sample temperature, apparently less thermal energy is available to generate free charge carriers. The SCR extends, but the Fermi level shifts only slowly away from the HOMO onset (cf. red and orange arrow in Fig. 6.10 (b)). This result is rather unexpected, since in the saturation region, free holes are efficiently generated from the shallow acceptor level at  $E_A < E_F$ . Actually, the transition between dopant reserve and dopant saturation  $E_F = E_A$  was found to occur at approx. MR 0.02 in ZnPc<sup>[183]</sup>

The Fermi level position and consequently the depletion zone width show strong swings dependent on the molar doping ratio (MR  $10^{-3}$ ... $10^{-4}$ ) and the thermal energy/temperature (130...90 K). Below 100 K, the thin-film runs into the trap-filling regime. It is almost entirely depleted. The Fermi level is deep within the energy gap and pinned to impurities, i.e. deep traps concentrations of approx.  $10^{17} \text{ cm}^{-3}$  (MR  $10^{-4}$ ).

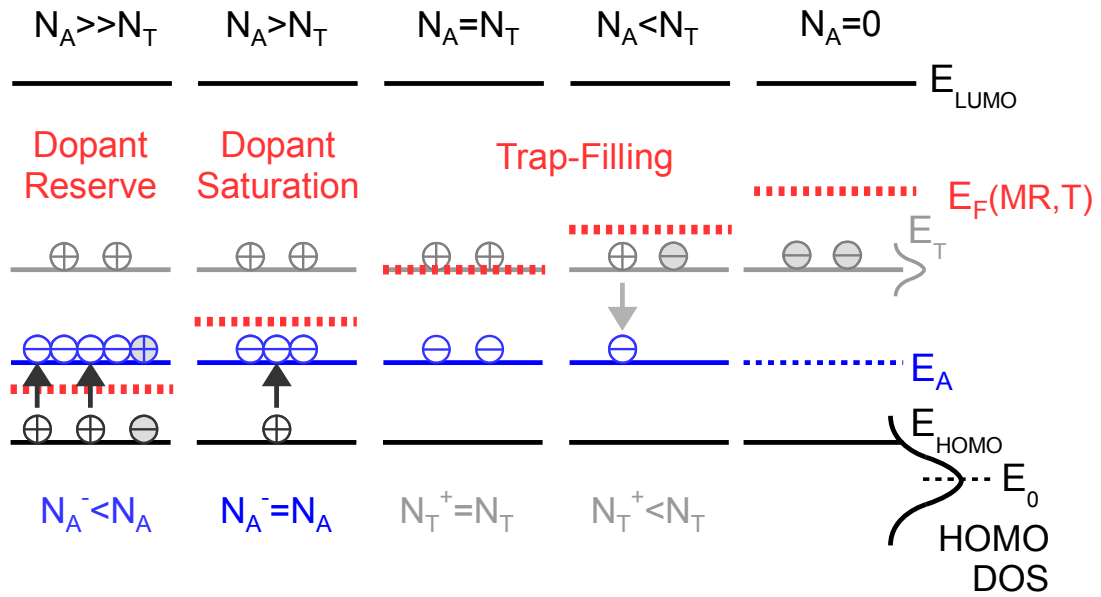


**Figure 6.11.:** Qualitative illustration of the statistical description of the doping process as introduced by Tietze *et al.*<sup>[181,183,207]</sup> Dopant activation is considered by an effective acceptor level  $E_A$ . Trap states at  $E_T$  hinder the doping process at low concentrations. Free holes are provided by doping for  $N_A > N_T$ . In this case, either dopant saturation ( $N_A^- = N_A$ ) or reserve ( $N_A^- < N_A$ ) is possible. With decreasing temperature, the CT complex dissociation is hindered and thus  $E_F$  transitions towards the gap-mid. Picture adapted from Ref.<sup>[183]</sup>

In summary, these findings strongly indicate a freeze-out of the p-doping effect in ZnPc upon cooling. In particular, the transition from dopant saturation to trap-filling regime, which was previously identified/observed by reduction of the doping ratio at RT, is here obtained (and consistently reproduced) by cooling a film of a fixed doping concentration from RT (dopant saturation) to  $< 100 \text{ K}$  (trap-filling only). Surprisingly, the number of free holes and, thus, the Fermi level position is strongly temperature controlled even in the

saturation regime, which emphasizes the demand for an adapted model beyond classical Fermi-Dirac statistics and thermal activation from a fixed dopant level  $E_A$ . A temperature dependence of the separation of the hole from the ionized dopant molecule (CT state dissociation) to release it into the disordered host system might be one reason for this difference to classical single crystal semiconductors and corresponding doping physics.

**Temperature-dependent UPS.** Pushing these investigations a little further, UPS studies are conducted for three differently p-doped ZnPc thin-films at various temperatures. The temperature is varied stepwise between 300 K and approx. 100 K (down and up again) via a liquid nitrogen flow through the sample holder in the UPS chamber and a heating element.

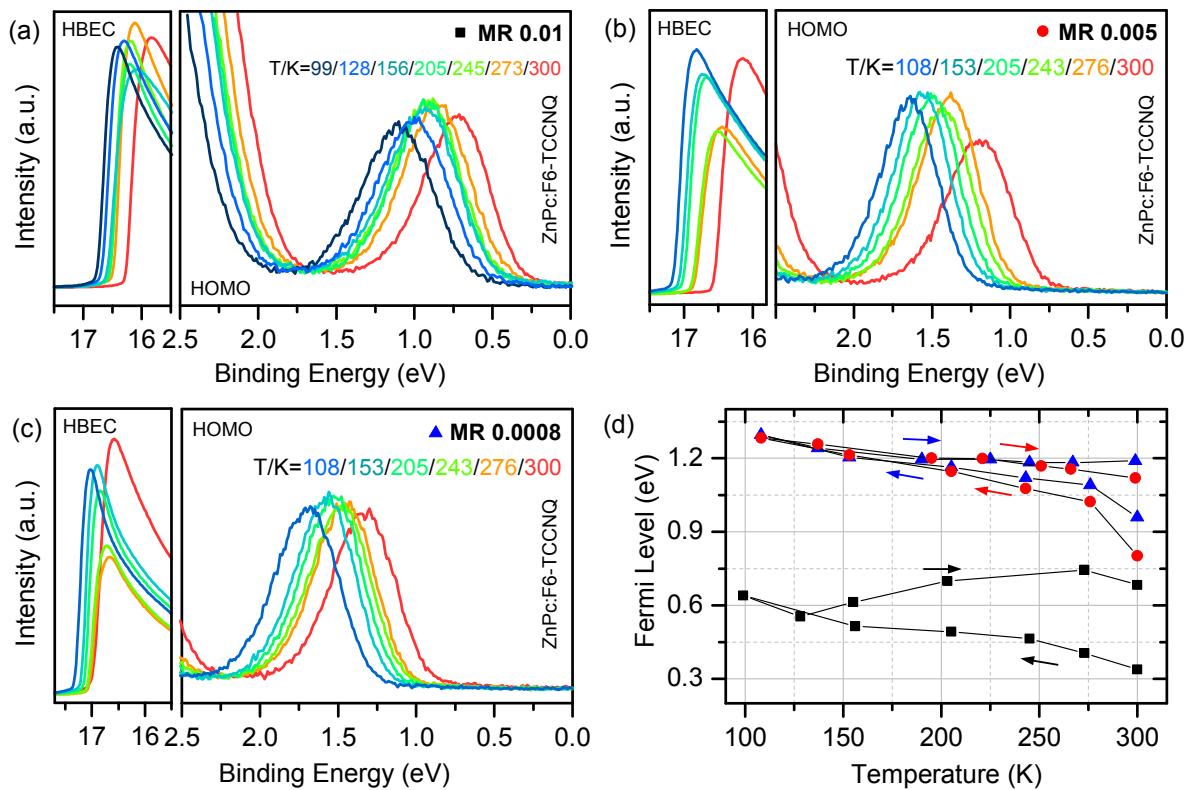


**Figure 6.12.:** UPS spectra of (a) MR 0.01, (b) MR 0.005, and (c) MR 0.0008 F<sub>6</sub>-TCNNQ doped ZnPc thin-films at various temperatures. (d) Determined Fermi level positions with respect to the HOMO onset under temperature variation for the doped thin-films.

The UPS spectra as well as the resolved Fermi level positions are shown in Fig. 6.12. In case of the MR 0.01 F<sub>6</sub>-TCNNQ doped sample,  $E_F$  shifts away from its initial position at 0.3 eV (RT) to 0.5 eV (200 K), and 0.7 eV (100 K). Both former values agree well with the previous estimations from Fig. 6.10 (b). The value obtained at 100 K exhibits a discrepancy of approx. 0.2...0.3 eV, which is most probably caused by the experimental error of the sample temperature. In the saturation regime,  $E_F$  depends heavily on the number of active dopants, i.e. the temperature, while the chamber cooling is here at its limit. In lightly doped samples,  $E_F$  is further away from the HOMO onset at RT. For MR 0.005, it is  $E_F = 0.8$  eV and for MR 0.0008 it is  $E_F = 0.95$  eV. Both results are equal to previous results shown by Tietze *et al.* (cf. Fig. 6.10 (b)).<sup>[183]</sup> Upon cooling, both samples feature a rapid increase of  $E_F$  within the first 50 K, where they pass the saturation regime. For temperatures below 200 K, both lightly doped thin-films are in the trap-filling regime. The Fermi level position is stable at approx. 1.2 eV (close to the value for an undoped ZnPc thin-film)<sup>[91,183]</sup> as the

majority of the dopants is frozen. These findings clearly indicate once more that the CT state dissociation could be temperature-dependent. The prevailing temperature and the initial doping MR determine  $E_F$ , which signifies either trap-filling, dopant saturation, or dopant reserve. Tietze demonstrated that for a very high doping concentration of MR 0.217, ZnPc remains in the dopant reserve regime ( $E_F \sim 0.25$  eV) down to 100 K.<sup>[91]</sup>

In the present cases, reheating the samples recovers  $E_F$  only entirely if the process is slow. Rapid heating as erroneously done for MR 0.01 (cf. black squares in Fig. 6.12 (d)) is suspected to vaporize dopants from the surface region.<sup>4</sup> Ideally, the introduced heat is kept minimal, which, however, renders such UPS(T) measurements very time-consuming (up to hours and days in total).

## 6.4. Summary

The interplay between charge carrier traps and molecular doping in organic semiconductors has been investigated by impedance spectroscopy and ultraviolet photon spectroscopy. In particular, doped thin-films and Schottky diodes comprising pentacene and ZnPc were examined. It was shown that the Fermi level position depends on the number of active dopants, which could be related to the incorporated molar doping ratio and the temperature. The latter seemed to control the CT transfer state dissociation, which is why a complete freeze-out was observed for p-ZnPc at temperatures below 100 K. Here, a descriptive model should be the aim of further investigation. During freeze-out, classical dopant reserve, doping saturation, and trap-filling were identified by comparison of impedance spectroscopy results and (temperature-dependent) UPS studies. Throughout all dopant regimes, the Fermi level position has been decisive for the trap response in the organic semiconductors. A change of the trap occupation due to the small-signal IS excitation occurs at the intersection of  $E_F$  and  $E_T$ . Consequently, undoped organic semiconductors revealed only a small trap capacitance, since most of the traps were 'inert'. Examining the trap capacitance for P5 and ZnPc, deep traps were identified at energies of approx. 0.52...0.65 eV above the hole transport level at RT. Upon doping, the deep trap concentrations saturated at approx.  $1 \times 10^{17} \text{ cm}^{-3}$  (P5) and  $5 \times 10^{17} \text{ cm}^{-3}$  (ZnPc), which was in accordance to previous UPS results.<sup>[183]</sup> In case of P5, an additional material purification step reduced the number of deep traps. For ZnPc, the attempt-to-escape frequency from the deep traps was identified to approx.  $\nu_0 = 1 \times 10^{11} \text{ s}^{-1}$ , which will gain importance in the thermally stimulated current simulations of Chapter 7-9.

Additionally, shallow trap distributions emerged at doping concentrations  $> \text{MR } 0.002$  in both materials. Their origin remained undetermined, but they were possibly residuals of the doping process or filled tailing states of the host DOS.

<sup>4</sup>note that the temperature is balanced by the cooling flow and the heating wire, which are both not 100 percent at the same place as temperature sensor and sample.



# Thermally Stimulated Currents in Organic Semiconductors

*Several methods to gain trap information from TSC spectra of organic semiconductors are assessed and applied to study the trap response of an aged pentacene Schottky diode and a 100 nm thick layer of the hole transporting MeO-TPD sandwiched between selective electrodes. The temperature shift of peak positions in the TSC spectra for varying heating rates  $\beta$  is controlled by the trap release. The peak position dependence on the extracting electric field is explained by modeling the dispersive transport in the disordered semiconductor system at low temperatures. Here, re-trapping additionally broadens the TSC spectra of the obtained Gaussian distributed trap levels.*

## 7.1. Assessments of TSC: Spectra Fitting, Hoogenstraaten-, $T^4$ -, and Chen's-Method

As previously reviewed in Sec. 4.3, numerous methods and approximations to extract trap parameters from thermally stimulated current (TSC) measurements are reported in literature.<sup>[310,311,315,317–321,323,326,327,330]</sup> In the following, these techniques are assessed on their capability to provide insight into trap densities, trap depths, and trap state distributions in small molecular organic semiconductors. Figure 7.1 (a) shows the TSC spectra of a pentacene (P5) Schottky diode consisting of 50 nm p-doped P5 (0.5 wt% F<sub>6</sub>-TCNNQ) and 50 nm intrinsic P5 sandwiched between ITO and Al contacts. The sample was aged, i.e. stored with intact encapsulation under ambient conditions and measured more than two years after fabrication. Filled electrically (5 V forward bias, 30  $\mu$ A) at 40 K, the diode exhibits a broad TSC spectrum featuring a shoulder at  $T_1$  around 80 K and a distinct peak at  $T_2$  between 100 K and 110 K. Both features shift to lower temperatures for smaller heating rates  $\beta$ , i.e. approximately by 15 K for  $T_1$  and 9 K for  $T_2$  when changing  $\beta$  from 7 K min<sup>-1</sup> to 1 K min<sup>-1</sup>. Simultaneously, the absolute TSC decreases, e.g. at the peak position  $T_2$  from 20.5 pA to 2.9 pA, since the trapped charge carriers are released at a slower pace for a longer time. Integrating the thermally stimulated current over time, however, yields a similar total net charge  $Q = 12.3...13.0$  nC for all  $\beta$ . Assuming a uniform trap state distribution for all 100 nm of P5, this results in a trap density  $N_T = 1.19...1.26 \times 10^{17}$  cm<sup>-3</sup> according to Eq. (4.48).

**Spectral Fitting.** The trap depths can be assessed via fitting the TSC spectra. Figure 7.1 (b) illustrates thermally stimulated current curves computed from

$$I(T) = (eA\mu\tau FN_T\nu) \exp \left[ -\frac{E_T - E_{Tr}}{k_B T} - \frac{\nu(E)}{\beta} \int_{T_0}^T \exp \left( -\frac{E_T - E_{Tr}}{k_B T'} \right) dT' \right] \quad (4.50)$$

after Haering/Adams<sup>[310]</sup> and Garlick/Gibson<sup>[317]</sup>. For a constant attempt-to-escape frequency  $\nu = 10^{11} \text{ s}^{-1}$ , two trap levels  $E_{T1} = 0.205 \text{ eV}$  and  $E_{T2} = 0.270 \text{ eV}$  are found to match with the shoulder and peak positions  $T_1$  and  $T_2$  in Fig. 7.1 (a). For sake of simplicity, the trap depths are taken here relatively to the transport level  $E_{Tr}$ . The electric field  $F$  is approximated by the difference in the work functions of the sandwiching electrodes, i.e.  $V_{bi} = 0.5 \text{ V}$ , divided by the total sample thickness.

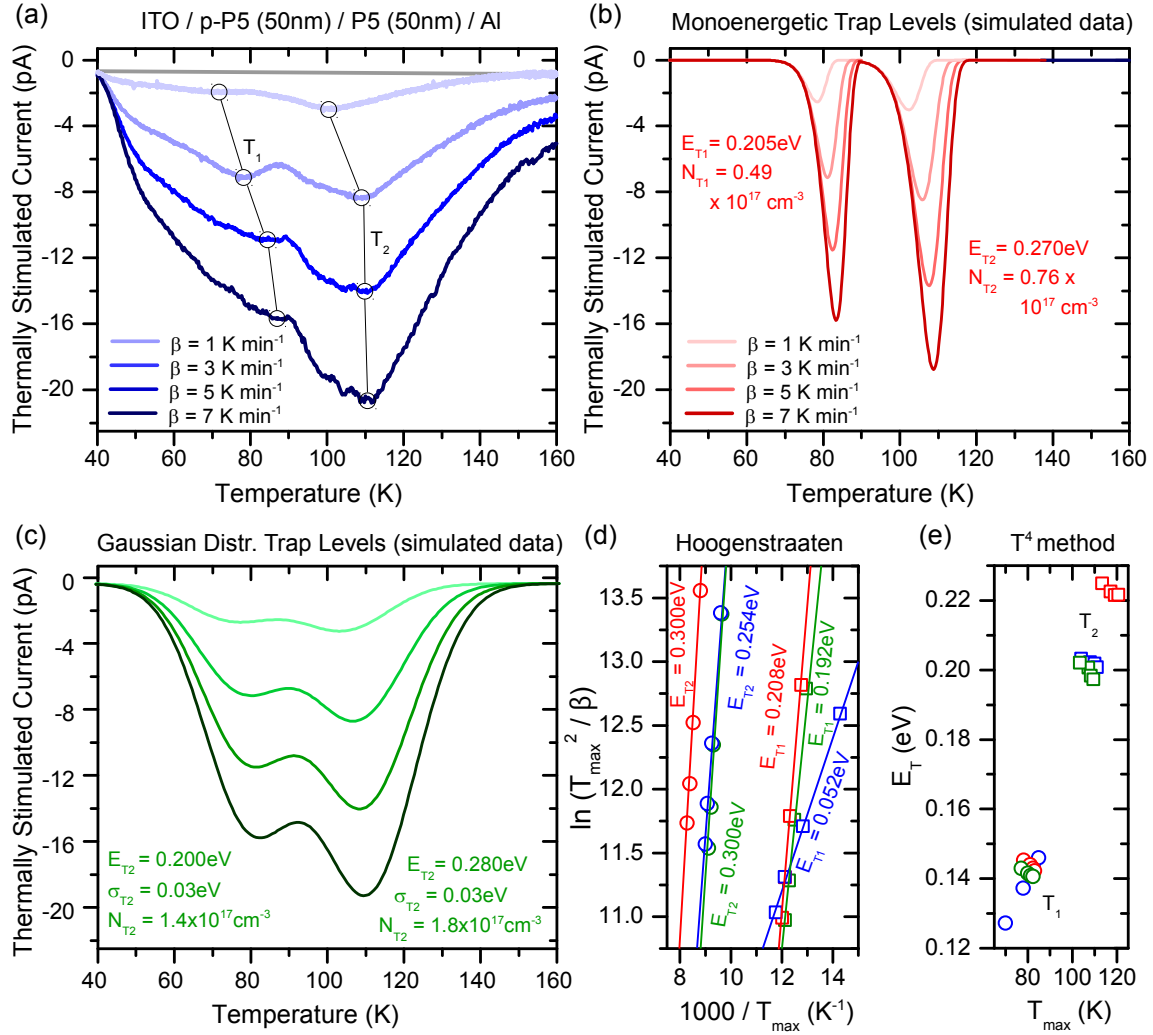


**Figure 7.1.:** (a) TSC spectra of an aged P5 Schottky diode for various linear heating rates  $\beta = 1 \dots 7 \text{ K min}^{-1}$ . Both TSC shoulder  $T_1$  and TSC peak  $T_2$  shift to higher temperatures when heating is faster. (b) Simulated TSC spectra employing different  $\beta$ , but only monoenergetic trap levels. (c) A better congruence between experiment and simulation is achieved when considering Gaussian distributed trap levels. (d) and (e) Examination of peak position versus heating speed  $\beta$  to check the reliability of the Hoogenstraaten- and  $T^4$ - method for the experimental TSC results (blue) and the simulated TSC from monoenergetic (red) and Gaussian distributed (green) trap levels  $T_1$  and  $T_2$ . All trap depths are relative to the hole transport level.

In the simulations, the shift of the features  $T_1$  and  $T_2$  towards lower temperatures for a lower heating speed  $\beta$  is reproduced. The trap site densities are  $N_{T1} = 0.49 \times 10^{17} \text{ cm}^{-3}$  and  $N_{T2} = 0.76 \times 10^{17} \text{ cm}^{-3}$ , which agrees with the TSC signal ratio of shoulder  $T_1$  to peak  $T_2$ . Their sum equals  $N_T \simeq 1.25 \times 10^{17} \text{ cm}^{-3}$  as obtained previously for Fig. 7.1 (a). The product  $\mu\tau = 4 \times 10^{-11} \text{ cm}^2 \text{ V}^{-1}$  is assumed to be temperature independent and accordingly scales the magnitude of the TSC spectra. However, the assumption of monoenergetic trap levels is physically unrealistic. It does not consider the DOS broadening by polarization effects generally

observed in organic semiconductors.<sup>[56,74,383]</sup> Consequently, the TSC features are sharp and steep, in strong contrast to the broad TSC features observed experimentally.

The agreement between simulation and experiment is greatly enhanced when assuming Gaussian distributed trap levels  $g(E)$ . Figure 7.1 (c) illustrates the TSC spectra resulting from

$$I(T) \propto \int_{-\infty}^{+\infty} dE g(E) \exp \left[ -\frac{E_T - E_{Tr}}{k_B T} - \frac{\nu}{\beta} \int_{T_0}^T \exp \left( -\frac{E_T - E_{Tr}}{k_B T'} \right) dT' \right]. \quad (4.60)$$

and Gaussian-type trap levels  $E_{T1} = 0.200$  eV and  $E_{T2} = 0.280$  eV (both with  $\sigma = \sigma_{T1} = \sigma_{T2} = 0.03$  eV and  $\nu = 10^{11} \text{ s}^{-1}$ ). The trapping site densities are  $N_{T1} = 0.55 \times 10^{17} \text{ cm}^{-3}$  and  $N_{T2} = 0.70 \times 10^{17} \text{ cm}^{-3}$ , and the product  $\mu\tau = 1.33 \times 10^{-10} \text{ cm}^2 \text{ V}^{-1}$ . Similar to Fig. 7.1 (a), the absolute TSC signal decreases for lower  $\beta$  and the features  $T_1$  and  $T_2$  shift to lower temperatures, as experimentally observed.

**Peak Position Methods.** Temperature shifts of TSC features with heating speed have been discussed in Sec. 4.3 to be decisive for the  $T^4$ - and the Hoogenstraaten approach towards  $E_T$ . Figure 7.1 (d) shows the plots of  $\ln T_{\max}^2/\beta$  versus  $1/T_{\max}$ . The slopes allow to determine  $E_T$  from<sup>[326,327]</sup>

$$\ln \left( \frac{T_{\max}^2}{\beta} \right) = \frac{E_T - E_{Tr}}{k_B T_{\max}} - \ln \left( \frac{E_T - E_{Tr}}{k_B \nu} \right). \quad (4.58)$$

In Fig. 7.1 (d), the results of the Hoogenstraaten method are compared for the measured and - serving as crosscheck - the simulated TSC data from Fig. 7.1 (a) to (c). The trap depths from the simulated TSC of the monoenergetic trap levels ( $E_{T1} = 0.208$  eV and  $E_{T2} = 0.300$  eV, red symbols) and the Gaussian distributed trap levels ( $E_{T1} = 0.192$  eV and  $E_{T2} = 0.300$  eV, green symbols) are exactly reproduced. In case of the measured P5 TSC spectra of Fig. 7.1 (a), the trap depths are found as  $E_{T1} = 0.052$  eV and  $E_{T2} = 0.254$  eV (blue symbols). Whereas the energetic depth  $E_{T2}$  revealed by the Hoogenstraaten method agrees with the predictive TSC spectra simulations fairly well, its accuracy seems to decrease for low trap energies. Signal shoulders as seen in Fig. 7.1 (a) are difficult to assess. At low heating rates  $\beta$ , they appear mostly flat, which increases the error on the feature temperature  $T_1$ . For intermediate heating rates, here at  $\beta = 3 \text{ K min}^{-1}$ , they can exhibit a peak. At high heating rates, signal shoulders tend to coincide with deeper lying trap features, i.e. here with  $T_2$ .

The trap depths  $E_{T1}$  and  $E_{T2}$  determined by the  $T^4$ -method are illustrated in Fig. 7.1 (e). The results are generally lower by 50 to 80 meV than those obtained via Hoogenstraaten method. Due to strong assumptions on  $\mu$ ,  $\tau$ , and  $\nu$ ,<sup>[312,330]</sup> the  $T^4$ -method is not considered any further in this thesis and shall not be used to examine TSC data for organic semiconductors.

**Chen's Method.** A different approach towards deriving the trap depth information from TSC spectra was suggested by Chen, who analyzed the symmetry of the spectral shapes.<sup>[320]</sup> His empirical studies led to the expression

$$E_T - E_{tr,h} = 2.8 k_B T_{\max}^2 / \alpha \quad (4.53)$$

with the form factors  $\omega = T_2 - T_1$  (i.e. the full width at half maximum of the TSC peak),  $\delta = T_2 - T_{\max}$ ,  $\tau = T_{\max} - T_1$ ,  $\alpha = \tau\omega/\delta$ , and  $\mu = \delta/\omega$ . Figure 7.2 illustrates the application of Chen's method to the data of Fig. 7.1. The monoenergetic trap exhibits a FWHM of  $\omega = 8.75$  K,  $\delta = 4.03$  K, and  $\tau = 4.72$  K. Following Eq. (4.53), this results in a trap depth  $E_T = 0.271$  eV, which is approx. identical to the initially assumed simulation parameter  $E_{T2} = 0.270$  eV. Another cross-check with Eq. (4.54) correctly yields the

utilized attempt-to-escape frequency  $\nu = 10^{11} \text{ s}^{-1}$ . However, in case of distributed trap levels, and thus broadened TSC spectra, Chen's method fails. Here, the extracted trap depth  $E_T = 0.098 \text{ eV}$  is far away from the initially assumed trap depth  $E_{T2} = 0.280 \text{ eV}$ . Therefore, the application of Eq. (4.53) to experimental TSC spectra of organic semiconductors is unreasonable. They are even more broadened, complex in shape, and hence not easily identified with a single peak shape, which further complicates symmetry examinations.

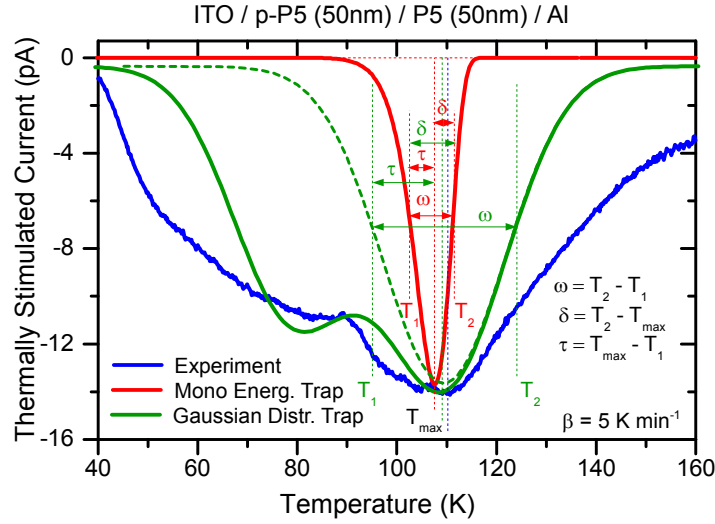


**Figure 7.2.:** Comparison of form factors  $\omega = T_2 - T_1$  (FWHM),  $\delta = T_2 - T_{\max}$ , and  $\tau = T_{\max} - T_1$  to examine the applicability of Chen's method. The data of Fig. 7.1 is re-arranged, i.e. showing the measured TSC spectrum of the aged P5 Schottky diode in blue for  $\beta = 5 \text{ K min}^{-1}$ . The simulated TSC spectra for a monoenergetic trap level ( $E_T = 0.270 \text{ eV}$ ) and Gaussian distributed trap levels ( $E_T = 0.280 \text{ eV}$ ,  $\sigma = 0.03 \text{ eV}$ ) are shown in red and green, respectively.

## 7.2. Dispersive Transport of Thermally Stimulated Currents

The previous section clarified that Chen's and the  $T^4$ -method are not adequate to examine typically broad thermally stimulated current spectra of organic semiconductors. The Hoogenstraaten method<sup>[326]</sup> and the trap spectra fitting after Haering/ Woods<sup>[310]</sup> and Garlick/Gibson<sup>[317]</sup> seemed to be appropriate candidates to resolve trap depth, density, and distribution from TSC spectra. However, they both share the assumption that charge carriers, once released from their initial trap states, travel with infinite speed towards the extracting electrode. This is in strong contradiction to the observed low charge carrier mobilities in disordered organic semiconductors, especially at low temperatures.<sup>[172,180,242,408]</sup> Here, a trap-controlled mobility has to be assumed.<sup>[168,409,410]</sup> The charge carriers travel only between multiple releases and re-trapping events, essentially slowing them down, and decreasing their mobility. Hence, the layer thickness of the organic semiconductor, or more exactly speaking the traveling distance of a released charge carrier, as well as the electric field and the mobility are likely to influence the TSC spectrum.

**Qualitative Description.** Figure 7.3 illustrates the situation for a sample temperature  $T'$  during the TSC run. Assuming a simplified trap distribution, the holes can interact here with trapping sites at energies  $E_{T1}$  to  $E_{T4}$  (from most shallow to deepest trap). Initially filled by holes prior to the TSC run, the traps emit holes when approaching their characteristic release temperature. In case of the most shallow trap energy  $E_{T1}$ , this refers to the temperature  $T_1$ . Released from a trap, the holes migrate assisted by the electric field  $F$



(built-in voltage + applied external voltage divided by the total sample thickness) towards the extracting electrode. The charge carrier movement is characterized by the mobility  $\mu(p, T, F)$  and hops occur in vicinity of the transport energy  $E_{Tr}(T)$ . Hence, a migrating hole exhibits an effective velocity  $v = \mu F$  in the organic semiconductor. Released at a spatial distance  $x_1$  from the contact, it reaches the extracting electrode after a traveling time  $t = x_1 / (\mu F)$ . Simultaneously, the sample temperature increases accordingly to the linear heating of the TSC run, i.e.

$$T(t) = \beta t + T_1. \quad (7.1)$$

The progressing heating causes the release of holes from energetically deeper trap levels, here  $E_{T2}$  and  $E_{T3}$  at temperatures  $T_2$  and  $T_3$ . Without any loss of generality, these release points can be situated closer towards the extracting electrode, e.g. at  $x_2$  and  $x_3$ . Hence, the emitted holes from both levels exhibit a (different and) shorter traveling distance to the electrode, as compared to the hole released earlier from  $E_{T1}$  at  $x_1$ . On the other hand, holes released at  $T_2$  and  $T_3$  face an altered energetic landscape on their way to the extraction (more shallow states are emptied). In case of a uniform trap distribution spread over the whole layer thickness of the organic semiconductor, a strong broadening of the corresponding TSC spectrum due to this type of dispersion is expected.

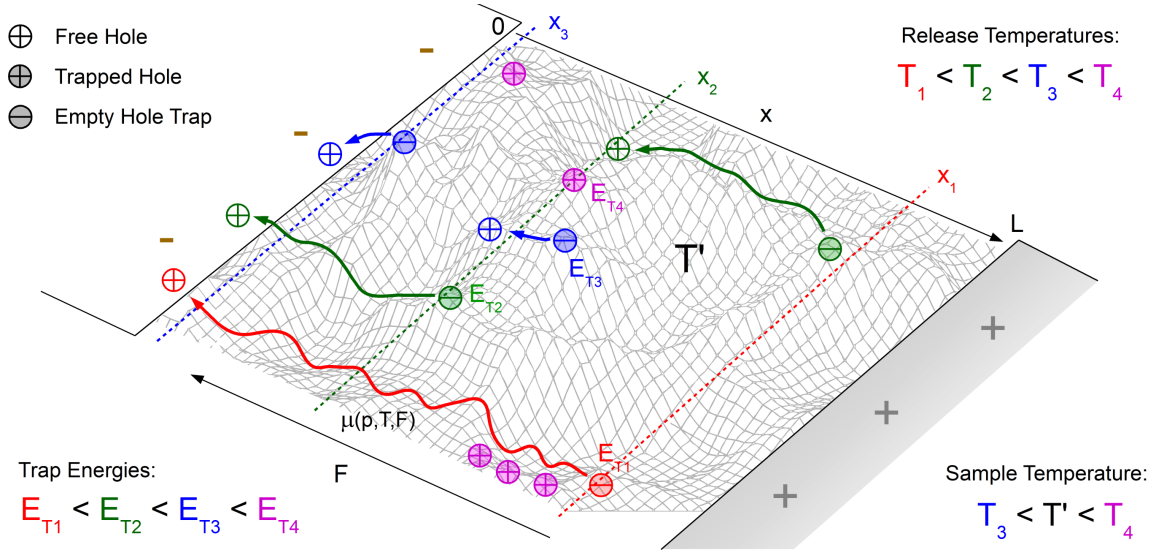


**Figure 7.3.:** Dispersive charge carrier transport in a disordered organic semiconductor of layer thickness  $L$  sandwiched between two electrodes. Holes initially trapped at energies  $E_{T1} > E_{T2} > E_{T3} > E_{T4}$  are released towards the transport level at their specific release temperatures  $T_1 < T_2 < T_3 < T_4$ . Motivated by an electric field  $F$ , they migrate with a mobility  $\mu(p, T, F)$  towards the extracting electrode (golden). In this picture, the sample temperature  $T'$  is below  $T_4$  but above  $T_3$ , i.e. traps at  $E_{T4}$  do not release charge carriers yet. The TSC detected at the electrode is a superposition of charge carriers released further away at lower temperatures and of those released closer to the contact at higher temperatures.

For sample geometries with multiple layers, released charge carriers originating from inner layers are delayed, thus revealing a deeper, i.e. false trap depth. In this context, Głowacki and Ulański compared the TSC spectra of 10...20  $\mu\text{m}$  thick PVK/PC<sup>1</sup> blends with thermally stimulated luminescence measurements.<sup>[411]</sup> Whereas the peak position for the latter remains unaffected, the peaks in the TSC spectra appeared at higher temperatures (up to 100 K more) and revealed a strong field dependence. For stronger electric extraction fields, the TSC spectra shifts to lower temperatures. Hence, the TSCs must be considered as combination of trap release and transport-peak phenomena, with an emphasis on charge carrier mobility similar to time-of-flight signals.<sup>[407,411]</sup>

<sup>1</sup>poly(N-vinylcarbazole)/polycarbona

**Physical Model.** Analytical solutions to dispersive TSCs were published by Arkhipov and Adriaenssens<sup>[409]</sup>, and later Nikitenko *et al.*<sup>[410]</sup>. The TSC depends on the charge carrier density  $p_c(x, t)$  in mobile states according to

$$I(t) = (eA\mu_c F/L) \int_0^L dx p_c(x, t) \quad (7.2)$$

for an organic semiconductor of film thickness  $L$ , sandwiched between two electrodes. Neglecting charge carrier diffusion and recombination, the charge carrier drift is governed by the continuity equation

$$\frac{\partial p(x, t)}{\partial t} + \mu_c F \frac{\partial p_c(x, t)}{\partial x} = 0 \quad (7.3)$$

with the charge carrier mobility  $\mu_c(p, F, T)$  and the electric field  $F$ . At an initial (and uniform) value of charge carrier density  $p_0 = p(x, 0) = \int dE \rho_0(E)$ , Eq. (7.3) is rewritten and yields the dispersive drift equation for the total charge carrier density

$$p(x, t) + \mu_c F \tau(t) \frac{\partial p(x, t)}{\partial x} = p_0. \quad (7.4)$$

Here, the function  $\tau(t)$  is the time-dependent lifetime of charge carriers at mobile states before capture by deep traps  $g(E)$  as

$$\tau(t) = \left[ \int_0^\infty dE g(E) W_d(E, t) \exp \left( -\nu(E) \int_0^t dt' \exp [-(E_T - E_{Tr})/kT(t')] \right) \right]^{-1}. \quad (7.5)$$

The product

$$W_d(E, t) = W_d(E, t_0) \exp \left( -\nu(E) \int_0^t dt' \exp [-(E_T - E_{Tr})/kT(t')] \right) \quad (7.6)$$

is the probability of a trap site to remain deep. Such deep traps do not release charge carriers captured until a distinct temperature is reached. Hence, deep traps lower the lifetime  $\tau(T)$  of holes in mobile states and thus also their effective drift mobility.  $W_d(E, t_0)$  is the same probability at time  $t_0$ , i.e. at the end of the initial isothermal filling and resting process step of the TSC. Since the preparation and the energy relaxation of charge carriers at prior times  $t < t_0$  are hardly assessable, Nikitenko *et al.* assumed<sup>[410]</sup>

$$W_d(E, t_0) = \begin{cases} 0, & E < E_{\min} \\ 1, & E > E_{\min} \end{cases} \quad (7.7)$$

including a distinct energy  $E_{\min}$ . With respect to the boundary conditions  $p_0 = p(x, 0)$  and  $p_c(x, 0) = 0$  and after changing the dependence from time to temperature according to Eq. (7.1), the solution of Eq. (7.4) reads<sup>[409]</sup>

$$\begin{aligned} I(T) &= (eA\mu_c F/L) \int_0^L dx p_c(x, T) \\ &= (eA\mu_c p_0 F \beta) \frac{d}{dT} \left( \tau(T) \left( 1 - \frac{p_d(T)}{p_0} \right) \right. \\ &\quad \left. \times \left[ 1 - \frac{\mu_c F \tau(T)}{L} \left( 1 - \exp \frac{-L}{\mu_c F \tau(T)} \right) \right] \right). \end{aligned} \quad (7.8)$$

Hereby, the function  $p_d(T)$  denotes the occupation of deep traps

$$p_d(T) = \int_0^\infty dE \rho_0(E) \exp\left(-\frac{\nu(E)}{\beta} \int_0^T dT' \exp[-(E_T - E_{Tr})/k_B T']\right). \quad (7.9)$$

TSC spectra ( $\beta = 5 \text{ Kmin}^{-1}$ ) calculated using Eq. (7.8) are presented in Fig. 7.4. A Gaussian distribution of traps with a trap depth of  $E_T = 0.1 \text{ eV}$  relative to the transport level, a width  $\sigma = 0.04 \text{ eV}$ , and a density of initially occupied states  $p_0 = 2 \times 10^{16} \text{ cm}^{-3}$  are assumed. In Fig. 7.4 (a), the extracting electric field is increased from  $1 \text{ MV/m}$  to  $9 \text{ MV/m}$  by enhancing the reverse readout voltages ( $V_{bi} + V_{bias} = -0.1 \dots -0.9 \text{ V}$ ) for an  $100 \text{ nm}$  thick organic thin-film. Consequently, the TSC peak shifts to lower temperatures for a fixed hole mobility  $\mu_c = 10^{-12} \text{ cm}^2 \text{ Vs}^{-1}$ . A similar trend is observed when the mobility  $\mu_c$  is increased in Fig. 7.4 (b) for a fixed readout voltage of  $-0.5 \text{ V}$ . Reducing the organic thin-film thickness from  $100 \text{ nm}$  to  $50 \text{ nm}$  further increases the extracting field (compare solid and dashed lines). Hence, TSC peaks appear at slightly lower temperatures and are approx. halved in intensity. Despite their peak temperature shifts with  $F$  and  $\mu_c$ , all equally thick organic layers release the same amount of net charge  $Q = 1.0 \text{ nC}$ , and all TSC spectra correctly yield the same  $p_0 = 2 \times 10^{16} \text{ cm}^{-3}$ .

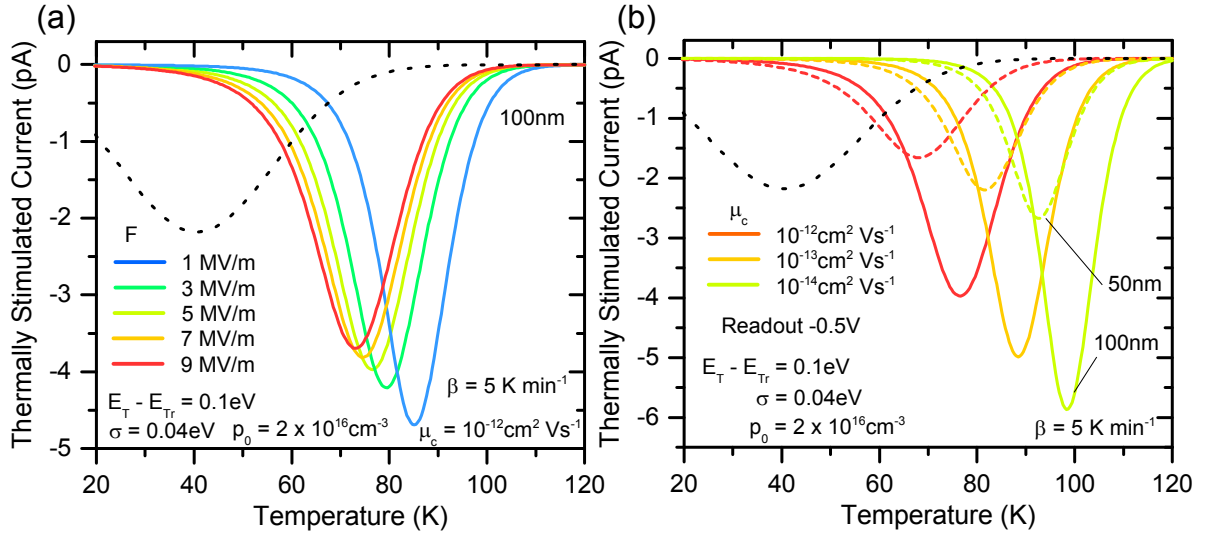


**Figure 7.4.:** TSC spectra regarding dispersive transport, computed from Eq. (7.8) for Gaussian distributed traps ( $E_T - E_{Tr} = 0.1 \text{ eV}$ ,  $\sigma = 0.04 \text{ eV}$ ,  $p_0 = 2 \times 10^{16} \text{ cm}^{-3}$ ), and a heating ramp  $\beta = 5 \text{ Kmin}^{-1}$ . **(a)** In a  $100 \text{ nm}$  thick organic semiconductor layer, the effective charge carrier mobility is assumed to be  $\mu_c = 10^{-12} \text{ cm}^2 \text{ Vs}^{-1}$ . An increase in the strength  $F$  of the extracting electric field shifts the TSC peak to lower temperatures. **(b)** For decreasing mobilities, the TSC (transport) peak appears at higher temperatures. Solid lines illustrate the TSCs for  $100 \text{ nm}$  ( $F = 5 \text{ MV/m}$ ), dashed lines for  $50 \text{ nm}$  ( $F = 10 \text{ MV/m}$ ) film thickness. For comparison, the solution of an entirely trap-release controlled TSC according to Eq. (4.60) is shown in both graphs in black dotted lines.

Interestingly, the electric field strength must be increased to  $F \geq 1 \text{ GV/m}$  at a mobility  $\mu_c = 10^{-12} \text{ cm}^2 \text{ Vs}^{-1}$  to match the TSC peak temperature calculated from Eq. (4.60) for an infinitely fast extraction of the released charge carriers (cf. black dotted lines in Fig. 7.4). At a readout voltage  $V = -0.5 \text{ V}$  (i.e.  $F = 5 \text{ MV/m}$ ), a mobility  $\mu_c \geq 10^{-9} \text{ cm}^2 \text{ Vs}^{-1}$  is required, respectively. Reviewing Eq. (7.8), this situation is described by the limiting case

$$\tau(t) \gg \frac{L}{2\mu_c F}, \quad (7.10)$$

where the lifetime of charge carriers in mobile states  $\tau(t)$  exceeds their mean traveling time towards the extracting electrode. The transient current is here controlled only by charge carrier release from initially filled traps only and reads

$$I(T) = -(eAL/2) \frac{d}{dT} p_d(T). \quad (7.11)$$

Combined with Eq. (7.9), Eq. (7.11) exhibits the same temperature dependence as the initial Eq. (4.60) and the extraction of charge carriers, once released, is not influenced by re-trapping.

**Experimental Results.** Figure 7.5 (a) illustrates TSC spectra in 100 nm MeO-TPD sandwiched between an ITO and an aluminum electrode. Usually, the readout voltage is close to 0 V, i.e. the built-in field is used to extract the released charge carriers. The latter is governed by the difference of the electrode work functions  $\phi$  and the interface dipoles  $\Delta$ , i.e. here  $V_{bi} \simeq \phi_{Al} - \phi_{ITO} + \Delta = -1.1$  eV.

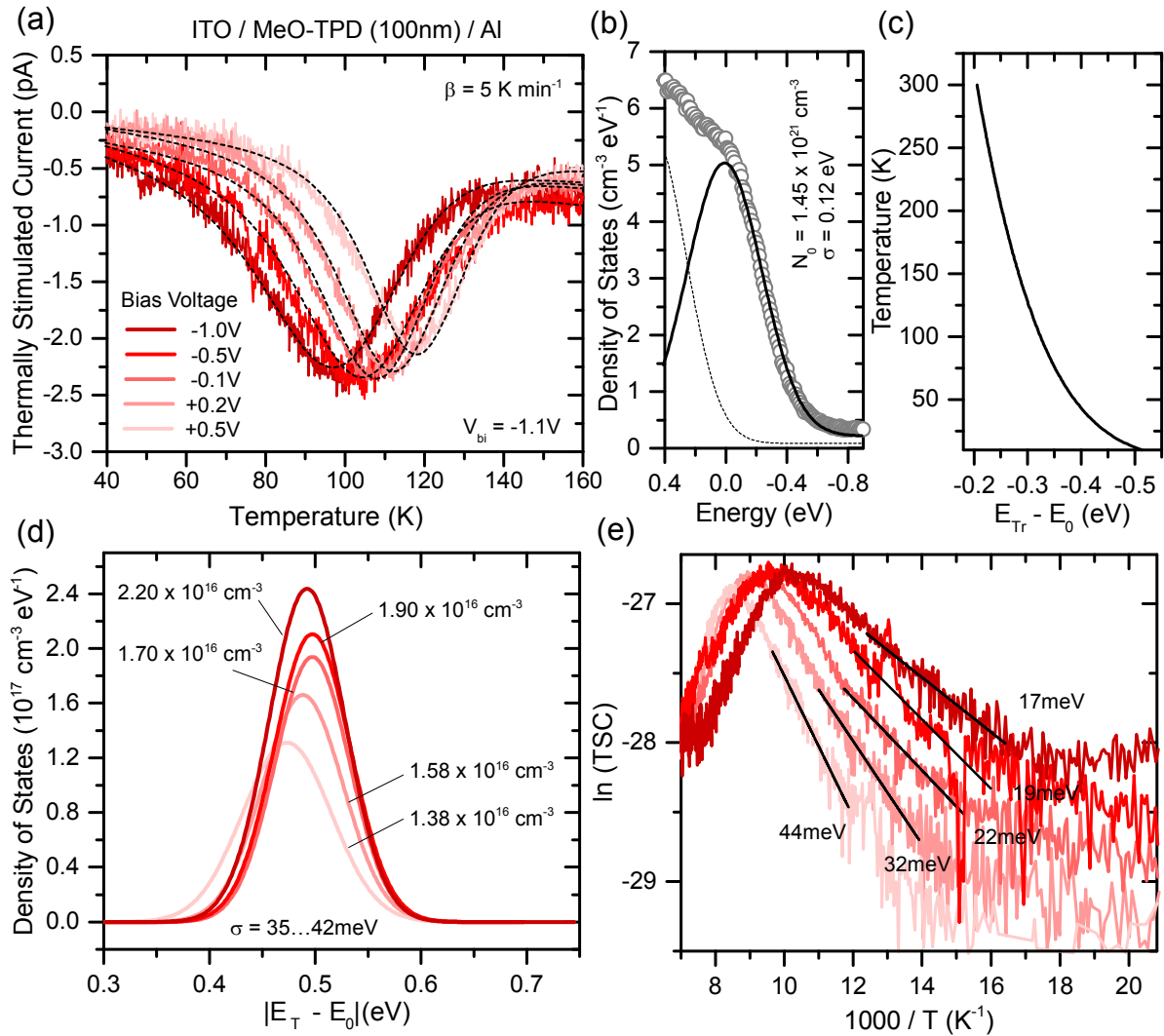


**Figure 7.5.:** (a) TSC spectra of an 100 nm MeO-TPD sandwich structure. Negative readout voltages add to the built-in voltage while positive ones partially compensate the inherent  $V_{bi}$ . Simulated TSC spectra regarding dispersive transport are shown in dashed lines. (b) Rescaled UPS spectrum (circles) and HOMO DOS fit (solid line) used to compute the (c) hole transport level  $E_{Tr}(T)$  in MeO-TPD. (d) DOS obtained at different read-out fields. (e) Initial rise examinations yield lower limits of the trap activation energies towards the transport level.

When applying reverse bias, the internal electric field increases and de-trapped holes speed up on their way to the collecting ITO electrode. Hence, the TSC peak appears already at lower temperatures (e.g. at  $T_{\max} = 96$  K for  $V_{\text{bias}} = -1.0$  V). Vice versa, the charge carriers slow down when a positive bias voltage is applied. The TSC peak moves to higher temperatures ( $T_{\max} = 119$  K at  $V_{\text{bias}} = +0.5$  V). In case of complete compensation of the built-in voltage, one would expect no charge carriers to be extracted anymore and therefore no TSC signal. However, this is not observed experimentally, since an elevated forward bias already causes injection of charge carriers from the ITO into the organic semiconductor. The resulting injection current superimposes the TSC. Thus, the extracted net charge decreases steadily with decreasing field strength from 0.85 nC at  $V_{\text{bias}} = -1.0$  V to 0.78 nC at  $V_{\text{bias}} = +0.1$  V and 0.71 nC at  $V_{\text{bias}} = +0.5$  V. The TSC spectra are fitted according to Eq. (7.8) (black dashed lines in Fig. 7.5 (a)), assuming a constant attempt-to-escape frequency  $\nu = 10^{11} \text{ s}^{-1}$ . The mobility is set independent of temperature to  $\mu_c = 4 \times 10^{-13} \text{ cm}^2 \text{ Vs}^{-1}$ .

In order to relate the trap energies to the HOMO center, the temperature dependent transport level position in MeO-TPD is considered (cf. Fig. 7.5 (c)). It has been previously calculated in Sec. 5.2 from the rescaled UPS HOMO DOS shown here in Fig. 7.5 (b). Regarding Eq. (7.7), the assumption

$$W_d(E, t_0, )|_T = \begin{cases} 0, & E \geq E_{\text{Tr}}(T) \\ 1, & E < E_{\text{Tr}}(T) \end{cases} \quad (7.12)$$

is reasonable, i.e. sites energetically closer to the HOMO center than the transport level  $E_{\text{Tr}}(T)$  at the distinct temperature  $T$  do not hinder the charge carrier migration. Sites at lower energies than  $E_{\text{Tr}}(T)$  are considered as deep states, lowering the lifetime  $\tau(T)$  of charge carriers in mobile states due to re-trapping.

The obtained densities of occupied gap states are presented in Fig. 7.5 (d). The trap distributions  $g(E)$  are found to be Gaussian-type with widths  $\sigma = 35 \dots 42$  meV, centered at 0.47...0.49 eV away from the HOMO center  $E_0$ . The fitted densities of initially filled traps  $p_0$  are on the order of  $1 \dots 2 \times 10^{16} \text{ cm}^{-3}$ , which is approximately doubling the amount of the extracted net charge in the TSC experiment. Three main reasons could explain, why the extracted charge carrier densities are generally lower than the initially assumed densities of occupied trap states. First, recombination is neglected in the model. Inherent minority charge carriers are able to recombine non-radiatively with holes prior to their extraction, especially when those are re-trapped in deep states. These recombining charges do not contribute to the TSC.<sup>[311]</sup> Furthermore, this consideration could explain the decrease in extracted net charge for decreasing extraction fields. The probability of a hole to recombine with an electron increases with its traveling time through the organic semiconductor. Second, charge carriers have been suspected to be electrostatically attracted to trap sites.<sup>[311,313]</sup> Werner *et al.* reported a Poole-Frenkel effect lowering the trap depth in TSCs of Alq<sub>3</sub>.<sup>[313]</sup> This observation can be interpreted as increased dissociation probability of trap-charge pairs. On the contrary, local electric fields of inherent (even deeper) traps could partially compensate the external electric field. As a consequence, such a field-assisted trap release becomes more improbable and the velocity of mobile charge carriers decreases. Third, the assumption of a constant mobility  $\mu_c$  disregarding its temperature dependence is a strong restraint. If the mobility is further reduced to  $\mu_c \simeq 10^{-15} \text{ cm}^2 \text{ Vs}^{-1}$ , the ratio of the extracted net charge and the charge initially occupying trap states approaches zero. The Gaussian distribution of trap sites must be widened and shifts to energies  $E_T - E_0 \sim 0.44$  eV. The latter is, however, in contradiction to the trap depth estimated from initial rise examinations on the TSC shown in Fig. 7.5 (e). The fits (black lines) yield an estimate for the lower limit of the trap site activation energies towards  $E_{\text{Tr}}(T)$  according to Eq. (4.49). They increase from  $\Delta E = 17$  meV for an external readout voltage of  $V_{\text{bias}} = -0.8$  V to  $\Delta E = 44$  meV for  $V_{\text{bias}} = +0.5$  V. Considering the transport level positions for MeO-TPD shown in Fig. 7.5 (c) (i.e.  $E_{\text{Tr}} - E_0 = 0.35 \dots 0.40$  eV

for  $T = 40...80$  K), the lower-limit estimates of the trap depth coincide at approx.  $E_T - E_0 \simeq 0.4$  eV. This is in fairly good agreement with the results obtained for the dispersive TSC model shown in Fig. 7.5 (d). In literature, the initial rise method is considered to be independent on the (re-) trapping kinetics,<sup>[318,322]</sup> since only a small temperature range at the beginning of the TSC peak is important. If the trap-containing thin-films are adjacent to the extracting electrode, a TSC signal is measured as soon as charge carriers are released.

### 7.3. Summary

Several ways to assess the trap information of organic semiconductors from TSC spectra have been discussed. In the first part of this chapter, TSC spectra of an aged pentacene Schottky diode were used as benchmark measurements. The spectra, each taken at a different TSC heating rate  $\beta$ , were typically broadened (approx. 100 K) and exhibited a signal shoulder and a signal peak. The characteristic temperatures  $T_{\max}$  of both features shifted to lower values for faster heating. TSC spectra simulations following the ansatz of Haering/Adams and Garlick/Gibson, i.e. assuming an immediate extraction of the trap-released charge carriers, reproduced the observed temperature shift. However, sharp signal peaks originating from monoenergetic trap levels only poorly matched the full experimental TSC signal. The agreement between simulation and experimental TSC spectra was significantly enhanced when Gaussian distributed trap levels were assumed ( $\sigma \sim 0.03...0.04$  eV). Furthermore, the capabilities of the  $T_{\max}$ -methods (Hoogenstraaten and  $T^4$ ) were analyzed. In case of clearly distinguishable signal peaks, the Hoogenstraaten method yields comparable results for simulated and experimental trap depths. Signal shoulders were hard to assess, i.e. showed a large error especially for low  $\beta$  and when overlapping with other peaks. The  $T^4$ - method had to be discarded due to its inherent and severe assumptions on the temperature dependence of mobility and attempt-to-escape frequency (originating from inorganic semiconductor physics), which caused large errors in  $E_T$ . The same applied to Chen's method of examining TSC peak symmetries, which was only valid in case of strictly monoenergetic trap levels.

In the second part of this chapter, a dispersive transport model for thermally stimulated currents reported earlier by Arkhipov/Adriaenssens and Nikitenko *et al.* was applied to TSC data for the intrinsic hole transporting material MeO-TPD. Here, the observed TSC peak around  $T_{\max} \simeq 100$  K shifted to lower temperatures for increasing readout voltages. The release of the initially stored charge carriers from trap sites was temperature-controlled. Motivated by the built-in field and an additional external electric field, the released holes performed an electric drift motion towards the extracting electrode. On their way, they were susceptible to re-trapping by sites at lower energies than the transport level. The re-trapping probability increased for thicker layers and lower charge carrier mobilities. For sufficiently large electric fields ( $F \geq 1$  GV/m) or mobilities ( $\mu_c \geq 10^{-9}$  cm<sup>2</sup>Vs<sup>-1</sup>), re-trapping becomes negligible and the results have been equal to the case of infinitely fast charge carrier extraction. For 100 nm thick MeO-TPD, Gaussian distributed traps ( $\sigma \simeq 0.04$  eV) were found at a depth  $E_T \simeq 0.5$  eV with respect to the HOMO center. The trap depth was found in accordance to lower level estimations from initial rise examinations on the TSC spectra. Populating a density of trap states  $p_0 = 2 \times 10^{16}$  cm<sup>-3</sup> prior the TSC run, only half of the charges were extracted and detected as current. Major reasons could be the recombination with minority charge carriers over deep states not considered here and/or too strong assumptions on the hole mobility ( $\mu_c = 10^{-12}$  cm<sup>2</sup>Vs<sup>-1</sup>, temperature independence), which were not included in the model. Since the extraction of trap-released charges in a TSC behaves similar to a time-of-flight experiment, such measurements are strongly suggested to reveal low-temperature mobility values of organic semiconductors. The benefit for the interpretation of TSC experiments would be tremendous. A possible approach is presented in Sec. 9.5.

# Doping Induced Gap States in Organic Neat and Blend Layers

*Shallow trap states are identified via the thermally stimulated current technique in organic semiconductor diodes containing p-doped Spiro-TTB. Layer thickness and dopant concentration of the p-Spiro-TTB are varied, which clearly assigns the observed TSC features to the doped bulk. The TSC spectra are fitted by the model of thermal release and dispersive transport of charge carriers, introduced in the previous chapter. It is suggested that the low-temperature mobility of thin-films governs the exact point in time, at which emitted charge carrier is extracted. Moreover, trap states are found in TSC spectra of p-doped ZnPc:C<sub>60</sub> 1:1 blend layers. UPS measurements indicate a significant energetic broadening of the HOMO DOS in the blend as compared to neat films. The trap states introduced by p-doping lay deeper in the gap than for p-Spiro-TTB and agree with results of impedance spectroscopy.*

## 8.1. Motivation

The examination of TSC spectra of intrinsic organic semiconductor thin-films is already complex.<sup>[312–314,409,410]</sup> Especially identification of absolute trap energies requires a significant effort in modeling and a number of assumptions, e.g. on the temperature dependent transport level<sup>[165,166]</sup> or the low-temperature mobility for the dispersive transport of released charge carriers<sup>[409,410]</sup> (cf. Ch. 7). Nevertheless, the accessible energy range of the organic semiconductor DOS, which is typically up to 1 eV away from the center towards mid-gap, encourages the application of TSC to current research topics.

When intermixing two different molecular species, Arkhipov *et al.* predicted already in 2005 a broadening of the intrinsic DOS.<sup>[277]</sup> In particular, this finding has become crucial for understanding charge carrier transport and its limitations in (ternary) blend bulk heterojunctions of today's organic solar cells.<sup>[109,412,413]</sup> By using TSC, Schafferhans and Domanski *et al.* reported for instance on broadened and overall increased trap densities in P3HT:PC<sub>61</sub>BM blends as compared to respective neat thin-films in 2011 and 2013.<sup>[46,312]</sup> For small molecule material combinations, we recently published first TSC spectra for ZnPc:C<sub>60</sub> blends.<sup>[40]</sup> The results are presented in Sec. 8.4. Trap data for state-of-the-art benchmark blends like DCV2-5T-Me<sup>3,3</sup>:C<sub>60</sub> are currently under investigation, however, a brief outlook is provided in Ch. 10.

Besides absorber blends, the precise working principle of molecular doping is still under debate. In contrast to the traditionally assumed integer charge transfer,<sup>[107,175]</sup> the group of Norbert Koch (Berlin, Germany) proposed a formation of hybrid states governing the charge transfer in various publications.<sup>[178,234,414]</sup> p-Doping of the host, i.e. the generation of a free hole, occurs after an electron from the host HOMO is promoted to the anti-bonding hybrid orbital (cf. Fig. 8.1). The energetic position of the hybrid levels depends on the specific host:dopant configuration, i.e. the host IP, the dopant EA, and their orientation towards each other. Calculations predict the anti-bonding hybrid orbital to be located in the energy gap of the host at the distance

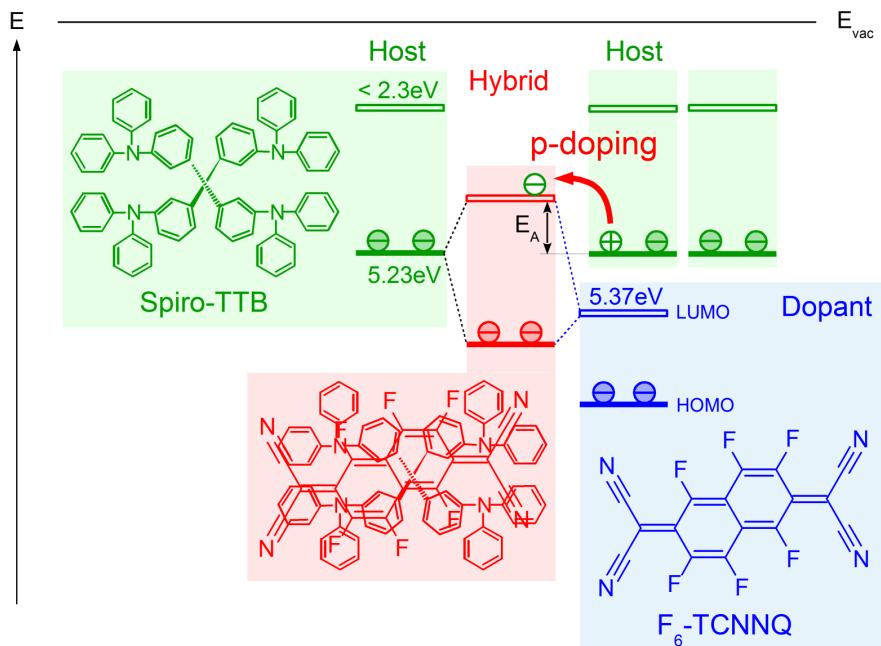


**Figure 8.1.:** Principle of molecular p-doping governed by hybrid formation.<sup>[178,183,234,414]</sup> Due to overlapping frontier orbitals, i.e. of the host HOMO (green, here Spiro-TTB) and the dopant LUMO (blue, here F<sub>6</sub>-TCNNQ), a bonding and an anti-bonding electronic hybrid orbital are established. In case of p-doping, an electron is transferred from the HOMO of another host to the unoccupied hybrid orbital to generate free charge carriers. The activation energy  $E_A$  of this process correlates with the energy splitting.

$E_A$  from the host HOMO. In case of P5:F<sub>4</sub>-TCNQ, Salzmann *et al.* found  $E_A = 0.6$  eV.<sup>[178]</sup> Similar results were published by Tietze *et al.*, who examined Fermi level shifts in host:dopant systems via UPS.<sup>[181,183,207]</sup> The generation of free holes is controlled by an acceptor level at the energy  $E_A$ . For P5:C<sub>60</sub>F<sub>36</sub>, they report  $E_A = 0.41$  eV with respect to the HOMO onset.<sup>[183]</sup> In case of MeO-TPD:C<sub>60</sub>F<sub>36</sub> and ZnPc:F<sub>6</sub>-TCNNQ, Tietze *et al.* found  $E_A = 0.46$  eV<sup>[181,207]</sup> and  $E_A = 0.27$  eV,<sup>[183]</sup> respectively. All those DOS energies are accessible via TSC. The samples examined in this thesis comprise the host material Spiro-TTB, which is trap-free in the relevant DOS range as shown in Sec. 8.2. Doped by F<sub>6</sub>-TCNNQ, it is a state-of-the-art HTL in OLEDs<sup>[355]</sup> and new perovskite-organic hybrid solar cells.<sup>[71]</sup> Spiro-TTB's chemical structure is similar to that of MeO-TPD. It is examined in sandwich devices and combined with different intrinsic hole transport materials to reduce the TSC leakage current. The results are discussed below in Sec. 8.2 and Sec. 8.3.

## 8.2. Doping Induced Gap States in Spiro-TTB

Figures 8.2, 8.3, and 8.4 summarize a series of measurements for p-Spiro-TTB combined with different HTL materials. The 50 nm thick Spiro-TTB layers are doped by 4 wt% (MR 0.126) of the p-dopant F<sub>6</sub>-TCNNQ. On top, either intrinsic ZnPc, P5, m-MTDATA, Spiro-TTB, NPB, MeO-TPD, or BF-DPB is deposited to a thickness of 100 nm. By default, the organic layers are sandwiched between aluminum electrodes.

**IV and Estimation of the Built-in Potentials.** The corresponding current-voltage characteristics, taken at room temperature, are shown in Fig. 8.2 (a). All structures exhibit diode-like IV curves with rectification ratios of up to 10<sup>6</sup> at  $\pm 1$  V. This asymmetry is ensured by p-doping of Spiro-TTB, which reduces the hole injection barrier at the adjacent Al electrode.



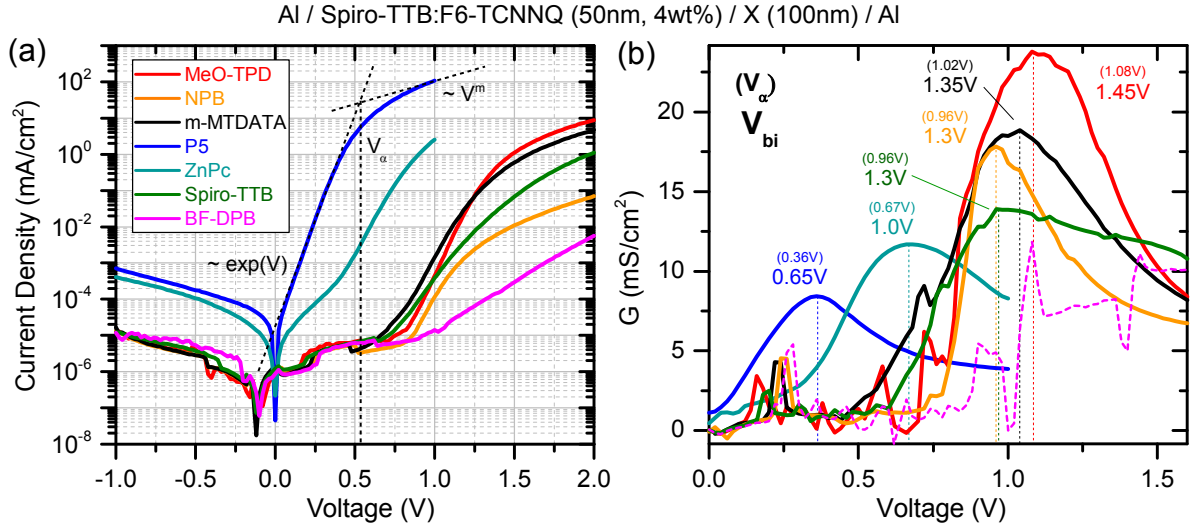


**Figure 8.2.:** (a) Current-voltage characteristics of TSC devices consisting of p-doped Spiro-TTB (50 nm, 4 wt% F<sub>6</sub>-TCNNQ) covered by various HTL materials and sandwiched between Al electrodes. The built-in voltages  $V_{bi}$  are determined approximately from transition points between the exponential and the polynomial regime (dashed lines). (b) For an alternative determination of  $V_{bi}$ , corresponding differential conductances  $G$  (cf. Eq. (8.1)) are plotted. The peak positions define the respective transition voltages  $V_{\alpha}$ , from which  $V_{bi}$  is approximated.<sup>[417]</sup>

When comparing the IV characteristics for the various cover HTLs, two differences are immanent. First, the magnitudes of both forward and reverse currents for P5 and ZnPc are at least two orders higher than for the remaining HTL materials. Despite the significantly smaller energy gaps of P5 (2.2 eV) and ZnPc (1.6 eV) as compared to e.g. NPB (3.1 eV) or MeO-TPD (3.2 eV), the differences in IV curves cannot be explained by higher thermally generated intrinsic charge densities.<sup>1</sup> More probable reasons are morphological differences, i.e. the crystallization grade of the thin-films, and possible impurity doping. Further, the reported hole mobilities are higher for P5 ( $10^{-1} \text{ cm}^2 \text{ Vs}^{-1}$ )<sup>[128,129]</sup> and ZnPc ( $10^{-3} \dots 10^{-4} \text{ cm}^2 \text{ Vs}^{-1}$ )<sup>[415]</sup> than those of NPB ( $10^{-4} \text{ cm}^2 \text{ Vs}^{-1}$ )<sup>[288]</sup> or MeO-TPD ( $10^{-5} \text{ cm}^2 \text{ Vs}^{-1}$ ).<sup>[240]</sup>

Second, the intersection between the exponential rise  $I \propto \exp(V)$  and the polynomial part  $I \propto V^m$  of the IV characteristics is influenced by the HTL choice. This transition point is commonly identified with the built-in potential of the diode.<sup>[114,305,416,417]</sup> Here, the built-in field is fully compensated by the external field and at higher voltages the IV curve is determined by trap-/space-charge limited mobility and ohmic resistance of the contacts. Since different tangents can be drawn at different points yielding different transition points, Mantri *et al.* suggested an alternative method to obtain  $V_{bi}$ .<sup>[417]</sup> They utilize the differential conductance function

$$G(V) = \frac{d \log I(V)}{d \log V} \quad (8.1)$$

which exhibits a well defined and sharp peak at the transition voltage  $V_{\alpha}$ . The transition voltage is correlated with the actual built-in voltage via  $V_{\alpha} \simeq 0.925 V_{bi} - 0.25$ .<sup>[417]</sup> As illustrated in Fig. 8.2 (b),  $V_{bi}$  is approx. 0.65 V for P5, around 1.0 V for ZnPc, and 1.3...1.45 V for m-MTDATA, NPB, MeO-TPD, and Spiro-TTB. These differences are most probably caused by interface dipole interactions  $\Delta$  between p-Spiro-TTB, the covering

<sup>1</sup>In a classical semiconductor with  $N_0 = 10^{21} \text{ cm}^{-3}$  and  $n_i = N_0 \times \exp(-E_g/2k_B T)$ , an intrinsic charge carrier density  $n_i \geq 10^{16} \text{ cm}^{-3}$  is thermally generated only for energy gaps  $E_g \leq 0.6 \text{ eV}$  at RT.

HTL, and the metal top contact (cf. Sec. 2.1.6).<sup>2</sup> For further work, UPS studies of the work function  $\phi$  and  $\Delta$  as well as  $C(V)$ -measurements to crosscheck  $V_{bi}$  are suggested.

In case of the p-Spiro-TTB/BF-DPB devices, the current density is only slowly rising with increasing voltage (cf. Fig. 8.2 (a): pink curve). Since the IP of BF-DPB was found at 5.38 eV on p-Spiro-TTB (IP = 5.11 eV), a significant hole transport barrier is expected at the internal interface between both materials.

**TSC Spectra of m-p-i-m Devices.** TSC spectra ( $\beta = 5 \text{ K min}^{-1}$ ) for the discussed devices are shown in Fig. 8.3. The TSC runs are performed starting at  $T_0 = 10 \text{ K}$  after an initial electrical filling ( $+5 \dots 15 \text{ V}$ ,  $\sim +10 \mu\text{A}$ ), to a maximum temperature of  $T = 200 \text{ K}$ . Without filling, no signal is detected. All samples share a relatively broad (approx. 60 K) TSC peak with an absolute signal height of at least 3 to 4 pA around 40 to 60 K. The corresponding trapping sites are suspected to be very shallow, i.e. close to the temperature dependent transport level position. Immediately after the measurement starts, charge carrier emission is detected ( $T < 20 \text{ K}$ ). Integration of the entire peaks yield a total extracted net charge of  $Q \simeq 2 \text{ nC}$ , which equals  $N_T \geq 4 \times 10^{16} \text{ cm}^{-3}$ . When intrinsic Spiro-TTB, NPB, or BF-DPB are utilized as cover HTLs (all IPs  $\geq 5.25 \text{ eV}$ , obtained in Sec. 5.1.2), no additional TSC features are observed up to  $T = 200 \text{ K}$ .

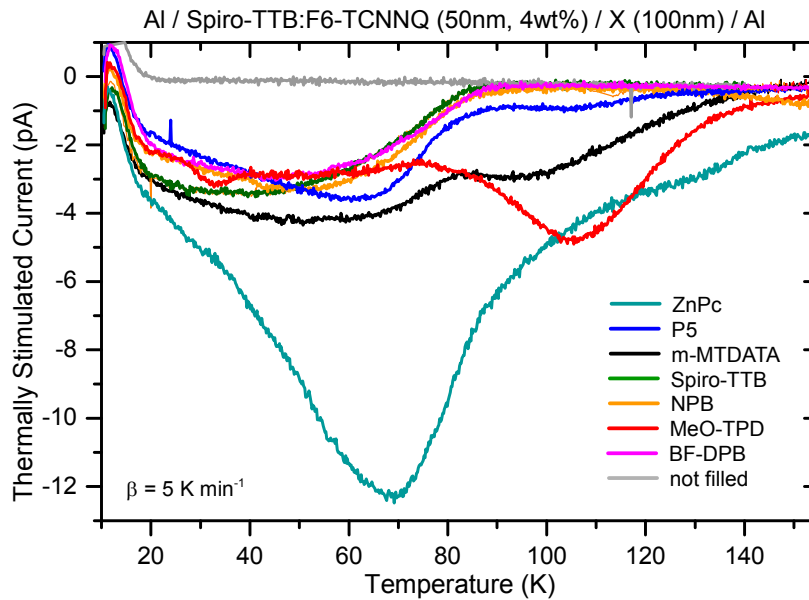


**Figure 8.3.:** TSC spectra of devices consisting of p-doped Spiro-TTB (50 nm, 4wt% F<sub>6</sub>-TCNNQ) with various HTL materials on top and sandwiched by aluminum electrodes ( $\beta = 5 \text{ K min}^{-1}$ ). Without an initial electrical filling, no significant TSC is recorded (gray line).

For P5, m-MTDATA, MeO-TPD, and ZnPc on top of the p-doped Spiro-TTB, the TSCs originating from the shallow states are superimposed by additional signals. In case of ZnPc, a huge TSC signal peaking at 70 K overlaps with the p-Spiro TSC spectrum. However, this is not that surprising as comparably large trap densities  $\sim 10^{18} \text{ cm}^{-3}$  were already found in ZnPc by UPS<sup>[183]</sup> and impedance spectroscopy (cf. Sec. 6). In case of P5 ( $T_{\text{max}} = 105 \text{ K}$ ), MeO-TPD (106 K), and m-MTDATA (98 K), smaller TSC peaks are visible. Interestingly, only HTL materials with IPs significantly smaller than 5.2 eV introduce additional TSC features. This observation is discussed more in detail in Ch. 9, in the context of oxygen and water related defects.

<sup>2</sup>An interesting observation was reported by Selina Olthof in case of lightly doped MeO-TPD (MR 0.05 of F<sub>4</sub>-TCNQ) and Ag contacts.<sup>[94]</sup> The work function of Ag changed from  $\phi = 4.2 \text{ eV}$  in bottom to  $\phi = 3.66 \text{ eV}$  in top contact configuration.

**Comparison to TSC Spectra of m-i-m Devices.** Figure 8.4 (a) shows a comparison of TSC spectra for 100 nm MeO-TPD (red) and m-MTDATA (black) with (thick lines) and without (thin lines) the 50 nm p-doped Spiro-TTB layer underneath. In presence of p-Spiro-TTB, the TSC spectra are identical to those in Fig. 8.3. Without p-Spiro-TTB, however, the broad TSC peaks around 40 K to 60 K are completely missing (cf. thin lines in Fig. 8.4 (a)). Only narrow peaks at higher temperatures are observed. These TSC peaks originate from the MeO-TPD and m-MTDATA HTLs. Interestingly, similar TSC features are found at almost identical temperatures in p-Spiro-TTB/HTL devices as well. In detail, MeO-TPD(100) shows a TSC peak at 106 K, which occurs at 107 K in p-Spiro-TTB(50)/MeO-TPD(100). For m-MTDATA(100) and p-Spiro-TTB(50)/m-MTDATA(100), TSC peaks are located at 101 K and 94 K, respectively. These findings are remarkable, as the additional 50 nm of p-Spiro-TTB would imply a longer pathway for released charge carriers on their way to the extracting ITO contact. Dispersive transport (cf. Sec. 7.2) implies an increased re-trapping probability, and thus a delayed TSC signal. Since the peak position, however, remains almost constant when an additional p-Spiro-TTB layer is inserted, three interpretations are conceivable.

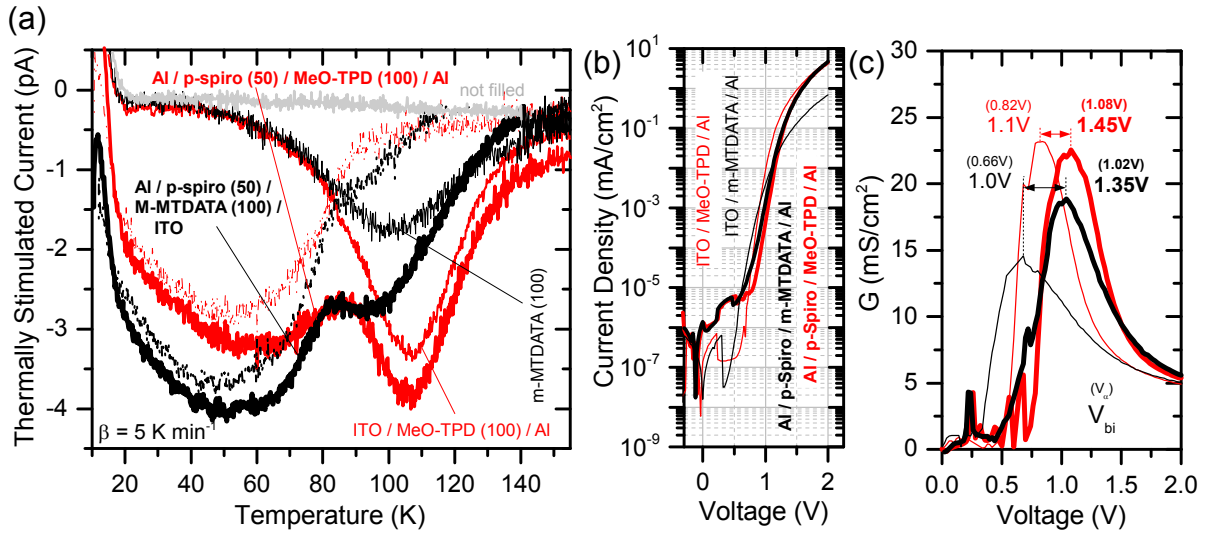


**Figure 8.4.:** (a) TSC spectra ( $\beta = 5 \text{ K min}^{-1}$ ) for 100 nm MeO-TPD (red) and m-MTDATA (black), grown on 50 nm p-Spiro-TTB (thick lines) or directly on the metal substrate (thin lines). Subtraction reveals the part of the TSC spectra originating from the p-doped Spiro-TTB layer (dashed lines). (b) IV curves of the devices at RT. (c) The differential conductance indicates small disparities in  $V_{bi}$  between devices of MeO-TPD (red) or m-MTDATA (black) w/ (thick lines) and w/o p-doped Spiro-TTB (thin lines).

First, the released charge carriers are minority carriers, i.e. electrons, and actually extracted towards the opposite contact. Hence, their extraction length would remain unchanged. At room temperature, the electric contacts are selective due to p-doping, i.e. the injection barrier for holes is way smaller than for electrons. At temperatures as low as 10 K, however, a strong freeze-out of the dopants is observed (cf. Sec. 6.3). Filling bias voltages of 10 V and above possibly compensate injection barriers and push electrons in the samples. Devices with p-Spiro-TTB exhibit a larger total layer thickness and hence a smaller overall electric field, which should delay the minority carrier extraction likewise. This is, however, not observed. Instead, TSC experiments in Sec. 9.5 unequivocally identified these gap states in MeO-TPD and m-MTDATA as hole traps. Second, the built-in field in the samples is affected, since the hole injecting contact is changed from Al/p-Spiro-TTB to pure ITO. Although the work functions of ITO and the doped layer ( $\phi = IP - HIB$ ) are equal at 4.7 eV at RT (cf. Sec. 5.1), possibly occurring interface dipoles  $\Delta$  with the adjacent HTL layer are not

negligible. Indications are indeed provided by the current-voltage characteristics at RT, shown in Fig. 8.4 (b) and (c). The determined built-in potential increases by approx. 0.3 eV at RT when ITO is substituted by Al/p-Spiro-TTB. Besides, the temperature dependence of  $V_{bi}$  has been neglected so far, which requires further research. The higher electric field can compensate the longer extraction pathway, explaining similar peak positions.

Third, the mobility of Spiro-TTB is greatly enhanced by doping, although parts of the dopants are still inactive due to the low sample temperatures. As discussed previously in Sec. 7.3,  $\mu(T)$ -measurements are strongly suggested to clarify this possibility.

Finally, the TSC spectra of the single cover HTLs MeO-TPD and m-MTDATA are subtracted from that of the p-Spiro-TTB/HTL devices. The results are depicted in Fig. 8.4 (a) by dotted lines. In both cases, the same shallow TSC peak between 20 and 80 K discussed earlier remains. It peaks with  $-3$  to  $-4$  pA. This trap signal is clearly attributed to the presence of the doped p-Spiro-TTB layer. In order to exclude an interface origin of the trap signal, layer thickness and doping concentration of the HTL are varied in the following. The p-Spiro-TTB is paired with an 100 nm intrinsic Spiro-TTB cover HTL, which does not contribute any additional TSC signal for temperatures  $T < 200$  K (cf. Fig. 8.3). Recorded thermally stimulated currents hence originate from the doped HTL exclusively.

### 8.3. Dependence on Layer Thickness and Doping Concentration

**Built-in Potentials and Hole Transport Levels.** Figure 8.5 (a) illustrates the current-voltage characteristics of various TSC sandwich samples. The F<sub>6</sub>-TCNNQ p-doped Spiro-TTB layer is varied in thickness in-between 0...50 nm and doping concentration by 1...8 wt% (MR 0.031...0.263). It is remarkable that the built-in potential is almost constant at  $V_{bi} = 1.2...1.3$  V (cf. Fig. 8.5 (b)). Even when the p-doped layer is completely omitted,  $V_{bi}$  remains unchanged for ITO/Spiro-TTB(100 nm)/Al (black line).

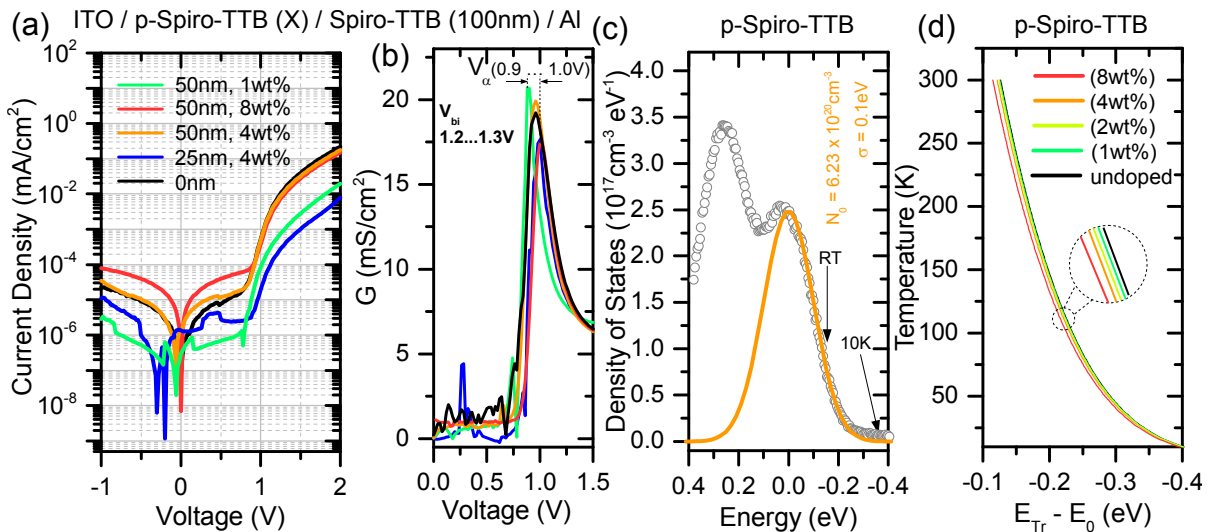


**Figure 8.5.:** (a) Current-voltage characteristics of various TSC sandwich devices at RT. Film thickness and doping concentration of the F<sub>6</sub>-TCNNQ doped Spiro-TTB are varied. (b) Plotting the differential conductance  $G(V)$  reveals that the built-in potential remains at  $V_{bi} = 1.2...1.3$  V. (c) Rescaled UPS spectrum (gray circles) and HOMO DOS fit (pink line) used to determine the (d) hole transport level  $E_{Tr}(T)$  in p-Spiro-TTB as discussed in Sec. 5.2. Black arrows indicate  $E_{Tr}(RT)$  and  $E_{Tr}(10K)$ .

In order to conclude on trap energies from the TSC spectra, the temperature dependent transport level in p-Spiro-TTB has to be considered. Figure 8.5 (c) shows the HOMO DOS of p-Spiro-TTB doped by 4 wt% F<sub>6</sub>-TCNNQ (MR0.126), which has been obtained via UPS in Sec. 5.1. It is rescaled to compensate the UPS signal broadening as discussed in Sec. 5.1.6 (cf. Tab. 5.1). The Gaussian width  $\sigma = 0.1$  eV was found earlier, coinciding with the value for intrinsic Spiro-TTB on p-Spiro-TTB (cf. Tab. 5.4). Differences in the DOS widths for varying doping concentrations could not be resolved. Hence,  $\sigma = 0.1$  eV is assumed for all MR. The host site density is taken accordingly to the dopant molar ratio, i.e.  $N_0 = 6.23 \times 10^{20} \text{ cm}^{-3}$  for MR0.126. In case of undoped,  $N_0$  equals the mole density of Spiro-TTB, which is  $N_0 = 7.13 \times 10^{20} \text{ cm}^{-3}$ . Calculated from Eq. (5.7), the hole transport level positions are plotted versus the sample temperature in Fig. 8.5 (d). At all temperatures, the differences of  $E_{Tr}$  for all considered doping concentrations are found to be below 10 meV.

**Influence of the Layer Thickness.** Figure 8.6 (a) compares fractional TSC measurements ( $\beta = 5 \text{ Kmin}^{-1}$ ) of devices, where the thickness of the p-doped Spiro-TTB (4 wt% F<sub>6</sub>-TCNNQ) layer is 25 nm (blue) or 50 nm (green), respectively. For both cases, 100 nm intrinsic Spiro-TTB are utilized as cover HTL. The TSC spectra exhibit the same broad signal peak centered at approx. 40 K like the samples discussed earlier in Sec. 8.2. Here, the absolute signal height is 4.5 pA for 50 nm and 2.25 pA for 25 nm p-Spiro-TTB, which is exactly the half. Furthermore, the TSC signal for 50 nm is twice that of 25 nm p-Spiro-TTB, not only at the peak center, but even for the whole peak distribution between 20 K and 80 K (cf. dark blue and dark green lines in Fig. 8.6 (a)). This fact strongly indicates that the TSC response is a bulk feature of the p-doped Spiro-TTB layer and not related to interface states. The integration of both spectra yield  $N_T = 4.6 \times 10^{16} \text{ cm}^{-3}$  (25 nm) and  $N_T = 4.8 \times 10^{16} \text{ cm}^{-3}$  (50 nm). The small deviation is due to doping concentration variance during device preparation.

For fractional TSC, the stop temperature is varied within 20...70 K in steps of 10 K. By emptying the traps up to  $T_{\text{stop}}$  and performing another TSC run without prior filling, the density distribution of occupied trap states is profiled. The obtained fractional TSC spectra are illustrated in Fig. 8.6 (a) for 25 nm and 50 nm in blue and green color gradients, respectively. Without any filling, or equally  $T_{\text{stop}} > 80 \text{ K}$ , no thermally stimulated currents are observed (gray lines).

The initial rise of each fractional TSC spectrum is analyzed according to Eq. (4.49) for a lower-limit estimate of the trap depth. The results are shown in Fig. 8.6 (b) in blue for 25 nm p-Spiro-TTB and green colors for 50 nm. The corresponding linear fits are depicted in red lines. For the lowest stopping temperatures, the activation energies  $\Delta E$  of the TSC are remarkably small, e.g. 8.5 meV (25 nm p-Spiro-TTB) and 11.0 meV (50 nm p-Spiro-TTB) at  $T_{\text{stop}} = 20 \text{ K}$ . The activation energies of the envelope TSC spectra (darkest blue and green lines) are  $\Delta E = 2.3 \text{ meV}$  and  $\Delta E = 6.5 \text{ meV}$ , thus even smaller. This means that the releasing trap sites at such low temperatures are very shallow, i.e. energetically close to the transport level. At higher stopping temperatures,  $\Delta E$  increases to values as high as 33.6 meV (25 nm) and 49.7 meV (50 nm) at  $T_{\text{stop}} = 60 \text{ K}$ . Above, at  $T_{\text{stop}} = 70 \text{ K}$ , the slight decrease of  $\Delta E$  is attributed to the reduced signal-to-noise ratio as a consequence of the low number of initially filled trap sites. Overall, the obtained activation energies are slightly lower for devices with 25 nm p-Spiro-TTB than for those with 50 nm. Since the built-in field is expected to be larger in the former, field-induced trap release<sup>[313]</sup> could explain this result.

The extracted trap DOS distributions are plotted in Fig. 8.6 (c). Hereby, all fractional TSC spectra are integrated and subtracted accordingly. The previously fitted activation energy  $\Delta E$  of each slice is added to the transport level position at the respective stop temperatures (cf. Fig. 8.5 (c)). This sum is the trap energy

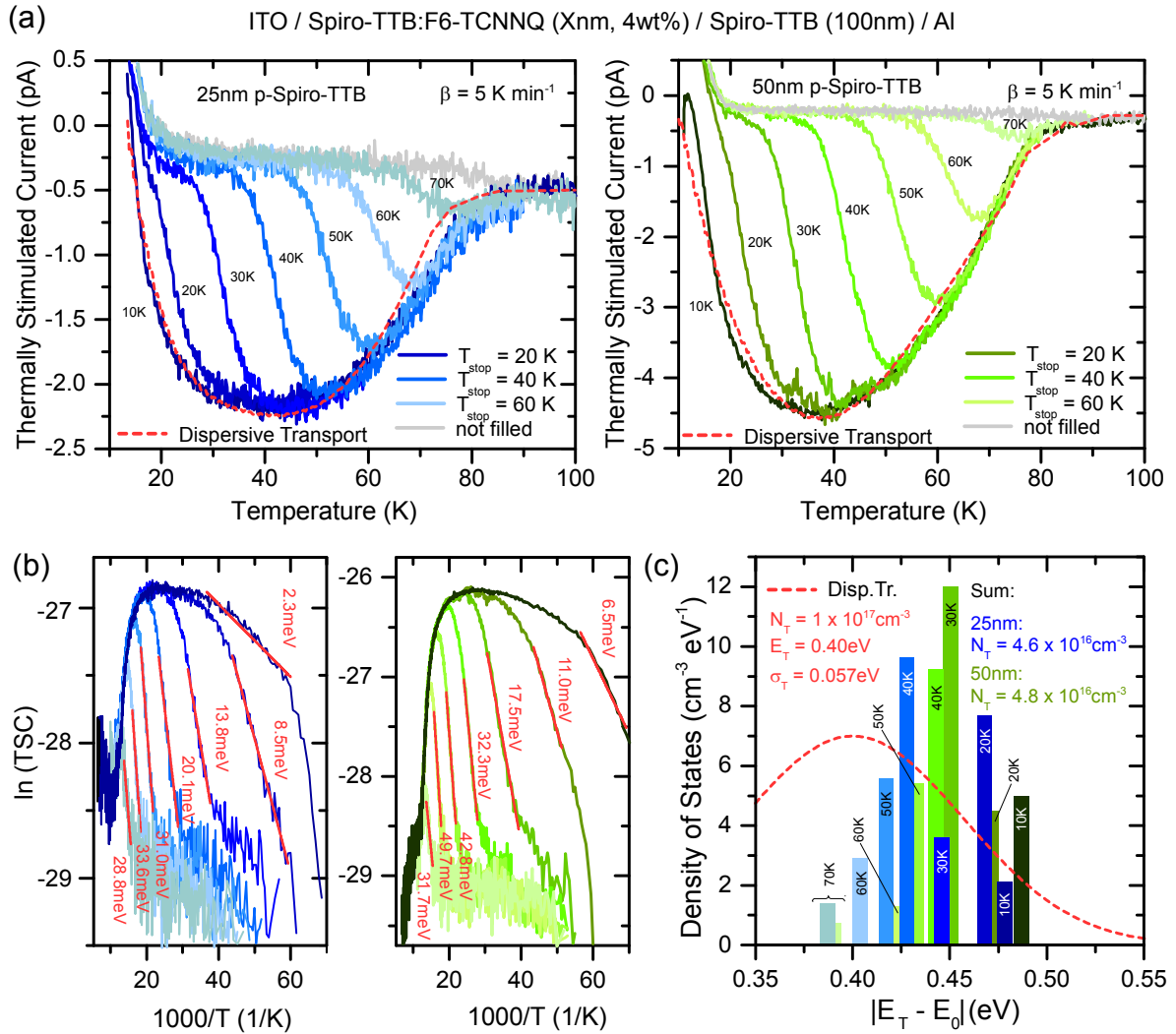


**Figure 8.6.:** (a) Fractional TSC spectra of Spiro-TTB p-doped by 4 wt% (MR 0.126) F<sub>6</sub>-TCNNQ for layer thicknesses of 25 nm (left) and 50 nm (right) at a linear heating rate  $\beta = 5 \text{ K min}^{-1}$  and pre-release temperatures  $T_{\text{stop}} = [20...70] \text{ K}$ . TSC runs without an initial filling procedure are presented in gray lines. The TSC peaks are simulated considering temperature dependent trap release and dispersive charge carrier transport (red dashed lines). The density distributions of occupied gap states are compared in (c) with results from initial rise examinations in (b). The trap depths are related to the Spiro-TTB HOMO center at  $E_0$ .

regarding the HOMO center of Spiro-TTB. For both samples, an in first-order Gaussian trap distribution centered at approx. 0.45 eV is found. Its smoothness could be, in principle, improved by shrinking the fractional TSC  $T_{\text{stop}}$  intervals from 10 K to 5 K.<sup>3</sup> The sums of all DOS slices are  $4.6 \times 10^{16} \text{ cm}^{-3}$  (25 nm) and  $4.8 \times 10^{16} \text{ cm}^{-3}$  (50 nm), which are the same as the integration results of the envelope TSC spectra (dark blue and dark green in Fig. 8.6 (a)). For the smaller layer thickness (25 nm) of p-Spiro-TTB, the trap distribution is located at slightly lower energies. Interestingly, the most shallow traps at approx.  $|E_T - E_0| = 0.38 \text{ eV}$  (light blue and light green bar) are determined from the fractional TSC measurements with the highest stop temperature ( $T_{\text{stop}} = 70 \text{ K}$ ). This is in contradiction to the steady increase of the activation energy from the initial rise examinations. The inconsistency might be due to an overestimate of the scaling of the transport

<sup>3</sup>This, however, would increase the required total TSC measurement time for a single sample from approx. 24 h to 48 h, which is not desirable.

level position with temperature. From the start of the TSC at  $T_0 = 10$  K to  $T = 50$  K, a strong shift of up to 100 meV is found (cf. Fig. 8.5 (d)). A re-adjustment of the transport level model in the limit of  $T \rightarrow 0$ , e.g. considering the temperature dependence of the inverse localization radius  $\gamma$ ,<sup>[418,419]</sup> could solve this inconsistency. However, this is beyond the scope of this thesis. In either case, the obtained trap depth span is well below typical DOS (trap) widths  $\sigma \simeq 50\text{...}100$  meV.<sup>[39,44,54,180,181,383]</sup>

Considering dispersive transport into the modeling of thermally stimulated currents (cf. Sec. 7.2), the results according to Eq. (7.8) are depicted in Fig. 8.6 in red dashed lines. Gaussian distributed trap centers ( $\sigma_T = 0.057$  eV) located at  $E_T = 0.40$  eV from the Spiro-TTB HOMO center towards gap-mid are found. The attempt-to-escape frequency  $\nu = 10^{11} \text{ s}^{-1}$  and the charge carrier mobility upon extraction  $\mu = 10^{-12} \text{ cm}^2 \text{ Vs}^{-1}$  are assumed constant. Here, the trap density is found to  $N_T = 1 \times 10^{17} \text{ cm}^{-3}$  for both layer thicknesses. However, this value is twice the trap density obtained by integration of the TSC spectra ( $4.6\text{...}4.8 \times 10^{16} \text{ cm}^{-3}$ ). Recombination losses as discussed earlier in Sec. 7 seem unreasonable in p-doped layers. The immediate release of trapped charge carriers at  $T \rightarrow 0$  indicates shallow traps close to the transport level. Here, the natural conclusion is that only half of the traps, i.e. those at lower energies than the transport level, have initially been filled. It is hence not surprising that only the lower energy flank of the Gaussian distributed trap DOS (red dashed line) matches with the results of the initial rise examinations (cf. Fig. 8.6 (c)).

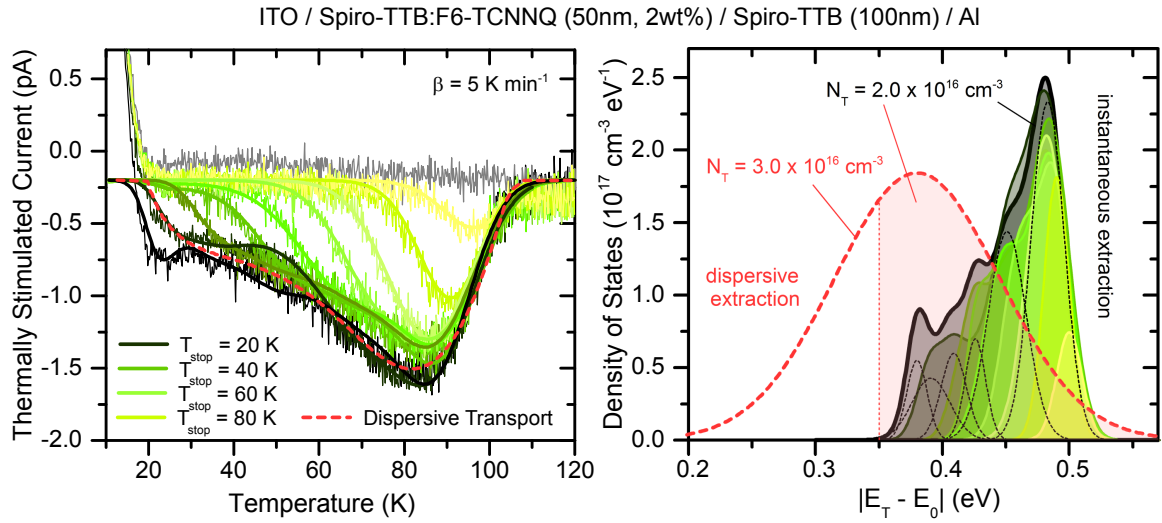
**Instant Extraction vs. Dispersive Transport.** As concluded in Sec. 7.2 from field-dependent experiments, dispersive transport with multiple re-trapping and release events governs the occurrence of the TSC in organic thin-films. Revisiting this debate suggests that besides the trap depth  $E_T$ , not only the electric extraction field, but also the charge carrier mobility determine when the TSC is detected.

Figure 8.7 (a) shows the (fractional) TSC spectra ( $\beta = 5 \text{ Kmin}^{-1}$ ) of 50 nm p-Spiro-TTB in combination with 100 nm intrinsic Spiro-TTB, sandwiched between ITO and aluminum. The doping concentration is 2 wt% F<sub>6</sub>-TCNNQ (MR 0.062). Remarkably, the TSC peak position shifts to 80...90 K (as compared to approx. 40 K for 4 wt% F<sub>6</sub>-TCNNQ), while the entire peak exhibits a strong asymmetry. Fractional TSC measurements for stop temperatures  $T_{\text{stop}} = 20\text{...}90$  K in steps of 10 K are shown in green gradient colors in Fig. 8.7 (a). Without any electrical filling, no signal is obtained (gray line).

In the limit of an instantaneous extraction of the released charge carriers ( $F$  or  $\mu$ , or both  $\rightarrow \infty$ ), the distribution of initially filled trap states is computed from Eq. (4.50) and given as respective colored solid lines. Figure 8.7 (b) illustrates the obtained DOS curves. Reproducing the TSC signals, which are very complex in shape up to  $T_{\text{stop}} = 60$  K, is only possible if a number of Gaussians are superimposed (black dashed lines). Their sums are projections of the corresponding fractional TSC spectra from the temperature to the energy scale. With respect to  $E_{\text{Tr}}(T)$  in Fig. 8.5 (d), the DOS maximum is found around  $|E_{T,\text{inst}} - E_0| = 0.49$  eV. The overall trap density is  $N_{T,\text{inst}} = 2.0 \times 10^{16} \text{ cm}^{-3}$ . Modeling the full TSC spectra in Fig. 8.7 (a) (black line) requires the assumption of no less than six Gaussian distributions for the DOS ( $\sigma = 8\text{...}15$  meV), which appears rather arbitrary.

However, taking into account the mechanism of dispersive transport for released charge carriers solves this problem. Here, a single Gaussian distribution of trapping sites ( $\sigma = 65$  meV,  $N_{T,\text{disp}} = 3.0 \times 10^{16} \text{ cm}^{-3}$ ) is sufficient to describe the obtained TSC. Again,  $\nu = 10^{11} \text{ s}^{-1}$  is assumed to be temperature-independent, the mobility of released charge carriers is reduced to  $\mu = 10^{-13} \text{ cm}^2 \text{ Vs}^{-1}$ . The TSC spectrum calculated from Eq. (7.8) and the obtained trap DOS are drawn as red dashed lines in Fig. 8.7 (a) and (b), respectively. In contrast to the limit of immediate extraction, the trap centers are found at shallower energies  $|E_{T,\text{disp}} - E_0| = 0.38$  eV when dispersive transport is assumed. In other words, the charge carriers are released





**Figure 8.7.:** (a) TSC spectrum of p-Spiro-TTB (50 nm, 2 wt% F<sub>6</sub>-TCNNQ) with 100 nm intrinsic Spiro-TTB ( $\beta = 5 \text{ K min}^{-1}$ ) (black). The fractional TSCs with  $T_{\text{stop}} = 20 \dots 90 \text{ K}$  are shown in gradient colors, while the experiment without prior trap filling is depicted in gray. Simulated TSCs in the limit of instant extraction are added as solid lines. The TSC simulated for temperature dependent charge carrier release and dispersive transport is shown as red dashed line. (b) Densities of occupied gap states in case of solely release-controlled TSC (gray to green according to  $T_{\text{stop}}$ ) and dispersive TSC transport model (red dashed line).

at lower temperatures, but they are delayed on their extraction. Integration of the DOS for dispersive transport (red in Fig. 8.7 (b)) up to the point where it starts in the limit of instant extraction, i.e.  $-0.35 \text{ eV}$  yields  $N'_T = 2.0 \times 10^{16} \text{ cm}^{-3}$ . This result is remarkable since it equals the trap density  $N_{T,\text{inst}}$  found previously. This finding provides another indication that recorded TSC spectra from organic semiconductors are a signal convolution of their filled trap DOS and a transport function  $\Theta$ .

**Influence of Doping Concentration.** Interestingly, the found trap depth  $|E_T - E_0| = 0.38 \text{ eV}$  is not affected by a change of the doping concentration from 4 wt% to 2 wt%. Less extrinsic F<sub>6</sub>-TCNNQ molecules in the amorphous Spiro-TTB host layer cause only a decrease of trap site density. The obvious peak temperature shift is most likely a transport phenomenon, which will fall into place when the MR is further varied. Figure 8.8 (a) shows TSC spectra for various doping concentrations 0...8 wt% of F<sub>6</sub>-TCNNQ (MR 0...0.263) in the 50 nm p-Spiro-TTB layer. All other sample stack parameters remain unchanged as compared to before. No TSC is recorded in case of undoped Spiro-TTB, which is consistent with the findings of Fig. 8.4. At 1 wt% F<sub>6</sub>-TCNNQ (MR 0.263), a strong asymmetric TSC spectrum with a peak at 98 K is observed. By increasing the dopant MR, the maximum peak position is shifted towards lower temperatures (84 K for 2 wt% and 40 K for 4 wt%). Eventually, it reaches  $T_{\text{max}} = 29 \text{ K}$  in 8 wt% Spiro-TTB:F<sub>6</sub>-TCNNQ. Here, the TSC spectral shape is almost symmetric. It is worth notable that already a significant current of 3 pA is flowing out of the device at the start  $T_0 = 10 \text{ K}$ . The activation energy is  $\Delta E \simeq 0$ , i.e. charge carriers are present near the transport level already at the beginning of the TSC run.

All TSC spectra are fitted (black dashed lines) according to the dispersive transport model by Eq. (7.8), considering the temperature dependent transport levels from Fig. 8.5 (d). The obtained DOS functions are illustrated in Fig. 8.8 (b). They are found as single Gaussian distributions ( $\sigma = 55 \dots 65 \text{ meV}$ ) centered at approx. 0.40 eV away from the HOMO center towards mid-gap. The trap density  $N_T$  increases with rising doping concentration from  $1.9 \times 10^{16} \text{ cm}^{-3}$  (1 wt%) and  $3.0 \times 10^{16} \text{ cm}^{-3}$  (2 wt%) to  $1.0 \dots 1.1 \times 10^{17} \text{ cm}^{-3}$



for 4...8 wt%. In the latter case, most likely not all trap states are filled at the beginning of the TSC run. A remarkable percentage could have already been released during the sample rest (cf. Sec. 4.3), indicated by the high TSC at  $T_0$ . An alternative explanation is that the quasi-equilibrium occupation of the trap sites during the filling process is far from unity for the entire trap DOS. Metaphorically speaking, a tilted reservoir can never be completely filled.

The peak temperature shift of the TSC spectra is attributed to a change in  $\mu$  of the released charge carriers. Estimated to approx.  $10^{-12} \text{ cm}^2 \text{ Vs}^{-1}$  for 8...4 wt% F<sub>6</sub>-TCNNQ, the mobility decreases further to  $10^{-13} \text{ cm}^2 \text{ Vs}^{-1}$  (2 wt%) and  $6 \times 10^{-14} \text{ cm}^2 \text{ Vs}^{-1}$  (1 wt%). Reasons for this trend are suggested in Sec. 8.5.

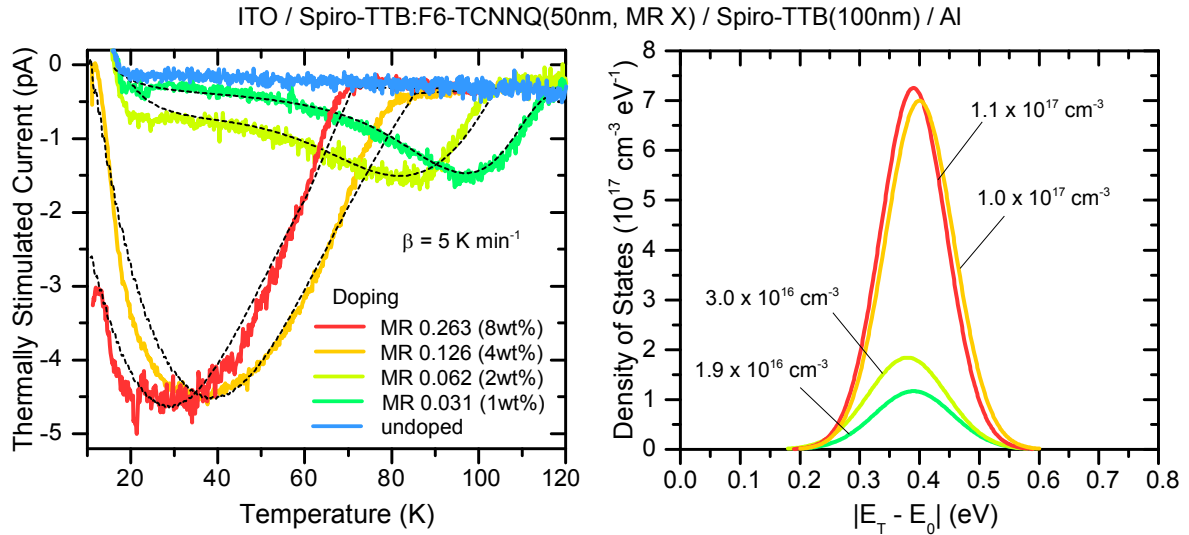


**Figure 8.8.:** (a) TSC spectra ( $\beta = 5 \text{ K min}^{-1}$ ) of p-Spiro-TTB (50 nm) covered by 100 nm intrinsic Spiro-TTB for varying doping density (0...8 wt% F<sub>6</sub>-TCNNQ, blue to red). Simulated TSC spectra considering trap-release to  $E_{Tr}(T)$  and dispersive transport to the collecting electrode are shown in black dashed lines. (b) Determined densities of occupied gap states for the different doping concentrations (turquoise: 1 wt% to red: 8 wt%).

## 8.4. Doping Induced Gap States in ZnPc:C<sub>60</sub> Blends

**Introduction.** Most recently, Fischer *et al.* employed molecular doping in ZnPc:C<sub>60</sub> absorber blends of organic solar cells.<sup>[40]</sup> Earlier investigations by Burtone *et al.* revealed a trap response in capacitance spectra, which however, require doped transport layers adjacent to the blend.<sup>[39,289]</sup> Fischer *et al.* added small amounts of the fluorinated fullerene C<sub>60</sub>F<sub>36</sub> to intentionally dope the ZnPc:C<sub>60</sub>. Hence, the induced energy level bending enabled the Fermi level to interfere with the intrinsic trap DOS. The depletion zone width, and thus the trap capacitance were varied by changing the sample temperatures in between 223...323 K. Following the approach of Walter *et al.*,<sup>[404,420]</sup> Gaussian distributed trap states were found at approx. 0.40 eV above the RT hole transport level position of ZnPc.<sup>[40]</sup> The deduced trap densities for 0.25 wt% and 0.5 wt% C<sub>60</sub>F<sub>36</sub> were  $2.3 \times 10^{16} \text{ cm}^{-3}$  and  $8 \times 10^{16} \text{ cm}^{-3}$ , respectively.

**Thermally Stimulated Currents in Doped Blend Layers.** Figure 8.9 (a) illustrates TSC spectra ( $\beta = 5 \text{ K min}^{-1}$ ) for various 200 nm ZnPc:C<sub>60</sub> blends sandwiched between ITO and aluminum. Undoped blend layers do not release thermally stimulated currents (gray line). Doped by 0.5 wt% C<sub>60</sub>F<sub>36</sub> (MR0.002) with respect to ZnPc, a strong TSC signal with an almost symmetrical peak at 131.4 K and 17.7 pA is recorded. For a

doping concentration of 0.25 wt% (MR 0.001), the TSC peak decreases slightly to 15.6 pA and shifts to higher temperatures, i.e.  $T_{\max} = 135.0$  K. For temperatures of 150 K and above, significant leakage currents  $> 1$  pA are observed. These contributions increase up to 15 pA (0.5 wt%) and 7.5 pA (0.25 wt%), and are present even without trap filling (dashed blue lines). Their occurrence is most probably attributed to progressing dopant activation during the heating. The additional thermal energy supports the generation of free charge carriers, which superimpose the TSC signal from traps. In order to evaluate the TSC signal originating only from initially filled traps, the 'not filled' TSC spectra (dashed lines) are subtracted. The results are shown in Fig. 8.9 (b).

By integration of the corrected TSC spectra in Fig. 8.9 (b), one obtains the total extracted net charges  $Q = 5.57$  nC (0.5 wt%) and  $Q = 4.98$  nC (0.25 wt%), which equal initially filled trap densities  $N_T = 2.8 \times 10^{16} \text{ cm}^{-3}$  and  $N_T = 2.4 \times 10^{16} \text{ cm}^{-3}$ , respectively. In comparison to the incorporated amount of dopant molecules ( $0.5 \times N_{0,\text{ZnPc}} \times \text{MR}$ ), the trap densities account only for 1.7% (0.5 wt%) and 3.0% (0.25 wt%) of the actually  $\text{C}_{60}\text{F}_{36}$  molecule density. Moreover, it is observed that the  $\text{ZnPc}:\text{C}_{60}$  samples require an increased filling current  $I_{\text{fill}}$  prior the TSC run. The spectra shown in Fig. 8.9 are recorded for  $I_{\text{fill}} \simeq 1$  mA. At 'default' values (cf. Sec. 7, Sec. 8.2 and Sec. 8.3) of  $I_{\text{fill}} \simeq 1 \mu\text{A}$ , no TSC peaks could be observed. It is suspected that in bipolar devices, such as the present hetero junction blends, recombination limits the occurrence of thermally stimulated currents. In case of electrical filling, only flooding the samples with a large amount of excess charge carriers (i.e. high fill currents) apparently guarantees a significant initial occupation of trap states for TSCs.

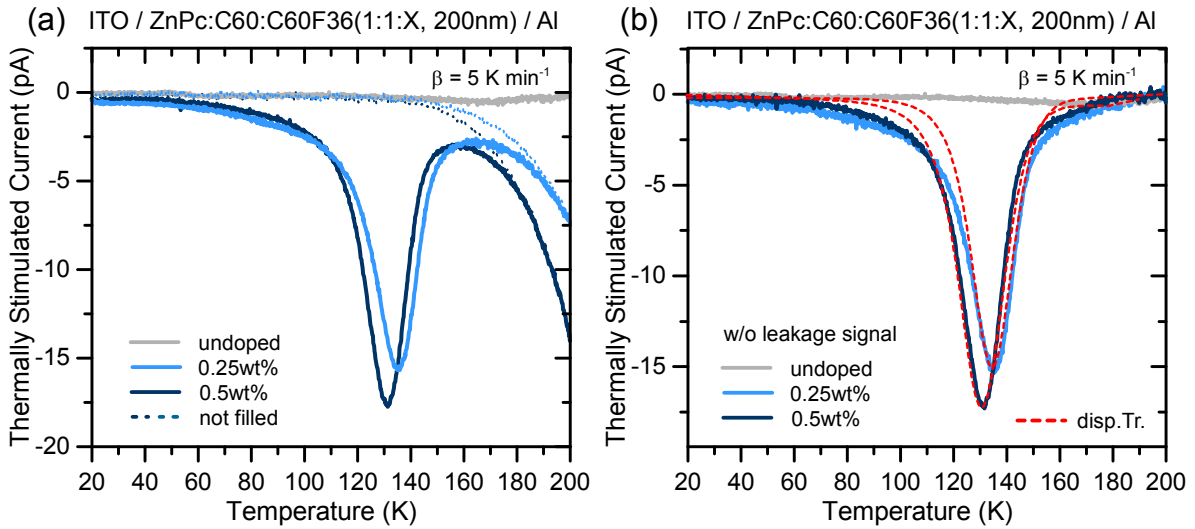


**Figure 8.9.:** (a) TSC spectra ( $\beta = 5 \text{ K min}^{-1}$ ) of various 200 nm  $\text{ZnPc}:\text{C}_{60}$  blend layers sandwiched between ITO and aluminum contacts. For the undoped blend (gray line), no significant TSC is recorded, whereas 0.5 wt% (dark blue) and 0.25 wt% (light blue)  $\text{C}_{60}\text{F}_{36}$ -doped blends exhibit a prominent TSC peak around 130 K. Without initial trap filling, only leakage signal (dashed lines) is observed. (b) TSC spectra from (a) after subtraction of the leakage current contribution. Red dashed lines illustrate computational TSC results assuming temperature-controlled trap release and dispersive transport.

In order to conclude on trap depths from Fig. 8.9, the TSC spectra must be analyzed with respect to the temperature dependent transport level. Therefore, UPS spectra of pure  $\text{ZnPc}$  (blue symbols), pure  $\text{C}_{60}$  (red), and the 1:1 blend (MR 0.7) (gray) taken from Ref. [362] (all on Au substrates) are presented in Fig. 8.10 (a). Black lines indicate Gaussian fits of the respective HOMO DOS. In case of pure  $\text{ZnPc}$ , the determined DOS width  $\sigma_{\text{UPS}} = 0.19 \text{ eV}$  agrees with the result obtained earlier in Sec. 5.1.3. Pure  $\text{C}_{60}$  exhibits the same  $\sigma_{\text{UPS}}$ , whereas its HOMO is shifted significantly to higher binding energies. When blending both host materials, the

HOMO DOS widths are increased to  $\sigma_{\text{UPS}} = 0.235 \text{ eV}$  (ZnPc) and  $\sigma_{\text{UPS}} = 0.230 \text{ eV}$  (C<sub>60</sub>)<sup>4</sup>. This tendency indicates a substantial increase of the system's energetic disorder due to molecular intermixing. At the same time, Tietze *et al.* reported from GIXRD a loss in crystallinity in blends as compared to neat thin-films.<sup>[362]</sup> The IPs of both blended hosts, however, are approx. 5.0 eV (ZnPc) and 6.4 eV (C<sub>60</sub>). Restricted by the EA of C<sub>60</sub>F<sub>36</sub> (5.38 eV)<sup>[208]</sup>, only p-doping of ZnPc is possible. Moreover, the blend is characterized by an effective gap,<sup>[372,399,421]</sup> i.e. electron transport happens via the C<sub>60</sub> LUMO and hole transport via the ZnPc HOMO. Consequently, the hole transport level position is calculated regarding the DOS parameters of ZnPc in the blend. Considering the signal broadening in the UPS spectra, the DOS width is rescaled to  $\sigma = 0.115 \text{ eV}$  (cf. Sec. 5.1.6). The inverse localization radius is taken to  $\gamma = 10^{-9} \text{ m}^{-1}$  and the Fermi level is at  $E_F - E_0 = -0.8 \text{ eV}$ . The site density of ZnPc in the blend is reduced to  $1.13 \times 10^{21} \text{ cm}^{-3}$  (MR 0.7). Figure 8.10 (b) shows a comparison of  $E_{\text{Tr}}(T)$  for ZnPc in neat (blue line) and 1:1 C<sub>60</sub> blended (orange) thin-films. For all temperatures, the difference between both situations is approx. 50...100 meV, and the transport level in the blended ZnPc is located deeper in the gap. The reason is the increased energetic broadening  $\sigma$ , as discussed earlier for the parameter variations in Sec. 5.2.1.

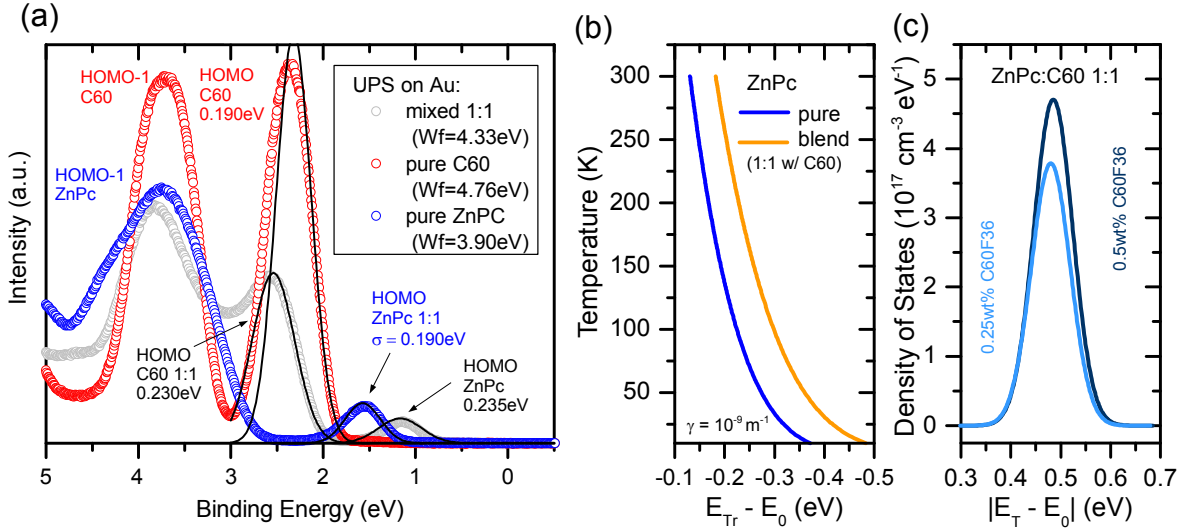


**Figure 8.10.:** (a) UPS spectra measured by Max L. Tietze and published in Ref.<sup>[362]</sup> of pure ZnPC (blue symbols), pure C<sub>60</sub> (red) and 1:1 vol% ZnPC:C<sub>60</sub> thin-films (gray), all evaporated on gold substrates. The respective HOMOs are fitted by Gaussian distributions (black lines), and the DOS widths  $\sigma$  are shown. (b) Temperature dependent hole transport levels in pure ZnPC (blue line) and ZnPC:C<sub>60</sub> blends (orange) as calculated from Eq. (5.7) (cf. Sec. 5.2). (c) Trap DOS obtained from the TSC spectra in Fig. 8.9 (b) for ZnPC:C<sub>60</sub> blends doped by 0.5 wt% (dark blue) or 0.25 wt% (light blue) C<sub>60</sub>F<sub>36</sub>.

By using the estimated  $E_{\text{Tr}}(T)$  and dispersive transport model for thermally released charge carriers, the TSC spectra in Fig. 8.9 (b) are fitted according to Eq. (7.8) (red dashed lines). The built-in potentials  $V_{\text{bi}} = 0.6 \text{ V}$  are taken from Ref.<sup>[40]</sup>, there obtained from C(V) measurements. By assuming hole mobilities  $\mu_h = 3 \times 10^{-13} \text{ cm}^2 \text{ Vs}^{-1}$  (0.5 wt%) and  $\mu_h = 1 \times 10^{-13} \text{ cm}^2 \text{ Vs}^{-1}$  (0.25 wt%), a Gaussian trap distribution ( $\sigma = 39 \text{ meV}$ ) is found at approx. 0.48 eV away from the HOMO center towards mid-gap. The densities of initially filled traps are estimated to be  $4.6 \times 10^{16} \text{ cm}^{-3}$  (0.5 wt%) and  $3.7 \times 10^{16} \text{ cm}^{-3}$  (0.25 wt%) (cf. Fig. 8.10 (c)).

Discrepancies in the fit, e.g. around 100 K, are most probably caused by the fact that the TSC spectra cover a large temperature range 60...180 K, where no experimental  $\mu_h(T)$  data is available and an average hole

<sup>4</sup>Still, the C<sub>60</sub> HOMO fit in the 1:1 blend is slightly influenced by the ZnPc sub-spectrum.

mobility had to be assumed. For example, if assuming a hole mobility  $\mu_h \sim 10^{-10} \text{ cm}^2 \text{ Vs}^{-1}$ , the calculated trap depth  $E_T$  increases further by approx. 0.1 eV. Results published on mobilities in ZnPc:C<sub>60</sub> blends, e.g. by Widmer *et al.*<sup>[422]</sup> or Fischer *et al.*<sup>[399]</sup>, only provide upper limit estimations of  $\mu_h$ . Both articles report  $\mu_h \simeq 10^{-7} \text{ cm}^2 \text{ Vs}^{-1}$  for electric fields  $F = 1.5 \times 10^5 \text{ V/cm}$ , charge carrier densities  $p \simeq 1 \times 10^{16} \text{ cm}^{-3}$ , and room temperature.<sup>[399,422]</sup> Here, the TSC experiments are conducted at  $F = 0.5 \times 10^5 \text{ V/cm}$  and considerably lower  $T$ , which is why mobilities in the order of  $10^{-10} \text{ cm}^2 \text{ Vs}^{-1}$  and below are not unrealistic. Furthermore, the trap densities and trap energies found agree well with the results from impedance spectroscopy published by Fischer *et al.* ( $N_T \simeq 10^{16} \text{ cm}^{-3}$  and  $|E_T - E_{Tr}| = 0.40 \text{ eV}$ ).<sup>[40]</sup> Since those results were obtained at considerably higher temperatures 223...323 K, where  $E_{Tr}(T)$  is closer to the HOMO center by more than 100 meV (cf. Fig. 8.10 (b)), it is consistent that the trap distribution appears in TSC at  $|E_T - E_{Tr}| = 0.21 \text{ eV}$  (at  $T_{\text{max}} = 130 \text{ K}$ ).

## 8.5. Summary: Indications for an Acceptor Level?

Thermally stimulated current spectra of doped organic semiconductors have been analyzed in this chapter. For the HTL material Spiro-TTB, p-doped by F<sub>6</sub>-TCNNQ, shallow trap signatures ( $|E_T - E_0| = 0.4 \text{ eV}$ ) close to the transport level were found. Already at the start of TSC experiments ( $T_0 = 10 \text{ K}$ ), charge carrier emission from trap states was recorded and a pronounced peak between  $T_0$  and  $T \simeq 60 \text{ K}$  was observed (MR0.126). Hereby, a thickness variation of the doped layer clearly identified the bulk as source of the TSC signal. In absence of the doped layer, only TSC features of the intrinsic cover HTLs (MeO-TPD, m-MTDATA) were observed. With p-Spiro-TTB layers present, however, the TSC spectra exhibit superpositions of features both layers. For further studies, trap-free (up to 150 K) intrinsic Spiro-TTB was chosen as cover HTL.

With decreasing dopant concentration (from MR0.253 to MR0.031), the TSC peak originating from the doped layer dissolved in shape and its main part shifted to higher temperatures ( $T = 80...100 \text{ K}$ ). The TSC spectra were fitted assuming a combination temperature-controlled release of trapped charge carriers and dispersive transport towards the extracting electrode. The required built-in potentials determining the extraction field were estimated from IV characteristics. Shifts of major parts of the TSC spectrum towards higher temperatures were explained by a decrease in hole mobility at lower doping concentrations from  $10^{-12}$  to  $10^{-14} \text{ cm}^2 \text{ Vs}^{-1}$ . Here, the accuracy of such examinations would strongly benefit from a complete data set  $\mu_h(T)$  at varying doping concentrations. Not only the hopping transport itself is temperature activated, but also the generation of additional charge carriers by doping, filling inherent deep traps. Besides CELIV<sup>5</sup> and time-of-flight experiments,<sup>[237,425]</sup> an additional possible TSC experiment is sketched in Fig. 8.11. Here, the transport layer *A* of unknown mobility  $\mu_A$  is evaporated between the extracting ITO contact and the p-doped layer *B*. By thickness variation of *A*, the TSC peak of *B* is re-located accordingly. At equal electric field strengths, the TSC peak should be recorded at lower  $T$  for thinner *A* and vice versa. Utilizing layers *B* with shallow trap centers allows a determination of  $\mu_A$  for low temperatures  $T < 100 \text{ K}$ , while *B* with deep traps provide access to  $\mu_A$  at  $T > 100 \text{ K}$ . In Sec. 9.5, this spacer layer concept is applied to estimate the hole mobility of intrinsic Spiro-TTB around  $T = 100 \text{ K}$ .

In C<sub>60</sub>F<sub>36</sub> p-doped ZnPc:C<sub>60</sub> 1:1 blends (MR0.002 and MR0.001), an almost symmetrical peak around 130 K was observed, which is absent in undoped blends. The electrical filling currents had to be increased to approx. 1 mA to achieve a saturation of the trap signal. Here, recombination in the bipolar devices was suspected to limit the TSC signal for lower filling currents of approx. 1  $\mu\text{A}$ . Moreover, this has been seen as reason why the measured trap densities  $10^{16} \text{ cm}^{-3}$  were only a few percent of the total dopant density. In order to compute trap depths, UPS spectra (taken from Ref.<sup>[362]</sup>) of neat and blended ZnPc and C<sub>60</sub>

<sup>5</sup>Charge carrier Extraction by Linearly Increasing Voltage<sup>[44,423,424]</sup>

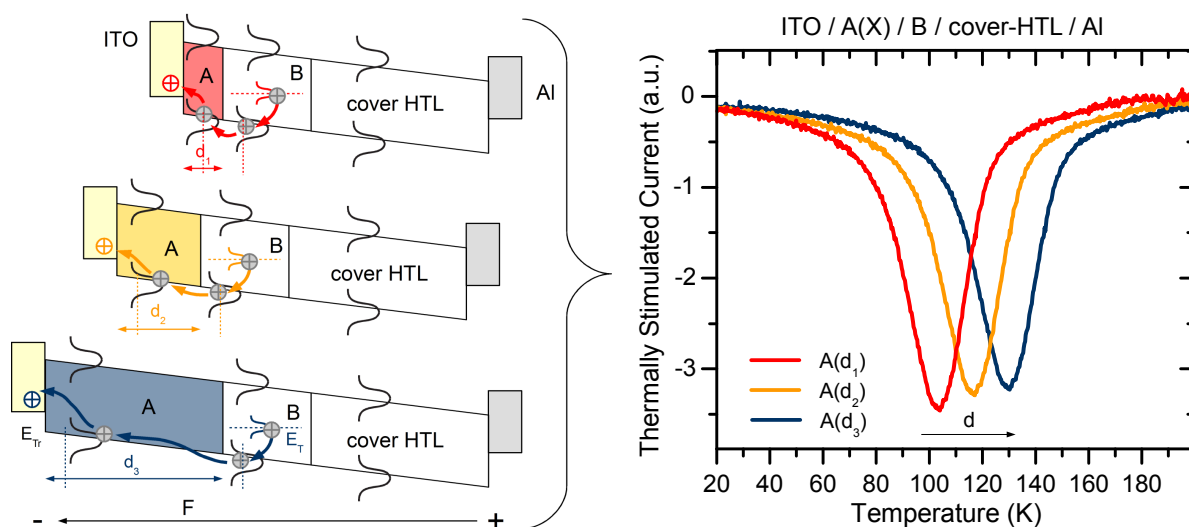


**Figure 8.11.:** Sketch of TSC experiments to estimate the low-temperature mobility of hole transport materials. The sandwich devices feature a trap-containing layer B, which emits thermally stimulated currents. The released charge carriers must pass transport layer A on their way to the extracting electrode. The recorded TSC signal is expected to shift to higher temperatures for an increasing layer thickness  $d$  of A.

were quantitatively analyzed. For the 1:1 blend, significant energetic broadening of both material's HOMOs was found. The temperature dependent hole transport level in the blend has been computed considering the rescaled HOMO of ZnPc ( $\sigma = 0.115$  eV). It has been located by up to 100 meV deeper in the gap as compared to neat ZnPc. Considering thermal release of the trapped charge carriers and dispersive transport to the extracting electrode, a Gaussian trap distribution ( $\sigma = 39$  meV) at  $E_T = 0.48 \pm 0.1$  eV above the HOMO center was identified. In the fitting process, also in this case, the main uncertainty has been the hole mobility. Here, a range from  $10^{-10}$  to  $10^{-13}$  cm<sup>2</sup>Vs<sup>-1</sup> had to be assumed. The obtained trap energies were comparable to the impedance spectroscopy results of identical devices reported by Fischer *et al.*<sup>[40]</sup> They related the observed signal responses to inherent charge carrier traps of the ZnPc:C<sub>60</sub> blend, which were 'visible' upon trap-filling by doping.<sup>[40]</sup> Here in this thesis, the TSC results on those blends and especially p-doped Spiro-TTB are seen different, i.e. caused by the doping itself. In undoped thin-films, no TSC signals are recorded, although electric filling provides excess charge carrier to populate possibly existing trap sites. More likely, the observed traps are directly caused by the dopant interaction with the host system. The following concluding paragraph and Fig. 8.12 (b) present an adapted hypothesis on 'how things actually are' in a (p-)doped organic semiconductor at low temperatures.

As discussed in Sec. 6.3, decreasing the sample temperatures freezes out the dopants, i.e. shifts the Fermi level towards mid-gap, where it is pinned at impurity levels (cf. Fig. 8.12 (a)). Tietze *et al.* found such deep trap levels at 1.6...2.2 eV with respect to the HOMO onset in the HTL materials MeO-TPD, ZnPc, and pentacene.<sup>[181,183]</sup> These trap levels, however, are too far away from the hole transport level to be accessible via TSC. Under filling conditions, i.e. at  $T_0 = 10$  K and forward bias of approx. 10 V, charge carriers are injected into the organic semiconductor. Although the energy barriers for electrons being much higher due to selective contacts, their injection can not be fully excluded at high voltages. Consequently, a split of  $E_F$  into two quasi-Fermi levels  $E_{F,h}$  and  $E_{F,e}$  is likely. The organic semiconductor is loaded and far away from its equilibrium state (cf. Fig. 8.12 (b)). Due to the low temperatures, however, a significant number

of charge carriers is 'frozen' and kept in trapping sites at  $E_T$ . Upon heat-up, they are sequentially released, starting with the most shallow states first (cf. Fig. 8.12 (c)). The (hole quasi-) Fermi level shifts towards mid-gap. At the same time, increasing sample temperatures enhance the host:dopant charge transfer and the generation of free charges.<sup>[91,180]</sup> Consequently, the Fermi level has to shift towards the HOMO as observed in UPS(T) equilibrium measurements of Sec. 6.3. Once  $E_F$  approaches the position of the trap level  $E_T$ , the capture of free holes from the host by the trap level  $E_T$  is probable (cf. Fig. 8.11 (d)). Interestingly, such a phenomenon is observed in TSC spectra of p-doped Spiro-TTB at higher temperatures ( $T \geq 140$  K). As shown in Fig. 8.12 (c), thermally stimulated currents of opposing sign, i.e. hole capture, are recorded. Apparently, the positive peak position shifts to higher temperatures for lower doping concentrations, i.e. from  $T_{\max} = 165$  K (8 wt%) to  $T_{\max} > 220$  K (1 wt%). More quantitative assertions, however, demand further high- $T$  TSC measurements for various doping concentrations in combination with UPS(T) evaluations of well-known host:dopant systems, i.e. MeO-TPD:C<sub>60</sub>F<sub>36</sub>, ZnPc:F<sub>6</sub>-TCNNQ, and P5:C<sub>60</sub>F<sub>36</sub>.

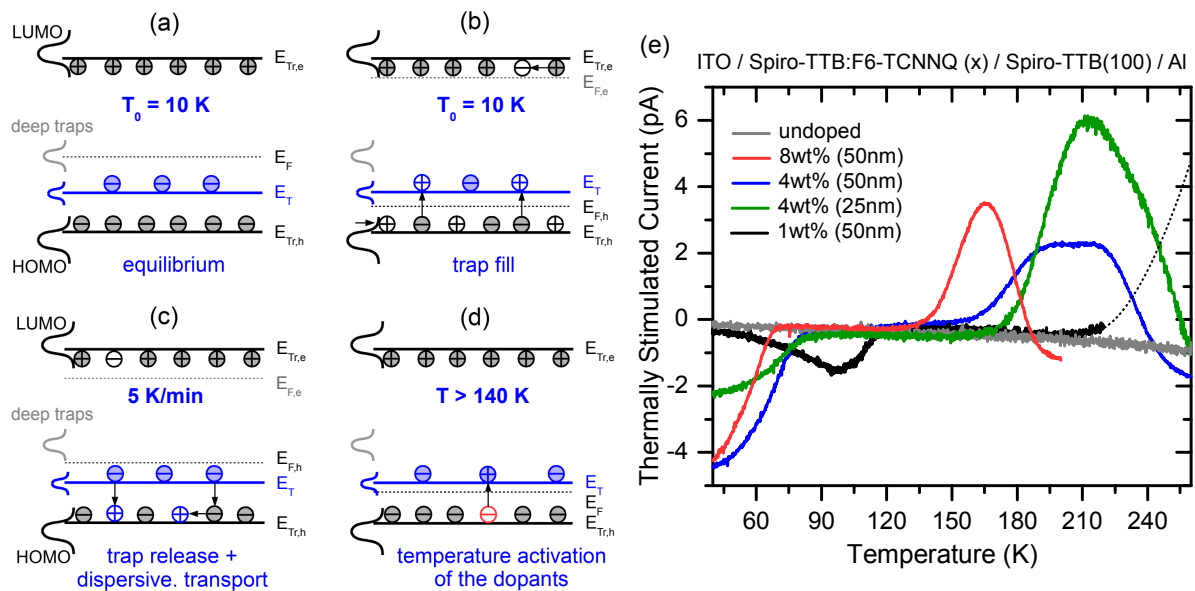


**Figure 8.12.:** Qualitative illustration of charge carrier occupation and (quasi-) Fermi levels  $E_F$  during a TSC procedure for a p-doped material with a trap distribution at  $E_T$ . (a) At ultra-low temperatures, dopant freeze-out is observed (cf. Sec. 6.3).  $E_F$  is at the intrinsic position, pinned by deep traps.<sup>[207]</sup> (b) By electrical filling, charge carriers are injected.  $E_F$  splits into two quasi-Fermi levels  $E_{F,h}$  and  $E_{F,e}$  of holes and electrons, respectively. (c) While heating, trapped charge carriers are released towards the transport levels, e.g. holes to  $E_{Tr,h}$ .  $E_F$  shifts towards mid-gap. (d) With increasing temperature, dopant:host charge transfer is gradually activated, and thus free holes generated.  $E_F$  shifts towards the HOMO. (e) TSC spectra of F<sub>6</sub>-TCNNQ doped Spiro-TTB for  $T \geq 120$  K. At increased sample temperatures, TSC signals of opposite sign as compared to the previous results are recorded which points towards a recombination or charge carrier injection mechanism but requires future investigations.

Besides, the nature of the trap levels observed in TSC remains actually unclear until further experiments can be performed. They could resemble energetic distortions of the host system, caused by Coulomb interactions between host and added (ionized) dopant molecules. In particular, a correlation of the trap states with a so far referred acceptor level, concluded from UPS studies,<sup>[181,183,207]</sup> could be envisioned. In that sense, the TSC features might indicate an underlying (temperature-dependent) self-trapping mechanism of the molecular doping, which originates from Coulomb attraction and, therefore, controls the overall doping efficiency. Nevertheless, extensive research is required for further clarification. An examination of various host:dopant systems should be the next step. The different acceptor levels  $E_A$  found by UPS already suggest

a scaling for different host materials.<sup>[181,183]</sup> Although the energy scale for UPS results is affected by signal broadening, the tendencies should apply to TSC results. Alternatively, the dopant strength can be varied to prove the concept of energy level splitting under hybrid formation.<sup>[234]</sup>





# Oxygen and Water Related Defects in Organic Hole Transporting Layers

*The influence of pure oxygen and ambient (humid) atmosphere on various organic hole transport materials are examined via the thermally stimulated current technique. While vacuum annealing during sample processing possibly limits impurity penetration, water and oxygen diffusion in the HTLs causes a steady increase of trap densities for fabricated samples. Oxygen-related trap centers are identified in pentacene, ZnPc, MeO-TPD, and m-MTDATA at site energies of 4.67-4.83 eV, strongly suggesting the existence of a global oxygen trap level in organic HTL materials. Utilizing the newly introduced spacer layer concept for TSC, those traps are found to be hole traps. Simultaneously, the low-temperature values of charge carrier mobilities are accessible, e.g. the hole mobility of intrinsic Spiro-TTB is determined to be approx.  $10^{-13} \text{ cm}^2 \text{ Vs}^{-1}$ .*

## 9.1. Motivation

Various publications report on the sensitivity of organic semiconductors to reactive molecular species, i.e. water, oxygen, or ambient air.<sup>[246,251–255]</sup> Due to the weak inter-molecular van-der-Waals interactions in an organic thin-film, small and mobile impurities are able to penetrate into it deeply.<sup>[256,257]</sup> Possible consequences are an increased morphological disorder<sup>[256]</sup> or locally induced dipole moments in the thin-film.<sup>[257,258]</sup> In this context, Nicolai *et al.* reported on a generic electron trap level ( $E_T = 3.6 \text{ eV}$  w.r.t. the vacuum level) in a series of conjugated polymers with various LUMO energies, caused by water-oxygen exposure.<sup>[43]</sup> They suspect the formation of  $(\text{H}_2\text{O})_n\text{-O}_2$  complexes<sup>[259,260]</sup> as well as photo-oxidation of the polymers in the vicinity of hydrated oxygen complexes. Besides the storage of impurities, chemical reactions (up to a complete fraction of the molecules as seen for the air-sensitive n-dopant  $\text{W}_2(\text{hpp})_4$ <sup>[220]</sup>) are expected to happen at reactive parts of the organic molecules. For example in pentacene (P5), either two oxygen or hydrogen atoms form double bonds with the carbon atoms at the 6,13-positions<sup>[249]</sup> and generate impurities within pentacene films.<sup>[261–264]</sup>

However, not only organic thin-films directly exposed to reactive gases are prone to degradation. Already the preparation can strongly affect the device stability. For polymeric P3HT:PCBM solar cells, Ecker *et al.* reported a rapid degradation when HTLs containing water-based solvents were utilized.<sup>[426]</sup> Hermenau *et al.* published extensive studies on the degradation of small molecule solar cells with different encapsulations (i.e. water vapor transmission rates WVTR) under various operation conditions.<sup>[427,428]</sup> The short circuit current, i.e. a measure for charge carrier transport, drastically decreased for longer times in moist atmosphere. Diffusion of water and oxygen at grain boundaries and through pinholes of the aluminum top contact was suspected.<sup>[427,428]</sup> Using TOF-SIMS<sup>1</sup> measurements on degraded ZnPc:C<sub>60</sub> solar cells, Hermenau *et al.*

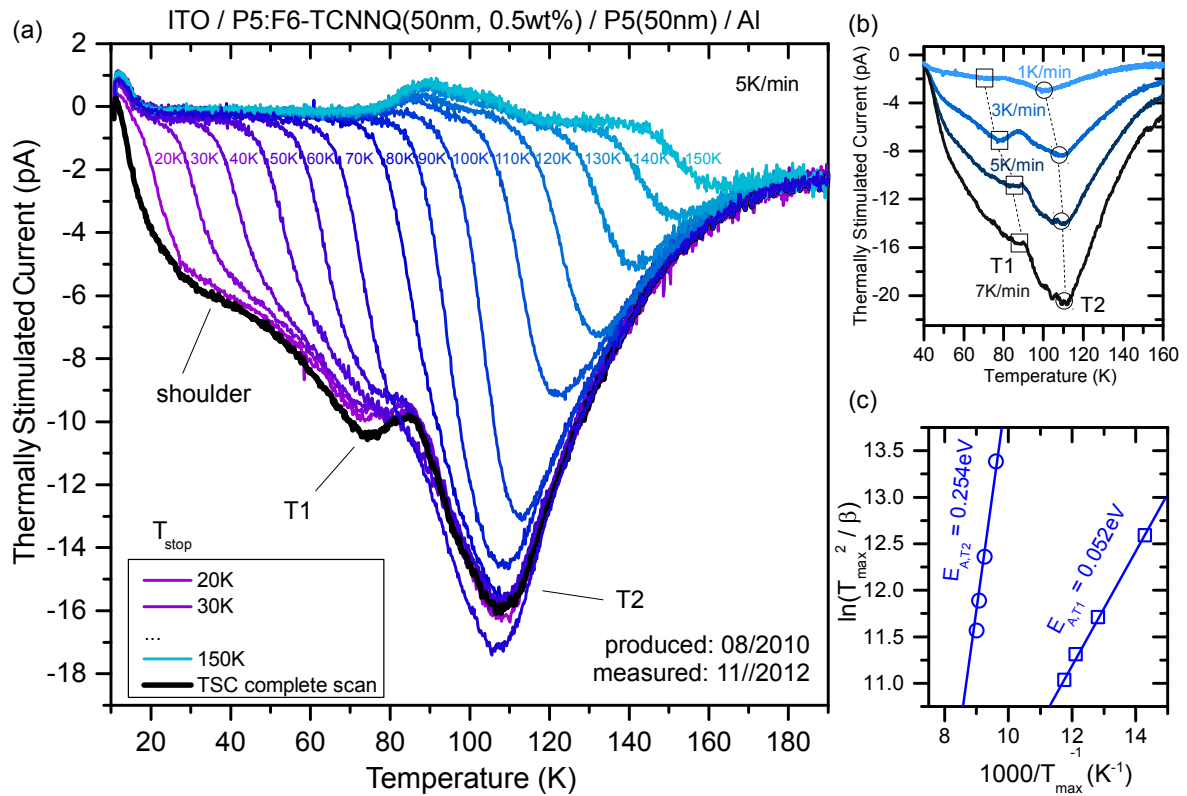
<sup>1</sup>time-of-flight secondary ion mass spectroscopy

identified a significant storage of water and oxygen in ZnPc and the MeO-TPD hole transport layer.<sup>[427]</sup>

In this chapter, the thermally stimulated current technique is applied to as-prepared and degraded organic semiconductors to quantify the amount and the energetic position of impurity traps. Motivated by the trap spectra found for aged pentacene presented in Sec. 9.2, the examinations are extended to various hole transporting materials in Sec. 9.3. In addition, the influence of oxygen residual gas and humid air during the sample preparation process is investigated in Sec. 9.4, while conclusions on the trap polarities are drawn in Sec. 9.5. Whenever an absolute trap energy is presented throughout the following sections, it is computed using the intrinsic transport level position of the respective HTL material (cf. Sec. 5.2.3). Changes of  $E_{Tr}(T)$  upon doping and/or impurities are hardly resolvable and thus not considered.

## 9.2. Aged Pentacene Schottky Diode

The Schottky diode discussed in this section consists of 50 nm P5 p-doped by 0.5 wt% F<sub>6</sub>-TCNNQ ( $MR 3.9 \times 10^{-3}$ ) and additional 50 nm intrinsic P5 as cover HTL, which minimizes TSC leakage currents. The sample is investigated via the thermally stimulated current technique roughly two years and three month after its fabrication. Up to this point, it was stored in ambient atmosphere at room temperature and with an unimpaired glass-glue-glass encapsulation.



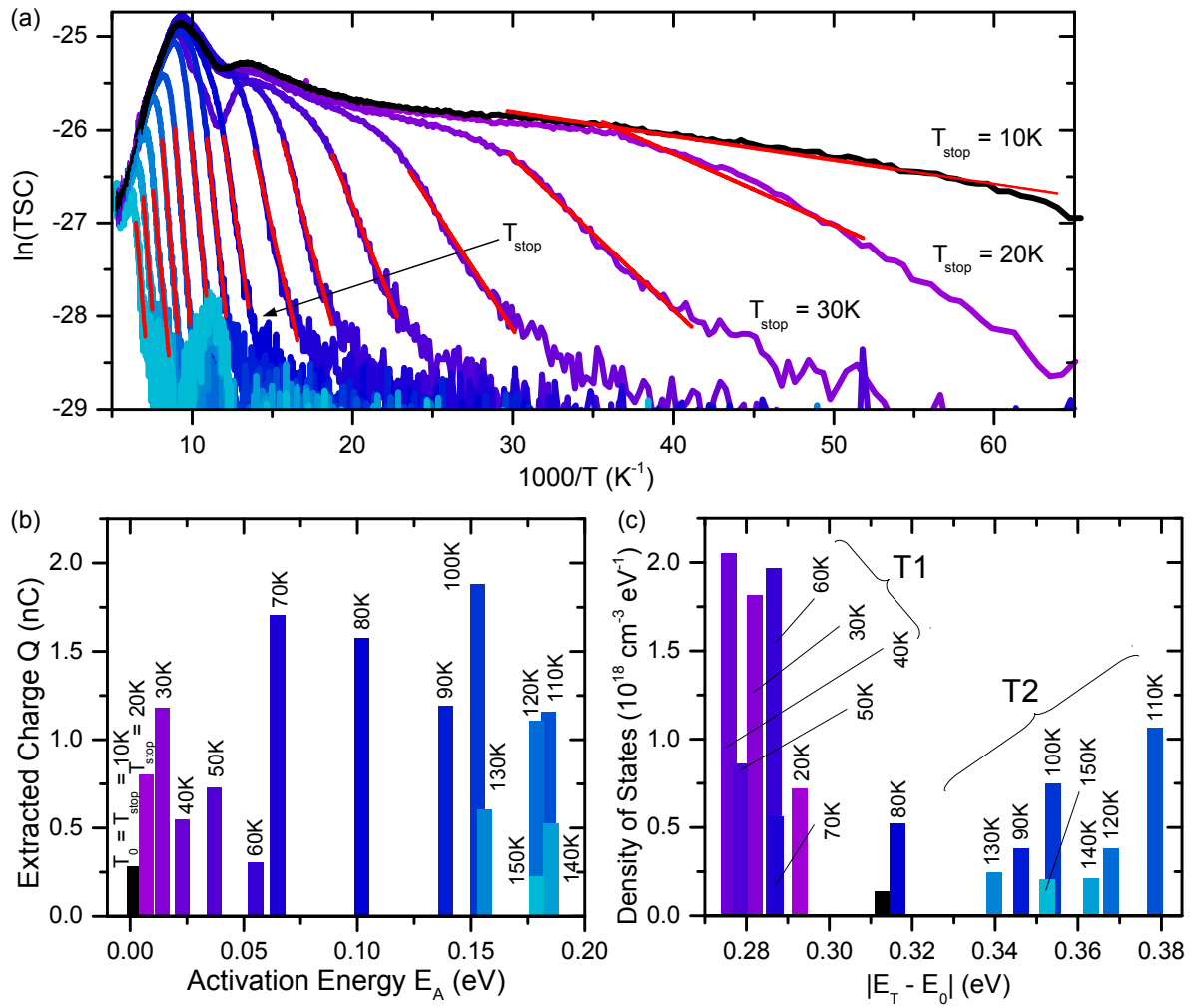
**Figure 9.1.:** (a) (Fractional) TSC spectra of an aged pentacene Schottky diode at a linear heating rate  $\beta = 5 \text{ Kmin}^{-1}$ . The device consists of 50 nm P5:F<sub>6</sub>-TCNNQ (0.5 wt%,  $MR 3.86 \times 10^{-3}$ ) and 50 nm intrinsic P5, both sandwiched between an ITO and an aluminum contact. It was measured more than two years after fabrication. The complete TSC (black line) features a shoulder and two peaks at T1 and T2. Fractional TSC spectra are taken for pre-release temperatures  $T_{stop} = [20...150] \text{ K}$ . (b) TSC spectra for varying heating  $\beta = 1...7 \text{ K min}^{-1}$ . Both TSC peaks T1 and T2 shift to higher temperatures for faster heating. (c) Examination of the peak positions the versus heating speed  $\beta$  to conclude on the trap depths with respect to the transport level (Hoogenstraaten method).<sup>[326,327]</sup>

Figure 9.1 shows (fractional) TSC spectra taken from the aged P5 Schottky diode. For the entire spectrum (black line), the integration yields a total net charge of 13.8 nC. Assuming a uniform trap state distribution for all 100 nm of P5, this yields a lower-limit trap density  $N_T = 1.34 \times 10^{17} \text{ cm}^{-3}$ . Uniformity is here, however, a strong approximation, as the TSC signal is obvious the superposition of more than one trap distribution. It features a broad shoulder around 40 K, a minor peak T1 at 75 K, and the most prominent peak T2 between 100 K and 120 K. Recalling the results from Ch. 8, p-doping induces a TSC response. Although the dopant MR is low here, parts of the TSC spectra are expected to originate from the doping process. Moreover, it is unknown if degradation affects both the host and the dopant system in the same fashion. Consequently, the occurrence of multiple trap distributions is not surprising.

For heating rates  $\beta = 1...7 \text{ K min}^{-1}$ , the peak positions T1 and T2 shift by several Kelvin as illustrated in Fig. 9.1 (b). Plotted according to Eq. (4.58),<sup>[326,327]</sup> an activation energy with respect to the transport level could be approximated to  $E_{A,T1} = 0.052 \text{ meV}$  and  $E_{A,T2} = 0.254 \text{ eV}$  (cf. Fig. 9.1 (c)). However, the Hoogenstraaten method of varying  $\beta$  requires far-reaching assumptions on the attempt-to-escape frequency  $\nu$ , the mobility  $\mu$ , and the carrier lifetime  $\tau$ , and has no solid base to judge trap levels in organic semiconductors (cf. discussion in Sec. 7.1).

Without exact knowledge of  $\mu(T)$  for doped and intrinsic P5 at this aged state, the model of temperature-controlled release and dispersive transport of trapped charge carriers is unfavorable to extract absolute trap depths as well. Hence, for the estimation of the trap energies, the initial rise of the fractional TSCs is fitted as illustrated in Fig. 9.2 (a) (red lines). The obtained TSC activation energies for each pre-release temperature  $T_{\text{stop}}$  are shown in Tab. 9.1. By integration and subtraction of consecutive TSC spectra, the extracted net charge  $Q$  is correlated to the energy axis, which is plotted in Fig. 9.2 (b). The largest share of the charges ( $Q = 6.36 \text{ nC}$ ) is extracted near the peak temperature  $T_2$ , i.e. for  $T_{\text{stop}} = 70...100 \text{ K}$  and activation energies  $E_A = 70...150 \text{ meV}$ . Below ( $T_{\text{stop}} = 10...60 \text{ K}$ , 3.85 nC) and above ( $T_{\text{stop}} = 110...150 \text{ K}$ , 3.62 nC), significantly less charges are extracted. The sum of all slices  $Q(T_{\text{stop}})$  equals the integral  $Q = \int I_{\text{TSC}}(t) dt$  for the entire TSC spectrum (black line) with  $Q = 13.8 \text{ nC}$ .

The density of initially occupied trap sites versus the site energy is obtained from Eq. (4.48), Fig. 9.2 (b), and the  $T$ -dependent transport level of P5 (cf. Sec. 5.2.3). The resulting DOS distribution is illustrated in Fig. 9.2 (c). While the trap energies are spread by approx. 100 meV, the majority of trap centers per eV is located around 0.28...0.30 eV from the HOMO center towards the gap-mid. Here, the amount of released charges per (activation) energy interval is considerably higher than for the rest of the fractional TSC spectra. Furthermore, two remarkable observations are made. First, the activation energy decreases again for higher pre-release temperatures, i.e.  $T_{\text{stop}} \geq 120 \text{ K}$ . This tendency has been seen earlier in Sec. 8 for Spiro-TTB:F<sub>6</sub>-TCNNQ, but it is apparent likewise in fractional TSC data in literature, e.g. for (oxygen-doped) P3HT by Schafferhans.<sup>[44,312]</sup> This anomaly can be caused at low-signal-to-noise ratios by the slow migration of charge carriers when only few charge carriers are released. Second, thermally stimulated currents of opposite, i.e. positive, sign are recorded around 100 K for fractional TSC runs with  $T_{\text{stop}} \geq 110 \text{ K}$  (cf. Fig. 9.1 (a)). Interestingly, those TSC signals appear at temperatures for which the trap DOS has been emptied in the pre-runs. Although an exact physical model is beyond the scope of this thesis, an interplay of the p-dopant F<sub>6</sub>-TCNNQ 'returning' from the freeze-out and the trap DOS is suggested (cf. Sec. 8.5).



**Figure 9.2.:** (a) Initial rise examination of the fractional TSC spectra from Fig. 9.1 (a). The pre-release temperature  $T_{\text{stop}}$  increases from right (dark violet,  $T_{\text{stop}} = 20$  K) to left (light blue,  $T_{\text{stop}} = 150$  K) in steps of 10 K. In black, the entire TSC spectrum with  $T_0 = T_{\text{stop}} = 10$  K is drawn. Red lines illustrate linear fits to extract the respective activation energies, presented in Tab. 9.1. (b) Extracted net charge  $Q$  with respect to the activation energies  $E_A$  of each fractional TSC run. (c) Calculated DOS distribution for P5 aged from initial rise examinations.

**Table 9.1.:** Activation energies  $E_A$  of the thermal release towards the temperature-dependent transport level for trapped charge carriers in aged P5. The energies are calculated from the initial rise of the fractional TSC spectra (cf. Fig. 9.2 (a)) for pre-release temperatures  $T_{\text{stop}}$ .

$T_{\text{stop}}$ (K)	$E_A$ (meV)	$T_{\text{stop}}$ (K)	$E_A$ (meV)	$T_{\text{stop}}$ (K)	$E_A$ (meV)
10	2	60	55	110	184
20	7	70	65	120	179
30	14	80	102	130	156
40	23	90	139	140	185
50	37	100	153	150	179

**Water Vapor and Oxygen Transmission.** Diffusion of impurities, i.e. water and/or oxygen, into the organic semiconductor layers are suspected to be the reason for the dominant TSC response in the aged P5 TSC spectra of Fig. 9.1 (a). Hermenau determined the water vapor transmission rates for the IAPP default glass-on-glass encapsulation sealed by UV-curable glue via electrical calcium tests<sup>[429]</sup> to  $\text{WVTR}_{\text{encap}} = 3.9 \times 10^{-5} \text{ g m}^{-2} \text{ d}^{-1}$ .<sup>[430]</sup> An additional diffusion barrier is the 100 nm aluminum top contact with a value of  $\text{WVTR}_{\text{Al}} = 8 \times 10^{-4} \text{ g m}^{-2} \text{ d}^{-1}$ .<sup>[428]</sup> The total water vapor transmission rate is given by the equation

$$\frac{1}{\text{WVTR}_{\text{total}}} = \frac{1}{\text{WVTR}_{\text{encap}}} + \frac{1}{\text{WVTR}_{\text{Al}}}, \quad (9.1)$$

as both diffusion resistances add up in series.<sup>[428]</sup> Consequently, this yields overall a  $\text{WVTR}_{\text{total}} = 3.7 \times 10^{-5} \text{ g m}^{-2} \text{ d}^{-1}$ , i.e. the overall diffusion barrier is governed by an intact encapsulation. After a period of approximately two years and three months, i.e. the time between fabrication and TSC measurement of the P5 diode in this section, an approximate amount of  $30 \text{ mg m}^{-1}$  water is accumulated in the organic layers. For comparison, Hermenau *et al.* found a degradation of the short circuit current in ZnPc:C<sub>60</sub> bulk heterojunction solar cells down to approx. 30% of its initial value for an accumulation of  $10 \text{ mg m}^{-1}$  water.<sup>[428]</sup> TOF-SIMS depth profiling revealed that significant amounts of water and molecular oxygen are captured in the absorbing ZnPc:C<sub>60</sub> blend layer and the p-MeO-TPD HTL of such OSCs.<sup>[427]</sup>

Similar to water, oxygen possesses a transmission rate through encapsulations and contacts,<sup>[431]</sup> which is, however, undetermined for the IAPP sample design up to now. Studies on P5/ZnPc solar cells by Yang *et al.* in ambient air for different humidity levels revealed separate time scales for water- and oxygen-induced degradation.<sup>[432]</sup> The authors suspect a faster diffusion speed for smaller water molecules as compared to larger oxygen molecules.

**Progressing Degradation.** Figure 9.3 (a) shows TSC spectra for the P5 Schottky diode at advancing ages. The shallowest curve (light blue) is taken 812 days after device fabrication. It features two peaks, one at  $T_1 = 82 \text{ K}$  and one at  $T_2 = 110 \text{ K}$ . The extracted net charge is  $Q = 9.3 \text{ nC}$  in total. After this first TSC run for the device, the encapsulation leaked and a variety of measurements has been performed in the following days, e.g. the fractional TSC run in Fig. 9.1 (a) or the heating rate variations in Fig. 9.1 (b). In between measurements, the sample has been stored in ambient atmosphere. After 18 days, the sample at the age of 830 days exhibits a TSC signal, significantly increased by approx. a factor of two (sky blue in Fig. 9.3 (a)). A total net charge of  $Q = 21.7 \text{ nC}$  is extracted. When the P5 Schottky diode is re-measured after additional 52 days at the age of 882 days in total, a net charge of  $36.4 \text{ nC}$  is released from trap states. Both former peaks coincide and result in one huge signal peak  $T'$ , which reaches a TSC of up to  $53 \text{ pA}$  at  $124 \text{ K}$  (dark blue line). Interestingly, the peak position is found at slightly higher temperatures than  $T_1$  and  $T_2$ , and the overall spectrum broadens. This could indicate a decreased charge carrier mobility with higher sample age, which agrees with the increasing amount of trap states in the device when aging it. The released charge carriers are delayed upon their extraction. Assuming uniform trap distributions, one obtains trap site densities  $N_{T,812 \text{ d}} = 9.0 \times 10^{16} \text{ cm}^{-3}$ ,  $N_{T,830 \text{ d}} = 2.1 \times 10^{17} \text{ cm}^{-3}$ , and  $N_{T,882 \text{ d}} = 3.5 \times 10^{17} \text{ cm}^{-3}$ .

Evidence for the proceeding degradation of the pentacene sample upon storage in air (with leaking encapsulation) is not only provided by the increasing TSC response. Figure 9.3 (b) compares the current-voltage characteristics of the P5 Schottky diode at room temperature for different ages. While the black curve has been measured immediately after sample fabrication, the blue characteristics are degraded. After 812 days, the forward/backward current densities decreased by one/two orders of magnitude (light blue line). At 882 days (dark blue) after numerous TSC experiments and storage in ambient air in between, the forward/backward direction is degraded by five/three orders of magnitude as compared to the fresh sample. The main reason is

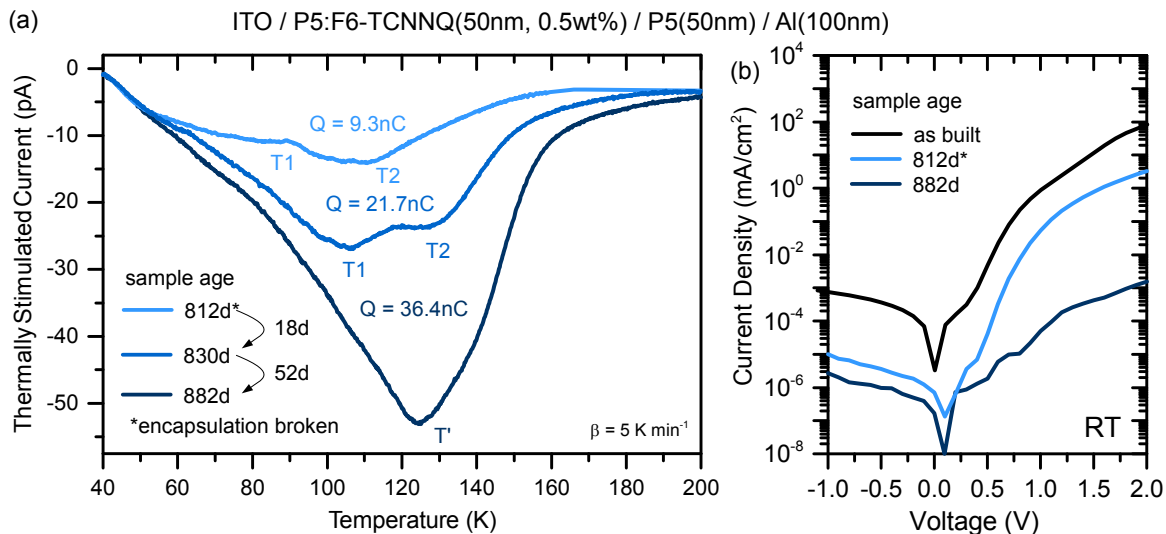


**Figure 9.3.:** (a) TSC spectra ( $\beta = 5 \text{ K min}^{-1}$ ) of the aged P5 Schottky diode, measured for different storage times. The first TSC run is taken 812 days after the sample fabrication (light blue, equal to Fig. 9.1 (a) black line). After that, the encapsulation leaks and the sample is stored in ambient (lab) atmosphere. Eventually, the P5 Schottky diode is re-measured by TSC after 18 days (sky blue) and again after 52 days (dark blue). Hereby, the extracted net charge from trap states increases from 9.3 nC (812 d) to 21.7 nC (830 d) and 36.4 nC (882 d). (b) Corresponding current-voltage characteristics at room temperature for the 812 d (light blue) and 882 d (dark blue) old sample, in comparison to the freshly prepared device (black).

here most probably the strongly increased amount of trap centers, which capture free charge carriers (thus reduce the leakage current in backward direction) and hinder the charge carrier motion in forward direction. In summary, aged pentacene exhibits an approx. 100 meV broad trap distribution at a depth of approx. 300 meV from its HOMO center towards mid-gap. The trap DOS increases substantially in density for longer storing times in ambient air, especially with damaged encapsulation. Water/oxygen is suspected to pass the encapsulation and the top contact diffusion barrier entering the organic layers and cause trapping sites. In the next section, the TSC examinations are extended to various other HTL materials to check if similar interactions are apparent.

### 9.3. Trap Signatures in Fresh and Aged HTLs

**Thermally Stimulated Currents from as-Prepared HTLs.** Revisiting the TSC spectra of p-doped Spiro-TTB paired with various intrinsic HTLs from Ch. 8.2, trap distributions with separate origins are observed. Figure 9.4 (a) shows TSC spectra for 50 nm Spiro-TTB:F6-TCNNQ (4 wt%) with 100 nm intrinsic ZnPc, P5, m-MTDATA, Spiro-TTB, NPB, MeO-TPD, or BF-DPB on top. All TSC spectra exhibit a broad signal between 20 K and 80 K peaking at approx. 3...4 pA, which originates from the p-Spiro-TTB layer as discussed in Ch. 8. Additionally, the low IP materials ZnPc (5.0 eV), P5 (5.0 eV), m-MTDATA (5.0 eV), and MeO-TPD (5.1 eV) feature second peaks at temperatures 70...110 K, while none appear for the higher IP materials Spiro-TTB (5.25 eV), NPB (5.3 eV), and BF-DPB (5.4 eV).<sup>2</sup> Omitting p-doped Spiro-TTB, i.e. for solely intrinsic HTLs sandwiched between selective electrodes, the TSC features around 70...110 K remain as shown in Fig. 9.4 (b). This fact proves beyond doubt that these particular trap signatures originate from the respective HTL materials.

<sup>2</sup>ionization potentials obtained via UPS on various substrates in Sec. 5.1.2, Sec. 5.1.3 and Tab. 5.3.

Interestingly, as-prepared intrinsic HTL materials show already significant thermally stimulated emission of charges, i.e.  $Q = 0.72$  nC (m-MTDATA),  $1.37$  nC (MeO-TPD),  $1.92$  nC (P5), and  $6.92$  nC (ZnPc). Assuming uniformity within the thin-films, the resulting lower estimate trap densities are  $N_T = 0.7 \times 10^{16} \text{ cm}^{-3}$  (m-MTDATA),  $1.3 \times 10^{16} \text{ cm}^{-3}$  (MeO-TPD),  $1.9 \times 10^{16} \text{ cm}^{-3}$  (P5), and  $6.7 \times 10^{16} \text{ cm}^{-3}$  (ZnPc). Hereby, ZnPc exhibits an exceptionally broad TSC signal from 20 up to 200 K (cyan line), which indicates the existence of multiple trap site distributions within the material. Remarkably, the TSC spectra from as-prepared pentacene shows double peaks T1 and T2 (blue line) similar to the TSC spectra of the aged P5 devices in Fig. 9.1 and Fig. 9.3. Here, however, they are at slightly lower temperatures 70 K (T1, fresh) and 92 K (T2, fresh) as compared to 82 K (T1, aged) and 110 K (T2, aged) in Sec. 9.2. Most probably, the mobility of the charge carriers during extraction in fresh devices is higher than for degraded samples. Consequently, released charge carriers are collected earlier (at lower  $T$ ) in the first case. Thin-films of intrinsic Spiro-TTB, NPB, and BF-DPB exhibit no TSC signal from sandwich devices (cf. Fig. 9.4 (b): green, orange, and pink line).

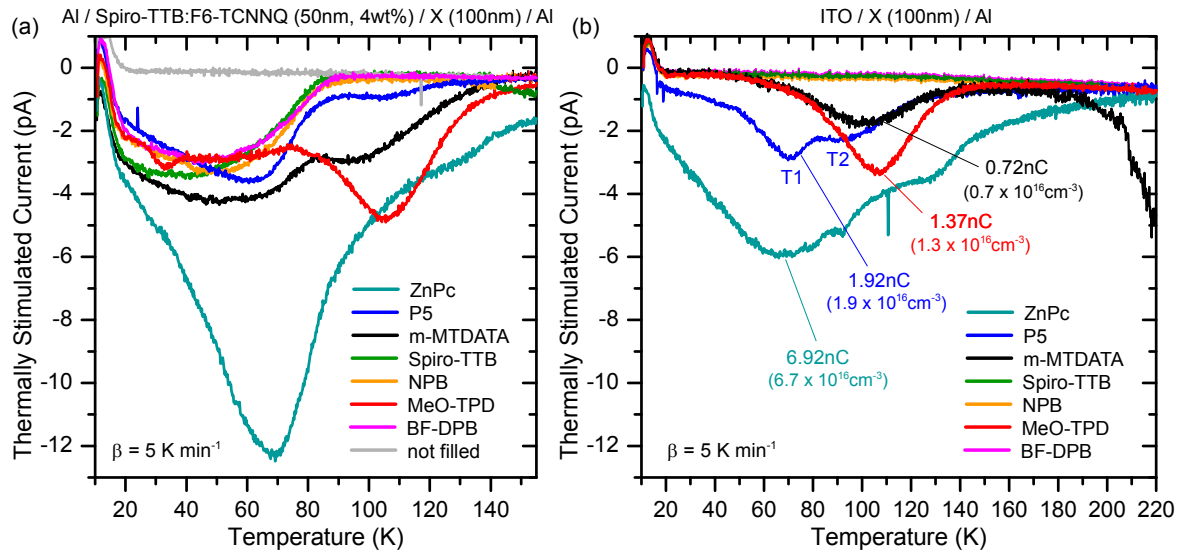


**Figure 9.4.:** TSC spectra ( $\beta = 5 \text{ K min}^{-1}$ ) of devices consisting of (a) p-doped Spiro-TTB (50 nm, 4 wt% F<sub>6</sub>-TCNNQ) with various HTL materials (100 nm) on top and sandwiched by aluminum electrodes or (b) solely 100 nm intrinsic HTL materials sandwiched between ITO and Al. Without an initial electrical filling, no significant TSC is recorded (gray line).

**Thermally Stimulated Currents from Degraded HTLs.** The susceptibility of pentacene, ZnPc, and MeO-TPD to water and oxygen degradation is investigated by removing the glass encapsulation of the samples and subsequent TSC experiments versus storage time. Between consecutive TSC runs, the samples are stored in ambient (lab) air, i.e. only the aluminum top contact prevents direct gas exposure of the organic thin-films. Diffusion at cracks, pinholes, and grain-boundaries in the aluminum layer determine its water vapor transmission rate (WVTR) and oxygen transmission rate (OTR) [427] as illustrated in Fig. 9.5 (d) (1). Figure 9.5 (a)-(c) show the TSC spectra from P5, ZnPc, and MeO-TPD thin-films for storage times of several days to few month in comparison to those of as-prepared thin-films. Throughout all experiments, the released net charge  $Q$ , i.e. the defect density  $N_T$ , is increasing for longer air exposure. In case of pentacene,  $Q$  ( $N_T$ ) more than tripled from  $1.92$  nC ( $1.9 \times 10^{16} \text{ cm}^{-3}$ ) to  $6.22$  nC ( $6.0 \times 10^{16} \text{ cm}^{-3}$ ) after four days. Within one month,  $7.19$  nC ( $7.0 \times 10^{16} \text{ cm}^{-3}$ ) was reached. Simultaneously, the TSC double peaks T1 and T2 shift to higher temperatures by several 10 K, which hints on a reduced extraction mobility due to more traps, a weaker built-in field caused by Coulomb interaction with traps, or both. Remarkably, a TSC of opposite sign



is observed from air exposed P5 around 160...200 K even without electrical filling prior the TSC run (dashed lines in Fig. 9.5 (a)). Although a detailed study on reasons is beyond the scope of this thesis, such a trend has been only seen for doped thin-films in Sec. 8.5. As oxygen is known to p-dope pentacene<sup>[433–435]</sup> and increasing leakage currents for temperatures  $T > 200$  K are recorded, unintentional p-doping by air exposure is likely.

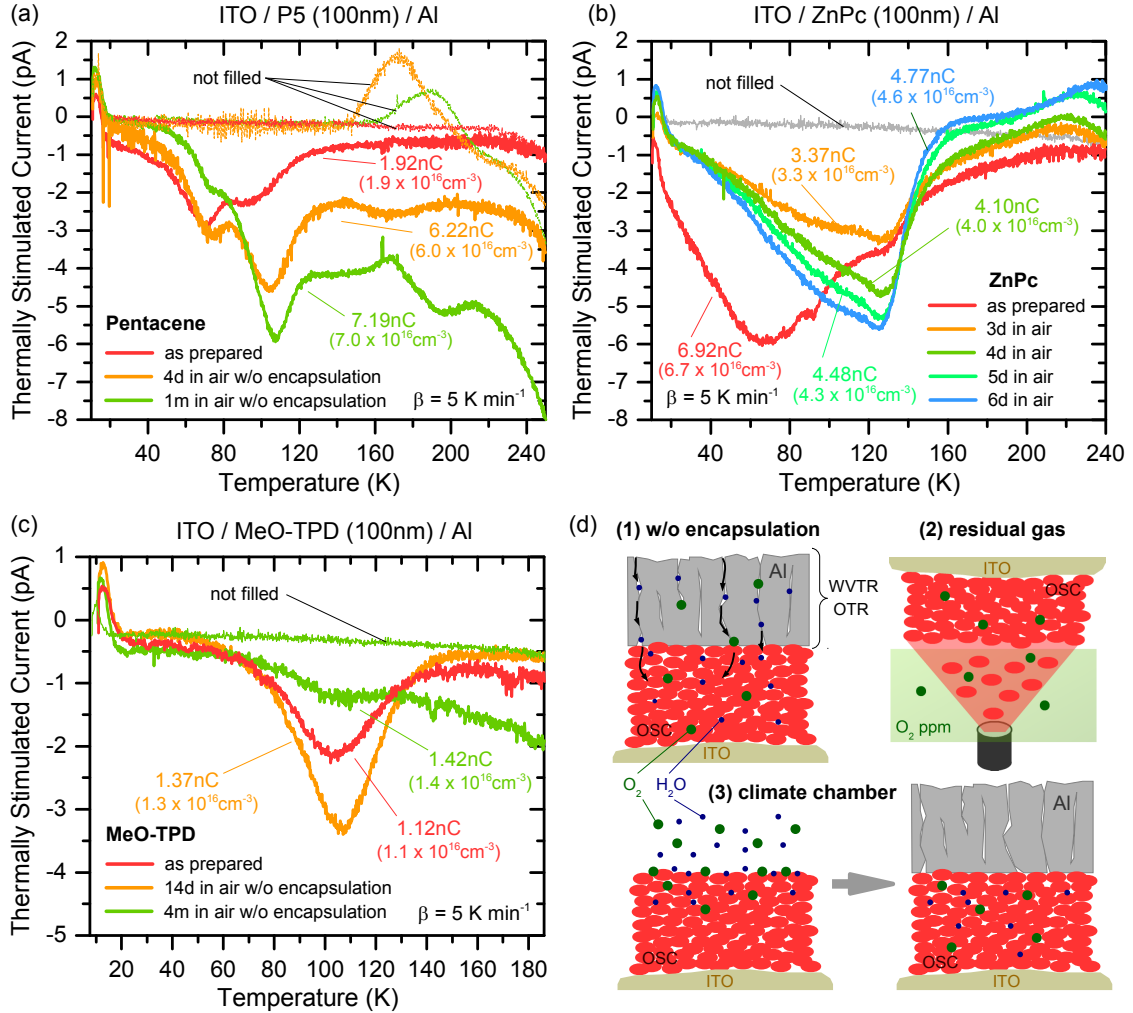


**Figure 9.5.:** TSC spectra ( $\beta = 5 \text{ K min}^{-1}$ ) of 100 nm (a) pentacene (b) ZnPc, or (c) MeO-TPD sandwiched between ITO and aluminum, as-prepared and for various ambient air exposure times. (d) Experiments to examine the influence of water and oxygen on HTL materials. Samples are stored in ambient air/ $\text{O}_2$  w/o encapsulation (1), residual gases are present during the organic layer deposition (2), or the HTL is exposed to humid air during the fabrication.

For ZnPc, the TSC spectrum shifts considerably to higher temperatures when the thin-film is exposed to ambient air (cf. Fig. 9.5 (b)). While neat ZnPc exhibits a broad TSC peak around 70 K (red line), its TSC maximum is found at approx. 130 K after air exposure. The extracted net charge drops from initially  $Q = 6.92 \text{ nC}$  (as-prepared) to 3.37 nC after three days in ambient air, eventually rising to 4.10 nC (4d), 4.48 nC (5d), and 4.77 nC (6d). At increasing air exposure times, an additional TSC distribution of opposite sign emerges for temperatures  $T > 160$  K. Similar to P5, this observation could hint at p-doping by oxygen as reported for phthalocyanines.<sup>[436,437]</sup> However, ZnPc is known to feature hole and electron traps.<sup>[39,40,91]</sup> Time-wise overlapping release/existence of both charge carrier species in the thin-films could



result in a compensatory TSC, governed by recombination processes. Upon ambient air exposure, hole and electron trap concentrations in ZnPc are possibly changing independently of each other. In consequence, the compensatory TSC might be reduced, e.g. as seen for 3 d air-exposed ZnPc in comparison to as-prepared ZnPc.

For MeO-TPD (cf. Fig. 9.5 (c)), a higher amount of net charge is extracted from more trapping sites for longer air exposure times, i.e.  $Q = 1.37 \text{ nC}$  ( $N_T = 1.3 \times 10^{16} \text{ cm}^{-3}$ ) after 14 days in ambient air (orange line) in comparison to  $1.12 \text{ nC}$  ( $N_T = 1.1 \times 10^{16} \text{ cm}^{-3}$ ) as-prepared (red line). After four month in air (green line), the trap density in MeO-TPD is further increased to  $N_T = 1.5 \times 10^{16} \text{ cm}^{-3}$ , whereby the largest chunk of the total net charge  $Q = 1.54 \text{ nC}$  is extracted at temperatures significantly above the intrinsic peak  $T = 110 \text{ K}$ . Again, a decreased mobility or/and electrical field is suspected to cause this trend.

In summary, the examined HTL materials P5, ZnPc, and MeO-TPD show strong susceptibility to ambient air without intact encapsulation. The extracted charge and thus the trap density increase with longer exposure times. However, up to this point, it can not be decided, whether water or oxygen impact cause the specific TSC features.

## 9.4. Influence of Oxygen and Humid Air During the Sample Preparation

As observed in Sec. 9.3, HTL materials are susceptible to air, i.e. exhibit increasing trap densities when exposed to ambient atmosphere. In order to distinguish whether water vapor or oxygen exposure is decisive for the degradation, two separate experiments are conducted as sketched in Fig. 9.5 (d) (2) and (3). First, oxygen is added to the Lesker deposition chamber during the evaporation of the HTL materials. While the overall chamber pressure is usually at approx.  $1 \times 10^{-7} \text{ mbar}$ , it is increased here to  $7 \times 10^{-6} \text{ mbar}$ . Hence, the oxygen partial pressure is  $6.9 \times 10^{-6} \text{ mar}$ , which equals an oxygen molar ratio of 0.986 in the residual gas mixture. However, this results only approx.  $5 \times 10^{16}$  oxygen molecules inside the evaporation chamber.<sup>3</sup>

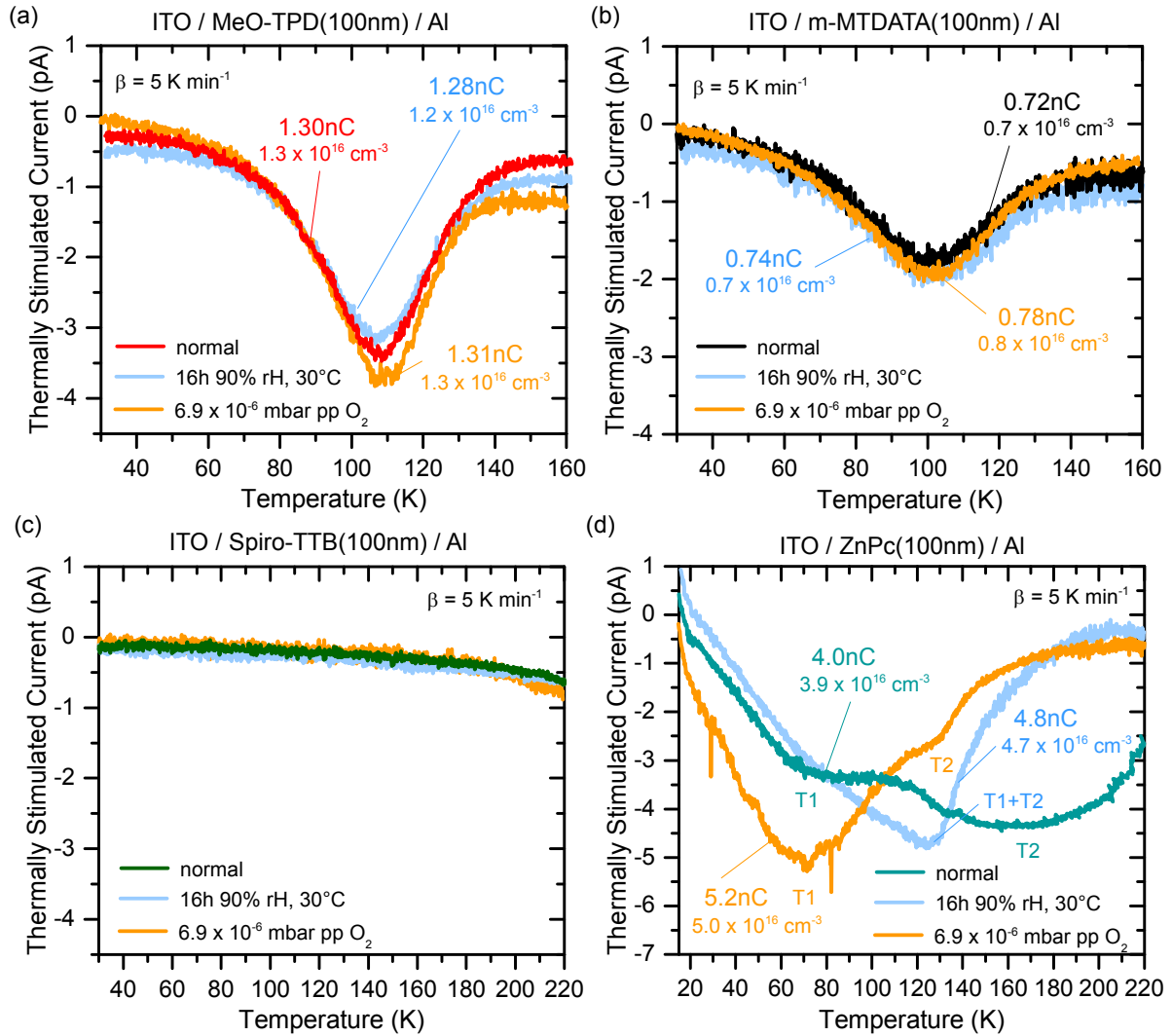
For the second experiment, the HTL layers are exposed to humid air for 16 h in a climate cabinet. The humidity is set to 90% rH at 30 °C. Afterwards, the sample is transferred to UHV again, where the aluminum top contact is evaporated on top.

Figure 9.6 compares TSC spectra of MeO-TPD (a), m-MTDATA (b), Spiro-TTB (c), and ZnPc (d) for the different processing conditions. In case of MeO-TPD and m-MTDATA, neither a spectral change nor an increase of the released net charge is obtained when the HTL is exposed to oxygen (orange lines) or humid air (light blue lines). The trap densities are constant at approx.  $1.3 \times 10^{16} \text{ cm}^{-3}$  (MeO-TPD) and  $0.7 \times 10^{16} \text{ cm}^{-3}$  (m-MTDATA). Furthermore and in accordance to previous results from Sec. 8.2 and Sec. 9.3, Spiro-TTB does not feature any TSC response in the examined temperature range, independently on the processing conditions.

ZnPc, however, shows significant TSC spectral changes (cf. Fig. 9.6 (d)) when exposed to oxygen (orange) or humid air (light blue). The HTL processed at standard conditions (cyan) exhibits an extended TSC spectrum with two prominent features: a shoulder T1 around 80 K and a broad peak T2 between 140 K and 200 K. Summing up both, a net charge of 7.6 nC is extracted, which results in a lower-limit estimate of the

<sup>3</sup>Assuming an ideal gas, i.e.  $p \cdot V = n \cdot R \cdot T$ , the oxygen amount in the  $V = 0.3 \text{ m}^3$  Lesker chamber is  $n = 8.3 \times 10^{-8} \text{ mol}$ . This equals  $n \cdot 6.022 \times 10^{23} = 5 \times 10^{16}$  oxygen molecules.

trap density of  $N_T = 7.4 \times 10^{16} \text{ cm}^{-3}$ . Evaporated under oxygen partial pressure, the shoulder T1 is more pronounced and occurs as a peak at 70 K. The broad signal T2 is almost vanishing, solely a small feature at 130 K remains. The majority of charge carriers are extracted at lower temperatures as compared to neat ZnPc, whereas the total net charge is  $5.2 \text{ nC}$  ( $N_T = 5.0 \times 10^{16} \text{ cm}^{-3}$ ). When ZnPc is exposed to humid air after processing the HTL, the extracted net charge is  $4.8 \text{ nC}$  ( $N_T = 4.7 \times 10^{16} \text{ cm}^{-3}$ ). Interestingly, the TSC spectrum is very similar to what has been recorded for complete ZnPc samples degraded via storing in air (cf. Fig. 9.5 (b)). In both cases, the TSC signal increases steadily until its maximum T1+T2 at 130 K, before it converges to zero again.



**Figure 9.6.:** TSC spectra ( $\beta = 5 \text{ K min}^{-1}$ ) of 100 nm intrinsic (a) MeO-TPD (red), (b) m-MTDATA (black), (c) Spiro-TTB (green), and (d) ZnPc (cyan), all evaporated at normal UHV Lesker conditions ( $p = 1 \times 10^{-7} \text{ mbar}$ ). TSC spectra for the same HTL materials evaporated at  $6.9 \times 10^{-6} \text{ mbar}$  oxygen partial pressure are presented in orange. Light blue lines represent the TSC spectra, at which the HTL materials are exposed to humid air (90% rH,  $30^\circ \text{C}$ ) for 16 h before the top contact is built. Only for ZnPc, the extracted net charge, i.e. the trap densities, increase significantly.

The interpretation of the present results in this section is not unambiguous. Materials with higher ionization potentials ( $\text{IP} \geq 5.2$ ) as Spiro-TTB or the similar NPB and BF-DPB are not affected trap-wise by humid or oxygen-containing processing conditions, at least for the scanned temperature range 10...220 K. The

highly amorphous MeO-TPD and m-MTDATA do not exhibit any change either. Only for the polycrystalline ZnPc,<sup>[353]</sup> the processing conditions influence its TSC spectrum. This disparity might be attributed to morphological issues. Impurity diffusion into densely packed amorphous layers is expected to happen on a longer timescale than for materials with a large number of grains and thus grain boundaries such as ZnPc or pentacene.<sup>[128]</sup> The necessary recovery of UHV conditions after gas exposure, prior to the top contact fabrication (approx. 1 h), on the other hand, is suspected to remove large portions of the impurities (vacuum annealing). Here, further studies with varying exposure times, humidities, partial pressures, temperatures (to speed up or slow down diffusion), and material systems are suggested. ZnPc, however, reveals a strong susceptibility to both oxygen and humid air. Due to the complex shape and evolution of the TSC spectra, it is not possible to conclude which peak corresponds to what impurity for the present data. Moreover, it is likely that hole and electron traps are introduced and the TSC is partially compensated due to internal recombination before successful extraction of the charge carriers. Hence, a way to identify the polarity of traps is presented in the following section.

## 9.5. Trap Polarity, O<sub>2</sub> Storage, and Low-T Mobility

**Spacer Layer Concept.** The species of the trap distributions, i.e. hole or electron trap, appearing in the TSC spectra can be easily identified when additional spacer layers (SLs) are placed between the trap-containing material and the adjacent extraction contacts. Consequently, the length of the extraction pathway for holes will be increased, if a thick SL is present next to the ITO. The TSC signal shifts to higher temperatures. Electrons are delayed during TSC runs when a thick SL is placed at the aluminum side. Ideally, Spiro-TTB is chosen as spacer material, since it is trap-free within a reasonable temperature range, i.e. no TSC signal originating from Spiro-TTB is recorded up to 220 K as discussed for Fig. 9.4 (b).

**Built-In Voltage via C(V) Spectroscopy.** TSC spectra and their peak positions must be compared at equal extraction fields  $F$  as discussed in Sec. 7.2. In good approximation, the extraction field is the quotient of the voltage (built-in + bias) and the total sample thickness. Hence, an exact built-in voltage estimate is required.

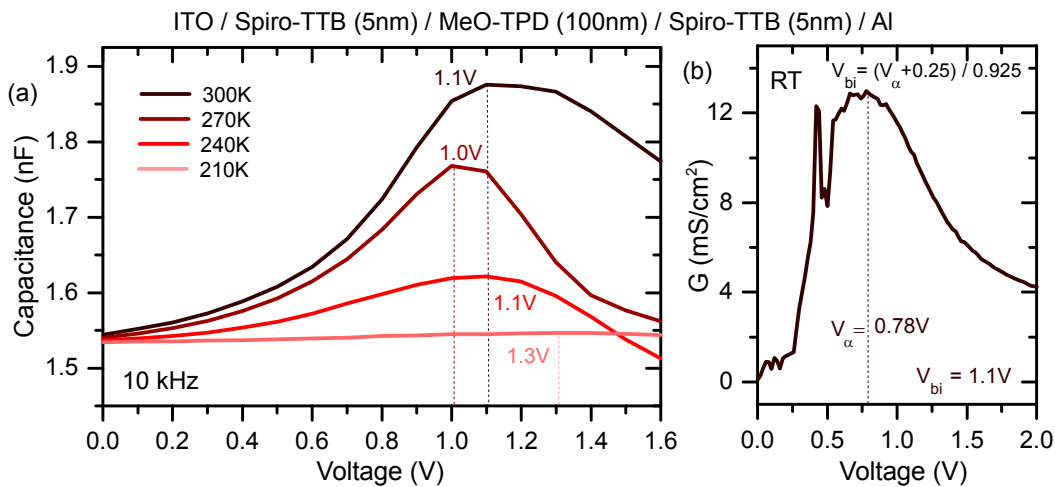


**Figure 9.7.:** (a) Built-in voltage  $V_{bi}$  estimation at different  $T$  for 100 nm MeO-TPD with two 5 nm Spiro-TTB spacer layers close to the sandwiching ITO and Al contacts. The C(V) experiments are conducted at 10 kHz. (b)  $V_{bi}$  estimate from the differential conductance function  $G(V)$ , i.e. the transition point  $V_\alpha$  (cf. 8.2) at room temperature.

In this section, capacitance-voltage measurement are conducted. The  $C(V)$  peak is identified with the built-in voltage  $V_{bi}$ . At voltages beyond  $V_{bi}$ , the depletion region collapses as more and more charge carriers are injected and flood the device. The  $C(V)$  spectra are typically taken for frequencies  $f = 10$  kHz, where the capacitive trap response is minimal. Figure 9.7 (a) depicts  $C(V)$  results for 100 nm MeO-TPD sandwiched by 5 nm Spiro-TTB at temperatures from 300 K to 210 K. Down to 240 K, the built-in potential is constant at  $1.1 \pm 0.1$  V. This results agrees with  $V_{bi}$  obtained from the transition voltage  $V_\alpha$  of the differential conductance function  $G(V)$ , shown in Fig. 9.7 (b). Below 240 K, the capacitance peak indicating  $V_{bi}$  shifts reasonably to higher voltages. The reason for that is seen in slower hopping transport at lower temperatures. Due to mobility loss,<sup>[180]</sup> the charge carriers require more forward bias, i.e. electric field, to flood the sample within an impedance high-frequency half-cycle. In the following, the built-in potential is considered to be temperature-independent, which is a reasonable assumption for intrinsic samples. The  $V_{bi}$  values are extracted at room temperature and 10 kHz. Hereby, each sample features the configuration ITO/Spiro-TTB/HTL/Spiro-TTB/Al to maintain equal interfaces, i.e. interface dipoles.

**Trap Polarity.** Figure 9.8 (a) shows TSC spectra of 100 nm MeO-TPD. The  $C(V)$  scans to estimate  $V_{bi}$  are plotted in Fig. 9.8 (b). For a symmetric configuration of 5 nm Spiro-TTB / MeO-TPD / 5 nm Spiro-TTB, a prominent peak appears around  $T_{max} = 109$  K (red line). The extracting field is approx.  $10 \times 10^4$  V cm<sup>-1</sup> ( $V_{bi} = 1.1$  V). When the SL thickness next to the ITO electrode is increased to 50 nm Spiro-TTB, the TSC peak shifts to 121 K (thin blue line). Here, a built-in voltage  $V_{bi} = 1.2$  V is obtained, which results in an electric field  $F = 7.7 \times 10^4$  V cm<sup>-1</sup>. By applying a reverse bias voltage of 0.45 V, the field strength is increased to  $10.6 \times 10^4$  V cm<sup>-1</sup>, i.e. similar to the symmetric configuration. The corresponding TSC spectra (thick blue line) has its signal peak at 115 K.  $\Delta T = 6$  K implies that released charge carriers are delayed upon extraction by the thick spacer layer near the ITO, which is the hole-selective contact. Evidently, the extracted charge carriers are holes and the trapping centers are hole traps. The control experiment confirms this result. When a 50 nm-thick Spiro-TTB spacer layer is located next to the aluminum contact, the TSC spectrum (green line) is not significantly affected. For an extraction field  $F = 10.6 \times 10^4$  V cm<sup>-1</sup> ( $V_{bi} = 1.65$  V), i.e. similar to the symmetric configuration, the TSC peak is at 110 K. The extracted net charge is equal at approx.  $1.4 \pm 0.2$  nC for all compared structures, which refers to a trap density  $1.4 \times 10^{16}$  cm<sup>-3</sup>.

Substituting MeO-TPD with m-MTDATA, the same observation is made (cf. Fig. 9.8 (d) and (e)). At similar extraction fields  $F = 8.2...9 \times 10^4$  V cm<sup>-1</sup>, the TSC peak is shifted to higher temperatures from  $T_{max} = 111$  K (black line) to 122 K (thick blue line) when the Spiro-TTB SL thickness between the ITO contact and the m-MTDATA is increased from 5 nm to 50 nm. In order to match the electric fields, a reverse bias of 0.37 V is required. Without reverse bias, the built-in voltage of approx. 0.9 V solely provides a substantially weaker extraction field  $F = 5.8 \times 10^4$  V cm<sup>-1</sup>. Consequently, the TSC peak is recorded even later at 126 K (thin blue line). Again, evidence is given that the trapped charge carriers are holes for this prominent TSC peak in m-MTDATA. Independently on the actual spacer layer thickness, a net charge of approx. 2.0 nC is collected from the samples. This number corresponds to a hole trap density of  $1.9 \times 10^{16}$  cm<sup>-3</sup>.

Examining ZnPc samples, again extended TSC spectra with several shoulders and peak features are conspicuous (cf. Fig. 9.8 (g)). For the symmetric configuration with 5 nm Spiro-TTB on each side of the 100 nm ZnPc layer, a broad peak with  $T_{max} = 190$  K is found (cyan line). In total, a net charge of 7.6 nC ( $N_T \geq 7.4 \times 10^{16}$  cm<sup>-3</sup>) is extracted by  $F = 11.8 \times 10^4$  V cm<sup>-1</sup>. When the SL thickness next to ITO is increased to 50 nm, suddenly a TSC peak of positive sign appears around 130 K (blue line) and significantly less charge, i.e. 2.7 nC ( $N_T \geq 2.6 \times 10^{16}$  cm<sup>-3</sup>), is extracted. The only reasonable explanation is here that

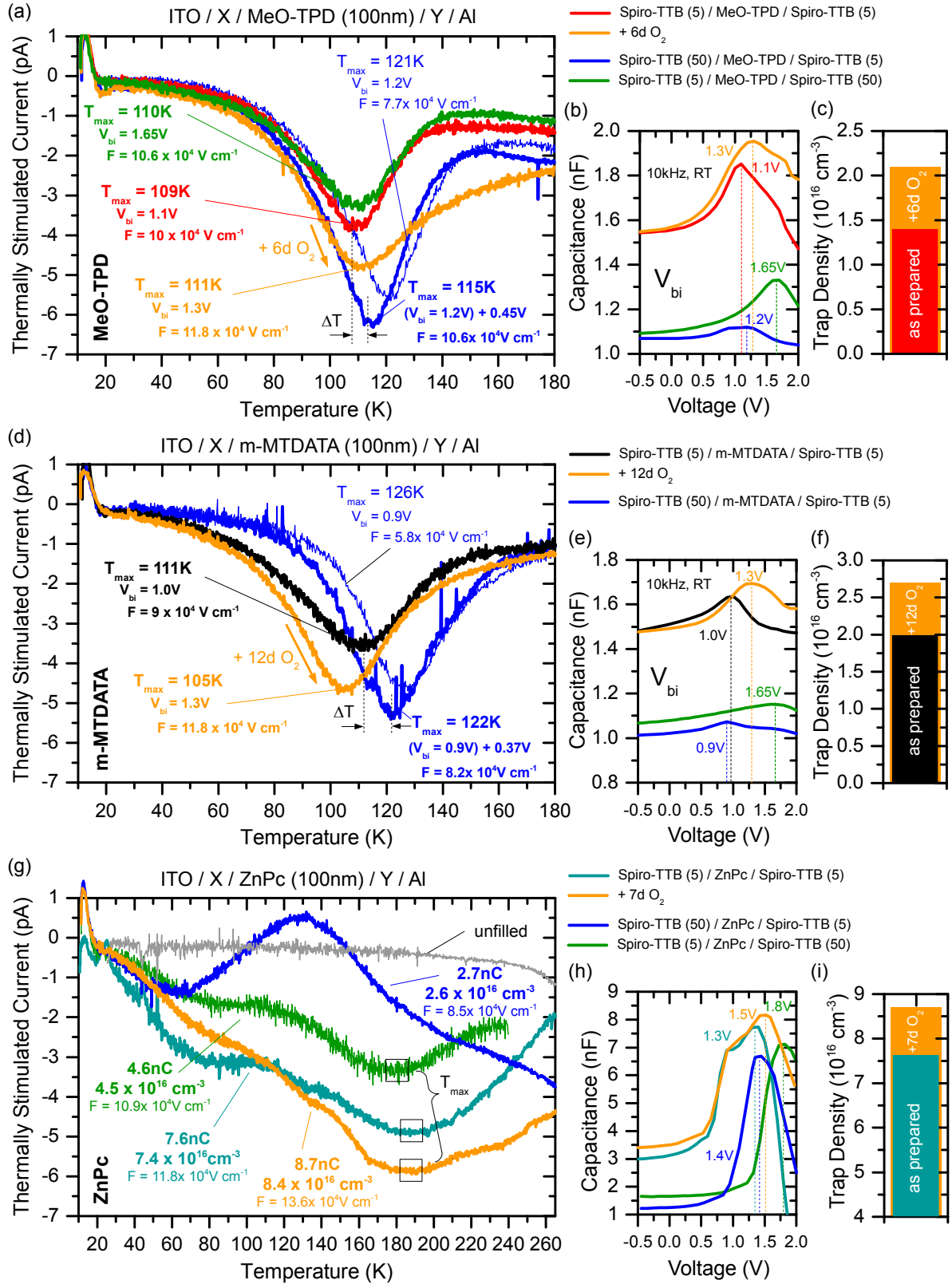


**Figure 9.8.:** TSC spectra ( $\beta = 5 K min^{-1}$ ) of 100 nm (a) MeO-TPD (red) (d) m-MTDATA (black), or (g) ZnPc (cyan) symmetrically sandwiched by 5 nm Spiro-TTB spacer layers (SLs). In blue (green), the SL next to ITO (Al) is increased to 50 nm, which delays holes (electrons) by  $\Delta T$ . Orange lines illustrate the symmetric samples after pure O<sub>2</sub> exposure for several days. (b),(e),(h) Built-in potentials via C(V). (c),(f),(i) Trap density increase upon O<sub>2</sub> exposure.

released holes are delayed by the thick SL next to ITO (note that the initial peak at  $T_{\max} = 190$  K is shifted to  $> 240$  K), while electron extraction is not hindered. A positive TSC occurs for 100 K to 160 K.

If the 50 nm Spiro-TTB SL is evaporated next to aluminum, the TSC spectrum remains unaffected in shape but its amplitude is reduced by approx. a factor 1.5 (green line). Despite the thicker sample as compared to the symmetric configuration, the extraction field is similar ( $10.9$  to  $11.8 \times 10^4$  V cm $^{-1}$ ). Interestingly, the built-in potential increases to 1.8 V from 1.4 V for the symmetric sample. Similar increases of  $V_{bi}$  are observed for all HTL materials (cf. Fig. 9.8 (b), (e), (h)). Although the formation of a considerable electric dipole is suspected at the Spiro-TTB / aluminum interface, the exact reason remains unclear here. The same goes for the reduced amount of extracted net charge of 4.6 nC ( $N_T \geq 4.5 \times 10^{16}$  cm $^{-3}$ ). One explanation might be increased recombination of released holes and electrons, which is more probable once electrons are delayed upon extraction, i.e. stay longer in vicinity of the holes. Consequently, less charge carriers reach their extraction point and the TSC is smaller.

**O<sub>2</sub>-Storage of HTL.** After the initial TSC measurements, the samples containing HTLs with symmetric configurations of Spiro-TTB are removed from the cryostat and put into a vacuum sealed degradation chamber. Prior, the chamber has been baked out for several hours at 110 °C to remove water traces. After purging with pure oxygen (Air Liquide, 99.995% purity), the samples are stored in complete oxygen atmosphere at approx. 2 bar for at least a week, until they are remeasured via TSC.

The results are illustrated in Fig. 9.8 in orange lines, respectively. Indisputably, the number of inherent traps increases for all examined HTLs, i.e. MeO-TPD, m-MTDATA, and ZnPc, when the samples are stored in oxygen. Furthermore, the impact of oxygen is clearly attributed to a distinct feature of each HTL's TSC spectrum. In case of MeO-TPD, the single peak at approx. 110 K grows. Compared to  $1.4 \times 10^{16}$  cm $^{-3}$  for as-prepared MeO-TPD, the trap density increases to  $2.1 \times 10^{16}$  cm $^{-3}$  after six days in pure O<sub>2</sub> (cf. Fig. 9.8 (c)). For m-MTDATA, the TSC peak at approx. 111 K is enlarged. After 12 days in pure O<sub>2</sub>, the trap density increases from initially  $2.0 \times 10^{16}$  cm $^{-3}$  to  $2.8 \times 10^{16}$  cm $^{-3}$ , shown in Fig. 9.8 (f). Although the ZnPc TSC spectrum is complex, i.e. revealing multiple trap distributions, the broad signal peak around 190 K grows remarkably. The lower-limit estimate of the trap density increases for seven days in oxygen from  $7.4 \times 10^{16}$  cm $^{-3}$  to  $8.4 \times 10^{16}$  cm $^{-3}$  (cf. Fig. 9.8 (i)). At the same time, the TSC signal below  $T = 120$  K is reduced. Here, further examinations for devices with spacer layer next to ITO are suggested to clarify if the number of electron traps is increasing likewise.

Remarkably, the built-in voltage of the samples is slightly increased by oxygen exposure, compare Fig. 9.8 (b), (e), and (h). Consequently, the extraction fields are higher and small shifts of the TSC spectra to lower temperatures than initially measured are observed. Probably, oxygen diffusion towards ITO could explain this phenomenon, since oxygen-treated ITO typically exhibits a higher work function.<sup>[99]</sup>

**Low-T Mobility Estimation.** The assumed charge carrier mobilities in the order of  $10^{-12}$  to  $10^{-14}$  cm $^2$ Vs $^{-1}$  to fit the TSC spectra of p-doped Spiro-TTB in Sec. 8.3 seemed rather arbitrary and require experimental validation, but are nearly not resolvable with common techniques such as OFET<sup>[129]</sup> or POEM.<sup>[422]</sup> Here, the TSC signal peak shift upon incorporation of a thick spacer layer allows to determine the charge carrier mobility in the latter. As indicated in Fig. 9.8 (a), the MeO-TPD TSC peak shifts by  $\Delta T = 6$  K from  $T_{\max} = 109$  K to 115 K in presence of 50 nm Spiro-TTB instead of 5 nm. For a linear heating rate  $\beta = 5$  Kmin $^{-1}$ , this equals a runtime difference of 1.2 min. In other words, the released holes need a traveling time of approx. 72 s to pass 45 nm Spiro-TTB on their way to the extracting electrode, which corresponds to a velocity  $v$  of  $6.3 \times 10^{-8}$  cm s $^{-1}$ . At a mean electric field of  $10.3 \times 10^4$  Vcm $^{-1}$ , a hole mobility of  $\mu = v/F = 6 \times 10^{-13}$  cm $^2$ Vs $^{-1}$  within the Spiro-TTB is estimated. When the calculation is done for the m-MTDATA TSC spectra (cf. Fig. 9.8 (d))

and  $\Delta T = 11$  K, one obtains  $\mu = 4 \times 10^{-13} \text{ cm}^2 \text{Vs}^{-1}$  at a mean electric field  $F = 8.6 \times 10^4 \text{ Vcm}^{-1}$ . These results are very satisfying, since they prove the charge carrier mobility assumptions taken earlier in Sec. 8.3 to be in the right order of magnitude.

## 9.6. Summary: Global Oxygen Trap

Trap distributions of various hole transport materials handled in presence of ambient air or pure oxygen were studied by the thermally stimulated current technique. Although interactions of organic semiconductors with ambient atmosphere such as degradation or doping effects had been observed earlier,<sup>[438]</sup> attention was drawn by growing TSC spectra signals from an aged pentacene Schottky diode. Here, the sample had been kept untouched in ambient (lab) atmosphere for more than two years. Its degradation, i.e. the increase of inherent trap densities up to  $10^{17} \text{ cm}^{-3}$  and the worsening of the current-voltage characteristics have been attributed to water/oxygen diffusion. Impurities pass the encapsulation glue and eventually the crackly aluminum top contact. Water vapor transmission rates have been assessed from literature values.<sup>[427]</sup> Oxygen transmission rates, however, had not been determined at that point, which sets up a future task.

In case of pentacene, TSC measurements revealed two prominent peaks around 80 K and 110 K, which coincided and formed a huge TSC signal peak for ongoing degradation. The TSC examinations were extended to further HTL materials, i.e. MeO-TPD, m-MTDATA, ZnPc, Spiro-TTB, NPB, and BF-DPB. A remarkable trend has been observed, as those materials with ionization potentials  $> 5.2$  eV, i.e. Spiro-TTB, NPB, and BF-DPB, did not show TSC features up to temperatures  $T \simeq 220$  K. In contrast, MeO-TPD and m-MTDATA had as-prepared one prominent peak around 100...110 K, while ZnPc exhibited a broad TSC signal distribution for 20...220 K. When samples incorporating one of the three latter HTLs were stored without encapsulation in ambient air, their TSC spectra changed within days due to impurity diffusion through the top contact. The trap densities increased, which was seen as the reason why the TSC features shifted to slightly higher temperatures at the same time. For ZnPc and P5, small thermally stimulated currents of opposite sign were recorded at  $T = 160...240$  K. Here, hole capture/recombination due to inherent electron traps or introduced oxygen-type dopant impurities was suspected.

In order to specify whether oxygen or water impurities have caused the signal increase of specific TSC features, the processing parameters during sample preparation were varied. Evaporated at an oxygen partial pressure of  $6.9 \times 10^{-6}$  mbar, the TSC spectra (i.e. the observed trap distributions) from MeO-TPD, m-MTDATA, and those materials with IP  $> 5.2$  remained unaffected. Similarly, no change of the TSCs was registered when the HTLs were exposed to humid air (90% rH, 30 °C) for 16 h prior to the fabrication of the top contact. Most probably, the exposure time and/or the number of impurities were too low. It has been suggested that water and oxygen diffusion into these densely packed amorphous organic semiconductor layers takes place considerably slowly and large impurity portions had been removed already by re-establishing UHV conditions prior to the top contact processing. However, a larger variation of processing parameters is strongly advised for future examinations. In case of ZnPc, the apparent trap densities after humid air/oxygen exposure were altered by several  $1 \times 10^{16} \text{ cm}^{-3}$  in comparison to standard sample fabrication. The polycrystalline growth with a high number of grain boundaries might have been beneficial for impurity diffusion. As ZnPc's TSC spectrum changes drastically upon humid air and oxygen exposure, the formation of additional hole and electron traps was suspected.

The polarity of inherent traps was successfully identified via TSC for the first time in literature by a series of TSC experiments utilizing quasi trap-free Spiro-TTB spacer layers. The comparison of symmetric and

asymmetric samples revealed TSC spectra shifts to higher temperatures, i.e. a delay of released holes, when a thick spacer layer was located between the trap-containing HTL and the hole extraction contact. By that, it was shown that the prominent TSC features in MeO-TPD and m-MTDATA originate from hole traps. ZnPc exhibits hole trap signatures around 190 K, in addition to more shallow electron trap features. When samples with MeO-TPD, m-MTDATA, and ZnPc were stored without encapsulation in a vacuum chamber filled with pure oxygen for a few days, the identified hole traps increased in site densities by up to 30%. Hence, after all previous ambiguous exposure experiments, the prominent HTL traps were assigned to oxygen impurities beyond any doubt.

Finally, the spacer layer configuration allowed to determine hole mobilities in intrinsic Spiro-TTB to  $4...6 \times 10^{-13} \text{ cm}^2 \text{Vs}^{-1}$  for temperatures as low as 100 K. At similar extraction fields, holes extracted from sandwiched MeO-TPD or m-MTDATA layers were delayed due to the additional traveling pathway, i.e. the Spiro-TTB spacer layer. Such low values are hardly accessible via common mobility extraction methods, e.g. OFET measurements<sup>[129]</sup> or POEM.<sup>[422]</sup> However, their estimate is crucial for theoretical predictions on thermally stimulated currents and their dispersive transport. The obtained mobility agrees very well with previous TSC modeling assumptions in the Ch. 8, discussing traps in p-doped Spiro-TTB.

## Global Oxygen Trap

The final chart Fig. 9.9 presents the essence of this chapter and combines the results of the previous sections. Figure 9.9 (a) depicts the temperature dependent positions of the hole transport level for the various HTL materials, as calculated in Sec. 5.2.3. These positions were computed for Gaussian-type hopping site distributions, whose widths had been estimated from (rescaled) UPS spectra in Sec. 5.1.6. Ionization potentials, i.e. the energetic differences between the vacuum level and the HOMO onsets, are assessed from the UPS spectra in Sec. 5.1. Figure 9.9 (b) shows TSC spectra of 100 nm MeO-TPD (red), m-MTDATA (black), and ZnPc (cyan). The oxygen-related features, identified previously in Fig. 9.8, are fitted in accordance to Sec. 7.2, i.e. assuming dispersive transport of thermally released holes. The results are drawn in dashed lines in Fig. 9.9 (b) and listed in Tab. 9.2. For pentacene, the trap distribution estimation from TSC's initial rise for aged P5 (cf. Fig. 9.9 (c)) is utilized.

Combining all those results, an energy scheme for all examined HTL materials is sketched in Fig. 9.9 (d). It shows the HOMO DOS on a logarithmic scale for each material at energies determined by their IP. The oxygen-related trap distributions are located at trap energies  $E_T = \text{IP} + 2\sigma - (E_0 - E_T)$ . Remarkably, the trap depths for all observed distributions are within a close range, i.e.  $E_T = 4.67...4.83 \text{ eV}$ . This finding strongly suggests the existence of a global oxygen trap, which should be relevant for all organic hole transport materials. For P5, MeO-TPD, and m-MTDATA, the trap DOS slightly exceeds the intrinsic HOMO DOS function around the trap energy. In case of ZnPc, a large number of gap states drastically exceeding the intrinsic DOS is obtained. The only reason why no TSC signal is observed for Spiro-TTB, BF-DPB, and NPB is seen in their significantly higher IP. If the TSC temperature scan range is further increased to RT and above, enough thermal energy will be provided to release charge carriers from these materials. However, the current cryostat setup is limited to only 300 K. Further experiments should clarify whether the trap densities could be decreased by post-annealing of the samples, i.e. oxygen is reversibly physisorbed or irreversibly chemisorbed. HTL storing in inert gases such as nitrogen or argon should not affect the TSC spectra. Moreover, predictive calculations on the energy levels of oxygen within the HTL material matrices are required.



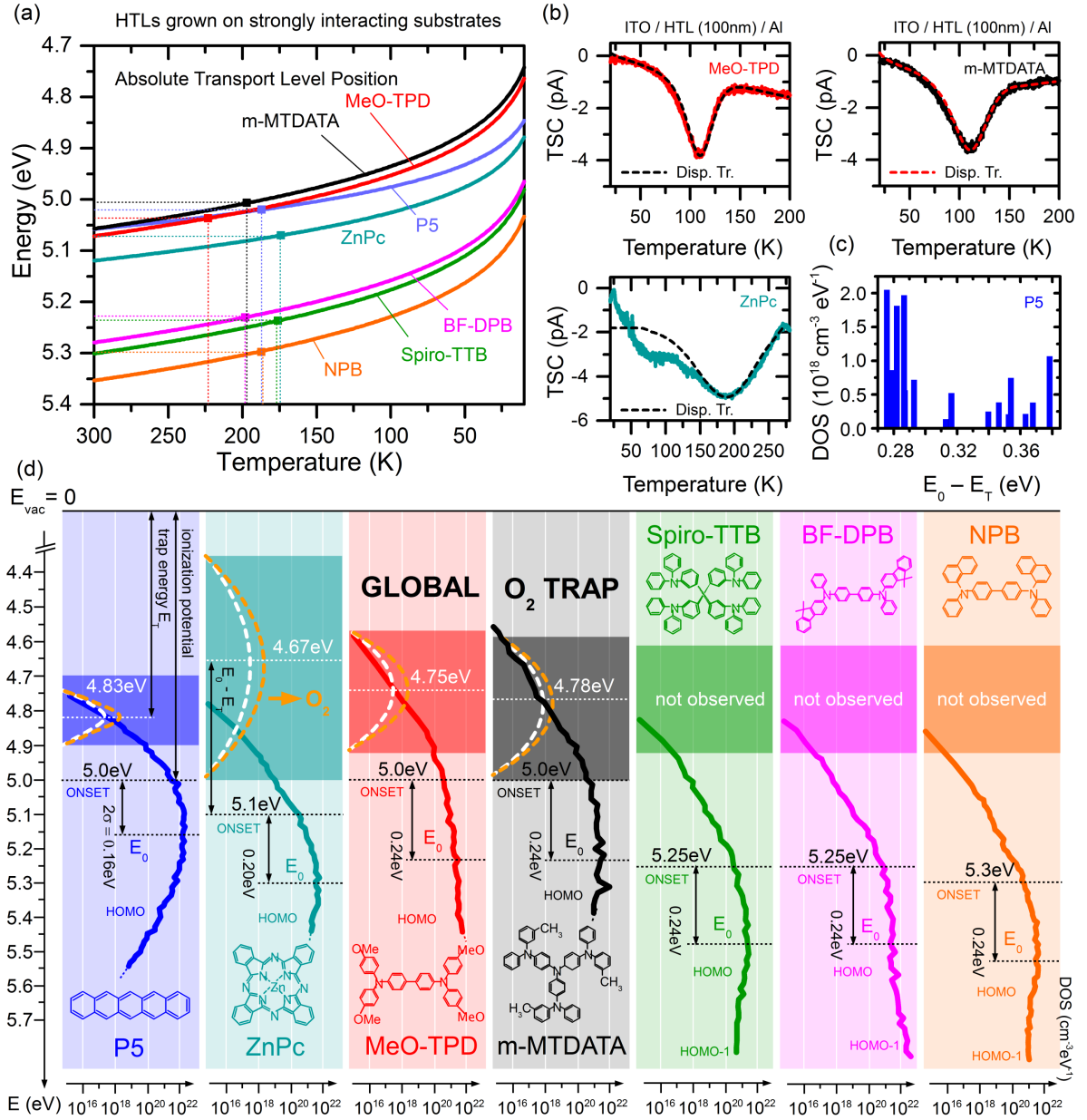


**Figure 9.9.:** (a) Hole transport level positions calculated in Sec. 5.2.3 versus temperature for the examined set of hole transporting materials, grown on strongly interacting substrates. The DOS parameters are found in Tab. 5.4. (b) TSC spectra of 100 nm MeO-TPD (red), m-MTDATA (black), and ZnPc (cyan). Oxygen-related features are fitted assuming dispersive transport of thermally released holes (dashed lines) according to Sec. 7.2. Hereby, the parameters and results are listed in Tab. 9.2. (c) Trap DOS for aged pentacene obtained from fractional TSC spectra in Fig. 9.1. (d) Global oxygen trap estimation for various HTL materials. The IPs, i.e. the difference between the vacuum level  $E_{\text{vac}}$  and the HOMO onset, are obtained via UPS in Sec. 5.1. UPS spectra, rescaled according to Sec. 5.1.6, illustrate the respective HOMO DOS. The absolute trap energies  $E_T$  are calculated from the individual trap depths ( $E_0 - E_T$ ), the IP and the HOMO disorder parameter  $\sigma$  as  $E_T = \text{IP} + 2\sigma - (E_0 - E_T)$ .

**Table 9.2.:** Sample parameters and fit results for the oxygen-related traps in TSC spectra of MeO-TPD, m-MTDATA, and ZnPc in Fig. 9.9 (b). Thermally stimulated release of trapped holes towards  $E_{\text{Tr,h}}(T)$ , shown in Fig. 9.9 (a), and dispersive transport are assumed.

	MeO-TPD	m-MTDATA	ZnPc
thin-film thickness (nm)	100	100	100
built-in potential $V_{\text{bi}}$ (V)	1.1	1.0	1.3
extraction field $F$ ( $\text{V cm}^{-1}$ )	$1 \times 10^5$	$9 \times 10^4$	$1.2 \times 10^5$
TSC heating rate $\beta$ ( $\text{K min}^{-1}$ )	5	5	5
attempt-to-escape frequency $\nu$ ( $\text{s}^{-1}$ )	$10^{11}$	$10^{11}$	$10^{11}$
trap depth ( $E_0 - E_T$ ) (eV)	0.49	0.46	0.63
trap width $\sigma$ (meV)	43	55	90
trap density $N_T$ ( $\text{cm}^{-3}$ )	$2.5 \times 10^{16}$	$3.1 \times 10^{16}$	$7.4 \times 10^{16}$
mobility $\mu$ ( $\text{cm}^2 \text{Vs}^{-1}$ )	$4 \times 10^{-13}$	$7 \times 10^{-13}$	$5 \times 10^{-11}$

## Conclusion and Outlook

It has been the aim of this thesis to identify and quantify charge carrier traps in organic semiconductors, and provide insights into the mechanisms causing them. Only by gaining that knowledge, material and device design of organic semiconductor applications can be improved to establish highly efficient organic electronics. Charge carrier traps were examined utilizing the techniques of photoelectron spectroscopy, impedance spectroscopy, and first and foremost thermally stimulated currents.

Since the latter scans the charge carrier emission of traps for a wide temperature range from almost room temperature down to 10 K, it was necessary to determine the temperature-dependent transport level positions  $E_{Tr}(T)$  for the examined materials. First, UPS measurements on the hole transport materials BF-DPB, Spiro-TTB, MeO-TPD, m-MTDATA, pentacene (P5), and ZnPc were performed and analyzed to gain information on the energetic disorder of their HOMO DOS. The disorder parameters  $\sigma_{UPS}$  obtained from the UPS spectra ranged between 0.15 eV (P5) and 0.24 eV (m-MTDATA). However, these results were broadened by approx. a factor two, which was corrected by rescaling the energy axis according to literature values of disorder parameters, yielding  $\sigma = 0.08...0.12$  eV. The UPS method most likely suffered from electron-phonon interaction, i.e. vibronic broadening, and secondary line excitations as well as a low signal-to-noise ratio for the current IAPP UPS setup. The examination of high-resolution UPS data<sup>[256,400]</sup> (Chiba, Japan) indicated that the HOMO DOS were in first order Gaussian distributed down to site densities of approx.  $10^{16} \text{ cm}^{-3} \text{ eV}^{-1}$ . For the present UPS data, the disorder parameters of all materials showed a weak substrate dependence, revealing a smaller  $\sigma$  when grown on weakly interacting organic substrates (Spiro-TTB:F<sub>6</sub>-TCNNQ) as compared to metal-type substrates. Only ZnPc thin-films featured a smaller  $\sigma$  on metal.

Hopping model calculations published by Arkhipov *et al.* were adapted and the obtained Gaussian distributions  $g(E)$  describing the HOMO DOS were used to compute  $E_{Tr}(T)$ . The influence of the HOMO DOS width as well as the number of states and the inverse localization radius on the transport level were discussed. In conclusion, more low energy states caused a charge carrier transport deeper in the gap. A strong delocalization (smaller  $\gamma$ ) had an identical effect. Introducing a charge carrier density raised the Fermi level in the DOS thus occupying low energy sites and shifting the transport level to towards the DOS center. The rescaled disorder parameters  $\sigma = [0.08...0.12]$  eV were used to finally determine the transport level positions of the HTL materials. In particular,  $E_{Tr}(RT)$  is above the HOMO onset. For decreasing temperatures, the transport levels relocate for several 100 meV towards the gap-mid.

One approach to identify charge carrier traps has been the exploit of the space charge region in doped organic semiconductors, where a substantial amount of deep traps hinders the generation of free holes.<sup>[183]</sup> In this thesis, Schottky diodes and p-doped thin-films comprising P5 and ZnPc were examined by impedance spectroscopy and (temperature-dependent) UPS. It was shown that the Fermi level position depends on the number of active dopants, which could be related to the incorporated molar doping ratio and the temperature. At room temperature, P5 (ZnPc) p-doped by a  $MR \geq 10^{-3}$  ( $10^{-2}$ ) was in dopant reserve and the doping

efficiency was considerably lower than 1. Moreover, the thermal energy seemed to control the CT transfer state dissociation, which is why a complete freeze-out was observed for p-ZnPc at temperatures below 100 K. During freeze-out, the classical semiconductor regimes of dopant reserve, doping saturation, and trap-filling were identified by comparison of impedance spectroscopy results and (temperature-dependent) UPS studies. Throughout all dopant regimes, the Fermi level position has been decisive for the trap response in the organic semiconductors. A change of the trap occupation due to the small-signal excitation occurs close to the intersection points of  $E_F$  and the trap distributions. Consequently, undoped/'frozen' organic semiconductors revealed only a small trap capacitance, since most of the traps were 'inert'. In P5 and ZnPc, deep traps were identified at energies of approx. 0.52...0.65 eV above the hole transport level at RT. Upon doping, the deep trap concentrations saturated at approx.  $1 \times 10^{17} \text{ cm}^{-3}$  (P5) and  $5 \times 10^{17} \text{ cm}^{-3}$  (ZnPc), and shallow trap distributions emerged at doping concentrations  $> \text{MR} 0.002$  in both materials. In case of P5, an additional material purification step reduced the number of deep traps. The found trap densities were in accordance to previous UPS results,<sup>[183]</sup> which, however, show a higher trap depth, most probably due to the energetic broadening of UPS.

The second approach to investigate charge carrier traps has been the thermally stimulated current (TSC) technique. Here, charge carriers were trapped at 10 K within the organic semiconductor thin-film and subsequently released via heating. Several methods to analyze thermally stimulated current (TSC) spectra were assessed. In conclusion, only a dispersive transport model reported earlier by Arkhipov/Adriaenssens and Nikitenko *et al.* described the extraction field- and sample thickness dependence of TSC spectra adequately. In that sense, a TSC run is a thermally stimulated time-of-flight experiment. At a critical release temperature, which depends on the trap depth, captured charge carriers are released to the temperature-dependent transport level. Typical attempt-to-escape frequencies were approx.  $\nu_0 = 1 \times 10^{11} \text{ s}^{-1}$ , as obtained earlier for deep traps in ZnPc by impedance spectroscopy. Motivated by the built-in field and an optional external electric field, the released charge carriers perform electric drift motions towards the extracting electrode. The time between release and recording the charge carriers at the measure unit is determined by their pathway length and their speed of motion. On their way, they are susceptible to re-trapping by sites at lower energies than the transport level. The dispersive transport model was applied to intrinsic MeO-TPD and successfully described the observed TSC peak around  $T_{\text{max}} \simeq 100 \text{ K}$ , which shifted to lower temperatures for increasing readout voltages. Gaussian distributed traps ( $\sigma \simeq 0.04 \text{ eV}$ ) were found at a depth  $E_T \simeq 0.5 \text{ eV}$  with respect to the HOMO center and a density of approx.  $2 \times 10^{16} \text{ cm}^{-3}$ .

Further, thermally stimulated current spectra of doped organic semiconductors have been analyzed. For the HTL material Spiro-TTB, p-doped by F<sub>6</sub>-TCNNQ, shallow trap signatures ( $E_0 - E_T = 0.4 \text{ eV}$ ) close to the transport level were found. Hereby, a thickness variation of the doped layer clearly identified the bulk as source of the TSC signal. With decreasing dopant concentration (from MR 0.253 to MR 0.031), the TSC peak originating from the doped layer dissolved in shape and its main part shifted to higher temperatures ( $T = 80 \dots 100 \text{ K}$ ). The latter trend was explained by a decrease in hole mobility at lower doping concentrations from  $10^{-12}$  to  $10^{-14} \text{ cm}^2 \text{ V s}^{-1}$ .

In C<sub>60</sub>F<sub>36</sub> p-doped ZnPc:C<sub>60</sub> 1:1 absorber blends (MR 0.002 and MR 0.001), a deep trap distribution was identified, which is absent in undoped blends. The trap densities of approx.  $10^{16} \text{ cm}^{-3}$  were only a few percent of the total dopant density. In order to compute trap depths, UPS spectra (taken from Ref.<sup>[362]</sup>) of neat and blended ZnPc and C<sub>60</sub> were quantitatively analyzed. For the 1:1 blend, significant energetic broadening of both material's HOMOs was found. The obtained trap energies at  $E_T = 0.48 \pm 0.1 \text{ eV}$  above the HOMO center were comparable to the impedance spectroscopy results of identical devices reported by Fischer *et*

*al.*<sup>[40]</sup> They related the observed signal responses to inherent charge carrier traps of the ZnPc:C<sub>60</sub> blend, which were 'visible' upon trap-filling by doping.<sup>[40]</sup> Here in this thesis, the TSC results on those blends and especially p-doped Spiro-TTB were seen different, i.e. caused by the doping itself. In undoped thin-films, no TSC signals are recorded, although electric filling provides excess charge carrier to populate possibly existing trap sites. More likely, the observed traps are directly caused by dopant (Coulomb) interaction with the host system. Furthermore, this interpretation coincides with the observation of shallow traps ( $N_T \simeq 10^{16} \text{ cm}^{-3}$ ) in p-doped P5 and ZnPc earlier via impedance spectroscopy.

Finally, the stability of various organic hole transporting materials upon water and oxygen exposure during sample fabrication and storage was examined via TSC. Trap densities in the order of  $N_T = 10^{16} \text{ cm}^{-3}$  were found in intrinsic pentacene, ZnPc, MeO-TPD, and m-MTDATA. These trap densities increased partially by more than 100 % when the de-encapsulated devices were stored in ambient air or pure oxygen atmosphere for few days. Polycrystalline P5 and ZnPc thin-films were more susceptible than amorphous MeO-TPD and m-MTDATA. It was suspected that impurities diffusively pass the aluminum top contact, i.e. the only remaining barrier between the atmosphere and the organic semiconductors, and penetrate into the thin-films. Similar TSC experiments were conducted for thin-films fabricated under oxygen partial pressure and exposed to moist air exposure during the fabrication. A necessary vacuum annealing step before the evaporation of the top contact seemed to minimize additional contamination, especially in amorphous-type thin-films.

The found traps in MeO-TPD, m-MTDATA, and ZnPc<sup>1</sup> were identified as hole traps by the exploit of release time differences when the trap-containing thin-films were sandwiched by 'trap-free' Spiro-TTB spacer layers. For the latter, a charge carrier mobility was determined to  $\mu = 10^{-13} \text{ cm}^2 \text{ Vs}^{-1}$  at approx. 100 K. This spacer layer concept and its capability to determine the polarity of trap distributions has been completely new to TSC experiments. Furthermore, it has emphasized the necessity to consider the charge carrier transport at low temperatures and not only their temperature-dependent release when analyzing TSC results.

Combining the knowledge gained of the temperature-dependent transport levels of the HTL materials and the dispersive transport of thermally released charge carriers, a global hole trap distribution caused by oxygen impurities was identified. For Pentacene, ZnPc, MeO-TPD, and m-MTDATA it has been found at energies of 4.7...4.8 eV. In case of materials with a higher ionization potential such as Spiro-TTB, BF-DPB, or NPB, this global trap has been suspected to occur in TSC experiments close to room temperature, which, however, were not accessible due to setup limitations.

## Outlook

Although the results of this work represent a step forward in understanding the nature of charge carrier traps in organic semiconductors, several questions and tasks remain untouched. It has to be the aim of further investigations to combine the largest possible quantum of results on trap spectroscopy, charge carrier transport, and thin-film aggregation, in particular assessing the energetic DOS disorder. Only by that, a coherent appraisal is obtained and weak points, e.g. of materials, can be studiously eradicated. The opportunities for chemistry, material science, and device design are here manifold. In the following, some starting points for further work shall be given. Hereby, their order does not represent their importance.

It has been shown in Chapter 5 that the UPS setup is rather limited in determining the energetic disorder of an organic semiconductor system. On one hand, the signal-to-noise ratio of the present IAPP system is bad in comparison to top-notch UPS systems such as in Chiba, Japan.<sup>[256,400]</sup> Additional, secondary line

<sup>1</sup>precisely: ZnPc exhibits hole and electron traps. The TSC spectra are superimposed.

emission, which could be suppressed by using a monochromator or even synchrotron radiation, is a big problem. Since replacements and additional personal are costly, a collaboration is highly recommended. On the other hand, the UPS method itself suffers from signal broadening as explained previously. The determined UPS disorder parameters do not equal the energetic disorder of the DOS, but have to be 'translated'. In the present thesis, this was done via comparison with literature values from computer simulations or charge carrier transport experiments. Hence, a workaround should be a catalog of UPS and non-UPS results for several materials, which allows to calculate a 'translation function' for the individual UPS system. Here, the group of Denis Andrienko (Mainz, Germany) shows great expertise in computing energetic disorders.<sup>[383]</sup> Possibly, charge carrier localizations  $1/\gamma$  can be determined for each material and thin-film formation in this context. Afterwards, a next, important step is the examination of the energetic disorder in doped films, mixed (blend) films, and blends grown at different substrate temperatures. The suspected DOS broadening should ascertainably affect the transport level positions.

Significant progress in understanding and analyzing thermally stimulated currents has been made by combining thermally stimulated charge carrier release and dispersive transport of the released charge carriers. However, the modeling requires some essential parameters to obtain correct trap depths. It has been found, that the charge carrier extraction is driven by the built-in potential  $V_{bi}$ , which was estimated from current-voltage characteristics and C(V) spectroscopy. The values seemed to be heavily influenced by interface dipoles between the organic semiconductors and the electrodes, which should be verified via UPS. Moreover, the independence of  $V_{bi}$  on the temperature has to be examined. Another crucial parameter has been the extraction mobility. For Spiro-TTB, a mobility of approx.  $10^{-13} \text{ cm}^2 \text{ Vs}^{-1}$  was found around 100 K by utilizing the new spacer layer concept. The ideal result would be a complete data set  $\mu(T)$  for all examined materials. Here, thin-films comprising different trap depths (i.e. release temperatures) could be combined with spacer layers of the sought material to yield further estimates of  $\mu(T)$ .

Concerning the shallow traps found in doped HTLs, additional experiments are required to conclude on their origin. Both impedance spectroscopy and TSC reveal shallow trap densities in the order of  $10^{16} \text{ cm}^{-3}$ , which arise only in case of p-doping. Up to now, it is not resolved if these are Coulomb distortions of the host system or additional, possible acceptor levels  $E_A$  as introduced by Tietze.<sup>[91,207]</sup> The next step has to be a comparative study of well-known material systems such as P5:C<sub>60</sub>, ZnPc:F<sub>6</sub>-TCNNQ, or MeO-TPD:F<sub>6</sub>-TCNNQ. Moreover, the examinations should be extended to n-doped systems.

The observed temperature-dependence of the Fermi level in ZnPc has raised several questions. Obviously, the number of the free charge carriers is determined by the ratio of inherent traps and active dopants. The latter relates to the introduced molar dopant ratio but at the same time to the most probably field- and temperature-dependent dissociation probability  $\zeta(F, T)$  of the charge transfer states host:dopant. These observations explain why a simple description in terms of Fermi-Dirac statistics is not complete and needs to be extended by a suitable description of  $\zeta$ . Furthermore, it has to be clarified if (more) active dopants cause (more) Coulomb traps within the host matrix. Combining those findings could explain the ambiguous trends in Mott-Schottky plots under temperature variation (e.g.  $N_A^-$  increasing with decreasing temperature).<sup>[401]</sup> Moreover, comparative studies of traps via impedance spectroscopy and TSC are highly suggested. Especially the hole capture parameter  $\beta = 10^{-9} \dots 10^{-10} \text{ cm}^3 \text{ s}^{-1}$ , which shifts the trap depth, should be verified.

In case of the identified global trap level in the HTL materials, further investigations are required. It has to be clarified, whether the traps are additional states at the oxygen impurities or originate from the

---

disturbed energetic order of the host. The latter option has to be checked by nitrogen or argon exposure of the organic semiconductors. The former task is more complicated and requires quantum mechanical calculations of the energy levels of (molecular) oxygen within the host matrices. Similar computations should be done for H<sub>2</sub>O complexes, which are expected to come into play when HTL materials are exposed to ambient air. Moreover, the oxygen transmission rates of the encapsulation barriers and especially the standard aluminum top contact need an evaluation, for instance via calcium tests. In that sense, impurity diffusion could be quantized and related to the actual increase in trap densities. In general, charge carrier transport experiments, e.g. conductivity or mobility measurements, would be required to show the negative impact of ambient air and especially oxygen on the various HTL materials. Since the existence of the global oxygen trap is assumed for all HTL materials, it should be observable via TSC for Spiro-TTB, BF-DPB, and NPB likewise - due to their higher IPs, however, close to room temperature. Sadly, the cryostat of the current TSC setup is restricted to temperatures below 325 K. In order to be able to scan deeper traps than done here in this thesis, another invest would be required, preferably in a fast-cooling small-volume cryostat.

Although it could not be outlined in detail in this thesis, old material batches quite often stored for some years after their initial purification featured higher trap densities. It is believed that storing of important materials should be done under vacuum conditions and not in packages of sealed foil in ambient air.

Last but not least, the trap studies should be extended to current high-performance OPV materials and help to further improve their efficiencies. In that sense, Fig. 10.1 illustrates TSC spectra, most recently recorded for complete DCV5T-Me<sub>3,3</sub>:C<sub>60</sub> solar cells. In contrast to the previously investigated thin-films, these samples were filled optically by illumination from a broadband white light source without additional bias voltage. The resulting filling current was at approx. 1 mA, which clearly demonstrates the functionality of organic solar cells at temperatures as low as 10 K. The obtained TSC spectra provide enough space for further investigations. In particular, shallow traps are suspected to originate from the doped transport layers and deeper traps from the absorber blend. However, for logical reasons, the solar cell stack should be reduced to a minimal number of layers to be able to conclude on the exact origin of the trap signals. Afterwards, the impact of manipulations such as a variation of the substrate temperature, the mixing ratios in the blend or a substitution of individual materials should be investigated.

ITO / C60:W2hpp4 (5nm, 4wt%) / C60 (15nm) / DCV2-5T-Me(3,3):C60 (2:1, X, 80°C) /  
BPAPF (5nm) / BPAPF:NDP9 (45 nm, 10wt%) / NDP9 (2nm) / Al

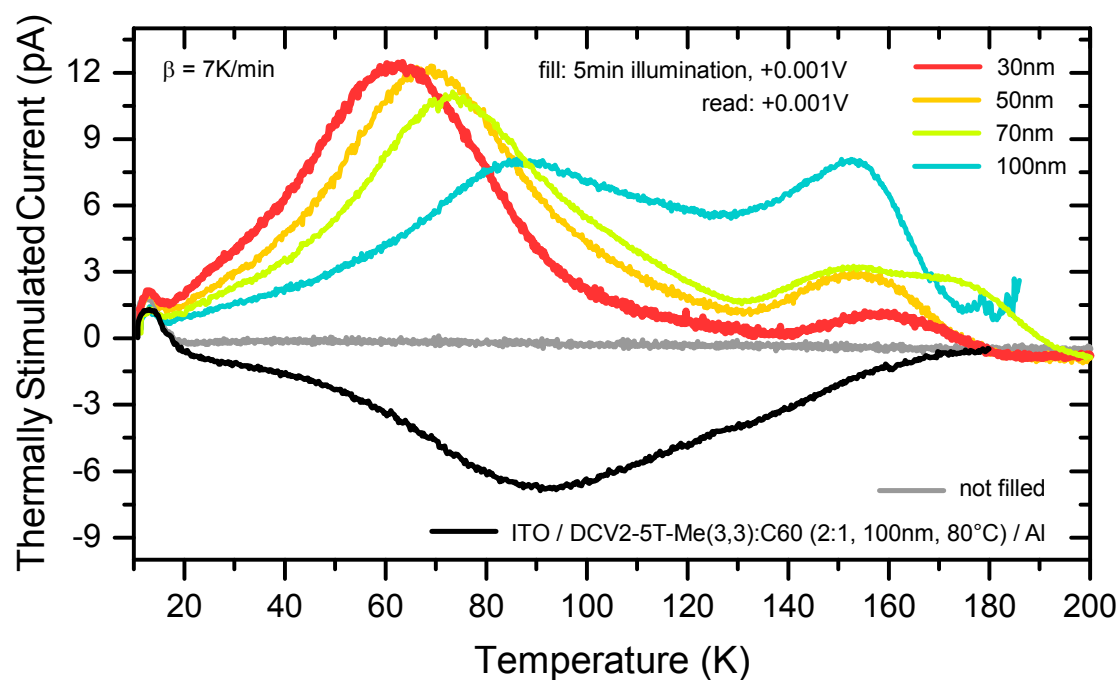


**Figure 10.1.:** TSC spectra ( $\beta = 5 \text{ K min}^{-1}$ ) taken for various DCV2-5T-Me(3,3):C<sub>60</sub> nip solar cells. The thickness of the absorbing blend layer is varied between 30 nm and 100 nm. Because of the inverted sample structure, the TSCs are at opposite sign. They reveal shallow traps most probably originating from the doped transport layers. The TSCs caused by deeper traps scale with the thickness of the blend layer. For comparison, already a single 100 nm blend layer of DCV2-5T-Me(3,3):C<sub>60</sub> (2:1) exhibits a broad TSC spectra (non-inverted sample). Measured together with Natalia Sergeeva, IAPP.



# Appendix

## A.1. Trap Capacitance Fitting - Burtone Model

**Listing A.1:** Simulation of Trap Capacitance in Organic Semiconductor Diodes

```

1 import pylab
2 import matplotlib.pyplot as plt
3 import numpy as np
4 from scipy import loadtxt
5 from mpmath import *
6
7 high_precision = 0 # needed when Fermi-D causes dev/0 error
8 mp.dps = 50 # standard float precision
9 _mpf0 = mp.mpf(0.0)
10 _dtype_object = np.dtype('object')
11 _cfunc_float = np.vectorize(float)
12
13 def mpfzeros(shape):
14     """construct an NumPy array of shape "shape"
15     filled with zero mpf's"""
16     res = np.empty(shape, object)
17     res2 = res.ravel()
18     for i in xrange(len(res2)):
19         res2[i] = mp.mpf(0.0)
20     return res
21
22 def mpparray2npfloat(a):
23     """convert a NumPy array of mpmath objects (mpf/mpc)
24     to a NumPy array of float"""
25     tmp = a.ravel()
26     res = _cfunc_float(tmp)
27     return res.reshape(a.shape)
28 def Ccombi_onepos(st_st, traps_gau, traps_exp, freq,
29                  transport, high_precision):
30
31     # loading simulation parameters from given array
32     Ev = st_st[0] # eV
33     Ec = st_st[1] # eV
34     Ef = st_st[2] # eV
35     T = st_st[3] # K
36     omega = 2*np.pi*freq

```

```
37 # Gaussian trap parameters
38 Nt_gau = traps_gau[0] # cm-3
39 sigma_gau = traps_gau[1] # eV
40 Et_gau = traps_gau[2] # eV
41
42 # exponential trap parameters
43 Nt_exp = traps_exp[0] # cm-3
44 T0_exp = traps_exp[1] # K
45
46 # mapping of energy intervals
47 E = np.linspace(Ev, Ec, 200)
48
49 # stationary model: equilibrium trap occupation + capacitance
50 if high_precision == 1:
51     ft = mpfzeros(200)
52     for i in range(0, len(ft)):
53         if transport == 0:
54             ft[i] = 1 - (1 / (1 + exp((E[i] - Ef) / (k * T))))
55         elif transport == 1:
56             ft[i] = 1 / (1 + exp((E[i] - Ef) / (k * T)))
57     else:
58         if transport == 0:
59             ft = (1 - (1 / (1 + np.exp((E - Ef) / (k * T)))))
60         elif transport == 1:
61             ft = 1 / (1 + np.exp((E - Ef) / (k * T)))
62
63 if transport == 0: # hole trap density distribution
64     g = ((Nt_gau / np.sqrt(2 * np.pi * sigma_gau ** 2))
65          * np.exp(-(E - Et_gau) ** 2 / (2 * sigma_gau ** 2)))
66     + (Nt_exp / (k * T0_exp) * np.exp((Ev - E) / (k * T0_exp)))
67 elif transport == 1: # electron trap density distribution
68     g = ((Nt_gau / np.sqrt(2 * np.pi * sigma_gau ** 2))
69          * np.exp(-(E - Et_gau) ** 2 / (2 * sigma_gau ** 2)))
70     + (Nt_exp / (k * T0_exp) * np.exp((E - Ec) / (k * T0_exp)))
71
72 nt_E = g * ft # trap occupation
73 Ct = q ** 2 / (k * T) * g * ft * (1 - ft) # equilibrium capacitance
74
75 # small signal model upon oscillatory excitation
76 if transport == 0:
77     epsilon = beta * Nc * np.exp((Ev - E) / (k * T))
78 elif transport == 1:
79     epsilon = beta * Nc * np.exp((E - Ec) / (k * T))
80
81 omega_t = epsilon / (1 - ft)
82 omega_t = mparray2npfloat(omega_t)
83 Ctraps_re = np.zeros(len(freq))
84 Ctraps_im = np.zeros(len(freq))
85
```

---

```

86  # capacitance calculation
87  for i in range (0, len(freq)):
88      Ctraps_re[i]= Area*np.trapz(E, (Ct/(1+(omega[i]/omega_t)**2)))/q
89      Ctraps_im[i]= Area*np.trapz(E, (Ct * (omega[i]/omega_t) /
90                                  (1+(omega[i]/omega_t)**2)))/q
91
92  return (E, ft, g, nt_E, omega_t, Ctraps_re, Ctraps_im)
93
94  # define global physical constants and sample parameters
95  k = 8.617343e-5 # eV K-1
96  q = 1.602176487e-19 # C
97  Nc = 1e20 # cm-3
98  T = 295 # K
99  d = 50e-7 # cm
100 A = 6.44e-2 # cm2
101 transport = 0 # 0..h-transport, 1..e-transport
102
103 # import banddiagram
104 method = 1 # 2..from OSOLsim, 1..from OLEDsim
105 profilepath = "Points_0.00.txt"
106 if method == 2:
107     profile = loadtxt(profilepath, dtype="float",
108                       usecols=(0,10,11,12,13), skiprows=47)
109 if method == 1:
110     profile = loadtxt(profilepath, dtype="float",
111                       usecols=(0,15,14,13,12), skiprows=1)
112
113 interfaces=[0,51]
114 profile = profile[profile[:,0] >= interfaces[0]]
115 profile = profile[profile[:,0] <= interfaces[1]]
116
117 x = profile[:,0]
118 Ec = profile[:,1]
119 Ev = profile[:,2]
120 Ef_n = profile[:,3]
121 Ef_p = profile[:,4]
122
123 x = x - x[0]
124 Ef[:] = -4.55 # set Fermi level position
125
126 # import measured data and trap parameters
127 filepath = "Cf_spectra.txt"
128 data = loadtxt(filepath, dtype="float", usecols=(0,1,2,3,4,5,6),
129               skiprows=7)
130 traps = loadtxt("traps_parameters.txt", dtype="float",
131                 usecols=(0,1,2,3,4,5), skiprows=1)
132 freqmeas = data[:,0] # Hz
133 Ctotmeas = data[:,5] # Ohm
134 Ztotmeas = data[:,3] # Ohm

```

```
135 Phmeas = data[:,4] # deg
136 beta = traps[5] # cm2 s-1
137
138 # Gaussian trap
139 Nt_gau = traps[0] # cm-3
140 sigma = traps[1] # eV
141 if transport == 0:
142     Et = Ev+traps[2] # eV
143 elif transport == 1:
144     Et = Ec-traps[2] # eV
145
146 # exponential trap
147 Nt_exp = traps[3] # cm-3
148 T0_exp = traps[4] # K
149
150 # initialize
151 freq = np.logspace(-3,7,100) # 1eX Hz
152 omega = 2*np.pi*freq
153
154 ft_x = np.zeros(shape=(200,len(x)))
155 g_x = np.zeros(shape=(200,len(x)))
156 nt_E_x = np.zeros(shape=(200,len(x)))
157 omega_t_x = np.zeros(shape=(200,len(x)))
158
159 Ctraps_re_x = np.zeros(shape=(len(freq),len(x)))
160 Ctraps_im_x = np.zeros(shape=(len(freq),len(x)))
161
162 Ctraps_re = np.zeros(len(freq))
163 Ctraps_im = np.zeros(len(freq))
164
165 E = np.zeros(shape=(200,len(x)))
166
167 # calculate spacial distribution of the trap capacitance
168 for i in range(0, len(x)):
169     print i
170     st_onepos=[Ev[i], Ec[i], Ef[i], T]
171     traps_gau=[Nt_gau, sigma, Et[i]]
172     traps_exp=[Nt_exp, T0_exp]
173     (E[:,i], ft_x[:,i], g_x[:,i], nt_E_x[:,i], omega_t_x[:,i],
174      Ctraps_re_x[:,i], Ctraps_im_x[:,i]) = Ccombi_onepos(
175      st_onepos, traps_gau, traps_exp, freq, transport, high_precision)
176
177 # spacial integration
178 for i in range(0, len(freq)):
179     Ctraps_re[i] = np.trapz(np.linspace(0,d,len(x)), Ctraps_re_x[i,:])
180     Ctraps_im[i] = np.trapz(np.linspace(0,d,len(x)), Ctraps_im_x[i,:])
181
182 # overall impedance: Rs, Rp & Cp from equivalent circuit fit
183 Rs=87.82 # Ohm
```

---

```

184 Rp=3.3445e6 # Ohm
185 Cp=6.7e-9 # F
186
187 Gp = 1/(Rp + (2 * np.pi * np.multiply(freq, Ctraps_im.T)))
188 Bp = 2 * np.pi * freq * (Cg + Ctraps_re.T)
189 Ypsq = (Gp**2) + (Bp**2)
190
191 Rtot = Rs + (Gp/Ypsq)
192 Xtot = -Bp/Ypsq
193 Ztotsq = Rtot**2 + Xtot**2
194
195 Ztot = np.sqrt(Ztotsq)
196 Ph = np.arctan(-Xtot/Rtot) * -180/np.pi
197 Ctot = (-Xtot)/(2 * np.pi * freq * (Ztotsq))
198
199 # plotting trap DOS, capacitance, modulus & phase
200 plt.figure(0, figsize=(15, 10))
201
202 ax1 = plt.subplot2grid((2,3), (0,0), colspan=2)
203 ax2 = plt.subplot2grid((2,3), (0,2))
204 ax3 = plt.subplot2grid((2,3), (1, 0))
205 ax4 = plt.subplot2grid((2,3), (1, 1))
206 ax5 = plt.subplot2grid((2,3), (1, 2))
207
208 print Ctotmeas
209
210 ax1.plot(freqmeas, Ctotmeas, "bo", freq, Ctot, "r-", linewidth=2.0)
211 ax1.set_xlabel('Frequency (Hz)')
212 ax1.set_ylabel('Capacitance (F)')
213 ax1.set_xscale('log')
214 ax1.set_xlim([1e1,1e6])
215 ax1.set_ylim([0, 25e-9])
216 ax1.set_title('Capacitance spectrum')
217 ax1.grid(True)
218
219 ax2.plot(x, Ec, "r-", x, Ev, "b-", x, Ef, "k:", linewidth=2.0)
220 ax2.set_xlabel('position (nm)')
221 ax2.set_ylabel('Energy (eV)')
222 ax2.set_title('Band diagram')
223 ax2.grid(True)
224
225 ax3.plot(freqmeas, Ztotmeas, "bo", freq, Ztot, "r-", linewidth=2.0)
226 ax3.set_xlabel('Frequency (Hz)')
227 ax3.set_ylabel('Modulus (Ohm)')
228 ax3.set_xscale('log')
229 ax3.set_yscale('log')
230 ax3.set_xlim([1e0,1e6])
231 ax3.grid(True)
232

```

```
233 ax4.plot(freqmeas, Phmeas, "bo", freq, Ph, "r-", linewidth=2.0)
234 ax4.set_xlabel('Frequency (Hz)')
235 ax4.set_ylabel('Phase angle (deg)')
236 ax4.set_xscale('log')
237 ax4.set_xlim([1e0,1e6])
238 ax4.grid(True)
239
240 ax5.plot(E[:,1], g_x[:,1], "k", linewidth=2.0, label="Ntgau=" +
241         str(Nt_gau) + "/ sigma=" + str(sigma) + "/ depth=" +
242         str(traps[2]) + "\n Ntexp=" + str(Nt_exp) +
243         "/ T0=" + str(T0_exp))
244 ax5.set_xlabel('Energy (eV)')
245 ax5.set_ylabel('Density of states (cm-3)')
246 ax5.set_title('Trap distribution')
247 ax5.legend(loc=2,prop={'size':9})
248 ax5.grid(True)
249
250 plt.suptitle("Burtone model for impedance analysis")
251 plt.show()
252
253 # export results
254 out = open("band_diagram.txt", "w")
255 out.write("Position (nm) \t Ec (eV) \t Ef (eV) \t Ev (eV) \n")
256 for i in range(0, len(x)):
257     out.write(str(x[i]) + " \t " + str(Ec[i]) + " \t " + str(Ef[i]) +
258             " \t " + str(Ev[i]) + " \n")
259 out.close()
260
261 out = open("trap_dos.txt", "w")
262 out.write("Energy (eV) \t Trap DOS[cm-3]\n")
263 for i in range(0, len(E[:,1])):
264     out.write(str(E[i,1]-Ev[1]) + " \t " + str(g_x[i,1]) + "\n")
265 out.close()
266
267 out = open("Impedance_fit.txt", "w")
268 out.write("Frequency (Hz) \t Capacitance (F) \t Modulus (Ohm) \t
269         Phase (deg)\n")
270 for i in range(0, len(freq)):
271     out.write(str(freq[i]) + " \t " + str(Ctot[i]) + " \t " +
272             str(Ztot[i]) + " \t " + str(Ph[i]) + "\n")
273 out.close()
```

---

## A.2. Python Calculation of the Transport Level

Listing A.2: Calculation of  $E_{Tr}$  w/ backward jumps and Gaussian or exponential DOS.

```

1  from numpy import *
2  from scipy.optimize import fmin
3  from scipy import loadtxt, integrate
4  import pylab
5
6  # physical constants
7  k = 8.617343e-5 # eV K-1
8  gamma = 1e9 # m-1
9
10 # DOS function
11 E0 = 0 # eV
12 sigma = 0.200 # eV
13 N = 1 * 1e27 # m-3
14 E0_exp = 0 # eV
15 T0_exp = 900 # K
16 N_exp = 1e21 # cm-3
17
18 # define temperature and energy axis
19 T_min = 10
20 T_max = 300
21 T_axis = linspace(T_max, T_min, 300)
22 E_axis = linspace(-15*sigma, 15*sigma, 300)
23
24 # set density of states
25 Gauss_DOS = (N/(sqrt(2 * pi)*sigma))*exp(-((E_axis - E0)**2)/
26 (2*(sigma**2))) # change to EXP_DOS for exp. DOS
27 def func(x, a):
28     return (N/(sqrt(2 * pi)*sigma))*exp(-((x - E0)**2)/
29 (2*(sigma**2)))*((a-x)**3)
30     # change to EXP_DOS * (a-x)**3 for exp. DOS
31
32 # initialize and calculate
33 Ej_initial_guess = 0.0
34 Ej = 0.0
35 Ej_level_results = []
36
37 for i in range(len(T_axis)):
38     print T_axis[i]
39     def residual(Ej):
40         return abs(((integrate.quad(func, -inf, Ej, args=(Ej,))[0])
41 - (6/pi * (gamma * k * T_axis[i])**3)))
42
43     result = fmin(residual, Ej_initial_guess)
44     print result
45     Ej_level_results.append(result[0])

```

```
46 # draw results
47 pylab.plot(T_axis, Ej_level_results, "ro")
48 pylab.xlabel("Temperature (K)")
49 pylab.ylabel("Ej - E_0 (eV)")
50 pylab.show()
51
52 # export results
53 out = open("calc_jump_level_wBackjumps.txt", "w")
54 out.write("Results: \n E0 = " + str(E0) + "\n sigma = " + str(sigma)
55 + "\n N = " + str(N) + "\n E0_exp = " + str(E0_exp) + "\n T0_exp = "
56 + str(T0_exp) + "\n N_exp = " + str(N_exp) + "\n\n")
57 out.write("Temperature (K) \t Ej - E0 (eV) \n")
58
59 for i in range(len(T_axis)):
60     out.write(str(T_axis[i]) + " \t "
61 + str(Ej_level_results[i]) + "\n")
62 out.close()
```

---

**Listing A.3:** Calculation of  $E_{Tr}$  w/o backward jumps and Gaussian + exponential DOS.

---

```
1 from numpy import *
2 from scipy.optimize import fmin
3 from scipy import loadtxt, integrate
4 import pylab
5
6 # physical constants
7 k = 8.617343e-5 # eV K-1
8 gamma = 1e9 # m-1
9 # DOS function
10 E0 = 0 # eV
11 sigma_array = [0.248] # eV
12 N_array = [5.91 * 1e26] # m-3
13 E0_exp_array = [-0.48] # eV
14 T0_exp_array = [0.345] # eV
15 N_exp_array = [6.62 * 1e25] # cm-3
16 E_cutoff_array = [-0.75] # eV
17
18 for a in range(len(sigma_array)):
19     sigma = sigma_array[a]
20     N = N_array[a]
21     E0_exp = E0_exp_array[a]
22     T0_exp = T0_exp_array[a]
23     N_exp = N_exp_array[a]
24     E_cutoff = E_cutoff_array[a]
25
26 # define temperature and energy axis
27 T_min = 10
28 T_max = 300
29 T_axis = linspace(T_max, T_min, 10)
```



```

30 E_axis = linspace(E_cutoff, 1, 300)
31
32 # set density of states
33 Gauss_DOS = (N/(sqrt(2 * pi)*sigma))*exp(-((E_axis - E0)**2)/
34         (2*(sigma**2)))
35 EXP_DOS = (N_exp/T0_exp * exp((-E0_exp+E_axis)/(T0_exp)))
36
37 def func1(x):
38     if x > E0_exp:
39         return (N/(sqrt(2 * pi)*sigma))*exp(-((x - E0)**2)/
40         (2*(sigma**2)))
41     elif x < E_cutoff:
42         return 0
43     else:
44         return (N_exp/T0_exp * exp((-E0_exp+x)/(T0_exp)))
45
46 N_E = []
47 for b in range(len(E_axis)):
48     N_E.append(func1(E_axis[b]))
49
50 # initialize and calculate
51 Etr_initial_guess = 0.0
52 Etr = 0.0
53 Etr_level_results = []
54
55 for i in range(len(T_axis)):
56     print T_axis[i]
57
58     def func2(x, Ej, r):
59         return func1(x) * (8*(1 - (x - Ej)/(2 * k * T_axis[i] * gamma
60         * r)) + 3*(1 - (x - Ej)/(2 * k * T_axis[i] * gamma * r))**4)
61
62     def target_sites(Ej, r):
63         return pi*(r**3)/12 * (11 * integrate.quad(func1, -inf, Ej)[0]
64         + integrate.quad(func2, Ej, Ej + (2*k * T_axis[i] * gamma
65         * r), args=(Ej, r))[0])
66
67     def func3(r, Ej):
68         return r**2 * (1 - exp(- target_sites(Ej, r)))
69
70     def func4(Ej, Etr):
71         return func1(Ej) * integrate.quad(func3, 0, (Etr - Ej)/
72         (2 * gamma * k * T_axis[i]), args=(Ej,))[0]
73
74     def residual(Etr):
75         return abs(((integrate.quad(func4, -inf, Etr, args=(Etr,))[0])
76         - 1/(4*pi)))
77
78     result = fmin(residual, Etr_initial_guess)

```

```
79     print result
80     Etr_level_results.append(result[0])
81
82     # export results
83     out = open("calc_transport_level_woBackjumps_" + str(a)
84               + ".txt", "w")
85     out.write("Results: \n E0 = " + str(E0) + "\n sigma = "
86             + str(sigma) + "\n N = " + str(N) + "\n E0_exp = " + str(E0_exp)
87             + "\n T0_exp = " + str(T0_exp) + "\n N_exp = " + str(N_exp)
88             + "\n\n")
89     out.write("Temperature (K) \t Etr - E0 (eV) \n")
90
91     for i in range(len(T_axis)):
92         out.write(str(T_axis[i]) + " \t "
93                 + str(Etr_level_results[i]) + "\n")
94     out.close()
```

---

Since minimizing the integral residuals in List. A.3 requires a calculation time around two hours per temperature point on a 2.7 GHz dual core CPU with 4 GByte RAM, optimization is necessary. Line 30 allows to limit the number of temperatures to an adequate amount. Here, it is set to 10. If further specific temperatures are needed, they can be added to the array 'T\_axis' using the .append function. A complete set of  $E_{Tr}(T)$  is obtained by using the previously calculated points from List. A.3 as grid points and applying the polynomial fit procedure given in List. A.4. By that, the precision of  $E_{Tr}(T)$  can be matched with the requirements of e.g. the temperature scale in TSC measurements. The time benefits are tremendous.

---

**Listing A.4:** Polynomial fit procedure to create complete  $E_{Tr}(T)$ .

---

```
1  from numpy import *
2  import pylab
3  import numpy.polynomial.polynomial as poly
4  from scipy import optimize, loadtxt
5
6  # import existing points E_tr(T)
7  filepath = "calc_transport_level_woBackjumps_0.txt"
8  data = loadtxt(filepath, dtype="float", usecols=(0,1), skiprows=9)
9  xdata = data[:,0]
10 ydata = data[:,1]
11
12 # fit and complete E_tr(T)
13 x_new = linspace(xdata.min(), xdata.max(), 300)
14 coefs = poly.polyfit(xdata, ydata, 10)
15 ffit = poly.polyval(x_new, coefs)
16
17 # draw results
18 pylab.plot(xdata, ydata, "ro", x_new, ffit, "r-")
19 pylab.title("Transport level neglecting backward jumps versus T")
20 pylab.xlabel("Temperature (K)")
21 pylab.ylabel("E_tr - E_0 (eV)")
22 pylab.legend(('data', 'fit'))
23 pylab.show()
```

```
24 # export results
25 out = open("calc_transport_level_woBackjumps_complete.txt", "w")
26 out.write("Temperature (K) \t E_tr - E_0 (eV) \n")
27 for i in range(len(x_new)):
28     out.write(str(x_new[i]) + " \t" + str(ffit[i]) + " \n")
29     out.write("\n\n")
30 out.close()
```

---

### A.3. Python TSC Experiment Procedure

Listing A.5: Measurement routine for TSC experiments.

```
1 import visa, string, sched, time, numpy
2 from struct import unpack
3
4 # establish GPIB communication with T-controller
5 class LakeShore336:
6     def __init__(self, LakeShore336Address):
7         self.LakeShore336Address = LakeShore336Address
8         self.LakeShore336 = visa.instrument("GPIB0::"
9                                             +str(LakeShore336Address))
10    def GPIBWrite(self, GPIBString):
11        GPIBResponse = self.LakeShore336.write(GPIBString)
12    def GPIBAsk(self, GPIBString):
13        GPIBResponse = self.LakeShore336.ask(GPIBString)
14        return GPIBResponse
15    def Reading(self, Channel):
16        Temperature = self.LakeShore336.ask("KRDG? "+str(Channel))
17        return Temperature
18 tc = LakeShore336("25::INSTR")
19
20 # establish GPIB communication with source measure unit
21 class Keithley2635:
22     def __init__(self, Keithley2635Address):
23         self.Keithley2635Address = Keithley2635Address
24         self.Keithley2635 = visa.instrument("GPIB0::"
25                                             +str(Keithley2635Address))
26    def GPIBWrite(self, GPIBString):
27        GPIBResponse = self.Keithley2635.write(GPIBString)
28    def GPIBAsk(self, GPIBString):
29        GPIBResponse = self.Keithley2635.ask(GPIBString)
30        return GPIBResponse
31 smu = Keithley2635("26::INSTR")
32
33 # define miscellaneous functions
34 def waituntil(loadT, stabletime, period=1):
35     mustend = time() + stabletime
36     while time() < mustend:
37         if (abs(float(tc.Reading("A")) - loadT) <= loadTtolerance)
38             and (abs(float(tc.Reading("B")) - loadT) <= loadTtolerance):
39             sleep(period)
40         else:
41             mustend = time() + stabletime
42             sleep(period)
43
44 def format_time(timevar):
45     m, s = divmod(timevar, 60)
```

---

```

46     h, m = divmod(m, 60)
47     timestring = "%2d h:%02d min:%02d s" % (h, m, s)
48     return timestring
49
50 # set TSC process parameters
51 loadT = [10] # K
52 loadTtolerance = 2 # K
53 loadlevel = -0.001 # V
54 loadtime = 300 # s
55 filling = [1]
56
57 resttime = 300 # s
58
59 rampRatesample = 7 # K/min
60 rampRatevaporizer = 7 # K/min
61 setpointsample = [150] # K
62 setpointvaporizer = [150] # K
63 stopT = [150] # K
64
65 nplc = 1
66 currentrange = 1e-12
67 releaselevel = -0.01 # V
68 measureinterval = 10 # s
69 measurecount = 1
70
71 # Sample identification
72 name = "OSOL1434P3_day2_release-0.01V"
73 pixel = 3
74
75 # generate log file for batch processing of TSC runs
76 out = open("C://TSC/" + name + "_" + str(pixel) + "_TSClog.txt", "w")
77 out.write("ID \t loadT [K] \t filling \t setpointsample [K] \t
78           setpointvaporizer [K] \t stopT [K] \n")
79
80 # ————— LakeShore 336 T-controller configuration —————
81 # Output Mode Command <output>,<mode>,<input>,<powerup enable>
82 tc.GPIBWrite("reset()")
83 tc.GPIBWrite("clear()")
84 tc.GPIBWrite("OUTMODE 1,1,1,0")
85 tc.GPIBWrite("OUTMODE 2,1,2,0")
86
87 # Control Loop Mode Command <loop>,<mode: =PID>
88 tc.GPIBWrite("ATUNE 1,2")
89 tc.GPIBWrite("ATUNE 2,2")
90 tc.GPIBWrite("RAMP 1,0,0")
91 tc.GPIBWrite("RAMP 2,0,0")
92
93 # ————— Definition of TSC procedure —————
94 def TSC(loadT, filling, setpointsample, setpointvaporizer, stopT, ID):

```

```
95
96 # no ramp heating for loadT + workaround to PID-autotune bug
97 tc.GPIBWrite("reset()")
98 tc.GPIBWrite("clear()")
99 tc.GPIBWrite("RAMP 1,0,0")
100 tc.GPIBWrite("RAMP 2,0,0")
101 tc.GPIBWrite("PID 1, 110,50,20")
102 tc.GPIBWrite("PID 2, 110,50,20")
103
104 # configure Keithley 2635 SMU
105 smu.GPIBWrite("reset()")
106 smu.GPIBWrite("smua.source.func = smua.OUTPUT_DCVOLTS")
107 smu.GPIBWrite("smua.source.limit1 = 0.01")
108 smu.GPIBWrite("display.smua.measure.func = display.MEASURE_DCAMPS")
109 smu.GPIBWrite("smua.measure.nplc = " + str(nplc))
110 smu.GPIBWrite("smua.measure.autorangev = 1")
111 smu.GPIBWrite("smua.measure.autozero = 1")
112 smu.GPIBWrite("smua.measure.count = " + str(measurecount))
113 smu.GPIBWrite("smua.measure.interval = 0.05")
114 smu.GPIBWrite("smua.nvbuffer1.clear()")
115 smu.GPIBWrite("smua.nvbuffer1.appendmode = 1")
116
117 # cooldown to load temperature and checking for stability
118 tc.GPIBWrite("clear()")
119
120 while (int(float(tc.GPIBAsk("SETP? 1"))) != loadT) or
121       (int(float(tc.GPIBAsk("SETP? 2"))) != loadT):
122     tc.GPIBWrite("SETP 1," + str(loadT))
123     tc.GPIBWrite("SETP 2," + str(loadT))
124     sleep(2)
125
126 print "Sample cooling to load point @ " + str(tc.GPIBAsk(
127     "SETP? 1")) + "/" + str(tc.GPIBAsk("SETP? 2")) + " K ..."
128
129 while ((float(tc.Reading("A")) - loadT) > 0) or
130       ((float(tc.Reading("B")) - loadT) > 0):
131     print "sample @ " + str(tc.Reading("A")) + " K, vaporizer @ "
132           + str(tc.Reading("B")) + " K"
133     sleep(10)
134
135 print "Sample dropped below load point @ " + str(tc.GPIBAsk(
136     "SETP? 1")) + "/" + str(tc.GPIBAsk("SETP? 2"))
137
138 sleep(60) # wait for temperature to be lower than LoadT for some
139           # time, approaching LoadT from T < LoadT
140
141 tc.GPIBWrite("RANGE 1,2") # change to "RANGE 1,3" for loadT > 10 K
142 tc.GPIBWrite("RANGE 2,2") # change to "RANGE 2,3" for loadT > 10 K
143
```

```

144     print "Approaching load point from below ..."
145
146     while (abs(float(tc.Reading("A")) - loadT) > loadTtolerance) or
147           (abs(float(tc.Reading("B")) - loadT) > loadTtolerance):
148         print "sample @ " + str(tc.Reading("A")) + " K, vaporizer @ "
149               + str(tc.Reading("B")) + " K"
150         sleep(10)
151
152     print "Load point temperature reached."
153     print "Waiting for temperature to be stable ..."
154     waituntil(loadT, 60)
155     print "Temperature has been stable for 60s @ " + str(loadT) +
156           " K +- " + str(loadTtolerance) + " K"
157
158     # applying trap filling
159     if filling == 1:
160         smu.GPIBWrite("smua.source.levelv = " + str(loadlevel))
161         print "Filling traps ..."
162         smu.GPIBWrite("smua.source.output = smua.OUTPUT_ON")
163
164         array_time = []
165         array_vaporizer = []
166         array_sample = []
167         array_measure = []
168
169         mustend = time() + loadtime
170         while time() < mustend:
171             smu.GPIBWrite("smua.measure.i(smua.nvbuffer1)")
172             array_vaporizer.append(float(tc.Reading("A")))
173             array_sample.append(float(tc.Reading("B")))
174             array_time.append(time())
175             listm = []
176             for i in range(1, measurecount+1):
177                 listm.append(float(smu.GPIBAsk("print(smua.nvbuffer1
178                                           .readings[" + str(i) + "])"))))
179             smu.GPIBWrite("smua.nvbuffer1.clear()")
180             array_measure.append(numpy.mean(listm))
181             sleep(1)
182
183         smu.GPIBWrite("smua.source.output = smua.OUTPUT_OFF")
184
185         # export measured filling currents
186         out = open("C://TSC/" + name + "_" + str(pixel) + "_ID" +
187                  str(ID) + "_TSC_fill.txt", "w")
188         out.write("Time [s] \t T_Sample [K] \t T_Vaporizer [K] \t
189                  Current [A]\n")
190
191         for i in range(0, len(array_measure)):
192             out.write(str(array_time[i]) + " \t " + str(array_sample[i])

```

```
193         + " \t " + str(array_vaporizer[i]) + " \t " +
194         str(array_measure[i]) + "\n")
195     out.close()
196
197     # rest time for sample
198     print "Sample rests for " + str(resttime) + " seconds."
199     smu.GPIBWrite("smua.source.levelv = -0.001")
200     smu.GPIBWrite("smua.source.output = smua.OUTPUT_ON")
201     sleep(resttime)
202     smu.GPIBWrite("smua.source.output = smua.OUTPUT_OFF")
203
204     # configure SMU for TSC measurement
205     smu.GPIBWrite("display.smua.measure.func = display.MEASURE_DCAMPS")
206     smu.GPIBWrite("smua.measure.autorangev = 1")
207     smu.GPIBWrite("smua.measure.count = " + str(measurecount))
208     smu.GPIBWrite("smua.measure.interval = 0.05")
209     smu.GPIBWrite("smua.nvbuffer1.clear()")
210     smu.GPIBWrite("smua.nvbuffer1.appendmode = 1")
211     smu.GPIBWrite("smua.source.levelv = " + str(releaselevel))
212
213     # start TSC ramping
214     tc.GPIBWrite("clear()")
215     tc.GPIBWrite("reset()")
216
217     print "Performing TSC ... " + str(tc.GPIBAsk("SETP? 1")) +
218           "/" + str(tc.GPIBAsk("SETP? 2"))
219
220     tc.GPIBWrite("RAMP 1,1," + str(rampRatevaporizer))
221     tc.GPIBWrite("RAMP 2,1," + str(rampRatesample))
222     tc.GPIBWrite("RANGE 1,3")
223     tc.GPIBWrite("RANGE 2,3")
224
225     sleep(10)
226     tc.GPIBWrite("SETP 1," + str(setpointvaporizer))
227     tc.GPIBWrite("SETP 2," + str(setpointsample))
228     array_time = []
229     array_sample = []
230     array_vaporizer = []
231     array_measure = []
232
233     out = open("C://TSC/" + name + "_" + str(pixel) + "_ID"
234              + str(ID) + "_TSC_run_preview.txt", "w")
235     out.write("Time \t T_Sample [K] \t T_Vaporizer [K] \t
236              Current [A]\n")
237
238     smu.GPIBWrite("smua.source.output = smua.OUTPUT_ON")
239
240     while float(tc.Reading("B")) <= stopT:
241         smu.GPIBWrite("smua.measure.i(smua.nvbuffer1)")
```



---

```

242     array_vaporizer.append(float(tc.Reading("A")))
243     array_sample.append(float(tc.Reading("B")))
244     array_time.append(float(time()))
245     listm = []
246     for i in range(1, measurecount+1):
247         listm.append(float(smu.GPIBAsk("print(smu.nvbuffer1
248                                     .readings[" +str(i) +"])))")
249     smu.GPIBWrite("smua.nvbuffer1.clear()")
250     array_measure.append(numpy.mean(listm))
251     out.write(str(array_time[-1]) + " \t " + str(array_sample[-1])
252             + " \t " + str(array_vaporizer[-1]) + " \t " +
253             str(array_measure[-1]) + "\n")
254     sleep(1)
255
256 out.close()
257 smu.GPIBWrite("smua.source.output = smua.OUTPUT_OFF")
258
259 # export TSC data
260 out = open("C://TSC/" + name + "_" + str(pixel) + "_ID"
261           + str(ID) + "_TSC_run.txt", "w")
262 out.write("Thermally stimulated current measurement \n — \n")
263 out.write("Sample: " + name + "\n")
264 out.write("Date: " + str(time()) + "\n — \n")
265 out.write("measurement ID: " + str(ID) + "\n — \n")
266 out.write("Parameters: \n")
267 out.write("\t Contact: D" + str(pixel) + "\n \t Load Temperature: "
268         + str(loadT) + " K \n \t Load Bias: " + str(loadlevel) + " V \n")
269 out.write("\t Load Time: " + str(loadtime) + "s \t Rest Time: "
270         + str(resttime) + "s \n")
271 out.write("Time \t T_Sample [K] \t T_Vaporizer [K] \t Current [A]\n")
272
273 for i in range(0, len(array_measure)):
274     out.write(str(array_time[i]) + " \t " + str(array_sample[i]) +
275             " \t " + str(array_vaporizer[i]) + " \t "
276             + str(array_measure[i]) + "\n")
277
278 out.close()
279 tc.GPIBWrite("RANGE 1,0")
280 tc.GPIBWrite("RANGE 2,0")
281
282 for p in range(0, len(loadT)):
283     TSC(loadT[p], filling[p], setpointsample[p], setpointvaporizer[p],
284         stopT[p], p)
285     out = open("C://TSC/" + name + "_" + str(pixel) + "_TSClog.txt", "a")
286     out.write(str(p) + " \t " + str(loadT[p]) + " \t " + str(filling[p])
287             + " \t " + str(setpointsample[p]) + " \t " +
288             str(setpointvaporizer[p]) + " \t " + str(stopT[p]) + " \n")
289     out.close()
290     print "done."

```

---

## A.4. Conductivities

In order to match the IP of the absorbing  $\text{CH}_3\text{NH}_3\text{PbI}_{3-x}\text{Cl}_x$  perovskite layer (5.4 eV) in hybrid solar cells and minimize hole extraction barriers, various HTL materials are tested. The results are published in Ref. [71] Here, the conductivity values obtained upon p-doping of the matrices are shown. For a solar cell application, at least  $\sigma = 10^{-5} \text{ S/cm}$  is required.

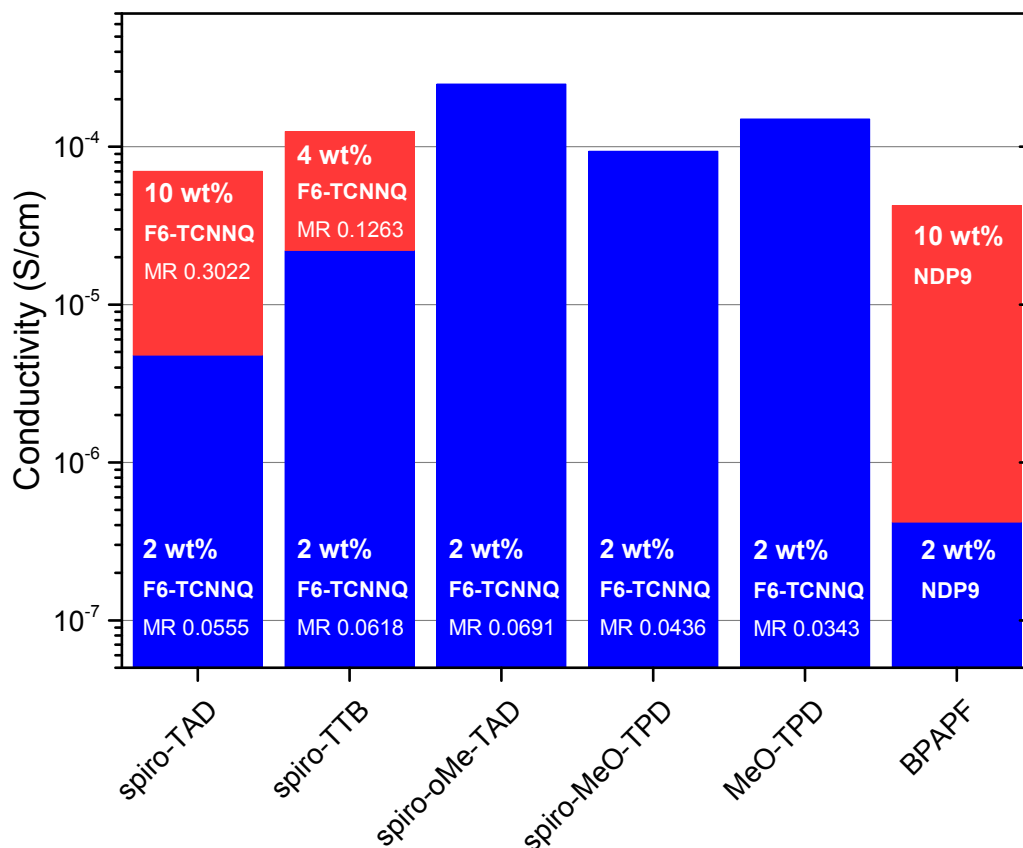


**Figure A.1.:** Hole conductivities of differently F<sub>6</sub>-TCNNQ doped HTL materials. In case of BPAPF, the only the Novaled property dopant NDP9 raise the conductivity due to its low-lying LUMO at approx. 5.4 eV.

## A.5. List of Important Abbreviations

AFM	atomic force microscopy
CT	charge transfer
DOS	density of states
EA	electron affinity
(E)CDM	(extended) correlated disorder model
(E)GDM	(extended) Gaussian disorder model
FET	field effect transistor
FFT	fast Fourier transformation
GI(XRD)	grazing incidence x-ray diffraction
HOMO	highest occupied molecular orbital
HTL	hole transporting layer
IP	ionization potential
IS	impedance spectroscopy
K	Kelvin
LCAO	linear combination of atomic orbitals
LUMO	lowest unoccupied molecular orbital
MR	molar ratio
NNH	nearest-neighbor-hopping
OFET	organic field effect transistor
OLED	organic light emitting diode
OPV	organic photovoltaics
OSC	organic solar cell
OTFT	organic thin-film transistor
PCE	power conversion efficiency
PES	photoelectron spectroscopy
ppm	parts per million
RT	room temperature
SCR	space charge region
SEM	scanning electron microscope
TSC	thermally stimulated currents
TSL	thermally stimulated luminescence
UHV	ultra high vacuum
UPS	ultraviolet photoelectron spectroscopy
VRH	variable range hopping
WR	weight ratio
XPS	x-ray photoelectron spectroscopy

## A.6. List of Important Symbols

$\chi$	atomic wave function
$\gamma$	inverse localization length
$C$	capacitance
$\Delta$	interface dipole
$\Delta E_B$	binding energy
$E$	energy
$E_A$	activation energy
$E_C$	conduction band energy
$E_F$	Fermi energy
$E_g$	energy gap
$E_{Tr}$	transport energy
$E_V$	valence band energy
$F$	electric field strength
$\eta$	doping efficiency
$\hat{H}$	Hamilton operator
$k_B$	Boltzmann constant
$\mu$	charge carrier mobility
$\nu$	attempt-to-escape frequency
$n$	free electron density
$N_A$	acceptor density
$N_A^-$	ionized acceptor density
$N_T$	trap density
$N_T^-$	occupied trap density
$p$	free hole density
$P$	polarization energy
$R$	resistance
$\sigma$	conductivity
$\sigma$	energetic disorder
$\Sigma$	off-diagonal disorder
$T$	temperature
$Z$	impedance

## A.7. List of used Materials

BF-DPB	N,N'-Bis(9,9-dimethyl-fluoren-2-yl)-N,N'-diphenyl-benzidine
C <sub>60</sub>	buckminster fullerene
C <sub>60</sub> F <sub>36</sub>	fluorinated buckminster fullerene
DCV2-5T-Me(3,3)	2,2'-((3'',4''-dimethyl-[2,2':5',2'':5'',2''':5''',2''':5''''-quiquethiophene]-5,5''''-diyl)bis(methanylylidene))dimalononitrile
F <sub>6</sub> -TCNNQ	1,3,4,5,7,8-hexafluorotetracyanonaphthoquinodimethane
m-MTDATA	4,4',4''-tris(3-methylphenylphenylamino)-triphenylamine
MeO-TPD	N,N,N',N'-tetrakis(4-methoxyphenyl)-benzidine
NPB	N,N'-Di(naphthalen-1-yl)-N,N'-diphenyl-benzidine
P5	pentacene
Spiro-TTB	2,2',7,7'-tetrakis-(N,N-di-methylphenylamino)-9,9'-spirobifluoren
W <sub>2</sub> (hpp) <sub>4</sub>	tetrakis(1,3,4,6,7,8-hexahydro-2H-pyrimido[1,2-a]pyrimidinato)ditungsten (II)
ZnPc	zinc-phthalocyanine



---

# Bibliography

- [1] *Global Wealth Report 2015*. Tech. Rep. October, Credit Suisse Research Institute (2015).
- [2] Danzhen, L. Hug, S. Ejdemyr, J. Beise, P. Idele, P. Gerland, F. Pelletier, L. Bassarsky, V. Gaigbe-togbe, D. Gu, V. Kantorova, N. Li, C. Sawyer, and T. Spoorenberg: *Child Mortality Report 2015*. Unicef Levels & Trends in Child Mortality (2015).
- [3] G. Mudur: *Atemlos in der Großstadt*. Max Planck Forschung **4**(10):18 (2010).
- [4] B. J. Laurens and R. Maino: *China's Emerging Financial Markets - Challenges and Opportunities*, vol. 8. Springer (2009), doi:10.1007/978-0-387-93769-4.
- [5] *GDP growth database* (2016).
- [6] J. Yang, Y. Liu, P. Qin, and A. A. Liu: *A review of Beijing's vehicle registration lottery: Short-term effects on vehicle growth and fuel consumption*. Energy Policy **75**:157 (2014), doi:10.1016/j.enpol.2014.05.055.
- [7] Y.-L. Zhang and F. Cao: *Fine particulate matter (PM<sub>2.5</sub>) in China at a city level*. Scientific Reports **5**(2014):14884 (2015), doi:10.1038/srep14884.
- [8] International Energy Agency: *Key World Energy Statistics 2015* 81 (2015).
- [9] L. Lindholt: *Arctic natural resources in a global perspective*. S. Glomsrød and I. Aslaksen, eds., *The Economy of the North*, chap. 3, 27–36, Statistisk sentralbyrå - Statistics Norway, Oslo–Kongsvinger (2008).
- [10] E. Stromquist and R. Johnston: *Opportunities and Challenges for arctic oil and gas development*. Tech. rep., Woodrow Wilson International Center For Scholars, Washington, US (2014).
- [11] B. Walsh: *The IEA Says Peak Oil Is Dead. That's Bad News for Climate Policy* (2013).
- [12] Opec: *OPEC Annual Statistical Bulletin 2015*. Tech. rep., Organization of the Petroleum Exporting Countries (2015).
- [13] T. C. Jones: *America, Oil, and War in the Middle East*. Journal of American History **99**(June):208 (2012), doi:10.1093/jahist/jas045.
- [14] R. B. Jackson, J. G. Canadell, C. Le Quéré, R. M. Andrew, J. I. Korsbakken, G. P. Peters, and N. Nakićenovic: *Reaching peak emissions*. Nature Climate Change **4** 1–4 (2015), doi:10.1038/nclimate2892.
- [15] *Global climate in context as the world approaches 1°C above pre-industrial for the first time*. Tech. Rep. November, Met Office United Kingdom, Exeter (2015).
- [16] J. L. Chen, C. R. Wilson, and B. D. Tapley: *Satellite Gravity Measurements Confirm Accelerated Melting of Greenland Ice Sheet*. Science **313**(5795):1958 (2006), doi:10.1126/science.1129007.
- [17] K. Compton, R. A. Bennett, and S. Hreinsdóttir: *Climate-driven vertical acceleration of Icelandic crust measured by continuous GPS geodesy*. Geophysical Research Letters **42**(3):743 (2015), doi:10.1002/2014GL062446.

- [18] a. J. Cook, a. J. Fox, D. G. Vaughan, and J. G. Ferrigno: *Retreating glacier fronts on the Antarctic Peninsula over the past half-century*. Science (New York, N.Y.) **308**(5721):541 (2005), doi:10.1126/science.1104235.
- [19] WWF Nepal Program: *An Overview of Glaciers, Glacier Retreat, and Subsequent Impacts in Nepal, India and China* 80 (2005).
- [20] B. Davies and N. Glasser: *Accelerating shrinkage of Patagonian glaciers from the Little Ice Age (~AD 1870) to the present day*. Journal of Glaciology **58**(212):1063 (2012).
- [21] N. Cannone, G. Diolaiuti, M. Guglielmin, and C. Smiraglia: *Accelerating climate change impacts on alpine glacier forefield ecosystems in the European Alps*. Ecological Applications **18**(3):637 (2008), doi:10.1890/07-1188.1.
- [22] G. Jouvet, M. Huss, H. Blatter, and M. Funk: *Modelling the retreat of Great Aletschglacier in a changing climate*. Journal of Glaciology **57**(206):1033 (2011), doi:10.3189/002214311798843359.
- [23] N. M. Kehrwald, L. G. Thompson, Y. Tandong, E. Mosley-Thompson, U. Schotterer, V. Alfimov, J. Beer, J. Eikenberg, and M. E. Davis: *Mass loss on himalayan glacier endangers water resources*. Geophysical Research Letters **35**(22):2 (2008), doi:10.1029/2008GL035556.
- [24] E. M. Fischer and R. Knutti: *Anthropogenic contribution to global occurrence of heavy-precipitation and high-temperature extremes*. Nature Climate Change **5**(April):1 (2015), doi:10.1038/nclimate2617.
- [25] C. Deutsch, H. Brix, T. Ito, and L. Thompson: *Climate-Forced Variability of Ocean Hypoxia*. Science **333**(6040):336 (2011), doi:10.1126/science.1202422.
- [26] J. D. Sutter and J. Berlinger: *Final draft of climate deal formally accepted in Paris* (2015).
- [27] M. C. Hatch, S. Wallenstein, J. Beyea, J. W. Nieves, and M. Susser: *Cancer rates after the Three Mile Island nuclear accident and proximity of residence to the plant*. American Journal of Public Health **81**(6):719 (1991), doi:10.2105/AJPH.81.6.719.
- [28] A. V. Yablokov, V. B. Nesterenko, A. V. Nesterenko, and J. D. Sherman-Nevinger: *Chernobyl: Consequences of the Catastrophe for People and the Environment*. Wiley-Blackwell, New York, 1st ed. edn. (2010).
- [29] P. Y. Lipsy, K. E. Kushida, and T. Incerti: *The fukushima disaster and Japan's nuclear plant vulnerability in comparative perspective*. Environmental Science and Technology **47**(12):6082 (2013), doi:10.1021/es4004813.
- [30] Federal Ministry for the Environment (BMU): *Long-term Scenarios and Strategies for the Development of Renewable Energy in Germany Considering Development in Europe and Globally*. Tech. rep., Federal Ministry for the Environment (BMU), Berlin (2012).
- [31] A. Breidhardt, A. Rinke, H.-E. Busemann, and S. Brown: *German government wants nuclear exit by 2022 at latest (Reuters)* (2011).
- [32] T. M. Eggenhuisen, Y. Galagan, a. F. K. V. Biezemans, T. M. W. L. Slaats, W. P. Voorthuijzen, S. Kommeren, S. Shanmugam, J. P. Teunissen, a. Hadipour, W. J. H. Verhees, S. C. Veenstra, M. J. J. Coenen, J. Gilot, R. Andriessen, and W. a. Groen: *High efficiency, fully inkjet printed organic solar cells with freedom of design*. J. Mater. Chem. A **3**(14):7255 (2015), doi:10.1039/C5TA00540J.



- [33] M. Kaltenbrunner, M. S. White, E. D. Głowacki, T. Sekitani, T. Someya, N. S. Sariciftci, and S. Bauer: *Ultrathin and lightweight organic solar cells with high flexibility*. Nature Communications **3**:770 (2012), doi:10.1038/ncomms1772.
- [34] C. W. Tang: *Two-layer organic photovoltaic cell*. Applied Physics Letters **48**(2):183 (1986), doi:10.1063/1.96937.
- [35] Heliateg GmbH: *Heliateg sets new Organic Photovoltaic world record efficiency of 13.2%*. Press Release, 8th February (2016).
- [36] NREL: *Best Research-Cell Efficiencies* (2016).
- [37] J.-H. Huang, Z.-Y. Ho, T.-H. Kuo, D. Kekuda, C.-W. Chu, and K.-C. Ho: *Fabrication of multilayer organic solar cells through a stamping technique*. Journal of Materials Chemistry **19**(24):4077 (2009), doi:10.1039/b903765a.
- [38] K. W. Chou, B. Yan, R. Li, E. Q. Li, K. Zhao, D. H. Anjum, S. Alvarez, R. Gassaway, A. Biocca, S. T. Thoroddsen, A. Hexemer, and A. Amassian: *Spin-cast bulk heterojunction solar cells: A dynamical investigation*. Advanced Materials **25**(13):1923 (2013), doi:10.1002/adma.201203440.
- [39] L. Burtone, J. Fischer, K. Leo, and M. Riede: *Trap states in ZnPc:C60 small-molecule organic solar cells*. Physical Review B - Condensed Matter and Materials Physics **87**:1 (2013), doi:10.1103/PhysRevB.87.045432.
- [40] J. Fischer, D. Ray, H. Kleemann, P. Pahnner, M. Schwarze, C. Koerner, K. Vandewal, and K. Leo: *Density of states determination in organic donor-acceptor blend layers enabled by molecular doping*. Journal of Applied Physics **117**(24):245501 (2015), doi:10.1063/1.4922587.
- [41] S. Olthof, S. Singh, S. K. Mohapatra, S. Barlow, S. R. Marder, B. Kippelen, and A. Kahn: *Passivation of trap states in unpurified and purified C60 and the influence on organic field-effect transistor performance*. Applied Physics Letters **101**(25):253303 (2012), doi:10.1063/1.4772551.
- [42] M. M. Mandoc, F. B. Kooistra, J. C. Hummelen, B. De Boer, and P. W. M. Blom: *Effect of traps on the performance of bulk heterojunction organic solar cells*. Applied Physics Letters **91**(26):2005 (2007), doi:10.1063/1.2821368.
- [43] H. T. Nicolai, M. Kuik, G. a. H. Wetzelaer, B. de Boer, C. Campbell, C. Risko, J. L. Brédas, and P. W. M. Blom: *Unification of trap-limited electron transport in semiconducting polymers*. Nature Materials **11**(8):1 (2012), doi:10.1038/nmat3384.
- [44] J. Schafferhans, A. Baumann, C. Deibel, and V. Dyakonov: *Trap distribution and the impact of oxygen-induced traps on the charge transport in poly(3-hexylthiophene)*. Applied Physics Letters **93**(9):093303 (2008), doi:10.1063/1.2978237.
- [45] C. G. Shuttle, N. D. Treat, J. D. Douglas, J. M. J. Fréchet, and M. L. Chabinyc: *Deep energetic trap states in organic photovoltaic devices*. Advanced Energy Materials **2**(1):111 (2012), doi:10.1002/aenm.201100541.
- [46] A. Domanski, I. Lieberwirth, E. Sengupta, K. Landfester, H.-J. Butt, R. Berger, J. Rauh, V. Dyakonov, and C. Deibel: *Effect of Morphological Changes on Presence of Trap States in P3HT: PCBM Solar Cells Studied by Cross-Sectional Energy Filtered TEM and Thermally Stimulated*. The Journal of Physical Chemistry C **117**(45):23495 (2013).

- [47] B. a. Gregg, S.-G. Chen, and R. a. Cormier: *Coulomb Forces and Doping in Organic Semiconductors*. Chemistry of Materials **16**(23):4586 (2004), doi:10.1021/cm049625c.
- [48] S.-J. Yoo and J.-J. Kim: *Charge Transport in Electrically Doped Amorphous Organic Semiconductors*. Macromolecular Rapid Communications **36**(11):984 (2015), doi:10.1002/marc.201500026.
- [49] E. Schrödinger: *Quantisierung als Eigenwertproblem*. Annalen der Physik (1926).
- [50] C. Cohen-Tannoudji, B. Diu, and F. Laloe: *Quantum mechanics vol.1*. Wiley-Interscience, New York (1977).
- [51] W. Demtröder: *Experimentalphysik 3: Atome, Moleküle und Festkörper*. Springer Verlag, Berlin Heidelberg New York, 3rd edn. (2005).
- [52] J. Brédas, D. Beljonne, V. Coropceanu, and J. Cornil: *Charge-transfer and energy-transfer processes in  $\pi$ -conjugated oligomers and polymers: a molecular picture*. Chemical Reviews **104**:4971 (2004).
- [53] M. Piacenza and S. Grimme: *Van der Waals interactions in aromatic systems: structure and energetics of dimers and trimers of pyridine*. ChemPhysChem **6**(8):1554 (2005), doi:10.1002/cphc.200500100.
- [54] D. Venkateshvaran, M. Nikolka, A. Sadhanala, V. Lemaire, M. Zelazny, M. Kepa, M. Hurhangee, A. J. Kronemeijer, V. Pecunia, I. Nasrallah, I. Romanov, K. Broch, I. McCulloch, D. Emin, Y. Olivier, J. Cornil, D. Beljonne, and H. Sirringhaus: *Approaching disorder-free transport in high-mobility conjugated polymers*. Nature **515**(7527):384 (2014), doi:10.1038/nature13854.
- [55] N. Karl: *Organic semiconductors*. H. J. Queisser, ed., *Festkörperprobleme 14 SE - 11*, vol. 14 of *Advances in Solid State Physics*, 261–290, Springer Berlin Heidelberg (1974), doi:10.1007/BFb0108470.
- [56] E. Silinsh: *Organic Molecular Crystals*. Springer-Verlag, Berlin Heidelberg New York (1978).
- [57] I. Vilfan: *Small polaron model of the electron motion in organic molecular crystals*. physica status solidi (b) **351** (1973).
- [58] C. Körner: *Oligothiophene Materials for Organic Solar Cells - Photophysics and Device Properties*. Ph.D. thesis, Technische Universität Dresden (2012).
- [59] D. L. Dexter: *A Theory of Sensitized Luminescence in Solids*. The Journal of Chemical Physics **21**(1953):836 (1953), doi:10.1063/1.1699044.
- [60] T. Förster: *Energiewanderung und Fluoreszenz*. Annalen der Physik **437**(1-2):55 (1948), doi:10.1007/BF00585226.
- [61] R. C. Powell and Z. G. Soos: *Singlet exciton energy transfer in organic solids*. Journal of Luminescence **11**:1 (1975), doi:10.1016/0022-2313(75)90077-0.
- [62] R. R. Lunt, N. C. Giebink, A. a. Belak, J. B. Benziger, and S. R. Forrest: *Exciton diffusion lengths of organic semiconductor thin films measured by spectrally resolved photoluminescence quenching*. Journal of Applied Physics **105**(2009) (2009), doi:10.1063/1.3079797.
- [63] G. M. Akselrod, P. B. Deotare, N. J. Thompson, J. Lee, W. a. Tisdale, M. a. Baldo, V. M. Menon, and V. Bulović: *Visualization of exciton transport in ordered and disordered molecular solids*. Nature communications **5**:3646 (2014), doi:10.1038/ncomms4646.

- [64] T. a. Ford, H. Ohkita, S. Cook, J. R. Durrant, and N. C. Greenham: *Direct observation of intersystem crossing in charge-pair states in polyfluorene polymer blends*. Chemical Physics Letters **454**:237 (2008), doi:10.1016/j.cplett.2008.02.021.
- [65] C. L. Lee, X. Yang, and N. C. Greenham: *Determination of the triplet excited-state absorption cross section in a polyfluorene by energy transfer from a phosphorescent metal complex*. Physical Review B **76**:1 (2007), doi:10.1103/PhysRevB.76.245201.
- [66] T. a. Ford, I. Avilov, D. Beljonne, and N. C. Greenham: *Enhanced triplet exciton generation in polyfluorene blends*. Physical Review B - Condensed Matter and Materials Physics **71**:1 (2005), doi:10.1103/PhysRevB.71.125212.
- [67] S. Hofmann, T. C. Rosenow, M. C. Gather, B. Lüssem, and K. Leo: *Singlet exciton diffusion length in organic light-emitting diodes*. Physical Review B - Condensed Matter and Materials Physics **85**:1 (2012), doi:10.1103/PhysRevB.85.245209.
- [68] J. D. a. Lin, O. V. Mikhnenko, J. Chen, Z. Masri, A. Ruseckas, A. Mikhailovsky, R. P. Raab, J. Liu, P. W. M. Blom, M. A. Loi, C. J. García-Cervera, I. D. W. Samuel, and T.-Q. Nguyen: *Systematic study of exciton diffusion length in organic semiconductors by six experimental methods*. Materials Horizons **1**:280 (2014), doi:10.1039/c3mh00089c.
- [69] S. D. Stranks, G. E. Eperon, G. Grancini, C. Menelaou, M. J. P. Alcocer, T. Leijtens, L. M. Herz, A. Petrozza, and H. J. Snaith: *Electron-hole diffusion lengths exceeding 1 micrometer in an organometal trihalide perovskite absorber*. Science **342**(October):341 (2013), doi:10.1126/science.1243982.
- [70] S. Bai, Z. Wu, X. Wu, Y. Jin, N. Zhao, Z. Chen, and Q. Mei: *High-performance planar heterojunction perovskite solar cells : Preserving long charge carrier diffusion lengths and interfacial engineering*. Nano Research **7**(12):1749 (2014), doi:10.1007/s12274-014-0534-8.
- [71] L. E. Polander, P. Pahner, M. Schwarze, M. Saalfrank, C. Koerner, and K. Leo: *Hole-transport material variation in fully vacuum deposited perovskite solar cells*. APL Materials **2**:081503 (2014), doi:10.1063/1.4889843.
- [72] C. D. Dimitrakopoulos and D. J. Mascaro: *Organic thin-film transistors: A review of recent advances*. IBM Journal of Research and Development **45**(1):11 (2001), doi:10.1147/rd.451.0011.
- [73] R. Ruiz, D. Choudhary, B. Nickel, T. Toccoli, K. C. Chang, A. C. Mayer, P. Clancy, J. M. Blakely, R. L. Headrick, S. Iannotta, and G. G. Malliaras: *Pentacene thin film growth*. Chemistry of Materials **16**:4497 (2004), doi:10.1021/cm049563q.
- [74] M. Pope and C. Swenberg: *Electronic Processes in Organic Crystals and Polymers*. Oxford University Press, Oxford, 2nd edn. (1999).
- [75] J. E. Anthony, A. Facchetti, M. Heeney, S. R. Marder, and X. Zhan: *N-Type organic semiconductors in organic electronics*. Advanced Materials **22**:3876 (2010), doi:10.1002/adma.200903628.
- [76] A. Facchetti: *Made to order: Organic semiconductors*. Nature Materials **12**(July):598 (2013), doi:10.1038/nmat3686.
- [77] J. Rivnay, A. Salleo, S. Mannsfeld, C. Miller, and M. Toney: *Determination of Organic Semiconductor Microstructure from the Molecular to Device Scale with Quantitative X-ray Scattering and Absorption Analyses*. Chemical Reviews **112**(10):5488 (2012), doi:10.1021/cr3001109.

- [78] S. C. B. Mannsfeld, M. L. Tang, and Z. Bao: *Thin film structure of triisopropylsilylethynyl-functionalized pentacene and tetraceno[2,3-b]thiophene from grazing incidence x-ray diffraction*. *Advanced Materials* **23**:127 (2011), doi:10.1002/adma.201003135.
- [79] J. E. Anthony: *Induced  $\pi$ -Stacking in Acenes*. T. J. Müller and U. H. F. Bunz, eds., *Functional Organic Materials: Syntheses, Strategies and Applications*, chap. 14, Wiley VCH, Weinheim, 1st edn. (2007).
- [80] J. L. Brédas, J. P. Calbert, D. a. da Silva Filho, and J. Cornil: *Organic semiconductors: a theoretical characterization of the basic parameters governing charge transport*. *Proceedings of the National Academy of Sciences of the United States of America* **99**(9):5804 (2002), doi:10.1073/pnas.092143399.
- [81] W. Brütting, C. Adachi, and R. J. Holmes: *Physics of Organic Semiconductors*. Wiley (2012).
- [82] S. Pfuetzner, C. Mickel, J. Jankowski, M. Hein, J. Meiss, C. Schuenemann, C. Elschner, A. a. Levin, B. Rellinghaus, K. Leo, and M. Riede: *The influence of substrate heating on morphology and layer growth in C 60: ZnPc bulk heterojunction solar cells*. *Organic Electronics: physics, materials, applications* **12**(3):435 (2011), doi:10.1016/j.orgel.2010.12.007.
- [83] C. Schünemann, D. Wynands, L. Wilde, M. P. Hein, S. Pfütznern, C. Elschner, K.-J. Eichhorn, K. Leo, and M. Riede: *Phase separation analysis of bulk heterojunctions in small-molecule organic solar cells using zinc-phthalocyanine and C<sub>60</sub>*. *Physical Review B* **85**(24):245314 (2012), doi:10.1103/PhysRevB.85.245314.
- [84] K. Xiao, W. Deng, J. K. Keum, M. Yoon, I. V. Vlassiouk, W. Kendal, A.-p. Li, I. I. Kravchenko, G. Gu, E. A. Payzant, G. Sumpter, S. C. Smith, J. F. Browning, D. B. Geohegan, K. W. Clark, E. a. Payzant, B. G. Sumpter, S. C. Smith, and F. James: *Surface-Induced Orientation Control of CuPc Molecules for the Epitaxial Growth of Highly Ordered Organic Crystals on Graphene*. *Journal of the American Chemical Society* **135**(9):3680 (2013), doi:10.1021/ja3125096.
- [85] H. J. Kim, J.-H. Lee, J. W. Kim, S. Lee, J. Jang, H. H. Lee, and J.-J. Kim: *Molecular alignment and nanostructure of 1,4,5,8,9,11-hexaazatriphenylene-hexanitrile (HATCN) thin films on organic surfaces*. *Journal of Materials Chemistry C* **1**:1260 (2013), doi:10.1039/c2tc00331g.
- [86] R. Resel, M. Ottmar, M. Hanack, J. Keckes, and G. Leising: *Preferred Orientation of Copper Phthalocyanine Thin Films Evaporated on Amorphous Substrates*. *Journal of Materials Research* **15**(04):934 (2000).
- [87] R. Naito, S. Toyoshima, T. Ohashi, T. Sakurai, and K. Akimoto: *Molecular orientation control of phthalocyanine thin film by inserting pentacene buffer layer*. *Japanese Journal of Applied Physics* **47**:1416 (2008), doi:10.1143/JJAP.47.1416.
- [88] Y. Zhou, T. Taima, T. Miyadera, T. Yamanari, M. Kitamura, K. Nakatsu, and Y. Yoshida: *Glancing Angle Deposition of Copper Iodide Nanocrystals for Efficient Organic Photovoltaics*. *Nano letters* **12**(8):4146 (2012).
- [89] D. Hong, Y. R. Do, H. T. Kwak, and S. Yim: *Structural templating and growth behavior of copper phthalocyanine thin films deposited on a polycrystalline perylenetetracarboxylic dianhydride layer*. *Journal of Applied Physics* **109**(2011) (2011), doi:10.1063/1.3553884.

- 
- [90] T. B. Fleetham, J. P. Mudrick, W. Cao, K. Klimes, J. Xue, and J. Li: *Efficient zinc phthalocyanine/C60 heterojunction photovoltaic devices employing tetracene anode interfacial layers*. ACS Applied Materials and Interfaces **6**:7254 (2014), doi:10.1021/am500472m.
  - [91] M. L. Tietze: *Molecular Doping Processes in Organic Semiconductors investigated by Photoelectron Spectroscopy*. Ph.D. thesis, Technische Universität Dresden (2014).
  - [92] Q. Chen, T. Rada, A. McDowall, and N. V. Richardson: *Epitaxial Growth of a Crystalline Organic Semiconductor : Perylene / Cu { 110 }.* Chemistry of Materials **14**(2):743 (2002), doi:10.1021/cm011185r.
  - [93] A. a. Virkar, S. Mannsfeld, Z. Bao, and N. Stingelin: *Organic semiconductor growth and morphology considerations for organic thin-film transistors*. Advanced Materials **22**:3857 (2010), doi:10.1002/adma.200903193.
  - [94] S. Olthof: *Photoelectron Spectroscopy on Doped Organic Semiconductors and Related Interfaces*. Ph.D. thesis, Technische Universität Dresden (2010).
  - [95] J. Hwang, A. Wan, and A. Kahn: *Energetics of metal–organic interfaces: New experiments and assessment of the field*. Materials Science and Engineering: R: Reports **64**(1-2):1 (2009), doi:10.1016/j.mser.2008.12.001.
  - [96] M. Oehzelt, N. Koch, and G. Heimel: *Organic semiconductor density of states controls the energy level alignment at electrode interfaces*. Nature communications **5**(May):4174 (2014), doi:10.1038/ncomms5174.
  - [97] C. Tengstedt, W. Osikowicz, W. R. Salaneck, I. D. Parker, C. H. Hsu, and M. Fahlman: *Fermi-level pinning at conjugated polymer interfaces*. Applied Physics Letters **88**(2006):1 (2006), doi:10.1063/1.2168515.
  - [98] M. Fahlman, a. Crispin, X. Crispin, S. K. M. Henze, M. P. de Jong, W. Osikowicz, C. Tengstedt, and W. R. Salaneck: *Electronic structure of hybrid interfaces for polymer-based electronics*. Journal of physics. Condensed matter : an Institute of Physics journal **19**:183202 (2007), doi:10.1088/0953-8984/19/18/183202.
  - [99] S. Braun, W. R. Salaneck, and M. Fahlman: *Energy-level alignment at organic/metal and organic/organic interfaces*. Advanced Materials **21**:1450 (2009), doi:10.1002/adma.200802893.
  - [100] H. Ishii, K. Sugiyama, E. Ito, and K. Seki: *Energy Level Alignment and Interfacial Electronic Structures at Organic/Metal and Organic/Organic Interfaces*. Advanced Materials **11**(8):605 (1999), doi:10.1002/(SICI)1521-4095(199906)11:8<605::AID-ADMA605>3.0.CO;2-Q.
  - [101] C. Shen and a. Kahn: *The role of interface states in controlling the electronic structure of Alq 3/reactive metal contacts*. Organic Electronics **2**:89 (2001), doi:10.1016/S1566-1199(01)00015-5.
  - [102] C. Shen, a. Kahn, and J. Schwartz: *Chemical and electrical properties of interfaces between magnesium and aluminum and tris-(8-hydroxy quinoline) aluminum*. Journal of Applied Physics **89**(1):449 (2001), doi:10.1063/1.1333740.
  - [103] M. G. Mason, C. W. Tang, L. S. Hung, P. Raychaudhuri, J. Madathil, D. J. Giesen, L. Yan, Q. T. Le, Y. Gao, S. T. Lee, L. S. Liao, L. F. Cheng, W. R. Salaneck, D. a. Dos Santos, and J. L. Brédas: *Interfacial chemistry of Alq3 and LiF with reactive metals*. Journal of Applied Physics **89**(2001):2756 (2001), doi:10.1063/1.1324681.

- [104] H. Vázquez, F. Flores, R. Oszwaldowski, J. Ortega, R. Pérez, and A. Kahn: *Barrier formation at metal-organic interfaces: Dipole formation and the charge neutrality level*. Applied Surface Science **234**:107 (2004), doi:10.1016/j.apsusc.2004.05.084.
- [105] H. Vázquez, F. Flores, and A. Kahn: *Induced Density of States model for weakly-interacting organic semiconductor interfaces*. Organic Electronics **8**:241 (2007), doi:10.1016/j.orgel.2006.07.006.
- [106] N. Hayashi, H. Ishii, Y. Ouchi, and K. Seki: *Examination of band bending at buckminsterfullerene (C<sub>60</sub>)/metal interfaces by the Kelvin probe method*. Journal of Applied Physics **92**(2002):3784 (2002), doi:10.1063/1.1504495.
- [107] K. Walzer, B. Maennig, M. Pfeiffer, and K. Leo: *Highly efficient organic devices based on electrically doped transport layers*. Chemical reviews **107**(4):1233 (2007), doi:10.1021/cr050156n.
- [108] S. Reineke, F. Lindner, G. Schwartz, N. Seidler, K. Walzer, B. Lüssem, and K. Leo: *White organic light-emitting diodes with fluorescent tube efficiency*. Nature **459**(7244):234 (2009), doi:10.1038/nature08003.
- [109] R. Meerheim, C. Körner, and K. Leo: *Highly efficient organic multi-junction solar cells with a thiophene based donor material*. Applied Physics Letters **105**(6):063306 (2014), doi:10.1063/1.4893012.
- [110] J. X. Tang, C. S. Lee, and S. T. Lee: *Electronic structures of organic/organic heterojunctions: From vacuum level alignment to Fermi level pinning*. Journal of Applied Physics **101**(2007):1 (2007), doi:10.1063/1.2710297.
- [111] J. X. Tang, K. M. Lau, C. S. Lee, and S. T. Lee: *Substrate effects on the electronic properties of an organic/organic heterojunction*. Applied Physics Letters **88**(2006):11 (2006), doi:10.1063/1.2209212.
- [112] I. G. Hill and A. Kahn: *Energy level alignment at interfaces of organic semiconductor heterostructures*. Journal of Applied Physics **84**(10):5583 (1998), doi:10.1063/1.368864.
- [113] I. Hill, D. Milliron, J. Schwartz, and A. Kahn: *Organic semiconductor interfaces: electronic structure and transport properties*. Applied Surface Science **166**:354 (2000), doi:10.1016/S0169-4332(00)00449-9.
- [114] S. Olthof, R. Meerheim, M. Schober, and K. Leo: *Energy level alignment at the interfaces in a multilayer organic light-emitting diode structure*. Physical Review B **79**(June):1 (2009), doi:10.1103/PhysRevB.79.245308.
- [115] R. J. Murdey and W. R. Salaneck: *Charge injection barrier heights across multilayer organic thin films*. Japanese Journal of Applied Physics, Part 1: Regular Papers and Short Notes and Review Papers **44**:3751 (2005), doi:10.1143/JJAP.44.3751.
- [116] S. Braun, M. P. De Jong, W. Osikowicz, and W. R. Salaneck: *Influence of the electrode work function on the energy level alignment at organic-organic interfaces*. Applied Physics Letters **91**(2007):11 (2007), doi:10.1063/1.2806938.
- [117] W. Zhao, E. Salomon, Q. Zhang, S. Barlow, S. R. Marder, and A. Kahn: *Substrate-dependent electronic structure of an organic heterojunction*. Physical Review B - Condensed Matter and Materials Physics **77**:1 (2008), doi:10.1103/PhysRevB.77.165336.
- [118] N. Tessler, Y. Preezant, N. Rappaport, and Y. Roichman: *Charge Transport in Disordered Organic Materials and Its Relevance to Thin-Film Devices: A Tutorial Review*. Advanced Materials **21**(27):2741 (2009), doi:10.1002/adma.200803541.

- [119] J. O. Oelerich, F. Jansson, a. V. Nenashev, F. Gebhard, and S. D. Baranovskii: *Energy position of the transport path in disordered organic semiconductors*. Journal of Physics: Condensed Matter **26**(25):255801 (2014), doi:10.1088/0953-8984/26/25/255801.
- [120] S. D. Baranovskii: *Theoretical description of charge transport in disordered organic semiconductors*. physica status solidi (b) **251**(3):487 (2014), doi:10.1002/pssb.201350339.
- [121] N. W. Ashcroft and D. N. Mermin: *Festkörperphysik*. Oldenbourg, München, 3rd edn. (2007).
- [122] K. Bolotin, K. Sikes, Z. Jiang, M. Klima, G. Fudenberg, J. Hone, P. Kim, and H. Stormer: *Ultra-high electron mobility in suspended graphene*. Solid State Communications **146**(9-10):351 (2008), doi:10.1016/j.ssc.2008.02.024.
- [123] V. Umansky, M. Heiblum, Y. Levinson, J. Smet, J. Nübler, and M. Dolev: *MBE growth of ultra-low disorder 2DEG with mobility exceeding  $35 \times 10^6 \text{ cm}^2/\text{Vs}$* . Journal of Crystal Growth **311**(7):1658 (2009), doi:10.1016/j.jcrysgro.2008.09.151.
- [124] M. Prince: *Drift mobilities in semiconductors. I. Germanium*. Physical Review **92**(3) (1953).
- [125] N. Karl, K. H. Kraft, J. Marktanner, M. Münch, F. Schatz, R. Stehle, and H. M. Uhde: *Fast electronic transport in organic molecular solids?* Journal of Vacuum Science & Technology A **17**(4):2318 (1999), doi:doi: 10.1116/1.581767.
- [126] W. Xie, K. A. McGarry, F. Liu, Y. Wu, P. P. Ruden, C. J. Douglas, and C. D. Frisbie: *High-mobility transistors based on single crystals of isotopically substituted rubrene- d 28*. Journal of Physical Chemistry C **117**(22):11522 (2013), doi:10.1021/jp402250v.
- [127] D. J. Gundlach, Y. Y. Lin, T. N. Jackson, S. F. Nelson, and D. G. Schlom: *Pentacene organic thin-film transistors-molecular ordering and mobility*. IEEE Electron Device Letters **18**(3):87 (1997), doi:10.1109/55.556089.
- [128] H. Kleemann, C. Schuenemann, A. a. Zakhidov, M. Riede, B. Lüssem, and K. Leo: *Structural phase transition in pentacene caused by molecular doping and its effect on charge carrier mobility*. Organic Electronics **13**(1):58 (2012), doi:10.1016/j.orgel.2011.09.027.
- [129] M. P. Hein, A. a. Zakhidov, B. Lüssem, J. Jankowski, M. L. Tietze, M. K. Riede, and K. Leo: *Molecular doping for control of gate bias stress in organic thin film transistors*. Applied Physics Letters **104** (2014), doi:10.1063/1.4861168.
- [130] T. Menke, D. Ray, H. Kleemann, K. Leo, and M. Riede: *Determining doping efficiency and mobility from conductivity and Seebeck data of n-doped C60 layers*. arXiv **1410.7119**(D):1 (2014).
- [131] J. Schafferhans, A. Baumann, A. Wagenpfahl, C. Deibel, and V. Dyakonov: *Oxygen doping of P3HT:PCBM blends: Influence on trap states, charge carrier mobility and solar cell performance*. Organic Electronics: physics, materials, applications **11**(10):1693 (2010), doi:10.1016/j.orgel.2010.07.016.
- [132] P. Pingel, R. Schwarzl, and D. Neher: *Effect of molecular p-doping on hole density and mobility in poly(3-hexylthiophene)*. Applied Physics Letters **100**(14):143303 (2012), doi:10.1063/1.3701729.
- [133] T. Sakanoue and H. Sirringhaus: *Band-like temperature dependence of mobility in a solution-processed organic semiconductor*. Nature Materials **9**(9):736 (2010), doi:10.1038/nmat2825.

- [134] A. S. Dhoot, G. M. Wang, D. Moses, and A. J. Heeger: *Voltage-Induced Metal-Insulator Transition in Polythiophene Field-Effect Transistors*. Physical Review Letters **96**(24):246403 (2006), doi:10.1103/PhysRevLett.96.246403.
- [135] B. Movaghar, M. Grünewald, B. Ries, H. Bässler, and D. Würtz: *Diffusion and relaxation of energy in disordered organic and inorganic materials*. Physical Review B **33**(8) (1986).
- [136] A. Miller and E. Abrahams: *Impurity conduction at low concentrations*. Physical Review **257** (1960).
- [137] N. Mott and W. Twose: *The theory of impurity conduction*. Advances in Physics **10**(38):107 (1961), doi:10.1080/00018736100101271.
- [138] S. Novikov, D. Dunlap, V. Kenkre, P. Parris, and a. Vannikov: *Essential Role of Correlations in Governing Charge Transport in Disordered Organic Materials*. Physical Review Letters **81**(20):4472 (1998), doi:10.1103/PhysRevLett.81.4472.
- [139] N. F. Mott: *Conduction in non-crystalline materials*. Philosophical Magazine **19**(160):835 (1969), doi:10.1080/14786436908216338.
- [140] Y. Preezant and N. Tessler: *Carrier heating in disordered organic semiconductors*. Physical Review B **74**(23):235202 (2006), doi:10.1103/PhysRevB.74.235202.
- [141] V. Ambegaokar, B. I. Halperin, and J. S. Langer: *Hopping Conductivity in Disordered Systems*. Physical Review B **4**(8) (1971), doi:doi:10.1103/PhysRevB.4.2612.
- [142] M. Vissenberg and M. Matters: *Theory of the field-effect mobility in amorphous organic transistors*. Physical Review B **57**(20):964 (1998).
- [143] G. Pike and C. Seager: *Percolation and conductivity: A computer study. I*. Physical Review B **10**(4) (1974).
- [144] M. Pollak: *A percolation treatment of DC hopping conduction*. Journal of Non-Crystalline Solids **8-10**:486 (1972).
- [145] M. Grünewald and P. Thomas: *A hopping model for activated charge transport in amorphous silicon*. physica status solidi (b) **94**(1):125 (1979), doi:10.1002/pssb.2220940113.
- [146] D. Monroe: *Hopping in exponential band tails*. Physical Review Letters **54**(2):146 (1985).
- [147] S. D. Baranovskii, T. Faber, F. Hensel, and P. Thomas: *The applicability of the transport-energy concept to various disordered materials*. Journal of Physics: Condensed Matter **9**(13):2699 (1997), doi:10.1088/0953-8984/9/13/007.
- [148] S. Baranovskii, H. Cordes, F. Hensel, and G. Leising: *Charge-carrier transport in disordered organic solids*. Physical Review B **62**(12):7934 (2000), doi:10.1103/PhysRevB.62.7934.
- [149] S. Baranovskii and I. Zvyagin: *Percolation approach to hopping transport in organic disordered solids*. physica status solidi (b) **287**(1):281 (2002).
- [150] H. Bässler: *Charge transport in disordered organic photoconductors a Monte Carlo simulation study*. physica status solidi (b) **175**(1):15 (1993).
- [151] Y. Gartstein and E. Conwell: *High-field hopping mobility in molecular systems with spatially correlated energetic disorder*. Chemical physics letters **245**(November):351 (1995).



- 
- [152] L. B. Schein: *Comparison of charge transport models in molecularly doped polymers*. Philosophical Magazine Part B **65**(4):795 (2006), doi:10.1080/13642819208204920.
- [153] S. Naka, H. Okada, H. Onnagawa, Y. Yamaguchi, and T. Tsutsui: *Carrier transport properties of organic materials for EL device operation*. Synthetic Metals **111-112**:331 (2000), doi:10.1016/S0379-6779(99)00358-6.
- [154] H. Murata, G. Malliaras, and M. Uchida: *Non-dispersive and air-stable electron transport in an amorphous organic semiconductor*. Chemical Physics Letters **339**(May) (2001).
- [155] H. H. Fong and S. K. So: *Hole transporting properties of tris(8-hydroxyquinoline) aluminum (Alq<sub>3</sub>)*. Journal of Applied Physics **100**(9):094502 (2006), doi:10.1063/1.2372388.
- [156] W. Pasveer, J. Cottaar, C. Tanase, R. Coehoorn, P. Bobbert, P. Blom, D. de Leeuw, and M. Michels: *Unified Description of Charge-Carrier Mobilities in Disordered Semiconducting Polymers*. Physical Review Letters **94**(20):1 (2005), doi:10.1103/PhysRevLett.94.206601.
- [157] R. Coehoorn, W. Pasveer, P. Bobbert, and M. Michels: *Charge-carrier concentration dependence of the hopping mobility in organic materials with Gaussian disorder*. Physical Review B **72**(15):155206 (2005), doi:10.1103/PhysRevB.72.155206.
- [158] C. Tanase, E. J. Meijer, P. W. M. Blom, and D. M. de Leeuw: *Unification of the Hole Transport in Polymeric Field-Effect Transistors and Light-Emitting Diodes*. Physical Review Letters **91**(21):216601 (2003), doi:10.1103/PhysRevLett.91.216601.
- [159] Z. Yu, D. Smith, a. Saxena, R. Martin, and a. Bishop: *Molecular Geometry Fluctuation Model for the Mobility of Conjugated Polymers*. Physical Review Letters **84**(4):721 (2000), doi:10.1103/PhysRevLett.84.721.
- [160] B. Hartenstein and H. Bässler: *Transport energy for hopping in a Gaussian density of states distribution*. Journal of non-crystalline solids **190**:112 (1995).
- [161] J. O. Oelerich, D. Huemmer, M. Weseloh, and S. D. Baranovskii: *Concentration dependence of the transport energy level for charge carriers in organic semiconductors*. Applied Physics Letters **97**(14):143302 (2010), doi:10.1063/1.3496045.
- [162] G. Schönherr, H. Bässler, and M. Silver: *Simulation of carrier transport and energy relaxation in a macroscopic hopping system of sites with a Gaussian energy distribution*. Philosophical Magazine Part B **44**(3):369 (2006), doi:10.1080/01418638108223559.
- [163] J. Cottaar, L. Koster, R. Coehoorn, and P. Bobbert: *Scaling Theory for Percolative Charge Transport in Disordered Molecular Semiconductors*. Physical Review Letters **107**(13):1 (2011), doi:10.1103/PhysRevLett.107.136601.
- [164] a. V. Nenashev, F. Jansson, J. O. Oelerich, D. Huemmer, a. V. Dvurechenskii, F. Gebhard, and S. D. Baranovskii: *Advanced percolation solution for hopping conductivity*. Physical Review B **87**(23):235204 (2013), doi:10.1103/PhysRevB.87.235204.
- [165] V. Arkhipov, E. Emelianova, and G. Adriaenssens: *Effective transport energy versus the energy of most probable jumps in disordered hopping systems*. Physical Review B **64**(12):125125 (2001), doi:10.1103/PhysRevB.64.125125.

- [166] A. Kadashchuk, Y. Skryshevskii, A. Vakhnin, N. Ostapenko, V. Arkhipov, E. Emelianova, and H. Bässler: *Thermally stimulated photoluminescence in disordered organic materials*. Physical Review B **63**(11):115205 (2001), doi:10.1103/PhysRevB.63.115205.
- [167] V. I. Arkhipov, P. Heremans, E. V. Emelianova, G. J. Adriaenssens, and H. Bassler: *Charge carrier mobility in doped semiconducting polymers*. Applied Physics Letters **82**(19):3245 (2003), doi:10.1063/1.1572965.
- [168] V. I. Arkhipov, J. Reynaert, Y. D. Jin, P. Heremans, E. V. Emelianova, G. J. Adriaenssens, and H. Bässler: *The effect of deep traps on carrier hopping in disordered organic materials*. Synthetic Metals **138**(1-2):209 (2003), doi:10.1016/S0379-6779(02)01267-5.
- [169] J. Bisquert: *Interpretation of electron diffusion coefficient in organic and inorganic semiconductors with broad distributions of states*. Physical chemistry chemical physics : PCCP **10**(22):3175 (2008), doi:10.1039/b719943k.
- [170] D. Mendels and N. Tessler: *The topology of hopping in the energy domain of systems with rapidly decaying density of states*. Journal of Physical Chemistry C **117**(47):24740 (2013), doi:10.1021/jp4089782.
- [171] R. Schmechel: *Gaussian disorder model for high carrier densities: Theoretical aspects and application to experiments*. Physical Review B **66**(23):235206 (2002), doi:10.1103/PhysRevB.66.235206.
- [172] I. I. Fishchuk, a. K. Kadashchuk, J. Genoe, M. Ullah, H. Sitter, T. B. Singh, N. S. Sariciftci, and H. Bässler: *Temperature dependence of the charge carrier mobility in disordered organic semiconductors at large carrier concentrations*. Physical Review B **81**(4):045202 (2010), doi:10.1103/PhysRevB.81.045202.
- [173] A. Mityashin, Y. Olivier, T. Van Regemorter, C. Rolin, S. Verlaak, N. G. Martinelli, D. Beljonne, J. Cornil, J. Genoe, and P. Heremans: *Unraveling the mechanism of molecular doping in organic semiconductors*. Advanced Materials **24**(12):1535 (2012), doi:10.1002/adma.201104269.
- [174] F. Löser, M. L. Tietze, B. Lüssem, and J. Blochwitz-Nimoth: *Conductivity Doping*. D. J. Gaspar and E. Polikarpov, eds., *OLED Fundamentals: Materials, Devices, and Processing of Organic Light-Emitting Diodes*, chap. 9, 504 pp, Boca Raton: CRC Press / Taylor & Francis Group, 1 edn. (2015).
- [175] B. Lüssem, M. Riede, and K. Leo: *Doping of organic semiconductors*. Physica Status Solidi (a) **210**(1):9 (2013), doi:10.1002/pssa.201228310.
- [176] M. Pfeiffer, A. Beyer, T. Fritz, and K. Leo: *Controlled doping of phthalocyanine layers by cosublimation with acceptor molecules: A systematic Seebeck and conductivity study*. Applied Physics Letters **73**(22):3202 (1998), doi:10.1063/1.122718.
- [177] B. Maennig, M. Pfeiffer, a. Nollau, X. Zhou, K. Leo, and P. Simon: *Controlled p-type doping of polycrystalline and amorphous organic layers: Self-consistent description of conductivity and field-effect mobility by a microscopic percolation model*. Physical Review B **64**(19):1 (2001), doi:10.1103/PhysRevB.64.195208.
- [178] I. Salzmann, G. Heimel, S. Duhm, M. Oehzelt, P. Pingel, B. M. George, A. Schnegg, K. Lips, R.-P. Blum, A. Vollmer, and N. Koch: *Intermolecular Hybridization Governs Molecular Electrical Doping*. Physical Review Letters **108**(3):035502 (2012), doi:10.1103/PhysRevLett.108.035502.

- [179] P. Pingel and D. Neher: *Comprehensive picture of p-type doping of P3HT with the molecular acceptor F4TCNQ*. Physical Review B **87**(11):115209 (2013), doi:10.1103/PhysRevB.87.115209.
- [180] S. Olthof, S. Mehraeen, S. Mohapatra, S. Barlow, V. Coropceanu, J.-L. Brédas, S. Marder, and A. Kahn: *Ultralow Doping in Organic Semiconductors: Evidence of Trap Filling*. Physical Review Letters **109**(17):1 (2012), doi:10.1103/PhysRevLett.109.176601.
- [181] M. L. Tietze, K. Leo, and B. Lüssem: *Quantification of deep hole-trap filling by molecular p-doping: Dependence on the host material purity*. Organic Electronics **14**(9):2348 (2013), doi:10.1016/j.orgel.2013.05.036.
- [182] P. Pahner, H. Kleemann, L. Burtone, M. L. Tietze, J. Fischer, K. Leo, and B. Lüssem: *Pentacene Schottky diodes studied by impedance spectroscopy: Doping properties and trap response*. Physical Review B **88**(19):195205 (2013), doi:10.1103/PhysRevB.88.195205.
- [183] M. L. Tietze, P. Pahner, K. Schmidt, K. Leo, and B. Lüssem: *Doped Organic Semiconductors: Trap-filling, Impurity Saturation, and Reserve Regimes*. Advanced Functional Materials **25**(18):2701 (2015), doi:10.1002/adfm.201404549.
- [184] B. A. Bolto and D. E. Weiss: *Electronic Conduction in Polymers. II. The Electrochemical Reduction of Polypyrrole at Controlled Potential*. Australian Journal of Chemistry **16**(6):1076 (1963).
- [185] B. A. Bolto, R. McNeill, and D. E. Weiss: *Electronic Conduction in Polymers. III. Electronic Properties of Polypyrrole*. Australian Journal of Chemistry **16**(6):1090 (1963).
- [186] R. McNeill, R. Siudak, J. H. Wardlaw, and D. E. Weiss: *Electronic Conduction in Polymers. I. The Chemical Structure of Polypyrrole*. Australian Journal of Chemistry **16**(6):1056 (1963).
- [187] C. Chiang, C. F. Jr, and Y. Park: *Electrical conductivity in doped polyacetylene*. Physical Review Letters **39**(17):1098 (1977).
- [188] Y. Yamamoto, K. Yoshino, and Y. Inuishi: *Electrical properties of phthalocyanine-halogen complexes*. Journal of the Physical Society of Japan **47**(6):1887 (1979).
- [189] L. S. Hung, C. W. Tang, and M. G. Mason: *Enhanced electron injection in organic electroluminescence devices using an Al/LiF electrode*. Applied Physics Letters **70**(2):152 (1997), doi:10.1063/1.118344.
- [190] J. Kido, K. Nagai, and Y. Okamoto: *Bright organic electroluminescent devices with double-layer cathode*. Electron Devices, IEEE ... **40**(7):1342 (1993).
- [191] J. Endo, T. Matsumoto, and J. Kido: *Organic Electroluminescent Devices Having Metal Complexes as Cathode Interface Layer*. Japanese Journal of Applied Physics **41**(Part 2, No. 7A):L800 (2002), doi:10.1143/JJAP.41.L800.
- [192] T. Oyamada, H. Sasabe, C. Adachi, S. Murase, T. Tominaga, and C. Maeda: *Extremely low-voltage driving of organic light-emitting diodes with a Cs-doped phenyldipyrrenylphosphine oxide layer as an electron-injection layer*. Applied Physics Letters **86**(3):033503 (2005), doi:10.1063/1.1852707.
- [193] R. Meerheim, K. Walzer, M. Pfeiffer, and K. Leo: *Ultrastable and efficient red organic light emitting diodes with doped transport layers*. Applied Physics Letters **89**(6):061111 (2006), doi:10.1063/1.2268354.

- [194] G. Parthasarathy, C. Shen, a. Kahn, and S. R. Forrest: *Lithium doping of semiconducting organic charge transport materials*. Journal of Applied Physics **89**(9):4986 (2001), doi:10.1063/1.1359161.
- [195] J. Kido and T. Matsumoto: *Bright organic electroluminescent devices having a metal-doped electron-injecting layer*. Applied Physics Letters **73**(20):2866 (1998), doi:10.1063/1.122612.
- [196] B. W. D'Andrade, S. R. Forrest, and A. B. Chwang: *Operational stability of electrophosphorescent devices containing p and n doped transport layers*. Applied Physics Letters **83**(19):3858 (2003), doi:10.1063/1.1624473.
- [197] D. R. Kearns, G. Tollin, and M. Calvin: *Electrical Properties of Organic Solids. II. Effects of Added Electron Acceptor on Metal-Free Phthalocyanine*. The Journal of Chemical Physics **32**(4):1020 (1960), doi:10.1063/1.1730844.
- [198] J. J. Andre, J. Simon, R. Even, B. Boudjema, G. Guillaud, and M. Maitrot: *Molecular semiconductors and junction formation: Phthalocyanine derivatives*. Synthetic Metals **18**(1–3):683 (1987), doi:http://dx.doi.org/10.1016/0379-6779(87)90961-1.
- [199] M. Maitrot, G. Guillaud, B. Boudjema, J. J. Andre, and J. Simon: *Molecular material-based junctions: Formation of a Schottky contact with metallophthalocyanine thin films doped by the cosublimation method*. Journal of Applied Physics **60**(7):2396 (1986), doi:10.1063/1.337151.
- [200] W. Gao and A. Kahn: *Controlled p-doping of zinc phthalocyanine by coevaporation with tetrafluorotetracyanoquinodimethane: A direct and inverse photoemission study*. Applied Physics Letters **79**(24):4040 (2001), doi:10.1063/1.1424067.
- [201] D. Ray and K. L. Narasimhan: *Measurement of deep states in hole doped organic semiconductors*. Journal of Applied Physics **103**(9):093711 (2008), doi:10.1063/1.2919058.
- [202] S. Olthof, W. Tress, R. Meerheim, B. Lussem, and K. Leo: *Photoelectron spectroscopy study of systematically varied doping concentrations in an organic semiconductor layer using a molecular p-dopant*. Journal of Applied Physics **106**(10):103711 (2009), doi:10.1063/1.3259436.
- [203] W. Gao and A. Kahn: *Controlled p doping of the hole-transport molecular material N,N-diphenyl-N,N-bis(1-naphthyl)-1,1-biphenyl-4,4-diamine with tetrafluorotetracyanoquinodimethane*. Journal of Applied Physics **94**(1):359 (2003), doi:10.1063/1.1577400.
- [204] J. Drechsel, M. Pfeiffer, X. Zhou, and A. Nollau: *Organic Mip-diodes by p-doping of amorphous wide-gap semiconductors: CV and impedance spectroscopy*. Synthetic metals **127**(1-3):201 (2002).
- [205] J. Blochwitz, T. Fritz, M. Pfeiffer, and K. Leo: *Interface electronic structure of organic semiconductors with controlled doping levels*. Organic Electronics **2**:97 (2001).
- [206] B. Maennig, M. Pfeiffer, a. Nollau, X. Zhou, K. Leo, and P. Simon: *Controlled p-type doping of polycrystalline and amorphous organic layers: Self-consistent description of conductivity and field-effect mobility by a microscopic percolation model*. Physical Review B **64**(19):195208 (2001), doi:10.1103/PhysRevB.64.195208.
- [207] M. Tietze, L. Burtone, M. Riede, B. Lüssem, and K. Leo: *Fermi level shift and doping efficiency in p-doped small molecule organic semiconductors: A photoelectron spectroscopy and theoretical study*. Physical Review B **86**(3):1 (2012), doi:10.1103/PhysRevB.86.035320.

- [208] R. Meerheim, S. Olthof, M. Hermenau, S. Scholz, A. Petrich, N. Tessler, O. Solomeshch, B. Lussem, M. Riede, and K. Leo: *Investigation of C60F36 as low-volatility p-dopant in organic optoelectronic devices*. Journal of Applied Physics **109**(10):103102 (2011), doi:10.1063/1.3590142.
- [209] M. Kröger, S. Hamwi, J. Meyer, T. Riedl, W. Kowalsky, and A. Kahn: *P-type doping of organic wide band gap materials by transition metal oxides: A case-study on Molybdenum trioxide*. Organic Electronics **10**(5):932 (2009), doi:10.1016/j.orgel.2009.05.007.
- [210] S. Hamwi, J. Meyer, T. Winkler, T. Riedl, and W. Kowalsky: *P-type doping efficiency of MoO3 in organic hole transport materials*. Applied Physics Letters **94**(2009):28 (2009), doi:10.1063/1.3159824.
- [211] M. Lehnhardt, S. Hamwi, M. Hoping, J. Reinker, T. Riedl, and W. Kowalsky: *Charge carrier densities in chemically doped organic semiconductors verified by two independent techniques*. Applied Physics Letters **96**(2010):1 (2010), doi:10.1063/1.3427416.
- [212] J. Meyer, P. R. Kidambi, B. C. Bayer, C. Weijtens, A. Kuhn, A. Centeno, A. Pesquera, A. Zurutuza, J. Robertson, and S. Hofmann: *Metal oxide induced charge transfer doping and band alignment of graphene electrodes for efficient organic light emitting diodes*. Nature Scientific Reports **4**:5380 (2014), doi:10.1038/srep05380.
- [213] S. Y. Kim, W. S. Jeon, T. J. Park, R. Pode, J. Jang, and J. H. Kwon: *Low voltage efficient simple p-i-n type electrophosphorescent green organic light-emitting devices*. Applied Physics Letters **94**(2009) (2009), doi:10.1063/1.3114378.
- [214] J. H. Lee, D. S. Leem, H. J. Kim, and J. J. Kim: *Effectiveness of p-dopants in an organic hole transporting material*. Applied Physics Letters **94**(2009):1 (2009), doi:10.1063/1.3107267.
- [215] T. Glaser, S. Beck, B. Lunkenheimer, D. Donhauser, A. Köhn, M. Kröger, and A. Pucci: *Infrared study of the MoO3 doping efficiency in 4,4-bis(N-carbazolyl)-1,1-biphenyl (CBP)*. Organic Electronics **14**(2):575 (2013), doi:10.1016/j.orgel.2012.11.031.
- [216] F. Cotton, N. Gruhn, J. Gu, and P. Huang: *Closed-shell molecules that ionize more readily than cesium*. Science **298**(5600):1971 (2002).
- [217] F. Albert Cotton, P. Huang, C. A. Murillo, and X. Wang: *Synthesis and reactivity of a very strong reducing agent containing a quadruple bond: structures of W2(hpp)4 and W2(hpp)4Cl2·4CH2Cl2*. Inorganic Chemistry Communications **6**(2):121 (2003), doi:10.1016/S1387-7003(02)00701-3.
- [218] F. Cotton and J. Donahue: *Expeditious access to the most easily ionized closed-shell molecule, W2(hpp)4*. Journal of the American Chemical Society **127**(31):10808 (2005).
- [219] T. Menke, D. Ray, J. Meiss, K. Leo, and M. Riede: *In-situ conductivity and Seebeck measurements of highly efficient n-dopants in fullerene C60*. Applied Physics Letters **100**(9):093304 (2012), doi:10.1063/1.3689778.
- [220] M. L. Tietze, F. Wölzl, T. Menke, A. Fischer, M. Riede, K. Leo, and B. Lüssem: *Self-passivation of molecular n-type doping during air exposure using a highly efficient air-instable dopant*. Physica Status Solidi (a) **210**(10):2188 (2013), doi:10.1002/pssa.201330049.
- [221] a. G. Werner, F. Li, K. Harada, M. Pfeiffer, T. Fritz, and K. Leo: *Pyronin B as a donor for n-type doping of organic thin films*. Applied Physics Letters **82**(25):4495 (2003), doi:10.1063/1.1583872.

- [222] J. H. Oh, P. Wei, and Z. Bao: *Molecular n-type doping for air-stable electron transport in vacuum-processed n-channel organic transistors*. Applied Physics Letters **97**(24):243305 (2010), doi:10.1063/1.3527972.
- [223] F. Li, M. Pfeiffer, A. Werner, K. Harada, K. Leo, N. Hayashi, K. Seki, X. Liu, and X.-D. Dang: *Acridine orange base as a dopant for n doping of C<sub>60</sub> thin films*. Journal of Applied Physics **100**(2):023716 (2006), doi:10.1063/1.2219374.
- [224] T. Menke, P. Wei, D. Ray, H. Kleemann, B. D. Naab, Z. Bao, K. Leo, and M. Riede: *A comparison of two air-stable molecular n-dopants for C<sub>60</sub>*. Organic Electronics **13**(12):3319 (2012), doi:10.1016/j.orgel.2012.09.024.
- [225] P. Wei, J. H. Oh, G. Dong, and Z. Bao: *Use of a 1 H -Benzoimidazole Derivative as an n -Type Dopant and To Enable Air-Stable Solution-Processed n -Channel Organic Thin-Film Transistors*. Journal of the American Chemical Society **132**(26):8852 (2010).
- [226] P. Wei, T. Menke, B. D. Naab, K. Leo, M. Riede, and Z. Bao: *2-(2-Methoxyphenyl)-1,3-dimethyl-1 H -benzoimidazol-3-ium Iodide as a New Air-Stable n-Type Dopant for Vacuum-Processed Organic Semiconductor Thin Films*. Journal of the American Chemical Society **134**(9):3999 (2012).
- [227] M. Pfeiffer: *Controlled Doping of Organic Vacuum Deposited Dye Layers: Basics and Applications*. Ph.D. thesis, Technische Universität Dresden (2000).
- [228] A. Werner: *N-type doping of organic thin films using a novel class of dopants*. Ph.D. thesis, Technische Universität Dresden (2003).
- [229] P. Pingel, L. Zhu, K. S. Park, J.-O. Vogel, S. Janietz, E.-G. Kim, J. P. Rabe, J.-L. Bredas, and N. Koch: *Charge-Transfer Localization in Molecularly Doped Thiophene-Based Donor Polymers*. The Journal of Physical Chemistry Letters **1**(13):2037 (2010), doi:10.1021/jz100492c.
- [230] Y. Zhang, B. de Boer, and P. W. M. Blom: *Controllable Molecular Doping and Charge Transport in Solution-Processed Polymer Semiconducting Layers*. Advanced Functional Materials **19**(12):1901 (2009), doi:10.1002/adfm.200801761.
- [231] J. Cornil, S. Verlaak, N. Martinelli, a. Mityashin, Y. Olivier, T. Van Regemorter, G. D'Avino, L. Muccioli, C. Zannoni, F. Castet, D. Beljonne, and P. Heremans: *Exploring the energy landscape of the charge transport levels in organic semiconductors at the molecular scale*. Accounts of chemical research **46**(2):434 (2013), doi:10.1021/ar300198p.
- [232] E. Aziz, a. Vollmer, S. Eisebitt, W. Eberhardt, P. Pingel, D. Neher, and N. Koch: *Localized Charge Transfer in a Molecularly Doped Conducting Polymer*. Advanced Materials **19**(20):3257 (2007), doi:10.1002/adma.200700926.
- [233] L. Zhu, E.-g. Kim, Y. Yi, and J.-I. Bre: *Charge Transfer in Molecular Complexes with 2,3,5,6-Tetrafluoro-7,7,8,8-tetracyanoquinodimethane (F<sub>4</sub> -TCNQ): A Density Functional Theory Study*. Chemistry of Materials **23**(23):5149 (2011), doi:10.1021/cm201798x.
- [234] H. Méndez, G. Heimel, A. Opitz, K. Sauer, P. Barkowski, M. Oehzelt, J. Soeda, T. Okamoto, J. Takeya, J.-B. Arlin, J.-Y. Balandier, Y. Geerts, N. Koch, and I. Salzmann: *Doping of organic semiconductors: impact of dopant strength and electronic coupling*. Angewandte Chemie (International ed. in English) **52**(30):7751 (2013), doi:v.

- [235] M. Lögdlund, R. Lazzaroni, and S. Stafström: *Direct observation of charge-induced  $\pi$ -electronic structural changes in a conjugated polymer*. Physical Review Letters **63**(17):1841 (1989).
- [236] D. Steinmüller, M. Ramsey, and F. Netzer: *Polaron and bipolaronlike states in *n*-doped bithiophene*. Physical Review B **47**(20):323 (1993).
- [237] V. Coropceanu and J. Cornil: *Charge transport in organic semiconductors*. Chemical Reviews **107**:926 (2007).
- [238] E. V. Tsiper and Z. G. Soos: *Charge redistribution and polarization energy of organic molecular crystals*. Physical Review B **64**:12 (2001), doi:10.1103/PhysRevB.64.195124.
- [239] L. Li, G. Meller, and H. Kosina: *Analytical conductivity model for doped organic semiconductors*. Journal of Applied Physics **101**(3):033716 (2007), doi:10.1063/1.2472282.
- [240] T. Menke, D. Ray, H. Kleemann, M. P. Hein, K. Leo, and M. Riede: *Highly efficient *p*-dopants in amorphous hosts*. Organic Electronics **15**(2):365 (2014), doi:10.1016/j.orgel.2013.11.033.
- [241] B. a. Gregg, S.-G. Chen, and H. M. Branz: *On the superlinear increase in conductivity with dopant concentration in excitonic semiconductors*. Applied Physics Letters **84**(10):1707 (2004), doi:10.1063/1.1668326.
- [242] S. Mehraeen, V. Coropceanu, and J.-L. Brédas: *Role of band states and trap states in the electrical properties of organic semiconductors: Hopping versus mobility edge model*. Physical Review B **87**(19):195209 (2013), doi:10.1103/PhysRevB.87.195209.
- [243] H. Kleemann, B. Lussem, and K. Leo: *Controlled formation of charge depletion zones by molecular doping in organic pin-diodes and its description by the Mott-Schottky relation*. Journal of Applied Physics **111**(12):123722 (2012), doi:10.1063/1.4730771.
- [244] K. Vandewal, K. Tvingstedt, A. Gadisa, O. Inganäs, and J. V. Manca: *Relating the open-circuit voltage to interface molecular properties of donor:acceptor bulk heterojunction solar cells*. Physical Review B **81**:1 (2010), doi:10.1103/PhysRevB.81.125204.
- [245] R. Schmechel and H. von Seggern: *Electronic traps in organic transport layers*. Physica Status Solidi (a) **201**(6):1215 (2004), doi:10.1002/pssa.200404343.
- [246] L. G. Kaake, P. F. Barbara, and X.-Y. Zhu: *Intrinsic Charge Trapping in Organic and Polymeric Semiconductors: A Physical Chemistry Perspective*. The Journal of Physical Chemistry Letters **1**(3):628 (2010), doi:10.1021/jz9002857.
- [247] I. Hulea, H. Brom, a. Houtepen, D. Vanmaekelbergh, J. Kelly, and E. Meulenkaamp: *Wide Energy-Window View on the Density of States and Hole Mobility in Poly(*p*-Phenylene Vinylene)*. Physical Review Letters **93**(16):166601 (2004), doi:10.1103/PhysRevLett.93.166601.
- [248] T. Sueyoshi, H. Fukagawa, M. Ono, S. Kera, and N. Ueno: *Low-density band-gap states in pentacene thin films probed with ultrahigh-sensitivity ultraviolet photoelectron spectroscopy*. Applied Physics Letters **95**(18):183303 (2009), doi:10.1063/1.3258351.
- [249] W. L. Kalb, S. Haas, C. Krellner, T. Mathis, and B. Batlogg: *Trap density of states in small-molecule organic semiconductors: A quantitative comparison of thin-film transistors with single crystals*. Physical Review B **81**(15):1 (2010), doi:10.1103/PhysRevB.81.155315.

- [250] D. Pai, J. Yanus, and M. Stolka: *Trap-controlled hopping transport*. The Journal of Physical Chemistry **429**(1976):4714 (1984).
- [251] O. Mitrofanov, D. V. Lang, C. Kloc, J. M. Wikberg, T. Siegrist, W.-Y. So, M. a. Sergent, and A. P. Ramirez: *Oxygen-Related Band Gap State in Single Crystal Rubrene*. Physical Review Letters **97**(16):166601 (2006), doi:10.1103/PhysRevLett.97.166601.
- [252] C. Krellner, S. Haas, C. Goldmann, K. P. Pernstich, D. J. Gundlach, and B. Batlogg: *Density of bulk trap states in organic semiconductor crystals: Discrete levels induced by oxygen in rubrene*. Physical Review B **75**(24):245115 (2007), doi:10.1103/PhysRevB.75.245115.
- [253] O. Armbruster, C. Lungenschmied, and S. Bauer: *Investigation of trap states and mobility in organic semiconductor devices by dielectric spectroscopy: Oxygen-doped P3HT:PCBM solar cells*. Physical Review B **86**(23):235201 (2012), doi:10.1103/PhysRevB.86.235201.
- [254] T. Cramer, T. Steinbrecher, T. Koslowski, D. Case, F. Biscarini, and F. Zerbetto: *Water-induced polaron formation at the pentacene surface: Quantum mechanical molecular mechanics simulations*. Physical Review B **79**(15):155316 (2009), doi:10.1103/PhysRevB.79.155316.
- [255] T. Hallam, C. M. Duffy, T. Minakata, M. Ando, and H. Sirringhaus: *A scanning Kelvin probe study of charge trapping in zone-cast pentacene thin film transistors*. Nanotechnology **20**(2):025203 (2009), doi:10.1088/0957-4484/20/2/025203.
- [256] F. Bussolotti, S. Kera, K. Kudo, A. Kahn, and N. Ueno: *Gap states in Pentacene Thin Film Induced by Inert Gas Exposure*. Physical Review Letters **110**(26):267602 (2013), doi:10.1103/PhysRevLett.110.267602.
- [257] L. K. Ono, P. Schulz, J. J. Endres, G. O. Nikiforov, Y. Kato, A. Kahn, and Y. Qi: *Air-Exposure-Induced Gas-Molecule Incorporation into Spiro-MeOTAD Films*. The Journal of Physical Chemistry Letters **5**(8):1374 (2014), doi:10.1021/jz500414m.
- [258] K.-J. Lee, K. Ihm, T.-H. Kang, and S. Chung: *H<sub>2</sub>O induced structural modification of pentacene crystal*. Surface Science **603**(24):3445 (2009), doi:10.1016/j.susc.2009.10.013.
- [259] A. J. Bell and T. G. Wright: *Structures and binding energies of O<sub>2</sub>-H<sub>2</sub>O and O<sub>2</sub>-H<sub>2</sub>O*. Physical Chemistry Chemical Physics **6**(18):4385 (2004), doi:10.1039/b407310j.
- [260] J. a. G. Gomes, J. L. Gossage, H. Balu, M. Kesmez, F. Bowen, R. S. Lumpkin, and D. L. Cocke: *Experimental and theoretical study of the atmospherically important O<sub>2</sub>-H<sub>2</sub>O complex*. Spectrochimica acta. Part A, Molecular and biomolecular spectroscopy **61**(13-14):3082 (2005), doi:10.1016/j.saa.2004.10.042.
- [261] C. C. Mattheus, J. Baas, A. Meetsma, J. L. D. Boer, C. Kloc, T. Siegrist, and T. T. M. Palstra: *A 2:1 cocrystal of 6,13-dihydropentacene and pentacene*. Acta Crystallographica Section E Structure Reports Online **58**(11):o1229 (2002), doi:10.1107/S1600536802018445.
- [262] J. Northrup and M. Chabiny: *Gap states in organic semiconductors:Hydrogen- and oxygen-induced states in pentacene*. Physical Review B **68**(4):041202 (2003), doi:10.1103/PhysRevB.68.041202.
- [263] O. D. Jurchescu, J. Baas, and T. T. M. Palstra: *Effect of impurities on the mobility of single crystal pentacene*. Applied Physics Letters **84**(16):3061 (2004), doi:10.1063/1.1704874.



- [264] D. Knipp and J. E. Northrup: *Electric-Field-Induced Gap States in Pentacene*. *Advanced Materials* **21**(24):2511 (2009), doi:10.1002/adma.200802173.
- [265] I. H. Hong, K. Jie Tan, M. Toh, H. Jiang, K. Zhang, and C. Kloc: *Impurities in zone-refining anthracene crystals*. *Journal of Crystal Growth* **363**:61 (2013), doi:10.1016/j.jcrysgro.2012.10.002.
- [266] G. Giri, E. Verploegen, S. C. B. Mannsfeld, S. Atahan-Evrenk, D. H. Kim, S. Y. Lee, H. a. Becerril, A. Aspuru-Guzik, M. F. Toney, and Z. Bao: *Tuning charge transport in solution-sheared organic semiconductors using lattice strain*. *Nature* **480**(7378):504 (2011), doi:10.1038/nature10683.
- [267] A. B. Chwang and C. D. Frisbie: *Temperature and gate voltage dependent transport across a single organic semiconductor grain boundary*. *Journal of Applied Physics* **90**(3):1342 (2001), doi:10.1063/1.1376404.
- [268] A. Di Carlo, F. Piacenza, A. Bolognesi, B. Stadlober, and H. Maresch: *Influence of grain sizes on the mobility of organic thin-film transistors*. *Applied Physics Letters* **86**(26):263501 (2005), doi:10.1063/1.1954901.
- [269] T. Yokoyama, C. B. Park, K. Nagashio, K. Kita, and A. Toriumi: *Grain Size Increase and Field-Effect Mobility Enhancement of Pentacene Thin Films Prepared in a Low-Pressure H<sub>2</sub> Ambient*. *Applied Physics Express* **1**:041801 (2008), doi:10.1143/APEX.1.041801.
- [270] B. Bräuer, R. Kukreja, A. Virkar, H. B. Akkerman, A. Fognini, T. Tylliszczak, and Z. Bao: *Carrier mobility in pentacene as a function of grain size and orientation derived from scanning transmission X-ray microscopy*. *Organic Electronics* **12**(11):1936 (2011), doi:10.1016/j.orgel.2011.08.007.
- [271] M. Weis, K. Gmucová, V. Nádaždy, E. Majková, D. Haško, D. Taguchi, T. Manaka, and M. Iwamoto: *Grain Boundary Effect on Charge Transport in Pentacene Thin Films*. *Japanese Journal of Applied Physics* **50**(4):04DK03 (2011), doi:10.1143/JJAP.50.04DK03.
- [272] E. M. Muller and J. a. Marohn: *Microscopic Evidence for Spatially Inhomogeneous Charge Trapping in Pentacene*. *Advanced Materials* **17**(11):1410 (2005), doi:10.1002/adma.200401174.
- [273] K. Puntambekar, J. Dong, G. Haugstad, and C. Frisbie: *Structural and Electrostatic Complexity at a Pentacene/Insulator Interface*. *Advanced Functional Materials* **16**(7):879 (2006), doi:10.1002/adfm.200500816.
- [274] M. Tello, M. Chiesa, C. M. Duffy, and H. Sirringhaus: *Charge Trapping in Intergrain Regions of Pentacene Thin Film Transistors*. *Advanced Functional Materials* **18**(24):3907 (2008), doi:10.1002/adfm.200800009.
- [275] S. Verlaak, C. Rolin, and P. Heremans: *Microscopic description of elementary growth processes and classification of structural defects in pentacene thin films*. *The journal of physical chemistry. B* **111**(1):139 (2007), doi:10.1021/jp0653003.
- [276] C. Koerner, C. Elschner, N. C. Miller, R. Fitzner, F. Selzer, E. Reinold, P. Bäuerle, M. F. Toney, M. D. McGehee, K. Leo, and M. Riede: *Probing the effect of substrate heating during deposition of DCV4T:C60 blend layers for organic solar cells*. *Organic Electronics* **13**(4):623 (2012), doi:10.1016/j.orgel.2011.12.017.

- [277] V. Arkhipov, P. Heremans, E. Emelianova, and H. Bässler: *Effect of doping on the density-of-states distribution and carrier hopping in disordered organic semiconductors*. Physical Review B **71**(4):045214 (2005), doi:10.1103/PhysRevB.71.045214.
- [278] O. Tal, Y. Rosenwaks, Y. Preezant, N. Tessler, C. Chan, and a. Kahn: *Direct Determination of the Hole Density of States in Undoped and Doped Amorphous Organic Films with High Lateral Resolution*. Physical Review Letters **95**(25):256405 (2005), doi:10.1103/PhysRevLett.95.256405.
- [279] G. Garcia-Belmonte, E. V. Vakarin, J. Bisquert, and J. Badiali: *Doping-induced broadening of the hole density-of-states in conducting polymers*. Electrochimica Acta **55**(21):6123 (2010), doi:10.1016/j.electacta.2009.08.019.
- [280] X. Jiang, Y. Harima, K. Yamashita, and Y. Tada: *Doping-induced change of carrier mobilities in poly(3-hexylthiophene) films with different stacking structures*. Chemical Physics Letters **364**(October):616 (2002).
- [281] J. R. Macdonald and E. Barsoukov: *Impedance Spectroscopy: Theory, Experiment, and Applications, Second Edition*. John Wiley & Sons, Inc. (2005), doi:10.1002/0471716243.
- [282] W. Lai and S. M. Haile: *Impedance spectroscopy as a tool for chemical and electrochemical analysis of mixed conductors: A case study of ceria*. Journal of the American Ceramic Society **88**:2979 (2005), doi:10.1111/j.1551-2916.2005.00740.x.
- [283] J. Bisquert, G. Garcia-Belmonte, F. Fabregat-Santiago, and P. R. Bueno: *Theoretical models for ac impedance of diffusion layers exhibiting low frequency dispersion*. Journal of Electroanalytical Chemistry **475**:152 (1999).
- [284] J. Bisquert: *Theory of the impedance of electron diffusion and recombination in a thin layer*. Journal of Physical Chemistry B **106**:325 (2002), doi:10.1021/jp011941g.
- [285] V. Freger: *Diffusion impedance and equivalent circuit of a multilayer film*. Electrochemistry Communications **7**:957 (2005), doi:10.1016/j.elecom.2005.06.020.
- [286] H. Martens, H. Brom, and P. Blom: *Frequency-dependent electrical response of holes in poly(p-phenylene vinylene)*. Physical Review B **60**(12):R8489 (1999), doi:10.1103/PhysRevB.60.R8489.
- [287] S. W. Tsang, S. K. So, and J. B. Xu: *Application of admittance spectroscopy to evaluate carrier mobility in organic charge transport materials*. Journal of Applied Physics **99**(2006) (2006), doi:10.1063/1.2158494.
- [288] N. D. Nguyen, M. Schmeits, and H. P. Loeb: *Determination of charge-carrier transport in organic devices by admittance spectroscopy: Application to hole mobility in alpha-NPD*. Physical Review B **75**:1 (2007), doi:10.1103/PhysRevB.75.075307.
- [289] L. Burtone, D. Ray, K. Leo, and M. Riede: *Impedance model of trap states for characterization of organic semiconductor devices*. Journal of Applied Physics **111** (2012), doi:10.1063/1.3693545.
- [290] M. Mesta, J. Cottaar, R. Coehoorn, and P. a. Bobbert: *Study of charge-carrier relaxation in a disordered organic semiconductor by simulating impedance spectroscopy*. Applied Physics Letters **104**(21):213301 (2014), doi:10.1063/1.4880355.

- [291] J. R. Macdonald: *Analysis of Impedance and Admittance Data for Solids and Liquids*. Journal of The Electrochemical Society **124**:1022 (1977), doi:10.1149/1.2133473.
- [292] L. Burtone: *Electrical Characterization of Organic Devices and Solar Cells by Impedance Spectroscopy*. Ph.D. thesis, Technische Universität Dresden (2013).
- [293] P. Diao, D. Jiang, X. Cui, D. Gu, R. Tong, and B. Zhong: *Studies of structural disorder of self-assembled thiol monolayers on gold by cyclic voltammetry and ac impedance*. Journal of Electroanalytical Chemistry **464**:61 (1999), doi:10.1016/S0022-0728(98)00470-7.
- [294] T. Ouisse, O. Stéphan, M. Armand, and J. C. Lepretre: *Double-layer formation in organic light-emitting electrochemical cells*. Journal of Applied Physics **92**(2002):2795 (2002), doi:10.1063/1.1499201.
- [295] D. M. Taylor and H. L. Gomes: *Electrical characterization of the rectifying contact between aluminium and electrodeposited poly(3-methylthiophene)*. J. Phys. D: Appl. Phys. **28**:2554 (1995).
- [296] P. Stallinga, H. L. Gomes, H. Rost, a. B. Holmes, M. G. Harrison, and R. H. Friend: *Minority-carrier effects in poly-phenylenevinylene as studied by electrical characterization*. Journal of Applied Physics **89**(2001):1713 (2001), doi:10.1063/1.1334634.
- [297] P. Stallinga: *Two-Terminal Devices: Admittance Spectroscopy. Electrical Characterization of Organic Electronic Materials and Devices*, 65–117, John Wiley & Sons, Ltd (2009), doi:10.1002/9780470750162.ch3.
- [298] G. I. Roberts and C. R. Crowell: *Capacitance energy level spectroscopy of deep-lying semiconductor impurities using schottky barriers*. Journal of Applied Physics **41**(1970):1767 (1970), doi:10.1063/1.1659102.
- [299] I. Balberg: *Relation between distribution of states and the space-charge-region capacitance in semiconductors*. Journal of Applied Physics **58**(1985):2603 (1985), doi:10.1063/1.335890.
- [300] D. L. Losee: *Admittance spectroscopy of impurity levels in Schottky barriers*. Journal of Applied Physics **46**(1975):2204 (1975), doi:10.1063/1.321865.
- [301] J. Bisquert: *Beyond the quasistatic approximation: Impedance and capacitance of an exponential distribution of traps*. Physical Review B **77**(23):1 (2008), doi:10.1103/PhysRevB.77.235203.
- [302] J. M. Montero and J. Bisquert: *Interpretation of trap-limited mobility in space-charge limited current in organic layers with exponential density of traps*. Journal of Applied Physics **110** (2011), doi:10.1063/1.3622615.
- [303] E. Knapp and B. Ruhstaller: *Numerical impedance analysis for organic semiconductors with exponential distribution of localized states*. Applied Physics Letters **99**(2011) (2011), doi:10.1063/1.3633109.
- [304] J. Bisquert: *Analysis of the kinetics of ion intercalation: Ion trapping approach to solid-state relaxation processes*. Electrochimica Acta **47**:2435 (2002), doi:10.1016/S0013-4686(02)00102-0.
- [305] M. Schober, S. Olthof, M. Furno, B. Lüssem, and K. Leo: *Single carrier devices with electrical doped layers for the characterization of charge-carrier transport in organic thin-films*. Applied Physics Letters **97**(2010) (2010), doi:10.1063/1.3460528.
- [306] M. Schober, M. Anderson, M. Thomschke, J. Widmer, M. Furno, R. Scholz, B. Lüssem, and K. Leo: *Quantitative description of charge-carrier transport in a white organic light-emitting diode*. Physical Review B **84**(16):165326 (2011), doi:10.1103/PhysRevB.84.165326.

- [307] M. Schober: *Charge Transport in Organic Light-Emitting Diodes*. Ph.D. thesis, Technische Universität Dresden (2012).
- [308] N. Von Malm, R. Schmechel, and H. Von Seggern: *Distribution of occupied states in doped organic hole transport materials*. Synth Met **126**(1):87 (2002), doi:10.1016/S0379-6779(01)00549-5.
- [309] C. Renaud and T.-P. Nguyen: *Study of trap states in polypyrrolofluorene based devices: Influence of aging by electrical stress*. Journal of Applied Physics **106**(5):053707 (2009), doi:10.1063/1.3195086.
- [310] R. Haering and E. Adams: *Theory and application of thermally stimulated currents in photoconductors*. Physical Review **117**(2):451 (1960).
- [311] a. Kadashchuk, R. Schmechel, H. Von Seggern, U. Scherf, and a. Vakhnin: *Charge-carrier trapping in polyfluorene-type conjugated polymers*. Journal of Applied Physics **98**(2005) (2005), doi:10.1063/1.1953870.
- [312] J. Schafferhans: *Investigation of defect states in organic semiconductors: Towards long term stable materials for organic photovoltaics*. Ph.D. thesis, Universität Würzburg (2011).
- [313] a. G. Werner, J. Blochwitz, M. Pfeiffer, and K. Leo: *Field dependence of thermally stimulated currents in Alq<sub>3</sub>*. Journal of Applied Physics **90**(1):123 (2001), doi:10.1063/1.1378813.
- [314] W. Weise, T. Keith, N. Von Malm, and H. Von Seggern: *Trap concentration dependence of thermally stimulated currents in small molecule organic materials*. Physical Review B - Condensed Matter and Materials Physics **72**:1 (2005), doi:10.1103/PhysRevB.72.045202.
- [315] C. Renaud, C. H. Huang, M. Zemmouri, P. L. Rendu, and T. P. Nguyen: *PHYSICAL JOURNAL Study of traps in polydiacetylene based devices using TSC*. Analysis **218**:215 (2007), doi:10.1051/epjap.
- [316] P. Yu, A. Migan-Dubois, J. Alvarez, A. Darga, V. Vissac, D. Mencaraglia, Y. Zhou, and M. Krueger: *Study of traps in P3HT:PCBM based organic solar cells using fractional thermally stimulated current (FTSC) technique*. Journal of Non-Crystalline Solids **358**(17):2537 (2012), doi:10.1016/j.jnoncrysol.2012.01.021.
- [317] G. F. J. Garlick and a. F. Gibson: *The electron trap mechanism of luminescence in sulphide and silicate phosphors*. Proceedings of the Physical Society **61**:101 (1948), doi:10.1088/0959-5309/61/1/317.
- [318] a. C. Lewandowski and S. W. S. McKeever: *Generalized description of thermally stimulated processes without the quasiequilibrium approximation*. Physical Review B **43**(10):8163 (1991), doi:10.1103/PhysRevB.43.8163.
- [319] R. Chen: *Generalization of a method for calculating activation energies of glow curves*. Chemical Physics Letters **11**(3):371 (1971), doi:10.1016/0009-2614(71)80511-0.
- [320] R. Chen: *On the calculation of activation energies and frequency factors from glow curves*. Journal of Applied Physics **40**(1969):570 (1969), doi:10.1063/1.1657437.
- [321] R. Chen: *On the kinetics of thermally stimulated conductivity*. Chemical Physics Letters **6**(3):125 (1970).
- [322] R. Chen: *Thermally stimulated current curves with non-constant recombination lifetime*. Journal of Physics D: Applied Physics **2**:371 (2002), doi:10.1088/0022-3727/2/3/309.

- 
- [323] T. Cowell and J. Woods: *The evaluation of thermally stimulated current curves*. British Journal of Applied Physics **18** (1967).
- [324] M. Meier, S. Karg, K. Zuleeg, W. Brutting, and M. Schwoerer: *Determination of trapping parameters in poly(p-phenylenevinylene) light-emitting devices using thermally stimulated currents*. Journal of Applied Physics **84**(1998):87 (1998), doi:10.1063/1.368004.
- [325] N. Gasanly, A. Aydinli, and Ö. Salihoglu: *Thermally stimulated current observation of trapping centers in undoped GaSe layered single crystals*. Crystal Research and ... 295–301 (2001).
- [326] W. Hoogenstraaten: *Electron traps in zinc-sulphide phosphors*. Philips research reports, Research laboratory of N. V. philips (1958).
- [327] R. H. Bube: *Photoconductivity of solids*. Wiley (1960).
- [328] T. Matsushima, M. Yahiro, and C. Adachi: *Estimation of electron traps in carbon-60 field-effect transistors by a thermally stimulated current technique*. Applied Physics Letters **91**(2007):2005 (2007), doi:10.1063/1.2779240.
- [329] K. Kawano and C. H. Adachi: *Evaluating carrier accumulation in degraded bulk heterojunction organic solar cells by a Thermally stimulated current technique*. Advanced Functional Materials **19**:3934 (2009), doi:10.1002/adfm.200901573.
- [330] Z. Fang, L. Shan, T. Schlesinger, and A. Milnes: *Study of defects in LEC-grown undoped SI-GaAs by thermally stimulated current spectroscopy*. Materials Science and Engineering: B **5**(3):397 (1990), doi:10.1016/0921-5107(90)90104-J.
- [331] N. Ueno: *Angle-resolved UPS of ultrathin films of functional organic molecules with synchrotron radiation: Determination of molecular orientation by quantitative analysis of photoelectron angular distribution*. Journal of Electron Spectroscopy and Related Phenomena **78**(0):345 (1996), doi:10.1016/S0368-2048(96)80095-8.
- [332] S. Hüfner: *Photoelectron spectroscopy : principles and applications*. Springer, Berlin; London, 3rd edn. (2011).
- [333] M. Seah and W. Dench: *Quantitative electron spectroscopy of surfaces: a standard data base for electron inelastic mean free paths in solids*. Surface and interface analysis **1**(1):2 (1979).
- [334] W. Salaneck: *Intermolecular relaxation energies in anthracene*. Physical Review Letters **40**(1) (1978).
- [335] E. Tsiper, Z. Soos, W. Gao, and A. Kahn: *Electronic polarization at surfaces and thin films of organic molecular crystals: PTCDA*. Chemical physics letters **360**(July):47 (2002).
- [336] M. Casu, Y. Zou, S. Kera, D. Batchelor, T. Schmidt, and E. Umbach: *Investigation of polarization effects in organic thin films by surface core-level shifts*. Physical Review B **76**(19):193311 (2007), doi:10.1103/PhysRevB.76.193311.
- [337] Specs GmbH: *Phoibos Hemispherical Energy Analyser Series - Manual*. Berlin (2007).
- [338] K. Schmidt: *Grundlagen molekularer Dotierung von organischen Halbleitern*. Ph.D. thesis, Technische Universität Dresden (2014).

- [339] L. Gross, Z. L. Wang, D. Ugarte, F. Mohn, N. Moll, W. a. Heer, P. Vincent, P. Liljeroth, C. Journet, G. Meyer, V. T. Binh, M. Poot, H. S. J. V. D. Zant, a. Aguasca, a. Bachtold, K. Kim, a. Zettl, P. Hung, H. W. C. Postma, M. Bockrath, X. Blase, and S. Roche: *only appears when looking at the I*. Science **325**(August):1110 (2009), doi:10.1126/science.1176210.
- [340] W. Han, H. Yoshida, N. Ueno, and S. Kera: *Electron affinity of pentacene thin film studied by radiation-damage free inverse photoemission spectroscopy*. Applied Physics Letters **103** (2013), doi:10.1063/1.4821445.
- [341] B. Lüssem, M. L. Tietze, H. Kleemann, C. Hoßbach, J. W. Bartha, A. Zakhidov, and K. Leo: *Doped organic transistors operating in the inversion and depletion regime*. Nature communications **4**:2775 (2013), doi:10.1038/ncomms3775.
- [342] B. Ehrler, M. W. B. Wilson, A. Rao, R. H. Friend, and N. C. Greenham: *Singlet exciton fission-sensitized infrared quantum dot solar cells*. Nano Letters **12**:1053 (2012), doi:10.1021/nl204297u.
- [343] D. N. Congreve, J. Lee, N. J. Thompson, E. Hontz, S. R. Yost, P. D. Reuswig, M. E. Bahlke, S. Reineke, T. Voorhis, and M. a. Baldo: *External Quantum Efficiency Above 100% in a Singlet-Exciton-Fission Based Organic Photovoltaic Cell*. Science **340**:334 (2013), doi:10.1126/science.1232994.
- [344] A. Maliakal, K. Raghavachari, H. Katz, E. Chandross, and T. Siegrist: *Photochemical Stability of Pentacene and a Substituted Pentacene in Solution and in Thin Films*. Chemistry of Materials **16**(13):4980 (2004), doi:10.1021/cm049060k.
- [345] A. R. Murphy and J. M. J. Fréchet: *Organic semiconducting oligomers for use in thin film transistors*. Chemical Reviews **107**(510):1066 (2007), doi:10.1021/cr0501386.
- [346] T. W. Kelley, D. V. Muyres, P. F. Baude, T. P. Smith, and T. D. Jones: *High Performance Organic Thin Film Transistors*. MRS Online Proceedings Library **771**:null (2003).
- [347] F. J. Meyer zu Heringdorf, M. Reuter, and R. Tromp: *Growth dynamics of pentacene thin films*. Nature **412**(August):517 (2001), doi:10.1038/35087532.
- [348] H. Kleemann: *Organic Electronic Devices - Fundamentals, Applications, and Novel Concepts*. Ph.D. thesis, Technische Universität Dresden (2012).
- [349] J. O. Rostalski and D. Meissner: *Monochromatic versus solar efficiencies of organic solar cells*. Solar Energy Materials and Solar Cells **61**:87 (2000), doi:10.1016/S0927-0248(99)00099-9.
- [350] J. Drechsel: *MIP-type organic solar cells incorporating phthalocyanine/fullerene mixed layers and doped wide-gap transport layers*. Organic Electronics **5**(4):175 (2004), doi:10.1016/j.orgel.2003.11.005.
- [351] S. Pfuetzner, J. Meiss, A. Petrich, M. Riede, and K. Leo: *Thick C60:ZnPc bulk heterojunction solar cells with improved performance by film deposition on heated substrates*. Applied Physics Letters **94**(2009):28 (2009), doi:10.1063/1.3154554.
- [352] W. Tress, S. Pfuetzner, K. Leo, and M. Riede: *Open circuit voltage and IV curve shape of ZnPc:C60 solar cells with varied mixing ratio and hole transport layer*. Journal of Photonics for Energy **1**:011114 (2011), doi:10.1117/1.3556726.
- [353] C. Schünemann, C. Elschner, a. a. Levin, M. Levichkova, K. Leo, and M. Riede: *Zinc phthalocyanine - Influence of substrate temperature, film thickness, and kind of substrate on the morphology*. Thin Solid Films **519**:3939 (2011), doi:10.1016/j.tsf.2011.01.356.

- [354] W. Gao and A. Kahn: *Controlled p-doping of zinc phthalocyanine by coevaporation with tetrafluorotetracyanoquinodimethane: A direct and inverse photoemission study*. Applied Physics Letters **79**(2001):4040 (2001), doi:10.1063/1.1424067.
- [355] C. Murawski, C. Fuchs, S. Hofmann, K. Leo, and M. C. Gather: *Alternative p-doped hole transport material for low operating voltage and high efficiency organic light-emitting diodes*. Applied Physics Letters **105**(11):113303 (2014), doi:10.1063/1.4896127.
- [356] T. Schwab: *Top-Emitting OLEDs - Improvement of the Light Extraction Efficiency and Optimization of Microcavity Effects for White Emission*. Ph.D. thesis, Technische Universität Dresden (2014).
- [357] M. Thomschke: *Inverted Organic Light Emitting Diodes - Optical and Electrical Device Improvement*. Ph.D. thesis, Technische Universität Dresden (2012).
- [358] T. P. I. Saragi, T. Spehr, A. Siebert, T. Fuhrmann-Lieker, and J. Salbeck: *Spiro Compounds for Organic Optoelectronics*. Chem. Rev. **107**(4):1011 (2007).
- [359] T. P. I. Saragi, T. Fuhrmann-Lieker, and J. Salbeck: *Comparison of charge-carrier transport in thin films of spiro-linked compounds and their corresponding parent compounds*. Advanced Functional Materials **16**:966 (2006), doi:10.1002/adfm.200500361.
- [360] M. Fröbel, A. Perumal, T. Schwab, C. Fuchs, K. Leo, and M. M. C. M. C. Gather: *White light emission from alternating current organic light-emitting devices using high frequency color-mixing*. Physica Status Solidi (a) **210**(11):2439 (2013), doi:10.1002/pssa.201330097.
- [361] T. Schwab, C. Fuchs, R. Scholz, A. Zakhidov, K. Leo, and M. C. Gather: *Coherent mode coupling in highly efficient top-emitting OLEDs on periodically corrugated substrates*. Optics express **22**(7):7524 (2014), doi:10.1364/OE.22.007524.
- [362] M. L. Tietze, W. Tress, S. Pfützner, C. Schünemann, L. Burtone, M. Riede, K. Leo, K. Vandewal, S. Olthof, P. Schulz, and A. Kahn: *Correlation of open-circuit voltage and energy levels in zinc-phthalocyanine: C<sub>60</sub> bulk heterojunction solar cells with varied mixing ratio*. Physical Review B **88**(8):085119 (2013), doi:10.1103/PhysRevB.88.085119.
- [363] T. Menke: *Molecular Doping of Organic Semiconductors: A Conductivity and Seebeck Study*. Ph.D. thesis, Technische Universität Dresden (2013).
- [364] M. Thelakkat, R. Fink, F. Haubner, and H.-W. Schmidt: *Synthesis and properties of novel hole transport materials for electroluminescent devices*. Macromolecular Symposia **125**:157 (1998), doi:10.1002/masy.19981250114.
- [365] C. H. Cheung, K. K. Tsung, K. C. Kwok, and S. K. So: *Using thin film transistors to quantify carrier transport properties of amorphous organic semiconductors*. Applied Physics Letters **93**(2008):2006 (2008), doi:10.1063/1.2972125.
- [366] W. Y. Gao and a. Kahn: *Electrical doping: the impact on interfaces of pi-conjugated molecular films*. Journal of Physics: Condensed Matter **15**:S2757 (2003), doi:10.1088/0953-8984/15/38/014.
- [367] G. Schwartz, M. Pfeiffer, S. Reineke, K. Walzer, and K. Leo: *Harvesting triplet excitons from fluorescent blue emitters in white organic light-emitting diodes*. Advanced Materials **19**:3672 (2007), doi:10.1002/adma.200700641.

- [368] Y. Shirota, Y. Kuwabara, H. Inada, T. Wakimoto, H. Nakada, Y. Yonemoto, S. Kawami, and K. Imai: *Multilayered organic electroluminescent device using a novel starburst molecule, 4,4',4'-tris(3-methylphenylphenylamino)triphenylamine, as a hole transport material*. Applied Physics Letters **65**(2011):807 (1994), doi:10.1063/1.112238.
- [369] X. Zhou, M. Pfeiffer, J. Blochwitz, a. Werner, a. Nollau, T. Fritz, and K. Leo: *Very-low-operating-voltage organic light-emitting diodes using a p-doped amorphous hole injection layer*. Applied Physics Letters **78**(4):410 (2001), doi:10.1063/1.1343849.
- [370] M. Aonuma, T. Oyamada, H. Sasabe, T. Miki, and C. Adachi: *Material design of hole transport materials capable of thick-film formation in organic light emitting diodes*. Applied Physics Letters **90**:48 (2007), doi:10.1063/1.2733627.
- [371] P. K. Koech, A. B. Padmaperuma, L. Wang, J. S. Swensen, E. Polikarpov, J. T. Darsell, J. E. Rainbolt, and D. J. Gaspar: *Synthesis and Application of 1,3,4,5,7,8-Hexafluorotetracyanonaphthoquinodimethane (F6-TNAP): A Conductivity Dopant for Organic Light-Emitting Devices*. Chemistry of Materials **22**(c):3926 (2010), doi:10.1021/cm1002737.
- [372] J. Meiss, A. Merten, M. Hein, C. Schuenemann, S. Schäfer, M. Tietze, C. Uhrich, M. Pfeiffer, K. Leo, and M. Riede: *Fluorinated zinc phthalocyanine as donor for efficient vacuum-deposited organic solar cells*. Advanced Functional Materials **22**:405 (2012), doi:10.1002/adfm.201101799.
- [373] A. Fischer, R. Scholz, K. Leo, and B. Lüssem: *An all C60 vertical transistor for high frequency and high current density applications*. Applied Physics Letters **101**(2012):20 (2012), doi:10.1063/1.4767391.
- [374] H. Kleemann, A. a. Günther, K. Leo, and B. Lüssem: *High-performance vertical organic transistors*. Small **9**(21):3670 (2013), doi:10.1002/sml.201202321.
- [375] K. Itaka, M. Yamashiro, J. Yamaguchi, M. Haemori, S. Yaginuma, Y. Matsumoto, M. Kondo, and H. Koinuma: *High-mobility C60 field-effect transistors fabricated on molecular-wetting controlled substrates*. Advanced Materials **18**:1713 (2006), doi:10.1002/adma.200502752.
- [376] A. Fischer, P. Pahner, B. Lüssem, K. Leo, R. Scholz, T. Koprucki, J. Fuhrmann, K. Gärtner, and A. Glitzky: *Self-heating effects in organic semiconductor crossbar structures with small active area*. Organic Electronics **13**(11):2461 (2012), doi:10.1016/j.orgel.2012.06.046.
- [377] A. Fischer, P. Pahner, B. Lüssem, K. Leo, R. Scholz, T. Koprucki, K. Gärtner, and A. Glitzky: *Self-heating, bistability, and thermal switching in organic semiconductors*. Physical Review Letters **110**(March):1 (2013), doi:10.1103/PhysRevLett.110.126601.
- [378] C. Elschner, A. a. Levin, L. Wilde, J. Grenzer, C. Schroer, K. Leo, and M. Riede: *Determining the C60 molecular arrangement in thin films by means of X-ray diffraction*. Journal of Applied Crystallography **44**:983 (2011), doi:10.1107/S002188981103531X.
- [379] C. Falkenberg: *Optimizing Organic Solar Cells - Transparent Electron Transport Materials for Improving the Device Performance*. Ph.D. thesis, Technische Universität Dresden (2011).
- [380] K. Schulze, C. Uhrich, R. Schüppel, K. Leo, M. Pfeiffer, E. Brier, E. Reinold, and P. Bäuerle: *Efficient vacuum-deposited organic solar cells based on a new low-bandgap oligothiophene and fullerene C60*. Advanced Materials **18**:2872 (2006), doi:10.1002/adma.200600658.



- [381] S. Duhm, G. Heimel, I. Salzmann, H. Glowatzki, R. L. Johnson, A. Vollmer, J. P. Rabe, and N. Koch: *Orientation-dependent ionization energies and interface dipoles in ordered molecular assemblies*. Nature materials **7**(4):326 (2008), doi:10.1038/nmat2119.
- [382] C. Schünemann, D. Wynands, K. J. Eichhorn, M. Stamm, K. Leo, and M. Riede: *Evaluation and control of the orientation of small molecules for strongly absorbing organic thin films*. Journal of Physical Chemistry C **117**(22):11600 (2013), doi:10.1021/jp400604j.
- [383] C. Poelking, M. Tietze, C. Elschner, S. Olthof, D. Hertel, B. Baumeier, F. Würthner, K. Meerholz, K. Leo, and D. Andrienko: *Impact of mesoscale order on open-circuit voltage in organic solar cells*. Nature Materials **14**(4):434 (2014), doi:10.1038/nmat4167.
- [384] V. Rühle, A. Lukyanov, F. May, M. Schrader, T. Vehoff, J. Kirkpatrick, B. Baumeier, and D. Andrienko: *Microscopic simulations of charge transport in disordered organic semiconductors*. Journal of Chemical Theory and Computation **7**(10):3335 (2011), doi:10.1021/ct200388s.
- [385] M. Schrader, R. Fitzner, M. Hein, C. Elschner, B. Baumeier, K. Leo, M. Riede, P. Bäuerle, and D. Andrienko: *Comparative study of microscopic charge dynamics in crystalline acceptor-substituted oligothiophenes*. Journal of the American Chemical Society **134**(13):6052 (2012), doi:10.1021/ja300851q.
- [386] I. Yavuz, B. N. Martin, J. Park, and K. N. Houk: *Theoretical Study of the Molecular Ordering, Paracrystallinity, And Charge Mobilities of Oligomers in Different Crystalline Phases*. Journal of the American Chemical Society **137**(8):2856 (2015), doi:10.1021/ja5076376.
- [387] N. R. Tummala, Z. Zheng, S. G. Aziz, V. Coropceanu, and J.-L. Brédas: *Static and Dynamic Energetic Disorders in the C<sub>60</sub>, PC<sub>61</sub>BM, C<sub>70</sub>, and PC<sub>71</sub>BM Fullerenes*. The Journal of Physical Chemistry Letters **6**(2015), doi:10.1021/acs.jpclett.5b01709.
- [388] P. Friederich, V. Meded, F. Symalla, M. Elstner, and W. Wenzel: *QM/QM Approach to Model Energy Disorder in Amorphous Organic Semiconductors*. Journal of Chemical Theory and Computation **11**(2):560 (2015), doi:10.1021/ct501023n.
- [389] B. Thole: *Molecular polarizabilities calculated with a modified dipole interaction*. Chemical Physics **59**(3):341 (1981), doi:10.1016/0301-0104(81)85176-2.
- [390] S. Yogev, E. Halpern, R. Matsubara, M. Nakamura, and Y. Rosenwaks: *Direct measurement of density of states in pentacene thin film transistors*. Physical Review B - Condensed Matter and Materials Physics **84**(16):1 (2011), doi:10.1103/PhysRevB.84.165124.
- [391] D. V. Lang, X. Chi, T. Siegrist, a. M. Sergent, and a. P. Ramirez: *Amorphouslike density of gap states in single-crystal pentacene*. Physical Review Letters **93**(8):8 (2004), doi:10.1103/PhysRevLett.93.086802.
- [392] D. Poplavskyy and J. Nelson: *Nondispersive hole transport in amorphous films of methoxy-spirofluorene-arylamine organic compound*. Journal of Applied Physics **93**(1):341 (2003), doi:10.1063/1.1525866.
- [393] V. Arkhipov, E. Emelianova, G. Adriaenssens, and H. Bässler: *Equilibrium carrier mobility in disordered organic semiconductors*. Journal of Non-Crystalline Solids **299-302**:1047 (2002), doi:10.1016/S0022-3093(01)01071-7.
- [394] V. Arkhipov, E. Emelianova, and G. Adriaenssens: *Effect of backward carrier jumps on variable-range hopping in disordered materials*. Physical Review B **65**(16):1 (2002), doi:10.1103/PhysRevB.65.165110.

- [395] A. Abate, D. R. Staff, D. J. Hollman, H. J. Snaith, and A. B. Walker: *Influence of ionizing dopants on charge transport in organic semiconductors*. *Physical Chemistry Chemical Physics* **16**(3):1132 (2014), doi:10.1039/c3cp53834f.
- [396] V. R. Nikitenko and M. N. Strikhanov: *Transport level in disordered organics: An analytic model and Monte-Carlo simulations*. *Journal of Applied Physics* **115**(7):073704 (2014), doi:10.1063/1.4866326.
- [397] D. Nabok, P. Puschnig, C. Ambrosch-Draxl, O. Werzer, R. Resel, and D. M. Smilgies: *Crystal and electronic structures of pentacene thin films from grazing-incidence x-ray diffraction and first-principles calculations*. *Physical Review B - Condensed Matter and Materials Physics* **76**(23):1 (2007), doi:10.1103/PhysRevB.76.235322.
- [398] H. Morisaki, T. Koretsune, C. Hotta, J. Takeya, T. Kimura, and Y. Wakabayashi: *Large surface relaxation in the organic semiconductor tetracene*. *Nature Communications* **5**:5400 (2014), doi:10.1038/ncomms6400.
- [399] J. Fischer, J. Widmer, H. Kleemann, W. Tress, C. Koerner, M. Riede, and K. Leo: *A charge carrier transport model for donor-acceptor blend layers*. *Journal of Applied Physics* **117**(045501) (2015), doi:10.1063/1.4906561.
- [400] F. Bussolotti, J. Yang, A. Hinderhofer, Y. Huang, W. Chen, S. Kera, A. T. S. Wee, and N. Ueno: *Origin of the energy level alignment at organic/organic interfaces: The role of structural defects*. *Physical Review B - Condensed Matter and Materials Physics* **89**(11):1 (2014), doi:10.1103/PhysRevB.89.115319.
- [401] K. Schmidt: *Grundlagen molekularer Dotierung von organischen Halbleitern*. Ph.D. thesis, Technische Universität Dresden (2014).
- [402] W. L. Kalb, K. Mattenberger, and B. Batlogg: *Oxygen-related traps in pentacene thin films: Energetic position and implications for transistor performance*. *Physical Review B - Condensed Matter and Materials Physics* **78**(3):1 (2008), doi:10.1103/PhysRevB.78.035334.
- [403] M. Kuik, L. Koster, G. Wetzelaer, and P. Blom: *Trap-Assisted Recombination in Disordered Organic Semiconductors*. *Physical Review Letters* **107**(25):1 (2011), doi:10.1103/PhysRevLett.107.256805.
- [404] T. Walter, R. Herberholz, C. Müller, and H. W. Schock: *Determination of defect distributions from admittance measurements and application to Cu(In,Ga)Se<sub>2</sub> based heterojunctions*. *Journal of Applied Physics* **80**(October):4411 (1996), doi:10.1063/1.363401.
- [405] R. Gresser, M. Hummert, H. Hartmann, K. Leo, and M. Riede: *Synthesis and characterization of near-infrared absorbing benzannulated aza-BODIPY dyes*. *Chemistry - A European Journal* **17**(10):2939 (2011), doi:10.1002/chem.201002941.
- [406] S. Kraner, J. Widmer, J. Benduhn, E. Hieckmann, T. Jägeler-Hoheisel, S. Ullbrich, D. Schütze, K. Sebastian Radke, G. Cuniberti, F. Ortman, M. Lorenz-Rothe, R. Meerheim, D. Spoltore, K. Vandewal, C. Koerner, and K. Leo: *Influence of side groups on the performance of infrared absorbing aza-BODIPY organic solar cells*. *Physica Status Solidi (a)* **7**:n/a (2015), doi:10.1002/pssa.201532385.
- [407] a. Kadashchuk, D. Weiss, P. Borsenberger, S. Nešpůrek, N. Ostapenko, and V. Zaika: *The origin of thermally stimulated luminescence in neat and molecularly doped charge transport polymer systems*. *Chemical Physics* **247**:307 (1999), doi:10.1016/S0301-0104(99)00169-X.

- [408] M. Bouhassoune, S. V. Mensfoort, P. Bobbert, and R. Coehoorn: *Carrier-density and field-dependent charge-carrier mobility in organic semiconductors with correlated Gaussian disorder*. Organic Electronics **10**(3):437 (2009), doi:10.1016/j.orgel.2009.01.005.
- [409] V. I. Arkhipov: *Thermally stimulated currents in amorphous semiconductors*. Journal of non-crystalline solids **181**:274 (1995).
- [410] V. R. Nikitenko, a. Kadashchuk, R. Schmechel, H. Von Seggern, and Y. Korosko: *Effect of dispersive transport and partial trap filling on thermally stimulated current in conjugated polymers*. Journal of Applied Physics **98**:1 (2005), doi:10.1063/1.2132092.
- [411] I. Glowacki and J. Ulanski: *Simultaneous measurements of thermoluminescence and thermally stimulated currents in poly(N-vinylcarbazole)/polycarbonate blends*. Journal of Applied Physics **78**(2):1019 (1995), doi:10.1063/1.360403.
- [412] L. Lu, W. Chen, T. Xu, and L. Yu: *High-performance ternary blend polymer solar cells involving both energy transfer and hole relay processes*. Nature communications **6**:7327 (2015), doi:10.1038/ncomms8327.
- [413] T. Moench, P. Friederich, F. Holzmueller, B. Rutkowski, J. Benduhn, T. Strunk, C. Koerner, K. Vandewal, A. Czyrska-Filemonowicz, W. Wenzel, and K. Leo: *Influence of Meso and Nanoscale Structure on the Properties of Highly Efficient Small Molecule Solar Cells*. Advanced Energy Materials **1**(1):1 (2015), doi:10.1002/aenm.201501280.
- [414] H. Méndez, G. Heimel, S. Winkler, J. Frisch, A. Opitz, K. Sauer, B. Wegner, M. Oehzelt, C. Röthel, S. Duhm, D. Többsens, N. Koch, and I. Salzmann: *Charge-transfer crystallites as molecular electrical dopants*. Nature Communications **6**:8560 (2015), doi:10.1038/ncomms9560.
- [415] S. Pfützner: *Studies on Organic Solar Cells Composed of Fullerenes and Zinc-Phthalocyanines*. Ph.D. thesis, Technische Universität Dresden (2011).
- [416] K. Harada, a. Werner, M. Pfeiffer, C. Bloom, C. Elliott, and K. Leo: *Organic Homojunction Diodes with a High Built-in Potential: Interpretation of the Current-Voltage Characteristics by a Generalized Einstein Relation*. Physical Review Letters **94**(3):1 (2005), doi:10.1103/PhysRevLett.94.036601.
- [417] P. Mantri, S. Rizvi, and B. Mazhari: *Estimation of built-in voltage from steady-state current-voltage characteristics of organic diodes*. Organic Electronics **14**(8):2034 (2013), doi:10.1016/j.orgel.2013.04.030.
- [418] M. Mladenovic: *Charge Carrier Localization and Transport in Organic Semiconductors : Insights from Atomistic Multiscale Simulations*. Advanced Functional Materials **25**(13):1915 (2015), doi:10.1002/adfm.201402435.
- [419] A. Y. B. Meneau, Y. Olivier, T. Backlund, M. James, D. W. Breiby, J. W. Andreasen, and H. Sirringhaus: *Temperature Dependence of Charge Localization in High-Mobility , Solution-Crystallized Small Molecule Semiconductors Studied by Charge Modulation Spectroscopy*. Advanced Functional Materials **1–8** (2015), doi:10.1002/adfm.201502502.
- [420] S. Khelifi, K. Decock, J. Lauwaert, H. Vrielinck, D. Spoltore, F. Piersimoni, J. Manca, A. Belghachi, and M. Burgelman: *Investigation of defects by admittance spectroscopy measurements in poly (3-hexylthiophene):(6,6)-phenyl C61-butyric acid methyl ester organic solar cells degraded under air exposure*. Journal of Applied Physics **110**(9) (2011), doi:10.1063/1.3658023.

- [421] M. Brendel, S. Krause, A. Steindamm, A. K. Topczak, S. Sundarraj, P. Erk, S. Höhla, N. Fruehauf, N. Koch, and J. Pflaum: *The Effect of Gradual Fluorination on the Properties of F<sub>n</sub>ZnPc Thin Films and F<sub>n</sub>ZnPc/C60 Bilayer Photovoltaic Cells*. Advanced Functional Materials n/a–n/a (2015), doi:10.1002/adfm.201404434.
- [422] J. Widmer, J. Fischer, W. Tress, K. Leo, and M. Riede: *Electric potential mapping by thickness variation: A new method for model-free mobility determination in organic semiconductor thin films*. Organic Electronics **14**(12):3460 (2013), doi:10.1016/j.orgel.2013.09.021.
- [423] G. Juska, K. Arlauskas, M. Viliunas, and J. Kocka: *Extraction current transients: new method of study of charge transport in microcrystalline silicon*. Physical review letters **84**(21):4946 (2000), doi:10.1103/PhysRevLett.84.4946.
- [424] G. Juška, K. Genevičius, R. Österbacka, K. Arlauskas, T. Kreouzis, D. Bradley, and H. Stubb: *Initial transport of photogenerated charge carriers in \$\$-conjugated polymers*. Physical Review B **67**(8):081201 (2003), doi:10.1103/PhysRevB.67.081201.
- [425] A. Kokil, K. Yang, and J. Kumar: *Techniques for characterization of charge carrier mobility in organic semiconductors*. Journal of Polymer Science, Part B: Polymer Physics **50**(15):1130 (2012), doi:10.1002/polb.23103.
- [426] B. Ecker, J. C. Nolasco, J. Pallarés, L. F. Marsal, J. Posdorfer, J. Parisi, and E. von Hauff: *Degradation Effects Related to the Hole Transport Layer in Organic Solar Cells*. Advanced Functional Materials **21**(14):2705 (2011), doi:10.1002/adfm.201100429.
- [427] M. Hermenau, M. Riede, K. Leo, S. A. Gevorgyan, F. C. Krebs, and K. Norrman: *Water and oxygen induced degradation of small molecule organic solar cells*. Solar Energy Materials and Solar Cells **95**(5):1268 (2011), doi:10.1016/j.solmat.2011.01.001.
- [428] M. Hermenau, S. Schubert, H. Klumbies, J. Fahlteich, L. Müller-Meskamp, K. Leo, and M. Riede: *The effect of barrier performance on the lifetime of small-molecule organic solar cells*. Solar Energy Materials and Solar Cells **97**:102 (2012), doi:10.1016/j.solmat.2011.09.026.
- [429] S. Schubert, H. Klumbies, L. Müller-Meskamp, and K. Leo: *Electrical calcium test for moisture barrier evaluation for organic devices*. Review of Scientific Instruments **82**(May 2013):1 (2011), doi:10.1063/1.3633956.
- [430] M. Hermenau: *Lebensdaueruntersuchungen an organischen Solarzellen*. Ph.D. thesis, Technische Universität Dresden (2012).
- [431] G. Dennler, C. Lungenschmied, H. Neugebauer, N. S. Sariciftci, M. Latrèche, G. Czeremuszkin, and M. R. Wertheimer: *A new encapsulation solution for flexible organic solar cells*. Thin Solid Films **511-512**(February 2016):349 (2006), doi:10.1016/j.tsf.2005.12.091.
- [432] H. B. Yang, Q. L. Song, C. Gong, and C. M. Li: *The degradation of indium tin oxide/pentacene/fullerene/tris-8-hydroxy-quinolino aluminum/aluminum heterojunction organic solar cells: By oxygen or moisture?* Solar Energy Materials and Solar Cells **94**(5):846 (2010), doi:10.1016/j.solmat.2010.01.006.
- [433] S. Ogawa, T. Naijo, Y. Kimura, H. Ishii, and M. Niwano: *Photoinduced doping effect of pentacene field effect transistor in oxygen atmosphere studied by displacement current measurement*. Applied Physics Letters **86**(25):1 (2005), doi:10.1063/1.1949281.

- 
- [434] C. K. Lu and H. F. Meng: *Hole doping by molecular oxygen in organic semiconductors: Band-structure calculations*. Physical Review B - Condensed Matter and Materials Physics **75**(23):2 (2007), doi:10.1103/PhysRevB.75.235206.
- [435] W. L. Kalb, F. Meier, K. Mattenberger, and B. Batlogg: *Defect healing at room temperature in pentacene thin films and improved transistor performance*. Physical Review B - Condensed Matter and Materials Physics **76**(18):1 (2007), doi:10.1103/PhysRevB.76.184112.
- [436] A. Twarowski: *Oxygen doping of zinc phthalocyanine thin films*. The Journal of Chemical Physics **77**(11):5840 (1982), doi:10.1063/1.443744.
- [437] T. D. Anthopoulos and T. S. Shafai: *Oxygen induced p-doping of ??-nickel phthalocyanine vacuum sublimed films: Implication for its use in organic photovoltaics*. Applied Physics Letters **82**(10):1628 (2003), doi:10.1063/1.1559649.
- [438] M. Jørgensen, K. Norrman, and F. C. Krebs: *Stability/degradation of polymer solar cells*. Solar Energy Materials and Solar Cells **92**(7):686 (2008), doi:10.1016/j.solmat.2008.01.005.



---

# Acknowledgments/Danksagung

Das Schönste immer zum Schluss. Obwohl ich diese Regel viel zu oft gern über den Haufen geworfen hätte und besonders in den letzten Monaten nichts mehr herbeigesehnt habe, als das Ende des Aufschreibens, ist dies hier zu tippen jetzt doch eine umso größere Freude. Ich möchte mich bei allen Menschen ganz herzlich bedanken, die mich auf dem langen Weg zur Fertigstellung dieser Doktorarbeit begleitet und unterstützt haben. Dafür vorab ein großes Danke!

- Mein besonderer Dank gilt Herrn Prof. Dr. Karl Leo, der mir die Möglichkeit gegeben hat, unter seiner wissenschaftlichen Leitung und Betreuung am Institut für Angewandte Photophysik zu promovieren und diese Doktorarbeit anzufertigen. Sein IAPP habe ich als Ort des Miteinanders erlebt, nicht nur zu Wandertagen und legendären Weihnachtsfeiern, sondern auch tagtäglich im Forschungsalltag. Im Speziellen danke ich Ihnen für das mir entgegengebrachte Vertrauen, dieses herausfordernde Thema bearbeiten zu dürfen, auch wenn es etwas länger gedauert hat, sowie Ihr großartiges Engagement um dieser Arbeit den letzten Schliff zu geben.
- Ein weiteres großes Dankeschön geht an Herrn Prof. Dr.-Ing. Björn Lüssem für die Übernahme des Zweitgutachtens dieser Arbeit, seine wissenschaftliche Neugier zum Thema Traps, seine wertvollen Anregungen und seine Motivationsgabe. Danke auch, dass Du als Gruppenleiter die OLED und die NewDevices Gruppe so gut zusammengehalten hast.
- I would like to give a shout-out and a huge thank you to Prof. Dr. Koen Vandewal. He showed great interest in my studies and proof-read large parts of my drafts, some over night, which allowed me to correct my stupidest errors already the next day.
- Dr. Max L. Tietze: Dir möchte ich besonders danken. Seit dem wir in einer Mittagspause zur Erkenntnis kamen, wie viele interessante Experimente man mit einem Drehshutter anstellen kann, hast Du mich mit Deinem Wissensdurst angesteckt. Egal ob beim UPSen und Probenbauen-im-Akkord im UFO, der Interpretation von 'random results' oder unterwegs nach Laborschluss, ich bin froh, Dich zu meinen Freunden zählen zu können. Und beim Lesen Deiner Diss lerne ich heute noch immer was.
- Techniker verschwinden leider oft irgendwo am Ende einer Danksagung in einer Aufzählung. Sven Kunze sei an dieser Stelle gedankt, da er oft die Feuerwehr ist, die den Brand löschen muss, den wir alle in den Laboren angesteckt haben. Seit dem ersten geplatzten Kühlschlauch zu Diplomzeiten hat er mir immer wieder aus der experimentellen Patsche geholfen. Ohne Dich wäre das TSC Setup dauerzickig und es im Büro und außerhalb nur halb so lustig!
- Martin Schwarze, Dir danke ich für die vielen UPS-Messungen, die Sisyphusarbeit des Spektren-Bereinigungs, Deine wissenschaftliche Diskussionsfreudigkeit und einen extrem guten Musikgeschmack.
- Den fleißigen Lesker-TechnikerInnen Tobias Günther, Andreas Wendel und Caroline Walde danke ich für die vielen exakt gebauten Proben, ohne die die TSC-Studien und damit ein guter Teil dieser Arbeit überhaupt nicht machbar gewesen wären! Danke auch Annette Petrich an der Materialsublimation.
- Dr. Janine Fischer danke ich besonders für die zahlreichen wissenschaftlichen Diskussionen, das geduldige Beantworten meiner Fragen zu allerlei Simulationskram, fürs Zuhören, Kuchen und Skifahren.

- Eine Arbeit mit Tippfehlern, falschen Beschriftungen und Argumentationsketten, die nur im wirren Autorenkopf Sinn machen, ohne fleißige Korrekturleser: Großes Danke an Max, Koen, Björn, Martin, Natalia, Daniel und Prof. Leo.
- Meinem ehemaligen Gruppenleiter Daniel Kasemann danke ich besonders fürs Rückenfreihalten und Geld-Freischaukeln zu Beginn der Schreibphase.
- Dr. Christian Körner danke ich sehr für die Einweisung in die Mysterien der Tieftemperaturphysik und die Bedienung des bitterkalten Kryostaten!
- Herrn Strauß und Herrn Posselt von der Heliumanlage der TU Dresden bin ich sehr dankbar für immer frischen kalten Stoff, manchen Plausch und ihre Flexibilität, wenn Freitag kurz vor Feierabend noch eine LHe-Kanne ausgetauscht werden musste.
- Daniel Dietrich sei gedankt für die Umbauten am Kryostaten und Andreas Büst für seine Hilfe bei der Gas-Degradationszelle.
- Dr. Lorenzo Burtone möchte ich danken für die Bereitstellung des ursprünglichen Simulationscodes zur Bestimmung von Traps aus Kapazitätsspektren und seine Hilfe bei der Einarbeitung in die Impedanzspektroskopie.
- Obwohl ich sie nie persönlich treffen konnte, danke ich Dr. Julia Rauh (geb. Schafferhans), deren Dissertation mir sehr beim Aufbau der Messapparatur und dem Verständnis von thermisch stimulierten Strömen geholfen hat.
- Im Weiteren danke ich Natalia Sergeeva für ihre kritischen Nachfragen, die mich immer wieder herausgefordert haben, meine Ergebnisse zu überdenken.
- Dr. Axel Fischer möchte ich für die produktive Zusammenarbeit zum self-heating in organischen Halbleitern und den entstanden Veröffentlichungen danken.
- Dr. Lauren Polander danke ich für den Einblick in die Welt der Perovskite und die erfrischende Zusammenarbeit.
- Dr. Jan Blochwitz-Nimoth und Dr. Tobias Canzler danke ich für die gute wissenschaftliche Zusammenarbeit bei der Dotantenstudie und die Möglichkeit, bei der Novald AG praxisnahe Erfahrungen zu sammeln.
- Für die stets rasche und unkomplizierte Hilfe bei IT- und Bürokratieproblemen danke ich herzlich Peter Leumer, Kai Schmidt, Dr. Angelika Wolf, Dr. Annette Polte, Dr. Christian Zschalig, Julia Barth und Johanna Katzschner.
- Tobi, Max, Janine, Lars und Koen möchte ich danken für einen echt genialen Ausflug zur MRS 2014 nach San Francisco! Das war unvergesslich! #sonnenbrillecool #professoryolo #testosterontietze
- Grüße und ein dickes Danke gehen raus an *Kunze & Partner*, die Crew von BEY 127a: Sven, Max, Christoph, Andreas und Bernhard. Danke für die schöne Bürozeit mit wissenschaftlichen und unterhalt-samen Diskussionen zwischen Klimmzugstange und Balkonien. Danke auch an Team Bierstube, für manch schönen Montag und einen tollen Bandauftritt 2013.
- Dominic Scharfe danke ich sehr für seine Unterstützung bei Programmierproblemchen, Gegenlesen des Simulationscodes und snu snu time.



- Was wären die letzten Jahre ohne die Gang? Obwohl wir uns langsam in alle Welt verstreuen und es auch für mich Zeit wird, hier den Laden zuzumachen, bin ich froh über unsere gemeinsame Zeit: Tubs, Sylv, Schmiddl, Markus, Marcman, Franzl, Nadja, Claudl und Vera - egal ob Physikerabend, Mensamädchen, Bergtour, Campuslauf oder Sushikoma. Um die Eingangsfrage zu beantworten: stinklangweilig oder gar nicht passiert. Weitermachen!
- Robert Schneider danke ich für manchen Flash, viele Tops und dafür, dass er mich während der gefühlt unendlich langen Schreibphase nicht komplett degenerieren lassen hat. Danke Freund!
- Meiner Familie, ganz besonders meinen Eltern und meiner Schwester, danke ich für ihre Hilfe und Unterstützung, nicht nur während meiner Studiums- und Promotionszeit, sondern in meinem ganzen bisherigen Leben. Ohne euch wäre das hier nicht möglich und ich aufgeschmissen.
- Von ganzem Herzen möchte ich Dir, Liane, danken, dass Du mich trotz aller meiner Zweifel ermutigt hast, diese Promotionsarbeit durchzuziehen. Danke, dass Du mich speziell während des letzten Jahres ausgehalten, aufgebaut und liebevoll unterstützt hast. Vielen Dank für Dein Verständnis, wenn ich nach durchgemessenen Nächten frühmorgens nochmal ins Institut musste, um die Heliumkanne zuzudrehen und aus 'ich-schreib-noch-fix-den-Satz-zuende' eine ganze Stunde wurde.

Ich denke, die einem Promovierenden am meisten gestellte Frage ist: "Und wann denkst Du, bist Du fertig?" Dies passiert ganz natürlich, schließlich wollen die Familie, der Partner, die Freunde, Kollegen und Betreuer ja Anteil nehmen und wissen, wie es um den Doktoranden steht, ob er vorankommt und wann wieder mit ihm zu rechnen ist. Insbesondere bei meinen Freunden und meiner Familie möchte ich mich entschuldigen, wenn sie von mir in den letzten Monaten hören mussten: "Tut mir Leid, keine Zeit." Umso mehr freue ich mich auf das Kommende und die Zeit mit Euch, nun wo ich die Frage beantworten kann: "Jetzt."

Die Freiheit, dahin aufzubrechen, wohin ich will.

Reinhold Messner



---

# Erklärung

Diese Dissertation wurde am Institut für Angewandte Photophysik der Fakultät Mathematik und Naturwissenschaften an der Technischen Universität Dresden unter wissenschaftlicher Betreuung von Prof. Dr. Karl Leo angefertigt.

Hiermit versichere ich, dass ich die vorliegende Arbeit ohne unzulässige Hilfe Dritter und ohne Benutzung anderer als der angegebenen Hilfsmittel angefertigt habe. Die aus fremden Quellen direkt oder indirekt übernommenen Gedanken sind als solche kenntlich gemacht. Die Arbeit wurde bisher weder im Inland noch im Ausland in gleicher oder ähnlicher Form einer anderen Prüfungsbehörde vorgelegt. Weiterhin versichere ich, dass keine früheren Promotionsverfahren stattgefunden haben. Ich erkenne die Promotionsordnung der Fakultät Mathematik und Naturwissenschaften an der Technischen Universität Dresden vom 23.02.2011 an.

---

Datum, Unterschrift